

UNCLASSIFIED

AD NUMBER	
AD387747	
CLASSIFICATION CHANGES	
TO:	unclassified
FROM:	confidential
LIMITATION CHANGES	
TO:	Approved for public release, distribution unlimited
FROM:	Distribution authorized to U.S. Gov't. agencies and their contractors; Critical Technology; AUG 1967. Other requests shall be referred to Air Force Rocket Propulsion Lab., Attn: AAFRPL/RPPR-STINFO, Edwards AFB, CA 93523.
AUTHORITY	
31 Aug 1979, DoDD 5200.10, per document marking; AFRPL ltr dtd 17 Jan 1986	

THIS PAGE IS UNCLASSIFIED

AD 387 747

AUTHORITY:

AFRPL

1trs 17 JAN 86



THIS REPORT HAS BEEN DELIMITED  
AND CLEARED FOR PUBLIC RELEASE  
UNDER DOD DIRECTIVE 5200.20 AND  
NO RESTRICTIONS ARE IMPOSED UPON  
ITS USE AND DISCLOSURE.

DISTRIBUTION STATEMENT A

APPROVED FOR PUBLIC RELEASE,  
DISTRIBUTION UNLIMITED.

# **SECURITY**

---

# **MARKING**

**The classified or limited status of this report applies to each page, unless otherwise marked.**

**Separate page printouts MUST be marked accordingly.**

---

**THIS DOCUMENT CONTAINS INFORMATION AFFECTING THE NATIONAL DEFENSE OF THE UNITED STATES WITHIN THE MEANING OF THE ESPIONAGE LAWS, TITLE 18, U.S.C., SECTIONS 793 AND 794. THE TRANSMISSION OR THE REVELATION OF ITS CONTENTS IN ANY MANNER TO AN UNAUTHORIZED PERSON IS PROHIBITED BY LAW.**

**NOTICE: When government or other drawings, specifications or other data are used for any purpose other than in connection with a definitely related government procurement operation, the U. S. Government thereby incurs no responsibility, nor any obligation whatsoever; and the fact that the Government may have formulated, furnished, or in any way supplied the said drawings, specifications, or other data is not to be regarded by implication or otherwise as in any manner licensing the holder or any other person or corporation, or conveying any rights or permission to manufacture, use or sell any patented invention that may in any way be related thereto.**



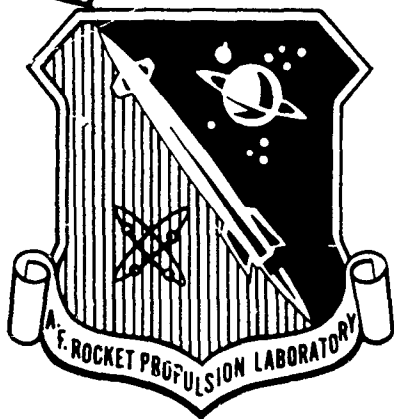
**CONFIDENTIAL**

AFRPL-TR-67-223 Vol II

**PROCEEDINGS OF THE  
AIR FORCE ROCKET PROPULSION LABORATORY  
TWO-PHASE FLOW CONFERENCE**

**15-16 MARCH 1967**

**NORTON AIR FORCE BASE  
SAN BERNARDINO, CALIFORNIA**



Technical Report AFRPL-TR-67-223, Vol. II

August 1967

LAWRENCE J. DELANEY  
AEROSPACE CORPORATION  
CONFERENCE GENERAL CHAIRMAN

RICHARD F. HOGLUND  
PURDUE UNIVERSITY  
CONFERENCE TECHNICAL COORDINATOR

1/LT PALMER W. SMITH  
AIR FORCE ROCKET PROPULSION LABORATORY  
CONFERENCE PROJECT OFFICER

IN ADDITION TO SECURITY REQUIREMENTS WHICH MUST BE MET, THIS DOCUMENT IS SUBJECT TO SPECIAL EXPORT CONTROLS AND EACH TRANSMITTAL TO FOREIGN GOVERNMENTS OR FOREIGN NATIONALS MAY BE MADE ONLY WITH PRIOR APPROVAL OF AFRPL (RPPR-STINFO) EDWARDS, CALIFORNIA 93523

**AIR FORCE ROCKET PROPULSION LABORATORY  
AIR FORCE SYSTEMS COMMAND  
UNITED STATES AIR FORCE  
EDWARDS, CALIFORNIA**

DOWNGRADED AT 3 YEAR INTERVALS;  
DECLASSIFIED AFTER 12 YEARS.  
DOD DIR 5200.10

**CONFIDENTIAL**

THIS DOCUMENT CONTAINS INFORMATION AFFECTING THE NATIONAL DEFENSE OF THE UNITED STATES WITHIN THE MEANING OF THE ESPIONAGE LAWS, TITLE 18, U.S.C., SECTION 793 AND 794, THE TRANSMISSION OF WHICH IN ANY MANNER TO AN UNAUTHORIZED PERSON IS PROHIBITED BY LAW.

## NOTICES

When U.S. Government drawings, specifications, or other data are used for any purpose other than a definitely related Government procurement operation, the Government thereby incurs no responsibility nor any obligation whatsoever, and the fact that the Government may have formulated, furnished, or in any way supplied the said drawings, specifications, or other data, is not to be regarded by implication or otherwise, or in any manner licensing the holder or any other person or corporation, or conveying any rights or permission to manufacture, use, or sell any patented invention that may in any way be related thereto.

**CONFIDENTIAL**

AFRPL-TR-67-223, Vol. II

(U) PROCEEDINGS OF THE  
AIR FORCE ROCKET PROPULSION LABORATORY  
TWO-PHASE FLOW CONFERENCE

Lawrence J. Delaney  
Aerospace Corporation  
Conference General Chairman

Richard F. Hoglund  
Purdue University  
Conference Technical Coordinator

1/Lt. Palmer W. Smith  
Air Force Rocket Propulsion Laboratory  
Conference Project Officer

In addition to security requirements which must be met, this document is subject to special export controls and each transmittal to foreign governments or foreign nationals may be made only with prior approval of AFRPL (RPPR-STINO), Edwards, California 93523.

DOWNGRADED AT 3 YEAR INTERVALS;  
DECLASSIFIED AFTER 12 YEARS.  
DOD DIR 5200.10

**CONFIDENTIAL**

This page is unclassified.

This document contains information affecting the national defense of the United States within the meaning of the Espionage Laws Title 18, U.S.C. Section 793 and 794 the transmission of which in any manner to an unauthorized person is prohibited by law

# UNCLASSIFIED

## TABLE OF CONTENTS

### PROCEEDINGS OF THE TWO-PHASE FLOW CONFERENCE

#### VOLUME II

	<u>Page</u>
SESSION III - PERFORMANCE LOSSES IN TWO-PHASE FLOW NOZZLES	
Session Chairman: Professor Frank E. Marble California Institute of Technology	
The Role of Approximate Analytical Results in the Study of Two- Phase Flow in Nozzles; F.E. Marble, California Institute of Technology . . . . .	407
Off-the-Cuff Remarks, Including Questions, Answers and Comments . . . . .	427
Nonequilibrium Phenomena of Two-Phase Flows; J.R. Kliegel, Dynamic Science . . . . .	435
Questions, Answers and Comments . . . . .	444
Gas-Particle Flow in Convergent Nozzles at High Loading Ratios; George Rudinger, Cornell Aeronautical Laboratory, Inc. . . . .	445
Questions, Answers and Comments . . . . .	458
Part I: Turbulent Mixing of Gas-Particle and Pure Gas Streams; D. Tirumalesa and R.S. Channapragada, CETEC Corporation . . . . .	461
Part II: Ignition and Combustion of a Boron Particle under Air- Augmentation Conditions; A. Gopalakrishnan, R. Anderson, and C.L. Miller, CETEC Corporation . .	493
Questions, Answers and Comments . . . . .	513
SESSION IV - TWO-PHASE PLUME PHENOMENA	
Session Chairman: Professor W.C. Kuby University of California Santa Barbara	
Two-Phase Flow Effects in Solid Propellant Rocket Plumes; W.C. Kuby, University of California . . . . .	519

UNCLASSIFIED

# UNCLASSIFIED

## Table of Contents (Cont'd)

	<u>Page</u>
Radiation from Particle-Laden Plumes; D. Carlson and A. Laderman, Philco-Ford Corporation . . . . .	551
Questions, Answers and Comments . . . . .	579
Experimental Measurements of Solid Propellant Rocket Exhaust Effects at High Altitudes	
Part I: Radiance and Impingement Characteristics of Saturn Auxiliary Solid Rocket Plumes; K.C. Hendershot, Cornell Aeronautical Laboratory, Inc. . . . .	585
Part II: Impingement Pressures, Forces, and Heat Transfer Rates in High Altitude Metalized Solid Propellant Rocket Exhaust Plumes; Leo Rute, AVCO/MSD . . .	611
Questions, Answers and Comments . . . . .	645
Shock Tube Studies of Hypervelocity Impact Phenomena; W.J. Hooker, A.L. Morsell, and R. Watson, Heliodyne Corporation . . . . .	647
Questions, Answers and Comments . . . . .	674
Open Forum - Chairman: Professor R.F. Hoglund, Purdue University	
Effects of Impingement of Rocket Exhaust Gases and Solid Particles on a Spacecraft; C.H. Lewis, Philco- Ford Corporation . . . . .	677
A Laser-Doppler Technique for the Measurement of Particle Velocity in Gas-Particle Two-Phase Flow; R.M. James, W.R. Babcock, and H.S. Seifert, Stanford University	691
Questions, Answers and Comments . . . . .	710
The Measurement of Gas and Particle Temperature in Rocket Motor Chambers and Exhaust Plumes; J.M. Adams, Aerojet-General Corporation . . . . .	713
Underexpanded Gas-Particle Jets; P.O. Jarvinen, Mithras Inc. . . . .	761

# UNCLASSIFIED

## Table of Contents (Cont'd)

	<u>Page</u>
Particle Drag Coefficient in Gas-Particle Flows; G. Rudinger, Cornell Aeronautical Laboratory, Inc. . .	769
Shock Tube Determination of Drag Coefficients of Small Spherical Particles; B.P. Selberg, Aerospace Corporation . . . . .	781
Questions, Answers and Comments . . . . .	806
Comments on Two-Phase Flow in the Rocket Chamber; Captain H. W. Gale, Air Force Institute of Technology	809
Methods for Predicting Particle Behavior in Two-Phase Flow; R.J. Zeamer, Hercules, Inc. . . . .	821
An Experimental Study of the Drag Coefficient of Burning Aluminum Droplets; R.L. Marshall, C.L. Pellett, and A.R. Saunders, NASA Langley Research Center	843

## DISTRIBUTION

FORM 1473

SESSION III

PERFORMANCE LOSSES IN TWO-PHASE FLOW NOZZLES

Session Chairman: Professor Frank E. Marble  
California Institute of  
Technology

**UNCLASSIFIED**

THE ROLE OF APPROXIMATE ANALYTICAL RESULTS  
IN THE STUDY OF TWO-PHASE FLOW IN NOZZLES

by

Frank E. Marble

Von Karman Laboratory of Fluid Mechanics  
and Jet Propulsion  
California Institute of Technology

**UNCLASSIFIED**



UNCLASSIFIED

THE ROLE OF APPROXIMATE ANALYTICAL RESULTS  
IN THE STUDY OF TWO-PHASE FLOW IN NOZZLES

Frank E. Marble

Von Kármán Laboratory of Fluid Mechanics  
and Jet Propulsion  
California Institute of Technology

Abstract

The small slip approximation to the theory of two-phase flow in rocket nozzles is reviewed to show that the inaccuracies associated with drag and heat transfer laws, and those associated with the fundamental approximation, are independent and that the former may be removed algebraically. Selected applications of the approximate theory are discussed to indicate that these stress the nature of the dependence of the results upon the relevant physical parameters and the possible consequence of scaling laws, rather than numerical accuracy too often limited by inaccurate initial data.

It is suggested that approximate analytical results may offer much more assistance to the rocket engineer than has yet been used to advantage.

UNCLASSIFIED

# UNCLASSIFIED

## Introduction

The performance losses caused in rocket nozzles by the presence of small solid particles in the exhaust, and other details of this two-phase flow, may be calculated with acceptable accuracy provided that accurate information on particle size, solid and gas properties, and the laws of particle and gas interaction are known. Numerical calculations may be tedious and time consuming and, even more important, sufficiently complex that any deep understanding of the physical processes is lost together with the capability to estimate the effects changes in material properties, nozzle shape, etc.

The approximate method that offers the best combination of simplicity, physical insight, and accuracy of results is the linearized analysis introduced by Rannie [1] and by Marble [2] and now in rather wide use for conventional nozzles of reasonable size. To be sure, the technique has limitations. In particular, the accuracy deteriorates when applied to very small nozzles or to regions of extreme acceleration.

The range of accurate applicability is very wide, however, and wider than appears to be realized at the present time. It is often erroneously supposed that approximations in the drag and heat transfer laws are related to the linearizations. This need not be the case if the problem is properly formulated.

It is the purpose of this paper to review the foundations of the linearized theory of one-dimensional, two-phase flow in nozzles and to re-examine some of the success this analysis has had in securing accurate results for and physical insight into some rather complex problems. Finally, the limitations of the linearized analysis will be investigated to clarify its range of applicability and some means of extending its range of usefulness will be discussed.

## The Linearized Theory of One-Dimensional Two-Phase Flow

For the usual mass fractions of solids in rocket exhaust and in view of the fact that the density of the solid is of the order  $10^3$  times that of the gas, the volume occupied by the solids may be neglected in the continuum equations for the gas. Then the equations of continuity, momentum, and the first law of thermodynamics may be written

$$\rho u A = \dot{m} \quad (1)$$

$$\rho u \frac{du}{dx} + \frac{dp}{dx} = F_p \quad (2)$$

$$\rho u c_p \frac{dT}{dx} - u \frac{dp}{dx} = (u_p - u)F_p + Q_p \quad (3)$$

where  $F_p$  is the effective force per unit volume exerted by the particles upon gas,  $Q_p$  is the heat transferred per unit volume from the particles to the gas, and  $(u_p - u)F_p$  is the dissipative work associated with the motion of particles relative to the gas.

# UNCLASSIFIED

The corresponding set of equations may be written for the solid phase, considering it as a sort of continuum and where  $\rho_p$  represents the mass of solid phase per unit volume rather than the density of material constituting the solid particles

$$\rho_p u_p A = \dot{m} \quad (4)$$

$$\rho_p u_p \frac{du_p}{dx} = -F_p \quad (5)$$

$$\rho_p u_p c \frac{dT_p}{dx} = -Q_p \quad (6)$$

where  $\kappa$  is the constant ratio of solid mass to gas mass flowing through any cross section of the nozzle.

Because of the approximations that we intend to employ, it is convenient to introduce the particle slip velocity

$$u_s = u - u_p \quad (7)$$

having the physical significance of the amount that the particle velocity lags behind the gas velocity in the accelerating flow. Similarly, the temperature and density of the particle cloud are replaced by

$$T_s = T - T_p \quad (8)$$

$$\rho_s = \kappa \rho - \rho_p \quad (9)$$

If the particle cloud were at all times in dynamic and thermal equilibrium with the gas, these three quantities defined in equations (7), (8), and (9) would vanish identically; they are measures of the deviation of the two-phase flow from a state of equilibrium.

The departure from equilibrium between the phases is governed by the exchange of momentum and heat, quantities that are given by  $F_p$  and  $Q_p$ . It has proven convenient to formulate these as

$$F_p = \frac{\rho_p a^2}{\lambda_v} \cdot \frac{u_s}{a} \cdot \alpha\left(\frac{u_s}{a}, k\right) \quad (10)$$

$$Q_p = \frac{\rho_p a c T_s}{\lambda_T} \cdot \beta\left(\frac{u_s}{a}, k\right) \quad (11)$$

The characteristic lengths  $\lambda_v$  and  $\lambda_T$  [2] are distances a particle would cover at the speed of sound while reducing initial velocity and temperature differences respectively to  $e^{-1}$  of their original values. When the spherical particles obey Stokes law and have a Nusselt number of unity, the functions  $\alpha$  and  $\beta$  are unity. For the flow regimes ordinarily encountered in nozzles,  $\alpha$  and  $\beta$  are still of order unity [1], but when the slip Mach number  $u_s/a$  or the Knudsen number  $k$  are very large, the values of  $\alpha$  and  $\beta$  may be seriously altered.

UNCLASSIFIED

# UNCLASSIFIED

It is convenient to construct a new set of equations [3] from (1) - (6), utilizing these new variables, the first three of which

$$\rho u A = m \quad (12)$$

$$\bar{c}_p (T - T_c) + \frac{1}{2} u^2 = \frac{\kappa}{1+\kappa} \{ c T_s + u u_s - \frac{1}{2} u_s^2 \} \quad (13)$$

$$\left( \frac{T}{T_c} \right) \left( \frac{p_c}{p} \right)^{\frac{\bar{\gamma}-1}{\bar{\gamma}}} = \exp \left\{ \frac{\kappa}{1+\kappa} \int_0^x \frac{1}{\bar{c}_p T} \left[ c \frac{dT_s}{dx} + u_s \frac{d}{dx} (u - u_s) \right] dx \right\} \quad (14)$$

resemble those that arise in conventional nozzle theory, the remaining three of which

$$\rho_s u + \kappa \rho u_s = \rho_s u_s \quad (15)$$

$$\left( 1 - \frac{\rho_s}{\kappa \rho} \right) \frac{a^2}{\lambda_v} \cdot \frac{u_s}{a} \cdot \alpha \left( \frac{u_s}{a}, k \right) + u \frac{du}{dx} = u \frac{du_s}{dx} \quad (16)$$

$$\left( 1 - \frac{\rho_s}{\kappa \rho} \right) \frac{a}{\lambda_T} \left( \frac{c_p}{c} \right) T_s \cdot \beta \left( \frac{u_s}{a}, k \right) + u \frac{dT}{dx} = u \frac{dT_s}{dx} \quad (17)$$

emphasize the slip quantities and involve the drag and heat transfer laws explicitly. The quantities  $\bar{c}_p$ ,  $\bar{\gamma}$ , reference 2, are the effective specific heat and isentropic exponent for the gas-particle mixture when the gas and solid are in complete dynamic and thermal equilibrium. When this state of equilibrium does hold, the slip quantities vanish identically, equations (15) (17) are redundant, and the right hand sides of equations (13) and (14) become 0 and 1, respectively. The nozzle flow described by these simplified forms of equations (12) - (14) is identified to that for conventional nozzle flow but with the gas properties modified by the mass and thermal capacity of the condensed phase. The nozzle performance under these conditions of equilibrium represents the maximum that can be obtained for the two-phase flow under fixed chamber and discharge conditions.

Under conditions which are appropriate to most rocket motors, the actual performance of the nozzle with suspended solids is rather close to the ideal because the slip quantities are not large. To be somewhat more precise about it, if the nozzle length  $L$  is the significant length for acceleration, then the distance  $x$  should be measured in terms of  $L$ ; accordingly, introduce the dimensionless distance along the nozzle as  $\xi \equiv x/L$ . Equation (15), for example, then may be written

$$\left( 1 - \frac{\rho_s}{\kappa \rho} \right) \frac{u_s}{a} \alpha \left( \frac{u_s}{a}, k \right) + \frac{\lambda_v}{L} \frac{u}{2} \frac{du}{d\xi} = \frac{\lambda_v}{L} \frac{u}{2} \frac{du_s}{d\xi} \quad (18)$$

where for nozzles of reasonable length and for particles of micron size, the ratio  $\lambda_v/L$  is small. But since  $(u/a^2)(du/d\xi)$  is of order unity, it follows that  $u_s/a$  is small. Physically, this means that the acceleration experienced by the particle in passing through the nozzle may be approximated by

# UNCLASSIFIED

the accelerations which would occur if the solid and gas were in complete equilibrium, the particle slipping at just such a velocity that the resulting drag balances this approximate inertial reaction.

From an analytical viewpoint, this approximation corresponds to an asymptotic expansion [2, 3] of the solution for small  $\lambda_v/L$  and is a singular one in that the highest derivatives of the slip quantities are suppressed in the process. Because use is almost never made of more than the first approximation, we shall not discuss the formal expansions here but simply note some properties of the equilibrium and first approximations to slip quantities, and the first order correction to the gas quantities.

As was first noted by Rannie [1] and subsequently employed to advantage by the present author [2, 3], it is most convenient to utilize as independent variable a thermodynamic quantity that varies monotonically along the nozzle axis. The gas pressure is such a quantity. This change in independent variable avoids difficulty with the perturbation quantities near the nozzle throat, which naturally occur when the distance  $x$  is used, and still permit flow field calculations for nozzles of fixed geometry.

The equilibrium solution is readily written down in terms of the pressure along the nozzle, where a superscript zero is employed to denote the equilibrium approximations

$$\frac{\rho^{(0)}}{\rho_c} = \left(\frac{p}{p_c}\right)^{1/\bar{\gamma}} \quad (19)$$

$$\frac{T^{(0)}}{T_c} = \left(\frac{p}{p_c}\right)^{\frac{\bar{\gamma}-1}{\bar{\gamma}}} \quad (20)$$

$$(u^{(0)})^2 = 2\bar{c}_p T_c \left\{ 1 - \left(\frac{p}{p_c}\right)^{\frac{\bar{\gamma}-1}{\bar{\gamma}}} \right\} \quad (21)$$

Similarly, the equilibrium relationship between nozzle area and pressure is

$$\frac{\rho_c a_c A^{(0)}}{\dot{m}^{(0)}} = \left(\frac{p}{p_c}\right)^{\frac{1}{\bar{\gamma}}} \left[ \frac{2}{\bar{\gamma}-1} \left\{ 1 - \left(\frac{p}{p_c}\right)^{\frac{\bar{\gamma}-1}{\bar{\gamma}}} \right\} \right]^{-\frac{1}{2}} \quad (22)$$

which, since the area is prescribed along the nozzle axis, corresponds to the equilibrium approximation to pressure along the axis. Note that, if the nozzle shape is prescribed, the mass flow is not known, the equilibrium approximation to the mass flow being denoted  $\dot{m}^{(0)}$  in equation (22).

Without reviewing the specific details, the first approximation to the slip quantities, denoted by a superscript unity, may be obtained quite simply. For the moment, let us assume that the functions

$$\alpha\left(\frac{u_s}{a}, k\right) \quad \text{and} \quad \beta\left(\frac{u_s}{a}, k\right)$$

UNCLASSIFIED

# UNCLASSIFIED

are unity; then the particle drag and heat transfer are given respectively by Stokes law and by a Pusselt number of unity. Then the approximate slip quantities are

$$u_s^{(1)} = -a^{(0)} \frac{\lambda_v}{L} \cdot \frac{1}{\bar{\gamma}} \frac{1}{p} \frac{dp}{d\xi} \quad (23)$$

$$T_s^{(1)} = T^{(0)} \frac{\lambda_T}{L} \cdot \frac{\bar{\gamma}-1}{\bar{\gamma}} \cdot \frac{c}{c_p} M^0 \frac{1}{p} \frac{dp}{d\xi} \quad (24)$$

$$\rho_s^{(1)} = \kappa \rho^{(0)} \frac{\lambda_v}{L} \cdot \frac{1}{\bar{\gamma}} \frac{1}{p} \frac{dp}{d\xi} \quad (25)$$

that is, they are given algebraically in terms of quantities that are either prescribed or are obtained from the conventional equilibrium solutions.

The first corrections to the solutions for the gas flow are less obvious since they involve approximations to the integral on the right hand side of equation (14). Explicitly, the correction to the gas temperature or the gas density is

$$\frac{T^{(1)}}{T^{(0)}} = \frac{\lambda_v}{L} \frac{\bar{\gamma}-1}{\bar{\gamma}} \frac{\kappa}{1+\kappa} \left\{ \eta M^0 \frac{1}{p} \frac{dp}{d\xi} + \frac{1}{\bar{\gamma}} \int_{p_c}^p \frac{1+(\bar{\gamma}-1)\eta M^0}{M^0} \frac{1}{p^2} \frac{dp}{d\xi} dp \right\} = -\frac{\rho^{(1)}}{\rho^{(0)}} \quad (26)$$

and the correction to the velocity is

$$\frac{u^{(1)}}{u^{(0)}} = \frac{-1}{(\bar{\gamma}-1)} M^0 \frac{\lambda_v}{L} \frac{\kappa}{1+\kappa} \left\{ \left( \frac{\bar{\gamma}-1}{\bar{\gamma}} \right) M^0 \frac{1}{p} \frac{dp}{d\xi} + \frac{\bar{\gamma}-1}{\bar{\gamma}^2} \int_{p_c}^p \frac{1+(\bar{\gamma}-1)\eta M^0}{M^0} \frac{1}{p^2} \frac{dp}{d\xi} dp \right\} \quad (27)$$

where

$$\eta \equiv \left( \frac{c}{c_p} \right)^2 \frac{\lambda_T}{\lambda_v} \quad (28)$$

For rocket applications, the item of especial significance is the loss of specific impulse and, for the ideally expanded nozzle, this may be written in the form of the fractional impulse loss, where  $I^{(0)}$  is the specific impulse for equilibrium flow

$$\begin{aligned} \frac{I^{(0)} - I}{I^{(0)}} &= \frac{(1+\kappa)u^{(0)} - [u^{(0)} + u^{(1)} + \kappa(u^{(0)} + u^{(1)} - u_s^{(1)})]}{(1+\kappa)u^{(0)}} \bigg|_{p=p_e} \\ &= -\frac{u^{(1)}}{u^{(0)}} + \frac{\kappa}{1+\kappa} \frac{u_s^{(1)}}{u^{(0)}} \bigg|_{p=p_e} \quad (29) \end{aligned}$$

Upon substitution from equations (23) and (26), after some algebraic reduc-

# UNCLASSIFIED

tion,

$$\frac{I^{(0)} - I}{I^{(0)}} = \frac{\lambda_v}{L} \frac{\kappa}{1+\kappa} \left( \frac{1}{\bar{\gamma}} M^{(0)}(p_e) \right)^2 \int_{p_c}^{p_e} \frac{1 + (\bar{\gamma} - 1) \eta M^{(0)2}}{M^{(0)}} \frac{1}{p^2} \frac{dp}{d\xi} dp. \quad (30)$$

There is no difficulty in evaluating this integral, since it involves no singularity, and the value of  $dp/d\xi$  can be evaluated from the equilibrium pressure and the known relationship between the cross-sectional area and  $x$ , the distance measured along the nozzle axis from the chamber exit. Since the equilibrium Mach number may be given explicitly in terms of the pressure ratio

$$M^{(0)2} = \frac{2}{\bar{\gamma} - 1} \left[ \left( \frac{p_c}{p} \right)^{\frac{\bar{\gamma} - 1}{\bar{\gamma}}} - 1 \right] \quad (31)$$

the integral in equation (30) may be expressed in terms of either  $M^{(0)}$  or  $p$ , the shape of the nozzle entering only through the term  $dp/d\xi$ .

The impulse loss resulting from the non-equilibrium flow in the nozzle is estimated in equation (30) for the case where expansion is carried out to a prescribed exit pressure,  $p_e$ . The complementary example, when the expansion is carried out to a prescribed outlet area, is evaluated in reference 2.

## The Nozzle Shape for Minimum Impulse Loss

Aside from the fact that equation (30) provides an estimate of the particle slip impulse loss that may be determined by an elementary quadrature, it provides a form appropriate for variational calculations. Because the nozzle shape enters in the integral only through the term  $dp/d\xi$ , a significant extremum problem may be posed to ask what shape the nozzle should have, when the nozzle length and pressure ratio are fixed, in order that the fractional loss of impulse shall be a minimum. It transpires that this calculation is a straightforward one and yields [3] the optimum shape

$$\xi \left( \frac{p}{p_c} \right) = \frac{H(p/p_c)}{H(p_e/p_c)} \quad (32)$$

where the function  $H(p/p_c)$  is defined by the integral

$$H(p/p_c) = \int_{p/p_c}^1 \sqrt{\frac{1 + (\bar{\gamma} - 1) \eta M^{(0)2}}{M^{(0)}}} \frac{dp}{p} \quad (33)$$

This simple formula may be evaluated directly since the relationship between the local pressure  $p$  and the equilibrium flow Mach number  $M^{(0)}$  is given by equation (31). This function  $H(p/p_c)$  is given in Figure 1 for two

## UNCLASSIFIED

ratios of the isentropic exponent  $\bar{\gamma}$  for equilibrium flow. It is of particular interest that the value of  $H(p/p_c)$  varies very nearly linearly with the logarithm of the expansion pressure ratio. As a result, it is easy to calculate the distribution of pressure along the nozzle, and this is given, through use of equation (32), in Figure 2 for a nozzle with a pressure ratio of 100. The near linearity of the  $\log(p_c/p)$  with distance along the nozzle is again to be noted.

The crudest approximation to the shape of the nozzle for minimum impulse loss is obtained by substituting the results of equation (32) into the pressure-area relation given by equation (22). The resulting shape of the optimum nozzle is shown in Figure 3 for comparison with a more conventional nozzle of the same expansion ratio.

The characteristics of the optimum shape then become quite clear. The contraction from the chamber is initially quite rapid; the throat region is greatly prolonged to reduce the usually high accelerations, and a reasonable degree of acceleration persists to the end of the nozzle. The fact that the optimum nozzle does not show small accelerations at the nozzle exit suggests that losses due to high slip within the nozzle are as important as particle slip at the nozzle exit. Rather, the acceleration is distributed so that both internal losses and particle slip losses at the exit are moderately small. This fact demonstrates the fallacy of judging impulse losses on the basis of particle lag alone. The fact that the particle velocity lag at the outlet of the optimum nozzle may be several times that of a typical nozzle demonstrates that a considerable portion of the impulse loss may be attributed to dissipation within the nozzle.

One interest in the optimum nozzle is the determination of how much of the particle lag loss in a conventional nozzle can be regained by modified contouring of the nozzle. The only straightforward manner of investigating this is to compare the specific impulse losses in conventional and optimum nozzles having the same length and the same prescribed pressure ratios.

The distribution of losses within the two nozzles is most easily shown by calculating the cumulative impulse loss at various stages along the expansion. The result gives the contribution to the impulse loss of all processes taking place to any point of the nozzle. The results of the cumulative loss calculations are shown in Figure 4 for both conventional and optimum contours. It is to be noted that the slope of the cumulative loss curve corresponds to values of particle slip velocity, confirming the conjecture that dissipation associated with particle slip is a principal contributing factor. The increment in loss which causes the conventional nozzle to have a lower impulse than the optimum occurs in the throat region of the conventional nozzle where the particle slip velocities are very high. Correspondingly, toward the end of the conventional nozzle, impulse losses are being accumulated very slowly, reflecting the low acceleration rate at the conventional nozzle discharge.

In terms of overall performance, the losses induced by the particle lag are not an exceedingly sensitive function of the nozzle shape, at least within the family of contours considered reasonable for the gas alone. As a consequence, one may conclude that, for practical nozzle shapes and reason-



# UNCLASSIFIED

able sizes, rather small gains in impulse may be expected from alterations to the nozzle contour. In terms of current practice, this gain would be a fraction of a per cent of the motor impulse.

On the other hand, a reasonable first estimate of the particle loss in a conventional rocket nozzle may be taken as the loss in the optimum nozzle of the same pressure ratio. This approximation may be made even more useful by noting [3] that the function  $H(p/p_c)$  may be taken very closely to be

$$H(p/p_c) \approx [4\eta(\bar{\gamma}-1)]^{1/4} \ln(p_c/p) \quad (34)$$

and consequently an adequate approximation to the impulse loss is

$$\frac{I^{(0)} - I}{I^{(0)}} \approx 2 \frac{\lambda_v}{L} \left( \frac{\kappa}{1+\kappa} \right) \eta(\bar{\gamma}-1) \left\{ \frac{\ln(p_c/p_e)}{\bar{\gamma} M_e^{(0)}} \right\}^2 \quad (35)$$

This result contains all of the elements that are of first importance in the problem of performance loss due to a solid phase in the exhaust. Furthermore, in spite of the fact that compromises have been made in absolute accuracy, the effect of change in parameters based upon this simple formula is quite accurate.

To summarize, the first interesting result of the first order analysis is that the difference between the particle lag loss in a conventional nozzle and that in the corresponding optimum nozzle is not very large. Consequently, it is usually unwarranted to construct exotic nozzle shapes, since this effort, carried out at the expense of many other features of the nozzle, will not reduce the particle loss by more than one third. This is not to imply that improvement in existing nozzles cannot be made, but rather that the gains will be small unless the original nozzle was very short, of very small scale, or possessed some unusual entrance condition or throat contour.

As a consequence, the performance of a conventional nozzle may be approximated by the performance of the optimum nozzle having the same pressure ratio or area ratio. The error made in this approximation is usually less than that resulting from inadequate knowledge of the particle size, gas properties, and detailed flow field.

## Droplet Agglomeration in Nozzles

The growth of liquid droplets in rocket nozzles, resulting from particle slip and collision, is another type of problem that demonstrates physical insight and simplicity that can be achieved through the approximate analytical treatment of two-phase flow problems. We wish to estimate the amount of growth in size that droplets may experience when they enter the nozzle as liquid and freeze subsequently as the gas and liquid temperatures fall along the flow path.

The agglomeration of small liquid droplets to form larger ones usually takes place through three separate mechanisms: (i) collision due to Brownian motion of very small droplets, (ii) collisions arising from turbulent diffusion, and (iii) collisions resulting from differential mean velocity

# UNCLASSIFIED

of droplets of different sizes. The relative importance of these mechanisms depends upon the magnitude of the acceleration field that produces the relative motion of different size droplets. In the rocket chamber, the Brownian or turbulent diffusion is dominant, but in the rocket nozzle, where accelerations of  $10^4$  g are common, the collisions from differential particle velocity probably control the agglomeration rate.

These differential slip velocities for particles of different radii, and the resulting collision processes, have been examined in reference 4 and these results may be used in estimating the rate of droplet growth during acceleration of the mixture through the nozzle. Although our scanty knowledge of physical details does not allow a reliable absolute calculation of droplet growth, it is possible to estimate the order of magnitude, the dependence of the process upon chamber pressure, nozzle geometry, and other factors of influence in experiments.

If  $m$  denotes the mass of a liquid droplet having a radius  $\sigma$ , we consider the droplet mass spectrum  $f(m)$  as continuous, and consequently

$$f(m)dm \quad (36)$$

is the number of droplets per unit volume having masses in the range  $m$  to  $m+dm$ . Now when the droplet sizes and flow conditions in the nozzle permit the approximate analytical treatment described earlier, the local velocity of the droplet of radius  $\sigma$  and mass  $m$  is just

$$u(m) = u^{(0)} - \lambda_v(m)M^{(0)} \frac{du^{(0)}}{dx} \quad (37)$$

where

$$\lambda_v(m) \equiv \frac{ma_c}{6\pi\sigma\mu_c} \quad (38)$$

is the velocity equilibration length for a droplet of mass  $m$  and radius  $\sigma$ . The quantities  $a_c$  and  $\mu_c$  are the sound speed and viscosity coefficient at the chamber conditions. The mass flow of droplets in the range  $(m, dm)$  is

$$m f(m)dm \cdot u(m)A \quad (39)$$

where  $A$  is the local nozzle area.

Droplets in the range  $(m, dm)$  are produced and lost by collision; it will be assumed that each collision [4] results in the formation of a new droplet having a mass equal to the colliding masses. The number of collisions per unit volume between droplets of mass  $m_1$  and mass  $m_2$  is then

$$f(m_1)dn_1 \cdot f(m_2)dm_2 \cdot \pi(\sigma_1 + \sigma_2)^2 |u(m_1) - u(m_2)|, \quad (40)$$

and employing the approximate relation, equation (37), for particle velocity, the collision number is

$$M \frac{du}{dx} \cdot f(m_1)dm_1 \cdot f(m_2)dm_2 \cdot \pi(\sigma_1 + \sigma_2)^2 |\lambda(m_1) - \lambda(m_2)|, \quad (41)$$

where subscripts and superscripts have been dropped that are not needed. It is to be noted, in particular, that the factor  $M(du/dx)$  is the only term re-

# UNCLASSIFIED

lating to the nozzle flow process, and this is separable from those terms that pertain to droplet spectrum and droplet geometry.

A droplet is removed from the range  $(m, dm)$  with each collision involving a member of this set. The rate of droplet mass loss for a length  $dx$  of the nozzle is then

$$(AM \frac{du}{dx}) dx \cdot mf(m) dm \int_0^{\infty} f(m') dm' \pi(\sigma + \sigma')^2 |\lambda(m) - \lambda(m')| \quad (42)$$

On the other hand, a droplet in the range  $(m, dm)$  is produced by a collision between droplets of mass  $m'$  and  $m'' = (m - m')$ . The production of these droplets in a length  $dx$  of the nozzle is

$$\frac{1}{2} (AM \frac{du}{dx}) dx \cdot m \int_{m'+m''=m} f(m') dm' \cdot f(m'') dm'' \cdot \pi(\sigma' + \sigma'')^2 |\lambda(m') - \lambda(m'')| \quad (43)$$

where the factor of  $\frac{1}{2}$  accounts for counting each collision twice when summing over all values of  $m', m''$ . The rate at which the mass flow of droplets in the range  $(m, dm)$  changes along the nozzle

$$\frac{d}{dx} \{mf(m) dm u dA\} \quad (44)$$

is then given by the difference between the production integral, equation (43), and the loss integral, equation (42).

This spectral equation may be written most conveniently by introducing a new independent variable

$$\xi = m/m_c \quad (45)$$

and a new spectral function

$$\varphi = \frac{\rho_c}{\rho} \cdot \frac{m_c}{r_c} f(m) \quad (46)$$

where  $m_c, n_c$  are the average mass and number density of particles in the chamber;  $\rho_c$  is the gas density in the chamber. Moreover, if we define a thermodynamic variable

$$\eta = \int_0^M \frac{dM}{[1 + \frac{\bar{\gamma}-1}{2} M^2]^{\bar{\gamma}/(\bar{\gamma}-1)}} \quad (47)$$

and a new characteristic length

$$l = \frac{1}{\pi n_c \sigma_c^2} \quad (48)$$

the spectral equation may be written [5]

UNCLASSIFIED

# UNCLASSIFIED

$$\frac{d}{d\eta} (\varphi d\xi) = \frac{1}{2} \frac{\lambda(m_c)}{l} \int_{\xi'=0}^{\xi} \varphi(\xi') d\xi' \cdot \varphi(\xi - \xi') d\xi \cdot g(\xi', \xi - \xi') - \frac{\lambda(m_c)}{l} \int_{\xi'=0}^{\infty} \varphi(\xi) d\xi \cdot \varphi(\xi') d\xi' g(\xi, \xi') . \quad (49)$$

The function

$$g(\alpha, \beta) = (\alpha^{1/3} + \beta^{1/3})^2 |\alpha^{2/3} - \beta^{2/3}| \quad (50)$$

arises from the term  $(\sigma + \sigma')^2 |\lambda(m) - \lambda(m')|$  after the appropriate change of variables. Accompanying this spectral equation is a statement that the total mass flow of liquid through the nozzle remains constant which, in terms of the new variables, is

$$\int_{\xi=0}^{\infty} \xi \varphi(\xi) d\xi = 1 . \quad (51)$$

Now the independent variable of the problem,  $\eta$ , is a thermodynamic quantity defined by the equilibrium flow of gas and droplets through the nozzle, and consequently, the change in the spectrum of droplet sizes from rocket chamber to any point in the nozzle depends only upon the change in thermodynamic state and not upon the configuration of the nozzle. Therefore, even without detailed calculations, it appears that the droplet growth will not depend upon the scale or shape of the nozzle but only upon the pressure or temperature ratio from the chamber. This result becomes obvious as a result of the approximate analysis and is valid so long as the small-slip approximation may be made.

Since it is our purpose to trace the general growth of particle size, it is sufficient to deal with the spectral mean droplet mass

$$\bar{\xi} \equiv \frac{\int_0^{\infty} \xi \varphi(\xi) d\xi}{\int_0^{\infty} \varphi(\xi) d\xi} \quad (52)$$

rather than with the details of the spectrum. Integrating the spectral equation (49) over the droplet mass and using the condition given by equation (51), we find that

$$\frac{d}{d\eta} \left( \frac{1}{\bar{\xi}} \right) = - \frac{1}{2} \frac{\lambda(m_c)}{l} \int_0^{\infty} \varphi(\xi) d\xi \int_0^{\infty} \varphi(\xi') d\xi' g(\xi, \xi') . \quad (53)$$

# UNCLASSIFIED

Since the result we desire, namely  $\bar{\xi}$ , is given in terms of an integral, this form is convenient for approximation and one has confidence that, because of the integrations involved, the result will not be sensitive to reasonable approximations in the dimensionless spectral function  $\varphi$ . To this end, a similarity solution has been investigated where the similarity variable is

$$\omega = \xi / \bar{\xi} \quad (54)$$

and the spectral function is of the form

$$\varphi(\xi, \eta) = k(\bar{\xi}) \cdot \psi(\omega) \quad (55)$$

It transpires, reference 5, that

$$k(\bar{\xi}) = (\bar{\xi})^{-2} \quad (56)$$

and

$$\bar{\xi} = \left(1 - C \frac{\lambda(m_c)}{\ell} \eta\right)^{-3} \quad (57)$$

where  $C = 1.181$  as a reasonable estimate.

In particular, we find that the ratio of the mean droplet radius at any point to the mean droplet radius in the chamber is

$$\frac{\bar{\sigma}}{\sigma_c} = \bar{\xi}^{1/3} = \frac{1}{1 - 1.18 \frac{\lambda(m_c)}{\ell} \eta} \quad (58)$$

Now the variable  $\eta$  is shown in Figure 5 as a function of the local Mach number or of the local gas temperature. The ratio  $\lambda(m_c)/\ell$  is

$$\frac{\lambda(m_c)}{\ell} = \frac{1}{6} \frac{\rho_c a_c \sigma_c}{\mu_c} \cdot \kappa \quad (59)$$

For a fixed chamber temperature,  $\lambda(m_c)/\ell$  increases linearly with the chamber pressure and with the initial droplet radius.

The mean particle radius that is to be observed in experiments is determined by the value of  $\eta$  at which the droplets solidify and the value of  $\lambda(m_c)/\ell$  determined from the initial state of the mixture in the chamber. In the case of aluminum oxide, solidification occurs at a value  $T/T_c = 0.667$ , corresponding to the value of  $\eta \approx \eta_s \approx 1.0$  at solidification. The value of  $\eta_s$  is insensitive to moderate variations of solidification temperature and chamber temperature. Moreover, it appears that  $\eta_s$  is insensitive to a particle temperature lag of several hundred degrees. Hence, for nozzles carrying aluminized propellants,  $\eta_s \approx 1.0$  is a rather good approximation.

As a consequence, the details of the observed particle sizes must depend only upon the ratio  $\lambda(m_c)/\ell$ . In particular, this quantity is directly proportional to the chamber pressure  $p_c$ , so that it appears that, as the chamber pressure rises, the final droplet radius increases also, in some cases quite rapidly. Since there is no adequate knowledge of initial droplet radii, equation (58) cannot be treated quantitatively. If we accept the assumption that the collision accommodation coefficient is unity, then the

# UNCLASSIFIED

pressure dependence of  $\bar{\sigma}$  may be employed to estimate the value of  $\sigma_c$  that is appropriate. Based on the data from reference 6 at 100 psi and 500<sup>c</sup>psi, equation (58) describes the variation adequately for  $\sigma_c \sim 0.05$  microns. It may or may not be relevant that experimental results often show a background of residual particles having a radius less than 0.1 microns. It is probable that, when equation (58) leads to very large droplet radii, as it easily may for appropriate values of the parameters, the final droplet radius may be determined by hydrodynamic instability of the liquid, a value that will not be independent of nozzle geometry.

## Concluding Remarks

In reviewing the foundations and some applications of the approximate calculation of two-phase flow in rocket nozzles, it is shown that the aim has been to obtain simple, useful analytic results, that contain the significant quantities of the problem and provide a physical insight into the true mechanism. The emphasis is upon the manner in which the desired results vary with the physical parameters of the problem rather than striving for detail that may not be warranted by the accuracy of data necessary for its solution. It appears that the areas where approximate analytical results provide convenient performance trends and scaling laws have yet to be used to maximum advantage.

Much of the inaccuracy attributed to these approximate calculations may be avoided by inverting the algebraic equations

$$\frac{u_s^{(1)}}{a^{(0)}} \alpha \left( \frac{u_s^{(1)}}{a^{(0)}}, k \right) = - \frac{\lambda_v}{L} \frac{1}{\bar{y}} \frac{1}{p} \frac{dp}{d\xi}$$

$$\frac{T_s^{(1)}}{T^{(0)}} \beta \left( \frac{u_s^{(1)}}{a^{(0)}}, k \right) = \frac{\lambda_T}{L} \frac{\bar{y}-1}{\bar{y}} \frac{c}{\bar{c}} \frac{1}{p} \frac{dp}{d\xi}$$

exactly for  $u^{(1)}$  and  $T^{(1)}$  rather than employing their low Reynolds number counterparts, equations (23) and (24). We emphasize that this algebraic step does not alter the ease with which subsequent results may be obtained; the approximations are valid under the conditions stated regardless of the drag and heat transfer laws. Although this fact was first indicated by Rannie [1] more than five years ago, it does not seem to have been employed by the practitioners in the field.

## References

1. Rannie, W. D.; "Perturbation Analysis of One-Dimensional Heterogeneous Flow in Rocket Nozzles," Progress in Astronautics and Rocketry: Detonation and Two-Phase Flow, Vol. 6, pp. 117-144, Academic Press, New York (1962).
2. Marble, Frank E.; "Dynamics of a Gas Containing Small Solid Particles," Proceedings of the 5th AGARD Colloquium, 1963, pp. 175-213, Pergamon Press, Oxford (1963).

## UNCLASSIFIED

3. Marble, Frank E.; "Nozzle Contours for Minimum Particle Lag Loss," AIAA Journal, Vol. 1, No. 12, pp. 2793-2801 (Dec. 1963).
4. Marble, Frank E.; "Mechanism of Particle Collision in the One-Dimensional Dynamics of Gas-Particle Mixtures," Physics of Fluids, Vol. 7, No. 8, pp. 1270-1282 (Aug. 1964).
5. Marble, Frank E.; "Droplet Agglomeration in Rocket Nozzles Caused by Particle Slip and Collision," Astronautica Acta, Vol. 13, (1967).
6. Sehgal, Robert; "An Experimental Investigation of a Gas-Particle System," Technical Report No. 32-238, Jet Propulsion Laboratory (16 March 1962).

UNCLASSIFIED

UNCLASSIFIED

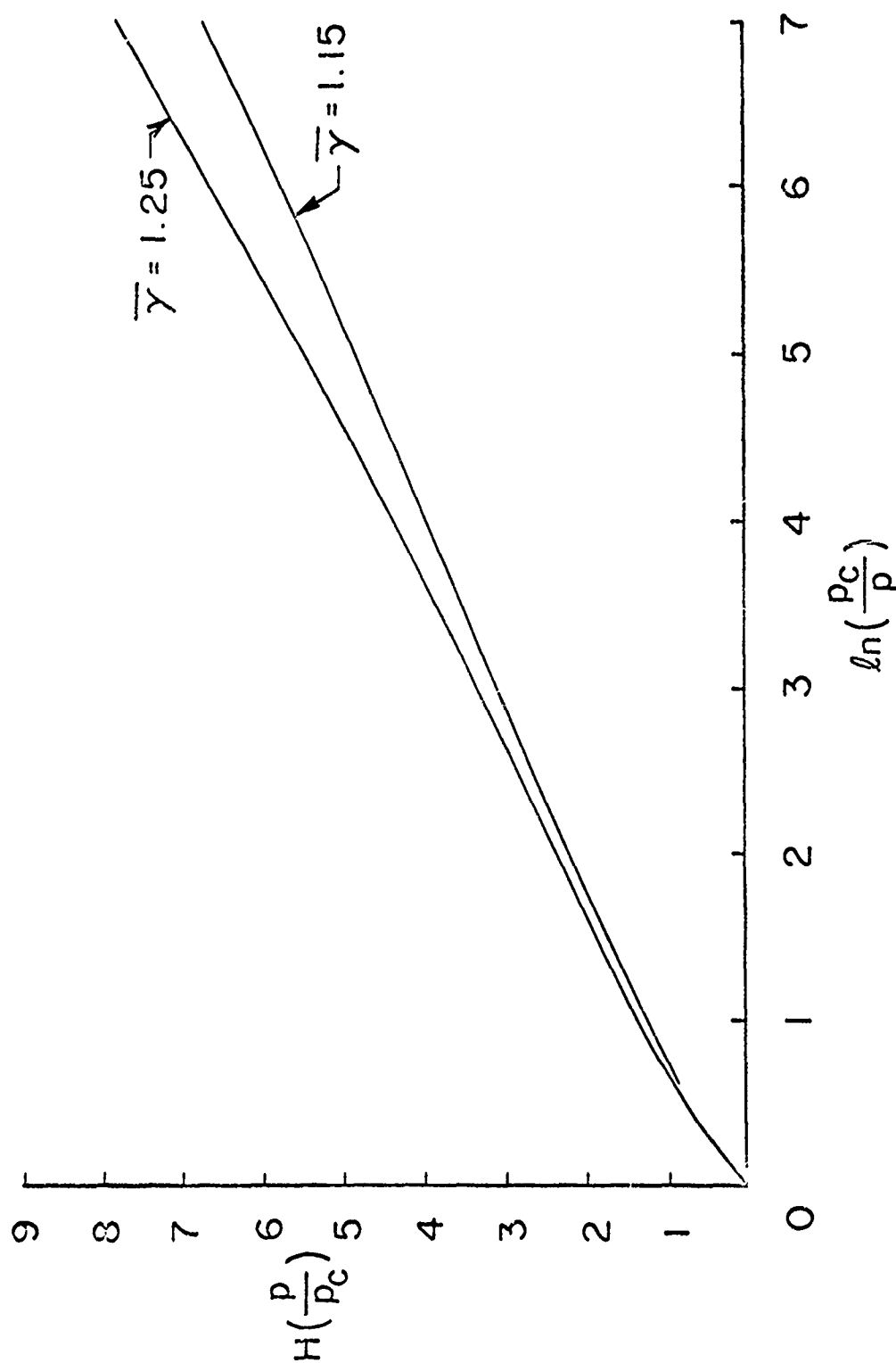
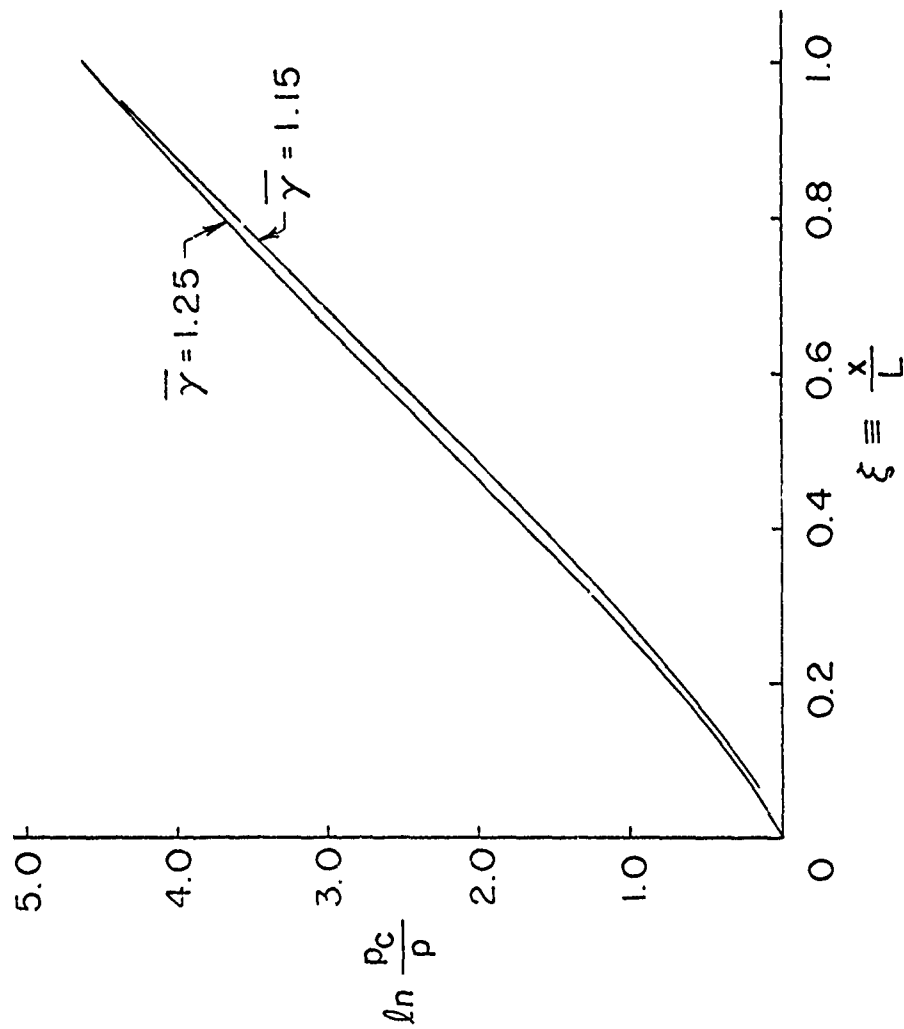


Figure 1. Values of  $H(p/p_c)$  as a Function of Pressure Ratio.

UNCLASSIFIED



UNCLASSIFIED



REDUCED 6.5" TO 5.5"

Figure 2. Pressure Distribution Along Nozzle of Optimum Contour.

UNCLASSIFIED

UNCLASSIFIED

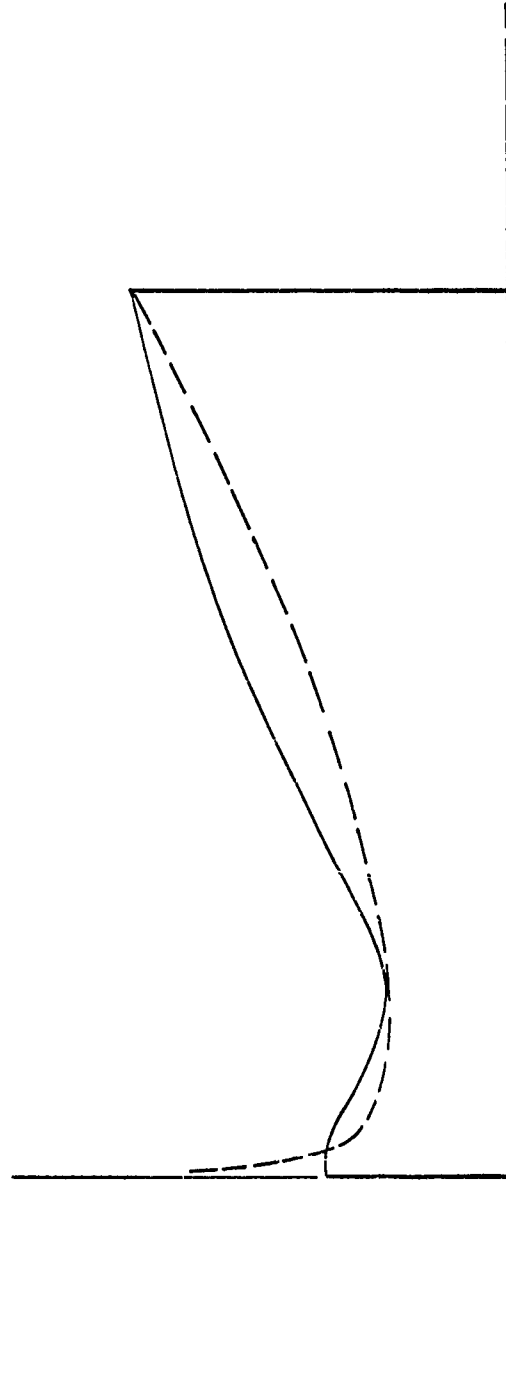


Figure 3. Comparison of Optimum Nozzle Contour with That of Conventional Nozzle.

UNCLASSIFIED

UNCLASSIFIED

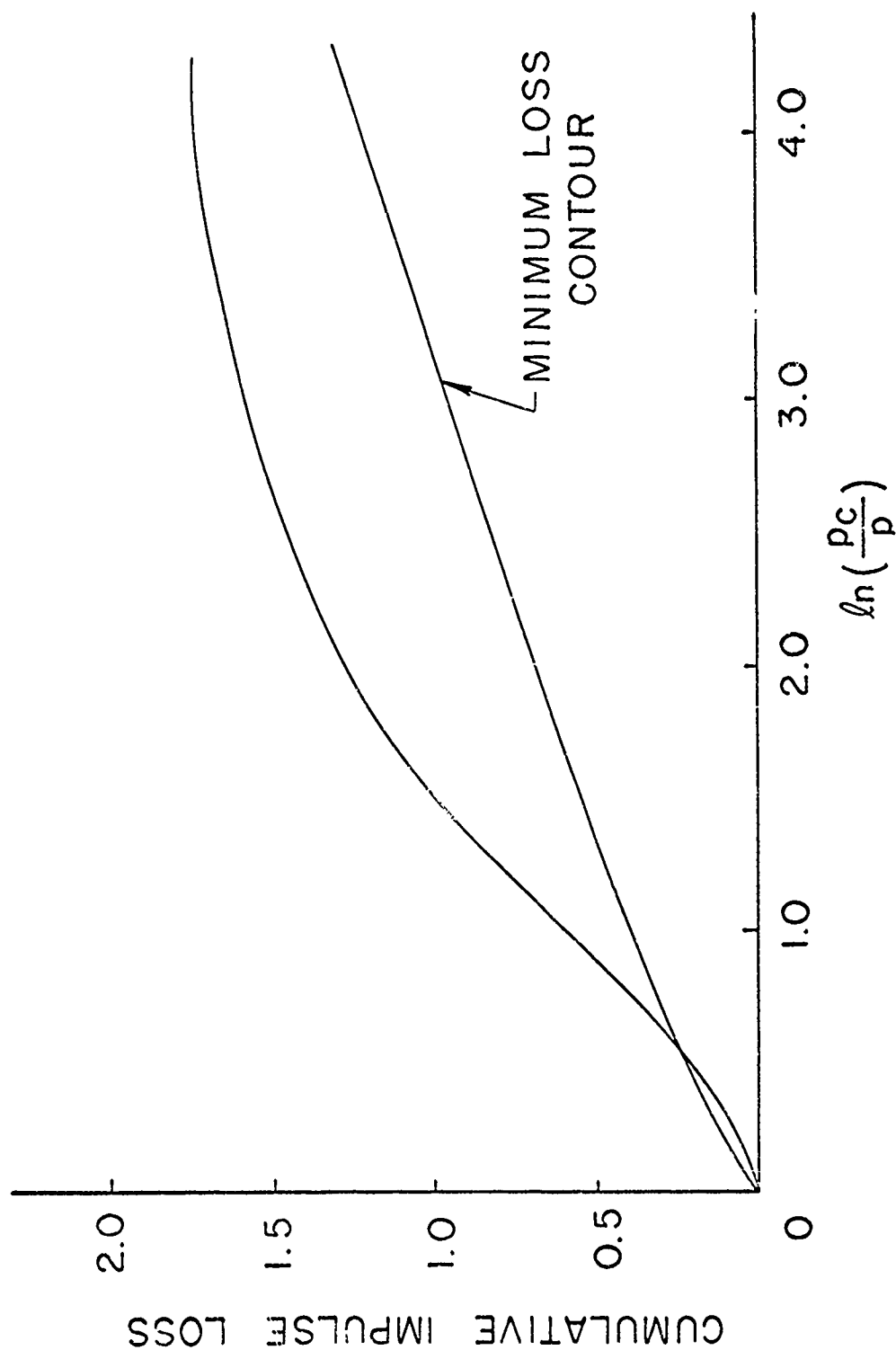


Figure 4. Comparison of Cumulative Impulse Loss Along Conventional Nozzle With That Along Optimum Nozzle.

UNCLASSIFIED

UNCLASSIFIED

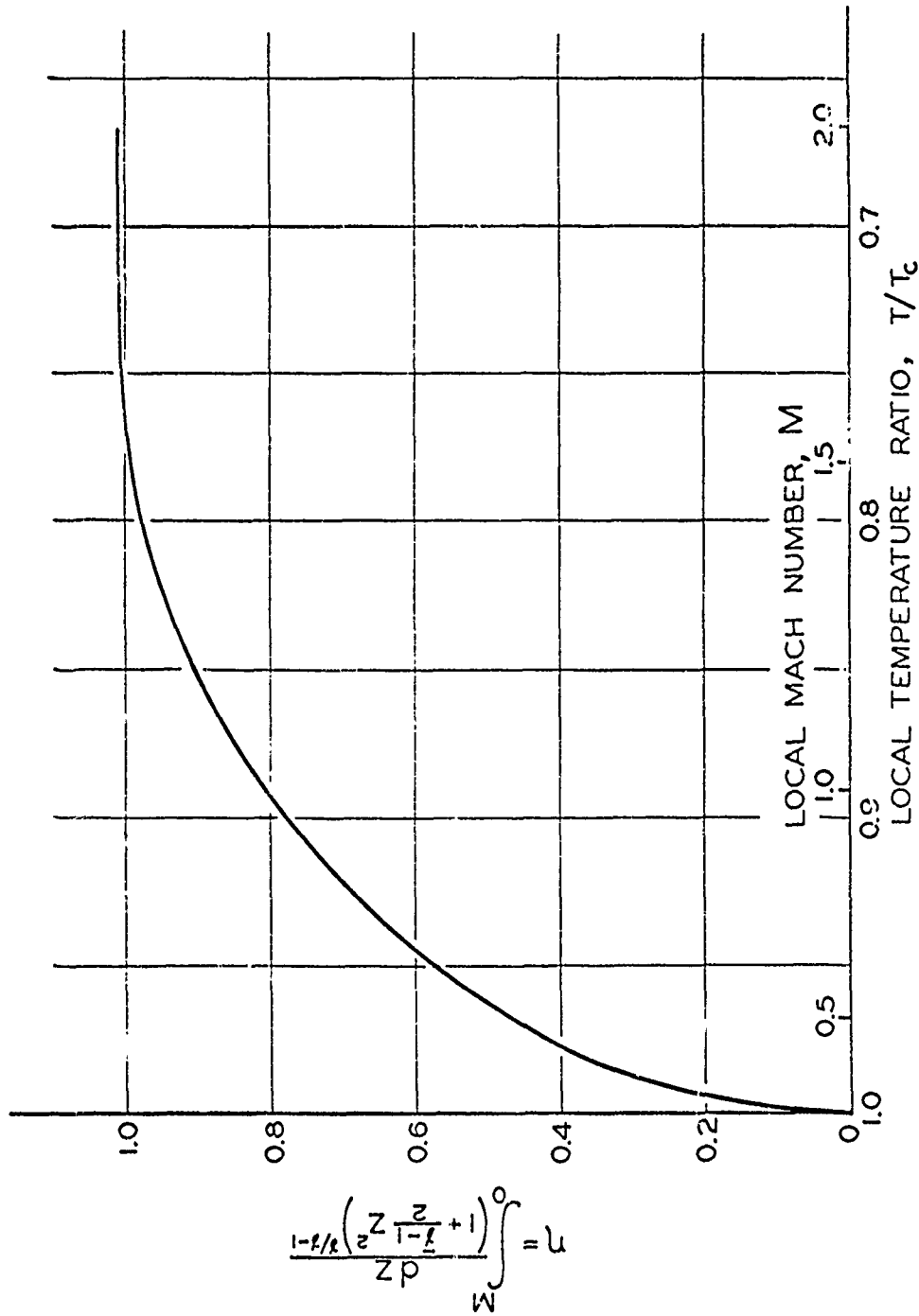


Figure 5. Values of State Variable  $\eta$  as a Function of Local Nozzle Temperature Ratio or of Local Nozzle Mach Number.

UNCLASSIFIED

## UNCLASSIFIED

J. R. Kliegel (Dynamic Science): Nonequilibrium Phenomena in Two-Phase "Nozzle Flow"

Off-the-cuff remarks by Jim Kliegel before he began his actual paper presentation.

J. R. Kliegel (Dynamic Science)

There are a number of fundamental questions in my mind regarding the interpretation of the work that was reported yesterday. I would like to take a couple of minutes and ask the question, "How does one relate the various burning experiments, the particle measurements, and the particle growth theories that were reported?" I believe this can be done in a fairly good way utilizing two basic principles. First, one should believe good experiments and question their interpretation, and secondly, one should utilize all available data and remember its accuracy. I would now like to go back through yesterday's session and give you some of my thoughts and interpretations, and mention some of the things I would like to have seen discussed. Yesterday afternoon was devoted mainly to studying what came out of the engine, and the morning was devoted to what happened between the grain and the throat. Much of the discussion pertained to grab sampling and what I would call the line-of-sight methods in which a picture, a hologram, or optical absorption techniques are used to determine particle sizes. Two particle growth theories were discussed; one was the maximum stable particle size theory, the other was the agglomeration growth theory. I would like to touch on each of these subjects as I view them from what was said and having read some of the reports that summarized this work.

I would classify grab sampling as an inaccurate measurement of a good sample in that what one has is what went through the engine, whether it is collected from the ultimate grab sampler, a huge tank, or after the firing either on the floor of the firing bay or in clouds. Because an inexact measurement is made from a good sample, one should count everything, although much discussion prevailed as to whether you count a thousand or all. As a suggestion, one might utilize in counting, a device similar to one the Weather Bureau has been using for years which

UNCLASSIFIED

## UNCLASSIFIED

scans electron microscope photographs and counts how many particles there are on the negative that are between a half micron and one, one and two, etc. This can be done with very little effort and gives accurate results. Grab sampling accuracy was also discussed at great length. I think we aren't keeping track of the measurement accuracy of grab samples. If one takes a large number of grab samples on a given engine (say 25 containing 4000 particles each), one obtains a statistical spread of about  $\pm 1.0 \mu$  in the mass mean size and distribution sigma. Since one gets such statistical spreads with grab sampling, I would classify it as an inexact measurement of what went through the engine. I believe it is a very representative measurement for the following reason, however: Everything correlates well, being log normal and, to my knowledge, one has never seen large deviations. I don't believe an experiment has ever been run that shows invalid samples within the accuracy of technique. People have turned collector plates upside down, normal and backward to the flow, in front of engines, both axially and radially, and behind engines, and their experience has been that if you collect something you get the same answer within a reasonable spread. Thus, it is rather difficult for me to believe that from so many diverse experiments you are not looking at a representative grab sample even though you get reasonable variations about the mean.

In the line-of-sight method there is a large, apparent discrepancy between what Dobbins has measured and what has been collected in the same tank. I would be inclined to accept both measurements as correct and question the interpretation. I believe the light-scattering technique is a very accurate way of measuring a certain property of the distributions, one moment. The difference may be that the line-of-sight can be a very biased sample in that one is looking line-of-sight through a plume. The line-of-sight plume particle distribution is quite different than the average distribution coming through the engine due to particle segregation as it passes through the nozzle. The light particles go to the outside, the heavy ones go down the middle, and the local particle to gas density varies with the particle lags. I thus believe you may be looking at a very biased sample with the line-of-sight method. I would suggest that

## UNCLASSIFIED

in the line-of-sight method you look at a calculation of where things went for that experiment and relate this to what was measured. I suspect you will find that grab samples and line-of-sight tank measurements are both right and that each method sees a different distribution. It may be a matter of interpretation, not experiment. I would believe both experiments.

The maximum stable particle size theory depends on having large particles coming into the nozzle that break up in the throat region. It is an experimental fact that you can break particles up by putting them through shocks or high shear regions, although one can argue about what Weber number one chooses to characterize this breakup. This theory appears valid for most engines since it fits the data on two counts. It gives a maximum size which no one measures things above and the particle distributions coming out the engine are log normal, which is the distribution for everything I know of that goes through a breaking down process whether it be grinding gravel into sand or breaking things up.

Since the maximum stable particle size theory appears to be applicable, one must now explain how the particles got to be large enough to break up. There are a couple of interesting things about the growth theory due to differential particle velocity lags. Is it possible that if the calculations were run from the head end of the chamber, one would find that particles would grow to larger than the maximum stable particle size by the nozzle inlet? This would be a very interesting calculation. The combustion experiments that were reported are very interesting and also relate to the maximum stable size theory. One thought that occurred to me in looking at the China Lake data is that the aluminum appears to vaporize and burn outside the drop at first, but one then gets oxide formulation on the drop surface. What we are really interested in is, where is the mass of the oxide found? If a large fraction of the oxide is formed on the aluminum drop then, since one started with something like a thirty micron aluminum drop, one has a large oxidizer drop. I would like to ask the China Lake people: "Can you find out what fraction of the aluminum oxide is formed in the polar cap as opposed to the fraction that is vaporized as aluminum and forms

UNCLASSIFIED

## UNCLASSIFIED

and condenses in the gas phase?" This may be the source of the very large drops of liquid alumina that then break up in the throat region and show up in the distributions collected outside the engine.

J. R. Kliegel (Dynamic Science): Questions, Answers and Comments:

Q./R. A. Dobbins (Brown University): A comment made in your spontaneously prepared paper was whether or not a plot of particle size on a log normal distribution is a sufficiency test for the validity of the statistical sample. If I understand correctly, you say any sample we make and plot on a log normal distribution which gives a straight line must be a statistically valid sample. Is that your statement?

A./J. R. Kliegel (Dynamic Science): No. I said that all samples I have seen by the grab sample technique give that.

C./R. A. Dobbins (Brown University): That does not imply a statistical validity.

C./J. R. Kliegel (Dynamic Science): That is correct. What I was trying to get at was one can postulate from the grab sample techniques an infinite number of ways that a biased sample is obtained. The observation I want to make is that all samples at least have the same distribution. One has not seen a distribution shift. One can argue about its slope and sigmas, but if there is a sample biasing, it is a funny bias, because you have not lost all the small or big ones, or obtained a terminated sample; it is still log normal and I think people have measured enough big and small ones to show that the distribution has not shifted from what they measured. The means and sigmas may have, however.

C./R. A. Dobbins (Brown University): I am not sure I understand all that you are getting at. One possibility would be this: we might get a sample that would be cut off all below a certain size, and this is going to result in a difference in plot on the log normal curve. I doubt if we are going to be able to detect the loss of all particles smaller than a certain size merely by plotting. I think this was brought out in some of yesterday's slides, therefore, I think there is indeed a critical problem in sampling to make certain that the sample is the same as the parent population, which is the one that all of us who have tried to measure particles have struggled with. I think we have to explore this a little more afterward.



UNCLASSIFIED

C./I. R. Kliegel (Dynamic Science): Let me clarify this. A typical mass mean size is three microns and size counts are typically made between 1/2 to six microns. Most measurements are in this range and everything is log normal. If the distribution is truly log normal, then we have the measurements in the size range where 95% of the mass is distributed. We have not seen very odd distributions like those that are all missing below 1-1/2 or above five microns. I would tend to accept the data, but I have questions as you do. I think that basically a lot of these things are unresolvable. I think I have more serious questions about interpretation.

C./R. A. Dobbins (Brown University): I would like to go on to a second point. You asked about a possibility that the optical technique which I described yesterday would be measuring the same distribution of sizes, but at a different moment and, therefore, getting different answers. This is one of the things that we have tried to avoid and have done everything we could think of to answer as to whether or not this happens. In the first series of tests, we conducted a test at three different radial stations right on the nozzle centerline, the optical axis going right through the nozzle centerline and at two stations moved off the nozzle centerline. In that particular case, we measured the same particle size at three different nozzle stations. The size is around 0.45 microns. Those particular tests were conducted at low pressures where the tank tests indicated there should be no large particles. So, then the past summer we conducted tests with the chamber pressure high where the tank tests indicate there should be very large particles present. Again we performed the same radial transverse. In this case, somewhat further away from the nozzle and at a larger radial span, we measure the same size as a function of radius, a minimum of around 0.5 microns. Then, if we take a criterion which you have given for the calculation of the particle velocity lag, and estimate the lag that we would have in the nozzle geometry that we use with that sort of size, we get a lag velocity ratio of 0.97. The velocity of the particles is about 97% of the velocity of the gas, which seems consistent as far as I can tell. It still remains that the optical method is sensitive to a different moment than the sampling method. It is very difficult to conceive that this difference in sensitivity would

UNCLASSIFIED

## UNCLASSIFIED

give the same results at low pressures, which it does, and it diverges by a factor of ten at high pressures. This is why we feel that there is a good possibility that they are not measuring the same quantity if there is actually a discrepancy.

C./F. C. Price (Aeronutronic): I think Jim Kliegel has gone too far in whitewashing of samples - like setting us back 80 years. When you think that a one-micron particle settles at 1/400th the speed of a 20-micron particle, and that things go pretty slow in boundary layers and they finally go to zero and at sometime that 400 is a lot higher than zero and one is almost at zero, one has to be careful in handling the particles. As Larry Delaney mentioned, he did something as I would; he spread samples out over the pad at far distances, and he got answers that were quite consistent. That does not prove anything to me. I think you have got to sample in different ways and you have got to worry that there isn't some allutriation effect. I also think that the log normal distribution will occur in many ways in statistical handling of particles. The particle growth and the breakup both give, or should give you, a nice log normal distribution. So, having log normal distributions does not indicate at all with any great enforcement that we have had particle breakup. I conducted an experiment a year or so ago. We had polyurethane particles between one and sixty microns. We wanted to get the particle size distribution because we were using them in cold-flow experiments. We wanted to know what came in and then what was picked up and counted; i.e., what fraction of the things we started with. So, as many of us do, I could see a very slow, cute way to do this. I atomized the particles with a high-velocity air jet into a chemistry hood with the glass slides placed on the bottom. I shot a tablespoon full of particles in there and then closed the hood and waited overnight and took out the slide. Then I went through the laborious counting of the particles and thought, "with all that work and all that careful preparation they must be right." But, I had a nagging worry that the hood leaked slightly. It wasn't turned on, of course, but there is some difference in air pressure in the building and outside. Maybe I had allutriated some of the small particles, so after all that work and getting a nice log normal distribution, I then shot them

## UNCLASSIFIED

into a closet where there wouldn't be any such action. Then I worried that the big particles went over, hit the wall, and didn't bounce back and that the small ones would drift down on the slide in the center, and I did put slides all over. We counted that. Then I discovered the way to do it is to put a diaphragm on a chamber and a little lump of particles - a little pile - on the diaphragm and explode the diaphragm. This gives you a good atomization of the particles. We counted those. Now we got what we think is right. Now we think we are smart. Both lines, the first and the last, were nice, straight log normal distributions, and I am convinced the first one was allutriated.

UNCLASSIFIED

# UNCLASSIFIED

## NONEQUILIBRIUM PHENOMENA OF TWO-PHASE NOZZLE FLOWS

James R. Kliegel

The nonequilibrium expansion losses associated with two-phase nozzle flows are qualitatively discussed. Particular attention is directed to how the various losses change with propellant system variations and the calculational methods currently employed to estimate these losses.

### INTRODUCTION

The simplest and most convenient method of comparing the performance of two propellant systems is by means of one-dimensional equilibrium thermodynamic performance calculations. Such calculations can be performed in a straightforward manner and are used as the reference performance from which the various nozzle expansion losses are subtracted to obtain the delivered engine performance. The expansion losses associated with two-phase nozzle flows are:

- divergence losses
- boundary layer viscous losses
- two-phase (velocity lag and thermal lag)
- expansion losses
- chemical recombination losses
- condensation losses
- shock losses

Although these losses are interrelated and dependent upon the engine and nozzle geometry, one generally treats them separately, neglecting the interactions between the various loss calculations. Utilizing this approach, the nozzle divergence loss is strictly a geometrical effect independent of the other expansion phenomena and will not be further considered in this discussion.

## UNCLASSIFIED

### DISCUSSION

Tables 1 and 2 give an approximate breakdown of the remaining expansion losses in two propellant systems having condensed exhaust products in typical 5,000 lb. thrust engines. The two columns in the tables list the maximum value of the individual losses when calculated individually and the probable value based on engine firing experience. Examination of the tables indicates the shift in loss mechanisms associated with changes in propellant systems. In a typical aluminized propellant system (Table 1) the probable two-phase flow losses are seen to be 2.5% while in the prepackage system having approximately the same percentage of condensibles, the two-phase flow losses drop to 0.2% due to the small size of the particles associated with the unburned carbon in the system. The recombination losses in the prepackage system have increased, however, so that the total expansion loss associated with both two-phase and recombination losses remains approximately the same for the two systems. Although data has been given on only two typical propellant systems, examination of additional systems has shown that the probable recombination and two-phase flow losses are approximately constant, independent of the propellant system in similar size engines. Thus, in trying to correlate experimental engine firing data with theoretical calculations, one must consider both types of expansion losses in order to obtain proper scaling effects over a wide range of engine sizes and between different propellant systems.

Although one would like to calculate both the recombination and two-phase flow losses together since they constitute the largest flow losses in actual two-phase nozzle flows, such a calculation is exceedingly complex.

Table 3 lists the number of significant species and chemical reactions which must be considered in such calculations for typical metalized propellant systems. Also listed in the table for reference purposes are the

## UNCLASSIFIED

same quantities for several typical liquid propellant systems having entirely gaseous exhaust products. Examination of the table reveals that the recombination chemistry associated with typical metalized propellant systems is exceedingly complex compared to that of typical liquid systems which can hardly be described as simple. It is, thus, much more difficult to accurately calculate the predominant nonequilibrium expansion losses (two-phase and recombination) in metalized systems than in typical nonmetalized liquid systems having all gaseous exhaust products. In addition, the fundamental data required for such calculations (particle size distribution and chemical reaction rates) are essentially lacking (especially the chemical rate or reactions involving metalized species).

Since it is extremely difficult to accurately calculate both the two-phase and recombination losses which occur in metalized systems due to the complexity of calculation and the lack of fundamental kinetic rate data, it would perhaps be fruitful to develop approximate methods of calculating these losses in order to determine how they interact and in determining semi-empirical engine performance scaling laws. The most successful approximate method of calculating two-phase flow losses are the constant fractional lag relationships which are strictly valid only when the velocity and thermal lags are constant. The validity of these relationships locally in most flows can be shown by examining the magnitude of the terms in the particle drag equation in various nozzle regions. Examination of Table 4 show that the first term (which is neglected in these approximations) is quite small compared to the other terms in the nozzle inlet and throat regions and is of importance only in the nozzle expansion section. From this order-of-magnitude comparison, one would expect that the constant fractional lag approximations would be in excellent agreement with

UNCLASSIFIED

## UNCLASSIFIED

exact numerical solutions in the nozzle inlet and throat regions and are reasonable representatives of the whole expansion which has been shown. Since particle lags and chemical recombination lags behave similarly, it is believed that a similar constant fractional lag approximation can be derived for recombination effects. Such solutions would be extremely useful in that they would allow one to perform accurate recombination and two-phase flow loss calculations in a simple and straightforward manner.

Two other loss phenomena which have been generally ignored in performance calculations are also listed in the tables. They are the condensation loss associated with lack of complete condensation in the nozzle which is encountered in some high temperature propellant systems and nozzle shock losses associated with non-ideal aerodynamic design of the nozzle. Consideration of these losses may be necessary in small engines or in engines where a large amount of nozzle erosion occurs during firing in order to completely characterize the engine behavior. Although it is believed that these losses are small in typical engines and are so listed in the tables, one cannot definitely prove this or ignore such losses in performance correlations at this time.

### CONCLUSIONS

Although the major nonequilibrium losses which occur in two-phase nozzle flows have been known for a relatively long time, the magnitude of the various (viscous, two-phase and recombination) losses are only approximately known. Part of this uncertainty is due to lack of basic data (particle size distributions and kinetic reaction rates) and part is due to a lack of fundamental understanding of the processes involved (turbulent boundary layer losses). Much further work is needed in these areas. It is suggested that due to the complexity of the recombination kinetics in

UNCLASSIFIED

## UNCLASSIFIED

metalized propellant systems, that an effort be spent to determine the predominant recombination effects in order to simplify the calculations. It is also suggested that simplified methods of calculating both two-phase and recombination losses be re-examined and improved in order that simple engineering calculations of both losses can be performed in a straightforward parametric phase.

J. R. Kliegel (Dynamic Science):

Q. R. F. Hoglund (Purdue University)

It is clear that the general two-phase flow expansion is a non-isentropic process and obviously all the entropy rise must appear in the gas. I was wondering - when you combine the chemically reactive system, which is usually characterized by utilization of free energy, with the two-phase flow system; if it isn't proper to include that entropy rise in the gas phase calculation, and does anybody really do this? It would seem to me that that is an effect on the order of things we are looking for - like a half of a per cent or more.

A. J. R. Kliegel (Dynamic Science)

The calculations I am referring to, trying to account for both the condensed phase and reactions, were calculations done using the non-equilibrium equations at integrating forward from equilibrium chamber conditions. The calculations account for the entropy generation due to particle lags and finite rate kinetics.

UNCLASSIFIED



# UNCLASSIFIED

TABLE 1

## Nozzle Losses - Aluminized Solid Propellants

<u>Category</u>	<u>Maximum</u>	<u>Probable</u>
Viscous Losses	2.0%	1.0%
Lag Losses	5.0%	2.5%
Recombination Losses	2.0%	1.0%
Condensation Losses	0.5%	0.3%
Shock Losses	<u>0.5%</u>	<u>0.2%</u>
Total Losses	10.0%	5.0%

# UNCLASSIFIED

TABLE 2

## Nozzle Losses - Liquid Prepackaged Propellants

<u>Category</u>	<u>Maximum</u>	<u>Probable</u>
Viscous Losses	2.0%	1.0%
Lag Losses	0.5%	0.2%
Recombination Losses	5.0%	3.0%
Condensation Losses	<u>0.5%</u>	<u>0.2%</u>
Total Losses	8.0%	4.4%

UNCLASSIFIED

# UNCLASSIFIED

TABLE 3

## Propellant System Chemistry

<u>Propellant</u>	<u>Species</u>	<u>Reactions</u>
Aluminized Solid	22	72
Beryllium Solid	22	65
Liquid Prepack	24	104
Aluminized Liquid Prepack	34	155
Beryllium Liquid Prepack	38	72
LOX/RP-1	9	16
H <sub>2</sub> /F <sub>2</sub>	5	6
A-50/N <sub>2</sub> O <sub>4</sub>	12	24
H <sub>2</sub> /O <sub>2</sub>	6	11

UNCLASSIFIED

TABLE 4

Constant Fractional Lag Solutions

Drag Equation

$$u \frac{dK}{dx} + K \frac{du}{dx} = \frac{9}{2} \frac{\mu_f r_p^{*2}}{m_p r_p^2} \frac{1-K}{K} u$$

Magnitude of Terms

Inlet	25	400	425
Throat	100	3000	3100
Expansion	-80	180	100

## UNCLASSIFIED

### QUESTIONS, ANSWERS & COMMENTS:

Q. R. F. Hoglund (Purdue University): It is clear that the general two-phase flow expansion is a non-isentropic process and all the entropy rise must appear in the gas. I was wondering - when you combine the chemically reactive system, which is usually characterized by minimization of free energy, with the two-phase flow system, if it isn't proper to include that entropy rise in the gas phase calculation. Does anybody really do this? It would seem to me that this is an effect on the order of things we are looking for - like a half a percent or more.

A. J. R. Kliegel (Dynamic Science): The calculations I am referring to, trying to account for both the condensed phase and reaction, were calculations done for the non-equilibrium chemical kinetic equations starting at equilibrium chamber conditions. The entropy rise is accounted for.

**UNCLASSIFIED**

GAS-PARTICLE FLOW IN CONVERGENT NOZZLES  
AT HIGH LOADING RATIOS

By

George Rudinger  
Cornell Aeronautical Laboratory, Inc.  
Buffalo, New York

**UNCLASSIFIED**

# UNCLASSIFIED

## GAS-PARTICLE FLOW IN CONVERGENT NOZZLES AT HIGH LOADING RATIOS

George Rudinger

Cornell Aeronautical Laboratory, Inc.

Buffalo, New York

In the analysis of gas-particle flow, it is often permissible to assume that the volume occupied by the particles can be neglected. As part of our ONR-sponsored Project SQUID, we have been investigating various flows that are so heavily loaded with particles that the particle volume should not be ignored.

Such flows may be used for the injection of powdered fuel into the combustion chamber of a rocket<sup>1</sup>; generally, they are important for the transport of powdered materials. As an important example of such flows, I should like to discuss the discharge of a gas-particle mixture from a high-pressure reservoir through a convergent nozzle where the pressure is low enough that the flow at the nozzle exit is always choked.

We shall assume that the flow may be considered as one-dimensional, and for this reason, the analysis will be restricted to the convergent part of the nozzle. Although the flow in the divergent part downstream of the throat would also be of great interest, it has been observed<sup>2</sup> that the particles in the divergent part of the nozzle tend to be concentrated in a narrow region along the nozzle axis. The assumption of a one-dimensional flow then would not be realistic. (Dr. Billings Brown has pointed out earlier that this phenomenon is particularly

UNCLASSIFIED

## UNCLASSIFIED

important for smaller rocket nozzles.)

We are not primarily concerned with obtaining numerical results for specific nozzle but rather with the understanding of the flow processes. Nevertheless, some representative nozzle must be assumed before any calculations can be performed. We shall assume that the shape of the nozzle is such that the ratio of the particle velocity  $v$  to the gas velocity  $u$  is equal to a constant  $K$ :

$$\frac{v}{u} = K \quad (1)$$

Such nozzles are known as "constant fractional lag nozzles" and have been analyzed by Kliegel<sup>3</sup> for the case of negligible particle volume. The present analysis extends Kliegel's work to flows in which the particle volume cannot be neglected. The assumed nozzle shape is, of course, arbitrary but not more so than any other shape that one might assume. It has the advantage of being mathematically convenient, and Kliegel has also pointed out that many actually used nozzles differ not too much from constant-fractional lag nozzles, particularly in the neighborhood of the throat.

If the particle volume cannot be neglected, one must make a careful distinction between the density of a phase, that is the mass of phase material per unit volume of the phase material and its concentration, that is the mass of phase material per unit volume of the mixture.

The relationships for steady nozzle flow are given by:

$$m = (1-\epsilon)puA \quad (2)$$

$$n = \epsilon dvA = \mu m \quad (3)$$

$$m \frac{du}{dx} + n \frac{dv}{dx} + A \frac{dp}{dx} = 0 \quad (4)$$

$$M(u \frac{du}{dx} + \lambda p \frac{dt}{dx}) + n(v \frac{dv}{dx} + c \frac{dt}{dx} + \frac{1}{d} \frac{dp}{dx}) \quad (5)$$



# UNCLASSIFIED

$$v \frac{dv}{dx} = \frac{18\mu}{D^2 d} (u-v) - \frac{1}{d} \frac{dp}{dx} \quad (6)$$

$$v \frac{dt}{dx} = \frac{12K}{D^2 dc} (T-t) \quad (7)$$

$$p = pRT \quad (8)$$

where  $m$  and  $n$  are the gas and particle flow rates,  $\epsilon$  is the volume fraction occupied by the particles,  $A$  the cross-sectional area of the nozzle,  $p$  the density of the gas phase,  $d$  the (constant) density of the particle material;  $T$  and  $t$  are the gas and particle temperatures,  $p$  is the gas pressure,  $c_p$  the specific heat of the gas at constant pressure and  $c$  that of the particle material;  $\mu$  is the viscosity and  $k$  the thermal conductivity of the gas,  $D$  is the diameter of the particles which are assumed to be spherical and of uniform size, and  $R$  is the gas constant. The ratio of the two flow rates,  $\mu = n/m$ , represents an important parameter of the analysis -- the loading ratio.

The effect of the finite particle volume appears in the continuity equations (2) and (3) where the usual density is replaced by the gas and particle concentrations  $(1-\epsilon)p$  and  $\epsilon d$ . The momentum equation (4) does not contain the particle volume fraction explicitly. In the energy equation (5), the last term is a consequence of the particle volume,<sup>4</sup> and it can be seen from Eq.(3) that the factor  $n/d$  is of order  $\epsilon$ . The equation of motion of a particle (6) includes a term for the pressure gradient because this driving force cannot be neglected if the particles have a finite volume. Since general flow properties rather than particular numerical solutions are desired, it seems permissible to assume Stokes drag in Eq. (6) and pure heat conduction in the heat balance eq. (7). The gas phase is assumed to be a perfect gas, Eq. (8).

UNCLASSIFIED

## UNCLASSIFIED

If Eq. (1) is introduced into the system of Eqs. (2) to (8), the cross-sectional area of the nozzle can no longer be prescribed but becomes part of the solution sought. One of the flow variables may be selected as the independent variable. The gas velocity  $u$  was chosen for this purpose, and all the variables may be expressed in terms of it. The longitudinal coordinate  $x$  may finally be found by integration of Eqs. (6) or (7).

The foregoing system of equations cannot be solved analytically and was programmed for numerical solutions by means of a digital computer. As usual in problems of this kind, the integration cannot be started from the reservoir conditions but must be started from the nozzle inlet where the gas has already reached a finite flow velocity  $u_0$ . This starting velocity was always taken to be 10% of the equilibrium speed of sound of the gas-particle mixture in the reservoir,  $a_R$ . A number of examples were computed to investigate the influence of various parameters on the solution, and it was noted that, for the higher loading ratios, both the gas and the particle temperatures remained practically constant throughout the nozzle. This observation is demonstrated in Figure 1, where the ratio of the throat temperature to the inlet temperature is plotted as a function of the loading ratio  $\mu$  for two values of the velocity ratio  $K$ . The particular conditions for these calculations are given in the insert of the figure, where  $\gamma$  is the specific-heat ratio of the gas,  $\mathcal{N}$  is the ratio  $C/C_p$ , and  $\beta$  is the ratio of the gas density in the reservoir to the density of the particle material. The stated values of  $\mathcal{N}$  and  $\beta$  represent typical conditions. A second abscissa scale also shows the particle volume fraction in the reservoir for the conditions

## UNCLASSIFIED

of these calculations. It can be seen that for loading ratios greater than about 5, or particle volume fractions greater than about 0.2%, the temperature changes are quite small. Lines representing temperature drops of 1% and 2% are shown in the figure.

This temperature behavior is readily explained: the heat capacity of the particles is so large compared with that of the gas that the temperature drop of the gas in the nozzle expansion is practically completely compensated by the heat transfer from the particles to the gas without significantly lowering the particle temperature. It is also instructive to look at the effective specific-heat ratio of the gas-particle mixture. It is given by:<sup>4</sup>

$$\Gamma = \gamma \frac{1 + \mu}{1 + \mu \gamma} \quad (9)$$

and for  $\gamma = 1.4$  and  $\mu = 1.0$ , this relationship is indicated by the following table:

$\mu$	$\Gamma$
0	1.4
1	1.167
10	1.027
100	1.003

Thus, the specific-heat ratio for  $\mu=10$  differs from unity by less than 3%, and for  $\mu = 100$ , its value is practically equal to unity. Since a value of unity for the specific-heat ratio indicates an isothermal flow, we find again that flows with sufficiently high particle loading should exhibit only small temperature changes.

The foregoing observations naturally lead one to the attempt to solve the basic equations by making the assumption that the energy equation (5) may be replaced by the condition of constant temperature. For

UNCLASSIFIED

# UNCLASSIFIED

a constant fractional lag nozzle, the solution is given by:

$$u^2 = u_o^2 + \frac{2RT}{1+\gamma K} \left[ \ln \frac{p_o}{p} + \frac{\epsilon_o}{1-\epsilon_o} \left(1 - \frac{p}{p_o}\right) \right] \quad (10)$$

$$\frac{\epsilon}{1-\epsilon} = \frac{\epsilon_o}{1-\epsilon_o} \frac{p}{p_o} \quad (11)$$

$$\frac{A}{A_o} = \frac{u_o p_o (1-\epsilon_o)}{u p (1-\epsilon)} \quad (12)$$

where the gas pressure is the independent variable and subscript zero indicates the prescribed conditions at the nozzle inlet. Equation (10) is transcendental and must be solved numerically for  $u$ , but the other flow variables are then readily obtained from Eqs. (11), (12), and (1).

The nozzle throat is reached when the derivative of  $A$  with respect to any of the other variables vanishes. With this additional requirement the throat pressure ratio  $p_t/p_o$  is given by the solution of the equation:

$$2 \ln \frac{p_o}{p_t} - \left( \frac{\epsilon_o}{1-\epsilon_o} \frac{p_t}{p_o} \right)^2 - 4 \frac{\epsilon_o}{1-\epsilon_o} \frac{p_t}{p_o} = 1 - \frac{1+\gamma K}{RT} u_o^2 - 2 \frac{\epsilon_o}{1-\epsilon_o} \quad (13)$$

The remaining throat conditions then follow again from Eqs. (10), (11), (12), and (1).

A considerable simplification of the described relationships would result if the particle volume fraction could be neglected.

Equations (10), (12), and (13) would then reduce to:

$$u^2 = u_o^2 + \frac{2RT}{1+\gamma K} \ln \frac{p_o}{p} \quad (14)$$

$$\frac{A}{A_o} = \frac{u_o p_o}{u p} \quad (15)$$

and the throat condition

$$\frac{p_t}{p_o} = \exp \frac{1}{2} \left( 1 - \frac{1+\gamma K}{RT} u_o^2 \right) \quad (16)$$

If the velocity of the nozzle inlet,  $u_o$ , is sufficiently small, Eqs. (14) and (16) become:

## UNCLASSIFIED

$$\frac{P_t}{P_o} = \frac{1}{\sqrt{e}} = 0.6065 \quad (18)$$

$$u_t^2 = \frac{RT}{1 + yK} \quad (17)$$

Note that under these conditions the throat pressure ratio becomes a constant, independent of all flow parameters.

At this point, it becomes imperative to investigate whether a significant range of the loading ratio exists that is high enough to allow the flow to be treated as isothermal and, at the same time, still low enough to neglect the volume occupied by the particles. The presented analytical solutions were therefore compared with solutions obtained by a digital computer mentioned earlier. Results of this comparison are shown in Figure 2 for the throat pressure, velocity, and cross-sectional area. The subscript "exact" refers to the computer solution while "approx." indicates the foregoing analytical solution. Solid lines are derived from the complete equations while the broken lines are based on the equations in which the particle volume has been neglected. The particular flow parameters used in this example are shown in the figure.

Clearly, the approximation of the complete equations becomes practically perfect for sufficiently high loading ratios. The simplified solution agrees with the "exact" solution to better than 3% for loading ratios between about 5 and 50. For much larger loading ratios, it becomes inaccurate because the particle volume then should not be neglected, and for loading ratios below 5 its accuracy decreases because the flow then should not be treated as isothermal. It is fortunate that the simplified theory is valid over a range of the loading

UNCLASSIFIED

# UNCLASSIFIED

ratio that is also important for the transport of powdered materials.

Equation 13 and its simplified forms 16 or 17 show that the throat conditions can be computed directly without having to perform the entire nozzle calculation. This convenient result is obtained under the assumption of a constant fractional lag nozzle and does not apply to nozzles of arbitrary shape. In md cases, a complete nozzle calculation must be performed to follow the flow through the nozzle until the throat is reached. A convenient criterion may be derived that may be used to establish when the throat has been reached in the course of the calculations. Equations 2 to 4 may be written in differential form:

$$\frac{d\hat{h}_G}{\hat{h}_G} + \frac{du}{u} + \frac{dA}{A} = 0 \quad (19)$$

$$\frac{d\hat{h}_p}{\hat{h}_p} + \frac{dv}{v} + \frac{dA}{A} = 0 \quad (20)$$

$$\int_G u \, du + \int_p v \, dv + dp = 0 \quad (21)$$

Where  $\hat{h}_G = (1-\epsilon)\rho$  and  $p = \epsilon d$  are the gas and particle concentration.

With the throat condition  $dA/A = 0$ , Eqs. 19 to 21 may be combined to a relationship for the throat velocity

$$U_t^2 = \left( \frac{d\hat{h}_G}{dp} + \left(\frac{v}{u}\right)^2 \frac{d\hat{h}_p}{dp} \right)^{-1} \quad (22)$$

For the special case  $v = u$ , this equation becomes:

$$U_t^2 = \frac{dp}{dp_{\text{Mixture}}} \quad (23)$$

since the sum of the gas and particle concentrations equals the density of the mixture  $p_{\text{mixt}}$ . Equation (23) is wellknown from nonequilibrium gas flows<sup>5</sup> and has been used to test for the arrival at the throat. Equation 22 thus represents the extension to nonequilibrium

## UNCLASSIFIED

gas-particle flows. Both Eqs. 22 and 23 are of general validity and independent of the nonequilibrium processes; neither can be used to derive the throat conditions directly.

A warning seems to be in order against the application of Eq 23 to gas-particle flows. The resulting errors are readily evaluated for a constant fractional lag nozzle. For  $v/u = K$ , Eqs. 2, 3, 19, 20, and 22 can be combined to:

$$U_t^2 = \frac{1}{1+\gamma K} \frac{dp}{d\zeta_G} \quad (24)$$

while Eq. 23 when combined with Eqs. 2, 3, 19, and 20 leads to:

$$U_t^{1^2} = \frac{K}{K+\gamma} \frac{dp}{d\zeta_G} \quad (25)$$

The ratio  $U_t^1/U_t$  is plotted in Fig. 3 and shows that the use of  $U_t^1$  instead of  $U_t$  would lead to large errors unless the loading ratio were quite low or the velocity ratio close to one.

To summarize the earlier discussion, it was shown that a heavily loaded flow in a constant fractional lag nozzle may be conveniently analyzed by treating it as isothermal. In general, the particle volume then cannot be neglected, but it is interesting to note that there exists an intermediate range of the particle loading for which both isothermal flow and negligible particle volume can be assumed with resultant extreme simplifications of the analysis.

It remains for further work to show whether or not similar simplifications may be obtained also for other gas-particle flows.

UNCLASSIFIED

# UNCLASSIFIED

## REFERENCES

1. H. L. Burge, R. W. Roberts, and E. V. Zettle, "Dense Phase Transport of Powdered Metals for a Tripropellant Rocket System". Chemical Engineering Progress Symposium Series No. 52, Vol. 60, pp. 30-38, 1964.
2. C. T. Crowe, P. G. Willoughby, R. W. Woolfolk, R. Dunlap, C. E. Woolbridge, R. W. Hermsen, A. G. Cattaneo, and W. J. Corcoran, "Dynamics of Two-Phase Flow in Rocket Nozzles". United Technology Center Report UTC 2102-FR, September 1965.
3. J. R. Kliegel, "Gas Particle Nozzle Flows". Ninth Symposium (International) on Combustion, Academic Press, Inc., New York, 1963, pp. 811-826.
4. G. Rudinger, "Some Effects of Finite Particle Volume on the Dynamics of Gas-Particle Mixtures". AIAA Journal, Vol. 3, pp. 1217-1222, 1965.
5. W. G. Vincenti and C. H. Kruger, Jr., "Introduction to Physical Gas Dynamics". John Wiley and Sons, Inc., New York, 1965, p. 287.

UNCLASSIFIED



UNCLASSIFIED

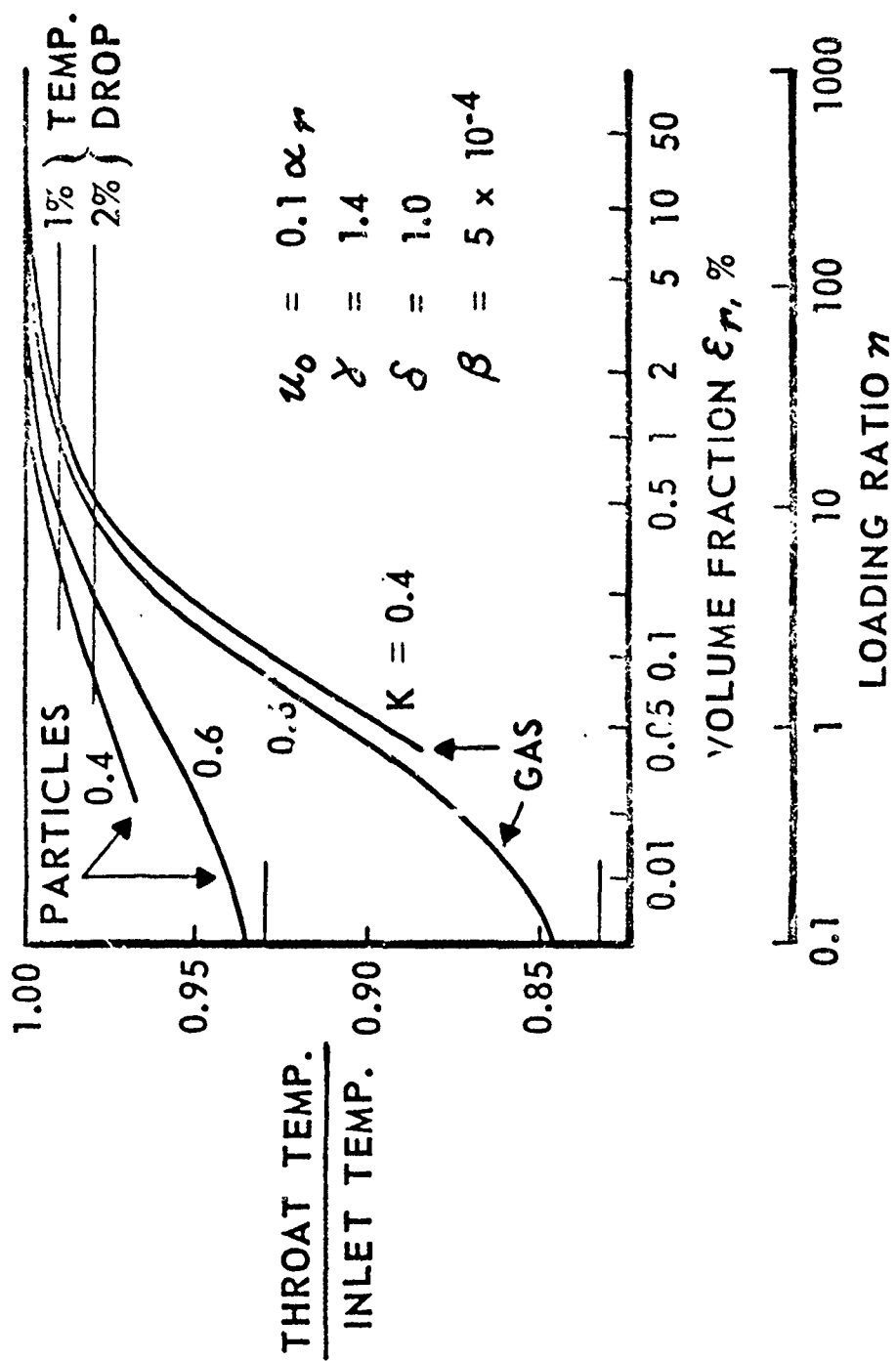


Figure 1. Temperature Ratios for Nozzle Throat.

UNCLASSIFIED

UNCLASSIFIED

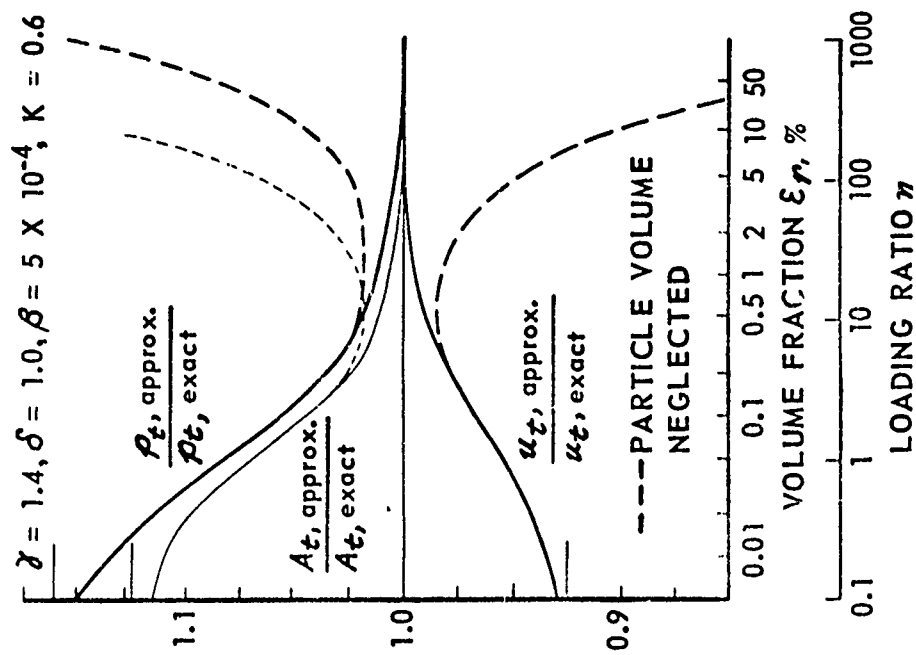


Figure 2. Approximation for Nozzle Throat.

UNCLASSIFIED

UNCLASSIFIED

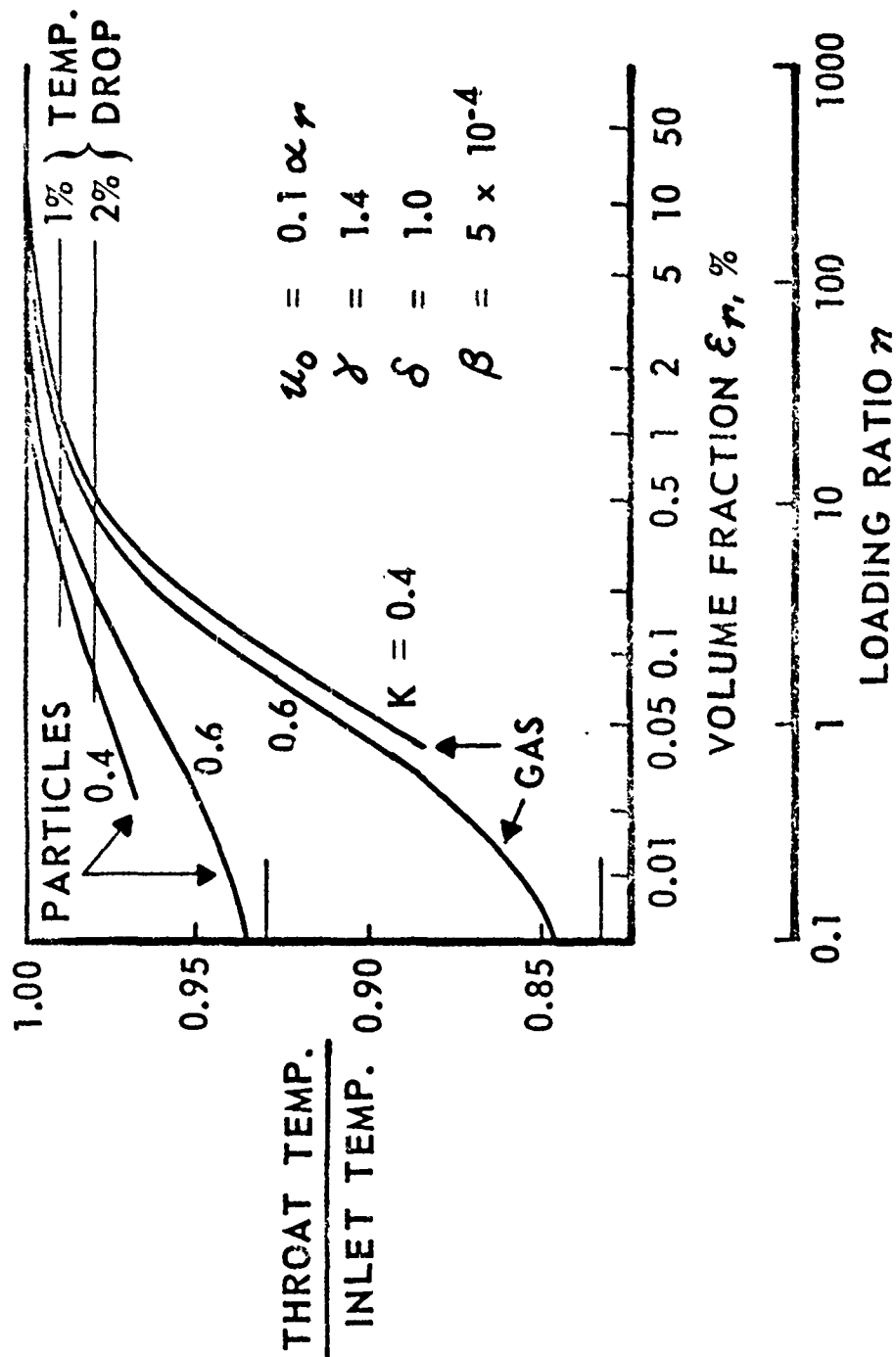


Figure 1. Temperature Ratios for Nozzle Throat.

UNCLASSIFIED

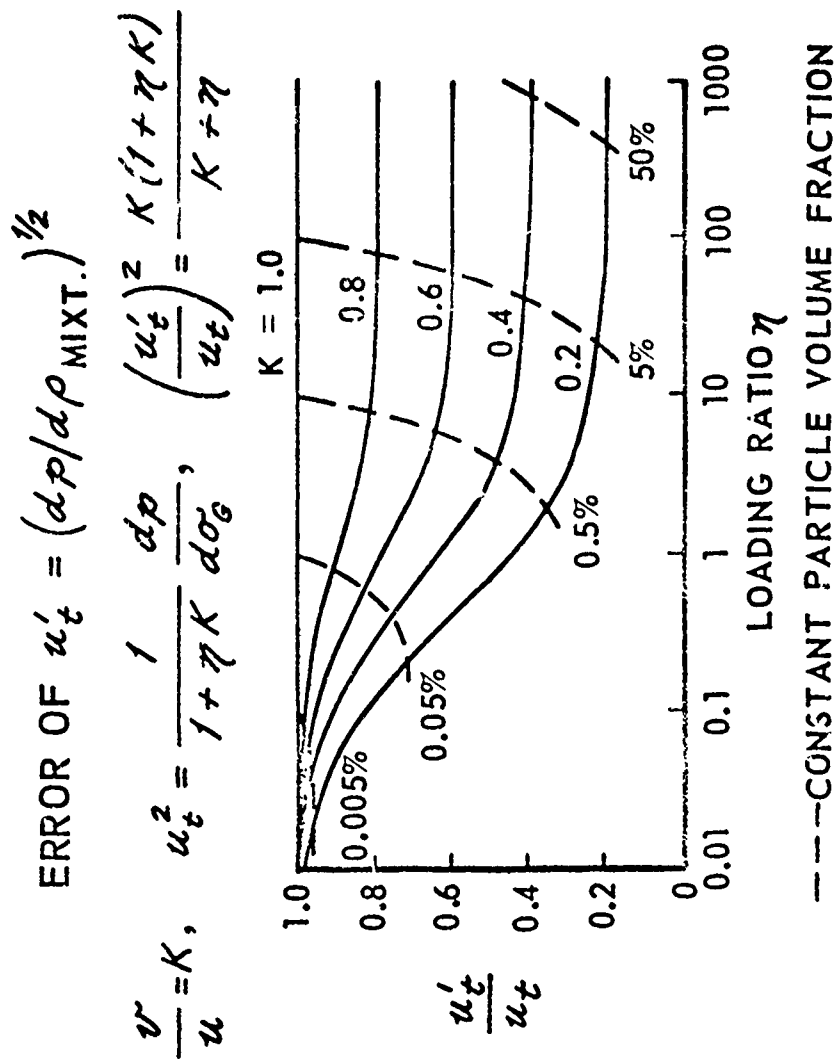


Figure 3.

# CONFIDENTIAL

## QUESTIONS, ANSWERS & COMMENTS:

Q./ J. R. Kliegel (Dynamic Science): Have these calculations been related to performance?

A./ G. Rudinger (Cornel Aeronautical Lab.): No, they have not. It is simply at the moment an attempt to solve the problem of a particular flow. It is part of a general study of the properties of such flows. Incidentally, since the approximation is so good, you can use these simplified equations even for a range outside of the immediate range. At least it would be a first approximation.

(C) Q./ A. Mager (Aerospace): It seems to me that if you were to apply this to performance you would have to add additional terms in the energy equation. I mean the particles are developing some energy. They are reacting, and consequently, the constant temperature assumption may not be as good as you think.

(C) A./ G. Rudinger (Cornell Aeronautical Lab.): If you have a chemical reaction going on, of course, then this is not quite enough. I might say here that loadings of this magnitude are not likely to be of significance for rocket propulsion, because the efficiency goes down very much with such high particle loadings. They would be more important for injection of powder into a rocket's chamber. That is one application that I have come across at Rocketdyne. As I said earlier, they are primarily of interest for transport of particle materials.

(C) Q./ R. F. Hoglund (Purdue University): Weren't the exhaust products of the pentaborane-hydrazine system in this range of particle loading?

# CONFIDENTIAL

## QUESTIONS, ANSWERS & COMMENTS:

A./ G. Rudinger (Cornell Aeronautical Lab.): I don't know.

Q./ W. Juran (Marquardt): If I followed you correctly, the analysis you have is based on the assumption that the solid particles and the gas are in thermal equilibrium, i.e., that the temperature of the particles and the gas is the same. Maybe I didn't follow you correctly. If I did, the question I ask is: Have you examined whether you have enough heat transfer there so that it is a good assumption? It seems like you did it in a fairly short time. If you have moderately large particles, I could see where you would not have an equilibrium temperature situation between them and the gas.

A./ G. Rudinger (Cornell Aeronautical Lab.): I am not worried about the possibility of having enough time for heat transfer. This solution is for a constant fractional lag nozzle. It only gives the relationship between the velocity and area. In order to get the longitudinal dimension, you have to integrate the equation of motion for whatever drag law you assume. There is an old study by Carrier, "Shock Waves in a Dusty Gas", where he pointed out that there is a reasonably good approximation if the Nusselt Number and the drag coefficient are related in such a way that the relationships can be used. One thing is important. Once you assume that the temperature is constant, you are not allowed to use the energy equation. In the energy equation, there are the terms  $U^2/2$  and  $C_p T$  and similar terms for the particles. Now, you cannot say the temperature is constant and therefore, we can neglect all the temperature terms. If you do,

# CONFIDENTIAL

## UNCLASSIFIED

### QUESTIONS, ANSWERS & COMMENTS:

you get a lot of nonsense. All we are saying here is that some terms are very large compared to other terms and you do not have to use this equation at all. Which means, as soon as you make the assumption that the temperature is constant, this is an approximation which is brought out by the exact calculation, but you cannot use this in the energy equation.

UNCLASSIFIED

**UNCLASSIFIED**

**TURBULENT MIXING OF GAS-PARTICLE  
AND PURE GAS STREAMS**

by

Duvvuri Tirumalesa

and

Roa S. Channapragada

CETEC Corporation  
Mountain View, California

**UNCLASSIFIED**



# UNCLASSIFIED

## TURBULENT MIXING OF GAS-PARTICLE AND PURE GAS STREAMS <sup>+</sup>

Duvvuri Tirumalesa\* and Rao S. Channapragada\*\*  
CETEC Corporation  
Mountain View, California

### ABSTRACT

An analytical solution to the turbulent mixing of a primary stream containing small solid particles with a pure gas secondary stream is presented. The compressible flow equations are transformed to the incompressible domain using Howarth transformation. In the transformed plane the mixing zone flow field is divided into three regions as near, transition and far fields defined by  $x \leq \lambda_m$  where  $\lambda_m$  is the momentum equilibration length for gas-particle velocity equilibration and  $x$  is the axial coordinate along the mixing zone.

The solution of the problem in the near and far fields is obtained by a power series expansion in  $x^* = x/\lambda_m$  and a local similarity variable. This leads to a solution for the gas stream function  $\psi_g$ , particle velocity lag,  $u_g$ , and particle gas density ratio  $\rho_p^*$  in terms of the well-known incompressible solutions.

Transforming back to the physical flow field, the compressible mixing zone spread and velocity profile are then predicted in terms of the incompressible spread parameter, the primary stream Crocco number, velocity ratio of the two streams and their total enthalpy ratios. A possible composite solution, valid uniformly throughout the flow field is considered.

### NOMENCLATURE

$a_1, a_2, a_3$	Constants of integration (Eq. 55).
$b$	Mixing zone width (Eq. 90).
$c$	Constant in mixing length (Prandtl-Tollmien formulation Eq. 89).

---

<sup>+</sup> Research sponsored by Edwards Air Force Base, Rocket Propulsion Laboratory, Contract No. FO4611-67-C-0011, under subcontract from Atlantic Research Corporation, Alexandria, Virginia.

\* Senior Staff

\*\* President

# UNCLASSIFIED

$c_1=(u_1-u_2)$	Constant in Gortler eddy viscosity formulation (Eq. 15', 19').
$c_p$	Specific heat of gas.
$c_{p,g}$	Constant in mixing length for particle or gas cloud (Eq. 84, 85).
$d_p$	Particle diameter.
$F_{p,x}, F_{p,y}$	Gas-particle interaction terms (Eq. 9, 10).
$h$	Static enthalpy.
$k_p$	Constant in Gortler eddy viscosity formulation for particles (Eq. 83', 86).
$k$	Gas thermal conductivity (Eq. 13).
$K = \xi_{p1} / \xi_1$	Initial particle loading.
$l$	Mixing length (Eq. 88').
$m_p$	Mass of particle
$n$	Number density or similarity exponent (Eq. 84).
$p$	Pressure.
$P = p / \xi_1 u_1^2$	
$Pr, Pr_t$	Laminar and turbulent Prandtl numbers.
$q$	Apparent heat conduction for gas (Eq. 4).
$Q_p$	Gas-particle heat conduction (Eq. 11).
$T$	Temperature.
$u, v$	x, y components of velocity.
$x, y$	Cartesian coordinates.
$y_i(x)$	$i=1$ primary, $2$ secondary, $p$ =particle boundaries of mixing zone in the compressible plane.
$\epsilon$	Eddy viscosity.
$\eta = \frac{\sigma_y}{x}$	Similarity variable.
$\eta' = \eta - \eta_{10}$	
$\eta_{10}$	Zeroeth order mixing zone boundary on primary side.
$\tau_m = m_p u_1 / 3 \pi d \mu$	Gas-particle momentum equilibration length.
$\tau_T = m_p u_1 c_p / 2 \pi d k$	Gas-particle thermal equilibration length.

# UNCLASSIFIED

$\mu$	Gas viscosity.
$\rho$	Density
$\alpha$	Jet spread parameter.
$\tau$	Shear stress.
$\psi$	Stream function.
$\lambda = \frac{u_2}{u_1}$	The ratio of secondary and primary stream velocities.

## Subscripts

p	Particle
g	Gas
s	Gas-particle lag
1	Primary stream
2	Secondary stream
f	Far field flow region
T	Turbulent or Tollmien
G	Gortler

## Superscripts

-	Incompressible, or mean of fluctuating quantities
*	Non-dimensional
'	Turbulent fluctuation components

## 1.0 INTRODUCTION

In recent times, the effect of the presence of solid particles in fluid flow has received considerable attention due to its importance in rocket nozzle flows.<sup>(1-6)</sup> In pure solid rockets, the unburned metalized propellant in the form of solid particles has an important effect on the properties of the exhaust stream (like temperature, exhaust velocity, radiation effects, etc.) which, in turn, affects the delivered thrust from such rockets. Considerable theoretical work has been done to study this effect on the exhaust stream,<sup>(1,2,3)</sup> to evaluate an optimum nozzle shape for minimum thrust losses.<sup>(4)</sup> In air-augmented solid rockets, that are currently being investigated, the particle loading consists of either aluminum, zirconium, or boron particles in the solid fuel. The primary exhaust containing these solid particles is

# UNCLASSIFIED

then mixed with pure air introduced into the secondary combustion chamber. Any analysis carried out to predict the ignition and combustion characteristics of these solid particles in the secondary combustion chamber must consider the effect of these particles on the mixing of the primary exhaust with the pure secondary air. At present, the theoretical analysis of the mixing zone is carried out by considering the particles to be in full thermal and velocity equilibrium with the gas. This could lead to considerable errors in the prediction of the performance of such air-augmented rockets due to velocity and thermal lags that would be present in any real flow situation. The aim of the present study is to evaluate the effect of these particle lags under simplifying assumptions.

## 2.0 ANALYSIS

In an air-augmented system, the primary and secondary streams will be bounded by the primary nozzle and either secondary combustion chamber or the shroud. The bounded flow would be axially symmetric. At the exit plane of the primary nozzle, there would be velocity and thermal lags between solid particles and gas. Also, these lags and the particle loading would not be necessarily uniform at the primary nozzle exit. In addition, there will be inviscid interaction between the primary and secondary streams. However, as a starting point in the analysis of the present paper, the following simplifying assumptions have been made, some of which may be removed at a later stage.

### 2.1 Assumptions

1. The turbulent mixing of two compressible, uniform, semi-infinite, two-dimensional streams is considered (see Fig. 1).
2. At the start of the mixing, the velocity and thermal lags of the particles are taken to be zero and a uniform particle loading is assumed.
3. The particle cloud is treated as a continuum.
4. Particle-particle interactions are neglected.
5. Fluid particle interactions are taken into account through Stokes drag law by considering the particles to be spherical. The particles are considered to have an average diameter " $d$ " and mass " $m_p$ ". The gas viscosity  $\mu$  is assumed to be constant.
6. Turbulent flow in the mixing zone with unit turbulent Prandtl number ( $Pr_t = 1$ ) is assumed.

# UNCLASSIFIED

7. The molecular transport terms are assumed to be negligible compared to the turbulent transport terms within the mixing zone.
8. Constant pressure mixing is assumed and axial pressure gradients are neglected.

## 2.2 Basic Equations

Under the above assumptions, the basic equations for the gas particle flows in the mixing zone (with the usual boundary layer approximations and without taking into account the effect of turbulent fluctuations of the particle cloud) (see Ref. 7 for details) are given by:

### GAS

$$\text{Mass: } (\rho u)_x + (\rho v)_y = 0 \quad (1)$$

$$\text{Momentum: } \rho(uu_x + vu_y) = \tau_y + F_{p,x} \quad (2)$$

$$\rho(uv_x + vv_y) = F_{p,y} - \frac{\partial p}{\partial y} \quad (3)$$

$$\text{Energy: } \rho(uh_x + vh_y) = q_y + \tau_{uy} + (u_p - u)F_{p,x} + Q_p \quad (4)$$

### PARTICLE CLOUD

$$\text{Mass: } (\rho_p u_p)_x + (\rho_p v_p)_y = 0 \quad (5)$$

$$\text{Momentum: } \rho_p(u_p u_{px} + v_p u_{py}) = -F_{p,x} \quad (6)$$

$$\rho_p(u_p v_{px} + v_p v_{py}) = -F_{p,y} \quad (7)$$

$$\text{Energy: } \rho_p(u_p h_{px} + v_p h_{py}) = -Q_p \quad (8)$$

$F_{p,x}$ ,  $F_{p,y}$ , the force terms due to gas-particle velocity lag are:

$$F_{p,x} = \rho_p u_l (u_p - u) / \tau_m \quad (9)$$

$$F_{p,y} = \rho_p u_l (v_p - v) / \tau_m \quad (10)$$

and  $Q_p$ , the heat transfer between gas and particles is:

$$Q_p = \rho_p c_p u_l (T_p - T) / \tau_T \quad (11)$$

$\tau_m$ ,  $\tau_T$ , the momentum and thermal equilibration lengths, are given by:

$$\tau_m = m_p u_l / 3\pi d \mu \quad (12)$$

# UNCLASSIFIED

$$\lambda_T = m_p u_1 c_p / 2\pi dk = 3 \text{ Pr } \lambda_m / 2 \quad (13)$$

It may be noted from Equation (7) that  $F_{p,y}$  is a higher order term like  $\partial p / \partial y$  in the boundary layer equations and that Eqs. (3) and (7) may be replaced by:

$$v_p \approx v \quad (14)$$

In Tollmien formulation, the eddy viscosity is:

$$\epsilon_T = \ell^2 u_y = x^2 u_y / 2 \sigma^3 \quad (15)$$

In Gortler's formulation, one has for the eddy viscosity:

$$\epsilon_G = c_1 x / 2 \sigma^2, \quad c_1 = (u_1 - u_2) \quad (15')$$

## BOUNDARY CONDITIONS

The boundary conditions at the mixing zone boundaries  $y_1(x)$  and  $y_2(x)$  (see Fig. 1) are:

$$\begin{aligned} \rho_p &= \rho_{p1}, \quad u = u_p = u_1, \quad u_y = 0, \quad v = v_p \text{ at } y = y_1(x) \\ u &= u_2, \quad u_y = 0 \text{ at } y = y_2(x) \end{aligned} \quad (16)$$

### 2.3 Transformation to Incompressible Plane

The problem in the physical plane may be treated conveniently in the transformed plane through the Howarth transformation:<sup>(12)</sup>

$$\bar{x} = x, \quad \bar{y} = \int_0^y \frac{\rho}{\rho_r} dy, \quad \psi(x, y) = \bar{\psi}(\bar{x}, \bar{y}) \quad (17)$$

and the gas stream function  $\psi = \bar{\psi}$  is given by

$$d\psi = \rho u dy - \rho v dx, \quad [d\bar{\psi} = \rho_r (\bar{u} d\bar{y} - \bar{v} d\bar{x})] \quad (18)$$

Coles<sup>(8)</sup> and Crocco<sup>(9)</sup> have considered the possibility of removing the restriction in the transformation of Equation (17). In order to reduce the complexity of the present problem, these modifications are not taken into account.

#### 2.3.1 Shear Stress

It has been shown in Ref. 10 that the turbulent shear stress is invariant under Howarth transformation. Hence, the shear stress for

# UNCLASSIFIED

Tollmien formulation is given by:

$$\tau_T = \rho \epsilon_{T u_y} = \rho_r \bar{\epsilon}_T \bar{u}_y = \bar{\tau} = \rho_r \bar{x}^2 \bar{u}_y^2 / 2 \bar{\sigma}^3 \quad (19)$$

or, for Gortler formulation we have

$$\tau_G = \rho \epsilon_{G u_y} = \rho_r \bar{\epsilon}_G \bar{u}_y = \bar{\tau} = \rho_{rc1} \bar{x} \bar{u}_y / 2 \bar{\sigma}^2 \quad (19')$$

where the incompressible jet spread parameter  $\bar{\sigma}$  is related to  $\sigma$  through the relation

$$\bar{\sigma} / \sigma = \rho_r / \rho \quad (20)$$

## 2.3.2 Particle Properties

For the particles, also, it is assumed that:

$$\psi_p(x, y) = \bar{\psi}_p(\bar{x}, \bar{y}) \quad (21)$$

where

$$d\psi_p = \rho_p(u_p dy - v_p dx), \quad [d\bar{\psi}_p = \bar{\rho}_p \bar{u}_p d\bar{y} - \bar{\rho}_p \bar{v}_p d\bar{x}] \quad (22)$$

with  $\bar{\rho}_p = \bar{\rho}_p(\bar{x}, \bar{y})$ . Under this assumption, one finds that

$$\rho_p u_p = \bar{\rho}_p \bar{u}_p \cdot \rho / \rho_r \quad (23)$$

Since the combination  $(u_p - u)$  enters into the x-momentum equation of the gas and particles ( $F_{p,x}$  in Eqs. (2) and (6)), it was assumed that  $\bar{u}_p(\bar{x}, \bar{y}) = u_p(x, y)$  in the transformation. Thus,  $\bar{\rho}_p$  is related to  $\rho_p$  through the relation

$$\bar{\rho}_p / \rho_p = \rho_r / \rho \quad (24)$$

Further, it is assumed that  $\lambda_m = \bar{\lambda}_m$  (24')

so that

$$F_{p,x} / \rho = u_1(u_p - u) \rho_p / \rho \lambda_m = \bar{u}_1(\bar{u}_p - \bar{u}) \bar{\rho}_p / \rho_r \bar{\lambda}_m \quad (25)$$

where

$$\bar{\lambda}_m = \bar{m}_p \bar{u}_1 / 3\pi \bar{d} \bar{\mu} \quad (26)$$

Thus, Eqs. (24) and (24') relate the particle properties in the physical (compressible) to those of the transformed (incompressible) planes (see Ref. 11 for discussion of these relations).

# UNCLASSIFIED

## 2.3.3 Basic Equations of Motion in the Transformed Plane

The mass and x-momentum equations for the gas and particles (Eqs. 1, 2, 5, 6) take the following form in the transformed incompressible plane (considering the shear stress and particle properties of Sections 2.3.1 and 2.3.2):

### GAS

$$(\rho_r \bar{u})_{\bar{x}} + (\rho_r \bar{v})_{\bar{y}} = 0 \quad (27)$$

$$\bar{u} \bar{u}_{\bar{x}} + \bar{v} \bar{u}_{\bar{y}} = \bar{\tau}_{\bar{y}} / \rho_r + (\bar{\rho}_p / \rho_r) \bar{u}_1 (\bar{u}_p - \bar{u}) / \bar{\tau}_m \quad (28)$$

### PARTICLES

$$(\bar{\rho}_p \bar{u}_p)_{\bar{x}} + (\bar{\rho}_p \bar{v}_p)_{\bar{y}} = 0 \quad (29)$$

$$\bar{u}_p \bar{u}_{p\bar{x}} + \bar{v}_p \bar{u}_{p\bar{y}} = -\bar{u}_1 (\bar{u}_p - \bar{u}) / \bar{\tau}_m \quad (30)$$

Note that the y-momentum equations, (3) and (7), are replaced by  $v_p \approx v$  as pointed out in Section 2.2. The shear stress term for Tollmien formulation is given by

$$\bar{\tau}_{\bar{y}} / \rho_r = (\bar{x}^2 \bar{u}_{\bar{y}}^2 / 2 \bar{\sigma}^3)_{\bar{y}} = \bar{x}^2 \bar{u}_{\bar{y}} \bar{u}_{\bar{y}\bar{y}} / \bar{\sigma}^3 \quad (31)$$

and for Gortler case by

$$\bar{\tau}_{\bar{y}} / \rho_r = c_1 \bar{x} \bar{u}_{\bar{y}\bar{y}} / 2 \bar{\sigma}^2 \quad (32)$$

Since Eqs. (28) and (30) contain the slip velocity  $(\bar{u}_p - \bar{u})$ , it is convenient to rewrite them in terms of the variables  $\bar{u}$ ,  $\bar{v}$ ,  $(\bar{u}_p - \bar{u}) = \bar{u}_s$  and, also, Eq. (27) is identically satisfied by the introduction of the gas stream function  $\bar{\psi}$  (Eq. 18).

Let us introduce the following non-dimensionalization,

$$x^* = \bar{x} / \bar{\tau}_m, \quad y^* = \bar{y} / \bar{\tau}_m$$

$$u^* = \bar{u} / c \bar{u}_1, \quad v^* = \bar{v} / c \bar{u}_1, \quad u_s^* = \bar{u}_s / c \bar{u}_1$$

$$\bar{\psi} = \rho_r c \bar{u}_1 \psi^*$$

$$\rho_p^* = \bar{\rho}_p / \rho_r K = \bar{\rho}_p / K \quad \text{where } K = \rho_{p1} / \rho_1 \text{ is the initial}$$

particle loading,  $c = 1$  in Tollmien formulation and equal to  $(u_1 + u_2) / 2u_1$ , in Gortler formulation. Eqs. (28) to (30) now become

$$u^* \rho_{p,x^*}^* + v^* \rho_{p,y^*}^* + (\rho_p^* u_s^*)_{x^*} = 0 \quad (34)$$



# UNCLASSIFIED

$$(1 + K \xi_p^*) (u^* u_{x^*}^* + v^* u_{y^*}^*) + K \xi_p^* \left[ u^* u_{s^* x^*}^* + v^* u_{s^* y^*}^* + u_{s^*}^* (u_{s^*}^* + u^*)_{x^*} \right] = -\tau_{y^*}^* / \xi_r \quad (35)$$

$$u^* u_{s^* x^*}^* + v^* u_{s^* y^*}^* + u_{s^*}^* (u_{s^*}^* + u^*)_{x^*} = -\tau_{y^*}^* / \xi_r - (1 + K \xi_p^*) u_{s^*}^* \quad (36)$$

where the approximation  $v_p^* \approx v^*$  is made use of.

## 2.4 Solution of the Problem in the Transformed Plane

In solving Eqs. (34) - (36) along with (18), the flow field will be divided into three regions,  $x^* \ll 1$ ,  $x^* \sim 1$ , and  $x^* \gg 1$ , designated as near, transition and far field regions, respectively. For the near field,  $x^* \ll 1$ , the distance  $\bar{x}$  traveled by the particles is very much less than the momentum equilibration length  $\bar{\lambda}_{in}$  and, thus, would deviate only slightly from their upstream values. Thus, in this region the solution may be obtained by expanding  $\psi^*$ ,  $u_{s^*}^*$ ,  $\xi_p^*$  in power series in  $x^*$  and a local similarity variable  $\eta^* = \bar{\sigma} y^* / x^*$  as follows:

$$\psi^* = \frac{x^*}{\bar{\sigma}} \left[ f_0(\eta^*) + x^* f_1(\eta^*) + \dots \right] \quad (37)$$

$$u_{s^*}^* = u_{0s}(\eta^*) + x^* u_{1s}(\eta^*) + \dots \quad (38)$$

$$\xi_p^* = R_0(\eta^*) + x^* R_1(\eta^*) + \dots \quad (39)$$

where the first terms correspond to the case of  $x^* \rightarrow 0$ .

For the far field case,  $x^* \gg 1$ , the particles would have traveled a distance much larger than the momentum equilibration length and, thus, would have reached very nearly the equilibrium values. In this region, the solution may be obtained by expanding  $\psi^*$ ,  $u_{s^*}^*$ ,  $\xi_p^*$  in power series in  $1/x^*$  and a local similarity variable  $\eta_f^* = (1 + K)^n \bar{\sigma} y^* / x^*$  as

$$\psi^* = \frac{x^*}{\bar{\sigma}} \left[ F_0(\eta_f^*) + \frac{1}{x^*} F_1(\eta_f^*) + \dots \right] \quad (40)$$

$$u_{s^*}^* = (1 + K)^{2n} \left[ \frac{1}{x^*} U_{1s}(\eta_f^*) + \dots \right] \quad (41)$$

$$\xi_p^* = 1 + (1 + K)^n \left[ \frac{1}{x^*} R_{1f}(\eta_f^*) + \dots \right] \quad (42)$$

The factor  $(1 + K)^n$  entering into  $\eta_f^*$ ,  $u_{s^*}^*$ ,  $\xi_p^*$  is arrived at by requiring that the equations for  $F_0$ ,  $U_{1s}$ ,  $R_{1f}$  when substituted in Eqs. (34-39) shall be independent of  $K$ . By carrying out this analysis, one finds that  $n = 1/3$  for Tollmien formulation and  $n = 1$  for Gortler formulation (see Ref. 11 for details).

Also, the mixing zone boundaries  $y = y_1(x)$  and  $y = y_2(x)$  and the limiting particle boundary  $y = y_p(x)$  are expanded in terms of the

# UNCLASSIFIED

similarity variables as

$$\eta_i = \eta_{i0} + x^* \eta_{i1} + x^{*2} \eta_{i2} + \dots, (i = 1, 2, p) \quad (43)$$

for the near field, and

$$\eta_{fi} = \eta_{fi0} + \frac{1}{x^*} \eta_{fi1} + \frac{1}{x^{*2}} \eta_{fi2} + \dots, (i = 1, 2, p) \quad (44)$$

for the far field where the subscripts  $i = 1, 2, p$  correspond to the primary, secondary and limiting particle boundaries (see Fig. 1).

## 2.4.1 Near Field Flow

By substituting the expansions (37, 38, 39, 43) in Eqs. (34, 35, 36, 16), one obtains the following equations and boundary conditions (see Ref. 10 for details).

### Tollmien Formulation Equations:

Zeroeth Order:

$$f_o + f_o''' = 0 \quad (45)$$

$$(u_{os} + f_o')' = 0 \quad (46)$$

$$R_o' c(\eta) + \eta R_o u_{os}' = 0 \quad (47)$$

First Order:

$$f_1''' f_o'' - f_1' f_o' + 2f_1 f_o'' + K R_o u_{os} = 0 \quad (48)$$

$$(u_{1s} + f_1')' c(\eta) + (u_{os} + f_o')(2f_1 + \eta u_{1s}) - \quad (49)$$

$$(u_{1s} + f_1')(u_{os} + f_o') - u_{os} = 0$$

$$R_1' c(\eta) - R_1(u_{os} + f_o' - \eta u_{os}') + R_o' \cdot \quad (50)$$

$$(2f_1 + \eta u_{1s}) - R_o(u_{1s} - \eta u_{1s}') = 0$$

where primes denote differentiation with respect to  $\eta$  and  $c(\eta)$  is defined as  $c(\eta) = f_o + \eta u_{os}$  (51)

Boundary Conditions:

$$f_o'(0) = 1, f_o''(0) = 0, f_o'(\eta_{210}) = \lambda, f_o''(\eta_{210}) = 0 \quad (52)$$

$$f_o(0) = \eta_{10}, u_{os}(0) = 0, R_o(0) = 1, c(\eta_{p0}') = 0$$

# UNCLASSIFIED

$$f_1(0) = 0, f_1'(0) = 0, f_1''(0) = \eta_{11} \eta_{10}, f_1'(\eta_{210}) = 0, \\ f_1'''(\eta_{210}) + \eta_{21} f_1''(\eta_{210}) = 0, u_{1s}(0) = 0 \quad (53)$$

$$R_1(0) = 0, R_1(\eta_{po}') + \eta_{p1} R_1'(\eta_{po}') = 0$$

where  $\eta'$  is defined as

$$\eta' = \eta - \eta_{10} \text{ and } \eta_{210} = \eta_{20} - \eta_{10} \quad (54)$$

Zero Order Equations:

Eq. (45) is the same as no particle result and has the solution

$$f_0 = a_1 e^{-\eta'} + e^{\eta'/2} \left[ a_2 \cos \sqrt{\frac{3}{2}} \eta' + a_3 \sin \sqrt{\frac{3}{2}} \eta' \right] \quad (55)$$

where  $a_1, a_2, a_3$  are constants of integration.

Eq. (46) integrates to

$$u_{0s} = 1 - f_0' \quad (56)$$

where the constant of integration is evaluated as unity from the boundary condition.

Eq. (47) can be readily integrated to

$$R_0 = \eta_{10} B(\eta)/c(\eta) \quad (57)$$

$$\text{where } B(\eta) = \int_{\eta_{10}}^{\eta} d\eta/c(\eta) \quad (58)$$

The integration is carried out from the edge of the mixing zone on the primary stream side and the constant of integration is evaluated to be zero from the boundary condition. The zeroeth order limiting particle boundary  $\eta_{po}'$  is obtained from  $c(\eta_{po}') = 0$ .

First Order Equations:

The first order correction to the gas stream function  $f_1$  given by Eq. (48) cannot be integrated as simply as above and has to be integrated numerically. One may also note that Eq. (48) contains the initial particle loading  $K = \eta_{p1}/\eta_{11}$  explicitly. However, one may evaluate  $f_1/K$  as a universal function. Also, after the limiting particle boundary is reached, one has to equate to zero the particle functions ( $u_{0s}, R_0$ ) in Eq. (48) for obtaining  $f_1$  beyond the particle boundary (P.B.). Thus, one has to solve

After the P.B.:

$$f_1''' f_0'' - f_1' f_0''' + 2 f_1 f_0'''' = 0 \quad (59)$$

# UNCLASSIFIED

# UNCLASSIFIED

The first order correction to the particle velocity lag is given by Eq. (49) which may be simplified up to the particle boundary with the aid of Eq. (56) to

Up to the P.B.:

$$(u_{1s} + f_1')'(f_0 + \eta u_{0s}) - (u_{1s} + f_1') - u_{0s} = 0 \quad (60)$$

which may be readily integrated to

$$(u_{1s} + f_1') = B(\eta) \cdot \int_{\eta_{10}}^{\eta} \frac{u_{0s} d\eta}{B(\eta)c(\eta)} \quad (61)$$

where  $c(\eta)$ ,  $B(\eta)$  are defined in Eqs. (51) and (58).

After the limiting particle boundary is reached, one has to put  $u_{0s} = 0$  in the above equation, thus one has

After the P.B.:

$$(u_{1s} + f_1')'f_0 - (u_{1s} + f_1')f_0' + f_0''(2f_1 + \eta u_{1s}) = 0 \quad (62)$$

The first order correction to particle loading  $R_1$  is given by Eq. (50) which up to the zero order limiting particle boundary may be simplified by the aid of Eq. (56) to

Up to the P.B.:

$$R_1'(f_0 + \eta u_{0s}) - R_1(1 - \eta u_{cs}') + R_0'(2f_1 + \eta u_{1s}) - R_0(u_{1s} - \eta u_{1s}') = 0 \quad (63)$$

which may be integrated to

$$R_1 = \frac{B^2(\eta)}{c(\eta)} \int_{\eta_{10}}^{\eta} \frac{D(\eta)d\eta}{B^2(\eta)} \quad (64)$$

$$\text{where } D(\eta) = R_0(u_{1s} - \eta u_{1s}') - R_0'(2f_1 + \eta u_{1s}) \quad (65)$$

The first order correction to the limiting particle boundary is obtained from

$$R_1(\eta'_{po}) + \eta_{pl}R_0'(\eta'_{po}) = 0 \quad (66)$$

## 2.4.2 Far Field Flow

The far field equations are obtained by substituting the expansions (40, 41, 42, 44) in the Eqs. (34, 35, 36, 16) as follows (see Ref. 11 for details):

# UNCLASSIFIED

## Tollmien Formulation Equations:

### Zeroeth Order:

$$(F_o''' + F_o) = 0 \quad (67)$$

$$U_{1s} + F_o'' F_o''' = 0 \quad (68)$$

$$(R_{1f} F_o + \eta_{f1}^* U_{1s})' = 0 \quad (69)$$

### First Order:

$$\left[ (1+K)^{2/3} / K \right] (F_o'' F_1'' + F_o F_1')' + F_o'' (R_{1f} F_o + \eta_{f1}^* U_{1s}) + (U_{1s} F_o)' = 0 \quad (70)$$

### Boundary Conditions:

$$(1+K)^{1/3} F_o'(0) = 1, F_o''(0) = 0, (1+K)^{1/3} F_o'(\eta_{f210}) = \lambda$$

$$F_o''(\eta_{f210}) = 0, (1+K)^{1/3} F_o(0) = \eta_{f10}, U_{1s}(0) = 0 \quad (71)$$

$$R_{1f}(0) = 0, F_o(\eta_{fpo}') = 0$$

$$F_1'(\eta_{f210}) = F_1'(0) = 0, (1+K)^{1/3} F_1''(0) = \eta_{f10} \eta_{f11}, \quad (72)$$

$$F_1''(\eta_{f210}) = \eta_{f21} F_o(\eta_{f210}), F_1(0) = F_1(\eta_{f210})$$

### Zero Order Equations:

Eq. (67) gives the zero order gas stream function  $F_o$  which satisfies the same equation in  $\eta_{f1}^*$  as the near field  $f_o$  in terms of  $\eta$ . Thus, the solution may be written as before to be

$$(1+K)^{1/3} F_o(\eta_{f1}^*) = a_1 e^{-\eta_{f1}'} + e^{\eta_{f1}'/2} \left[ a_2 \cos \frac{\sqrt{3}}{2} \eta_{f1}' + a_3 \sin \frac{\sqrt{3}}{2} \eta_{f1}' \right] \quad (73)$$

where  $\eta_{f1}' = \eta_{f1}^* - \eta_{f10}^*$ , and  $\eta_{f10}^*$  is the edge of the mixing zone on the primary stream side and  $a_1, a_2, a_3$  are constants of integration and have the same values as in Eq. (55). The factor  $(1+K)^{1/3}$  in front of  $F_o$  in Eq. (73) is introduced to have  $a_1, a_2, a_3$  the same values as before since the boundary conditions given in Eq. (71) contain the factor  $(1+K)^{1/3}$  compared to those given in Eq. (52).

Eq. (68) gives the zero order velocity lag readily which, with the aid of Eq. (67), may be written as

# UNCLASSIFIED

$$U_{1s} = F_0 F'' \quad (74)$$

Eq. (69) for the zero order particle loading may be readily integrated to yield

$$R_{1f} = -\eta_f^* F_0'' \quad (75)$$

where Eq. (74) for  $U_{1s}$  is used.

The limiting particle boundary is obtained from

$$F_0(\eta_{fpo}) = 0 \quad (76)$$

First Order Equations:

Only the first order correction to the gas stream function is given in the present note by the Eq. (70) which up to the limiting particle boundary reduces with the aid of Eq. (74) and (75) to

Up to the P.B.:

$$\left[ (1 + K)^{2/3} / K \right] (F_0'' F_1'' + F_0' F_1')' + F_0'^2 F_0'' = 0 \quad (77)$$

which may be readily integrated to

$$\left[ (1 + K)^{2/3} / K \right] F_1' = F_0'' \left[ - \int F_0'^2 / F_0'' d\eta_f^* + \text{const} \right] \quad (78)$$

from which one finally obtains  $F_1$  as

$$\left[ (1 + K)^{2/3} / K \right] F_1 = \int F_0'' \left[ - \int F_0'^2 / F_0'' d\eta_f^* \right] d\eta_f^* + A_1 F_0' + A_2 \quad (79)$$

Beyond the limiting particle boundary, Eq. (70) has to be re-written by equating the particle functions  $U_{1s}$ ,  $R_{1f}$  to zero, thus leading to

Beyond the P.B.:

$$\left[ (1 + K)^{2/3} / K \right] (F_0'' F_1'' + F_0' F_1') = 0 \quad (80)$$

which may be integrated to

$$(1 + K)^{2/3} / K (F_0'' F_1'' + F_0' F_1') = \text{constant} \quad (81)$$

## 2.4.3 Gortler Formulation

Sections 2.4.1 and 2.4.2 dealt with the solution of the problem with the Tollmien formulation of the eddy viscosity. One can get similarly another set of equations for the Gortler formulation of eddy viscosity by substituting Eq. (32) for the turbulent shear stress in Eqs. (34) to (36) and using the expansions (37-29) for the near field and Eqs. (40) to (42) for the far field. Only the salient features of this are given here

## UNCLASSIFIED

(see Ref. 11) for details) which are:

(1) The first order gas velocity functions  $f_0(\eta)$  and  $F_0(\eta_f)$  satisfy the no-particle (or pure gas) equation, namely,

$g''' + gg'' = 0$  ( $g = f_0$  or  $F_0$  and prime denotes differentiation with respect to  $\eta$  or  $\eta_f$ ).

(2) As already pointed out earlier, the exponent  $n$  in Eqs. (40)-(42) takes the value unity in contrast to Tollmien case where it is  $1/3$ .

(3) The dependence of zeroeth order particle velocity lag and particle loading functions on  $f_0$  or  $F_0$  are the same as in the Tollmien formulation.

### 2.4.4 Some Results

As an illustration of the solution, the functions  $f_0'$ ,  $f_1'/k$ ,  $u_{0s}$ ,  $u_{1s}$ ,  $R_0$ ,  $R_1$  and  $F_0'$ ,  $(1+K)^{2/3} F_1'/k$ ,  $U_{1s}$ ,  $R_{1f}$  for  $K = 0.5$  and  $u_2 = 0$  are presented in Figs. 2, 3, 4 for the Tollmien formulation. Note that the explicit use of  $K$  occurs only in the calculation of  $R_1$  whereas all other functions are universal functions. Even though  $f_0'$  is the same as no particle result, it is added in the figure for the sake of completeness. It is seen from Fig. 4 that the particle loading  $R_0$  in the near field decreases from its freestream value to some finite value near the limiting particle boundary where it becomes indeterminate due to the singular nature (i.e., varying from a finite value to zero beyond the limiting particle boundary). The particle velocity lag,  $u_{0s}$ , at this point is finite. In the far field the first order correction to the particle loading  $R_{1f}$  changes from a negative value near freestream to a positive value near the limiting particle boundary. Noting that the first term in Eq. (42) is unity, one can see that the total particle loading (up to first order) initially decreases and then increases to a finite value at the limiting particle boundary as in the near field case. The first order correction to the particle velocity lag  $U_{1s}$  (the zeroeth order correction  $U_{0s} = 0$ , i.e., fully equilibrated with gas velocity) (Fig. 3) passes through a maximum reaching zero value near the limiting particle boundary in contrast to the near field result ( $u_{1s}$ ) which monotonically increases to a finite value at the limiting particle boundary. (i.e., the particles move with gas velocity).

## 3.0 DISCUSSION

In this section, four points concerning the analysis given earlier are considered, namely,

- (1) The effect of particle turbulence on the flow equations (Eqs. 1-8).
- (2) The eddy viscosity formulation and the jet spread parameters.
- (3) Extension of the solution in the incompressible plane to the transition region ( $x^* \approx 1$ ).

UNCLASSIFIED

# UNCLASSIFIED

(4) Inverse transformation from the incompressible to compressible plane.

## 3.1 The Effect of Particle Turbulence on Flow Equations

The compressible equations of motion for the gas and particles in the mixing zone (Eqs. 1-8) are obtained by (i) assuming the particle cloud as a continuum and (ii) considering each flow quantity to be composed of a mean and fluctuating component and taking the time average to obtain the equations satisfied by the mean values. As the particle cloud is being treated as a continuum, the particle properties are also to be treated as consisting of a mean and a fluctuating component. As shown in Ref. 7, this leads to the following modifications:

(a) The x-momentum equation for the gas remains unaffected.

(b) The x-momentum equation for the particle cloud contains a shear stress term similar to the gas case, which is dependent on particle properties alone. This leads to the introduction of a particle eddy diffusivity if one follows the pure gas case. Thus, the shear stress for the particle cloud is given by

$$\tau_{Tp} = \overline{\rho_p u_p' v_p'} = \overline{\rho_p} \epsilon_{Tp} \bar{u}_{py} \quad (82)$$

The eddy viscosity for particle cloud in Tollmien formulation is given by

$$\epsilon_{Tp} = l_p^2 \bar{u}_{py} = c_p^2 x^2 \bar{u}_{py} \quad (83)$$

and for Gortler formulation as

$$\epsilon_{Tp} = k_p x (\bar{u}_{pmax} - \bar{u}_{pmin}) \quad (83')$$

In these formulations the constants  $c_p$ ,  $k_p$  are to be determined experimentally. However, one could propose the constants to be of the form

$$(c_p, k_p) = (c_g, k_g) \left( \frac{n_p d_p}{n_g d_g} \right)^n \quad (84)$$

such that  $c_p, k_p \rightarrow c_g, k_g$  in the limits of particles tending to gas properties or particle cloud tending to zero where subscript  $g$  denotes gas and the exponent  $n$  is a constant. From the zeroeth order far field results (i.e.,  $u_p \rightarrow u$ , or  $U_{os} \rightarrow 0$ ), one finds that the effect of the presence of particles is essentially that of increasing the jet spread parameter from  $\bar{\sigma}$  in the near field to  $(1 + K)^n \bar{\sigma}$  in the far field. The  $c_g$  and  $k_g$  are essentially  $(1/2 \sigma^3)^{1/2}$  and  $(2 \sigma^2)^{-1}$ . Thus, it appears reasonable to postulate that

$$c_{particle} = c_p = \left[ \left( 1 + \frac{\rho_{p1}}{\rho_{i1}} \right)^{3n} 2 \sigma^3 \right]^{-1/2} = \left[ 2(1 + K) \sigma^3 \right]^{-1/2} \quad (84a)$$



# UNCLASSIFIED

in the Tollmien formulation where  $n = 1/3$  and

$$k_{\text{particle}} = k_p = [2\sigma^2(1+K)^{2n}]^{-1} = [2\sigma^2(1+K)^2]^{-1} \quad (84b)$$

in the Gortler formulation where  $n = 1$ . The jet spread parameter occurring in these equations is the no-particle value.

(c) The y-momentum equation for the gas remains unaffected as long as  $p$  is defined to include the apparent normal stresses.

(d) The y-momentum equation for the particle cloud introduces an apparent normal stress term (y component). The y-momentum equations for the gas and particle cloud can be combined to yield two alternate equations, namely,

$$p_{\text{total}} = \bar{p} + \bar{\rho} \overline{v'^2} + \bar{\rho}_p \overline{v_p'^2} = \text{const.} \quad (85)$$

where the second and third terms are the apparent normal stresses due to the gas and particle cloud. The second equation is

$$\frac{1+K}{K} \frac{u_1}{\lambda_m} \bar{\rho}_p (\bar{v}_p - \bar{v}) = - \left[ \bar{p} + \bar{\rho} \overline{v'^2} - \frac{1}{K} \frac{\bar{\rho}_p}{\bar{\rho}} \overline{v_p'^2} \right]_y \quad (86)$$

or

$$\frac{u_1}{\lambda_m} \bar{\rho}_p (\bar{v}_p - \bar{v}) = - \left[ \bar{p} + \bar{\rho} \overline{v'^2} - \frac{\bar{\rho}_p}{\bar{\rho}} \overline{v_p'^2} \right]_y \quad (86')$$

where bars and primes denote mean and fluctuating components respectively. Eq. (86) may be interpreted as saying that the gas-particle y velocity lag is driven by the y gradient of the difference between the particle and gas normal (including the apparent) stresses.

(e) The apparent normal stresses in Eqs. (85) and (86) may be replaced in terms of  $\epsilon_T$ ,  $\epsilon_{Tp}$  and  $\bar{v}$ ,  $\bar{v}_p$  if one follows the analogy of the turbulent shear stress. Then, one can write

$$\bar{\rho} \overline{v'^2} = \bar{\rho} \epsilon_T \bar{v}_y \quad (87a)$$

and

$$\bar{\rho}_p \overline{v_p'^2} = \bar{\rho}_p \epsilon_{Tp} \bar{v}_{py} \quad (87b)$$

(See Ref. 13, Schlichting for the incompressible case). Thus, one can replace the y-momentum equations by

$$\bar{p} + \bar{\rho} \epsilon_T \frac{\partial \bar{v}}{\partial y} + \bar{\rho}_p \epsilon_{Tp} \frac{\partial \bar{v}_p}{\partial y} = p_i \quad (85a)$$

and

$$\frac{1+K}{K} \frac{u_1}{\lambda_m} \bar{\rho}_p (\bar{v}_p - \bar{v}) = - \frac{\partial \bar{p}}{\partial y} - \left[ \bar{\rho} \left( \epsilon_T \frac{\partial \bar{v}}{\partial y} - \frac{1}{K} \frac{\bar{\rho}_p}{\bar{\rho}} \epsilon_{Tp} \frac{\partial \bar{v}_p}{\partial y} \right) \right]_y \quad (86a)$$

or

$$\frac{u_1}{\lambda_m} \bar{\rho}_p (\bar{v}_p - \bar{v}) = - \frac{\partial \bar{p}}{\partial y} - \left[ \bar{\rho} \left( \epsilon_T \frac{\partial \bar{v}}{\partial y} - \frac{\bar{\rho}_p}{\bar{\rho}} \epsilon_{Tp} \frac{\partial \bar{v}_p}{\partial y} \right) \right]_y \quad (86b)$$

UNCLASSIFIED

# UNCLASSIFIED

Thus, the effect of particle turbulence would complicate the basic equations of motion in the compressible plane through the introduction of: (1) particle turbulent shear stress  $\tau_{TP}$ , (2) the apparent normal stresses due to particles  $\bar{\rho}_p v_p'^2$  in the definition of pressure, (3) the particle  $y$  velocity lag being related to the  $y$  gradient of the particle normal stress replacing  $v_p \approx v$  approximation of the no-particle turbulence case. With these modifications, one has to look into the utility of the Howarth transformation in solving the problem. This is being presently looked into.

## 3.2 The Eddy Viscosity Formulation and the Jet Spread Parameters

Two possible formulations for the eddy viscosity are the Prandtl-Tollmien mixing length concept and Prandtl-Gortler constant transport coefficient model. Even though the equations for the later case have been worked out, no solutions for these equations are obtained as it has been shown in Ref. 12 that Prandtl-Tollmien formulation is more in accord with experiment for the distribution of eddy viscosity, shear stress and velocity profile across the mixing zone. Thus, only the Prandtl-Tollmien formulation would be discussed.

The eddy viscosity in the mixing length concept is derived by assuming that  $|\bar{v}'| \propto |\bar{u}'|$  and  $|\bar{u}'| = \ell \bar{u}_y$

$$\epsilon \bar{u}_y = \overline{v'u'} = c_1 |\bar{v}'| \cdot |\bar{u}'| = c_1 \ell_2 |\bar{u}'| \cdot |\bar{u}'| = c_1 c_2 \left( \frac{\partial \bar{u}}{\partial y} \right)^2 = \ell^2 \bar{u}_y^2 \quad (88)$$

$$\text{or} \quad \epsilon = \ell^2 \bar{u}_y \quad (88')$$

(See Schlichting) where  $c_1, c_2$  are constants which are absorbed into  $\ell_1$  to give  $\ell$ , the mixing length. For free turbulence, i.e., jets and wakes, the mixing length  $\ell$  is taken to be proportional to the axial distance, i.e.,

$$\ell = cx \quad (89)$$

where  $c$  is a constant of proportionality. In other words, the mixing length is taken to be independent of the transverse coordinate and is linearly dependent on the axial coordinate. The  $y$  independence has been questioned in Ref. 12 for the simple Howarth transformation and in Ref. 14 for the more general transformation of Coles (Refs. 8, 9).

For the gas-particle case, even the linear dependence on axial coordinate seems to be questionable. To understand this, let us look at how  $\ell = cx$  has been arrived at. Again from Schlichting (Ref. 13), the rate of increase of the width  $b$  of the mixing zone is

# UNCLASSIFIED

$$\frac{Dl}{Dt} = u_{max} \frac{dl}{dx} = v = l \frac{\partial u}{\partial y} = \frac{l}{b} u_{max} = \text{const. } u_{max} \quad (90)$$

or

$$\frac{db}{dx} = \text{const. i.e., } b \propto x \quad (91)$$

$$\therefore l = \text{const. } b = \text{const. } x = cx \quad (92)$$

Here the assumptions are that  $\frac{Db}{Dt} = u_{max} \frac{db}{dx}$ ,  $\frac{\partial u}{\partial y} = \frac{u_{max}}{b}$  and  $\frac{l}{b} = \text{const.}$  In the present analysis, the  $b, x$  dependence is obtained from the mixing zone boundaries given by

$$\frac{\bar{\sigma} y^*}{x^*} = \eta_i = \eta_{i0} + x^* \eta_{i1} + x^{*2} \eta_{i2} + \dots \quad (93a)$$

for the near field and

$$(1+k)^{1/3} \frac{\bar{\sigma} y^*}{x^*} = \eta_{fi} = \eta_{fi0} + \frac{1}{x^*} \eta_{fi1} + \frac{1}{x^{*2}} \eta_{fi2} + \dots \quad (93b)$$

for the far field, with  $i = 1, 2$  defining the primary and secondary boundaries and  $\eta_{ij}$ ,  $\eta_{fij}$  are constants obtained as part of the solution. Thus, for the near field we have

$$\frac{\bar{\sigma} l}{x^*} = \eta_1 - \eta_2 = (\eta_{10} - \eta_{20}) + x^* (\eta_{11} - \eta_{21}) + x^{*2} (\eta_{12} - \eta_{22}) + \dots \quad (94a)$$

and for the far field

$$(1+k)^{1/3} \frac{\bar{\sigma} l}{x^*} = (\eta_{f10} - \eta_{f20}) + \frac{1}{x^*} (\eta_{f11} - \eta_{f21}) + \dots \quad (94b)$$

Now, the mixing zone width for the near and far field is given by

$$l = \frac{x^*}{\bar{\sigma}} \left[ (\eta_{10} - \eta_{20}) + x^* (\eta_{11} - \eta_{21}) + \dots \right] \quad (95a)$$

and

$$l = (1+k)^{-1/3} \frac{x^*}{\bar{\sigma}} \left[ (\eta_{f10} - \eta_{f20}) + \frac{1}{x^*} (\eta_{f11} - \eta_{f21}) + \dots \right] \quad (95b)$$

for the far field. For the far field case, the  $b, x$  dependence is in accord with the  $b \propto x$  dependence up to the first order by choosing the origin of the co-ordinate system properly. This is to be expected since  $b \propto x$  dependence is essentially for the far field. For the near field, however, the inclusion of the first order term leads to a quadratic dependence. This means that the linear dependence of  $l$  on the axial coordinate  $x$  is not strictly valid in the near field to the first order.

For the results presented in this paper (i.e.,  $\lambda = u_2/u_1 = 0$ )

$$\frac{1}{K} \frac{\eta_{11} - \eta_{21}}{\eta_{10} - \eta_{20}} = 6.5\%$$

# UNCLASSIFIED

# UNCLASSIFIED

i.e., for particle loading of the order of unity, the coefficient of the quadratic term for  $b, x$  dependence is not very large. Thus, it seems at least for this case that linear dependence of  $b, x$  may be a good approximation. Calculations will be carried out for other values of  $\lambda$  for a definitive answer to this question. Also, possible complications of the problem by taking quadratic dependence into account are being presently looked into.

Further, it is seen from the far field result that the mixing zone spread is also dependent on the initial particle loading  $K$  through the factor  $(1 + K)^{1/3}$ . If one so wishes, this factor may be incorporated into the jet spread parameter  $\bar{\sigma}$  such that the jet spread parameter varies from  $\bar{\sigma}$  in the near field to  $(1 + K)^{1/3} \bar{\sigma}$  in the far field. Then a jet spread parameter which is valid in all regions of the flow field (near, transition, far fields) may be formulated as

$$\sigma_{g.p.} = (1 + K D(x^*))^{1/3} \cdot \sigma_0 \quad (96)$$

where  $\sigma_{g.p.}$  is the gas particle value and  $\sigma_0$  is the pure gas value and  $D(x^*)$  is a function such that  $D(x^*) \rightarrow 0, 1$  in the near and far fields. A simple formulation would be exponential dependence, i.e.,

$$D(x^*) = e^{-1/x^*} \quad (97)$$

Since  $\bar{\sigma}$  is related to the constant of proportionality  $c$  in the mixing length, this means that there is a further  $x$  dependence of the mixing length, namely,

$$l = cx = \frac{x}{(2\sigma_{g.p.}^3)^{1/2}} = \frac{x}{[2(1 + K e^{-1/x^*}) \sigma_0^3]^{1/2}} \quad (98)$$

in addition to the quadratic dependence in the near field already discussed.

### 3.3 Extension of Solution to $x^* = 0(1)$

We have, so far, considered the near ( $x^* \ll 1$ ) and far ( $x^* \gg 1$ ) fields. For  $x^* = 0(1)$ , it is not possible to write any simple expansions. Thus, we will try to see if these results for far and near fields can be joined together to obtain a solution uniformly valid for all  $x^*$ .

For this purpose, let us first note that, for the zero order solutions to be independent of  $K$ , the similarity coordinate  $\eta$  for the far field needs the introduction of the parameter  $(1 + K)^n$  and the same factor with different exponents in  $u_s^*$  and  $\rho^*$ . This may be interpreted as saying that the incompressible jet spread parameter varies from  $\bar{\sigma}$  in the near field to  $(1 + K)^n \bar{\sigma}$  in the far field, so that one may write  $\bar{\sigma}(x^*)$  as

$$\bar{\sigma} = [1 + K D(x^*)]^n \cdot \sigma_0 \quad (99)$$

# UNCLASSIFIED

where  $\sigma_0$  is the no-particle value and  $D(x^*)$  is a function dependent on  $x^*$ , two simple expressions for which are

$$D(x^*) = x^*/(1 + x^*) \quad (100)$$

or

$$D(x^*) = e^{-1/x^*}$$

Choosing the latter form as in Section 3.2, one may combine the near and far field zero order results as follows:

$$\psi^* = \frac{x^*}{\sigma_0} f_0^*(\eta^*) \quad (101)$$

$$u_s^* = e^{-x^*} (u_{0s} - U_{1s}) + (1 + ke^{-1/x^*})^{2/3} (1 - e^{-1/x^*}) U_{1s} \quad (102)$$

$$\rho^* = e^{-1/x^*} + (R_0 - R_{1f}) e^{-x^*} + (1 + ke^{-1/x^*})^{1/3} (1 - e^{-1/x^*}) R_{1f} \quad (103)$$

where  $u_{0s}(\eta^*)$  is given in Eq. (56) and  $U_{1s}(\eta^*)$  is given in Eq. (74),  $R_0(\eta^*)$  given in Eq. (57) and  $R_{1f}(\eta^*)$  is given in Eq. (75) and  $f_0$  is the Tollmien function given in Eq. (55) and  $\eta^*$  is

$$\eta^* = \frac{\sigma y^*}{x^*} = (1 + ke^{-1/x^*})^n \sigma_0 y^*/x^* \quad (104)$$

Also,  $u_{0s}$  etc. are taken to be functions of  $\eta^*$ .

It is readily seen that Eqs. (101) to (104) reduce to the zero order terms of the near and far field expansions for  $x^* \rightarrow 0$  or  $\infty$  and have the proper dependence on  $x^*$  or  $1/x^*$ . One can take into account the first order corrections also by appropriate modification to Eqs. (101) to (103).

## 3.4 Inverse Transformation from Incompressible to Compressible (Physical) Plane

If the earlier results are to be useful in predicting the mixing zone spread, the particle loading and velocity distribution within the mixing zone in an actual problem, one has to determine the inverse transformation.

The transformation given in Eq. (17) may be inverted to

$$y = \int_0^{\bar{y}} \frac{\rho_2}{\rho} d\bar{y} \quad (105)$$

or

$$y = \frac{\rho_2}{\rho_1} \int_0^{\bar{y}} \frac{\rho_1}{\rho} d\bar{y} \quad (105')$$

# UNCLASSIFIED

where  $\rho_1$  is the gas density in the primary stream. Thus, the inverse transformation requires the knowledge of  $\rho_1/\rho$  variation in the incompressible plane and also the reference density  $\rho_r$ . The question of  $\rho_r$  will be taken up in the next section.

The density variation may be related to the velocity variation under some simplifying assumptions. If the gaseous composition of the primary and secondary streams is the same, then one has for constant pressure mixing

$$\frac{h}{h_1} = \frac{C_p T}{C_p T_1} = \frac{p/\rho}{p/\rho_1} = \frac{\rho_1}{\rho} \quad (106)$$

where the perfect gas law  $p = \rho RT$  is made use of, and  $p$  is constant due to the assumption of constant pressure mixing. Thus, the density variation in the incompressible plane can be determined from the knowledge of enthalpy variation. The enthalpy variation will be obtained from the energy equations, Eqs. (4) and (8).

## 3.5 Integration of the Energy Equations

The particle and gas energy equations are:

$$\rho_p(u_p h_{p,x} + v_p h_{p,y}) = -Q_p \quad (8)$$

$$\rho(u h_x + v h_y) = q_y + \tau u_y + (u_p - u)F_{p,x} + Q_p \quad (4)$$

where

$$Q_p = \rho_p C_p u_1 (T_p - T) / \lambda_T \quad (11)$$

and

$$F_{p,x} = \rho_p u_p (u_p - u) / \lambda_m \quad (9)$$

and

$$\lambda_T = \frac{3}{2} Pr \lambda_m = \frac{3}{2} \lambda_m (Pr=1) \quad (13)$$

where  $Pr$  is the laminar Prandtl number  $Pr = \mu c_p / k$  and will be assumed to be unity. It is already assumed that the turbulent Prandtl number is unity, i.e.,  $Pr_t = 1$  (see Section 2.1).

As a first attempt in integrating the energy equations, (8) and (4), it will be assumed that the enthalpies are functions of velocities only, i.e.,

$$h = h(u) \quad (107)$$

$$h_p = h_p(u_p) \quad (108)$$

Under this assumption, by writing  $h = c_p T$  and  $h_p = c_s T_p$  where  $c_p$  and  $c_s$  are the specific heats of the gas and solid particles, Eqs. (8) and (4) may be rewritten as

# UNCLASSIFIED

$$c_s (u_p T_{p_x} + v_p T_{p_y}) = -c_p u_1 (T_p - T) / \lambda_T$$

or

$$c_s \frac{dT_p}{du_p} (u_p u_{p_x} + v_p v_{p_y}) = -c_p u_1 (T_p - T) / \lambda_T$$

or with the aid of the momentum equation (6)

$$- \frac{dT_p}{du_p} (u_p - u) / \lambda_m = - \frac{c_p}{c_s} (T_p - T) / \lambda_T$$

or

$$\frac{dT_p}{du_p} = \frac{\lambda_m}{\lambda_T} \frac{c_p}{c_s} \frac{(T_p - T)}{(u_p - u)} \quad (109)$$

The assumption of  $Pr_t = 1$  may be written as

$$1 = Pr_t = (\rho c_p / k_T) = \frac{\tau}{u_y} \frac{c_p}{T_y} = \frac{\tau c_p T_y}{\tau u_y} = \frac{\tau_{h_y}}{\tau u_y} \quad (110)$$

where  $k_T$  is the apparent heat conduction coefficient and  $q$  is apparent heat conduction. From Eq. (110) one obtains

$$q = \tau_{h_y} / u_y \quad (111)$$

Eq. (4) may, thus, be rewritten as

$$\rho \frac{dh}{du} (u u_x + v u_y) = (\tau_{h_y} / u_y)_y + \tau u_y + (u_p - u) F_{p,x} + Q_p$$

which, with the aid of Eq. (2) becomes

$$\frac{dh}{du} \left[ \tau_y + \frac{(u_p - u) \rho u_1}{\lambda_m} \right] = \frac{dh}{du} \tau_y + \left( \frac{d^2 h}{du^2} + 1 \right) \tau u_y + \rho u_1 \cdot \left[ \frac{(u_p - u)^2}{\lambda_m} + \frac{c_p (T_p - T)}{\lambda_T} \right] \quad (112)$$

which for  $h$  to be a function of  $u$  alone requires, firstly,

$$\frac{d^2 h}{du^2} + 1 = 0$$

or

$$h = -\frac{u^2}{2} + A_1 u + A_2 \quad (113)$$

UNCLASSIFIED

# UNCLASSIFIED

and further, that

$$h_u = (u_p - u) + \frac{\lambda_m c_p}{\lambda_T} \cdot \frac{(T_p - T)}{(u_p - u)} \quad (114)$$

which, with the aid of Eq. (109) becomes

$$h_u = (u_p - u) + c_s \frac{dT_p}{du_p} = (u_p - u) + \frac{dh_p}{du_p} \quad (115)$$

or

$$\frac{dh}{du} + u = \frac{dh_p}{du_p} + u_p \quad (116)$$

Since  $h$  is a function of  $u$  alone and  $h_p$  is a function of  $u_p$  alone, one has

$$\frac{dh}{du} + u = A_3 \quad (117)$$

and

$$\frac{dh_p}{du_p} + u_p = A_3 \quad (118)$$

where  $A_3$  is a constant.

Eq. (117) is essentially the same as Eq. (113) and, thus, one may identify  $A_3$  with  $A_1$ . Thus,

$$\frac{dh_p}{du_p} = -u_p + A_1$$

or

$$h_p = \frac{u_p^2}{2} + A_1 u_p + A_4 \quad (119)$$

The constants of integration  $A_1, A_2, A_4$  may be determined from the boundary conditions at either edge of the mixing zone, namely,  $h = h_1$  for  $u = u_1$  and  $h = h_2$  for  $u = u_2$  and  $h_p = h_{p1}$  for  $u_p = u_1$ . Thus, one has

$$h_1 + \frac{u_1^2}{2} = H_{10} = A_1 u_1 + A_2 \quad (120)$$

$$h_2 + \frac{u_2^2}{2} = H_{20} = A_1 u_2 + A_2 \quad (121)$$

$$h_{p1} + \frac{u_1^2}{2} = A_1 u_1 + A_4 \quad (122)$$



# UNCLASSIFIED

which gives

$$A_1 = \frac{H_{10} - H_{20}}{u_1 - u_2} = \frac{H_{10}}{u_1} \frac{(1 - \beta)}{(1 - \lambda)} \quad (123)$$

$$A_2 = H_{10} - A_1 u_1 = H_{10} \frac{(\beta - \lambda)}{(1 - \lambda)} \quad (124)$$

$$A_4 = h_{p1} + \frac{u_1^2}{2} - H_{10} \frac{(1 - \beta)}{(1 - \lambda)} = H_{10} \left[ \frac{c_s}{c_p} - \frac{1 - \beta}{1 - \lambda} \right] \quad (125)$$

where  $\lambda$ ,  $\beta$  are the secondary to primary velocity and enthalpy ratios,

$$\lambda = u_2/u_1, \quad \beta = H_{20}/H_{10}$$

respectively,  $H_{10}$ ,  $H_{20}$  the total enthalpies of the gas in the primary and secondary streams and  $\frac{c_s}{c_p} H_{10} = H_{p10}$  is the particle total

enthalpy in the primary stream (one can write it in this fashion since thermal lag of the particles was assumed to be zero outside the mixing zone).

## 3.6 Interdependence of $h$ and $h_p$

In the previous section, it was assumed that gas enthalpy  $h$  depends on  $u$  alone while the particle enthalpy depends on  $u_p$  alone, leading to some very simple results. However, we have seen in the analysis given in Section 2 that while  $u$  is independent of  $u_p$  to the zeroth order approximation, the higher order approximations would introduce the  $u_p$  dependence whether it be in the near or far field. Further,  $u_p$  is always dependent on  $u$  to whatever approximation it may be in both near and far fields. Thus, it appears that this assumption of  $h = h(u)$  and  $h_p = h_p(u_p)$  has to be modified in any improved analysis. For the present, we shall content ourselves with the simple results and with the interdependence already present in the higher order terms for  $u$  and  $u_p$ .

## 3.7 Evaluation of the Integration in Equation (115')

Now, one may proceed with the evaluation of the integral in Eq. (105') which with the aid of Eqs. (106) and (113) becomes

$$\begin{aligned} y &= \left( \rho_\infty / \rho_1 \right) \int_0^{\bar{y}} \rho_1 / \rho \, d\bar{y} = \frac{\rho_\infty}{\rho_1} \int_0^{\bar{y}} (h/h_1) \, d\bar{y} \\ &= \left( \rho_\infty / \rho_1 h_1 \right) \int_0^{\bar{y}} \left( -\frac{u^2}{2} + A_1 u + A_2 \right) d\bar{y} \end{aligned} \quad (126)$$

# UNCLASSIFIED

Since the velocity is obtained in terms of  $\eta$  in Section 2 and since  $u = \bar{u}$  under the transformation, let us change to  $\eta$  as the integration variable. Then

$$y = (\rho_2/\rho_1) \int_0^{\bar{y}} (h/h_1) d\bar{y} = \int_0^{\eta} \frac{\rho_2 h}{\rho_1 h_1} \frac{\bar{x}}{\bar{\sigma}} d\eta$$

or

$$\bar{\sigma} \frac{y}{x} = (\rho_2/\rho_1 h_1) \int_0^{\eta^*} \left( -\frac{u^2}{2} + A_1 u + A_2 \right) d\eta^* \quad (127)$$

Since  $\eta = \frac{\bar{\sigma} y^*}{x^*} = \frac{\bar{\sigma} \bar{y}}{\bar{x}}$ ,  $\bar{x} = x$  and where  $\bar{\sigma}$  is the incompressible jet spread parameter for the gas-particle mixing as given in Eq. (104).

## 3.8 Mixing Zone Properties

### A. Mixing Zone Spread:

From Eq. (127), using the no-particle value for  $\bar{\sigma}_0$  to evaluate  $\bar{\sigma}$  and using the solutions for  $u$  obtained in Section 2, one can readily calculate the spread of the mixing zone into the primary and secondary streams, once  $\rho_r$  is defined.

### B. Particle Velocity Lag:

From  $u_s^*$  and  $u^*$ , the particle velocity lag distribution in the mixing zone may be determined by noting that  $u_p = u + u_s$ .

### C. Particle Temperature Distribution:

Eq. (119) with the knowledge of  $u_p$  will determine the particle temperature distribution within the mixing zone.

### D. Particle Loading Distribution:

Since we have chosen in our transformation  $\frac{q_p}{\rho} = \frac{\bar{\rho}_p}{\bar{\rho}_r} = \rho^*$ , knowing  $\rho^*$  from Section 2 gives the particle loading distribution within the mixing zone.

## REFERENCES

1. Marble, F. E., "Dynamics of a Gas Containing Small Solid Particles," Paper presented at the 5th AGARD Combustion and Propulsion Colloquium, Braunschweig, April 1962.
2. Clarke, H. L., Jr. and D. J. Carlson, "Normal Shock Location in Underexpanded Gas and Gas Particle Jets," AIAA J. Vol. 2, No. 4, pp. 776-777, April 1964.
3. Doughman, Lewis C. H., Jr., "Radial Lag of Solid Particles in a DeLaval Nozzle," AIAA J. Vol. 3, No. 1, pp. 169-170, Jan. 1965.

## UNCLASSIFIED

4. Marble, F. E., "Nozzle Contours for Minimum Particle Lag Loss," AIAA J. Vol. 1, No. 12, pp. 2793-2801, Dec. 1963.
- 5(a) Rudinger, G., "Some Effects of Finite Particle Volume on the Dynamics of Gas Particle Mixtures," AIAA J. Vol. 3, No. 7, pp. 1217-1222, July 1965.
- (b) Carlson, D. J., "Experimental Determination of Velocity Lag in Gas-Particle Nozzle Flow," AIAA J. Vol. 3, No. 2, pp. 356-357, Feb. 1965.
- (c) Fulmer, R. D. and D. P. Wirtz, "Measurement of Individual Particle Velocities in a Simulated Rocket Exhaust," AIAA J. Vol. 3, No. 8, pp. 1506-1508, Aug. 1965.
- 6(a) Hultberg, J. A. and S. L. Soo, "Two Phase Flow Through a Nozzle," Astronautica Acta, Vol. II, No. 3, pp. 208-216, (1965).
- (b) Soo, S. L., et al., "Concentration and Mass Flow Distribution in a Gas-Solid Suspension," I&EC Fundamentals, Vol. 3, pp. 98, May 1964.
7. Tirumalesa, Duvvuri, "Turbulent Flow Equations for Gas-Particle Flow," Tech. Rpt., CETEC Corp., Mt. View, Calif.
8. Coles, D. E., "The Turbulent Boundary Layer in a Compressible Fluid," Rand Corp. Rpt. R-403-PR (1962).
9. Crocco, L., "Transformations of the Compressible Turbulent Boundary Layer with Heat Exchange, AIAA J. Vol. 1, No. 12, pp. 2723-2727, Dec. 1963.
10. Deverall, L. I. and R. S. Channapragada, "Invariancy of Total Shear Stress for Compressible Turbulent Flows," AIAA J. Vol. 3, No. 8, p. 1513, Aug. 1965.
11. Tirumalesa, Duvvuri, "Turbulent Mixing of Gas-Particle and Pure Gas Streams," Tech. Rpt., CETEC Corp., Mt. View, Calif.
12. Channapragada, R. S. and J. P. Woolley, "Turbulent Mixing of Parallel Compressible Free Jets," Paper presented at AIAA Propulsion Joint Specialists Conference, Colorado Springs, Colorado, June 14-18, 1965.
13. Schlichting, "Boundary Layer Theory," (4th Edition) McGraw-Hill Book Co., Inc., New York.
14. Tirumalesa, Duvvuri, "Invariancy of Shear Stress for the General Transformation of Coles," Tech. Memo, CETEC Corp., Mt. View, Calif.

UNCLASSIFIED

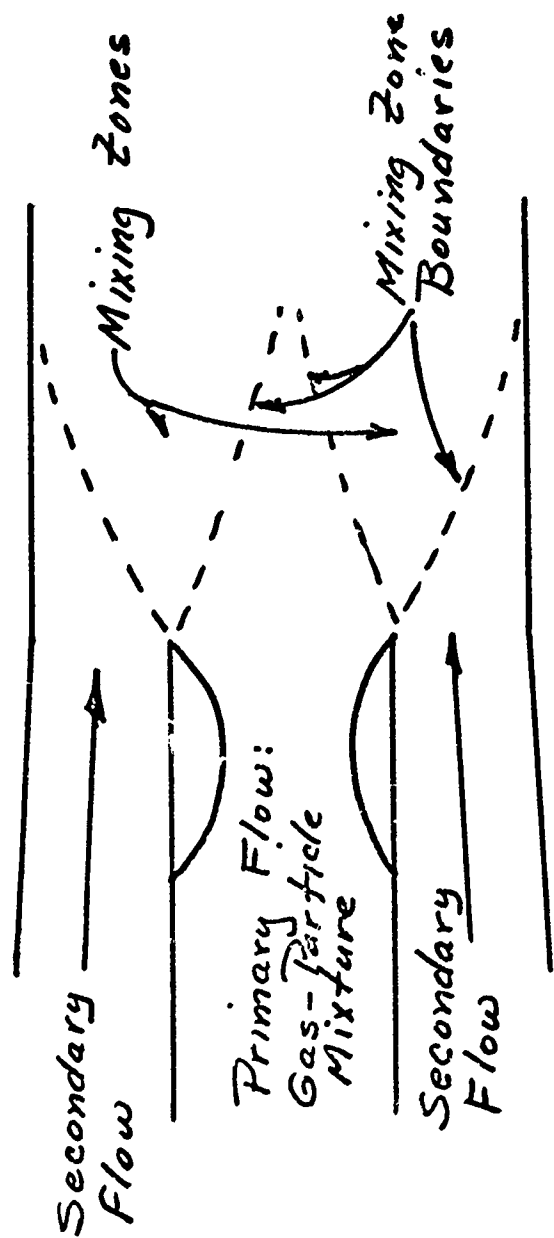


Figure 12. Schematic Diagram of Two Phase Mixing.

UNCLASSIFIED

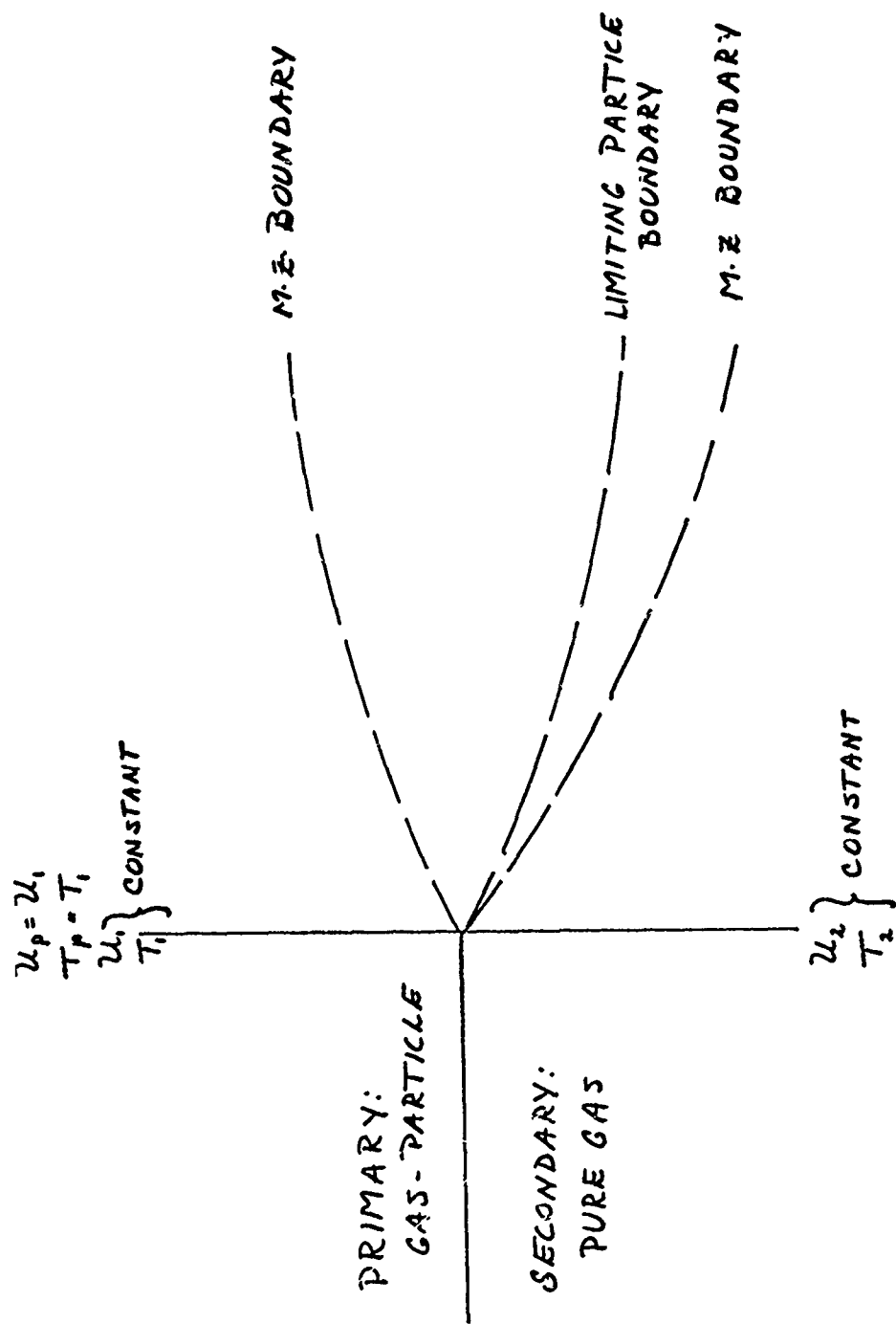


Figure 1b. Single Plane Interaction.

UNCLASSIFIED

UNCLASSIFIED

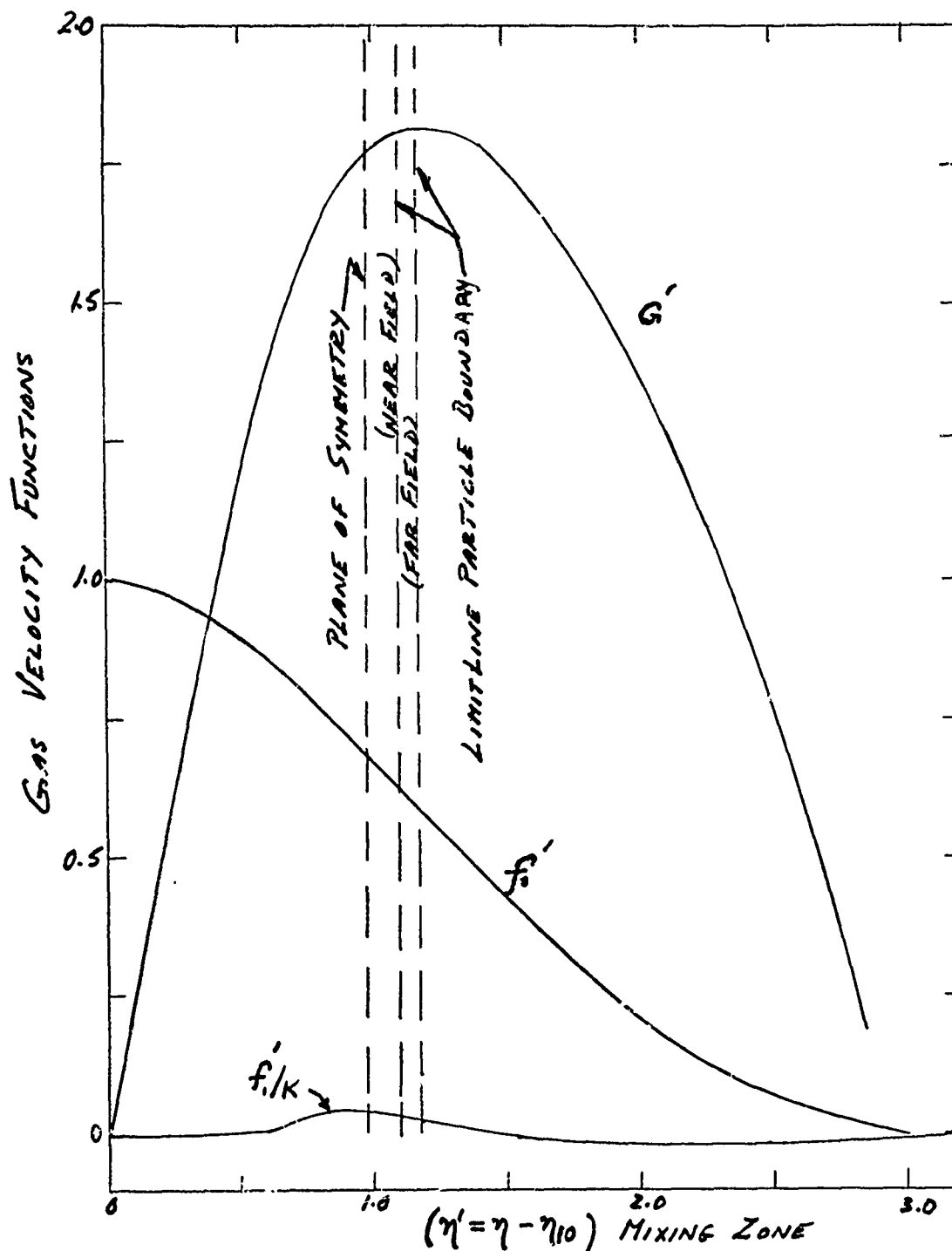


Figure 2. Gas Velocity Distribution Across the Mixing Zone.

UNCLASSIFIED

UNCLASSIFIED

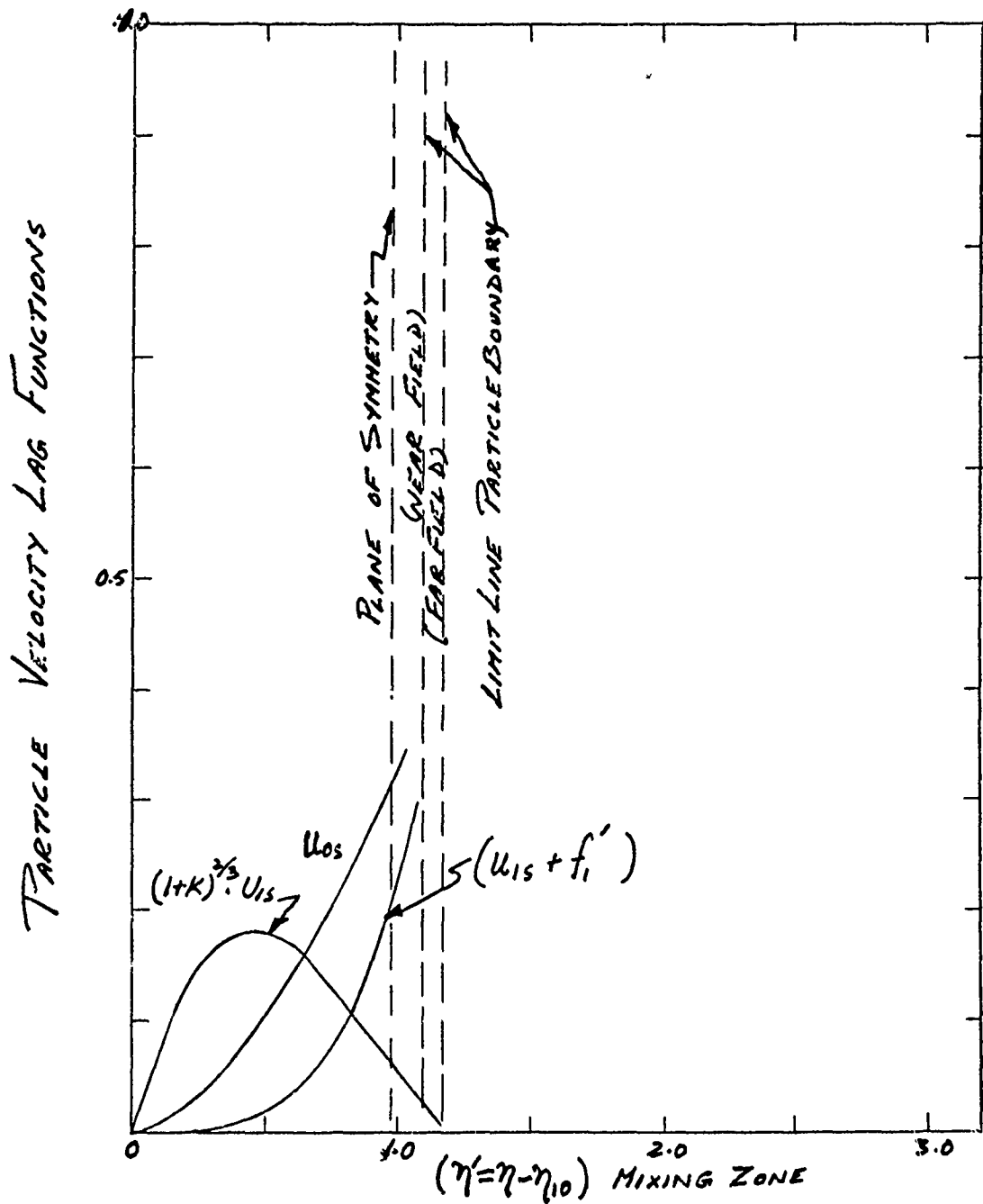


Figure 3. Particle Velocity Lag Distribution.

UNCLASSIFIED

UNCLASSIFIED

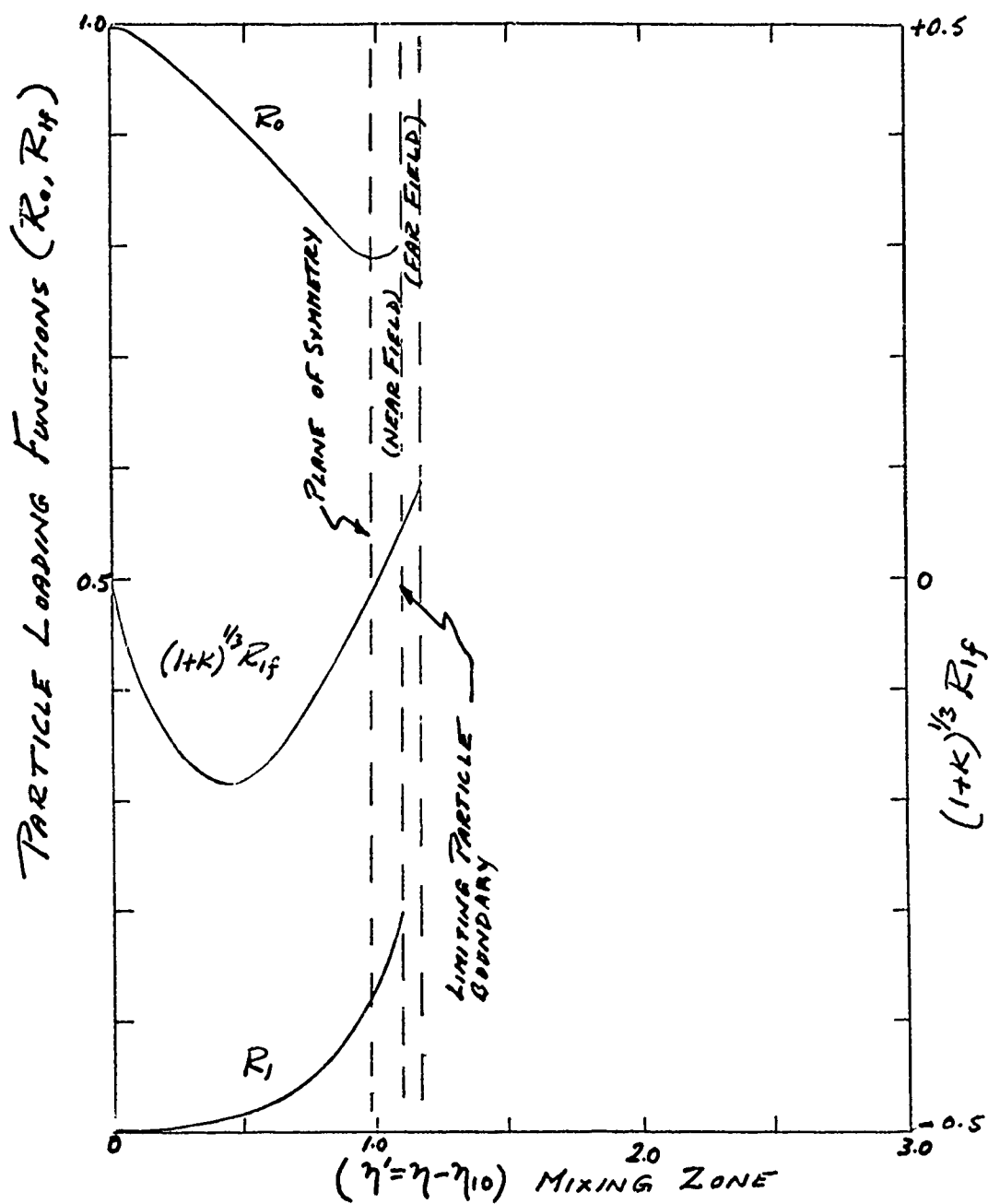


Figure 4. Particle Loading Distribution.

UNCLASSIFIED



# UNCLASSIFIED

## Ignition and Combustion of a Boron Particle Under Air Augmentation Conditions<sup>+</sup>

A. Gopalakrishnan<sup>\*</sup>, R. Anderson<sup>\*\*</sup>, and  
C. L. Miller<sup>\*\*\*</sup>

CETEC Corporation  
Mountain View, California

### Abstract

An analytical description of boron particle ignition is given as a function of gas temperature, composition and boron particle size. The ignition and combustion processes are considered analytically as three consecutive phases. First, the particle heat up history is considered to occur from ambient temperature conditions to the level where surface oxidation is observed. This temperature is taken to be of the order of 1800°K. Second, the ignition interval is assumed to be controlled by surface reaction and is assumed to begin at the 1800°K level and culminate at the normal boiling point of 2825°K. Third, steady burning is assumed to occur above this boiling point.

Calculations are presented to show the effects of initial gas temperature and boron particle size on the heat up and ignition history. In addition, a comparison is shown between the results of two mathematical analysis, one in which the assumption of a lumped thermal capacity in the boron particle is made and the second which considers the transient nature of the heating process.

---

<sup>+</sup> Research Sponsored by Edwards Air Force Base, Rocket Propulsion Laboratory, under Contract No. FO4611-67-C-0011. Under subcontract to Atlantic Research Corporation.  
<sup>\*</sup> Technical Staff

<sup>\*\*</sup> Vice President, R&D

<sup>\*\*\*</sup> Senior Staff

UNCLASSIFIED

# UNCLASSIFIED

## INTRODUCTION

The research programs presently being performed to determine the characteristics of high temperature combustion of metals have been motivated to a large extent by three major applications. These include their use in the production of high temperatures in flames, as additives in the forms of powder or wires in solid propellant rockets and as essential components of the reacting medium in the secondary combustion chamber of air augmented rockets. Since an improvement in the performance of the combustion system used in each of these three applications depends upon additional information, these programs have emphasized the mechanisms and physical parameters influential in the kinetics of metal combustion. This knowledge is required to predict and generate the conditions which will lead to improved ignition characteristics and increased combustion efficiency within the practical confines of the combustion chamber.

# UNCLASSIFIED

## TECHNICAL BACKGROUND

Various metals, by means of an exothermic reaction with their environment, are being utilized as sources of energy in a large number of liquid, solid propellant and hybrid rocket systems. Specific metals as aluminum, beryllium and boron are of interest as ingredients in propellant formulations primarily because of their high heats of combustion in combination with conventional oxidizers. However, in order to obtain the maximum advantage available through the use of these metals, those variables that directly affect the ignition and combustion time as well as efficiency must be established. Since these factors can be determined by careful experimentation and critical theoretical analyses, a thorough study of their ignition and combustion characteristics under selected pre-ignition and combustion environments which include conditions similar to those encountered within the rocket motor combustion chamber is warranted.

### An Approximate Analysis of Ignition and Combustion of Single Boron Particles in Air

The number of experimental efforts on ignition and combustion of boron particles are few and very few data have been reported. The following discussion is a brief summary of a mathematical analysis used to interpret experimental data gathered by Macek during a study on the ignition and combustion processes of boron particles 45-53 microns in diameter. The primary objective of this work is to develop an analytical technique that can be used to predict the time required for heat up and ignition of metal boron particles. The experimental approach by Macek is adequately described<sup>(1, 2, 3)</sup> and the observations are listed in Table I.<sup>(4)</sup>

UNCLASSIFIED

UNCLASSIFIED

TABLE I  
Combustion of Boron in 20% Oxygen Atmosphere

Ambient Temperature °K	Residence Time to Ignition (msec)	Total Residence (rough estimate) (msec)	Remarks
1850	no ignition	50	No combustion
1980	10-12	50	Particles glow dull yellow at 10-12 msec. Faint green visible at about 30 msec. Combustion probably negligible.
2070	7-8	40	Initial yellow becomes clear green which persists throughout.
2210	5	30-40	Strong green throughout. Appreciable combustion at 16 msec. Fairly complete combustion at 25-30 msec; residual boron size is 5-10 microns.
2410	3	25-35	Strong green throughout. Unburnt metal particle sizes are 20-40 microns at 8 msec, 5-30 microns at 12 msec. 5-10 microns at 20 msec. Still burning at 30 msec.
2650	2-3	20-25	Individual trajectories not clear because of highly luminous background. Green visible throughout. Some unburnt metal at 15-20 msec.

UNCLASSIFIED

## UNCLASSIFIED

The boron particle history from its initial contact with environmental hot-gases to its burnout is considered to be composed of three successive phases, each governed by differing physical or chemical mechanisms. The time interval from an initial exposure to the thermal energy source until the particle emits a yellow glow ( $T_p \approx 1850^\circ\text{K}$ ) can be considered as heat-up time. During this phase, the particle is heated by convection from the surrounding hot gas. The time interval between this yellow glow and a sustained green gas phase luminosity ( $T_p \approx 2825^\circ\text{K}$ ) is taken as the ignition interval. Throughout this second period the energy generated as a result of a surface reaction as well as heat gain from or loss to the surrounding gas determines the thermal history of the particle. The time interval between sustained luminosity and particle extinction is defined as the steady burning time. In the following sections, each of these three phases are discussed in order.

### Heat-Up Time for a Particle Brought into Contact with a Hot Gas

The heating up of a spherical particle initially at a uniform temperature by means of convective heat transfer from a high temperature gas surrounding it, has been treated, in the past, on the basis of its lumped thermal capacity. It has been assumed to a first approximation that the temperature is uniform within the particle at all times as a result of its high thermal conductivity. This approach is the one used by Dickenson and Marxman.<sup>(5)</sup> Under these assumptions the differential equation governing the average particle temperature,  $T_p$ , is as follows:

$$\frac{dT_p}{dt} = \frac{6 K Nu}{d^2 \rho_p C_p} (T_g - T_p) \quad (2.1)$$

$$T_p(0) = T_o$$

UNCLASSIFIED

# UNCLASSIFIED

where

- $\rho_p$  = Particle density
- $C_p$  = Specific heat
- $d$  = Particle diameter
- $T_g$  = Environmental gas temperature
- $Nu$  = Nusselt number
- $K$  = Thermal conductivity of the gas

The solution of this equation gives

$$T_g - T_p(t) = (T_g - T_o) e^{-mt} \quad (2.2)$$

where

$$m = \frac{6K Nu}{d^2 \rho_p C_p}$$

In Macek's experiments,<sup>(4)</sup> the particles were initially at about 300°K and the measured heat-up time is considered as the time required for the particle surface to increase from this initial temperature to 1850°K. In figure 1, the experimentally measured value of the length of this heat up period as a function of differing gas temperatures is compared to the corresponding theoretical value determined through the use of equation 2.2. While Equation (2.2) indicates an exponential decay of

$$\left( \frac{T_g - T_p}{T_g - T_o} \right)$$

with time, Figure 1 shows that the data does not follow this dependence and moreover the best exponential fit of the data when back extrapolated does not give the correct initial condition. It appears that in the case of short heat-up times, the lumped capacity analysis is not good enough; whereas, for larger heating times, the analysis with necessary corrections could be used to account for the differing initial condition. If the heat transfer coefficient (or a characteristic time) calculated from an

UNCLASSIFIED

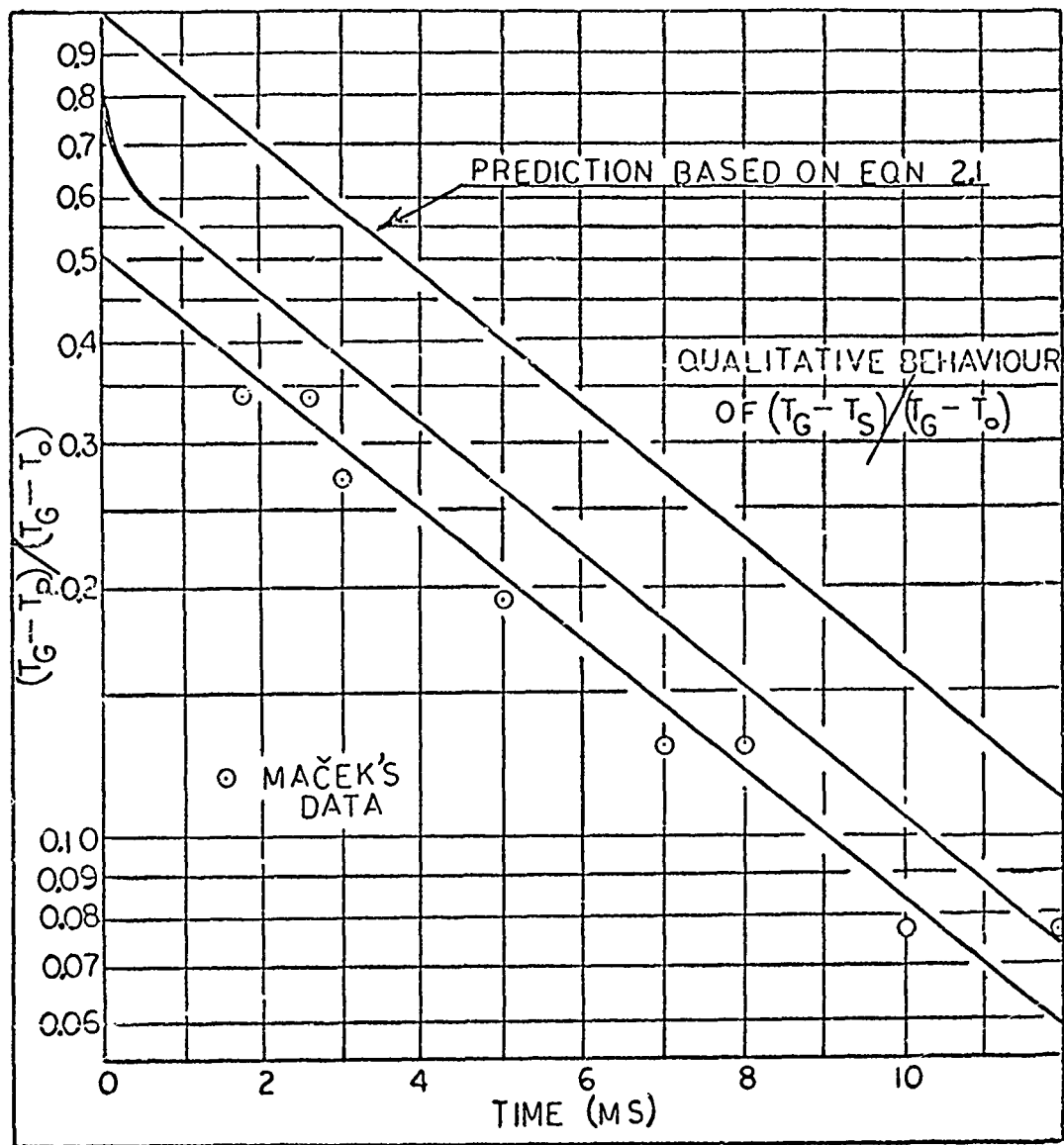


Figure 1. A Comparison of Macek's Data with the Mathematical Analyses.

UNCLASSIFIED

# UNCLASSIFIED

exponential fit of the data is used along with Equation (2.2) to predict the value of these heat-up periods, these predicted values will fall along the top straight line of Figure 1. The difference in magnitude of the non-dimensional temperature rise that exists between the experimental and theoretical curves could arise from the fact that, even though for longer times, characteristic times required for the decay of  $(T_g - T_{\text{average}})$  and  $(T_g - T_{\text{surface}})$  are the same, the magnitudes of these temperature defects are different. This is further clarified by means of the following analysis which takes into account the temperature distribution within the particle during its heat-up period.

The space-time dependent particle temperature,  $T(r, t)$ , will be governed by the following differential equation and boundary conditions.

$$\frac{\partial T}{\partial t} = \alpha \left( \frac{\partial^2 T}{\partial r^2} \right) + \frac{2}{r} \left( \frac{\partial T}{\partial r} \right); \quad 0 \leq r \leq R, t > 0 \quad (2.3)$$

$$K_p \frac{\partial T}{\partial r} = h_1 (T_g - T) \text{ at } r = R \quad (2.4)$$

$$T(r, 0) = T_0 \text{ (at } t = 0) \quad (2.5)$$

where

$$\alpha = \text{Thermal diffusivity of the particle} = \frac{K_p}{\rho C_p}$$

$$K_p = \text{Thermal conductivity of the particle}$$

$$h_1 = \text{Heat transfer coefficient between the particle and the gas} =$$

$$\left( \frac{K \text{ Nu}}{d} \right)$$

$$R = \text{Radius of the particle} = 0.5 d$$

$$\text{If we define } h = \frac{h_1}{K_p} \quad (2.6)$$

$$\text{and } v(r, t) = T(r, t) - T_g \quad (2.7)$$

the above set of equations reduce to the following:

$$\frac{\partial v}{\partial t} = \left( \frac{\partial^2 v}{\partial r^2} + \frac{2}{r} \frac{\partial v}{\partial r} \right); \quad 0 \leq r \leq R, t > 0 \quad (2.8)$$



# UNCLASSIFIED

$$\frac{\partial v}{\partial r} + hv = 0; r = R \quad (2.9)$$

$$v(r, 0) = T_o - T_g; (at t = 0) \quad (2.10)$$

This problem is readily solved using standard methods (Refer: Carslaw and Jaeger, <sup>(6)</sup> p. 238) and the solution is given below.

$$v(r, t) = \frac{2h(T_o - T_g)}{r} \sum_{n=1}^{\infty} e^{-\alpha \beta_n^2 t} \left[ \frac{R^2 \beta_n^2 + (Rh - 1)^2}{\beta_n^2 \{R^2 \beta_n^2 + (Rh - 1)\}} \right] \left[ \sin R \beta_n \sin r \beta_n \right] \quad (2.11)$$

where  $\pm \beta_n$  are the roots of Equation (2.12)

$$R \beta_n \cot(R \beta_n) + Rh = 1 \quad (2.12)$$

Equation (2.11) can be used to evaluate the time dependent surface temperature of the particle,  $T_s(t)$ . In nondimensional form, this is given by Equation (2.13) below.

$$\frac{T_g - T_s}{T_g - T_o} = \frac{2h}{R} \sum_{n=1}^{\infty} e^{-\alpha \beta_n^2 t} \sin^2 R \beta_n \left[ \frac{R^2 \beta_n^2 + (Rh - 1)^2}{\beta_n^2 \{R^2 \beta_n^2 + Rh(Rh - 1)\}} \right] \quad (2.13)$$

During the evaluation of the surface temperature history from Equation (2.13) in which parameters typical of boron particles in the 50 micron range of diameter were utilized, it is evident that only the first term in the infinite series solution is of importance at times longer than about 0.1 millisecond. Furthermore, the solution can be simplified by using a truncated series expansion of the trigonometric terms when  $(Rh)^2$  is small in comparison to  $(Rh)$ . These simplifications are completely valid in the case of the small diameter particles under consideration. The resulting expression is rather simple and shows, in the form given below, its similarity to Equation (2.2) as derived from the lumped capacity analysis.

# UNCLASSIFIED

# UNCLASSIFIED

$$\frac{T_g - T_s}{T_g - T_0} = \left( \frac{1 - Rh}{1 + Rh} \right) e^{-mt} \quad (2.14)$$

$$\text{where } m = \frac{6K Nu}{\rho_p C_p d^2} \quad (2.15)$$

Thus, we have

$$\left( \frac{T_g - T_s}{T_g - T_0} \right)_{\text{space-dependent analysis}} = \left( \frac{1 - Rh}{1 + Rh} \right) \left( \frac{T_g - T_s}{T_g - T_0} \right)_{\text{lumped capacity analysis}} \quad (2.16)$$

Thus, one would expect the later time nondimensional surface temperature data points to lie on an exponential curve, which, when extrapolated, should give an intercept of  $\left( \frac{1 - Rh}{1 + Rh} \right)$  on the  $t=0$  axis. The best fit through Macek's data gives an intercept of about 0.52. The analysis points to the way of getting an accurate surface temperature history for small diameter particles using a modified lumped capacity analysis. The predicted heat-up times based on the above analysis are given in Table II and they compare well with Macek's data as seen from Figure 2.

## Ignition Time for a Particle, Accounting for Heat Exchange Between the Particle and its Surroundings

As mentioned earlier, the ignition time is considered here as the time interval between the first appearance of the yellow glow of the particles and its sustained green phase luminosity. This, in turn, is the time taken for the particle to be heated from  $1850^\circ\text{K}$  to  $2825^\circ\text{K}$ . Early in this phase, the surface reaction and the hot surrounding gas contribute to the heating of the particle. As these combined processes continue, the temperature of the particle can rise above that of its environment in which case the particle loses energy to its environment. The continued heating of the particle to its steady burning temperature will depend upon the rate at which the surface reaction proceeds and its relationship to the environmental gas temperature and the particle diameter.

UNCLASSIFIED

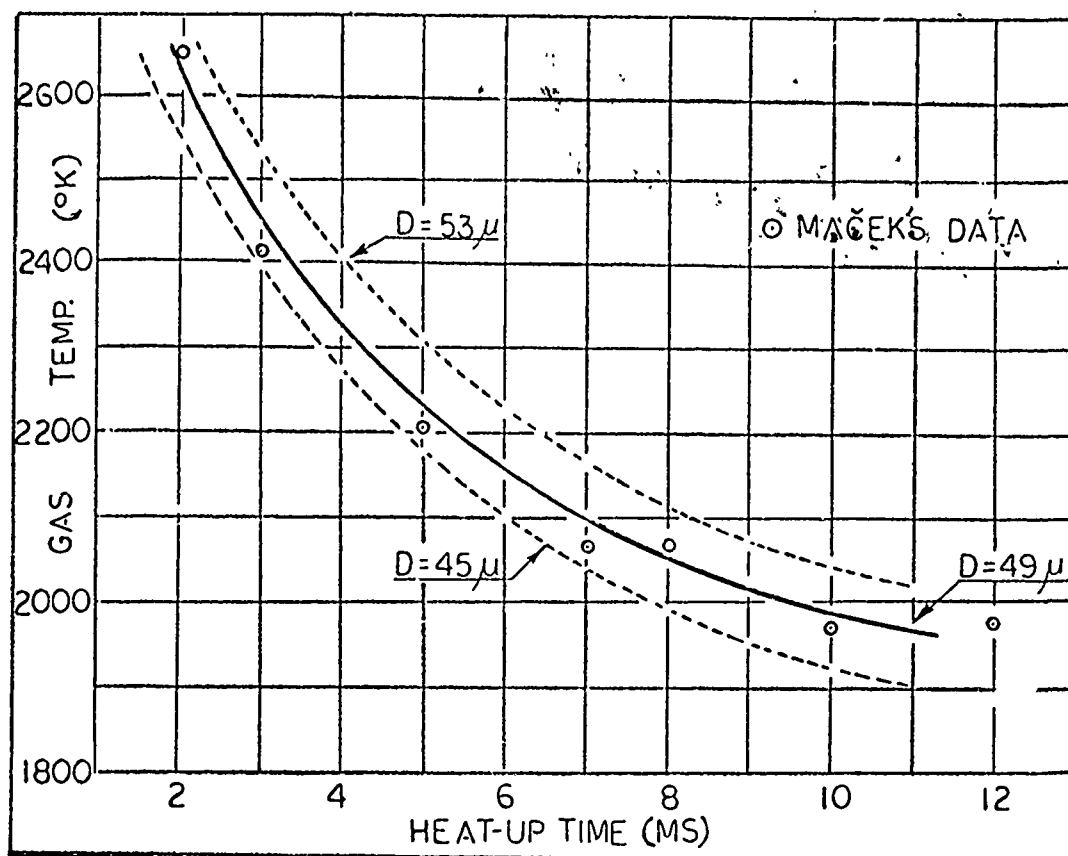


Figure 2. A Comparison of the Predicted Particle Heat Up Times with the Data of Macek.

UNCLASSIFIED

# UNCLASSIFIED

The overall differential equation describing the average temperature of the particle during this phase is as follows:

$$\frac{dT_p}{dt} = \frac{6Z}{d \rho_p C_p} (\text{Exp} - E_s/RT_p) X_{O_2} \frac{P}{RT_g} \Delta H_r + \frac{6K \text{Nu}}{d^2 \rho_p C_p} (T_g - T_p) \quad (2.17)$$

where the new symbols stand for the following quantities:

- $Z$  = Arrhenius Pre-Exponential Factor, cm/sec
- $E_s$  = Activation Energy of Surface Reaction
- $P$  = Total Pressure
- $X_{O_2}$  = Mole Fraction of Oxygen
- $\Delta H_r$  = Heat of Reaction, cal/gm

The first term on the right-hand side is the rate of rise in temperature due to surface reaction. The second term accounts for the heating or cooling effect of gas depending on whether  $T_g$  is greater or less than  $T_p$  at any instant. Equation (2.17) can be rewritten as

$$\frac{dT_p}{dt} = \psi e^{-\beta/T_p} + \theta (T_g - T_p) \quad (2.18)$$

where  $\psi$  and  $\theta$  are abbreviations for the group of parameters appearing in equation (2) and  $\beta = E_s/R$ . Equation (2.18) is non-linear in natu. and approximations have been made to obtain closed form solutions in connection with the theory of thermal explosions. (7, 8)

However, in order to obtain sufficient accuracy in the results over a wide range of gas temperatures a computer program was developed for the numerical integration of the above equation. Using the value of  $\theta$  which best correlated the heat-up times observed by Macek and the value of  $\psi$  as computed by this program from one experimental ignition point, the remainder of the predicted ignition times were calculated. These calculated values are compared with experimental data in Table II. Figure 3 shows the same results in a graphical form. Except for the data point at  $T_g = 2650^\circ\text{K}$ , for which Macek's estimation of heat-up and

UNCLASSIFIED

TABLE II  
Comparison of Predicted Heat-up and Ignition  
Times with the Experimental Data of Macek

T <sub>gas</sub> , °K	Heat-up Time		Ignition Time	
	Predicted	Macek's Data	Predicted	Macek's Data
1980	10.3 ms	10-12 ms	18.0 ms*	18.0 ms
2070	7.6 ms	7-8 ms	13.4 ms	12-13 ms
2210	5.3 ms	5 ms	9.6 ms	10 ms
2410	3.3 ms	3 ms	7.0 ms	7.0 ms
2650	1.9 ms	2 ms	5.3 ms	3.0 ms

\*Ignition time for this data point taken as time to reach 2825°K from 1980°K.

UNCLASSIFIED

UNCLASSIFIED

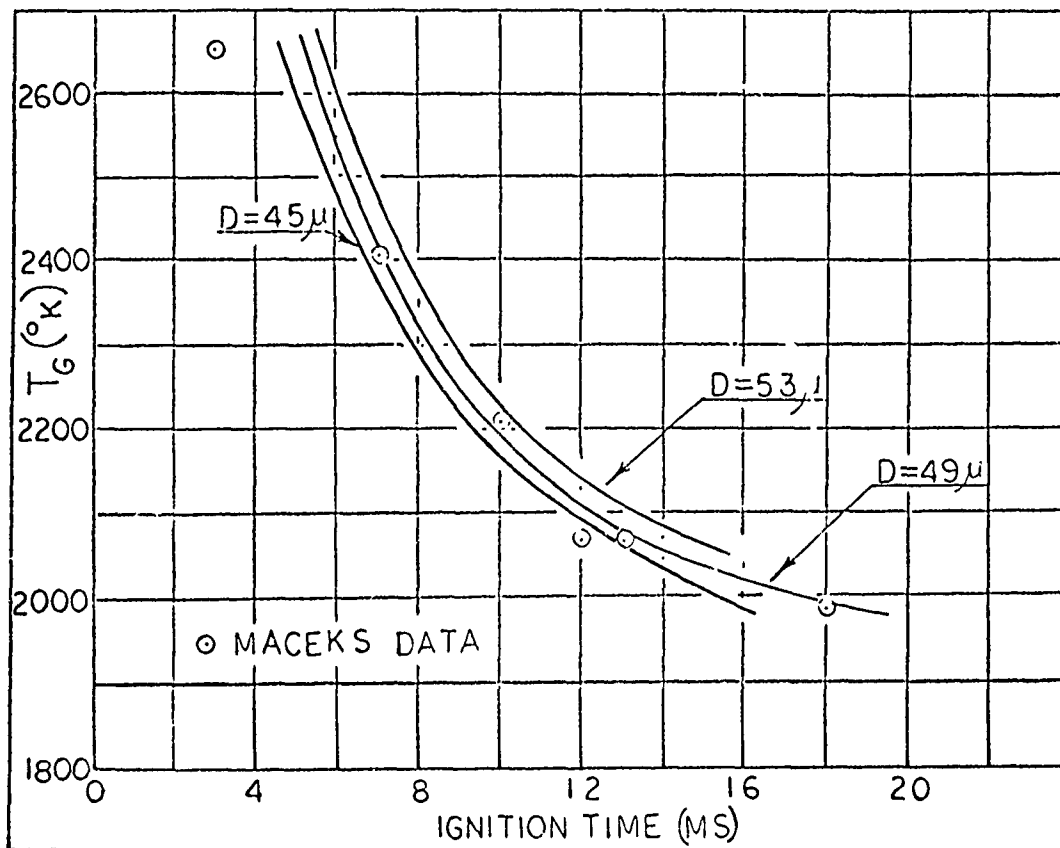


Figure 3. A Comparison of the Predicted Particle Ignition Times with the Data of Macek.

UNCLASSIFIED

## UNCLASSIFIED

ignition times have the greatest possible error, the prediction compares well with data.

In these computer studies convective heating is assumed to be the sole heating mechanism until the particle temperature reaches  $1845^{\circ}\text{K}$ .

Beginning at a temperature of  $1850^{\circ}\text{K}$ , surface reaction heating as well as convective energy transfer is considered as present. Between  $1845^{\circ}\text{K}$  and  $1850^{\circ}\text{K}$ , a transition zone has been assumed to exist whereby the mathematical continuity of the rate of temperature rise is preserved throughout the heating. In other words the surface reaction is assumed to begin at  $1845^{\circ}\text{K}$  and to reach its equilibrium rate at that particle temperature corresponding to  $1850^{\circ}\text{K}$ . The temperature width of this transition zone is controllable in the computer program and its effect on the heat-up time as well as a suitable choice for its value are currently being investigated. It should be noted, however, that the initiation and development of the yellow glow of the particle is really dependent on the physical and chemical mechanisms which govern the rupture, melting or vaporization of the oxide layer on the particle and that this complex phenomenon could, at best, be adequately represented by means of a suitable transition zone.

Effects of variation of particle size and the surrounding gas temperature are given in Figure 4 and Figure 5. The constant Nusselt number assumption results in an increase in heat transfer coefficient for a decreased particle diameter. It can be seen from equation (2.17) that even though the rate of temperature rise due to surface reaction also increases with decrease in diameter, the associated increase in the rate of heat transfer by convection is more predominant. Thus, it is evident that smaller diameter particles, in an environment which is not at a very high temperature, reach an equilibrium temperature sufficiently above the gas temperature so that its rate of heat loss is equal to the heating rate due to surface reaction. In cases where this equilibrium is reached below the vaporization temperature of the particle material, the

UNCLASSIFIED

UNCLASSIFIED

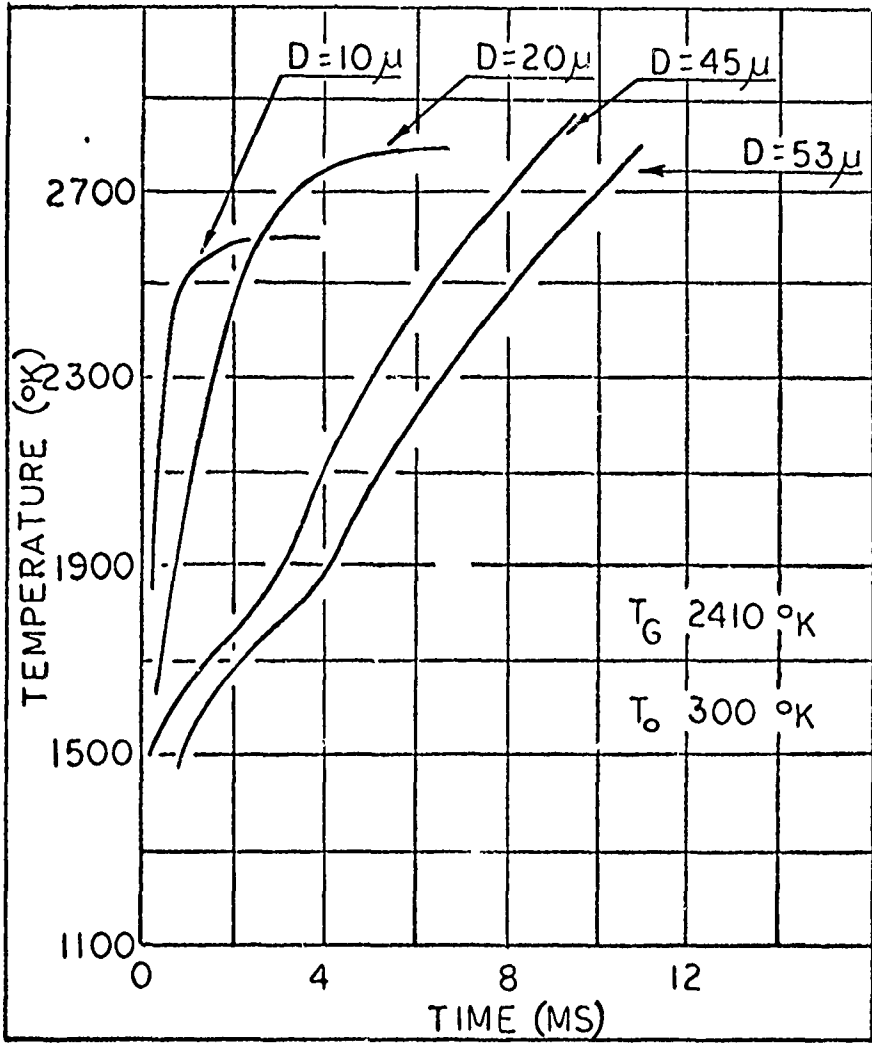


Figure 4. Effect of Diameter on Particle Temperature History.

UNCLASSIFIED



UNCLASSIFIED

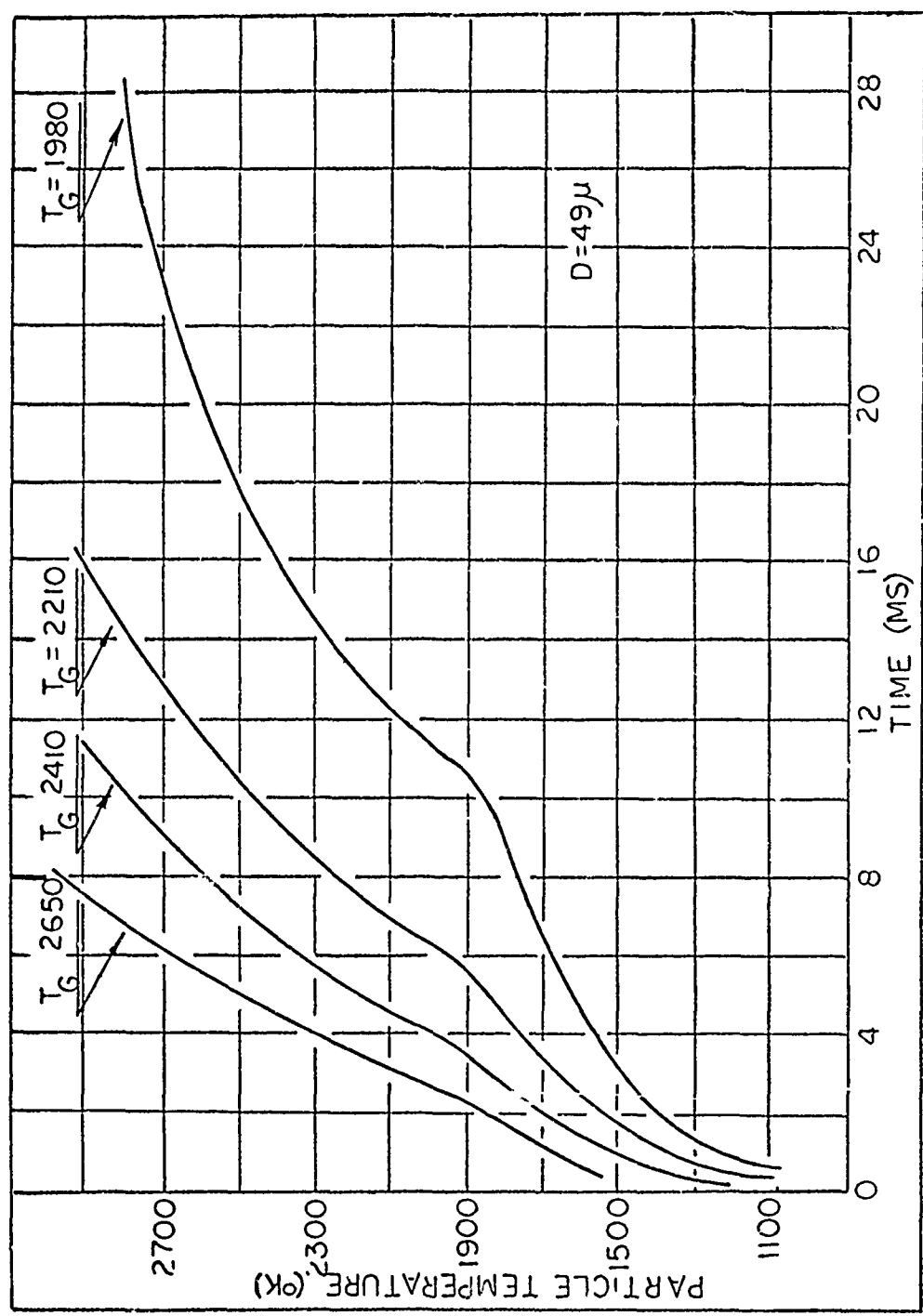


Figure 5. Effect of Gas Temperature on Particle Temperature History.

UNCLASSIFIED

## UNCLASSIFIED

depletion of the particle progresses due to surface reaction alone. As the particle diameter decreases still further, the equilibrium temperature also decreases and the surface reaction will eventually result in the complete consumption of the particle.

The limitations of the constant Nusselt number assumption as applied to the conditions associated with gas particle flows in rocket chambers have yet to be studied. Predictions based on Stoke's flow are strictly applicable only to continuum, incompressible flow and Reynold's numbers near unity. The flow regimes encountered by the micron-sized particles are such that appropriate corrections must be made to account for inertial, compressibility and rarefaction effects. The conclusions regarding the effect of particle diameter on the heating history is thus restricted to Stoke's flow assumption.

### Steady Burning of the Particles

During the final phase, boron particles undergo steady burning at a rate which depends on the mechanism controlling the process. For example, if the gas phase kinetic rates are very fast, in comparison to mass diffusion processes, and no surface reaction occurs, the steady burning rate is proportional to the square of the diameter.<sup>(9)</sup> This also assumes that no oxygen penetrates the combustion zone to the particle surface. This combustion model is classically referred to as the diffusion flame model. A second situation that needs to be considered is the case where significant molecular oxygen penetrates the combustion zone and reaches the surface. In this case the burning rate, in the limit, would be linearly proportional to the diameter. Smaller diameter particles, in an environment not at a very high temperature, may reach an equilibrium temperature below the vaporization limit and their combustion will occur solely through the surface reaction mechanism. The actual dependence of diameter would lie somewhere between these two models.

## UNCLASSIFIED

depletion of the particle progresses due to surface reaction alone. As the particle diameter decreases still further, the equilibrium temperature also decreases and the surface reaction will eventually result in the complete consumption of the particle.

The limitations of the constant Nusselt number assumption as applied to the conditions associated with gas particle flows in rocket chambers have yet to be studied. Predictions based on Stoke's flow are strictly applicable only to continuum, incompressible flow and Reynold's numbers near unity. The flow regimes encountered by the micron-sized particles are such that appropriate corrections must be made to account for inertial, compressibility and rarefaction effects. The conclusions regarding the effect of particle diameter on the heating history is thus restricted to Stoke's flow assumption.

### Steady Burning of the Particles

During the final phase, boron particles undergo steady burning at a rate which depends on the mechanism controlling the process. For example, if the gas phase kinetic rates are very fast, in comparison to mass diffusion processes, and no surface reaction occurs, the steady burning rate is proportional to the square of the diameter.<sup>(9)</sup> This also assumes that no oxygen penetrates the combustion zone to the particle surface. This combustion model is classically referred to as the diffusion flame model. A second situation that needs to be considered is the case where significant molecular oxygen penetrates the combustion zone and reaches the surface. In this case the burning rate, in the limit, would be linearly proportional to the diameter. Smaller diameter particles, in an environment not at a very high temperature, may reach an equilibrium temperature below the vaporization limit and their combustion will occur solely through the surface reaction mechanism. The actual dependence of diameter would lie somewhere between these two models.

# UNCLASSIFIED

## REFERENCES

- (1) Friedman, R., and A. Macek, "Ignition and Combustion Characteristics of Aluminum Particles in Hot Ambient Gas," *Combustion and Flame*, Vol. 6, 1962.
- (2) Friedman, R., and A. Macek, "Combustion Studies of Single Aluminum Particle," *Ninth International Symposium on Combustion*, New York, Academic Press, 1963.
- (3) Macek, A., R. Friedman, and J. M. Semple, "Techniques for the Study of Combustion of Beryllium Particles," *American Institute of Aeronautics and Astronautics Heterogeneous Combustion Conference*, December 1963, AIAA Preprint No. 63-485.
- (4) Sargent, W. and R. Anderson, "Investigation of the Air Augmented Rocket Combustion and Mixing Process," *Atlantic Research Corporation and CETEC Corporation, Quarterly Report No. 1, Contract FO4611-67-C-0011, February 1967*, data of Macek reported herein.
- (5) Dickinson, L. A. and G. A. Marxman, "Problems with Propellants Developed for Air Augmentation," *ICRPG/AIAA Solid Propulsion Conference*, Washington, D.C., July 19-21, 1966.
- (6) Carslaw, H. S. and J. C. Jaeger, "Conduction of Heat in Solids," *Oxford Press*, 1959.
- (7) Gray, P. and J. J. Harper, "The Thermal Theory of Induction Periods and Ignition Delays," *Seventh International Symposium on Combustion*, 1958.

## UNCLASSIFIED

- (8) Kinbara, T. and K. Akita, "An Approximate Solution of the Equation for Self-Ignition," Combustion and Flame, Vol. 4, No. 2, 1960.
- (9) Coffin, K. P. and R. S. Brokaw, NACA Tech. Note 3929, February 1957.

# CONFIDENTIAL

## QUESTIONS, ANSWERS & COMMENTS:

(C) C. / N. S. Cohen (LPC): As first brought out by R. Levin in earlier comments made at this conference, there are metals other than aluminum, beryllium, or their hydrides which are of interest in propulsion. In the air augmentation application, boron is of particular interest and much work remains to be done with respect to boron combustion and oxide particle formation and growth.

(C) Analysis of gas-particle flow in the mixing region of the afterburner is an exceedingly difficult problem, but a very important one. The ability of the particles to diverge with the gas and encounter mixing with air, will have bearing upon particle afterburning and the length of duct required to establish complete encountering of the particles with air or with hot oxygen-rich gaseous products of combustion. Analysis such as outlined in this paper can serve to compare, for example, trajectories of 50-micron particles versus those of 0.5 to 5-micron particles, when emanating from centrally located orifice or from various gas generator nozzle configurations. Perhaps initial qualitative trends can be established from uncoupled flow solutions, as was the case in early studies of gas-particle nozzle flow.

(U) Gas-particle nozzle flow can be expected to have great bearing in instances where measurement of "gas generator" performance alone are attempted. Where the great majority of species flowing through the nozzle are solid particles, not only can the performance loss be large, but the effect of very small particles assumes much greater significance.

CONFIDENTIAL

# CONFIDENTIAL

## QUESTIONS, ANSWERS & COMMENTS:

(C) The two-phase flow loss is of particular significance regarding air augmented performance because the values of fuel specific impulse are so high. As noted by R. Anderson in the presentation, the properties of boric oxide relative to boron are quite different from the case of aluminum or beryllium. The low oxide boiling point in the case of boron may prevent condensation at combustion temperatures in the afterburner; although this would eliminate the two-phase flow loss, it would be traded for a condensation energy loss. Where condensation does occur, in regions apart from the burning boron particle, the low boiling point may promote a delay in oxide particle growth such that the resulting two-phase flow loss would be very small. Particle size measurement from the exhaust of direct-connect tests is certainly warranted, to assess this important question.

C./ R. F. Hoglund (Purdue University): I think you might trade that for a nozzle condensation problem, however, with boric oxide.

Q./ H. A. Singer (Rocketdyne): I want to ask, in connection with the mixing study, whether you assume a single particle size uniform across the simulated rocket exhaust stream? Perhaps Dr Anderson's last comment about super-imposing the mixing without the particle combustion answered it, but do you plan to take into account any particle phase change essentially from a solid to the gas during your mixing analysis or is this going to be essentially a mixing analysis with no phase change whatsoever?

# CONFIDENTIAL

## UNCLASSIFIED

### QUESTIONS, ANSWERS & COMMENTS:

A./ R. Anderson (CETEC Corp): I think the best way to answer this is that first of all, we are developing the mixing analysis to help us correlate the first tests, and the tests are planned with inert particles with no phase change. Now in the additional mixing analysis, we are going to take into consideration the loss of mass from the particles as they are consumed as in the case of boron by surface reactions, and in the event of phase change. I might comment that in the analysis of the ignition of boron particles, we have not considered the phase change directly. We have simply, however, from a thermodynamics standpoint. In other words, what you would see is the temperature of the particle as a function of time history. Once you reach the melting point of boron, it should level out for a short time because of the latent heat of melting. Heat sink effect comes in. We are taking this into consideration in our planning, although we have not done it yet.

Q./ J. H. Morgenthaler (Bell Aerosystems): It seems to me the mixing analysis that you are doing is really no better than the eddy viscosity model which you assume, i.e., changing the model gives you about any results you want. I question whether those models that you are applying are really valid for this particular geometry and problem.

A./ R. S. Channapragada (CETEC Corp.): I think that is a very important point. In all the computer programs to date on two-phase flow mixing and any analysis that has been done on supersonic mixing, the results are directly a function of what eddy viscosity model one picks. In

UNCLASSIFIED



## CONFIDENTIAL

### QUESTIONS, ANSWERS & COMMENTS:

our analysis, we said let's pick the simplest model of eddy viscosity; however, we have left it an open parameter as far as the computer program is concerned. We can modify the eddy viscosity model accordingly.

C./R. Anderson (CETEC Corp.): The intent here is also to use the mixing analysis strictly as a framework. The constants and the parameters in the mixing analysis will be zeroed in by the experimental data.

C./R. F. Hoglund (Purdue University): I think there are several things not yet taken into account. For one thing, you have (as usual) assumed constant pressure all the way across your mixing layer; the intensive heat release around each reacting particle is probably going to violate that assumption locally. I don't think we have any real idea what the eddy viscosity is in a reacting particle laden stream. On the other hand, this justifies your use of a simple sigma correlation or its equivalent, the Prandtl mixing length concept, as a first approximation.

C./R. Anderson (CETEC Corp.): This is why we went to the non-reacting mixing case first.

(C) C./R. S. Channapragada (CETEC Corp.): I think the open question is, what is the eddy viscosity for a reactive flow?

(C) C./A. Mager (Aerospace): I would like to make a comment on this last issue because this question of reactivity came in again. In fact, I raised it myself before and I was planning to say something about it now. There is some question here about how much this reactivity is going to matter. One can perhaps do some guessing. The

## CONFIDENTIAL

## CONFIDENTIAL

### QUESTIONS, ANSWERS & COMMENTS:

issue is this - you are not really working the problem inside the nozzle; you are working it outside. Now of course, there are some cases where even outside it does not matter, but let's say that you are working with nozzles which expand the flow quite a bit, and you are operating outside of the atmosphere as it might happen in some cases. Then I sort of doubt that this reactivity is going to matter, i.e., that the reactivity of the particles is going to affect the flow process in a situation of this type, because the heat transfer coefficient and the resulting transfer of the heat from the particles to the gas which surrounds it will probably be quite low. I mean here that the density is low and the pressure is low; consequently the particles themselves, in spite of the fact that they are developing some energy, and so on, will not be contributing very much to the process that you are analyzing in the main. Of course, the situation in connection with afterburning, that is, where you want to add thrust, is not quite that simple; because then if your heat transfer coefficient is poor, your afterburning will not produce much force and so on, and you can argue that that is the wrong way to go.

(C) C. S. Channapragada (CETEC Corp.): Since we got into this problem of eddy viscosity which is an unsolved problem, let me bring up one other point. In the nonreactive case, as we use the sigma for the gas particle flows, we find that the eddy viscosity is less than that for the gas phase only. That means that the tendency of the particles is to suppress the total fluctuations of the gas phase. This is one result; I didn't want to report it here because we are trying

CONFIDENTIAL

## CONFIDENTIAL

### QUESTIONS, ANSWERS & COMMENTS:

to report this in another conference where we are directly involving the L/D ratio of the secondary combustor in our analysis. However, this is without a reaction; so with reaction now we have to go the other way around. How much, we don't know yet.

(C) C./R. Anderson (CETEC Corp.): This has allowed us in the present state to give a rough estimate of the length of the secondary combustion chamber or L/D as a function of particle size of the material issuing from the primary generators. It has helped a great deal, we feel, in assisting ARC in development of propellants for this application. I think the test data that has come out of the Applied Physics Lab. (Johns Hopkins University) program to date shows that they are pushing 100 percent secondary combustion efficiency; we feel pretty good.

SESSION IV

TWO-PHASE PLUME PHENOMENA

Session Chairman: Prof. W. C. Kuby  
University of California  
Santa Barbara

**UNCLASSIFIED**

**TWO-PHASE FLOW EFFECTS IN  
SOLID PROPELLANT ROCKET PLUMES**

By: W. C. Kuby  
Associate Professor,  
Department of Mechanical Engineering  
University of California  
Santa Barbara, California

**UNCLASSIFIED**

# UNCLASSIFIED

## TWO PHASE FLOW EFFECTS IN SOLID PROPELLANT ROCKET PLUMES

W. C. Kuby\*

University of California, Santa Barbara, California

### Abstract

The effect of condensed phase species in the exhaust of current solid propellant rocket motors on various plume phenomena is reviewed. Essentially, the phenomena of interest are the same as those attendant in studies of liquid propellant rocket engine plumes, but one must also consider the role of the condensed species in altering the salient gas properties or introducing independent contributions. The independent particle effects considered are radiation and particle impingement heat transfer, hypervelocity damage, particle impingement forces and moments, and communication attenuation. In addition to the independent contributions it is seen that the particles effect gas dynamic structure by reducing the distance to the normal shock in a highly underexpanded plume and significantly altering the gas properties due to non-equilibrium flow conditions. In the discussion of each effect, the state of knowledge is reviewed and conclusions as to the significance of particle contributions are made when possible.

### Nomenclature

B	black body function
C	heat capacity of particle
g	gravitational constant
J	conversion factor
$\dot{m}_p$	mass flux of particles impinging
$n(r)$	number of particles of radius between $r$ and $r+dr$
N	total number of particles
$\dot{q}$	heat flux per unit area
r	particle radius
S	target shear strength
T	temperature
u,v	velocities
V	volume of target lost
$V_0$	volume of projectile
x	distance along motor axis
z	distance normal to motor axis

The author wishes to express his appreciation to Dr. A.J. Laderman, Mr. D.J. Carlson, Dr. S.R. Byron and Mr. C.H. Lewis for their valuable discussions relating to this work and for their assistance in acquiring much of the information reported.

\* Associate Professor, Department of Mechanical Engineering

# UNCLASSIFIED

## Greek

$\rho$	density
$\sigma$	absorption cross-section
$\sigma_s^a$	scattering cross-section
$\langle \rangle$	mean value

## Subscripts

ch	chamber conditions
eff	effective quantity
p	particle phase
t	total quantity
w	wall conditions

The use of metallic fuel constituents in modern solid propellant rocket motors has brought attention to the role of condensed metal oxide combustion products in rocket plume effects. Essentially, the effects of interest are the same as those attendant in studies of liquid propellant plumes but the new problems are basically the determination of the role of the condensed species in either altering the gas properties or by introducing independent contributions based on their own properties. In the former case one must consider the effect of the inclusion of the particle phase on the gas dynamic structure; in the second category the following effects are important: (1) particle cloud radiation from the viewpoint of both heat transfer and discrimination, (2) particle impingement on immersed bodies which leads to increased heat transfer, hypervelocity damage, or body forces, and (3) communication attenuation caused by the generation of free electrons by thermionic emission from the high temperature, condensed phase. In this paper each of the effects will be discussed with the exception of particle plume radiation with regard to discrimination. In general, the pertinent information on this subject is classified beyond the allowable level of this paper and thus, cannot be discussed in any manner.

## Gas-Particle Interactions

In order to determine the plume effects salient to the gas phase, one must be able to describe the gas phase properties as a function of location and time. One of the important parameters pertinent to such supersonic jets issuing from underexpanded nozzles is the distance from the nozzle exit plane to the normal shock wave existing in such flows. Both the strength and the location of the shock wave is important since the high temperature flow behind the shock may well dominate the particular plume phenomena of interest. The effect on the normal shock location by gas particle plumes has been studied experimentally by Lewis and Carlson (1). The results of this study are shown in Figures 1 and 2. Figure 1 shows results for gas only flows in which the exit pressure ratio is shown as the function of the non-dimensional distance to the normal shock. In Figure 2 the variation of this distance with the particle loading is demonstrated. Typical solid propel-

## UNCLASSIFIED

lants which may have loadings of .4 to .6 are seen to exhibit quite large variations of normal shock location from that of gas only plumes having a comparable isentropic heat capacity ratio.

It appears that if one is primarily concerned with describing the gas flow properties, it is important to include in the flow field calculations, the non-equilibrium nature of the two phase flow. This is demonstrated by the work of Marble (2) in which he computes the nozzle contour required to maximize the exhaust  $I_{sp}$ . If the non-equilibrium nature of the two phase flow is unimportant in effecting the gas properties, one would expect maximum  $I_{sp}$  for a minimum exit condensed phase lag. However, it is found that the optimum contour results in a larger exit lag than does a typical nozzle contour. The cause of this result is that the optimum nozzle contour leads to minimized dissipation, which leads to a maximization in the gas phase velocity, rather than a maximization of the particle velocity. This result clearly indicates the importance of the non-equilibrium effects on the gas flow properties.

Conversely, however, if one is primarily interested in the particle trajectories and the particle properties, it appears to be adequate to describe the gas flow field in an uncoupled manner which does not account for the effects of dissipation and heat transfer between the particles and the gas. In such a description, the gas properties of the two phase flow are taken as the equilibrium values of the gas and particles together. Comparisons of results using the uncoupled solution with those using a coupled, one-dimensional solution and an axi-symmetric, characteristic solution indicate the uncoupled solution is in excellent agreement within the error introduced by uncertainties such as nozzle internal shock waves, gas transport properties, size distribution, etc. (3). The accuracy of an uncoupled solution increases for small loadings and for large motors in which the lags are small. Figure 3 shows the results of such an uncoupled computer program for various particle sizes. It is noted that there are two uncoupled solutions for the particle radius of 5 microns, one using a gas flow field description which results in a constant Mach number in the radial direction, varying only as a function of the axial distance and the other using a characteristic solution for the gas field. The differences would be more pronounced for smaller particle sizes. This result is included to demonstrate that the use of a proper flow field description may well be more important than the coupling effects when computing particle trajectories in plumes. The time and cost savings of using an uncoupled solution with a method of characteristics gas flow field description rather than a similar coupled version make this a most attractive concept.

### Radiation Effects

The radiation produced by the condensed phase in a solid propellant rocket exhaust has been studied considerably in the past. Since the solid phase radiates in a continuum and since the

UNCLASSIFIED



# UNCLASSIFIED

particle temperature is higher than the gas temperature, due to lag effects, it has been believed that the particle radiation may dominate the plume radiation. There are currently two calculation methods used to determine the particle cloud emissivity. One, by Fontenot (4), is extremely simple to apply and has had relatively good results in predicting radiative transport from plumes. However, the method is based on the optical properties of graphite which differ markedly from those of alumina. The second method by Morizumi and Carpenter (5) assumes gray radiation and then computes mean properties on this basis. Since this assumption is false, the results are questionable and naturally yield incorrect spectral details. The success of either of these methods seems somewhat fortuitous. A more complete discussion of both these methods is given in another paper within this same document by Laderman and Carlson. In order to best describe the state-of-the-art in our knowledge of the various parameters necessary to make an adequate radiative calculation, the results obtained using a new and rather detailed computer program technique will be discussed (6).

The particle trajectories, temperatures and velocities are determined using an uncoupled solution as discussed previously. The propellant characteristics, ambient conditions, and nozzle contours are used as inputs and the subsonic and transonic flow fields are computed using a pseudo, two-dimensional routine (7). This solution is then mated to a characteristics program in which the supersonic flow and plume gas dynamics are determined (8). The various flow properties resulting are stored in an orthogonal mesh for use in computing the particle trajectories. For these computations the gas was assumed to be in equilibrium at all times. The particle trajectories are then computed using these flow field results by integrating the particle momentum and energy equations using a modified Euler technique. The drag and heat transfer coefficients used take into account inertial, compressible and rarefaction effects (9). Any number of particle sizes can be computed and one has the option of computing both center line and limiting-stream line trajectory cases.

The results of the trajectory programs are then used to compute the average scattering and absorption properties of the plume as a function of position. These are given as:

$$\langle \sigma_a \rangle = \int_0^\infty \frac{n(r)\sigma_a(r)dr}{N} \quad \langle \sigma_s \rangle = \int_0^\infty \frac{n(r)\sigma_s(r)dr}{N}$$

$$\langle \sigma_a \rangle B(T_{\text{eff}}) = \int_0^\infty \frac{n(r)\sigma_a(r)B(T(r))}{N} dr$$

## UNCLASSIFIED

In a final routine the radiation is integrated over the field determined, to any prescribed target. The integration is performed along lines of sight and the total power computed by numerical integration of the angular distribution of the line of sight results. Three models are used for the integration procedure. First, a best estimate is computed by the one-dimensional beam approximation (10). Second, a high estimate is obtained by summing the radiation along lines of sight and attenuating this radiation by absorption only and third, a low estimate is obtained by attenuating the radiation by absorption and scattering but considering all scattered radiation to be lost. (That is, no multiple or forward scattering).

In each of the above cases, the field along the line of sight is divided into slabs normal to the line of sight which are semi-infinite, homogeneous and isothermal. The properties chosen for each slab are those for the mid point. The accuracy of this approximation is maintained by limiting the change in the black body radiation based on the local effective temperature over the slab thickness to an arbitrary percent of the local value. The radiation from a collection of particles depends on the absorption cross-section, the backward scattering factor, the effective black body function and the optical depth defined as

$$\tau = N(\langle \sigma_a \rangle + \langle \sigma_s \rangle) \times$$

This radiation is, at most, directly proportional to the absorption cross-section and the optical depth. The dependence on the effective black body function, however, is much stronger. For instance, at a wave length of two microns, the black body function goes approximately as  $T^p$  where  $p$  varies from 6 to  $2\frac{1}{2}$  for the temperature range of 600 to 3000 degrees Kelvin. Also, for plumes, the greatest changes in the properties other than temperature occur in the region where the temperature gradient is large; thus, the magnitude of the effective black body function seems the best criterion for slab thickness.

Using this computer technique, the radiation from an S-II ullage solid propellant rocket plume was computed at an altitude of 120,000 ft. These results were compared with measurements made at AEDC using a narrow view radiometer positioned 6 in. from the exit plane and 5 ft. from the axis of the plume (11). The view of the radiometer could be approximated by a single line of sight normal to the axis through the plume 6 in. from the exit. The spectral radiation flux computed for the plume over the wave length region of .5 to 10 microns is shown in Figure 4. As can be seen, a considerable portion of the total flux is produced at wave lengths for which extrapolation of the data was necessary. The total flux was 2.65 BTU/Ft<sup>2</sup>Sec. as compared to an experimental result of approximately 18 BTU/Ft<sup>2</sup>Sec. It should be noted that the experimental value includes the total flux to at least 15 microns (the detector used is reported to have a flat response to that wave length (12)).

## UNCLASSIFIED

In order to determine the cause of the deviation between the computed and the experimental values, the following problem sources have been considered; (1) the computational model for the radiation integration, (2) the extrapolation of the optical data for alumina, (3) the effect of liquid particle super cooling, (4) the effect of particle size distribution, (5) contribution of gas radiation, (6) radiation from additional solid phase particle matter in the exhaust, and (7) the so-called search light effect. A brief discussion of the significance of each of these effects will be given.

Since the case used for this computation is for an optically thin cloud, it does not represent a good test of the radiative transport model used; however, conversely, the radiative model has a small effect upon the result obtained. In essence, the computation could have been made by simply summing the radiative contributions of the individual particles over the line of sight. This was done and found to compare favorably with the computer results. For this reason, it is felt that the radiative transport model used has little effect on the results obtained for this calculation.

In order to compute the average optical properties of the plume as a function of position, one has to have the appropriate optical data for alumina, i.e., the refractive index as a function of temperature and wave length. The data used in this calculation is shown in Figure 5 (13,14,15). The solid lines represent regions in which experimental data exist and the dotted lines represent extrapolation of this data. If one only considers the radiation below a wavelength of 2.3 microns, the result is 1.45 BTU/Ft<sup>2</sup>Sec. By using the extrapolation of Figure 5 for the liquid particles, the prediction was increased to 2.65 over the entire wavelength region of interest. Since the total flux at this measuring station is dominated by the liquid particle radiation, it is clearly desirable to extend the optical data for liquid alumina to the longer wavelengths indicated. (The contention that the liquid particles dominate the total flux will be discussed later). Although the extension of the liquid data is desirable, it is only speculative that the disagreement will be resolved by increased radiation in the long wavelength region; however, a considerable portion of it (see Laderman and Carlson herein) can be accounted for by a more favorable extrapolation technique.

The effect of super cooling of the particles below their fusion point and the effect of a larger particle size distribution than assumed, can be discussed together since the essential feature of each phenomena is that a larger mass fraction of alumina is liquid at the measuring station. If one assumes thermodynamic equilibrium of the solid phase, the size distribution used indicates that 38% by mass of the particles will be liquid and that the minimum liquid diameter is 6 microns. The optical data in Figure 5 indicates an increase in the absorbtivity of alumina of about one hundred-fold when it melts at 2 microns. Thus, it is clear that the radiation from the plume will be dominated by the 38%

## UNCLASSIFIED

of the mass that is liquid. At best, by virtue of super cooling, the percent liquid could be increased to 100% which would give about a 2 1/2-fold increase in the radiation. The same 2 1/2-fold increase could be accomplished by choosing a particle size distribution which was essentially larger than the 6 micron minimum diameter. In addition to the increase in the mass fraction of liquid, a larger size distribution would introduce, because of increased lag, more mass at temperatures greater than the melting temperature so that there would also be an increase in the average liquid absorptivity. From these arguments it is clear that super cooling and/or increased size distribution could account for much of the discrepancy found. The particle size distribution assumed was consistent with the results of Cheung and Cohen (16) using the skew-symmetric distribution formula suggested by Bauer and Carlson (17). No direct evidence concerning super cooling is known to this author.

The contribution of gas-only radiation was determined by Marshall Space Flight Center (18) and is shown in Figure 6. The integrated radiation flux under this curve is 3.6 BTU/Ft<sup>2</sup>Sec. or 23% of the experimental value. It is clear from this result that the gas phase radiation must be included in the total radiation calculations. An additional source of gas radiation may result from non-equilibrium effects which could increase this equilibrium estimate substantially; however, additional work must be done in this area in order to evaluate the possibility.

Further investigation of other possible sources of continuum radiation has uncovered a very important factor not previously recognized. The S-II Ullage motor contains 2% ferric oxide as a burning rate enhancer which should be condensed in the exhaust. Since no particle size data or optical data at elevated temperatures exists for this material, this material is lumped with the alumina in the present calculations. However, the ferric oxide optical data that does exist indicates that the value of  $n_2$  at a wavelength of one micron and room temperature is about 15 times the value for liquid alumina at its melting point and over 7 orders of magnitude larger than the room temperature value for alumina. If the value of  $n_2$  for ferric oxide increases with temperature as does the alumina value, its importance is obvious. The possibility of ferric oxide being the primary continuum radiator is qualitatively substantiated by tests at Cornell Aeronautical Laboratory (19) and Aeronutronic (20). In the former tests, radiation results for small scale SI-B Retro-rockets, which contain 2% ferric oxide but no alumina, and S-II Ullage motors, which have a like amount of ferric oxide but 8% alumina, are shown in Table 1. As can be seen, the radiation values normalized by pressure (motor size and exit temperatures were not significantly different between the two cases) are comparable. If the dominant radiation is continuum, it cannot be ascribed to Al<sub>2</sub>O<sub>3</sub>, but could be Fe<sub>2</sub>O<sub>3</sub>.

In addition to the ferric oxide content, one must not overlook the

UNCLASSIFIED

## UNCLASSIFIED

possibility of the non-equilibrium formation of carbon particles. The report on the experimental measurements notes the presence at the end of the test of soot on a probe that was in the plume. It is not known whether this carbon matter is present only on start-up and/or shut-down (which would not effect the experiment) or is present during the steady state burn. It was also noted that part of the ablative nozzle was lost during the test. This nozzle ablation could have possibly introduced solid carbon into the plume mixing region. Unfortunately the importance of carbon radiation cannot be quantitatively estimated, but the possibility of its contribution must be noted.

The experimental results from Aeronutronic (20) pertain to both ferric oxide and carbon radiation and are shown in Figures 7-11. These results were obtained by measuring the radiation from the combustion effluent of a hydrogen-oxygen motor and introducing into the combustion region alumina, carbon and ferric oxide in varying amounts. In each test, the first two or three seconds of the run were made using hydrogen and oxygen alone. Then the run was continued with the introduction of the additional constituents. Each of the figures shows a typical spectral measurement in both regions for comparison. Figure 7 which shows the results of a run of hydrogen-oxygen with methanol and aluminum added, features the appearance of a very strong emission band in the 4.3 micron region. This band can be attributed to  $\text{CO}_2$  which is formed by the carbon-oxygen reactions. There also appears an increase in the 1.3 micron region which can probably be attributed to a relatively strong continuum radiator. This emitter may be alumina resulting from the combustion of aluminum or some unburned carbon resulting from non-equilibrium effects. In Figure 8, carbon particles were added to a hydrogen-oxygen-alumina mixture and the result was a decided increase in the continuum radiation in the 1 to 2 micron region. This clearly indicates the role of solid carbon in the effluent. Figures 9 and 10 are included to show what appears to be an influence of ferric oxide. A slurry mixture consisting of alumina, water and one-half percent by weight of ferric oxide was added to the hydrogen-oxygen flame and the results are shown in Figure 9. Of primary interest is the appreciable increase in the emission in the 1 to 2.3 micron region and the absence of any measurable change beyond that point. This is somewhat similar to the pure alumina emission although the increased emission in this case cannot be ascribed with certainty to either constituent alone. The results of Figure 10 were obtained using 1% ferric oxide in the same mixture. The resulting increase in the emission may be seen in this result. In this instance the change in radiance level at the 2.3 micron wavelength is more apparent and may be resulting from the ferric oxide. The significance of the importance of ferric oxide radiation is that other burn rate controls could be used with a resulting decrease in the continuum radiation level.

The final source of error considered is the omission in the model of the search light effect along lines of sight which do not directly view the exit or throat of the nozzle. For the S-II Ullage motor, since the

## UNCLASSIFIED

cloud is optically thin, the throat area would appear to be the closest possible source of black body radiation at the temperature of the chamber. If we assume that the cloud scatters isotropically, the scattered radiancy is

$$I_{sc} = \frac{1}{2} < \sigma_s > N_t B(T_{ch}) \Delta x \Delta \Omega$$

while the direct radiation in the line of sight is

$$I_o = < \sigma_a > N_t B(T_{eff}) \Delta z$$

The ratio of the scattered to the direct radiation flux is therefore

$$\frac{I_{sc}}{I_o} = \frac{1}{2} \frac{< \sigma_s >}{< \sigma_a >} \left( \frac{T_{ch}}{T_{eff}} \right)^4 \frac{\Delta x}{\Delta z} \Delta \Omega$$

Substituting numerical values in the above equation, the contribution from the scatter light effect is seen to be less than 5% of the particle radiation. This small contribution is due to the low 90° scattering lobe for the alumina particles and the small steradiancy of the black body emission at the throat that is intercepted by the detector. Such a 5% variation based on the particle radiation is seen to be a small contribution to the total discrepancy.

Based on the above discussion, it appears that there are still some serious uncertainties in both the values of the optical properties of alumina and other emitting species in the plume and the state and size distribution of the condensed phases present. Also, at least for the case discussed herein, the radiator from the gas phase cannot be considered negligible in comparison with the total flux. These uncertainties lead to predicted radiation values which are considerably in error when compared to experimental results. The state-of-the-art therefore appears to be somewhat limited by the proper acquisition of the basic data necessary.

### Particle Impingement Effects

Another basic plume phenomena augmented by the addition of a condensed phase in the plume is that of impingement of the plume upon vehicles immersed in it. In the limit of small gas density and body size, the particle lag is large compared to the scale of the problem and

UNCLASSIFIED

# UNCLASSIFIED

little change in particle trajectory occurs prior to impact. In this low density limit the force resulting from the gas stagnation on the body may be small compared to the particle contribution and the forces can be calculated directly from the knowledge of the particle surface interaction. In the other limit of high gas density and large body size, the particles achieve equilibrium with the gas flow and therefore do not impinge upon the body. In this instance the two phase flow behaves as in the equilibrium case described previously in that the particles effectively alter the gas molecular weight and heat capacity. The intermediate case, of course, is a very difficult problem to solve.

The accurate determination of the mass and momentum fluxes of the particles on an immersed body is dependent upon predicting the number density and velocity as a function of position in the plume and then determining the nature of the particle surface interaction. The former problem has been discussed in some detail in this paper and in greater detail in previous papers on gas-particle flows. Some comments, however, will be made here pertaining to the nature of the particle surface interaction. Three particular effects will be discussed, namely; heat transfer to the vehicle, hypervelocity damage, and the imposition of forces and moments on the vehicle.

If the particles impact upon the immersed surface but do not possess sufficient kinetic energy to cause a hypervelocity impact, the result of this impingement of particles is that there is a transfer of the particle kinetic and thermal energy to the walls. The particles which impinge upon the wall may stick to the wall and form a liquid or solid layer. Some may also rebound off the wall and transfer only a portion of their energy dependent on the time scale of the interaction. It has been suggested to use proportionality factors analagous to the accommodation factors defined in free molecular flow in order to describe the amount of energy which the particle contain that is transferred to the wall during the various types of collisions noted (21). Thus, one can write the heat flux due to particle impingement as

$$\dot{q}_p = \dot{m}_p \left[ \alpha_t C (T_p - T_w) + \alpha_k \frac{u^2}{2gJ} \right]$$

where  $\alpha_t$  and  $\alpha_k$  are these proportionality factors. Table 2 shows some results for particle impingement heat transfer calculations based on this accommodation coefficient approach. In each case the particle energy was obtained by an uncoupled solution for two phase flow. The total heat flux to the surface was either computed from experimental data or estimated. The combined contribution of conductive and radiative fluxes was then computed and subtracted from the total heat flux. The coefficients noted were obtained by dividing the total heat flux minus the convective and radiative effects by the total energy of the impinging particle cloud. In the two helium tunnel results obtained at

## UNCLASSIFIED

Aeronutronic (22), it is seen that the thermal energy was negligible and thus the accommodation coefficient can be related directly to the kinetic energy. In the other two firings reported by Boeing (23), this is not the case and no break down can be given. It is not clear why such a large discrepancy exists between the S-II Ullage result and the other three results. It is possible that this difference comes about through a variation in the particle-surface interaction; however, the S-II Ullage result was obtained using both copper and teflon cylinders. The 6C3-11.4 result was obtained using a micarta test sample. It is clear from these results that although empirically determined accommodation coefficients are not particularly reliable and no theoretical means is available to compute such a transfer situation, the impingement flux can be a considerable portion of the total flux and thus must be considered.

If the impinging particles have sufficient velocity the impact can be considered a hypervelocity one. There has been considerable experimental work done on this subject using rather large projectiles of the size of 1 millimeter to 1 centimeter impacting on metal or ceramic plates. One such study by Sorenson (24) resulted in an empirical correlation between the volume removed per unit volume of projectile with the projectile kinetic energy and the strength of the target. This is given below:

$$\frac{V}{V_0} = 0.12 \left( \frac{\rho_p}{\rho_t} \right)^{\frac{1}{2}} \left( \frac{\rho_p v^2}{S} \right)^{0.845}$$

In an attempt to test this single particle correlation as a means of predicting hypervelocity impact damage caused by a cloud of micron size particles, Lewis, Hackett, and Kuby (25) carried out experiments in a helium tunnel seeded with micron sized alumina particles. Aluminum targets were used and the results normalized according to the empirical relation reported by Sorenson. These results are shown in Figure 11. From these results, it appears that there is approximately a 2 order of magnitude decrease in the normalized damage predicted from the results of Sorenson. Gault and Moore (26), using a simple theoretical model to predict the effect of projectile size variation (not included in the Sorenson equation) would tend to predict these experimental results. Another explanation for the variation found is that the brittle nature of the projectile used in the cloud experiments reduces the damage from that caused by the ductile projectiles used in the Sorenson experiments. Also included in Figure 12 is a spread of data obtained by accelerating micron size alumina particles in a rocket engine. For these tests there was no means of maintaining a proper surface temperature control from which a reasonable strength could be computed. As a result, the large variation in the results could quite possibly be attributed to extremely high surface temperatures and resulting low surface strengths or melt layers. Although these results were obtained in a velocity range

UNCLASSIFIED



## UNCLASSIFIED

which is near the lower limit for hypervelocity phenomena, it should be noted that the velocities obtained in the micron sized, cloud impingement experiments were within the range of the experiments conducted by Sorenson. Thus we must conclude that although an explanation for these results is not evident, there appears to be a considerable reduction in hypervelocity damage in the micron size range as compared to the larger centimeter projectiles.

The final impingement phenomena to be discussed is the resulting force and momentum vectors imposed upon the vehicle by particle impact. Table 3 (27) shows the results of a sample calculation computed for a hypothetical motor. The results are given as a function of axial position from the exit plane and show the pressure load caused by the gas plume impingement. The results in Table 3 indicate the variation of the imposed pressure resulting from plume impingement and the force per unit area resulting from particle impingement as a function of axial distance from the exit plane. As one goes further out from the motor exit, the gas pressure decreases and finally becomes negligible. In this region, however, the particle impingement force, is still sizeable. Surface pressures as low as  $5 \times 10^{-4}$  psi can adversely effect the dynamic stability of objects located in the exhaust plume (27).

In order to bracket the uncertainty in determining the particle surface interaction, one can consider two limiting cases; inelastic and elastic collisions. The equations for these two collisions are written as follows:

$$\begin{array}{ll} \text{inelastic} & F/A = \rho_p v_p^2 \sin \theta \\ \text{elastic} & F/A = 2\rho_p v_p^2 \sin^2 \theta \end{array}$$

where the angle  $\theta$  is between the incoming particle trajectory and the surface. From these equations it is seen that the force from an elastic collision is twice that from an inelastic collision at  $90^\circ$  impact angle; however, at  $30^\circ$  impact angle, the two forces are equal. If one were to use the mean of these two limiting cases for calculations, the maximum variation would only be one third of the mean. Since uncertainties relating to the particle trajectory and number density calculations may be at least this large, it is clear that the determination of the force is not particularly uncertain.

However, there exists a very large uncertainty in the moment of this force dependent upon the model chosen. For instance, in an elastic collision the force is always normal to the surface, however, in an inelastic collision the force is in the direction of the particle trajectory. Thus, in the case of non-normal impactions, the model will greatly effect the resulting force vector direction and thus, the moments on the vehicle.

# UNCLASSIFIED

## Communication Attenuation

A final effect of two phase plumes that is to be discussed is that of increased attenuation of communication through the vehicle plume. In general, this attenuation results from the interaction of electromagnetic waves with free electrons produced in the plume. These electrons may be produced, in their order of importance, by four phenomena; after-burning, alkali metal ionization, gas specie ionization, and particle ionization. In general, the first phenomena dominates the situation at low altitude, but at altitudes greater than about 30 to 40 kilometers, after-burning becomes minimal, and the plume plasma becomes important. Solid propellants contain alkali metal impurities in their constituents, and the low ionization potentials of these alkali metals make them prime producers of electrons within the plume; the gas phase also is ionized to a certain degree as evidenced by high altitude, gas-only plume results. However, although considerable work has been performed in determining the work function for alumina at elevated temperatures, there has been no direct evidence that this phenomena adds significantly to the plume ionization level. In fact, in a series of studies made by Carpener, et.al. (28), with a view to determining the magnitude of the microwave attenuation associated with exhaust plasmas typical of state-of-the-art solid propellants, it was found that the principle electron producer was the alkali metal impurities.

In recent studies of the effects of exhaust plasmas upon signal transmission associated with the Apollo Program and reported by Baghdady and Ely (29), some pertinent results have been obtained. In particular, three different conditions of solid propellant retro-rocket firings have been encountered with significantly different effects on attenuation phenomena. In the first, with retros firing at altitudes of between 60 and 75 kilometers, the attenuation values were approximately 30 to 35 db. However, when a combination of retro-rockets and ullage rockets were fired simultaneously at altitudes between 60 and 75 kilometers, the value of the attenuation was recorded in excess of 60 db. In these tests the ullage rockets were fired 1/10th of a second before the retro-rocket ignition and continued to burn after the retro-rocket termination. There was no attenuation during the single engine firing time. In the third case, the retro-rocket and ullage rockets were fired simultaneously between 85 and 90 kilometers with a resulting attenuation between 15 and 35 db. The explanations given by the authors for these phenomena are as follows: In the simultaneous motor firing cases, the increased attenuation resulted from increased ionization in the two plume impingement region. In the third condition, at the higher altitudes, the reduction in attenuation was caused by the increased spreading of the plume at the higher altitudes. This reduces the electron density and since the attenuation is directly proportional to the square of the plasma frequency, which in turn is directly proportional to the electron density, one would expect the attenuation to decrease. Before one can be absolutely certain of this result, however, one must consider the collision frequency and the path length in the plasma are also

UNCLASSIFIED

# UNCLASSIFIED

changing with altitude.

These results and the explanations given indicate that the electron producing phenomena are associated with the gas phase or more exactly, a non-lagging phase. If the phenomena were associated with the particles, then at the higher altitudes one would not expect a significant decrease in the electron density since the particles would not spread at these flow conditions. The fact that the significant change does result seems to indicate that the ionization phenomena is associated with the gas phase.

## Conclusion

In the preceding discussion, the effect of condensed phase species on various plume phenomena have been considered. These effects result from either an altering of the gas properties or from an independent contribution based on the particle properties. In the former case it was shown that the distance from the nozzle exit to the normal shock which forms in a highly underexpanded gas jet is significantly reduced with increasing particle loadings. Also the gas properties are dependent on the non-equilibrium extent of the two phase flow but the proper consideration of the non-equilibrium effect on the gas flow field is not significant to the determination of the particle properties. Thus, an "uncouple" solution seems to be adequate in particle trajectory computations for low lag nozzles or small solids loadings.

With regard to independent particle effects the following were discussed, namely radiation heat transfer, particle impingement, and communication attenuation. For the case of radiation the accuracy of analytic techniques is limited by inadequate data on condensed phase species identification, optical properties, size distribution, and thermodynamic state. With regard to impingement effects, experimental results indicate that the heat transfer to an immersed vehicle is significantly enhanced by particle impaction; however, at present no analytic or empirical predictive technique appears satisfactory. Conversely, hypervelocity damage may be much less important than anticipated since there appears to be a significant effect of particle size that reduces the damage caused by micron size particle clouds. It was also shown that the force or moment imposed by particle impingement is significant at low gas densities, i.e., large axial distances from the motor exit, and that the magnitude of the force can be predicted adequately in the zero lag limit (low gas density, small body) by using the mean of a purely elastic and inelastic collision model. However, the moment imposed has a large uncertainty, particularly for oblique impacts. Finally, it was concluded that the particulate phase has little effect on communication attenuation.

# UNCLASSIFIED

## References

1. C.H. Lewis and D.J. Carlson, AIAA J. 2, 777 (1964).
2. F.H. Marble, AIAA J., 1, 2793 (1963).
3. D.J. Carlson, et al., "A Study of High Altitude Rocket Plume Phenomena (U)," Aeronutronic Publication No. S-2380, December 1963 (Secret).
4. J.E. Fontenot, "Thermal Radiation from Solid Rocket Plumes at High Altitude," AIAA Journal, 3, 970 (1965).
5. S.J. Morizumi and H.J. Carpenter, J. Spacecraft, 1, (1964).
6. A.J. Laderman, W.C. Kuby, S.R. Byron, D.J. Carlson, C.H. Bartky, "Study of Thermal Radiation, Particle Impingement Heating and Flow Field Analysis of Solid Propellant Rocket Exhausts," Aeronutronic No. U-4045, April (1966).
7. W.C. Kuby, et. al., "An Investigation of Recombination and Condensation Effects in Rocket Nozzles," Aeronutronic Publication No. C 1720 (1962), (Conf.).
8. R.J. Prozan, "Development of a Method of Characteristics Solution for Supersonic Flow of an Ideal, Frozen or Equilibrium Reacting Gas Mixture," LMSC/HREC A782535-A, Lockheed Missiles & Space Company, Huntsville, Alabama, April 1966.
9. D.J. Carlson and R.F. Hoglund, AIAA J., 2, 1980 (1964).
10. C.H. Bartky and E. Bauer, J. Spacecraft, 3, 1523-1527 (1966).
11. W.C. Rochelle, "Theoretical and Experimental Investigation of Heating from Saturn Solid Propellant Rocket Exhausts," Presented AIAA Second Propulsion Joint Specialists Conf., U.S. Air Force Academy, Colo. Spr., Colo., June 1966.
12. Private Communication, J. Reardon, Hayes International, Birmingham, Ala., Sept. 1966.
13. D.J. Carlson, "Emittance of Condensed Oxides in Solid Propellant Combustion Products," Tenth Symposium (Intern.) on Combustion, Cambridge, England, Paper 119 (August 17-21, 1965).
14. D.A. Gryvnak and D.E. Burch, "Optical and Infrared Properties of  $Al_2O_3$  at Elevated Temperatures," Aeronutronic Publication No. U-2623, May 31, 1964.

UNCLASSIFIED

## UNCLASSIFIED

15. J.M. Adams and S.E. Colucci, "The Spectroscopic Measurement of Gas and Particle Temperature in Metalized Propellant Combustion," Paper S66-175, presented at ICRPG/AIAA Solid Propulsion Conf., Wash., D.C., July 18-21, 1966.
16. H. Cheung and N.S. Cohen, AIAA J., 3, 250 (1965).
17. E. Bauer and D.J. Carlson, J. Quant. Spectrosc. Radiat. Transfer, 4, 363, (1964).
18. Private Communication, W.C. Rochelle, Marshall Space Flight Center, Huntsville, Ala., Dec. 1966.
19. K.C. Hendershot, "Research on Base Heating of Rocket Motor Vehicles Using Shock Tube Techniques," Cornell Aeronautical Laboratory Monthly Progress Report No. 19, CAL Project No. HM-2045-Y, Sept. 1966.
20. F.C. Price, et. al., "Final Technical Report: Internal Environment of Solid Rocket Nozzles," Philco Research Laboratories Publication No. U-2709, July 30, 1964.
21. W.C. Kuby, "The Internal Environment of a Solid Propellant Rocket Nozzle," AIAA Preprint No. 64-158, Presented Jan. 1962, Palo Alto, California.
22. A.J. Laderman, W.C. Kuby, S.R. Byron, D.J. Carlson, C.H. Bartky, "Study of Thermal Radiation, Particle Impingement Heating and Flow Field Analysis of Solid Propellant Rocket Exhausts," Aeronutronic No. U-4045, April (1966).
23. D.D. Jacobs, "Launch Vehicle Aerothermodynamic Design Assurance," Boeing Doc. No. D 515441-2, Nov. 1966.
24. N.R. Sorenson, Proc. of Seventh Symposium on Hypervelocity Impact, Vol. VI, 281 (1965).
25. C.H. Lewis, R.D. Hackett, and W.C. Kuby, "Effects of Impingement of Rocket Exhaust Gases and Solid Particles on a Spacecraft," Aeronutronic Interim Report Under Contract 951246, Jet Propulsion Lab, Nov. 1966.
26. D.E. Gault and H.J. Moore, Proc. of Seventh Symposium on Hypervelocity Impact, Vol VI, 341 (1965).
27. Private Communication, A.J. Laderman, Aeronutronics, Newport Beach, California, March 1967.
28. E.L. Carpener, J.B. Chown, I.A. Dickinson, and J.E. Nanevich, AIAA J., 4, 1339-1354 (1966).

UNCLASSIFIED

**UNCLASSIFIED**

29. E.J. Baghdady and O.P. Ely, Proc. of IEEE, 54, 1134-1146 (1966).

**UNCLASSIFIED**

# UNCLASSIFIED

Table I

Comparison of Radiation Measurements from Subscale Motor as Reported by  
Cornell Aeronautical Laboratory

	S-I B Retro	S-II Ullage
Exit Pressure, $P_e$	61 psia	14.6 psia
Radiation at $2\mu$ , $W$	0.1	0.025
$\frac{W}{P_e}$	$2.23 \times 10^{-3}$	$1.71 \times 10^{-3}$

UNCLASSIFIED

Table II

## RESULTS FOR PARTICLE IMPINGEMENT HEAT FLUX

Motor	Altitude	Model	$\dot{Q}_{tot.}$ BTU/in <sup>2</sup> sec	$\dot{Q}_{p-R}$	$\alpha_{tot}$	$\alpha$ K.E.	% Al <sub>2</sub> O <sub>3</sub>
Helium T <sub>O</sub> = 540°R P <sub>O</sub> = 100 psia	100 K ft	Teflon flat Cylinder Dia <sub>O</sub> = 1"	.1 *	~0	.05	.05	10
Helium T <sub>O</sub> = 1000°R P <sub>O</sub> = 100 psia	100 K ft	Teflon flat Cylinder Dia <sub>O</sub> = 1"	.1 *	~0	.04	.04	10
SIL Ullage T <sub>O</sub> = 6340°R P <sub>O</sub> = 930 psia	Sea Level	3" Dia Hemispherical end of Cylinder	20.8	3.5	.25	?	7.8
6 C3 - 11.4 T <sub>O</sub> = 6150°R P <sub>O</sub> = 727 psia	Sea Level	Blunt nose cone	15.7	3.5	.06	?	30.7

\* Estimated

UNCLASSIFIED



# UNCLASSIFIED

Table III

## SAMPLE IMPINGEMENT FORCE COMPUTATION

Specific Impulse	270 sec
Total Mass Flow Rate	0.93 lbs/sec
Exit Plane Mach No.	4.24
Exit Plane Static Pressure	1.0 psia
Nozzle Half Angle	15°
Nozzle Exit Area	11 in <sup>2</sup>
Particle Size	5.0 micron dia.
Particle Mass Fraction	1.0
Exit Plane Particle Velocity	4000 ft/sec

<u>x</u>	<u>P<sub>s</sub></u>	<u>F/A</u>
ft.	psia	lb sec/in <sup>2</sup> sec
2	0.37	1.2
4	9.2 X 10 <sup>-2</sup>	.37
10	1.5 X 10 <sup>-2</sup>	6.7 X 10 <sup>-2</sup>
100	1.5 X 10 <sup>-4</sup>	7.4 X 10 <sup>-4</sup>

UNCLASSIFIED

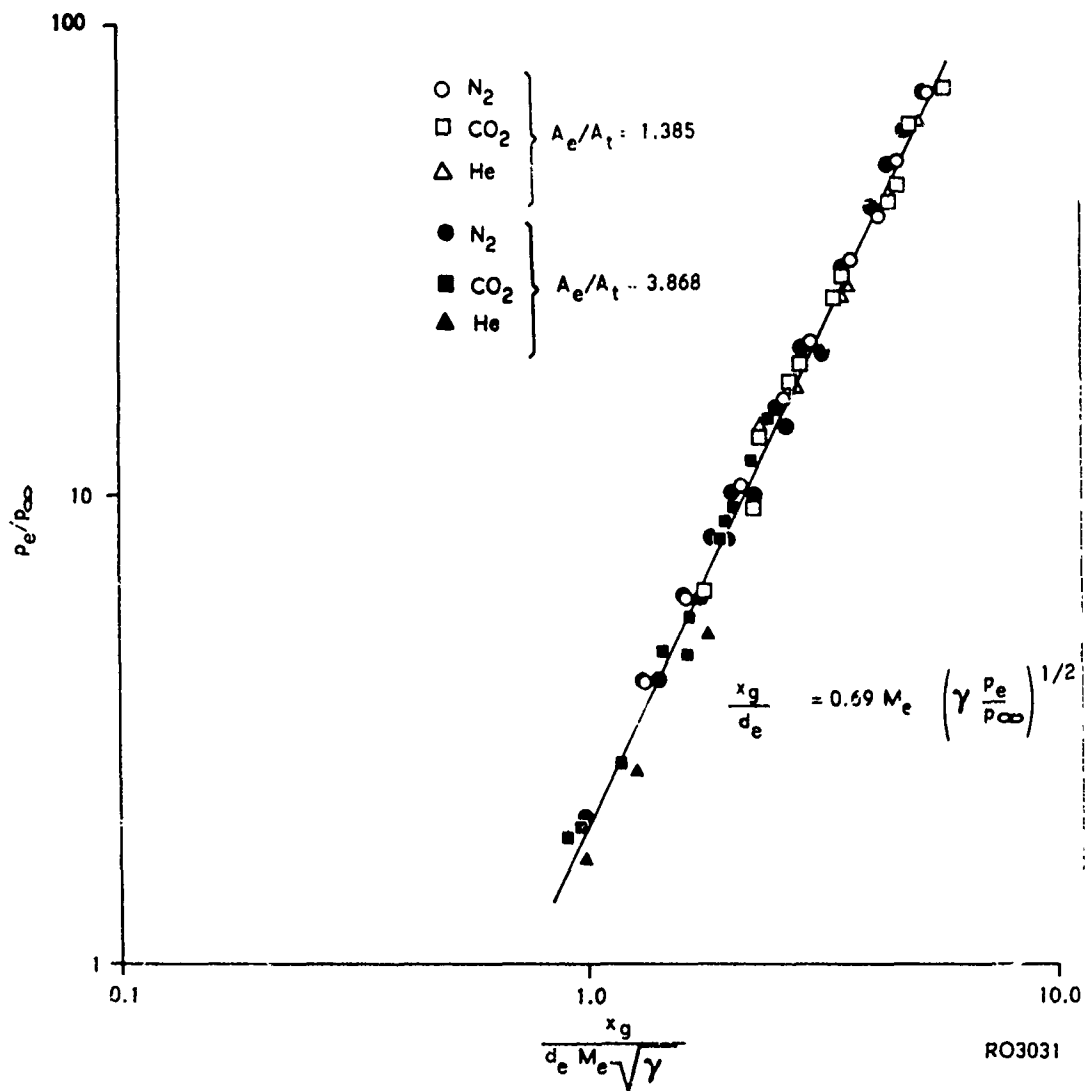


Figure 1. Distance to the Normal Shock in Gas-Only Flows Normalized by  $d_e M_e \sqrt{\gamma}$ .

UNCLASSIFIED

UNCLASSIFIED

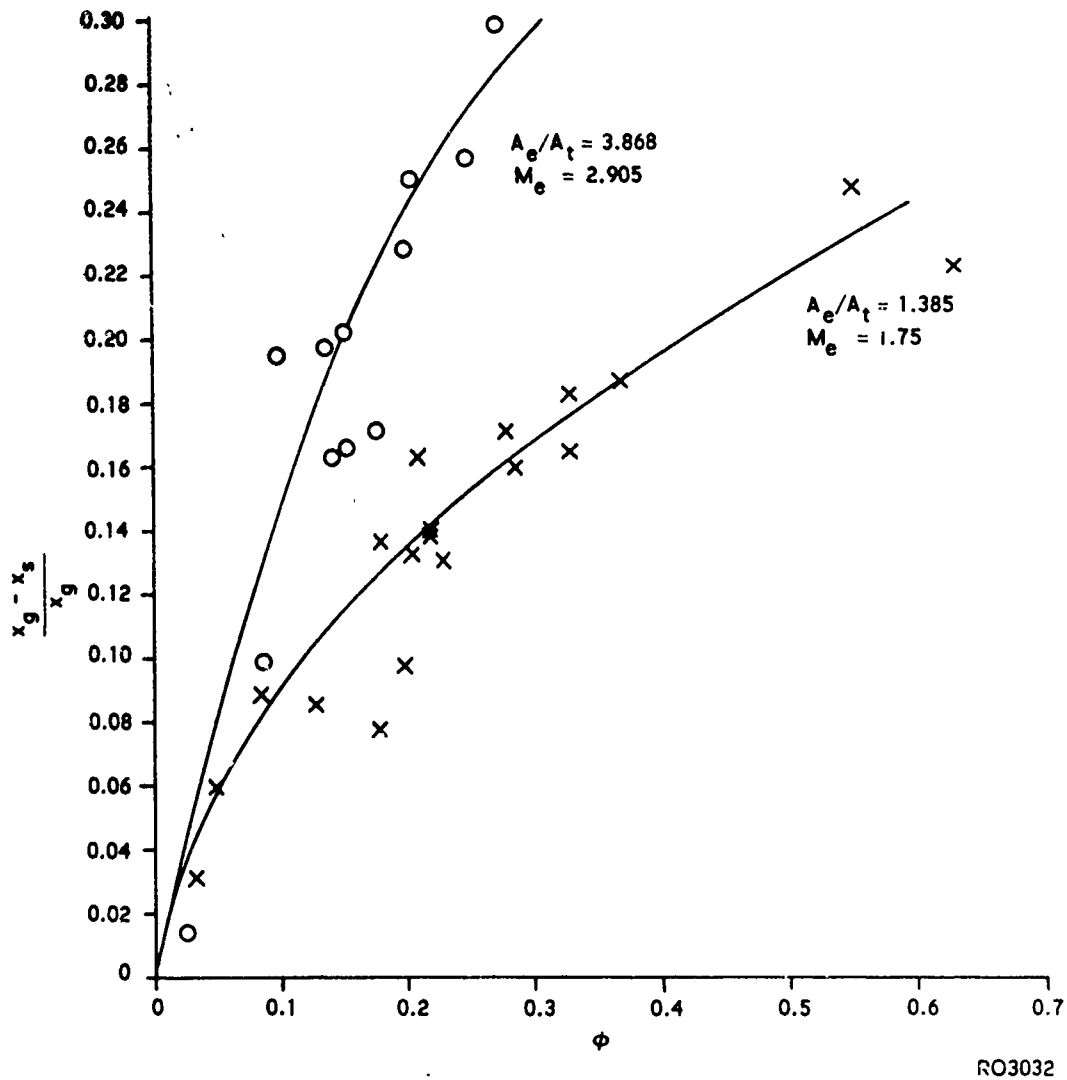


Figure 2. Fractional Change in the Distance to the Normal Shock as a Function of Particle Mass Fraction.

UNCLASSIFIED

UNCLASSIFIED

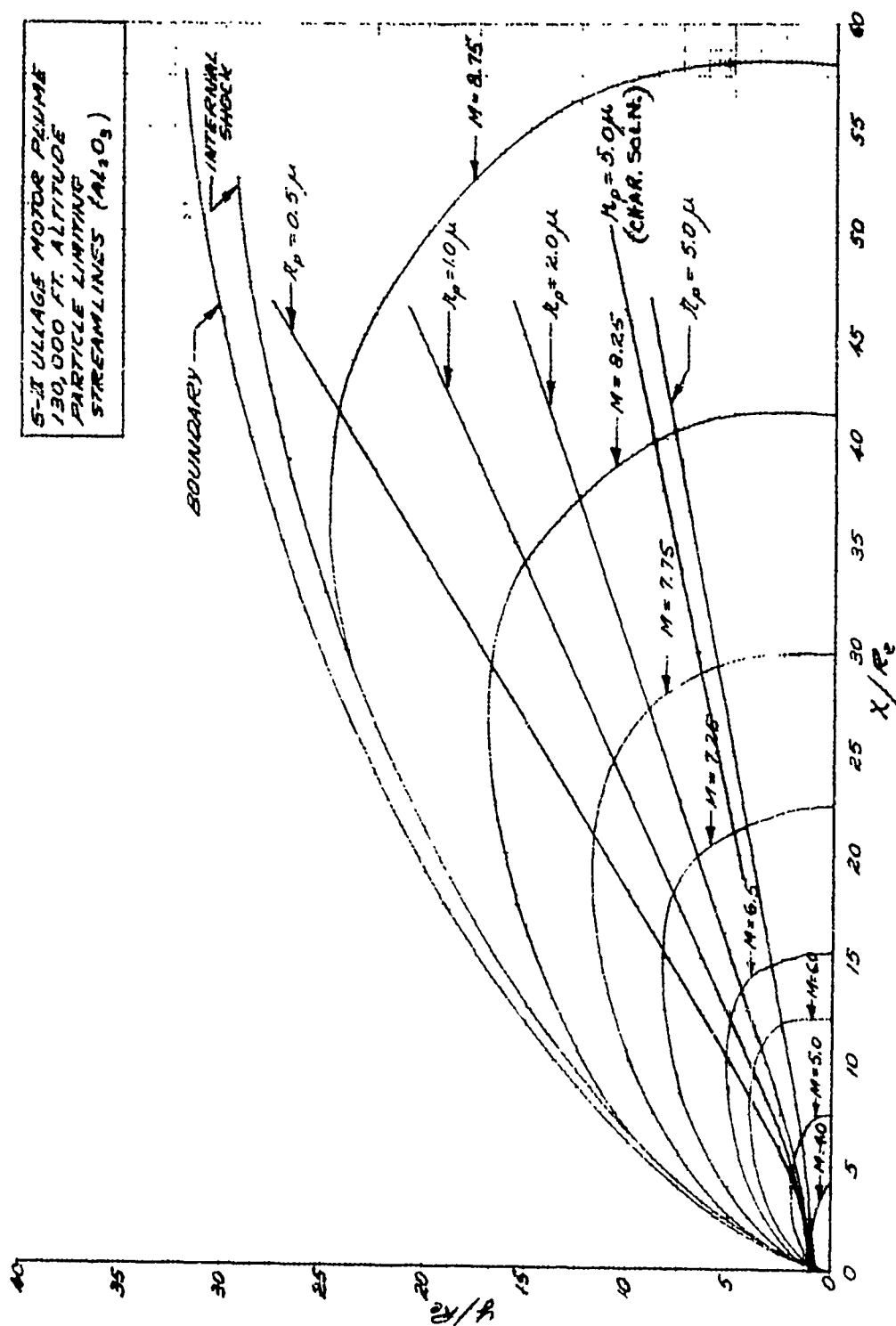


Figure 3. Limiting Particle Trajectories in the Exhaust Plume of an S-II Ullage Motor Firing at an Altitude of 130,000 ft. as computed using an uncoupled Flow Solution.

UNCLASSIFIED

UNCLASSIFIED

Computed Radiative Flux From S-II Ullage Motor, Normal to Axis  
0.5 Ft. From Exit Plane.

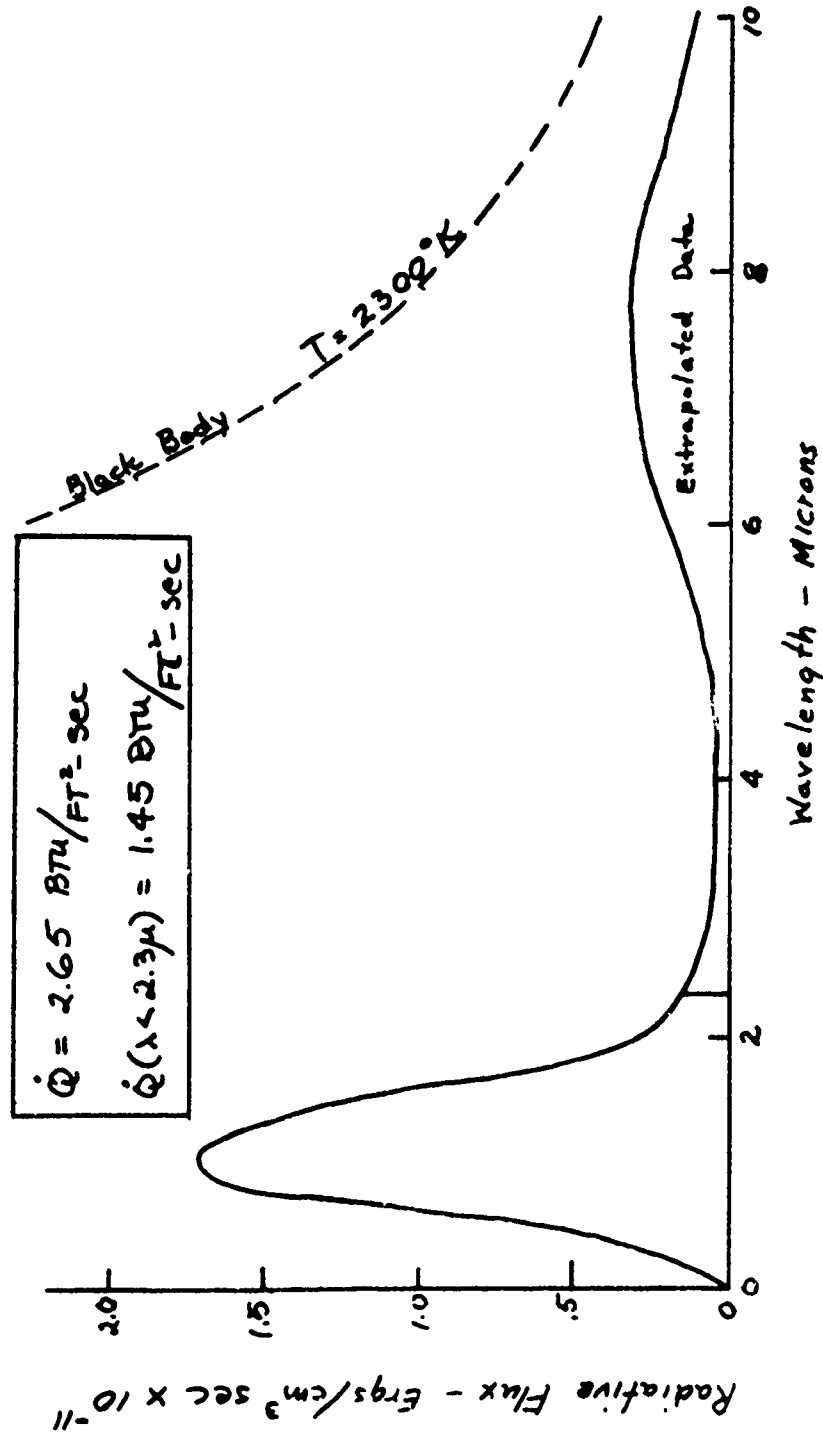


Figure 4. Computed Spectral Radiation Flux from the Condensed Phase in an S-II Ullage Motor Plume Firing at 130,000 ft. Altitude. Result is Given for a Line of Sight Normal to the Motor Axis and 0.5 ft. from the Nozzle Exit.

UNCLASSIFIED

UNCLASSIFIED

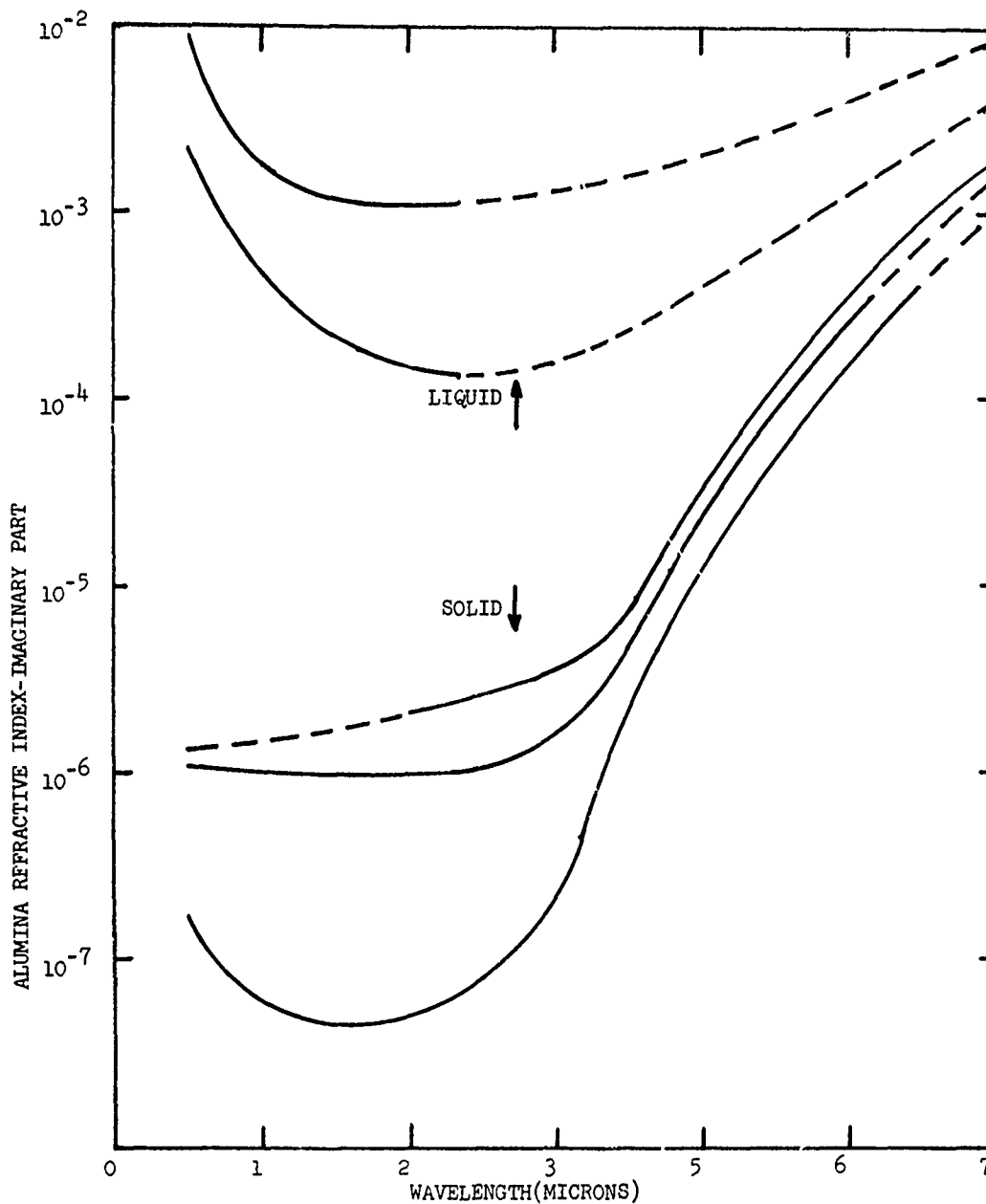


Figure 5. Imaginary Part of Refractive Index of Aluminum Oxide at Various Wavelengths and Temperatures. Solid Lines Represent a Fit of Experimental Data and Dashed Lines Indicate Extrapolation of the Data.

UNCLASSIFIED

UNCLASSIFIED

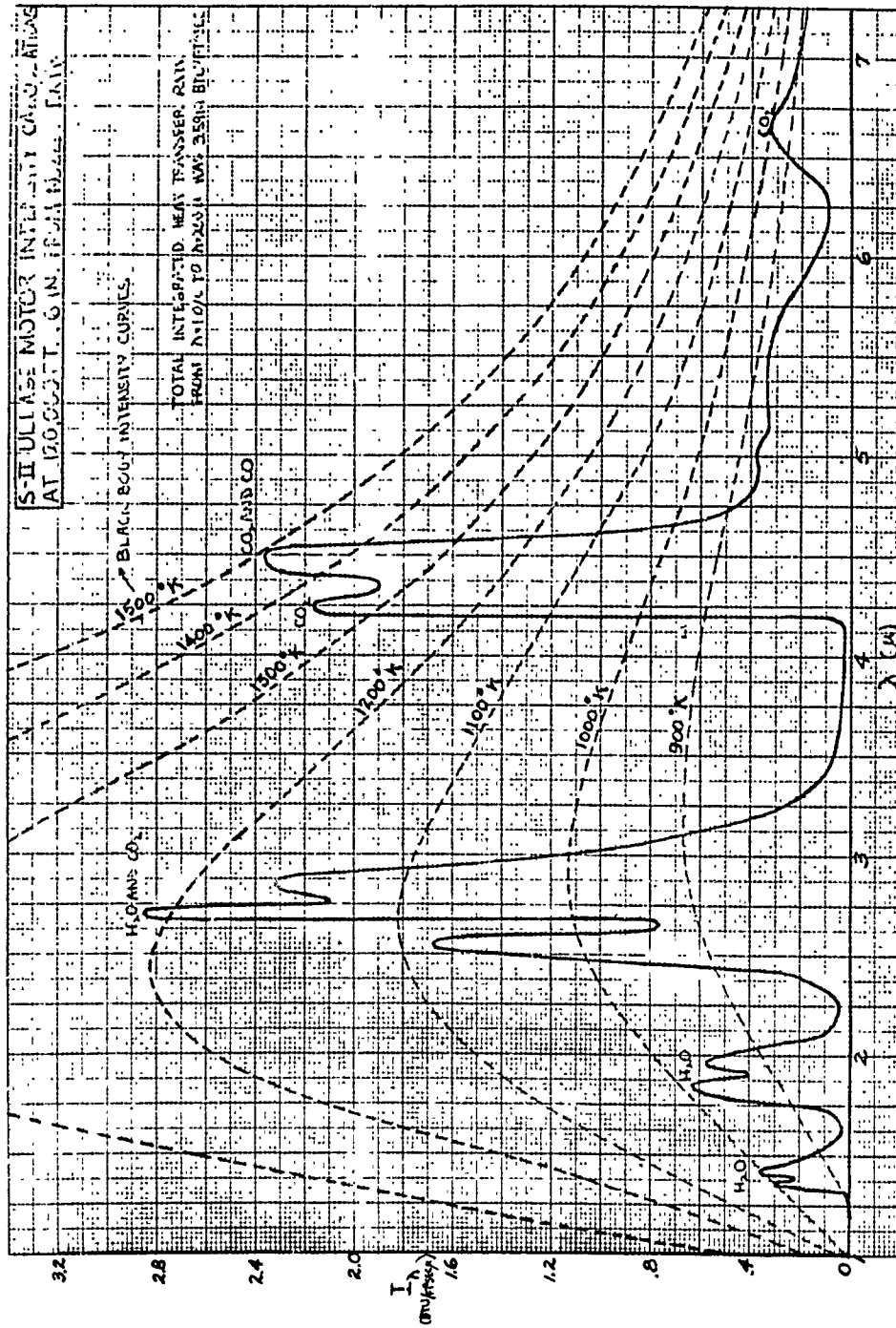
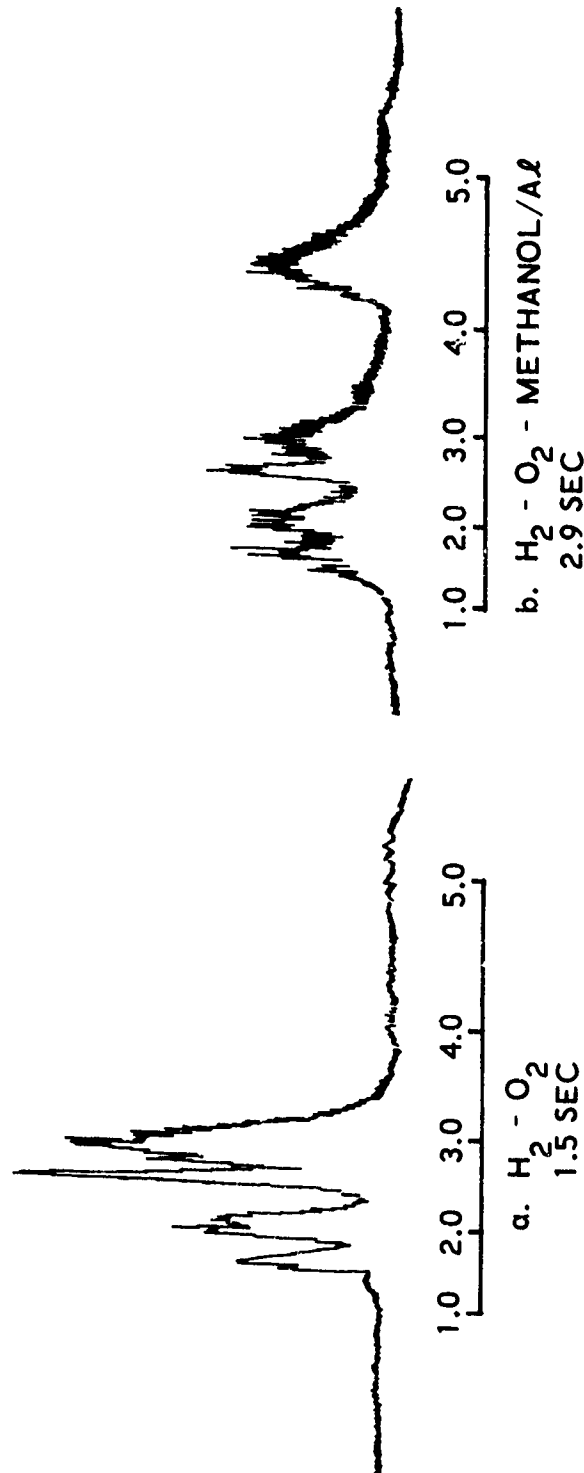


Figure 6. Computed Spectral Radiation Flux from the Gas Phase of an S-II Ullage Motor Firing at 120,000 ft. Altitude. Result is Given for a Line of Sight Normal to the Motor Axis and 0.5 ft. from the Nozzle Exit.

UNCLASSIFIED

UNCLASSIFIED



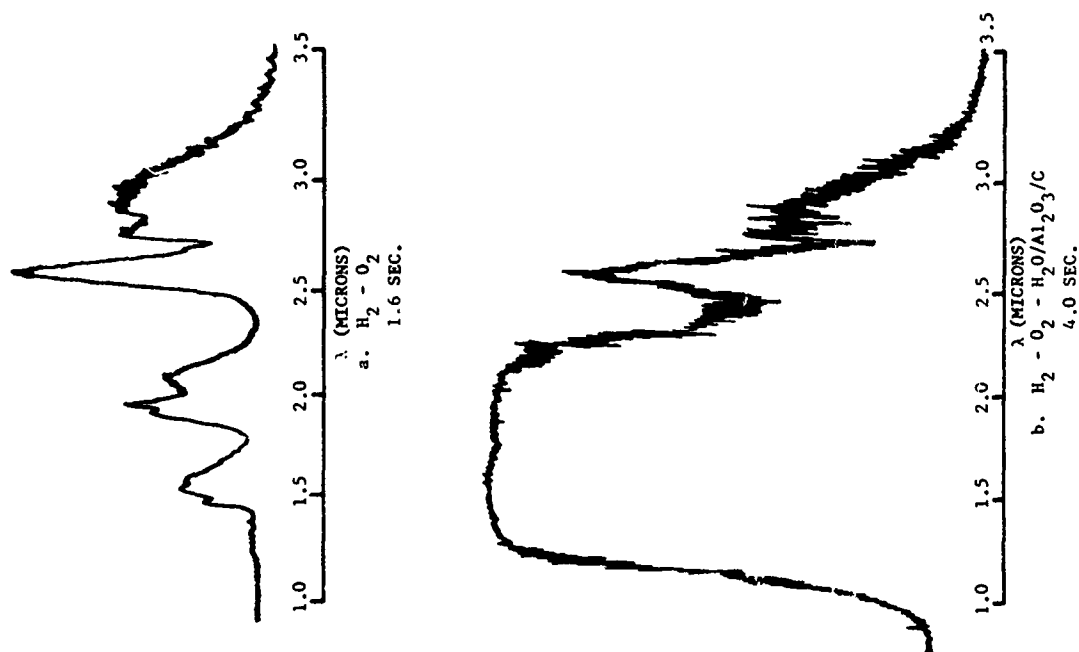
UNCLASSIFIED

Figure 7. Comparative Spectral Measurements at Combustion Temperatures from H<sub>2</sub>-O<sub>2</sub> Engine with Methanol and Aluminum Added.



UNCLASSIFIED

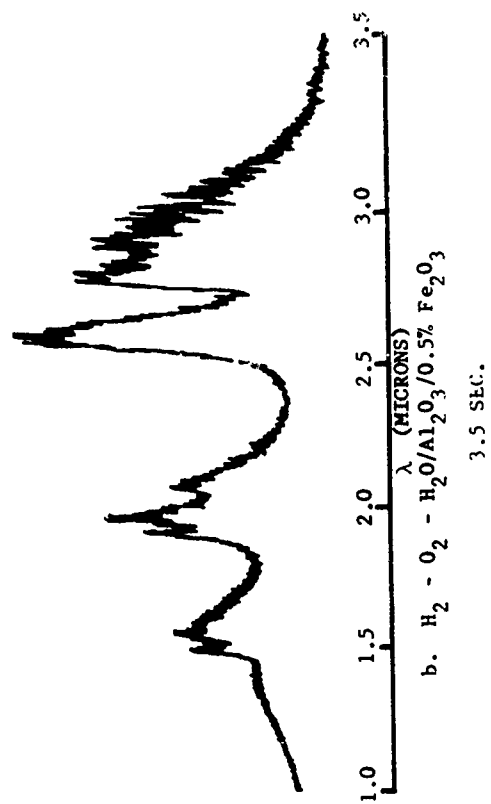
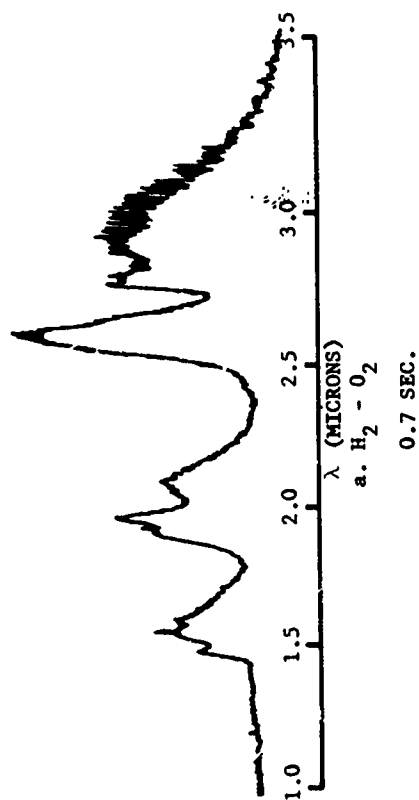
Figure 8. Comparative Spectral Measurements at Combustion Temperatures from an  $H_2-O_2$  Engine with Water, Alumina, and Carbon Added.



UNCLASSIFIED

UNCLASSIFIED

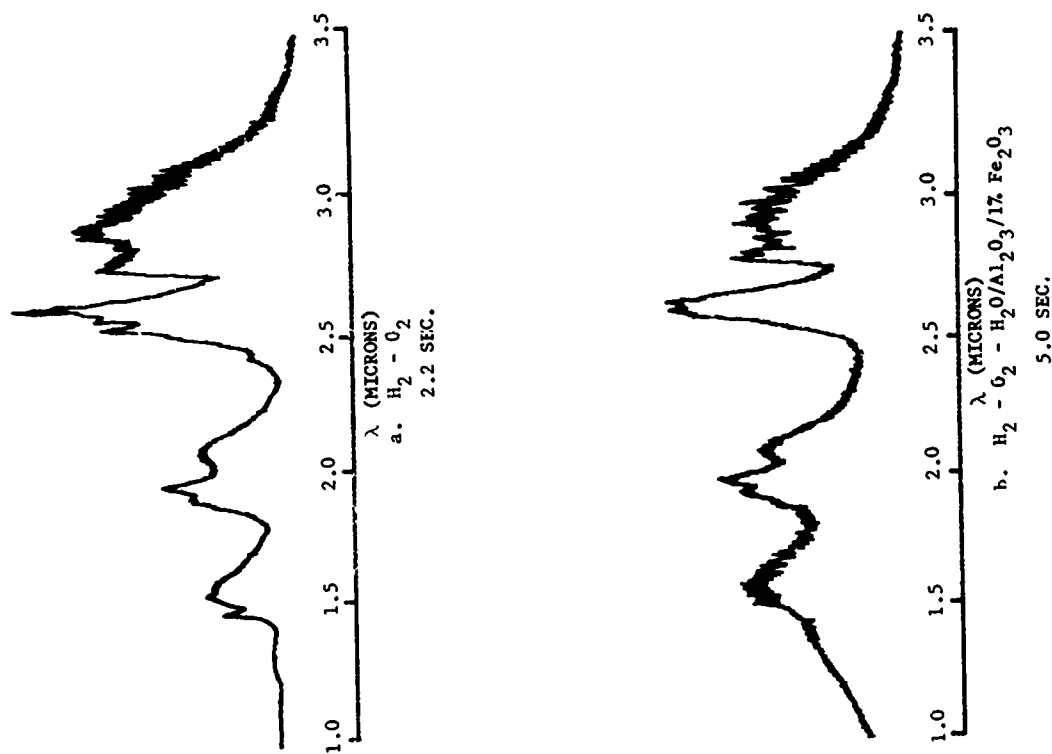
Figure 9. Comparative Spectral Measurements at Combustion Temperatures from an  $H_2-O_2$  Engine with Water, Alumina and 0.5% Ferric Oxide Added.



UNCLASSIFIED

UNCLASSIFIED

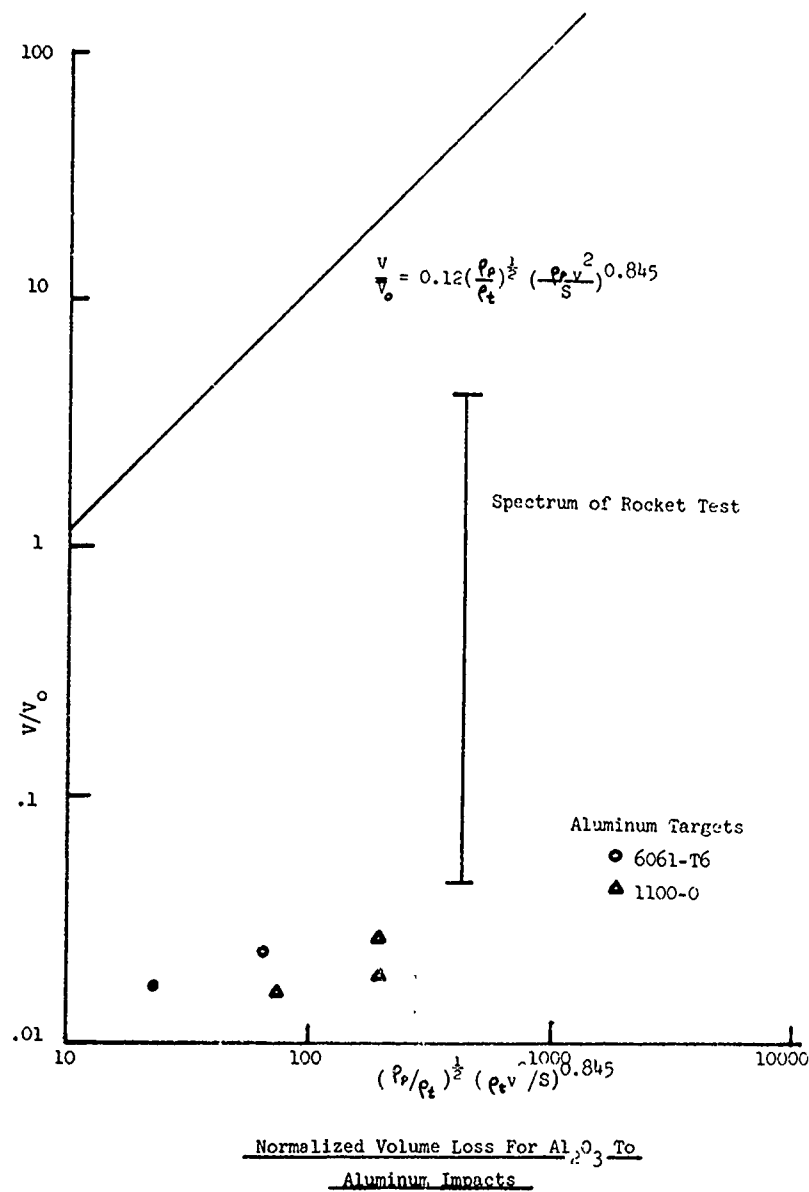
Figure 10. Comparative Spectral Measurements at Combustion Temperatures from an  $H_2-O_2$  Engine with Water, Alumina and 1% Ferric Oxide.



UNCLASSIFIED

UNCLASSIFIED

Figure 11. Hypervelocity Impingement Damage from Micron-Size Particle Clouds of Alumina Impinging on Aluminum Target Compared with a Typical Single, Large-Particle Correlation Equation.



UNCLASSIFIED

549/550

**UNCLASSIFIED**

**RADIATION FROM PARTICLE LADEN PLUMES**

By: A. J. Laderman  
D. J. Carlson

Philco-Ford Corporation  
Aeronutronic Division  
Applied Research Laboratories  
Newport Beach, California

**UNCLASSIFIED**

# UNCLASSIFIED

## CONTENTS

	PAGE
ABSTRACT . . . . .	iii
INTRODUCTION . . . . .	1
SCOPE OF THE PROBLEM . . . . .	3
GENERAL CALCULATION SCHEME . . . . .	5
COMPARISON BETWEEN THEORY AND EXPERIMENT . . . . .	7
RADIATION FROM INHOMOGENEOUS NONISOTHERMAL, OPTICALLY THICK PLUME	10
CONCLUSIONS. . . . .	14
REFERENCES . . . . .	15
ILLUSTRATIONS. . . . .	17

UNCLASSIFIED

# UNCLASSIFIED

## RADIATION FROM PARTICLE LADEN PLUMES

By

A. J. Laderman and D. J. Carlson

Aeronutronic Applied Research Laboratories  
Philco-Ford Corporation  
Newport Beach, California

### ABSTRACT

Existing methods for calculating radiation from the particulate material which is present in a two-phase rocket exhaust plume are reviewed. The scope of the problem is defined and limitations common to current methods are summarized. The significance of using the appropriate optical properties of the individual particles to predict spectral radiancy of the plume is demonstrated by comparison of theoretical results with experimental observations. Finally, an approximate technique for calculating radiation from an optically thick nonisothermal and inhomogeneous plume is proposed.

UNCLASSIFIED

**UNCLASSIFIED**

## INTRODUCTION

The purpose of this paper is to compare existing methods for predicting radiation from a two-phase rocket exhaust plume, to demonstrate the significance of using appropriate optical data on the results of such predictions, to indicate areas of uncertainties concerning the problem, and to propose a new approximate technique for calculating radiation from an optically thick, nonisothermal and inhomogeneous particle cloud.

There currently exist relatively few methods for calculating plume radiation. The previous paper<sup>1</sup> describes one method, a computerized technique which takes into account the appropriate optical properties of the individual particles comprising the plume. The remaining few methods are summarized in Figure 1 which shows a partial listing of organizations involved in two-phase plume radiation calculations and the methods employed.

The method of Babco and Edwards<sup>2</sup> is an analytical technique which provides a closed form solution for the local emissivity of an isothermal dispersion of isotropic scattering particles of the same size. The analysis is restricted to conically shaped plumes where the local number density of particles diminishes as the inverse square of the distance from the cone vertex. In addition, the solution is limited to small cone angles and strongly scattering dispersions.

**UNCLASSIFIED**



## UNCLASSIFIED

Morizumi and Carpenter<sup>3</sup> were the first to present a comprehensive analysis of the problem. Their calculation scheme is similar to that described by Kuby,<sup>1</sup> except that the treatment of optical properties is over-simplified by assuming a constant particle emissivity. Their method offers the advantages, however, that once the plume-flow field is known, the radiation calculations can be performed essentially by hand.

Fontenot's method<sup>4</sup> is a simplification of the analysis of Morizumi and Carpenter. However, Fontenot's description of alumina optical properties is based on data obtained for soot-laden flames.

# UNCLASSIFIED

## SCOPE OF THE PROBLEM

Before proceeding, it is instructive to review the scope of the problem to summarize limitations common to all the methods previously described. This is illustrated in Figure 2, where the major aspects of the problem have been grouped in four main categories: Radiation Mechanisms, Fluid Mechanics, Radiation Parameters, and Atmospheric Effects.

Because of inadequate information concerning some of these items, the listing of Figure 2 can be considerably reduced. Consequently, only thermal emission is considered because nonequilibrium processes are not yet well defined. Furthermore, the searchlight effect is unimportant for optically thick plumes and afterburning does not occur at high altitudes.

With respect to the fluid mechanic problems, there exist a number of computerized techniques for determining the gas and particle plume flow fields which provide local values of temperature, velocity, and concentration. Although the fluid mechanical structure of the plume has received a considerable amount of attention, much remains to be done. At low altitudes, interaction between unburned exhaust products and the ambient air (afterburning) introduces a host of uncertainties involving chemical equilibria, solid particle effects, etc. The shockwave structure is fairly well understood for the near field, but quantitative description of the fluid state downstream of the near field shocks becomes tenuous. At high altitudes, nonequilibrium effects become important, both

UNCLASSIFIED

## UNCLASSIFIED

in the exhaust gas itself and in the region where exhaust gas and ambient air interact. In addition, the effects of multiple nozzles introduces a further uncertainty. There is no attempt here to better define these problems, but the method proposed remains applicable as knowledge of the structure improves.

Solar scattering and atmospheric attenuation are also excluded because these processes are primarily of concern to problems of detection and can be ignored in calculation of base heating.

The remaining category, radiation parameters, is expanded in Figure 3. To determine the gas phase radiation, it is necessary to know the local species concentrations throughout the plume and the appropriate gas emissivities. The concentrations are found from the gas flow field results while the emissivities can be evaluated from existing theoretical band models or are available directly from experimental measurements, particularly for the more significant emitters such as  $H_2O$  and  $C_2O$ .

Likewise, calculation of the particle continuum requires specification of particle concentrations which is provided by the local size distribution arising from calculations of the plume structure. In addition, the local size distribution and the physical state of the particles are required to determine the optical properties of the particle plume.

When the plume is optically thin, the contributions from the gas bands and the particle continuum can be added to find the total radiation. However, when the plume is optically thick, the radiation from one phase is altered by the presence of the other. In this case, the gas and particle contributions must be combined in an appropriate manner yet to be developed. The radiative behavior of the plume will also depend on gradients in pressure, temperature, and concentration on the different emitters which are present and, as just mentioned, on the optical thickness.

UNCLASSIFIED

# UNCLASSIFIED

## GENERAL CALCULATION SCHEME

In general, a method for calculation of plume radiation will require the elements shown in Figure 4. There, the circled quantities represent input data and the boxed items denote calculation routines. Thus, a thermochemical calculation is needed to specify the chamber temperature and specie concentrations and the variation of these parameters throughout the nozzle and plume expansion. These results, together with the nozzle geometry, are used to determine the gas flow field in some manner such as the method of characteristics. Specification of the initial particle size distribution then allows calculation of the particle plume, consisting of the local particle temperature, velocity, and number density.

At this point, treatment of the problem has varied. In the method of Morizumi and Carpenter,<sup>3</sup> the plume is divided into cylindrical segments, whose axis is normal to the line-of-sight from the target. An averaging technique is used to determine an effective temperature,  $\bar{T}$ , for the segment and the optical thickness along the line-of-sight is found by summing overall particle sizes. A constant emissivity of 0.25 is assumed for all particles and the apparent plume emissivity,  $\epsilon_a$ , is evaluated from theoretical curves for scattering and absorbing cylinders of arbitrary optical thickness (isothermal, homogeneous, and single-size scattering centers). The heat flux from the segment is calculated finally from the equation:

$$\dot{q} = F \epsilon_a \bar{T}^4$$

UNCLASSIFIED

## UNCLASSIFIED

where the factor  $F$  accounts for the view geometry, and the total heat flux is found by summation over the segments.

On the other extreme, the method described by Kuby<sup>1</sup> starts with the complex index of refraction  $m = n_1 - in_2$  and uses Mie theory<sup>5</sup> to find the absorption and scattering cross sections,  $\sigma_a$  and  $\sigma_s$ , as a function of wavelength. Knowing the plume structure, the local values, averaged over particle size, of  $\langle \sigma_a \rangle$ ,  $\langle \sigma_s \rangle$ , and  $\langle R^\circ \rangle$  where  $R^\circ$  is the blackbody function, can be calculated. The plume is then divided into slabs normal to the line-of-sight, where each slab assumes the values of  $\langle \sigma_a \rangle$ ,  $\langle \sigma_s \rangle$ , and  $\langle R^\circ \rangle$  at its midpoint, and the radiative equation of transfer is applied to each slab. Solving the resulting set of simultaneous equations, with appropriate boundary conditions yields, finally, the spectral radiance of the plume along the line-of-sight.

In the example discussed later, the plume is optically thin, in which case it is also possible to find the total particle heat flux simply by summation of all contributions throughout the plume without regard to scattering contributions. Because, in this case, the gas phase radiation was important, it has been indicated in Figure 4 that a similar calculation could be made for this contribution.

UNCLASSIFIED

# UNCLASSIFIED

## COMPARISON BETWEEN THEORY AND EXPERIMENT

During firings of the Saturn II ullage motor at AEDC and OAL, several radiometer measurements were made which can be used as a basis for comparison with the theoretical calculations. At AEDC,<sup>6</sup> a Hayes FF1, narrow view (8 millirad x 8 millirad at 20 feet) detector, located 6 inches downstream of the exit plane and 5 feet from the plume centerline, Figure 5, was used to measure total radiation. The detector response was flat to 15 microns.<sup>7</sup> The results of this test indicated an average steady state flux of 18 Btu/ft<sup>2</sup> sec, or 6.53 watts/cm<sup>2</sup>-ster.

At OAL,<sup>8</sup> several spectral measurements were made over the wavelength interval from 0.5 to 3 microns. Results of these tests, shown in Figure 6, indicate that (1) on the basis of the AEDC test result, over half of the radiative flux occurs at wavelengths greater than 3 microns, and (2) in the observed spectral interval (1.7 to 3  $\mu$ ) the gas band radiation is approximately one third of the particle continuum.

To compute the plume radiation for these conditions, the following assumptions were made:

- (1) The initial particle size distribution was based on existing data for similar sized motors.
- (2) Alumina was considered to be the only continuum emitter and optical properties in the far infrared were based on an extrapolation of existing data.

UNCLASSIFIED

## UNCLASSIFIED

The optical property data are shown in Figure 7, where the imaginary part of the complex refractive index,  $n_2$ , is plotted as a function of wavelength for various temperatures. The solid phase data are based on the measurements of Gryvnak and Burch<sup>9</sup> over the spectral range from 1/2 to 6 microns. For the liquid phase, data<sup>10</sup> are available only in the range from 1/2 to 2.5 microns. To extend the calculations into the far infrared, the liquid data were extrapolated by paralleling the  $n_2$  curve to the solid  $n_2$  curves. The extrapolation choice is not as critical as it appears, however, because the particle emissivity becomes unity for this size distribution when  $n_2$  exceeds  $\sim 2 \times 10^{-2}$ .

With the data of Figure 7, absorption and scattering cross sections were calculated using Mie theory and radiation from the optically thin plume determined on the basis of the particle plume structure computed in Reference 11. The gas contribution was calculated using the experimental data 12,13,14,15 on gas emissivities for  $H_2O$  and  $CO_2$ .

The theoretical particle continuum was 36 percent of the total measured flux while the gas contribution was 23 percent of the measured radiation. The calculated radiancy in the visible spectrum is in good agreement with the OAL observation, while the integrated continuum radiancy in the interval from 1.7 to 3 microns is about 10 percent of the experimental observation (excluding the gas bands). However, in spite of the difference in the magnitudes of the theoretical and experimental spectral radiances in this region, the spectral distribution is similar.

The calculation of particle radiation was repeated using the method of Morizumi and Carpenter.<sup>3</sup> This result, shown also in Figure 6, corresponds to 87 percent of the total measured radiation. With the gas contribution then, this method predicts 110 percent of the measured value. However, the spectral distribution of radiancy resulting from the gray-body assumption made by Morizumi and Carpenter<sup>3</sup> is incorrect. With this assumption, the bulk of the radiation originates from the 1/2 to 4 micron interval, in contrast to the OAL measurements. If, in fact, the OAL and AEDC

UNCLASSIFIED

## UNCLASSIFIED

measurements are both correct, then a large fraction of the radiation must occur at longer wavelengths as indicated by the present results.

Several possible causes have been advanced to explain the source of the discrepancy between theory and experiment noted above. These include presence of other continuum emitters, supercooling of alumina, and searchlight emission.

In addition to 8 percent of  $\text{Al}_2\text{O}_3$ , the Saturn II ullage motor contains 2 percent of ferric oxide which is used as a burn rate controller. Although this material is present in the plume in the condensed phase, there are no data on optical properties available at the temperatures typical of the rocket plume. Existing room temperature data, however, show that in the infrared  $n_2$  for ferric oxide is greater than  $n_2$  of alumina at its melting point. Thus, even in small quantities, ferric oxide may contribute significantly to plume radiation. Furthermore, the possibility that the particles are comprised of a mixture of alumina and ferric oxide, with radiative properties exceeding those for pure alumina, cannot be overlooked.

Supercooling of the alumina would result in particles of all sizes retaining a liquid-like emissivity. Because  $n_2$  for the liquid is several orders of magnitude greater than that for the solid, the particle radiation is proportional to the mass fraction of particles in the liquid phase which, for the present calculation, is 40 percent. However, because the radiation at long wavelengths ( $> 5$  microns) becomes blackbody limited, supercooling would increase the theoretical particle continuum to only 48 percent of the total measured flux.

Searchlight emission dominates direct emission in the interval from 1 to 4 microns where the particle emissivity is low.<sup>11</sup> However, by including the searchlight effect the particle continuum is increased to 44 percent of measurement. If both supercooling and searchlight are accounted for, the calculated particle radiation is 59 percent of the measured radiant flux.

UNCLASSIFIED



# UNCLASSIFIED

## RADIATION FROM INHOMOGENEOUS NONISOTHERMAL, OPTICALLY THICK PLUME

In the following, a new approximate technique for calculating radiation from an inhomogeneous, nonisothermal, optically thick particle plume, which accounts for the spectral and temperature variation of optical properties, is described. It is assumed that the particle plume structure, in terms of local temperature and number density as a function of particle size, can be determined. With this information, the radiation calculations can be made essentially by hand, using the summation procedures developed below.

Absorption and scattering efficiency factors  $Q_a (= \sigma_a/2\pi r)$  and  $Q_s (= \sigma_s/2\pi r)$ , determined from Mie theory, are shown in Figure 8 as a function of  $n_2x$  and  $x$ , respectively, where  $x = 2\pi r/\lambda$  is the size parameter.  $Q$  is actually a function of  $x$ , as well as  $n_2x$  and the separation resulting from size is indicated on Figure 8. In addition, in the vicinity of the knee of the curves,  $Q$  varies about the mean curves shown; however, for the present method, only the mean values are considered.

In the case of a homogeneous isothermal plume, the equation of radiative transfer can be solved to yield the apparent plume emissivity  $\epsilon_a$  as a function of optical thickness  $\tau$  with  $Q_a/Q_t (= Q_a + Q_s)$  as parameter.<sup>16</sup> This is shown in Figure 9, where three regions of interest can be delineated. The first corresponds to a plume that is optically thin to both absorption and scattering and is bounded on the right by the line  $\tau \approx 1.0$ . The second is the region between  $\tau \approx 1.0$  and a line (which we will denote as  $\tau_1$ )

UNCLASSIFIED

# UNCLASSIFIED

drawn through points on each  $Q_a/Q_t$  curve where the curves just begin to deviate from a straight line. This region corresponds to a plume that is thin to absorption but thick to scattering. The third region is that to the right of the line  $\tau_1$  which corresponds to the case where self-absorption becomes significant. When the  $Q_a/Q_t$  curve becomes horizontal, the plume is thick to self-absorption and the apparent plume emissivity,  $\epsilon_a$ , acquires its maximum value.

Let the line which passes through the intersection of the extension of the straight portions of the  $Q_a/Q_t$  curves be labelled  $\tau_c$ . The line  $\tau_c$  is defined now as the boundary which separates the region to the left which is thin to self-absorption (but thick to scattering) from the region to the right which is thick to both self-absorption and scattering. The apparent emissivity  $\epsilon_a$  is then a maximum when  $\tau \geq \tau_c$  as shown for the case of a cylinder in Figure 10.

To calculate the radiation from the plume, we select several lines-of-sight and divide the plume into cylindrical segments where axes are normal to these lines-of-sight. Along each line we sum the contribution to the quantities  $\epsilon_a$ ,  $\tau$ , and  $R$

$$\epsilon_a = \int_0^{Z_c} \sum_r NAQ_a dz \quad (1)$$

$$\tau = \int_0^{Z_c} \sum_r NAQ_t dz \quad (2)$$

$$R = \int_0^{Z_c} \sum_r NAQ_a R^0 dz \quad (3)$$

UNCLASSIFIED

# UNCLASSIFIED

where  $Z$  is the distance along the line-of-sight,  $Z_c$  its value when  $\tau = \tau_c$ ,  $A$  is the geometric area of the particle of radius  $r$ ,  $N$  the number density of particles of radius  $r$ ,  $R^0$  is the blackbody function corresponding to the temperature of particles of radius  $r$ , and the summation is made locally over all particle sizes. It is to be emphasized that the spectral radiance is found by performing the calculations indicated in Equations (1) through (3) at selected wavelengths in the interval of interest.

For the case of a homogeneous, isothermal plume,  $Q_a/Q_t$  is a constant and the above equations are exact to the left of the line  $\tau_1$  on Figure 9. When  $\tau > \tau_1$ , the calculation is continued, ignoring self-absorption. Thus, in the  $\epsilon_a, \tau$  plane of Figure 9, the trajectory of the calculation proceeds along the straight line extension of the  $Q_a/Q_t = \text{constant}$  curve until  $\tau = \tau_c$ . At this point, the calculation is terminated because the plume is now optically thick to self-absorption. The error in the calculation increases from zero at  $\tau = \tau_1$ , reaches a maximum (of 40 percent) at  $\tau = \tau_c$ , and diminishes to zero again as the physical length of the plume increases beyond the value corresponding to  $\tau_c$ . It is obvious, from Equation (3), that the radiance of the plume is given by

$$R = R^0 \int_0^{Z_c} \sum_r NAQ_a dZ = R^0 \epsilon_a$$

when  $\tau \geq \tau_c$ , which is the maximum value given by the exact solution.

For inhomogeneous nonisothermal plumes,  $Q_a/Q_t$  is not constant and the calculation proceeds along an arbitrary trajectory in Figure 10. However, the error introduced by this method should not exceed that discussed above, as long as the gradient in  $R$  is not large in the vicinity of  $\tau_c$ . The method has not yet been tested for this case; however, in the absence of experimental spectra of optically thick plumes, a good test would be a comparison between the results of this technique and those obtained using the method of Reference 11.

UNCLASSIFIED

## UNCLASSIFIED

It should be pointed out, finally, that because the present method predicts an apparent emissivity equal to, or in excess of, the actual plume emissivity, the method is conservative and thus well-suited to engineering calculations.

UNCLASSIFIED

# UNCLASSIFIED

## CONCLUSIONS

On the basis of the preceding discussion, it is not possible to isolate, conclusively, the physical mechanisms responsible for the plume emission; however, the following conclusions can be made.

Gas phase radiation clearly cannot be ignored without demonstrating that its contribution is negligible. This is particularly true of lightly loaded solid propellant motors such as the Saturn II ullage motor.

Particle radiation is not graybody. Optical data appropriate to particle size and wavelength must be used to predict spectral radiancy.

While supercooling can explain 48 percent of the measured radiation from the Saturn II ullage plume, this requires a particular arbitrary extrapolation of the liquid alumina optical data. Searchlight emission provides an alternative explanation of the observed radiation and the two effects combined account for 59 percent of the total experimental measurement.

Other solids, particularly iron oxide and possibly carbon, cannot be dismissed as significant or even dominant contributors to particle radiation.

UNCLASSIFIED

# UNCLASSIFIED

## REFERENCES

1. Kuby, W. C., "Review of Two-Phase Plume Effects," presented at AFRPL two-phase Flow Conference, Norton AFB, San Bernardino, California, 15-16 March 1967.
2. Bobco, R. P. and Edwards, R. H., Radiation from an Absorbing Scattering Conical Dispersion with Non-Uniform Density, Hughes Aircraft Co, Space Systems Division, Report No. 21, SSD 60571R, December 1966.
3. Fontenot, J. E., AIAA Journal, 3, 970 (1965)
4. Morizumi, S. J., and Carpenter, H. J., J. Spacecraft, 1, 501 (1964)
5. van de Hulst, Light Scattering by Small Particles, (John Wiley and Sons, Inc., New York, 1957).
6. Rochelle, W. C., "Modified SIC Ordnance Disconnect Heating Analysis and SII Ullage Motor Test Results," NASA/MFSC Memorandum for File, AT-20-65, 23 November 1965.
7. Reardon, J., Hayes International (Private Communication).
8. Rochelle, W. C. (Private Communication).
9. Gryvnak, D. A. and Burch, D. E., J. Opt. Soc. Am., 55, 625 (1965)
10. Carlson, D. J., "Emittance of Condensed Oxides in Solid Propellant Combustion Products," pp 1413-1424, Tenth Symposium (International) on Combustion, (The Combustion Institute, Pittsburgh, 1965).

UNCLASSIFIED

## UNCLASSIFIED

11. Laderman, A. J., Kuby, W. C., Byron, S. R., Carlson, D. J., and Bartky, C. D., Study of Thermal Radiation, Particle Impingement Heating, and Flow Field Analysis of Solid Propellant Rocket Exhausts, Aeronutronic Publication No. U-4045, April 1967.
12. Ferriso, C. C., Ludwig, C. B., and Acton, L., J. Opt. Soc. Am., 56, 171 (1966).
13. Ferriso, C. C., and Ludwig, C. B., J. Chem. Phys., 41, 1668 (1964).
14. Ludwig, C. B., Ferriso, C. C., and Abeyta, C. N., J. Quantit. Spectr. and Radiat. Transfer, 5, 281 (1965).
15. Ferriso, C. C., and Ludwig, C. B., App. Opt., 3, 1435 (1964).
16. Bartky, C. D., and Bauer, E., J. Spacecraft, 3, 1523 (1966).

UNCLASSIFIED

UNCLASSIFIED

USER	METHOD
JPL	MC
NASA/MSFC	MC
HERCULES	MC
THIOKOL	APPX TECH
BOEING	MC, F
BROWN ENGR	MC, F
HUGHES	BE
TRW	MC

BE BOBCO AND EDWARDS  
F FONTENOT  
MC MORIZUMI AND CARPENTER

Figure 1. Heat Transfer Computational Schemes.

UNCLASSIFIED



**RADIATION MECHANISMS**

- THERMAL EMISSION
- NONEQUILIBRIUM EMISSION
- SEARCHLIGHT EFFECT
- AFTERBURNING

**FLUID MECHANICS**

- FLOW FIELD STRUCTURE
- MULTIPLE NOZZLE EFFECTS

**RADIATION PARAMETERS**

- GASEOUS SPECIES
- PARTICULATE EMITTERS
- CLOUD PROPERTIES

**ATMOSPHERIC EFFECTS**

- ATMOSPHERIC ATTENUATION
- SOLAR SCATTERING

UNCLASSIFIED

UNCLASSIFIED

Figure 2. Scope of the Problem.

UNCLASSIFIED

- GASEOUS EMITTERS
  - SPECIE CONCENTRATIONS
  - OPTICAL PROPERTIES
- PARTICULATE EMITTERS
  - SPECIE CONCENTRATIONS
  - LOCAL SIZE DISTRIBUTION
  - PHASE STATE
  - OPTICAL PROPERTIES
- CLOUD RADIATIVE BEHAVIOR
  - PARTICLE CONTINUUM
  - GAS SPECTRUM
  - GRADIENTS
  - MIXTURES OF EMITTERS
  - OPTICAL THICKNESS

Figure 3. Radiation Parameters.

UNCLASSIFIED

UNCLASSIFIED

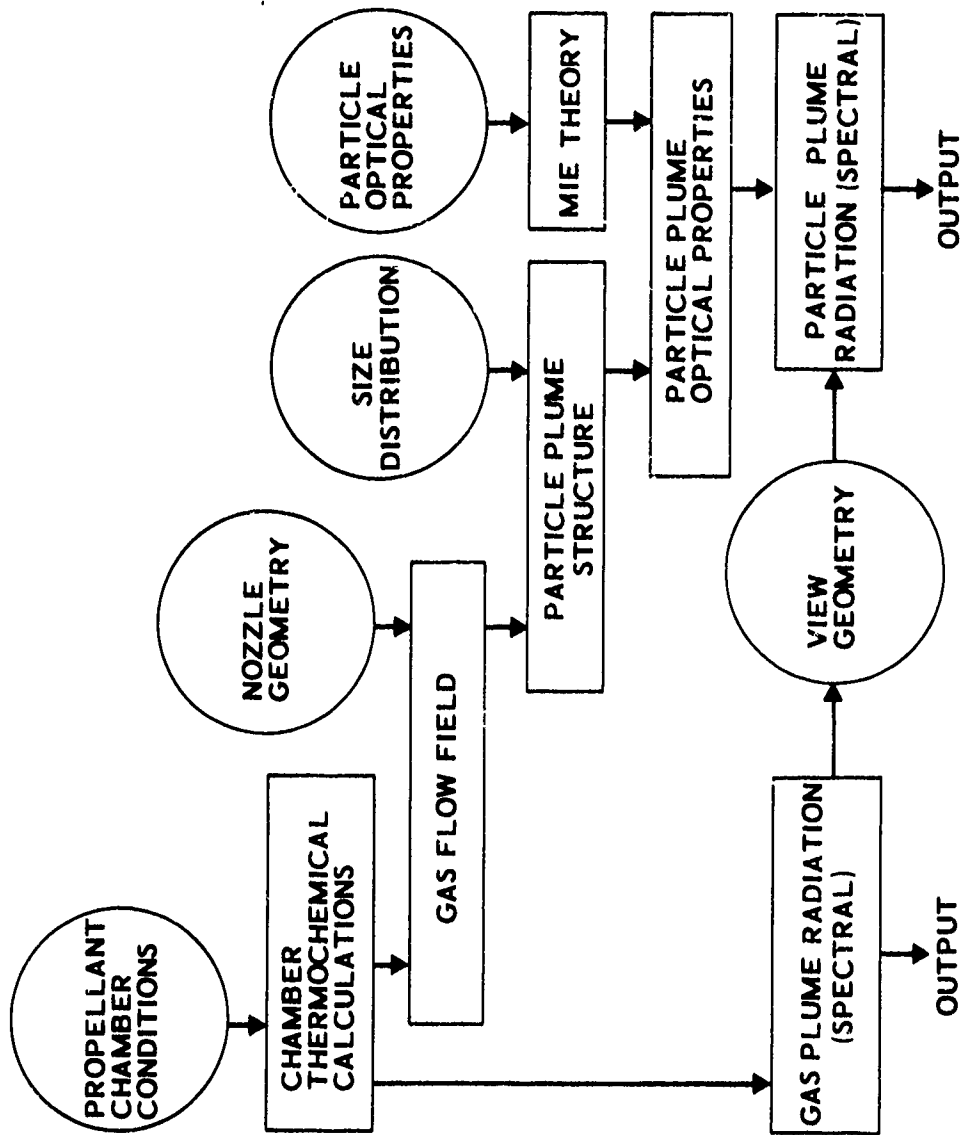


Figure 4. Flow Chart for Plume Radiation Calculations.

UNCLASSIFIED

UNCLASSIFIED

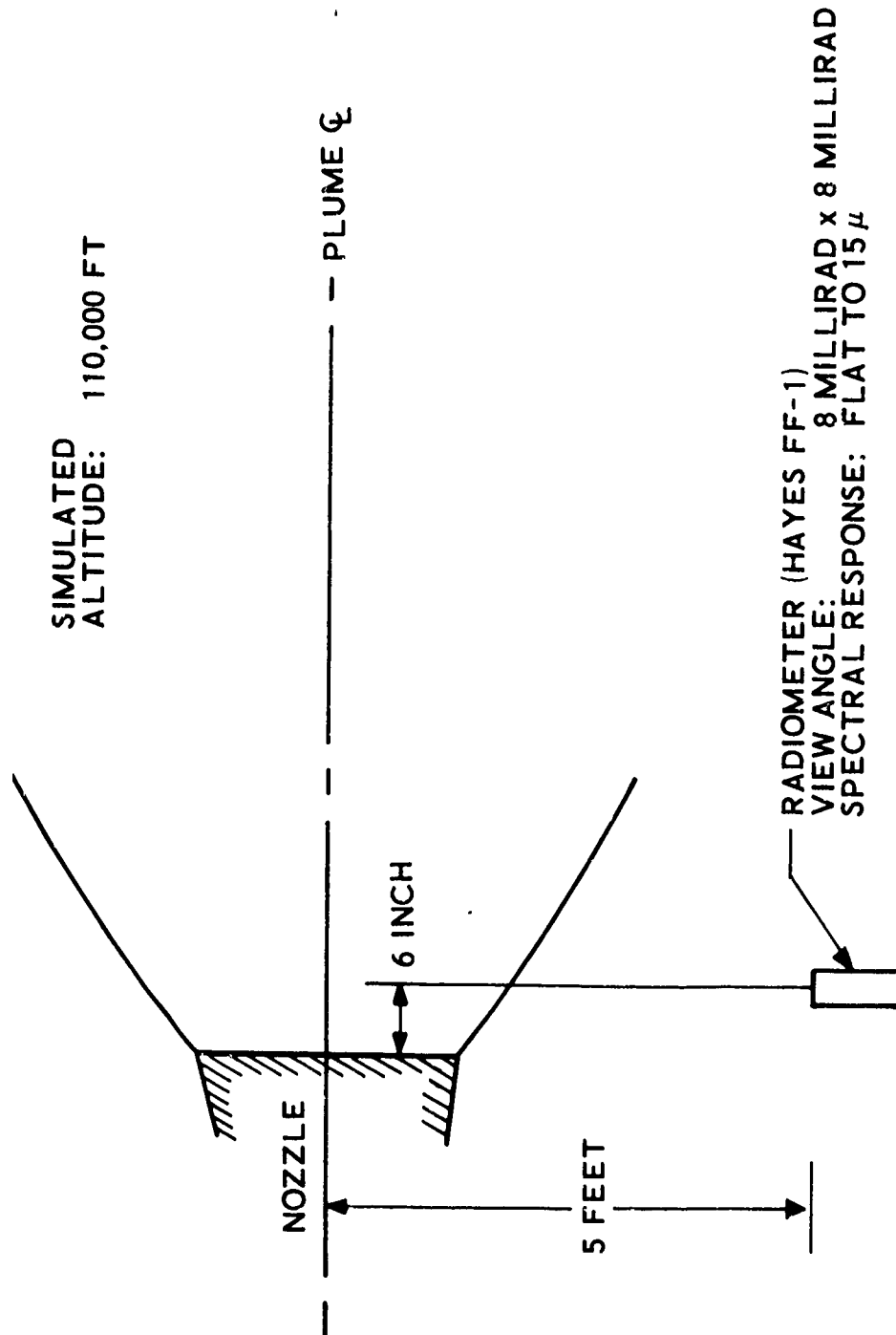


Figure 5. SII Ullage Experiment.

UNCLASSIFIED

UNCLASSIFIED

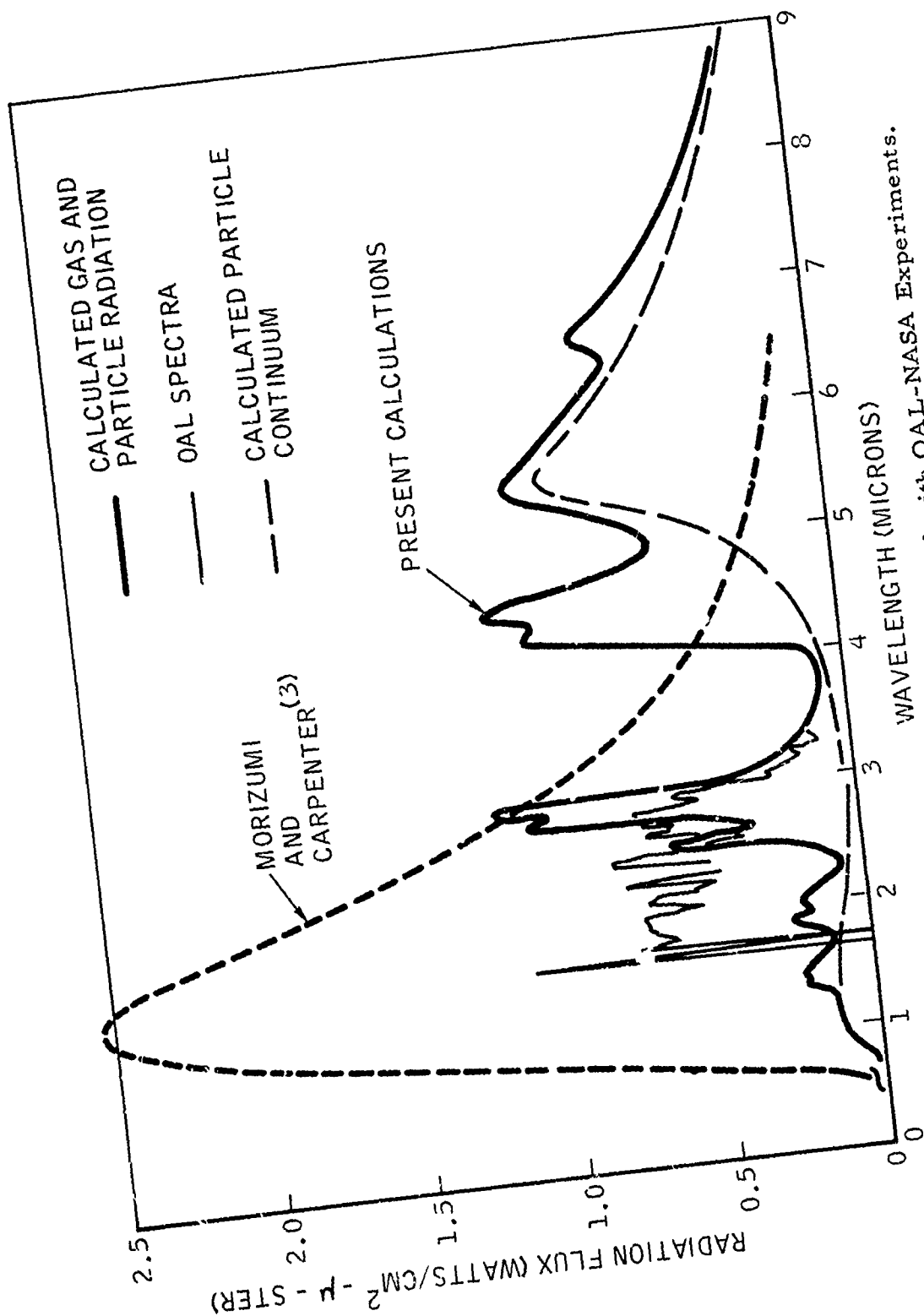


Figure 6. Theoretical Predictions Compared with OAL-NASA Experiments.

UNCLASSIFIED

UNCLASSIFIED

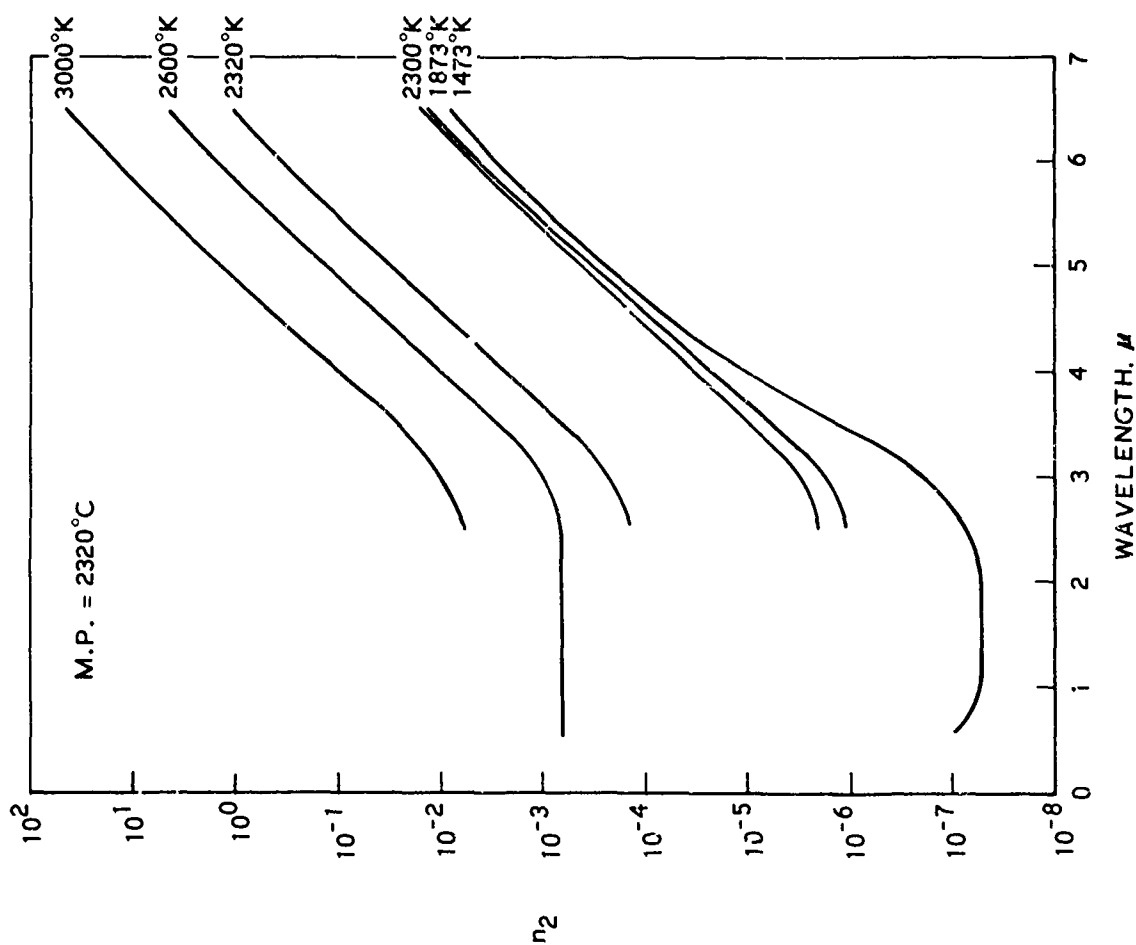


Figure 7. Imaginary Part of Refractive Index for Alumina.

UNCLASSIFIED

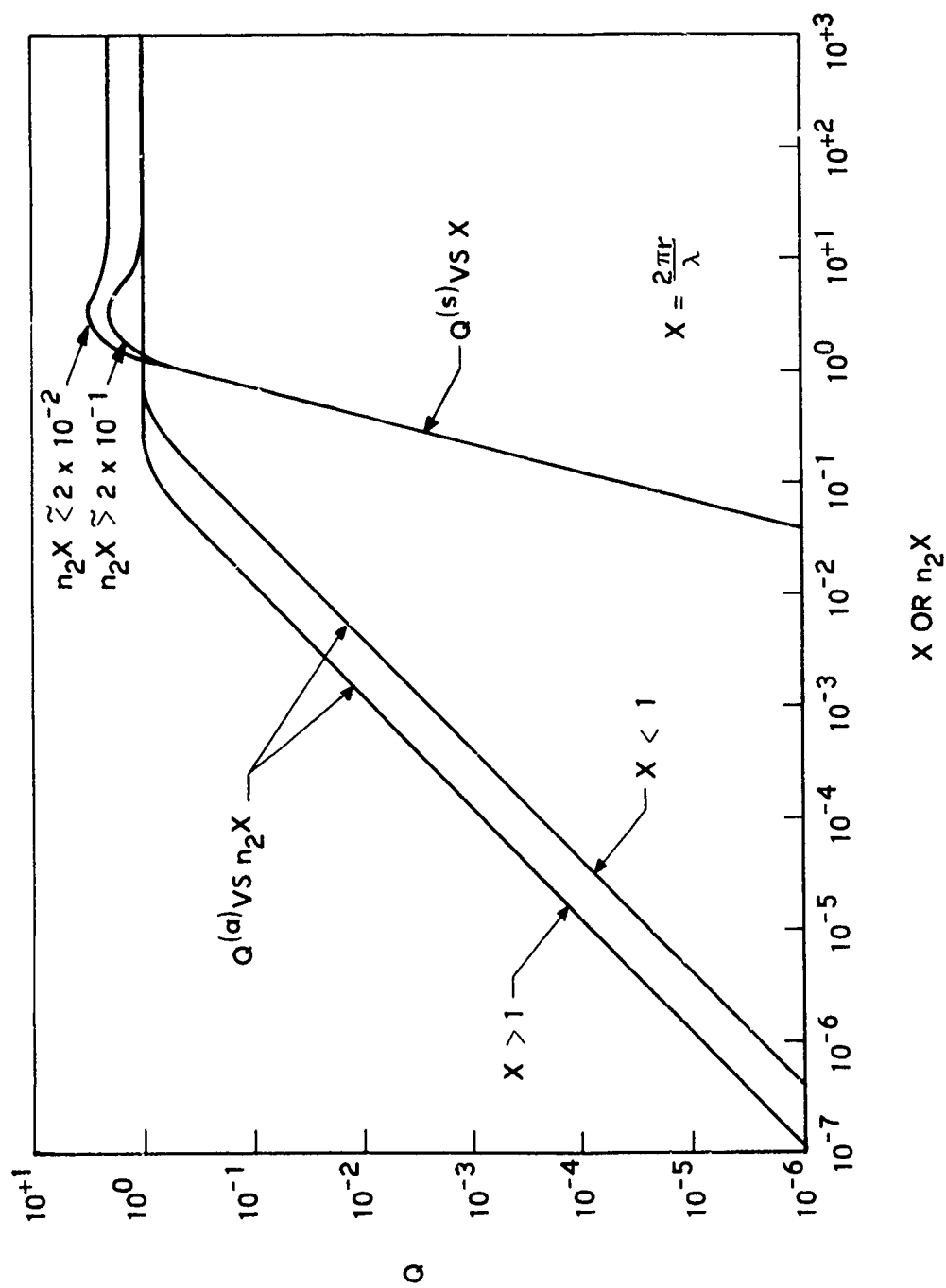


Figure 8. Mean Values of Efficiency Factor for  $n_1 = 1.74$ .

UNCLASSIFIED

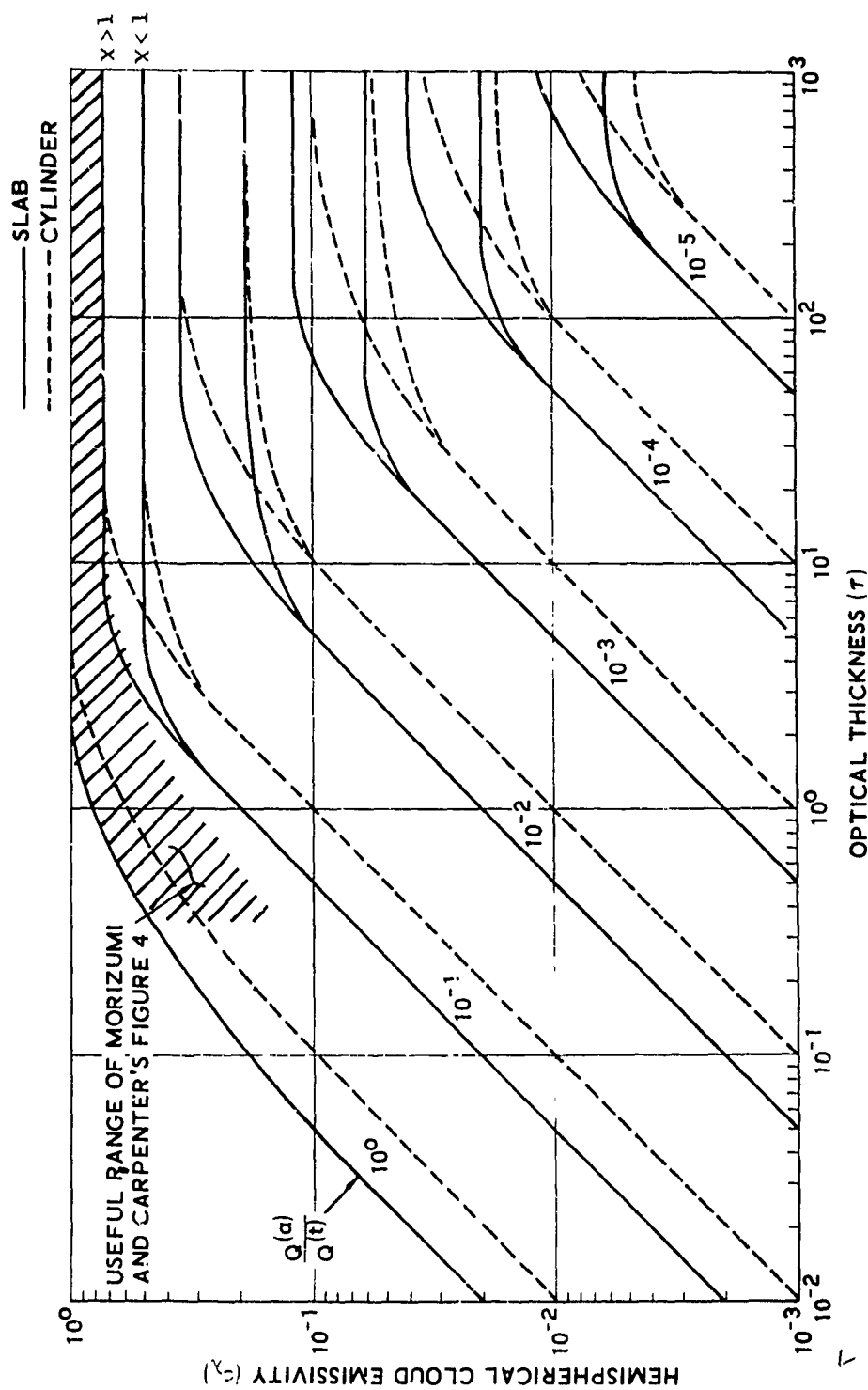


Figure 9. Hemispherical Cloud Emissivity.

UNCLASSIFIED



UNCLASSIFIED

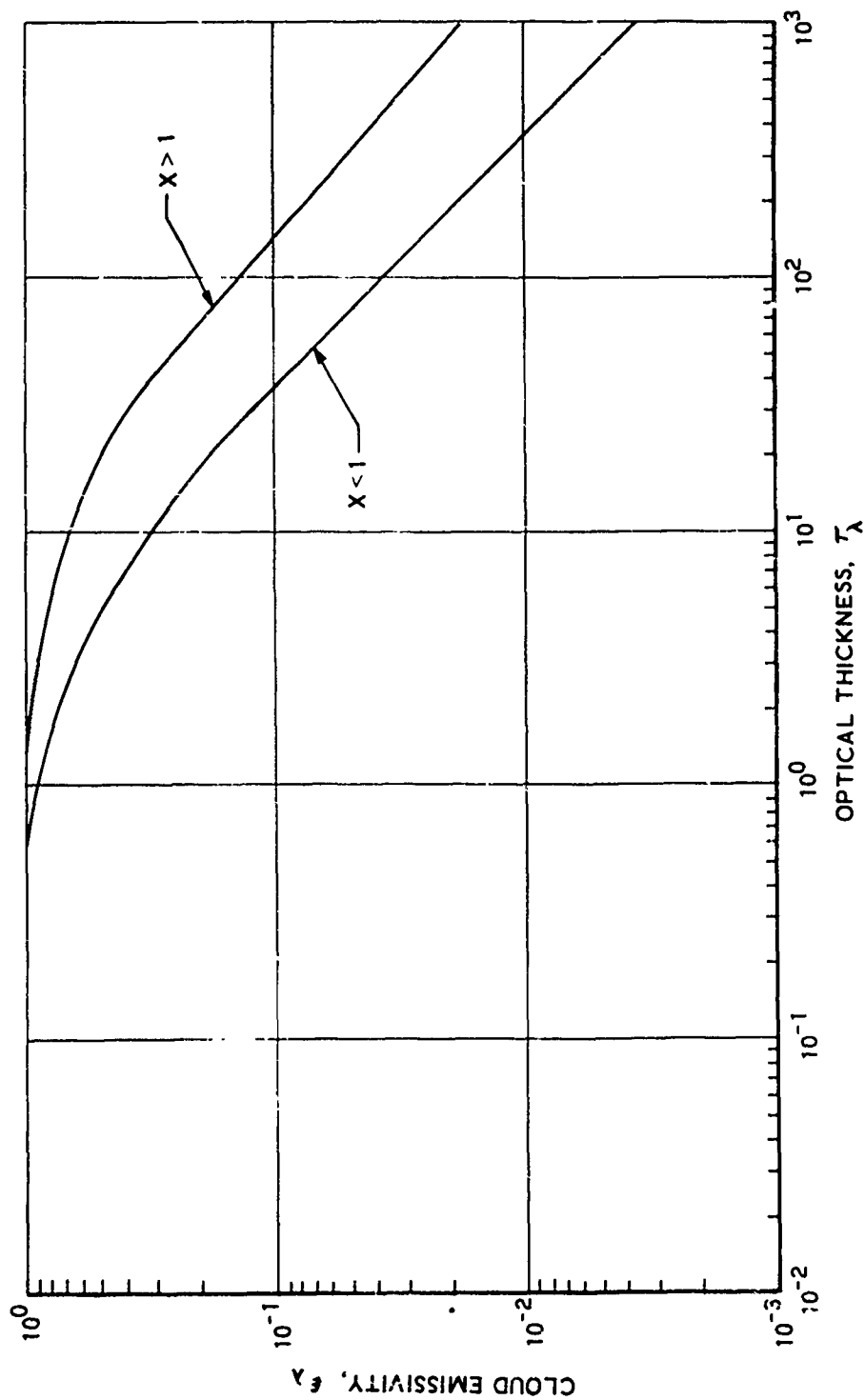


Figure 10. Hemispherical Cloud Emissivity Showing Maximum  $\epsilon_a$  as a Function of  $\tau$  for a Cylinder.

UNCLASSIFIED

# CONFIDENTIAL

## QUESTIONS, ANSWERS & COMMENTS\*

(C) C. J. M. Adams (Aerojet): I would like to mention here that it is very important to be able to extrapolate properly the absorption index for the refractive oxide, particularly in the case of optically thin plumes or low temperature plumes where the peak radiation occurs in the infrared region. I suggest that in order to perform extrapolation, rather than doing it arbitrarily, that we actually use the optical theory to do this; the electron model for optical properties of metal. Now, this doesn't work too well for dielectrics. We can't calculate the refractive index absolutely this way for dielectrics. You can do a pretty good job of it for metals, but in the case of dielectrics, we do have some points here from which to start the extrapolation. For instance, we could use the second derivative of the absorption index with respect to wave lengths and get a good extrapolation this way.

(C) The other comment I have has to do with the calculation of spectral emittance, and as I have shown in a recent paper, you can predict that the spectral emittance of an optically thick cloud goes through a minimum without any knowledge whatsoever of the particle size distribution. This is significant in that if you have a one-foot deep cloud of beryllium oxide particles in the case of a one-foot exhaust cone on a rocket motor, you can show that the spectral emittance in the visible region is as high as 5/10th as a bare minimum i.e., it has to be above 5/10ths. I think that some of the calculations that have been done in

\*Includes questions, answers and comments on paper by W. C. Kuby.

# CONFIDENTIAL

579

THIS DOCUMENT CONTAINS INFORMATION AFFECTING THE NATIONAL DEFENSE OF THE UNITED STATES WITHIN THE MEANING OF THE ESPIONAGE LAWS, TITLE 18, U.S.C., SECTION 793 AND 794, THE TRANSMISSION OF WHICH IN ANY MANNER TO AN UNAUTHORIZED PERSON IS PROHIBITED BY LAW.

## CONFIDENTIAL

### QUESTIONS, ANSWERS & COMMENTS:

the past, have underestimated the emittance of these optically thick clouds and even without a real extensive knowledge of the particle size distribution, we can show at least a minimum and get a good conservative answer for radiation.

(C) C./A. Mager (Aerospace): As I listen to this summary of the state-of-the-art, and also this second paper, I note that there is one aspect of plume radiation that is not getting any attention and in fact, it may be important. That is the radiation at very high altitude. The tendency is, and I think quite rightly so, to say well there will be no after-burning because the density of the atmosphere drops down and consequently there isn't anything to burn with. However, the atmosphere is not the atmosphere that we are used to thinking of. For example, the atmosphere has very peculiar species in it; monatomic oxygen, for example. It would be interesting to investigate the possible interaction of both the plume and the particles with an atmosphere of this type. I don't know whether anybody has done any work of this type, but it might be interesting to do it.

(C) C./W. C. Kuby (Univ. of Calif., Santa Barbara): I might refer you for some information along these lines to the BAMRAC proceedings.

(C) Q./W. G. Courtney (TCC): I would like to bring up a couple of points. We have done some work with the radiation emitted by AlO gas molecules reacting with atomic oxygen. This has an enormous emissivity obviously because it is a chemi-luminescent kind of reaction and there is some worry in my mind that we might be getting into that kind of thing

## CONFIDENTIAL

# CONFIDENTIAL

## QUESTIONS, ANSWERS & COMMENTS.

with a rocket plume even down on Earth. Secondly, I wonder are you going to consider scattering, search-light effect, in your plume radiation model? I might remind you that I go out and fire a plume and measure radiation and I have a plume emissivity of  $10^5$ .

A./A. J. Laderman (Aeronutronic): The scattering is accounted for in this calculation.

(C) C./W. G. Courtney (Thiokol): But you only end up with a plume emissivity of one. I'm sorry, I mean the search-light effect.

A./A. J. Laderman (Aeronutronics): No, the search-light effect is not included.

(C) Q./W. G. Courtney (Thiokol): In the visible range, my emissivity is around 0.2 which is normal; but if we fire a plume, we measure  $10^5$ . My first point is, I wonder if we should re-introduce radar attenuation problems and also modulation? Yes, the Saturn perhaps does not have too many problems but with some of the other low flying vehicles, they do have a significant Db. We have done a fair amount of work these, especially where the modulation is becoming increasingly sensitive from an operational viewpoint.

(C) A./W. C. Kuby (Univ. of Calif., Santa Barbara): My comments were not that low flying vehicles do not have significant attenuation. I was questioning the role of a condensed specie in supporting this attenuation and was suggesting that the attenuation, particularly for low flying vehicles, was a result of (1) afterburning and (2) ionization from alkali metals. It has been shown by the SRI people, particularly in

# CONFIDENTIAL

# CONFIDENTIAL

## QUESTIONS, ANSWERS & COMMENTS:

their contract with JPL to characterize solid propellants, that there are alkali metals in solid propellant effluents and that these can account for the electron densities that are measured by microwave techniques. I am not saying that these motors do not have attenuation; I am merely questioning whether the condensed phase is contributing to that attenuation.

(C) Q./R. J. Zeamer (HI): There are several applications to which plume radiation calculations can be made - one of which is base heating, the base heating of the rocket that goes into the high atmosphere. The method you described looks to be very laborious involving tremendous calculation effort, one after another stacked on top of one another. It also involves detailed inputs, say the properties of the various species and particles which make up the plume. Morizumi and Carpenter's method looks very straight-forward and simple where we have used it. I want to ask two questions: First, is Morizumi/Carpenter really as incorrect as your curve indicated and, second, do you think your method is ready for immediate application by people like us?

(C) A./A. J. Laderman (Aeronutronic): First of all, in the calculation I presented, I made the Morizumi/Carpenter type calculation. It took me about 8 hours. Don Carlson made what we call "our" calculation and I think it took 4 hours. While you need detailed information on the optical properties, these are essentially tabulated for you in the curves I presented; the Mie calculation does not need to be repeated. You do it once, and the information is available. All you

# CONFIDENTIAL

## QUESTIONS, ANSWERS & COMMENTS:

to do is to select a wave length of interest and a particle size distribution. Morizumi and Carpenter have to do the same as far as the size distribution is concerned. They need as much information about the plume flow field as we do. Secondly, they do not predict the appropriate spectral distribution. They can't. They make the assumption that they have a grey body, and if you look at the optical properties of the particles, you can see that this is just not the case. Finally, yes, the method is essentially ready to be used.

(C) C./A. J. Laderman (Aeronutronic): I might mention just one thing in this respect; it hasn't been tested thoroughly. We have checked it for an isothermal homogeneous plume and in the limit of an optically thick, i.e., totally self-absorbing cloud, and we get exactly the answer predicted by the exact theory. It's in the intermediate range where there is a deviation - there is an error - but it is a conservative error and I think that this is appropriate for engineering calculations. We have not yet checked it for a non-homogeneous non-isothermal plume and the method of checking that we are considering right now is to use Bill Kuby's computer technique, constructing an arbitrary plume, to get what we might consider an exact answer and check this against our calculations. However, as I say, as long as the gradient and the radiancy is small, between the limits  $\tau_1$  and  $\tau_2$ , in other words, where the plume begins to become self-absorbant, then I would not anticipate a large error - no larger than what I have already mentioned.

# CONFIDENTIAL

583

THIS DOCUMENT CONTAINS INFORMATION AFFECTING THE NATIONAL DEFENSE OF THE UNITED STATES WITHIN THE MEANING OF THE ESPIONAGE LAWS, TITLE 18, U.S.C., SECTION 793 AND 794, THE TRANSMISSION OF WHICH IN ANY MANNER TO AN UNAUTHORIZED PERSON IS PROHIBITED BY LAW

# CONFIDENTIAL

## QUESTIONS, ANSWERS & COMMENTS:

Q. M. J. Baker (Boeing, Huntsville): You talked about isothermal slabs. How do you average these temperatures to get an isothermal slab? Do you use a procedure like Morizumi and Carpenter did?

(C) A. J. Laderman (Aeronutronics): We don't need an isothermal slab in our case. Kuby's technique uses isothermal slabs, not a technique like Morizumi and Carpenter's. He divides the plume up into slabs over which the gradients are small so that it approaches the isothermal case for each slab.

(C) C. W. C. Kuby (Univ. of Calif., Santa Barbara): The method used to divide it up into so-called isothermal slabs is to integrate over the number distribution, by multiplying the cross-section of each particle, which is a function of its temperature and its radius at a particular wave length of interest, times the number of particles of that radius times the black body function evaluated at the temperature of that size particle. Then within a differential volume this gives me the total radiation that is generated within. I also have defined an average cross section and a total number of particles of all sizes for that differential element, and I calculate an effective temperature that will allow me to multiply all the average quantities together times a black body function and come up with the same generated radiation for the differential body.

**UNCLASSIFIED**

EXPERIMENTAL MEASUREMENTS OF SOLID PROPELLANT  
ROCKET EXHAUST EFFECTS AT HIGH ALTITUDES

Part I: RADIANCE AND IMPINGEMENT CHARACTERISTICS OF  
SATURN AUXILIARY SOLID ROCKET PLUMES

by

KENNETH C. HENDERSHOT  
Cornell Aeronautical Laboratory, Inc.  
Buffalo, New York

Part II: IMPINGEMENT PRESSURES, FORCES, AND HEAT TRANSFER  
RATES IN HIGH ALTITUDE METALIZED SOLID PROPELLANT  
ROCKET EXHAUST PLUMES

by

LEO RUTE  
AVCO/MSD  
Wilmington, Massachusetts

**UNCLASSIFIED**



# UNCLASSIFIED

## PART I - RADIANCE AND IMPINGEMENT CHARACTERISTICS OF SATURN AUXILIARY SOLID ROCKET PLUMES (UNCLASSIFIED)

by

Kenneth C. Hendershot  
Head, Propulsion Section  
Hypersonic Facilities Department  
Cornell Aeronautical Laboratory, Inc.  
Buffalo, New York

### ABSTRACT

A short-duration experimental technique for investigating radiative properties and impingement effects of solid propellant rocket exhaust plumes at high altitudes is described. Experimental measurements of the spectral radiance characteristics of several Saturn auxiliary solid propellant rocket motors are presented and discussed. Results of a one-tenth scale model investigation of impingement effects of solid propellant retro-rockets on the Saturn S-IB and S-IVB stages are also presented.

### INTRODUCTION

Operational requirements of rocket boosters, spacecraft and reentry vehicles presently in use or under development in this country often require the firing of rocket engines in close proximity to the vehicle or other nearby bodies. At high altitudes, the resulting highly expanded exhaust plumes may impinge on the parent vehicle and/or adjacent bodies, causing excessive convective heating, particle erosion or deposition, and undesirable perturbing pressure forces. Aside from the effects resulting from direct plume impingement, the rocket exhaust plumes can also generate significant radiant heating loads on nearby surfaces, interfere with the transmission and reception of RF communication and guidance signals, and enhance the detection, tracking, and discrimination characteristics of the parent vehicle.

Available analytical techniques for predicting the impingement effects and radiative properties of highly expanded rocket exhaust plumes are currently questionable, particularly when 1) two-phase flow (i. e., solid propellant rocket exhausts) and 2) transitional or non-continuum flow conditions are encountered. As a result, it is often necessary to resort to an experimental determination of the plume effects preferably at full scale and in a fully simulated test environment.

UNCLASSIFIED

## UNCLASSIFIED

Under the sponsorship of the Marshall Space Flight Center of NASA, the Cornell Aeronautical Laboratory (CAL) has perfected a short-duration experimental testing technique which provides exact duplication of solid propellant rocket exhaust gases (composition, temperature, etc.) in the proper high altitude environment, and in many cases at full scale. Further, fast response instrumentation originally developed for shock tunnel use provides the required capability for obtaining measurements during the short test period. Based on this experimental concept, several test programs have recently been conducted at CAL for NASA/MSFC and AVCO/RAD to investigate solid propellant exhaust plume effects at high altitudes.

The first part of this paper presents a brief description of the short-duration experimental technique, the instrumentation employed, and some initial results of the NASA/MSFC-sponsored studies conducted by CAL which involved 1) an evaluation of the spectral radiance characteristics of a number of scale Saturn auxiliary solid propellant rockets and 2) a scale model investigation of the impingement effects of solid propellant retro-rockets on several Saturn stages. The results of a full-scale test program conducted for AVCO/RAD by CAL to determine forces, pressures and convective heating resulting from impingement of a small (100 pound thrust) solid motor on separated bodies at very high altitudes ( $> 400,000$  feet) are presented and discussed by AVCO/RAD in Part II of the paper.

### SHORT-DURATION ROCKET EXPERIMENTAL TECHNIQUE

Although simple in concept, the short-duration approach to rocket testing represents a unique combination of nonsteady gasdynamic processes, utilized for many years in shock tunnel operation, and comparatively conventional solid propellant rocket motor technology. The principles involved may be briefly described as follows: the rocket and test model are installed inside a nominal-sized vacuum chamber which can be evacuated by conventional vacuum pumps to the desired test altitude. By procedures discussed later, the rocket is rapidly brought to the design operating conditions (pressure and temperature) which are sustained for a short period of time. During the operating period, the composition and thermodynamic properties of the actual rocket engine exhaust gases are completely duplicated since the same propellants are used. The rocket flow duration need only be long enough to assure attainment of steady-state operating conditions and allow the desired measurements to be made. Appropriate measurements (described later) are made with fast

## UNCLASSIFIED

response instrumentation originally developed for shock tunnel use but equally well suited for this application. The accumulative rocket starting transient and instrumentation response time are sufficiently small that the measurements can be made before the ambient pressure disturbances created by the rocket exhaust flow have time to travel to the end of the vacuum chamber and reflect back to alter the environmental pressure in the vicinity of the rocket exhaust. That is, until the fact that the test chamber is of finite length is communicated back to the test region by shock or acoustic wave processes, the rocket exhaust plume behaves as if it were in free space. For the test conditions and vacuum chamber employed for the test programs described in this paper, the ambient pressure remained constant at the initial value for 10-12 milliseconds, more than adequate time to obtain the required data.

A typical solid propellant rocket system consisting of a combustion chamber, flow nozzle, propellant holder inserts, nozzle diaphragm and ignition system is illustrated in Fig. 1. Operating features of the combustor are as follows: replaceable propellant holders of the proper surface geometry having thin sheets of solid propellant (on the order of 0.040-0.050 inches thick) cemented to their surfaces are inserted in the combustion chamber. The solid propellant is of the same type employed in the tactical rocket being simulated and is generally obtained directly from the rocket manufacturer in brick form. Cutting of the propellant into thin sheets is readily accomplished by means of a modified carpenter's plane. The propellant surface (burning) area is adjusted as required to provide the desired steady state combustion pressure.

During operation, the nozzle entrance is initially sealed with a mylar or scored copper diaphragm, sized to rupture at the design chamber pressure. The combustion chamber volume is filled to a low pressure (approximately 5 psia) with an oxygen-rich  $H_2-O_2$  mixture ( $O/F = 20/1$ ). Ignition of this mixture with a spark plug and subsequent constant volume combustion nearly instantaneously exposes the solid propellant to a high temperature ( $\approx 5000^\circ F$ ) oxidizing environment, resulting in a uniform ignition of the entire propellant surface in a very short time. Following ignition, the solid propellant combustion products are contained in the combustion chamber until the nozzle diaphragm ruptures at the design pressure. The flow from the combustion chamber then remains steady until the propellant charge is consumed.

UNCLASSIFIED

## UNCLASSIFIED

For a typical propellant thickness of 0.040 inches, and a representative burn rate of 0.4 inches/second, steady flow duration is on the order of 100 milliseconds. However, the useful test duration is ordinarily not limited by the steady flow period from the rocket, but rather by the arrival of the reflected starting wave in the testing region ( $\approx 10$  milliseconds). A representative oscilloscope record of the chamber pressure history of the 1/10 scale Saturn retro-rocket employed for tests discussed later in this paper is shown in Fig. 2.

### TEST INSTRUMENTATION

Perhaps of even more importance to the success of short-duration rocket testing techniques than the combustor/model system is the associated instrumentation. Indeed, regardless of the experimenter's ability to precisely simulate the necessary flow conditions and external environment, the experiment would be useless if suitable measurements could not be made. Fortunately, much of the instrumentation originally developed to satisfy the demanding requirements of shock-tunnel applications has been found to be ideally suited for short-duration rocket tests. Brief descriptions of the instrumentation employed in the experimental programs discussed herein follow:

#### Heat Transfer Measurements

Convective heating rates on bodies or surfaces subjected to exhaust plume impingement are obtained with thin-film heat transfer gages already in use for many years<sup>(1, 2)</sup>. These gages have microsecond response and operate on the principle of sensing the transient surface temperature of a suitable substrate material. The sensing element is an extremely thin ( $\approx 1$  micro-inch) platinum strip fused on the front surface of a Pyrex glass substrate which conforms to the local surface contour of the model. Since the heat capacity of the platinum strip is negligible, the film temperature is equal to the instantaneous surface temperature of the Pyrex substrate, and is related to the heat transfer rate to the model by the theory discussed in Ref. 1. The output of the heat transfer gage is fed through an analog network (Ref. 3) which converts the signal from one representing temperature to a signal directly proportional to the instantaneous heat transfer rate. A typical heat transfer gage temperature history and the corresponding analog circuit heating rate output is shown in Fig. 3.

# UNCLASSIFIED

## Pressure Measurements

Model surface pressures are measured with flush mounted fast response piezoelectric transducers, specifically designed and developed by CAL for short-duration testing<sup>(4, 5)</sup>. The transducers are characterized by rapid response ( $< 1$  msec rise time), high sensitivities (pressures as low as 0.0002 psia were measured during the programs described in this paper) and include internal acceleration compensation. A photograph and representative calibration and operating characteristics of a typical piezoelectric transducer are shown in Fig. 3.

## Force Measurements

Body forces and moments resulting from rocket plume impingement (discussed by AVCO/RAD in Part II of the paper) were determined from model acceleration measurements. In such an acceleration balance technique, the test model is suspended in the test chamber by very fine wires which are in turn attached through soft mounts (rubber bands) to the tank ceiling. This mounting procedure results in a floating model which is free to accelerate both linearly (axial, lateral, and normal directions) and in rotation (pitch and yaw) during the test event. Model weight is normally kept as low as possible to maximize acceleration levels and measurement sensitivity.\* Accelerations are measured by CAL-developed high frequency response piezoelectric accelerometers, appropriately located in the model to sense the desired acceleration components. The measured linear accelerations, in combination with the model mass and moment of inertia, provide the required force and moment data. For the particular model geometry and test configuration employed during the AVCO/RAD program described in Part II, force levels as low as 0.005 pounds were successfully resolved by this technique<sup>(6)</sup>.

## Spectral Radiance Measurements

Spectral radiance measurements of the Saturn solid propellant auxiliary rockets were made with a Warner & Swasey Model 501 Rapid-Scan spectrometer provided to CAL by NASA/MSFC. This instrument has recently been

---

\*It should be noted, however, that although model movement is necessary to the acceleration measurement technique, displacements are normally less than 0.005 inches during the short test event, thus assuring negligible change in the model/rocket geometrical relationship.

## UNCLASSIFIED

described in detail in the literature<sup>(7,8)</sup> and only the highlights of its operation will be considered here.

With the Model 501, radiation is collected from the test region by means of a variable-focus Cassegrain optical system, passed through a double-pass grating monochromator and onto dual exit slits and detectors. Between the first and second pass of the grating, the radiation beam is incident on a rotating wheel equipped with corner mirrors on its periphery. Positioning of the corner mirrors is such that rotation of the wheel causes the second pass radiation to be swept, in wavelength, across the dual exit slits.

The  $1.7 \rightarrow 3.1 \mu$  and  $3.0 \rightarrow 5 \mu$  wavelength intervals are scanned simultaneously, with the detector output signals being displayed and photographed on oscilloscopes. Variation of the time interval required for scanning the wavelength spectrum from  $1.7 \rightarrow 5 \mu$  is provided with plug-in modules, with a one-millisecond per scan interval being selected for these tests. This allowed a total of four separate data scans to be obtained during a 5 millisecond time interval. Finally, an integral temperature-controlled global secondary radiation standard in the instrument allows conversion of the observed data to units of absolute radiance.

For the test program discussed herein, the spectrometer was located outside the test chamber, viewing the exhaust plumes through a sapphire window. The external optical path between the window and detectors was flushed with dry nitrogen to eliminate absorption of radiation by atmospheric  $H_2O$  and  $CO_2$ .

### SATURN AUXILIARY SOLID PROPELLANT ROCKET TESTS - EXPERIMENTAL RESULTS

#### Measurements of Exhaust Plume Spectral Radiance

Exhaust plumes from several scaled model engines of the type employed on various stages of the Saturn vehicle were investigated to determine their spectral radiance in the  $1.7$  to  $5 \mu$  wavelength interval. In order to provide a consistent basis for comparison between engines, the exit diameter of all nozzles was maintained constant at 1.25 inches, with the throat and divergent sections of the nozzles being appropriately scaled to duplicate the full-scale engines. (Since the full-scale nozzles differ in size, the scale factor varied between individual nozzles during this test.) Spectrometer field of view

## UNCLASSIFIED

(defined by the width and height of the entrance slit) was constant for all rockets and extended over the full diameter of the nozzle exit plane (1.25 inches high by 0.125 inches wide). This field-of-view corresponded to a spectral slit width (resolution) of approximately  $0.05 \mu$ . Table I summarizes the geometries of the scale solid rocket nozzles evaluated along with some pertinent full-scale rocket characteristics provided by the rocket manufacturers and Ref. 9.

Spectral data were obtained over the  $1.7$  to  $5 \mu$  wavelength interval for a total of five different Saturn retro and ullage rocket configurations. To illustrate the type of results obtained, typical raw spectral data obtained from the scale S-II ullage motor configuration are reproduced in Fig. 4. (Similar data were obtained for each of the rockets tested.) In Fig. 4, the first spectral scan was initiated approximately 5 msec. after the start of rocket exhaust flow, and the consecutive 1 msec. scans (separated in time by  $0.25$  msec.) progress from top to bottom of the record. Excellent reproducibility between successive scans is readily apparent, confirming the steady character of the rocket combustion process and exhaust flow. For all configurations tested, scan-to-scan repeatability was within  $\pm 7\%$  during any given run, and within  $\pm 10\%$  on separate rocket firings. Also indicated in Fig. 4 are some of the more prominent infrared spectral bands ( $H_2O$ ,  $CO_2$  and  $HCl$ ), which were present for all of the propellants evaluated. Although the line structure in the  $HCl$  band is in evidence in the  $3 \rightarrow 5 \mu$  spectral record, resolution of the spectrometer was inadequate to separate the  $4.3 \mu CO_2$  and  $4.7 \mu CO$  band.

Accounting for the spectral response of the detectors and optical system transmission characteristics, spectral radiance was determined as a function of wavelength for each of the rocket exhaust flows as shown in Fig. 5. All the rocket flows indicate similar spectral characteristics, with the dominant features being the  $4.3 \mu CO_2$  and  $2.7 \mu H_2O$  bands. It is interesting to note that while the S-IC and S-I retros, and S-II ullage rocket exhausts exhibit nearly identical radiance levels in the  $2.7 \mu H_2O$  band, the S-I retro has significantly lower radiance at shorter wavelengths. Only the S-IB retro-rocket plume exhibits any sizeable continuum radiation (as indicated by the radiance level in the  $2$  to  $2.2 \mu$  region where no significant molecular radiation bands exist) and even in this case the continuum radiation level is considerably lower than the radiation from the  $H_2O$  and  $CO_2$  bands. Finally, as indicated in the legend of Fig. 5, the peak radiance levels for all five rockets in the  $4.3 \mu CO_2$  band are found

UNCLASSIFIED

## UNCLASSIFIED

to vary in the same sequence as the product of the individual nozzle exit pressures and temperatures.

Based on the spectral data obtained for the S-IB retro-rocket, an order-of-magnitude calculation was made for the radiant heat flux to a point immediately beneath the nozzle lip. The computed value of  $2.3 \text{ Btu/ft}^2\text{-sec.}$  (estimated to be high as a result of the simplifying assumptions made in the calculation) agreed very favorably with the measured value of  $1.5 \text{ Btu/ft}^2\text{-sec.}$  obtained during the one-tenth scale retro-rocket plume impingement test program discussed next in the paper.

### S-IB/S-II Retro-Rocket Plume Impingement Study

During the staging sequence of the Up-rated Saturn booster stages, four forward firing 35,000 pound thrust solid propellant Recruit rockets are employed to separate the spent S-IB lower stage from the S-IVB upper stage. As a result of the forward location of these retro-rockets on the S-IB stage, exhaust impingement on the base of the separated S-IVB stage presents a potentially serious heating problem. In addition to S-IVB base impingement, failure of one of the four retro-rockets to fire can produce an asymmetrical separation. Trajectory predictions of the S-IB stage based strictly on the rocket thrust vectors indicate no difficulties with such a separation. However, uncertainties exist as to the actual effective force vector on the stage as a result of rocket plume impingement and exhaust spreading over the interstage structure at the 200,000 foot staging altitude.

In order to study this impingement problem, a one-tenth scale test program was recently conducted at CAL for NASA/MSFC. During this investigation, pressure and heat transfer data were obtained over both the S-IB/S-IVB interstage and S-IVB base region at various separation distances. The results of this program are briefly summarized in the following paragraphs.

The complete test model assembly included a sector of the S-IB interstage, one of the four retro-rockets, and a separable S-IVB base as shown in Fig. 6a. More detailed close-up views of the retro-rocket and interstage are presented in Fig. 6b, illustrating the  $9.5^\circ$  outward cant of the retro-rocket nozzle, the inclined impingement ramp immediately beneath the nozzle, and some of the pressure and heat transfer instrumentation locations. The reader's attention is directed in particular to the most forward of the four heat transfer



## UNCLASSIFIED

gages located on the ramp, directly beneath the nozzle lip. This gage sensed both convective and radiative heating rates, and provided the experimentally measured  $1.5 \text{ Btu/ft}^2\text{-sec.}$  radiant heating rate value discussed in the preceding section of this paper. A photograph of a representative test firing at the nominal staging altitude of 200,000 feet is presented in Fig. 2, where only the incandescent solid particles in the central region of the exhaust plume are actually visible.

During the program, convective heating rate measurements were obtained over most of the interstage surface, as illustrated in Fig. 7 which shows a typical experimental heating rate distribution along the projected nozzle centerline. Also shown in Fig. 7 is a theoretical heating rate distribution based on a turbulent flat plate flow theory as predicted by Rochelle in Ref. 10. Further, an actual in-flight data measurement obtained during the first Uprated Saturn flight (SA-201) is also included for reference. This flight test data point is shown both as originally measured at full scale and also as adjusted upward to model scale by a factor of  $1.58^*$ . The overall agreement between theory, scale model results, and full-scale flight test data is seen to be excellent up to a region approximately 5 inches (50 inches full scale) from the nozzle exit. Distortion of the flow field as a result of shock and expansion wave interactions precluded any realistic theoretical heating rate predictions beyond this point.

Similar to the heating rate distributions obtained over the interstage surface, a comprehensive pressure survey was also made as typified by the data of Fig. 8 which presents the interstage axial pressure distribution along the projected retro-rocket nozzle centerline. The abrupt change in pressure near the three-inch axial station is attributed to a shock wave emanating from the ramp/interstage juncture, an observation which is generally confirmed by pitot pressure surveys made in the flow field above the interstage surface. Similar surface pressure distributions obtained along alternate longitudinal

---

\*The theoretical analysis of Ref. 10, based on Eckert's flat plate theory, predicts the axial convective heating rate to vary as  $x^{-0.2}$  (where  $x$  is the distance along the interstage surface measured from the plume impingement point on the ramp). Accordingly, if it is assumed that the 0.1 scale model properly simulates the full-scale rocket exhaust properties and the theory of Ref. 10 is valid, the model heating rates should consequently be  $(0.10)^{-0.2}$  ( $= 1.58$ ) times larger than the full-scale values.

## UNCLASSIFIED

rays on the interstage have allowed a comprehensive picture of the impingement-induced pressure field acting on the interstage surface to be developed, as evidenced by the pressure map presented in Fig. 9a. (Also shown as Fig. 9b is the corresponding convective heating rate distribution over the interstage surface.) It is interesting to note that an integration of the pressure field of Fig. 9a yields a full-scale side force on the interstage of nearly 5000 pounds, or approximately 15% of the total rocket thrust.

In addition to the interstage pressure and heating data obtained, the experimental program also provided an evaluation of the thermal environment in the base region of the S-IVB stage as a function of separation distance. The photograph of Fig. 10 illustrates the S-IVB stage base region, identifying the various components subjected to direct plume impingement and the related instrumentation locations. Also shown in Fig. 10 is a representative heating rate variation for one of the components (the helium sphere) as a function of separation distance. It may be observed that the heating rates on the helium sphere increased reasonably uniformly with increasing separation at all three instrumentation locations ( $Q_{14}$  is on the back side of the sphere, not visible in the photograph of Fig. 10), reaching maximum (and approximately constant) values at a separation distance of about 24 inches. Similar behavior with separation distance was exhibited by most of the components in the S-IVB base region.

In addition to the impingement heating and pressure measurements obtained for the S-IB and S-IVB stages, a pitot pressure survey was also made of the retro-rocket flow field in the vicinity of the interstage surface to provide some experimental verification of the plume flow field predictions of Ref. 11. Details of the pitot pressure rake installation on the interstage are shown in Fig. 11, along with a photograph taken during an actual rocket firing. Results of the pitot pressure survey are summarized in Fig. 12, where the experimentally determined flow field Mach numbers are compared with the theoretical exhaust plume calculations from Ref. 11. Agreement between the experimental data and theory is seen to be quite good at the two survey locations closest to the rocket exit. Plume Mach numbers tend to increase in the radial direction away from the plume centerline until encountering the oblique impingement shock emanating from the interstage ramp. Measured flow field Mach numbers just ahead of, and immediately downstream of, the interstage separation plane are seen to be somewhat lower than predicted for the free

# UNCLASSIFIED

plume, probably as a result of the oblique impingement shock and/or other shock/expansion wave systems generated by the interstage ramp and stringer geometries.

## SUMMARY AND CONCLUSIONS

The applicability of the short-duration rocket testing technique for studying the radiation characteristics and impingement effects of solid propellant rocket exhaust flows at high altitudes has been demonstrated. Measurements of the spectral radiance of several Saturn auxiliary solid propellant rocket exhaust flows are presented along with an interpretive discussion of the significance of these results. Experimental pressure and heating rate data obtained from a one-tenth scale model of the Saturn S-IB/S-IVB stages have been shown to agree well with theoretical predictions and full-scale flight test results.

## ACKNOWLEDGMENTS

The author wishes to acknowledge the contributions of Mr. R. J. Dennis, Mr. M. Urso, and his other colleagues at CAL to the experimental investigations discussed above.

The work was performed under Contract NAS 8-20027 with NASA/George C. Marshall Space Flight Center with Mr. Homer Wilson as technical director.

UNCLASSIFIED

# UNCLASSIFIED

## REFERENCES

1. Vidal, R. J.: "Transient Surface Temperature Measurements," CAL Report No. 114, March 1962.
2. Bogdan, L.: "Heat Transfer Instrumentation," CAL Report WTH-021, March 1963.
3. Skinner, G. T.: "Analog Network to Convert Surface Temperature to Heat Flux," CAL Report No. 100, AD 247277, February 1960. Also ARS Journal, Vol. 30, No. 6, pp. 569-570 (June 1960).
4. Martin, J. F.; Duryea, G. R. and Stevenson, L. M.: "Instrumentation for Force and Pressure Measurements in a Hypersonic Shock Tunnel," CAL Report 113, January 1962 (Presented at the 2nd National Symposium on Hypervelocity Techniques, Denver, Colorado, March 19-20, 1962).
5. MacArthur, R. C. and Martin, J. F.: "Use of Field Effect Transistors in Shock Tunnel Instrumentation Circuits," Presented at IEEE 2nd International Congress on Instrumentation in Aerospace Simulation Facilities, Stanford University, California, 29-31 August 1966.
6. Hendershot, K. C. and Sergeant, R. J.: "An Experimental Investigation of Solid Propellant Rocket Plume Impingement Effects on Bodies at High Altitude," CAL Report No. AA-2302-Y-1, 31 January 1967.
7. Klein, L. and Penzias, G. J.: "Spectral Radiance Measurements of Model Rocket Exhaust Gases at Simulated Altitude, Using a Rapid Scanning Spectrometer," AIAA Paper No. 67-10, 5th Aerospace Sciences Meeting, New York, N. Y., 23-26 January 1967.
8. Dolin, S. A.; Kruegle, H. A. and Penzias, G. J.: "A Rapid-Scan Spectrometer that Sweeps Corner Mirrors Through the Spectrum," Applied Optics, Vol. 6, No. 2, February 1967.
9. Eilerman, R. N.: "Saturn Auxiliary Solid Propulsion Applications," AIAA Paper No. 66-946, 3rd Annual Meeting, Boston, Mass., November 29-December 2, 1966.
10. Rochelle, W. C.: "Theoretical and Experimental Investigation of Heating from Saturn Solid Propellant Rocket Exhausts," AIAA Paper No. 66-653, Second Propulsion Joint Specialist Conference, Colorado Springs, Colo., 13-17 June 1966.
11. Unpublished communication from NASA/MSFC to CAL, 1966.

UNCLASSIFIED

UNCLASSIFIED

Table I  
Saturn Solid Propellant Rockets Used for Spectral Radiance Tests

ROCKET	PROPELLANT TYPE	PROPELLANT COMPOSITION (FROM REF.9)	P <sub>c</sub> PSIA (APPROX.)	FULL SCALE THRUST LBS (APPROX.)	NOZZLE GEOMETRY		
					EXPANSION RATIO	NOZZLE HALF ANGLE	MODEL SCALE
S-IV & S-IV B ULLAGE (TX-280)	THIOL TP-L-8183	BINDER 19.5% OXIDIZER 78.0% OTHER SOLIDS 2.5%	1000	—	20.6	CONTOURED	0.175
S-I B & S-II RETRO (TE-M-29-4 RECRUIT)	THIOL TP-E-8035	BINDER 74% OXIDIZER 23% OTHER SOLIDS 3%	1700	36,000	4.25	15°	0.141
S-I C RETRO (TE-424)	THIOL TP-E-8104	BINDER 20.9% OXIDIZER 72.0% OTHER SOLIDS 7.1%	1600	85,000	8.78	15°	0.063
S-I RETRO	AEROJET-GENERAL AMP-512DS MOD 3	ALUM. POWDER 35% VEG. OIL 1% POTASSIUM PER- CHLORATE OXIDIZER 64%	1400	—	6.67	15.5°	0.108
S-II ULLAGE (RS-U-501)	ROCKETDYNE RDS-509	RUBBER BINDER 12% AMMONIUM PER- CHLORATE OXIDIZER 82% ALUM. & OTHER METALS 6%	1000	20,000	8.25	12°	0.103

UNCLASSIFIED

UNCLASSIFIED

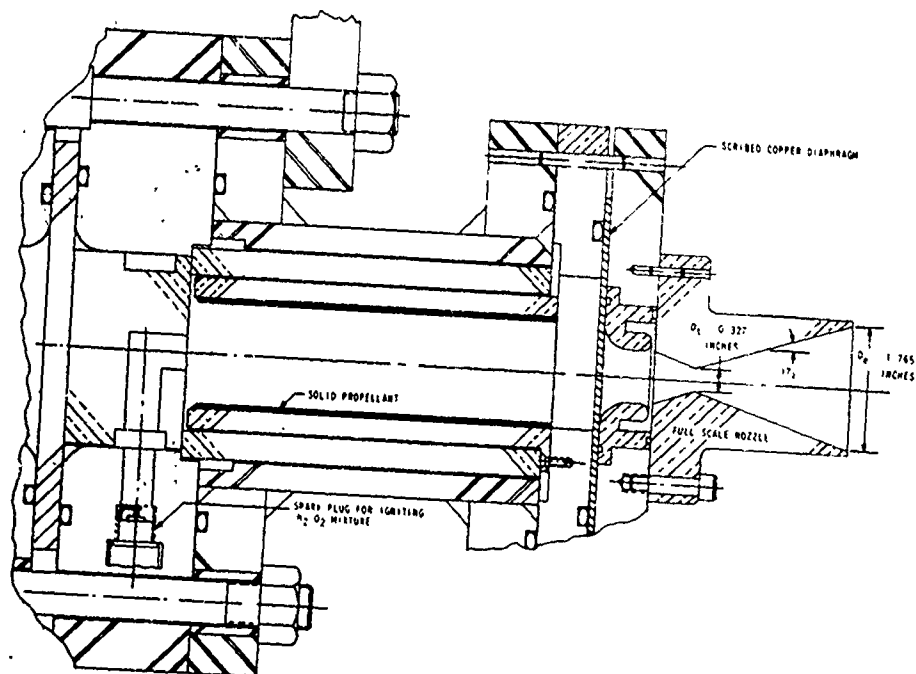
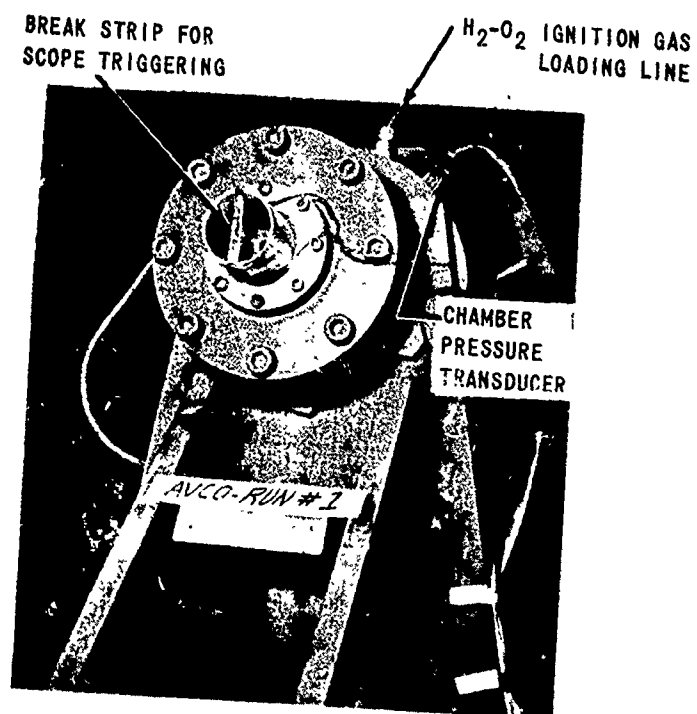


Figure 1. Solid Propellant Combustor Assembly.

UNCLASSIFIED

UNCLASSIFIED

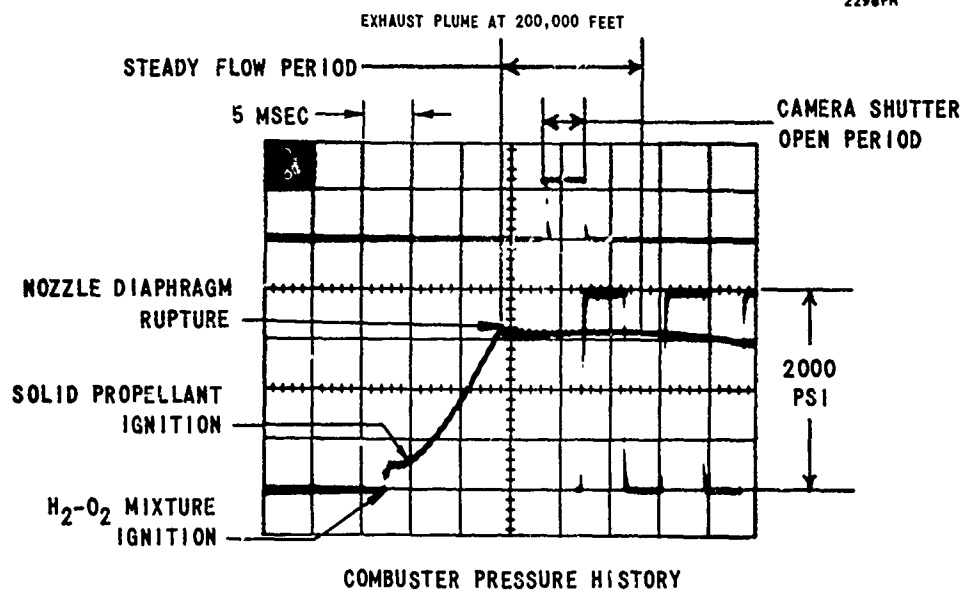
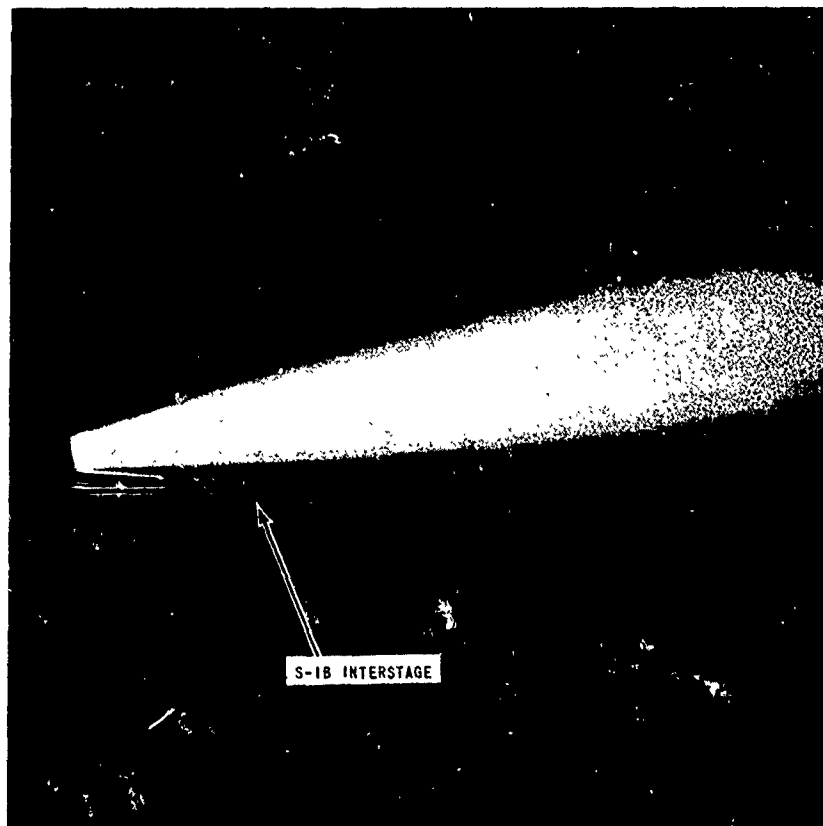


Figure 2. One-Tenth Scale Saturn Solid Propellant Retro-Rocket Operating Characteristics.

UNCLASSIFIED

UNCLASSIFIED

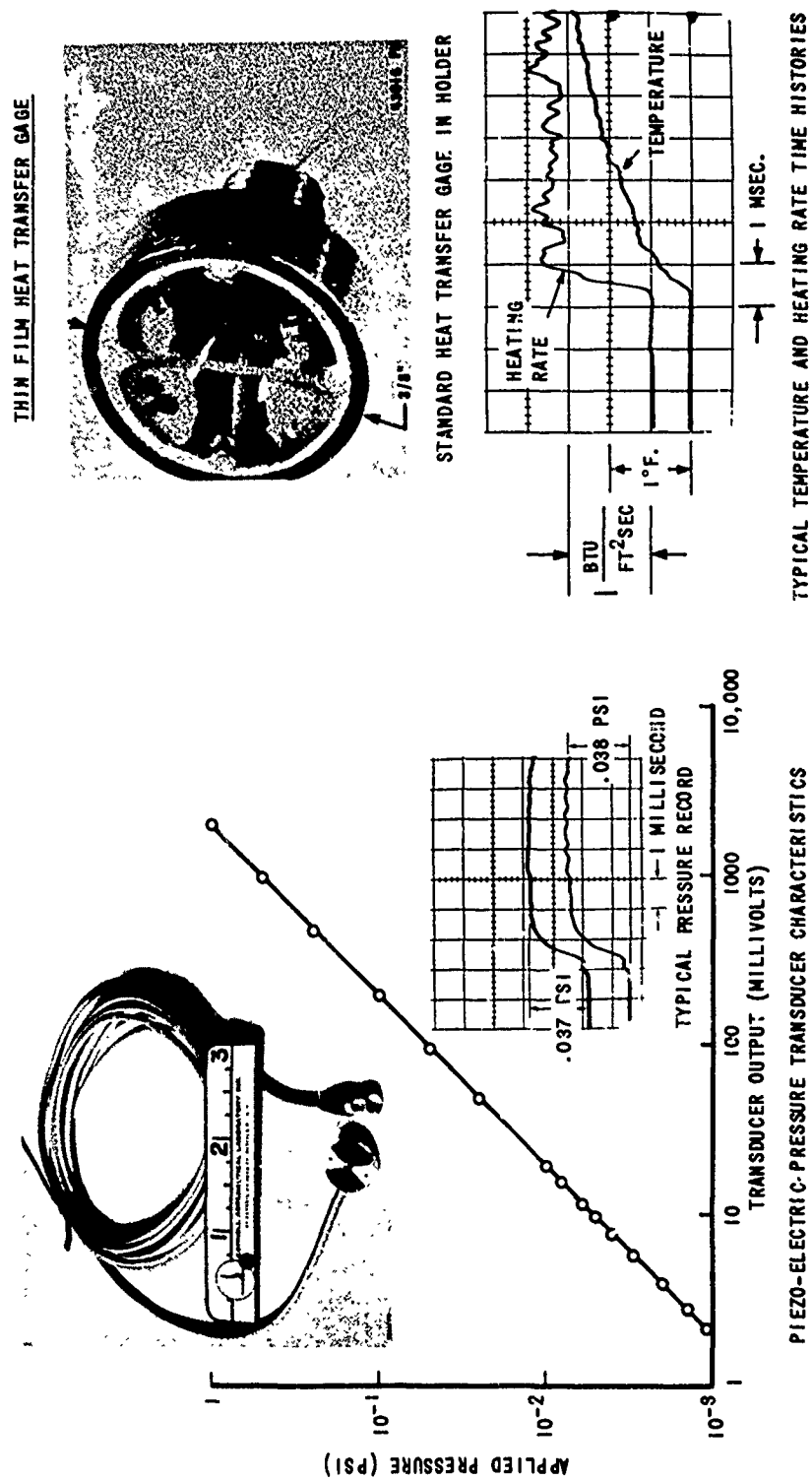


Figure 3. Heat Transfer and Pressure Transducers Used in Short-Duration Retro-Rocket Impingement Program.

UNCLASSIFIED



UNCLASSIFIED

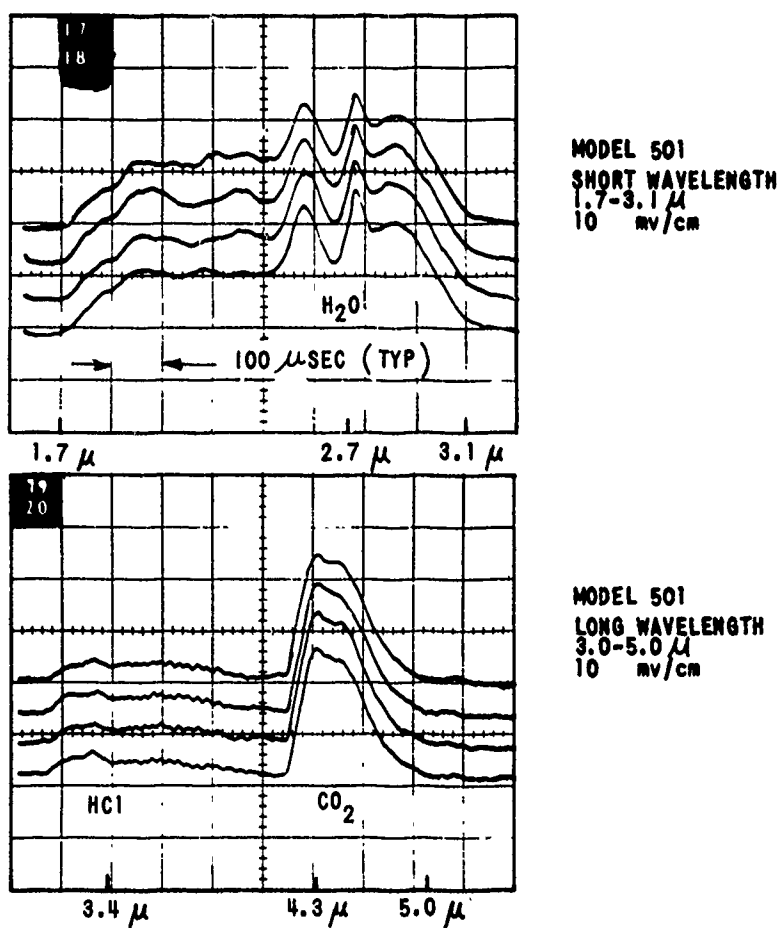


Figure 4. S-II Ullage Spectrometer Records.

UNCLASSIFIED

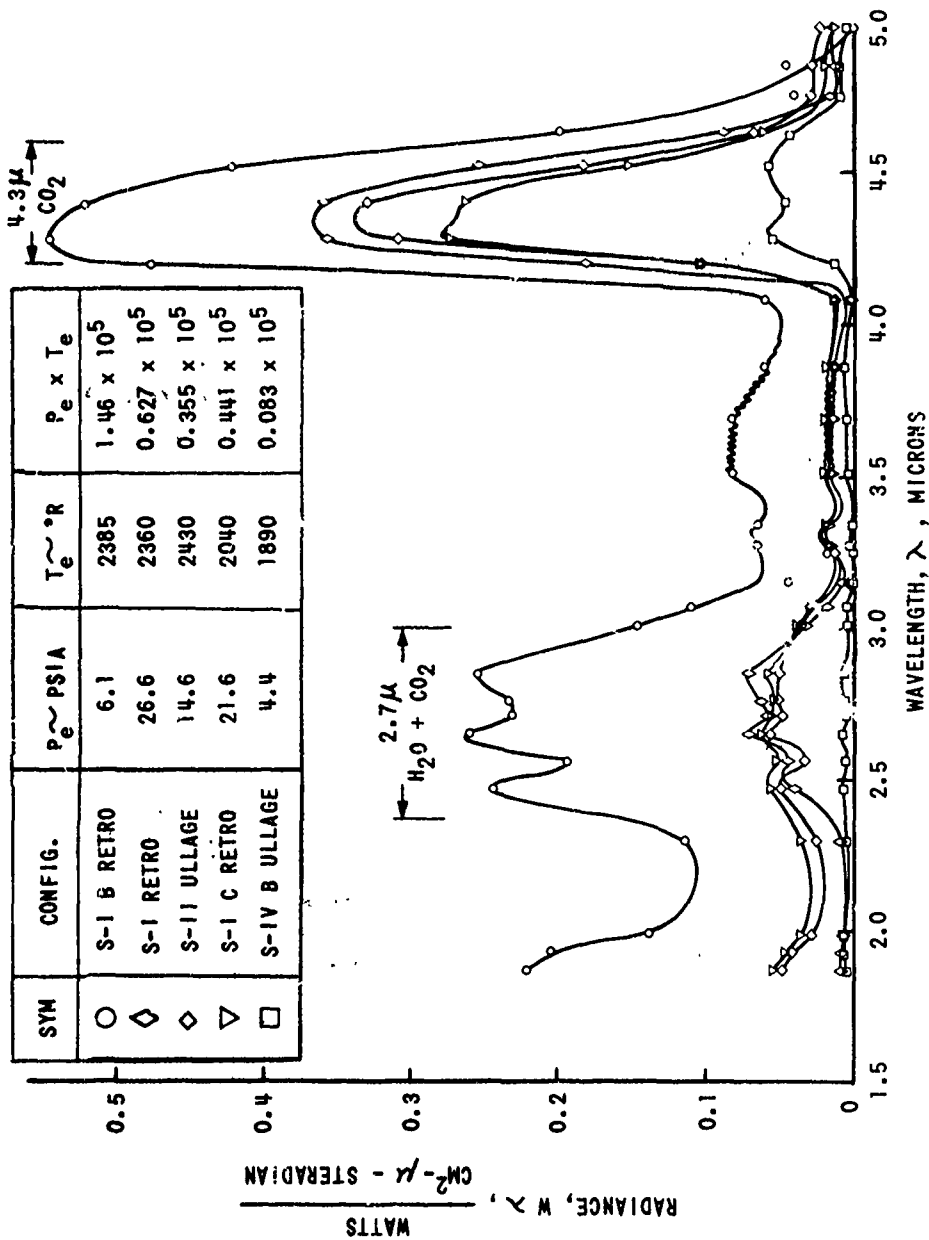


Figure 5. Spectral Radiance of Saturn Solid Propellant Exhaust Plumes.

UNCLASSIFIED

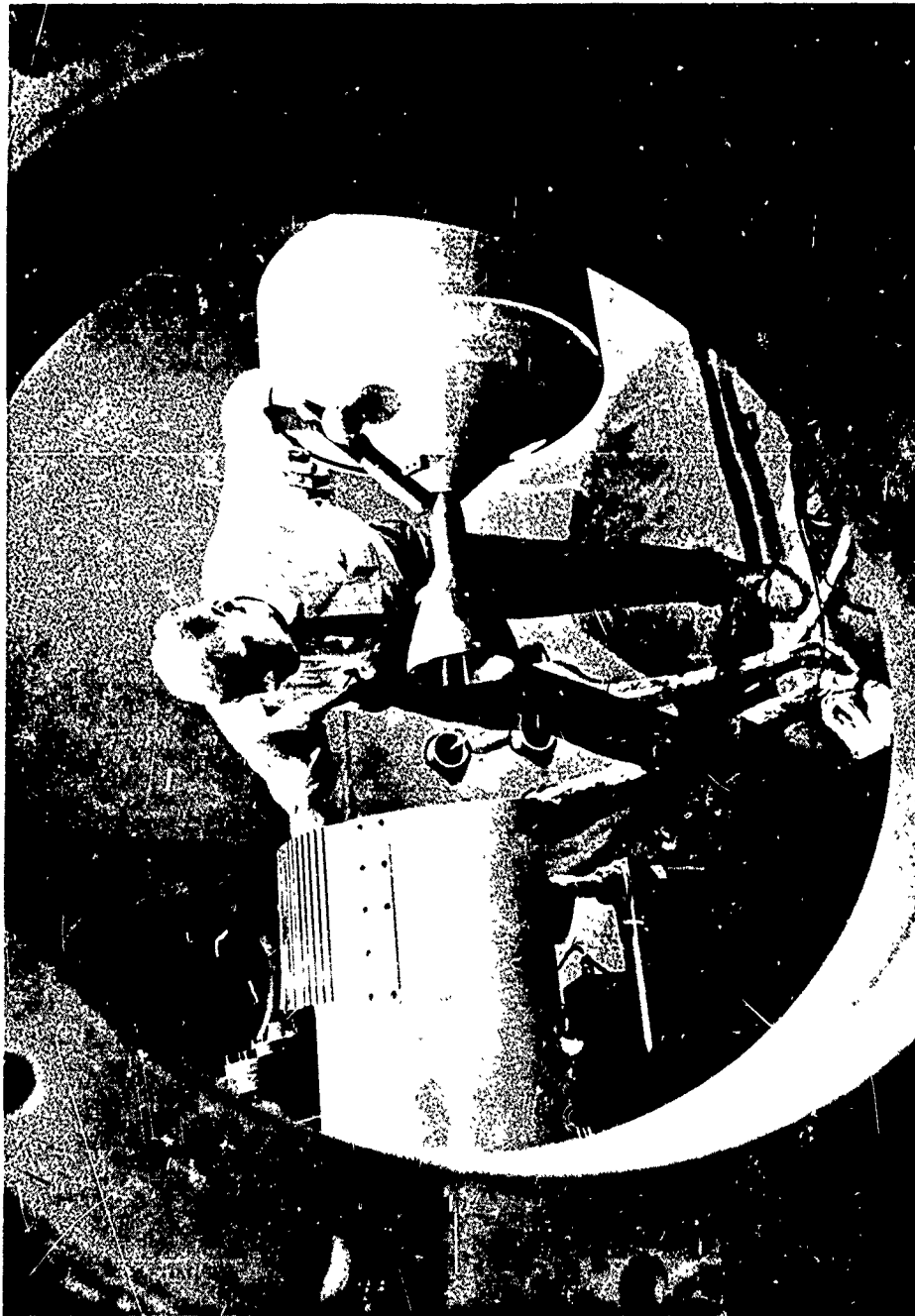


Figure 6a. S-IB/S-IVB Retro-Rocket Model Installation.

UNCLASSIFIED

UNCLASSIFIED

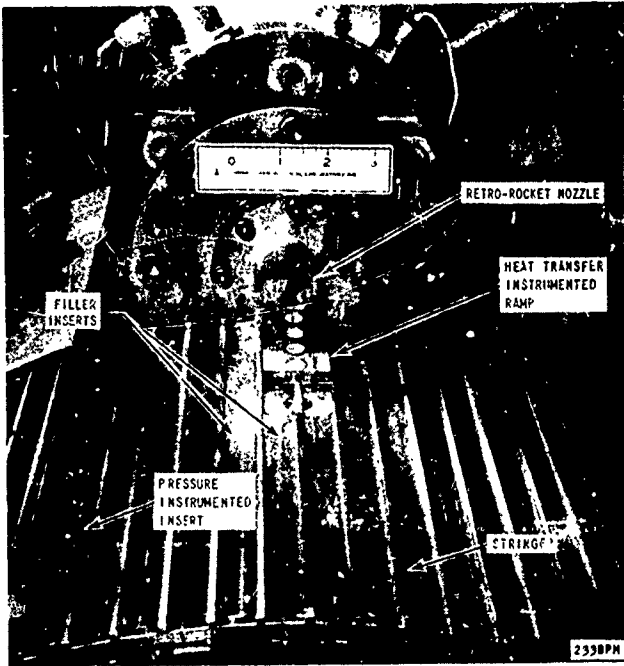
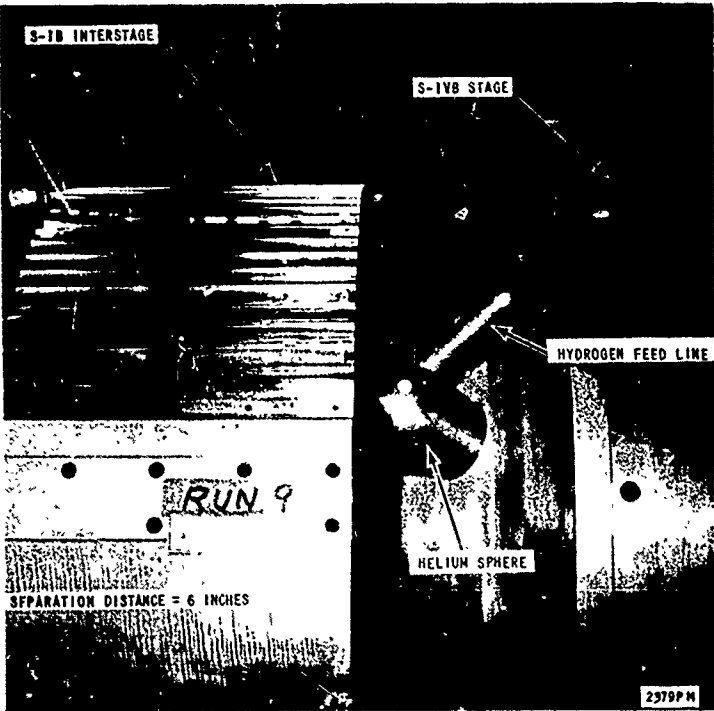


Figure 6b. One-Tenth Scale S-IB/S-IV B Separation Model Configuration.

UNCLASSIFIED

UNCLASSIFIED

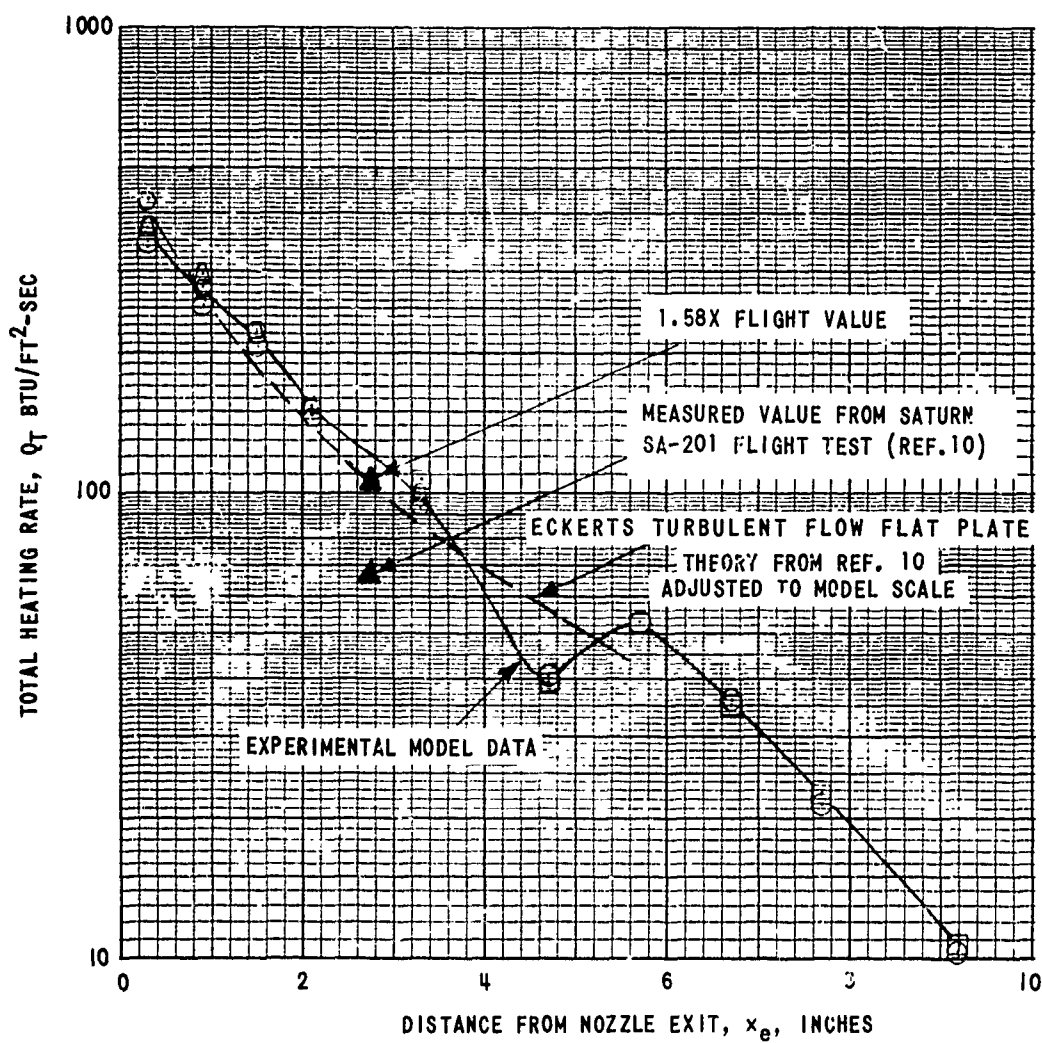
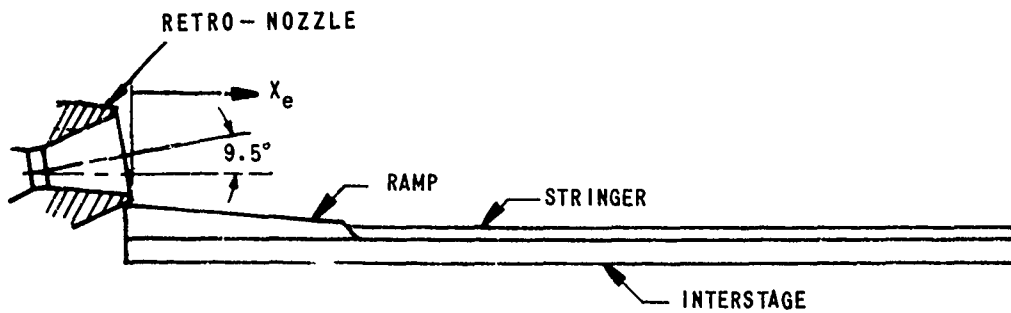


Figure 7. S-IB Interstage Centerline Heating Rate Distribution ( $\theta = 0$  Degrees).

UNCLASSIFIED

UNCLASSIFIED

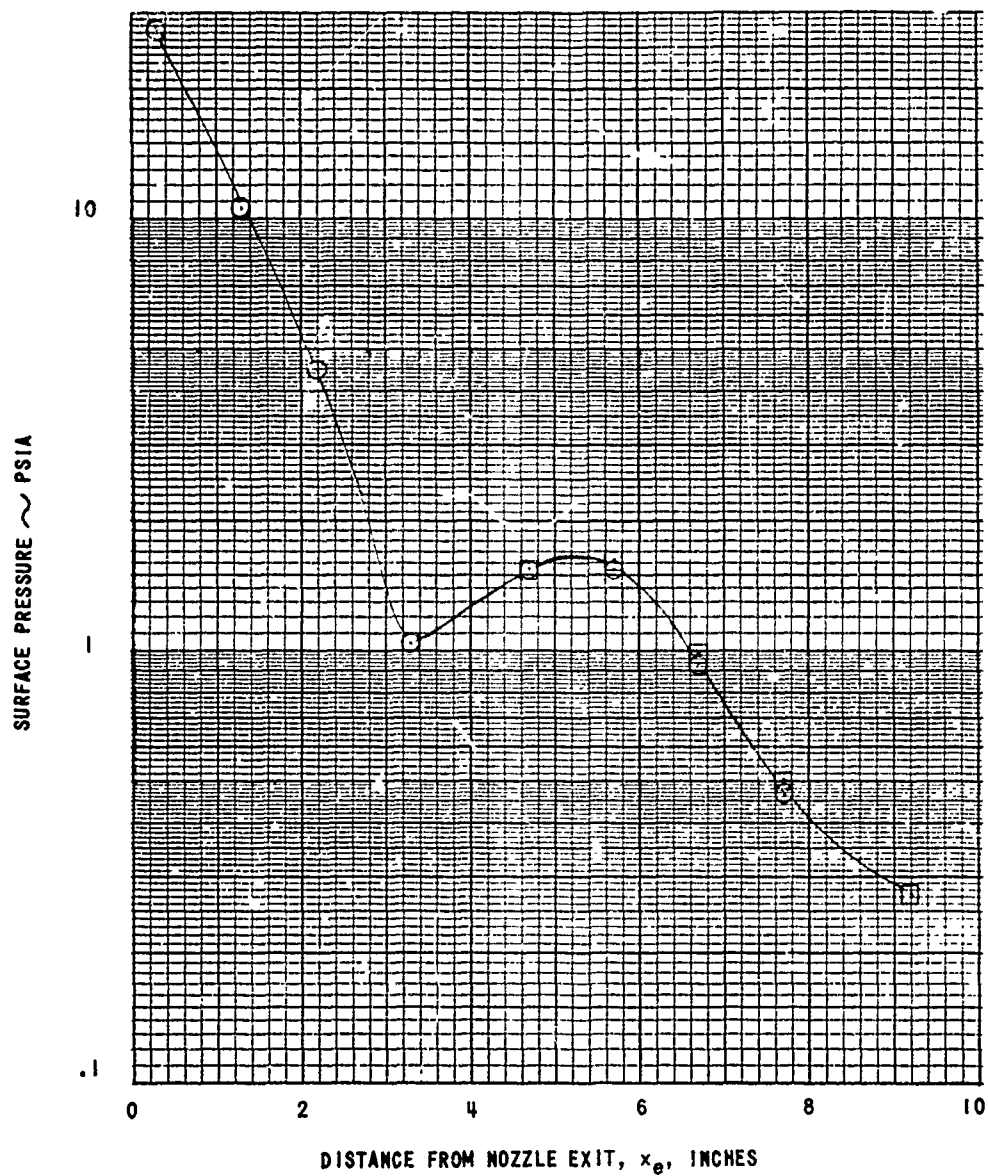
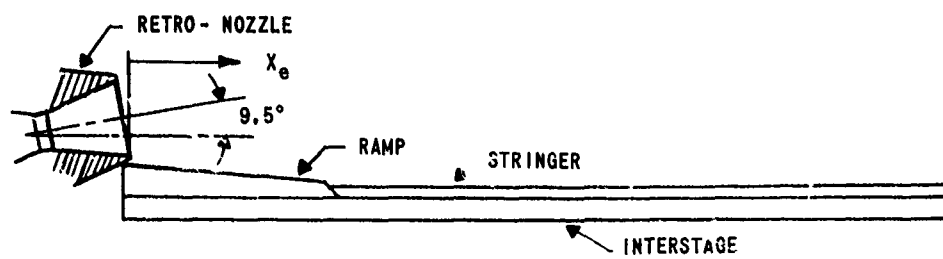


Figure 8. S-IB Interstage Centerline Pressure Distribution ( $\Theta = 0$  Degrees).

UNCLASSIFIED

UNCLASSIFIED

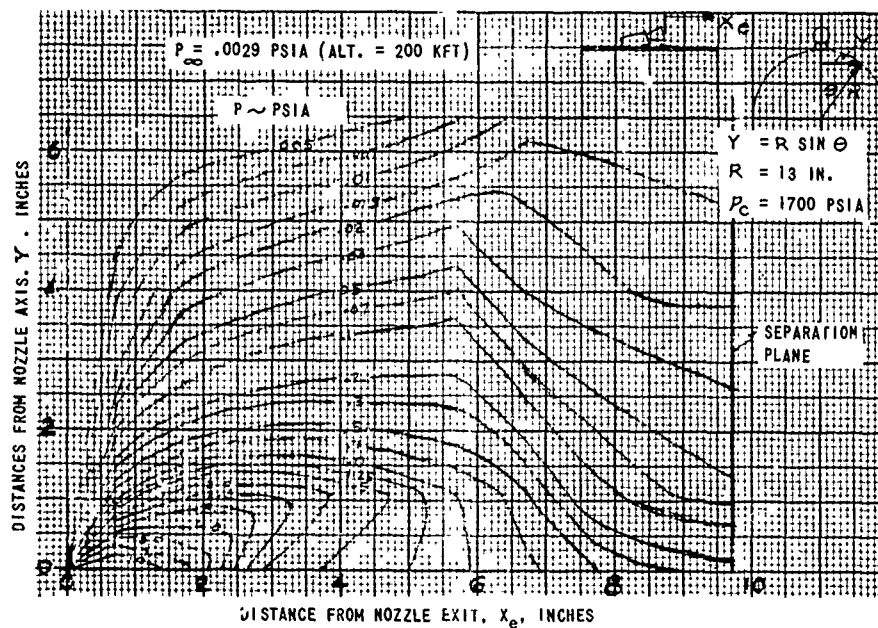


Figure 9a. S-IB Interstage Surface Pressure Distribution.

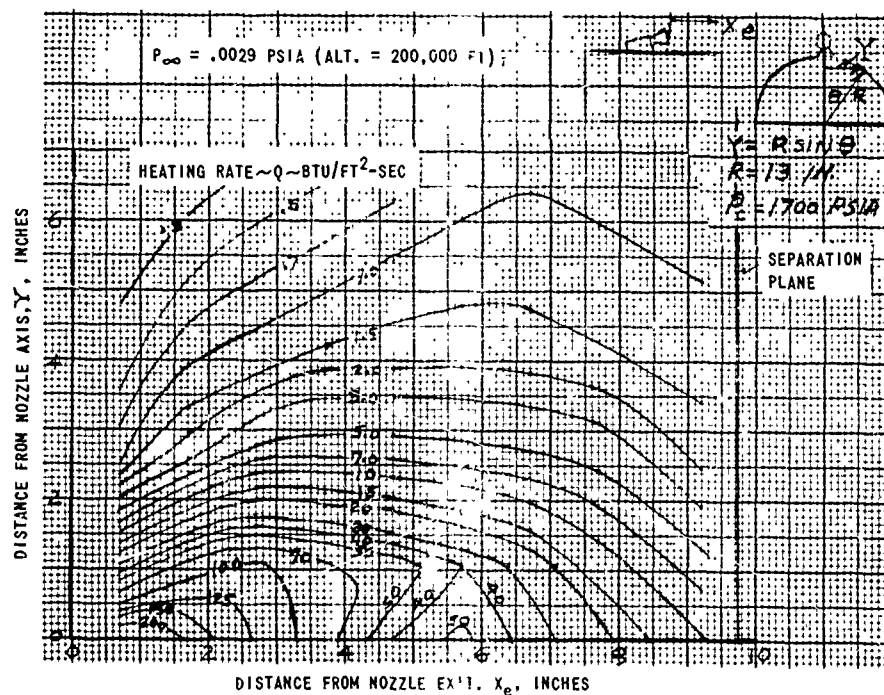
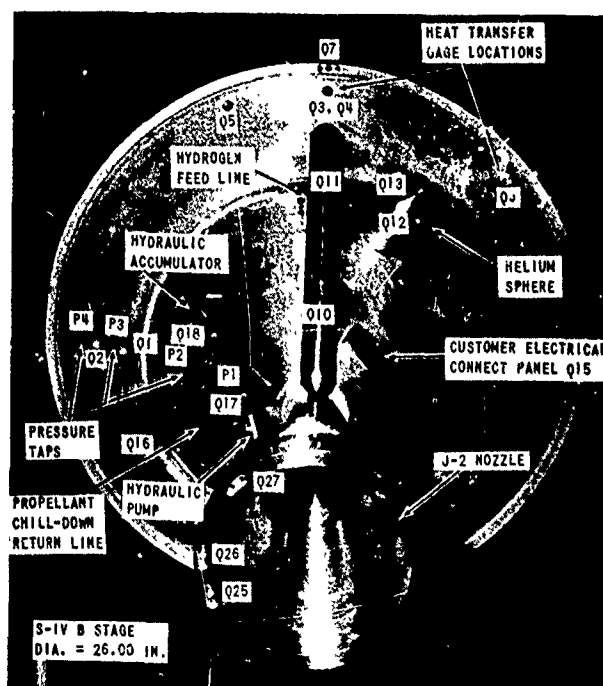


Figure 9b. S-IB Interstage Surface Convective Heating Distribution.

UNCLASSIFIED

UNCLASSIFIED



S-IV B STAGE BASE REGION CONFIGURATION

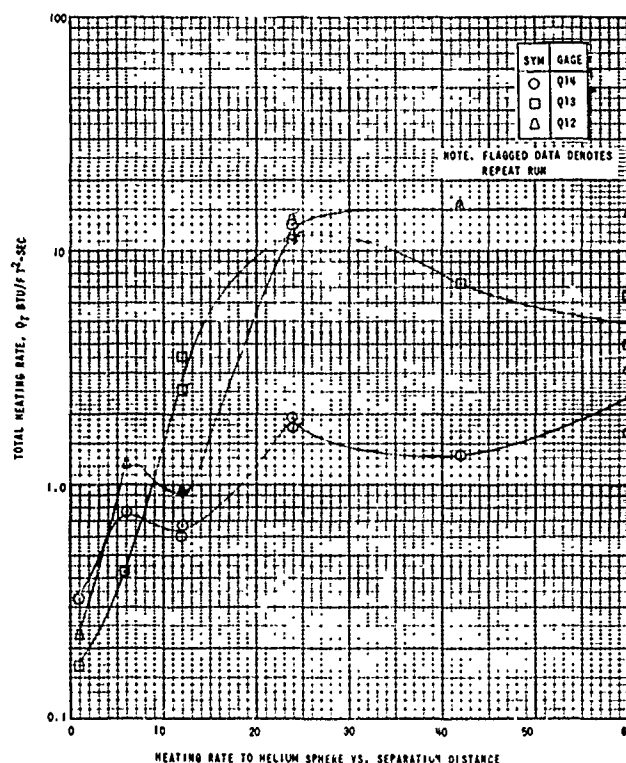
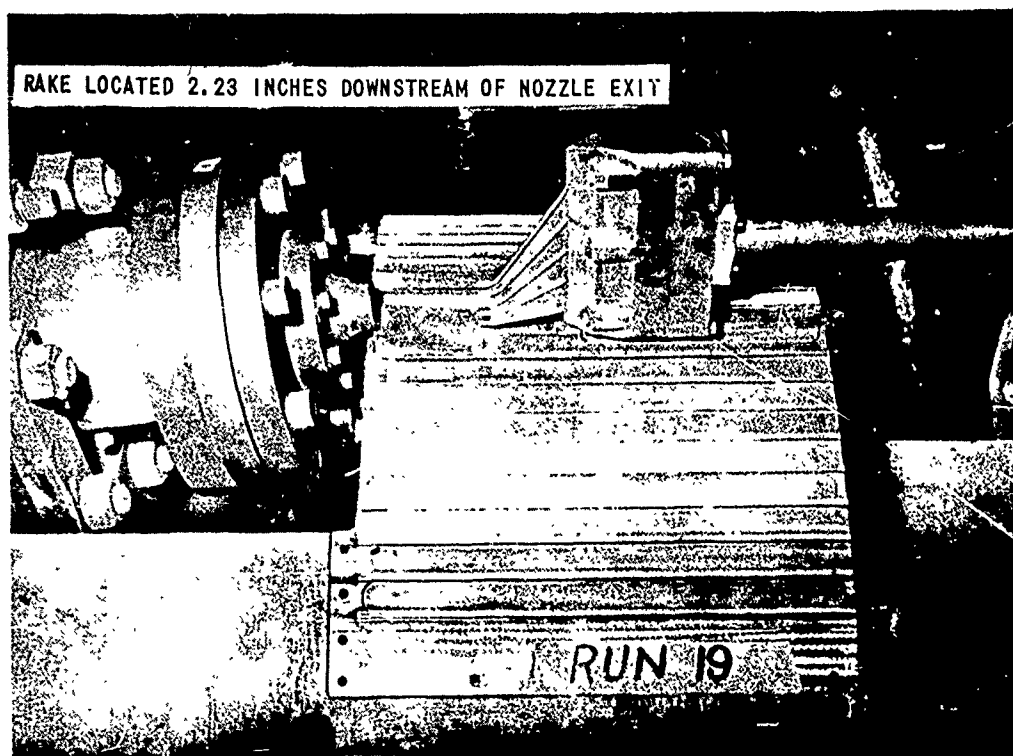


Figure 10. Typical S-IV B Base Heating Results.

UNCLASSIFIED



UNCLASSIFIED



S-1B INTERSTAGE WITH PITOT PRESSURE SURVEY RAKE INSTALLED



RETRO-ROCKET FIRING

Figure 11. Interstage Pitot Pressure Survey Test Configuration.

UNCLASSIFIED

UNCLASSIFIED

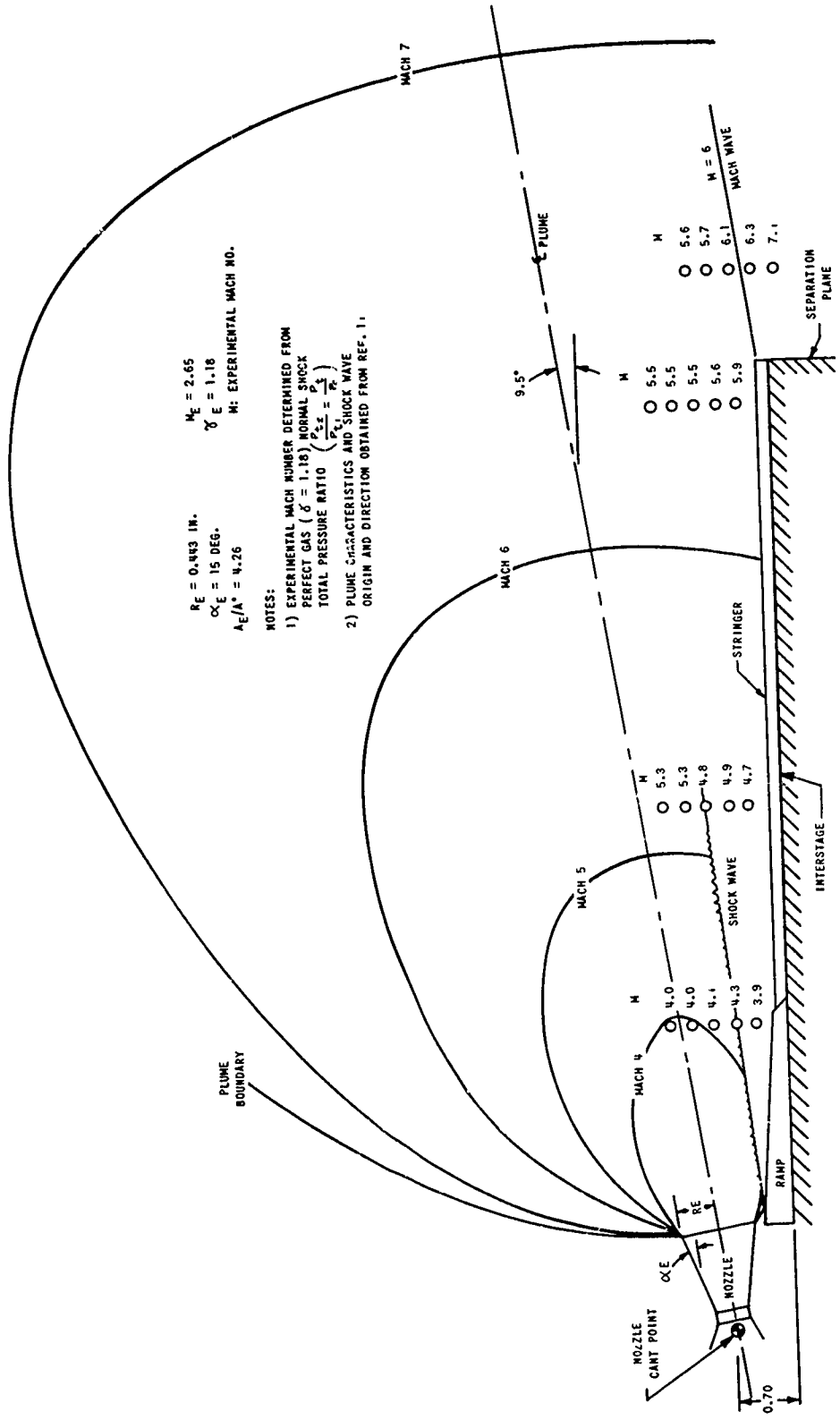


Figure 12. Comparison of Experimental and Theoretical S-IB Plume Flow Field Mach Numbers at 200,000 Feet Altitude.

UNCLASSIFIED

# UNCLASSIFIED

## PART II - IMPINGEMENT PRESSURES, FORCES, AND HEAT TRANSFER RATES IN HIGH ALTITUDE METALIZED SOLID PROPELLANT ROCKET EXHAUST PLUMES (UNCLASSIFIED)

by

Leo Rute  
Group Leader, Experimental Aero/Thermo Section  
Avco Missile Systems Division  
Wilmington, Massachusetts

### ABSTRACT

Results of an experimental investigation, subjecting a cylindrical body to the impingement of a metalized solid rocket exhaust plume at variable axial and radial locations relative to the nozzle exit plane are presented. The relative force contributions of gas and particles are compared. The applicability of infinite cylinder theory to a finite cylinder located in the plume flow field is assessed.

### INTRODUCTION

The operation of rocket motors at high altitudes with near-vacuum conditions results in a severely underexpanded flow of exhaust gases at the nozzle exit. In the process of exhaust gases adjusting to ambient pressure, large plumes develop. Their effects upon objects subjected to plume impingement and possibly engulfment are of interest and concern, where pressure and temperature effects may produce undesirable or detrimental consequences.

### STATE-OF-THE-ART DISCUSSION

The flow field exiting from a rocket exhaust nozzle can be satisfactorily analyzed (if fully gaseous) by means of the well-known method of characteristics. However, the introduction of metalized propellants considerably complicates this

UNCLASSIFIED

## UNCLASSIFIED

problem. While in a purely gaseous plume one is confronted with a gaseous stream which behaves in accordance with the dictates of the disturbance in the stream and the corresponding gas dynamics, the introduction of metalized propellants poses an entirely different problem. Now the rocket exhaust contains metallic particles which, depending on their distance from the exit plane, may be in liquid, solidifying, or solid state. Excepting those in completely solidified state, upon impact these particles can be expected to adhere to the object in their path. The effects of force contributions and localized heat sources due to "individual" droplets, obviously, cannot be analyzed in a straight-forward manner, being dependent on uncertainties such as droplet size, number of droplets, their phase and thermodynamic states as functions of spatial location, speed and angle of approach, distribution of particles at a particular flow cross section of interest, etc.

As a first approach to treating the two-phase flow problem, the gaseous flow field and the particles flow field may be considered uncoupled and analyzed independently. However, it is apparent that with increasing amounts of solid constituents in the exhaust, the uncoupled systems approach must become less and less satisfactory.

Because of the lack of available experimental data and present theoretical approaches being subject to the enumerated and other considerations, Avco/MSD decided to conduct a series of rocket firing tests designed to determine rocket exhaust impingement effects of metalized propellant exhaust upon cylindrical bodies. In order to have these tests present reality as closely as possible, the nozzle geometry of an actual rocket nozzle was duplicated, the actual propellant was used in the rocket firings and for the duration of the test time the altitude in Cornell Aeronautical Laboratory's (CAL) high altitude chamber was maintained in the vicinity of 400,000 feet.

# UNCLASSIFIED

## TEST EQUIPMENT

### ROCKET NOZZLE AND PROPELLANT

A duplicate of an actual rocket nozzle, having the dimensions:

cone half angle	17.5	degrees
area ratio	29.2	degrees
exit diameter	1.765	inches

and a representative average operating chamber pressure of 680 psia was installed in CAL's 10 foot diameter x 30 foot long high altitude chamber. Prior to each firing, the combustion chamber was fueled with the actual propellant obtained by CAL from Lockheed Propulsion Company (LPC), Redlands, and identified as LPC-619A (a solid aluminized polycarbutene propellant) - and the altitude chamber was evacuated to an altitude of approximately 400,000 feet.

### TEST MODELS

Of the two dimensionally equal (4 inch diameter, 26 inches long) cylindrical bodies, the 100 lb. model was instrumented for pressure and heat transfer measurements, and the 7 lb. model transmitted force measurements by means of accelerometers. The details of the instrumentation are discussed in Part I.

## TEST PROGRAM

This test program concentrated on systematically exploring the change in high altitude impingement effects of metalized solid rocket propellant exhaust plumes encountering a cylindrical body at selected distances from the nozzle exit plane as listed in the following table. The test arrangement is shown schematically in the accompanying figures.

UNCLASSIFIED

# UNCLASSIFIED

$\bar{x}/R_e$	$R/R_e$	$R/R_e$	$R/R_e$	$R/R_e$
-30			10	
-20			10	
-10			10	
0	-2.27	0	10	30
10	-2.27	0	10	30
20	-2.27	0	10	30
30	-2.27	0	10	30
40	-2.27	0	10	30
60	-2.27	0	10	30
80		0	10	30

where

$\bar{x}$  = axial distance from nozzle exit plane to upstream flat end of cylinder.

$R$  = radial distance from nozzle center line to axial stagnation line  
(windward side) of cylinder.

$R_e$  = nozzle exit radius (0.8825 inches)

Note that negative  $\bar{x}/R_e$ 's refer to positions where portions of the model extend upstream of the rocket nozzle exit plane. At  $\bar{x}/R_e = -30$ , the entire cylinder is upstream of the nozzle exit plane.

## EXPERIMENTAL RESULTS

### MEASUREMENTS

Figures 1 through 5 show pressure measurements taken along the stagnation line (windward side) at various cylinder positions in the plume as indicated by the sketch in each Figure. Figures 6 through 8 present similar measurements

# UNCLASSIFIED

along a ray located 90 degrees from the stagnation line. Figures 9 through 11 and 12 through 14 give heat transfer rate measurements along the stagnation line and 90 degrees ray, respectively. Figure 15 presents heat transfer rate measurements on the upstream flat end of the cylinder along two mutually perpendicular radii.

## ANALYSIS

The data may be examined with two particular objectives in mind.

1. Assess if and where infinite cylinder theory is valid.
2. Determine the relative contributions of gas and particle flows to the total impingement force.

Figures 16 through 18 superimpose pressure measurements at fixed radial cylinder positions, thereby simulating an infinite cylinder arrangement. From Figure 16, it is clear that in the strong flow field region ( $R/R_e = -2.27$ : nozzle and cylinder axes coincide) end effects are not negligible, and an infinite cylinder trend is not achieved until the far downstream regions are reached. As the model moves farther and farther away (axially and radially) from the nozzle exit plane, infinite cylinder behavior is approached more and more.

Similar comments hold for the heat transfer rates in Figures 20, 21 and 23. With the majority of heat transfer gages destroyed due to particle impingement, no conclusions can be drawn from Figure 22.

## RELATIVE CONTRIBUTIONS OF GAS AND PARTICLE FLOWS

A comparison of integrated pressure forces\* and total force measured independently should reveal the relative contributions of particle and gas flows (aerodynamic skin drag not specifically accounted for):

\*The cosine-type circumferential pressure distribution equation of Reference 1 was modified to pass through the three measured pressure values at each of the nine (9) instrumented axial sections.

## UNCLASSIFIED

As the model moves into the far upstream and the far downstream regions and recognizing the behavior of the flow field - one may expect decreasing particle contributions, so that at far enough upstream and downstream stations total measured force and integrated pressure forces should approach each other. This theory is borne out by the data of Figures 24 and 25: At  $R/R_e = 10$ , integrated pressure forces and measured total force are in practically complete agreement at the upstream and near upstream stations. As the cylinder moves farther downstream, the relative difference widens, reaches a maximum and then decreases again such that both measured force and integrated pressure forces approach a common constant value. This is in agreement with the behavior of the flow field: As the body moves downstream from the near-nozzle position, an increasing section of the cylinder intercepts particle flow lines coming from the strong near-nozzle particle flow field. With further increasing downstream distance, lower particle regions are entered, and particle impingement effects decrease. The same behavior is observed at the  $R/R_e = 30$  position.

Comparing forces at  $R/R_e = 10$  with those at  $R/R_e = 30$ , one notices that in addition to dealing with a generally lower force level in the latter case, the maximum appears farther downstream. Both trends agree with the to be anticipated flow behavior: As the radial distance from the nozzle axis increases, lighter and lighter particles with therefore decreasing impingement effects are intercepted, on one hand, explaining the generally lower force level at  $R/R_e = 30$ , and on the other hand, particle streamlines intercepted at the near radial locations are being missed at the farther out stations and are not again intercepted until moving farther downstream, explaining the later occurring maximum at  $R/R_e = 30$ .

However, another explanation must be sought for the behavior at  $R/R_e = 0$ . Here, the cylinder stagnation line is tangent to the nozzle axis and, therefore, in effect, the cylindrical surface is not subject to any impingement. However,



# UNCLASSIFIED

again visualizing the flow field and recalling the previous comments about the adherence of liquid and solidifying particles, it then appears that the particle bombardment of the front end of the cylinder contributes the force difference in the normal direction. Since the impinging particle streamlines approach the front end of the cylinder at varying angles, their momentum is transferred to the cylinder in the axial as well as the normal direction, and considering the strong particle flow field in the immediate vicinity of the nozzle, substantial particle contributions can be made.

## ADDITIONAL TESTS AND TEST RESULTS

In addition to the presented results axial force measurements were taken, also. Moreover, similar tests were performed with a cone/cylinder configuration. These results are presently under study.

## CONCLUSIONS

Cylindrical bodies were subjected in a high altitude (approximately 400,000 feet) chamber to metalized solid propellant rocket exhaust plumes at systematically varied locations in the flow field. The analysis of the pressure, heat transfer rate, and force measurements indicates the following:

1. For the test conditions discussed here (type of propellant, etc.) particle effects can be as much as triple impingement forces due to gas flow alone.
2. With increasing radial distance from the rocket nozzle axis, particle force contributions decrease as the lighter-particle regions are entered and the number of particle streamlines actually striking the body diminishes.

UNCLASSIFIED

## UNCLASSIFIED

3. Starting from a position upstream of the nozzle exit plane, as the model moves in the downstream direction (at any  $R/R_e = \text{const.}$ ) the force contribution due to particle impingement increases, reaches a maximum, and then decreases again as the body moves from the particle-free upstream region through maximum impingement into regions of diminishing particle population.
4. Contrary to the Newtonian impact approach, the adherence of liquid and solidifying particles upon impact on the front end of the cylinder necessitates the taking into account of an all-directions momentum transfer.

### RECOMMENDATIONS FOR FUTURE INVESTIGATIONS

The present test series concentrated on determining the change in impingement effects on a cylinder as a function of spatical coordinates, i.e., all other conditions such as rocket characteristics, propellant, etc., remained the same from test to test.

1. To obtain a comprehensive picture of the behavior of metalized solid rocket propellant exhaust effects, further tests need to be performed in order to include such variables as propellant composition, nozzle geometry, as well as separate out the effects of skin drag. Also, the investigating of other than cylindrical shapes is desirable.
2. It is recommended that a sufficient number of circumferential pressure measurements be made at selected stations along the test body in order to arrive at an analytical expression best representing the type of pressure distributions existing around bodies in highly non-uniform flow fields.

UNCLASSIFIED

# UNCLASSIFIED

3. In view of the number of heat transfer gages destroyed by direct particle hits, there exists the need for developing from direct impact protected instrumentation which is, nevertheless, quick-responsive and sensitive.

## ACKNOWLEDGMENT

The author is pleased to acknowledge the efforts of Mr. L. C. Winans in determining the integrated pressure forces.

Appreciation is expressed to Messrs. K. C. Hendershot and R. J. Sergeant of Cornell Aeronautical Laboratory, Inc., for their constant cooperation.

## REFERENCES

Degen, M., "Evaluation of Forces and Moments from Pressure Data on Bodies of Revolution," Unpublished Report.

UNCLASSIFIED

UNCLASSIFIED

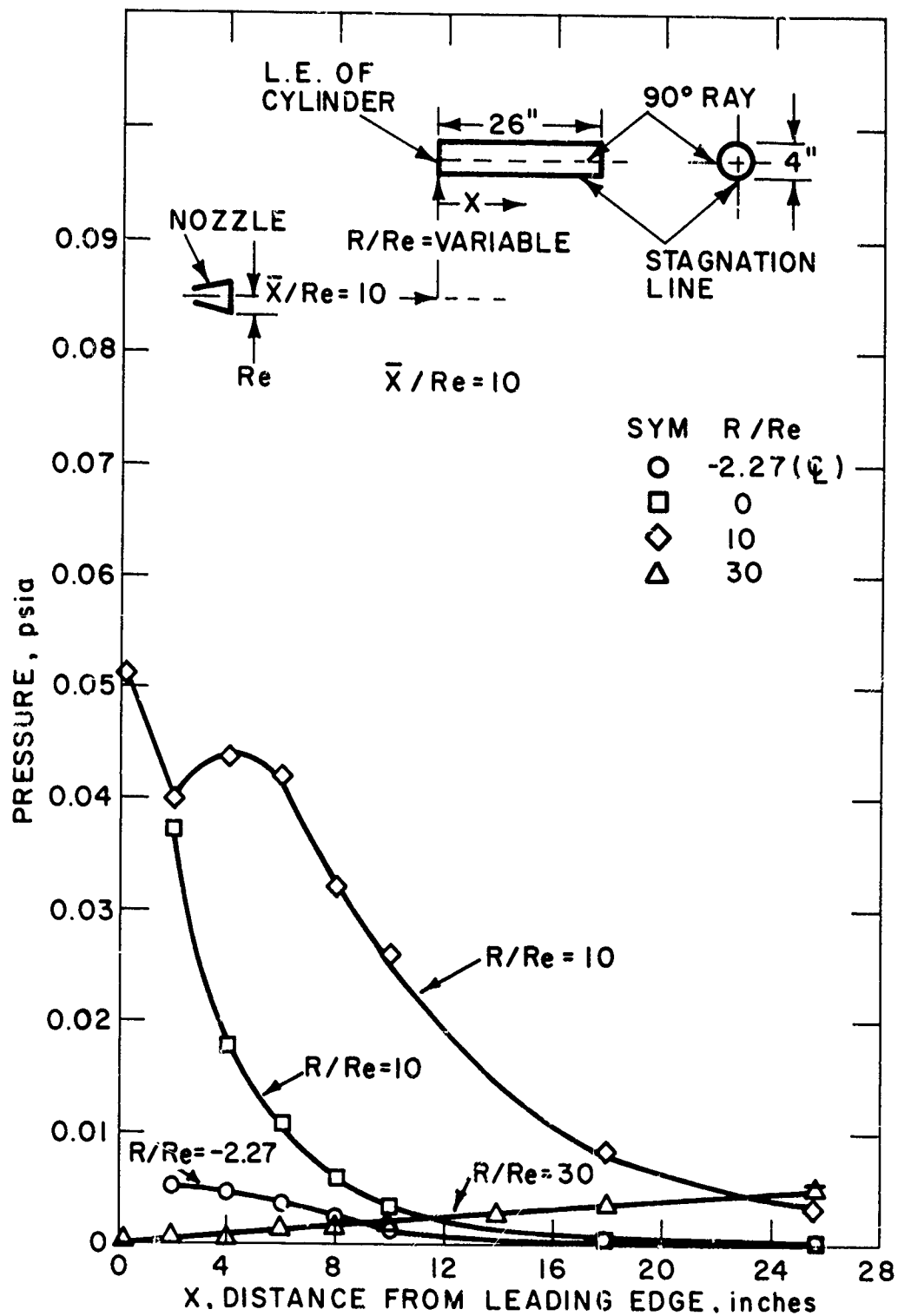


Figure 1. Axial Pressure Distribution Along Stagnation Line.

UNCLASSIFIED

UNCLASSIFIED

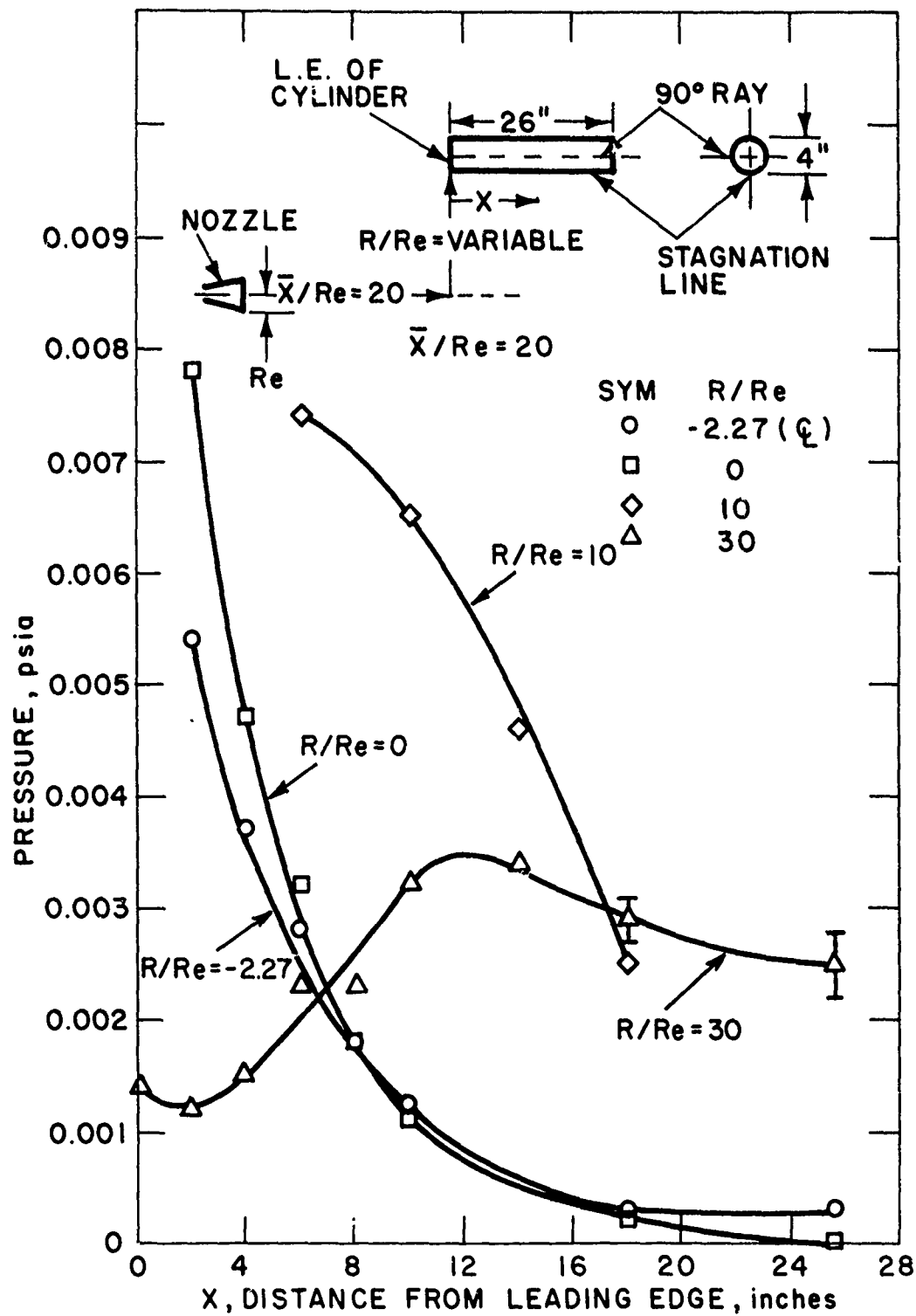


Figure 2. Axial Pressure Distribution Along Stagnation Line.

UNCLASSIFIED

UNCLASSIFIED

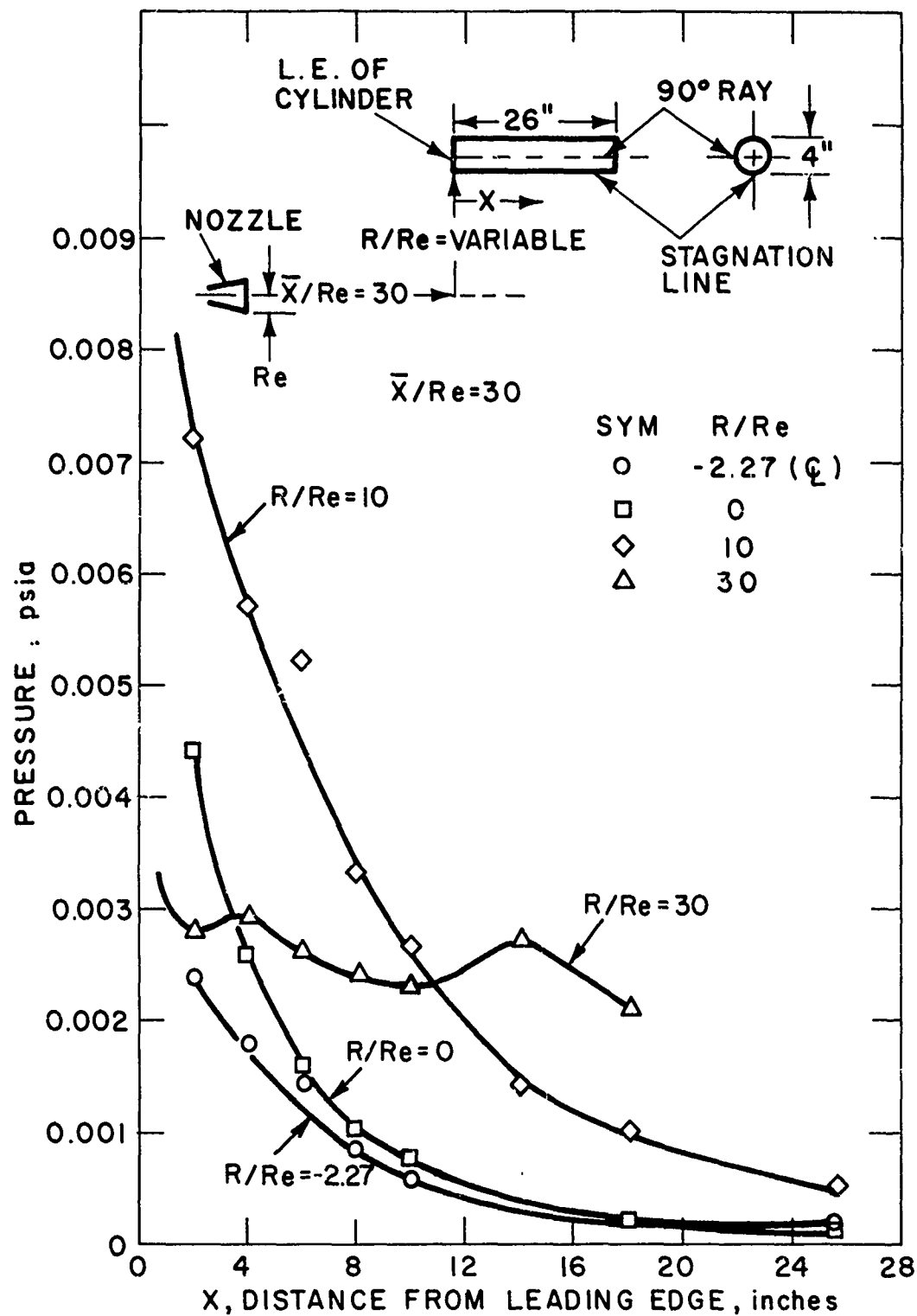


Figure 3. Axial Pressure Distribution Along Stagnation Line.

UNCLASSIFIED

UNCLASSIFIED

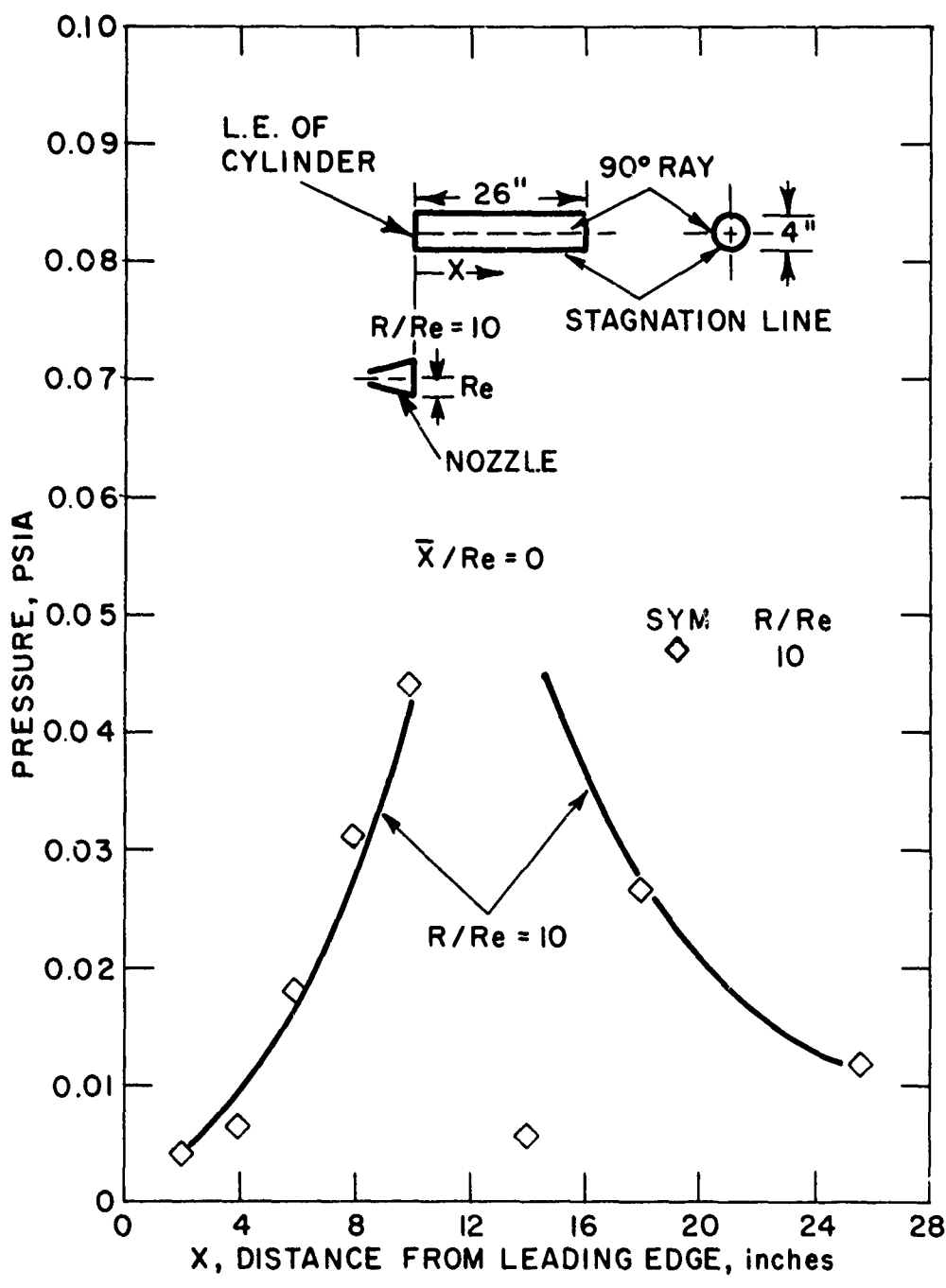


Figure 4. Axial Pressure Distribution Along Stagnation Line.

UNCLASSIFIED

UNCLASSIFIED

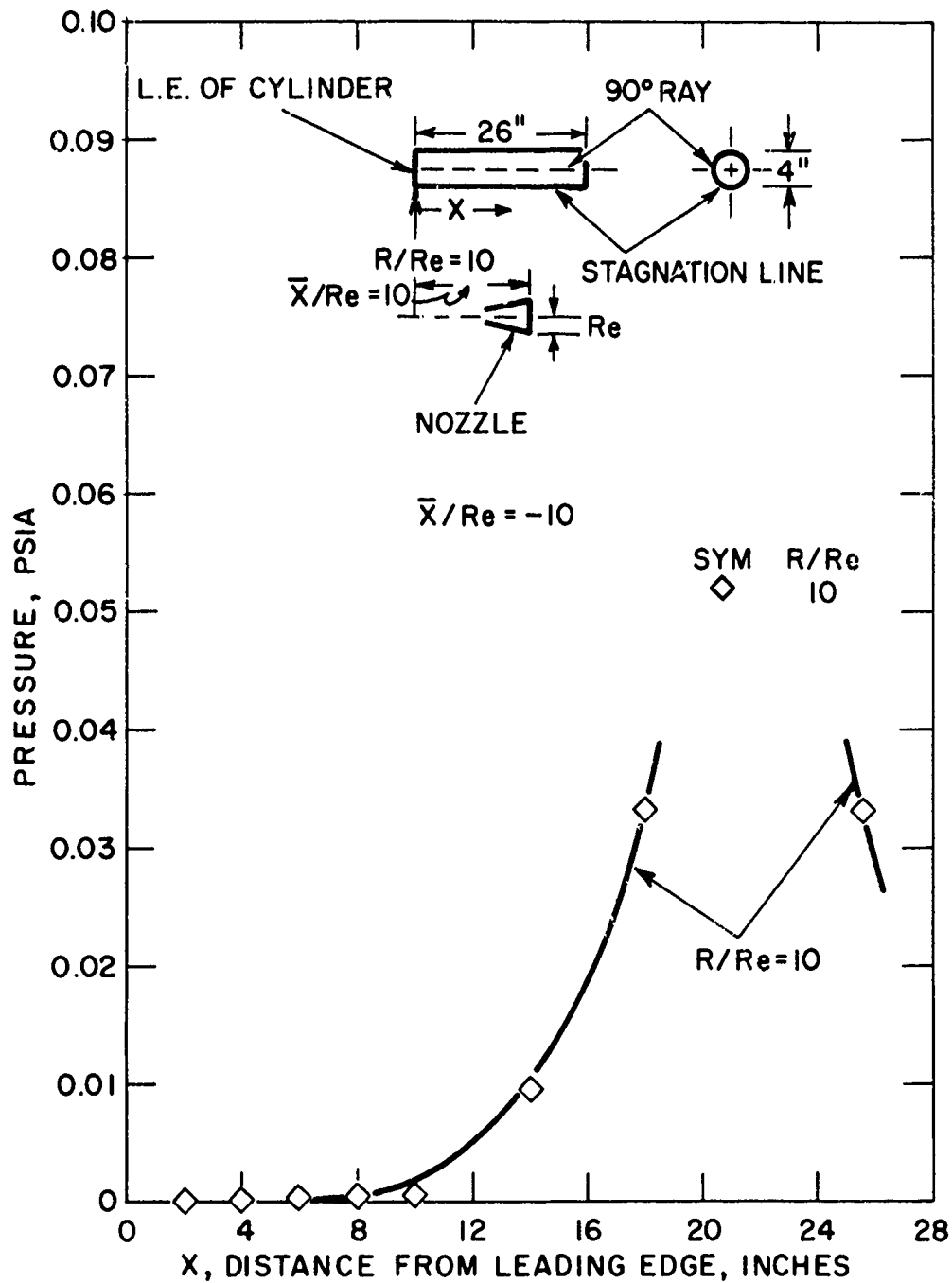


Figure 5. Axial Pressure Distribution Along Stagnation Line.

UNCLASSIFIED



UNCLASSIFIED

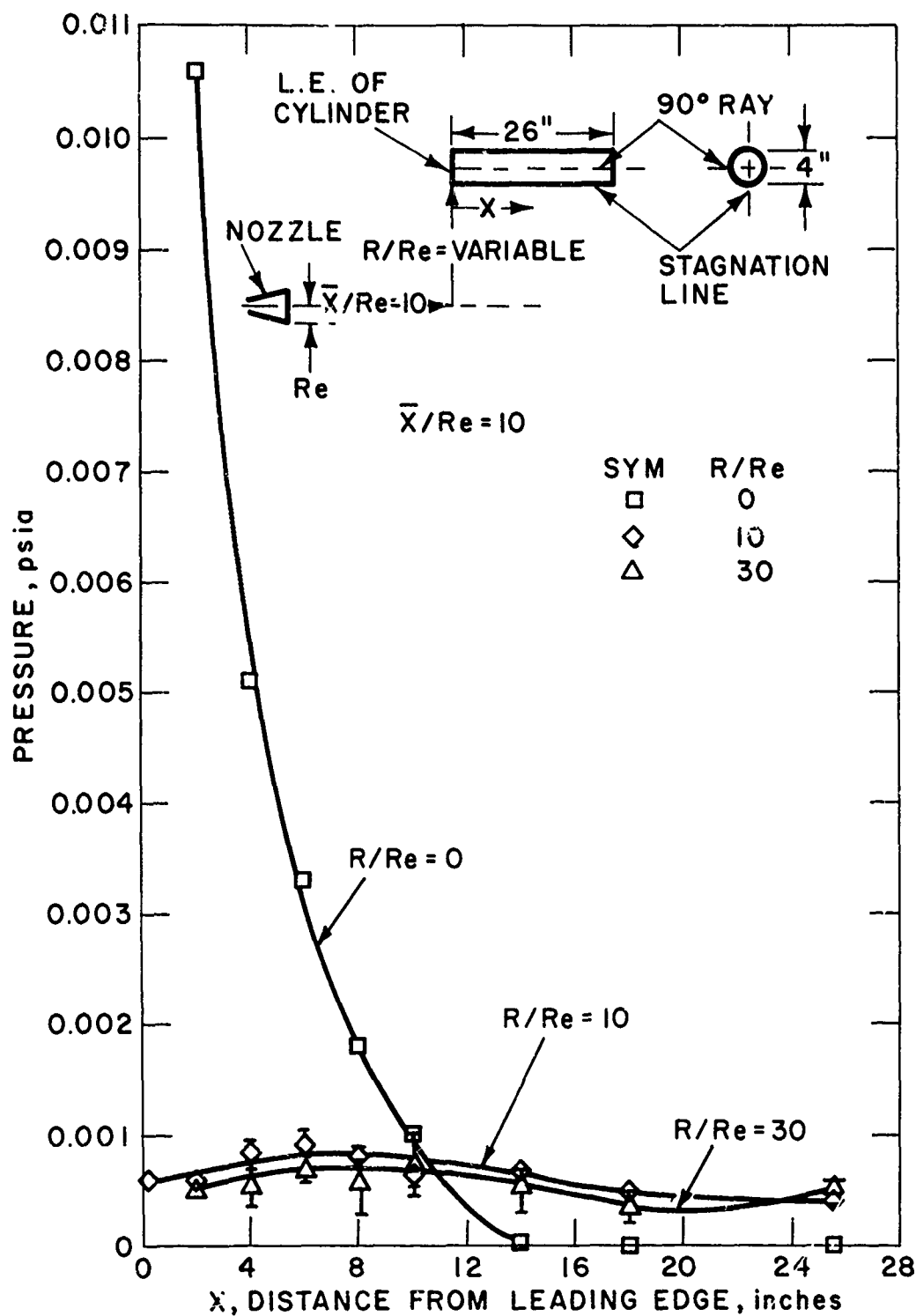


Figure 6. Axial Pressure Distribution Along Ray  $90^\circ$  from Stagnation Line.

UNCLASSIFIED

UNCLASSIFIED

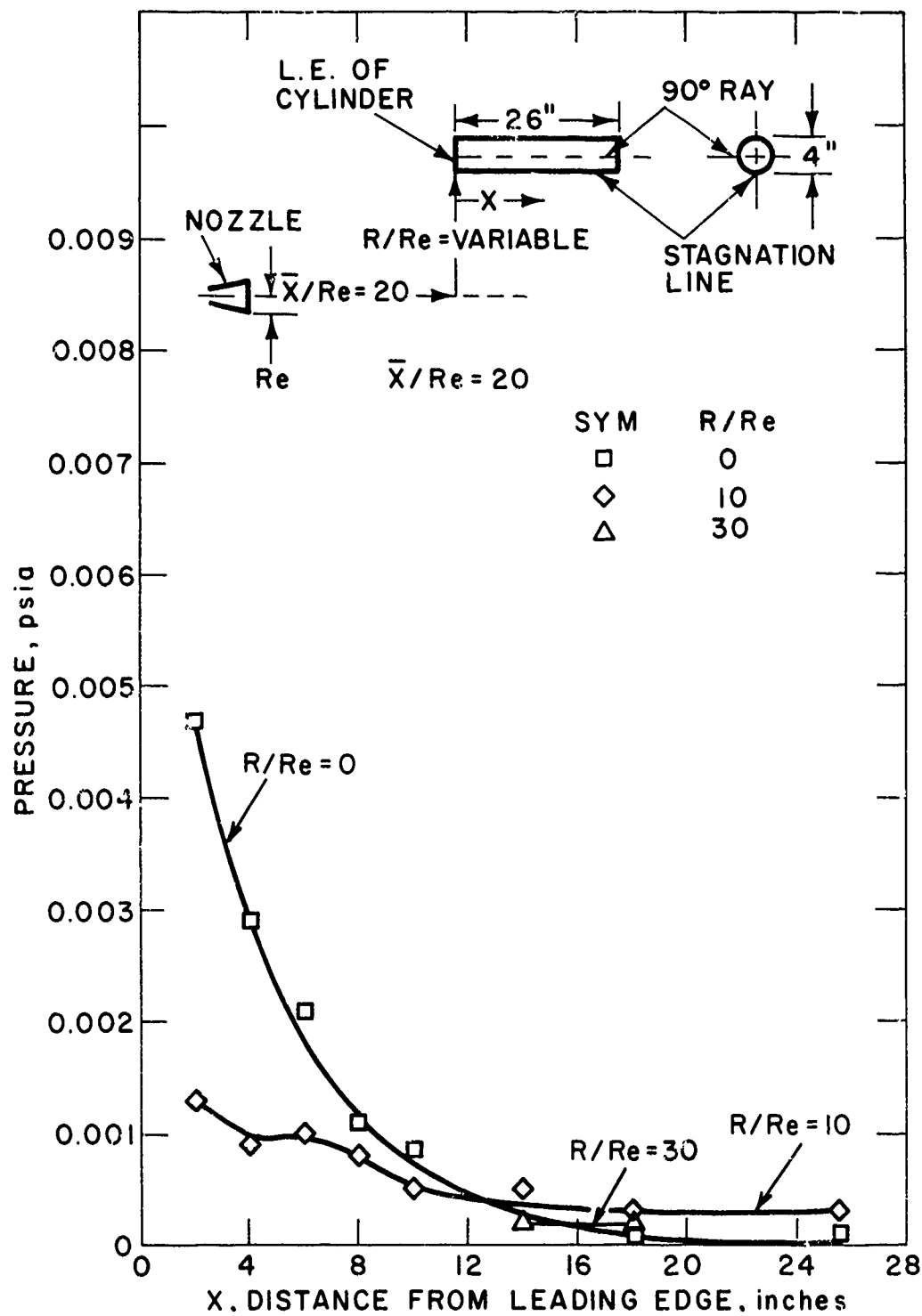


Figure 7. Axial Pressure Distribution Along Ray  $90^\circ$  from Stagnation Line.

UNCLASSIFIED

UNCLASSIFIED

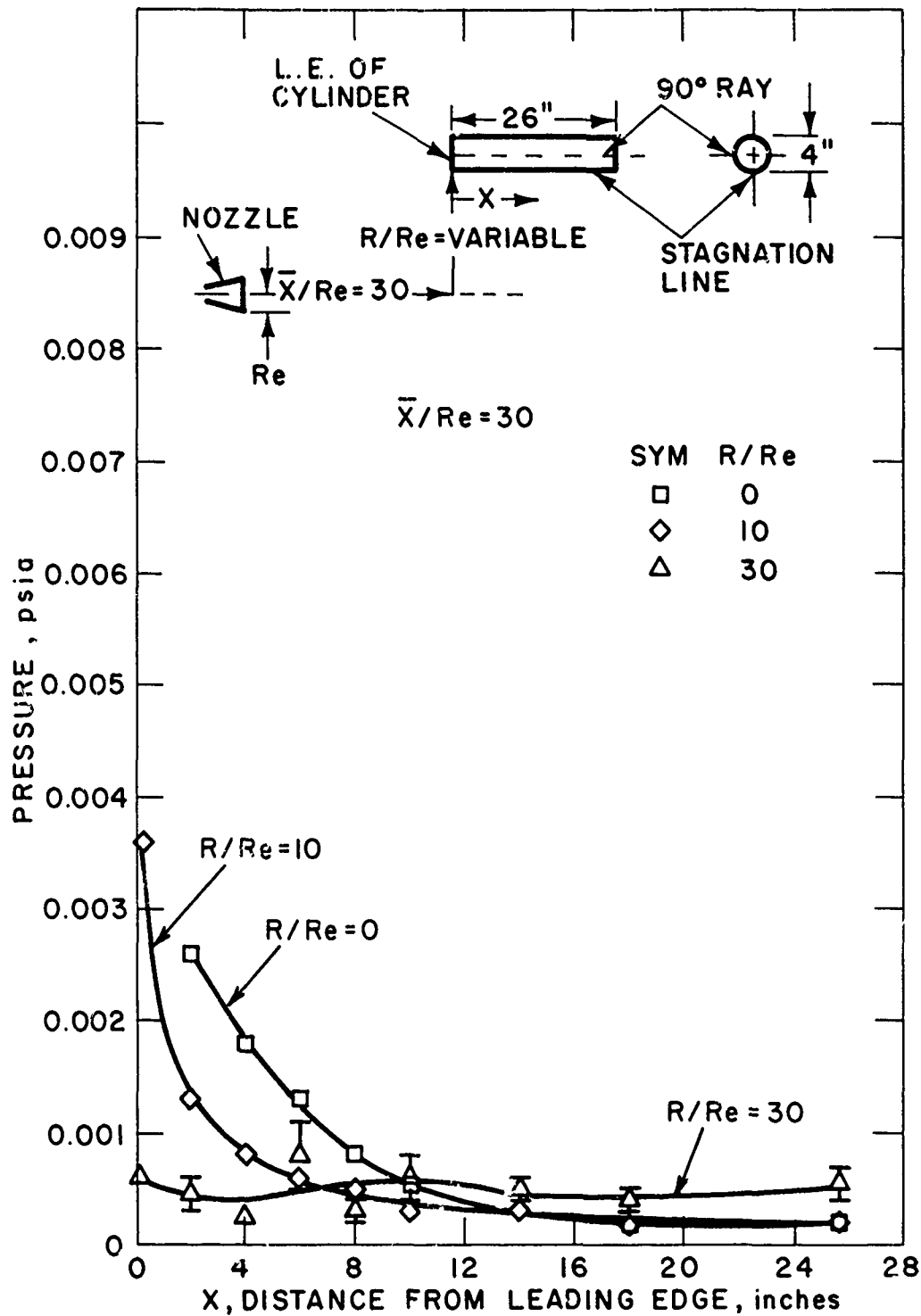


Figure 8. Axial Pressure Distribution Along Ray  $90^\circ$  from Stagnation Line.

UNCLASSIFIED

UNCLASSIFIED

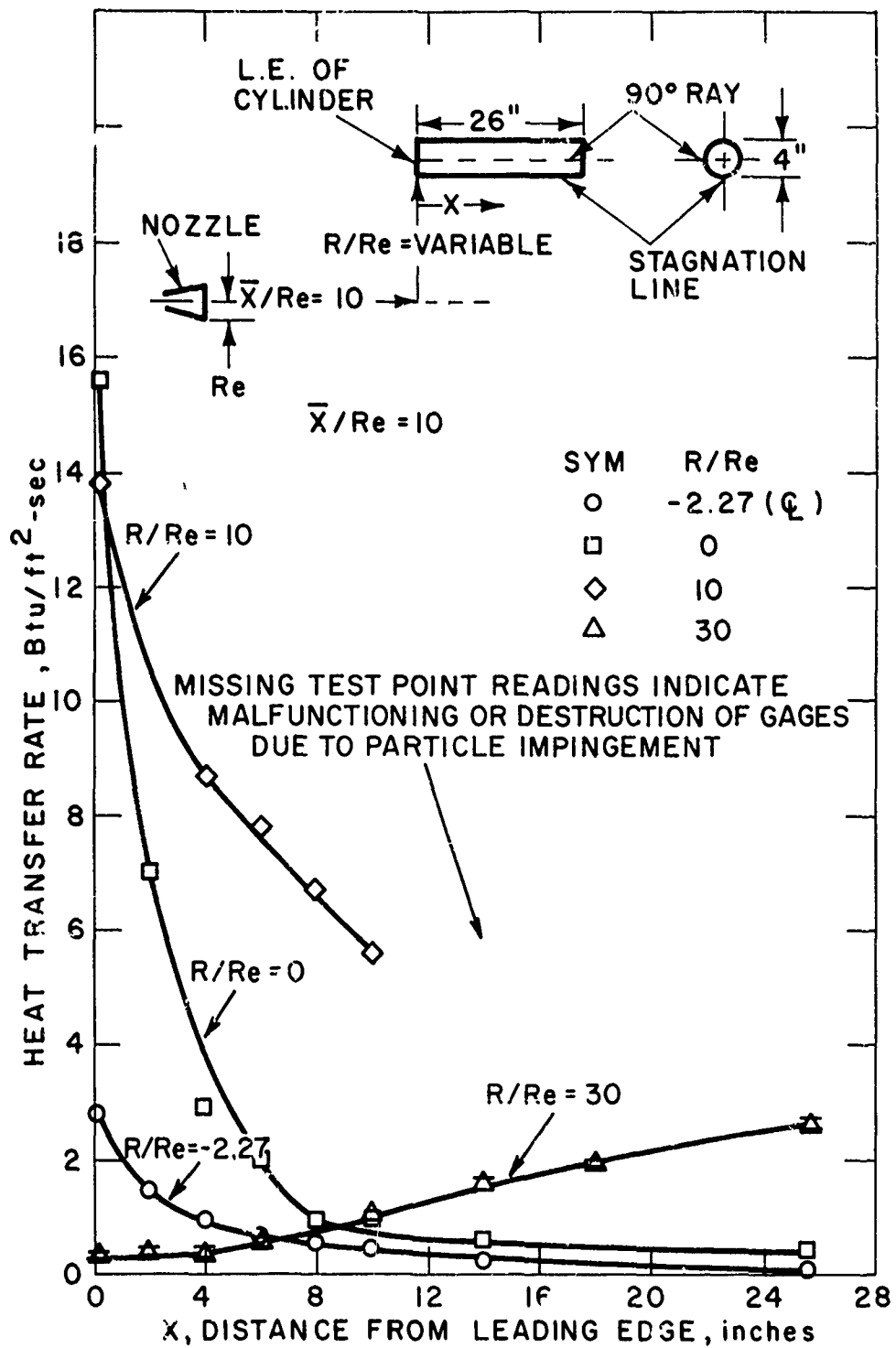


Figure 9. Heat Transfer Rate Distribution Along Stagnation Line.

UNCLASSIFIED

UNCLASSIFIED

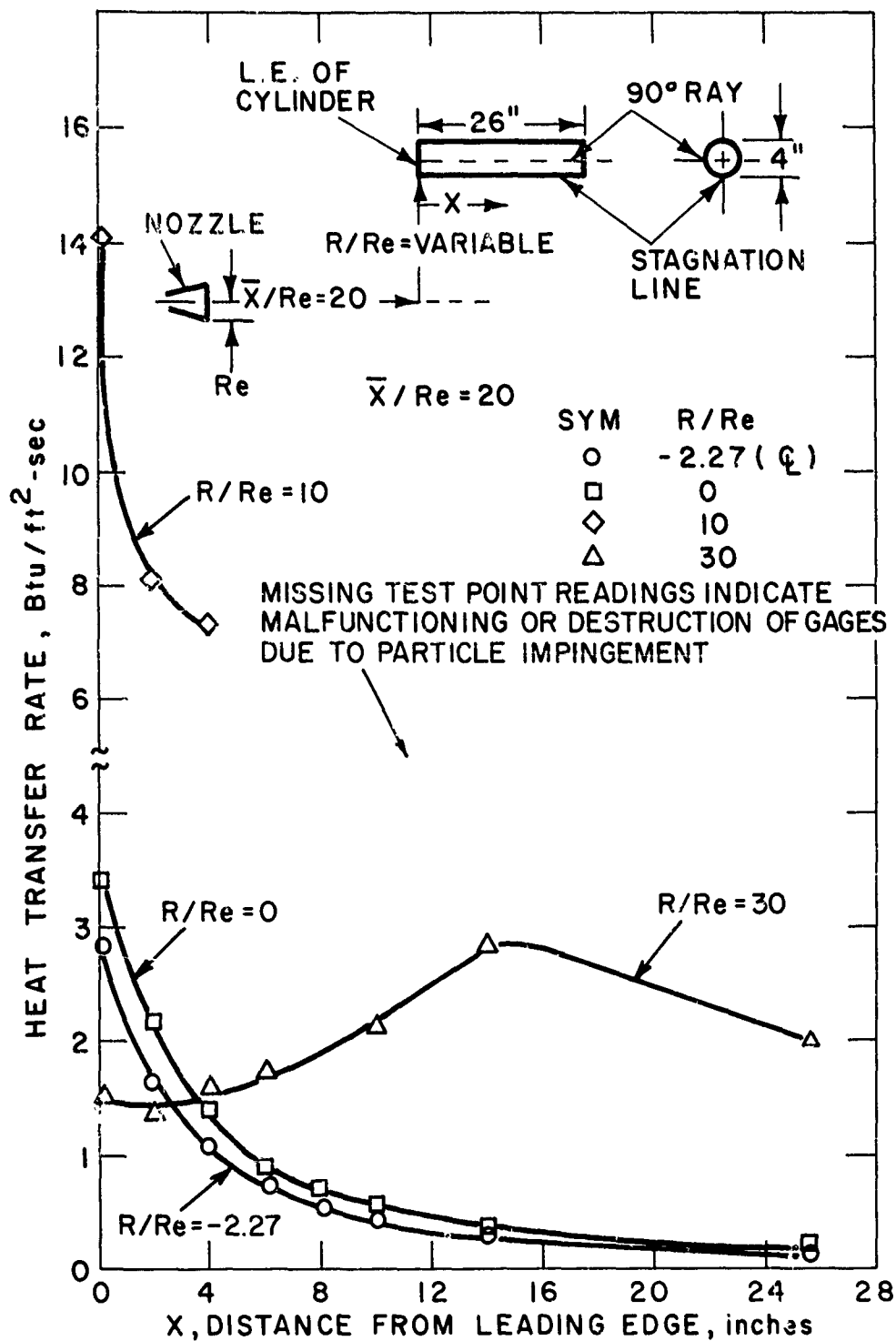


Figure 10. Heat Transfer Rate Distribution Along Stagnation Line.

UNCLASSIFIED

UNCLASSIFIED

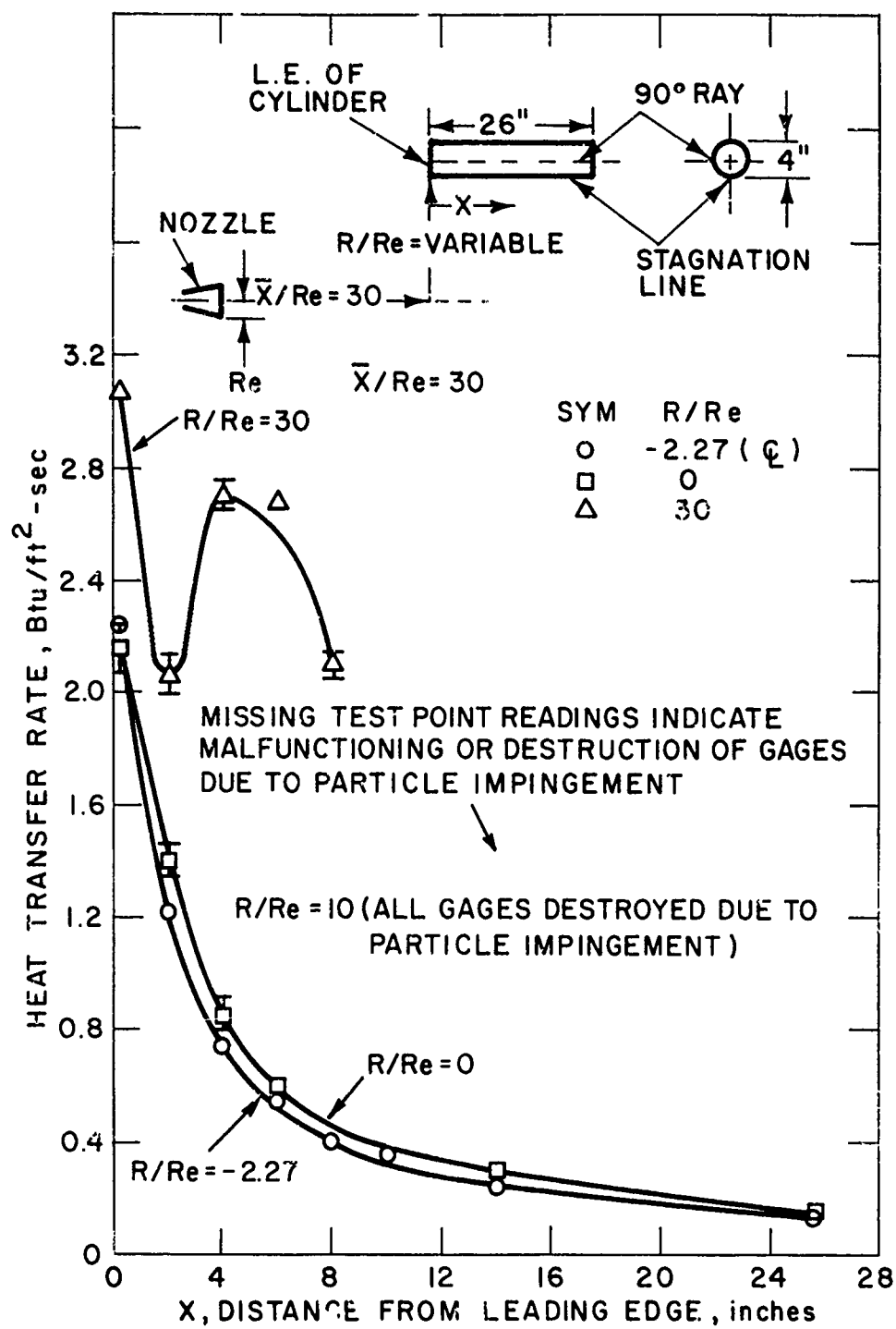


Figure 11. Heat Transfer Rate Distribution Along Stagnation Line.

UNCLASSIFIED

UNCLASSIFIED

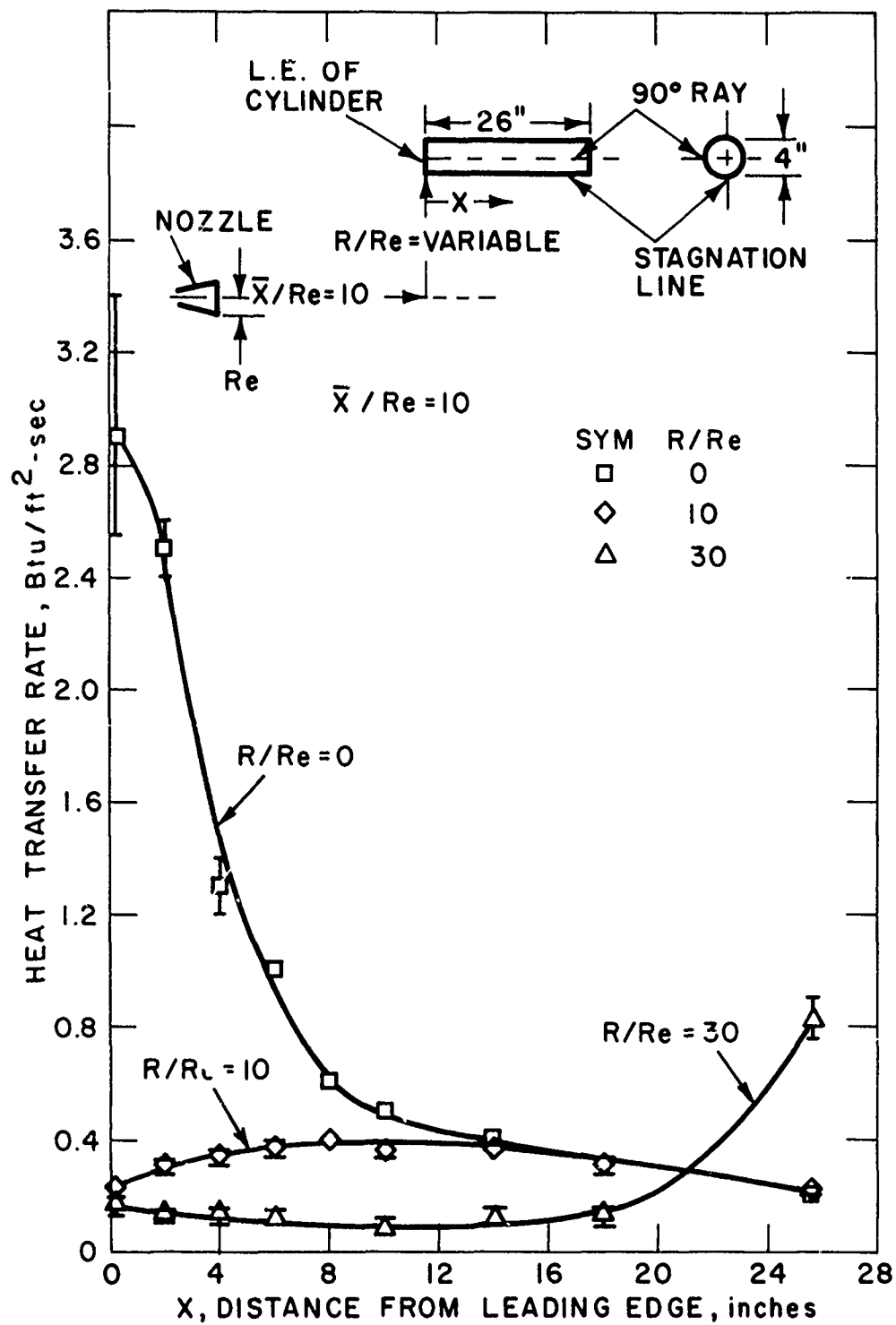


Figure 12. Heat Transfer Rate Distribution Along Ray 90° from Stagnation Line.

UNCLASSIFIED

UNCLASSIFIED

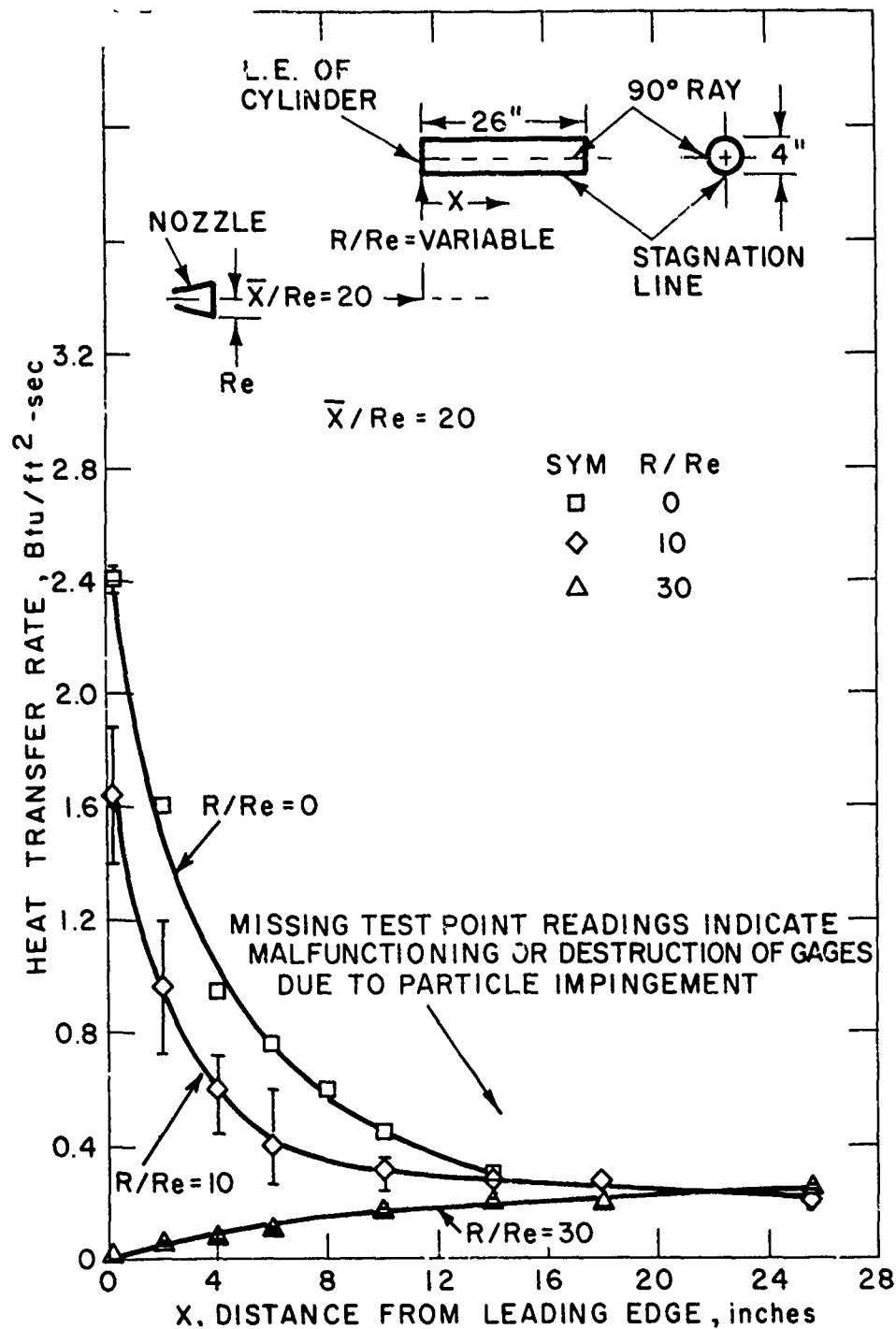


Figure 13. Heat Transfer Rate Distribution Along Ray 90° from Stagnation Line.

UNCLASSIFIED



UNCLASSIFIED

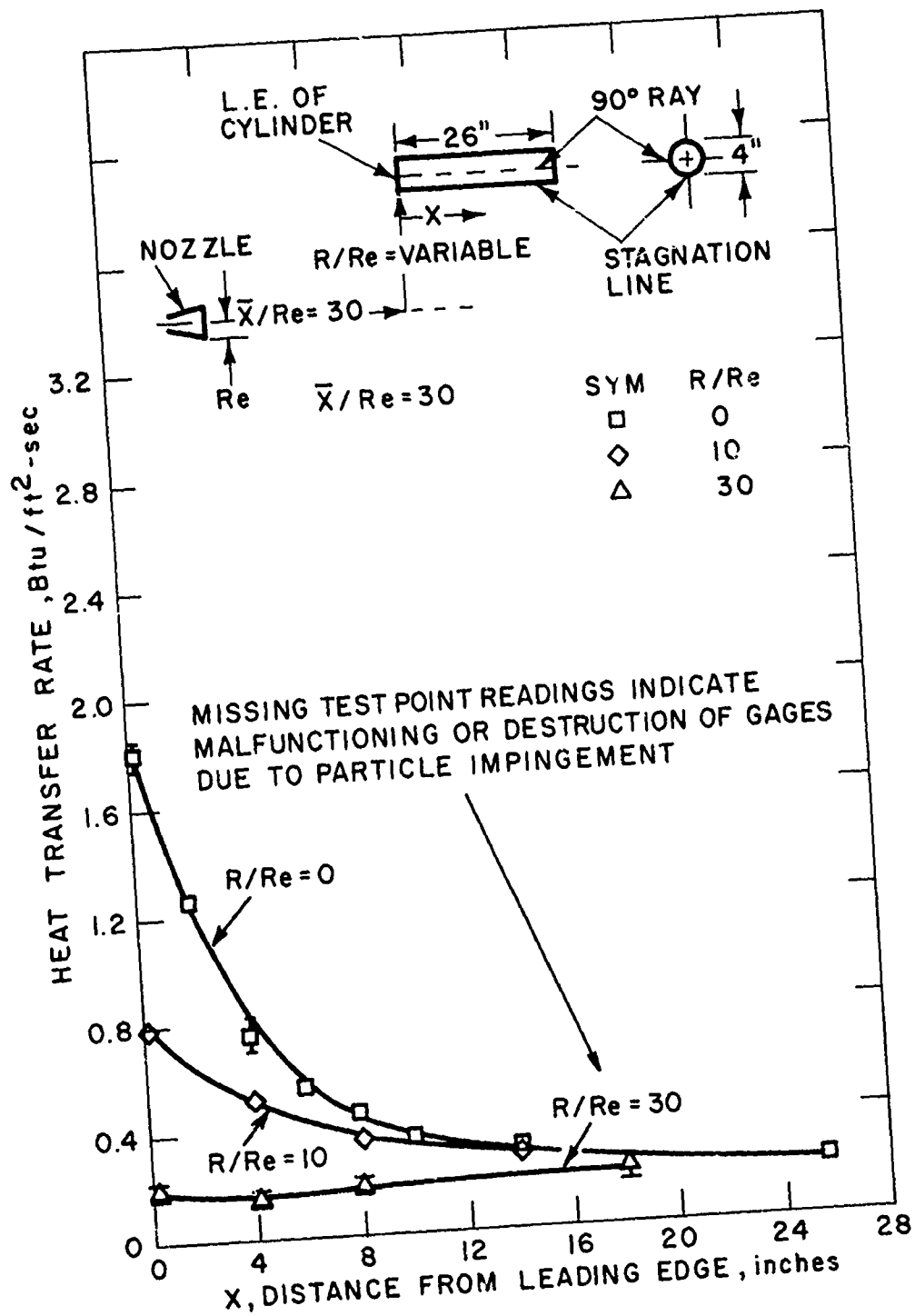


Figure 14. Heat Transfer Rate Distribution Along Ray 90° from Stagnation Line.

UNCLASSIFIED

UNCLASSIFIED

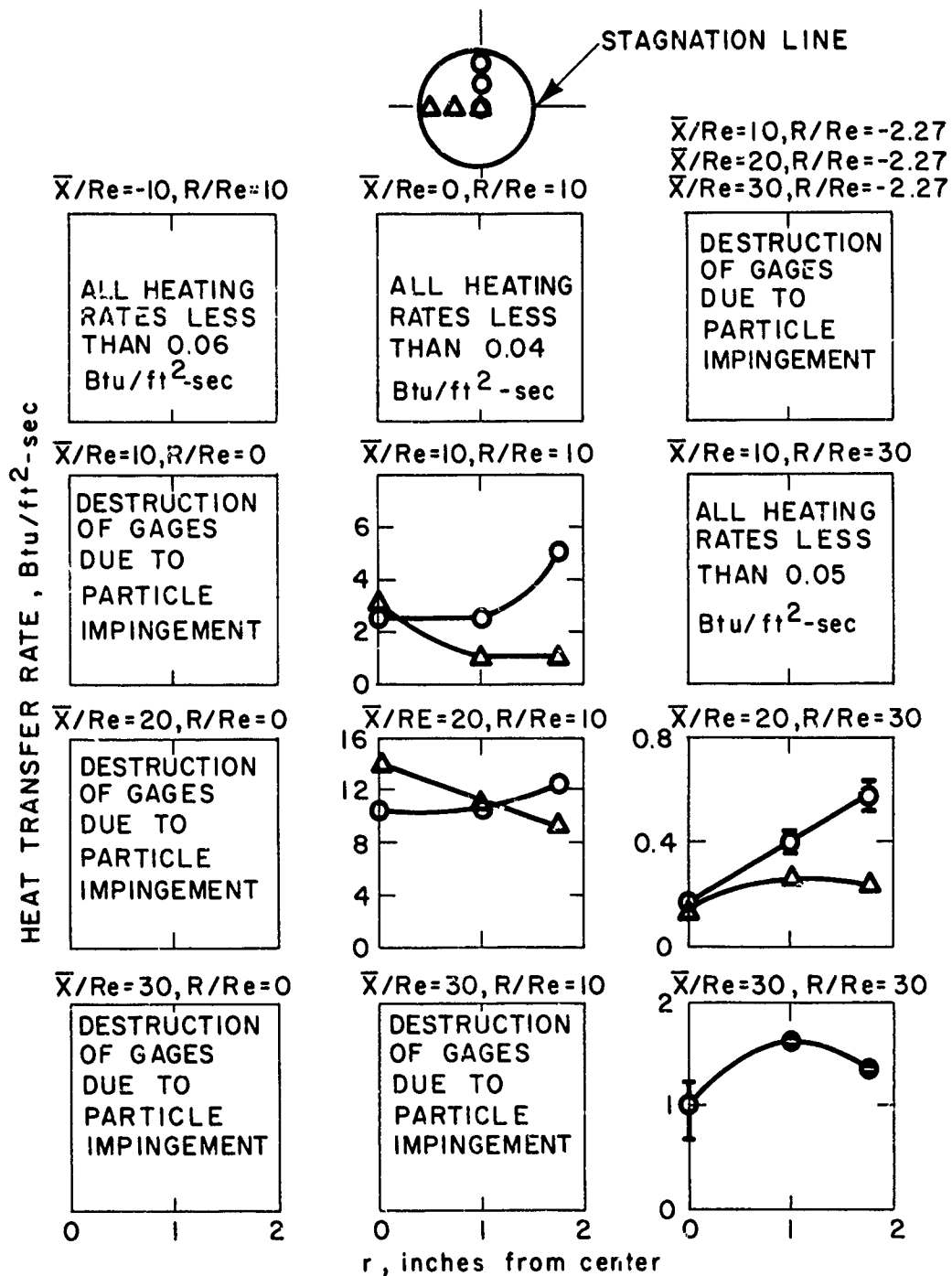


Figure 15. Radial Heat Transfer Distribution on Front of 4-inch Cylinder.

UNCLASSIFIED

UNCLASSIFIED

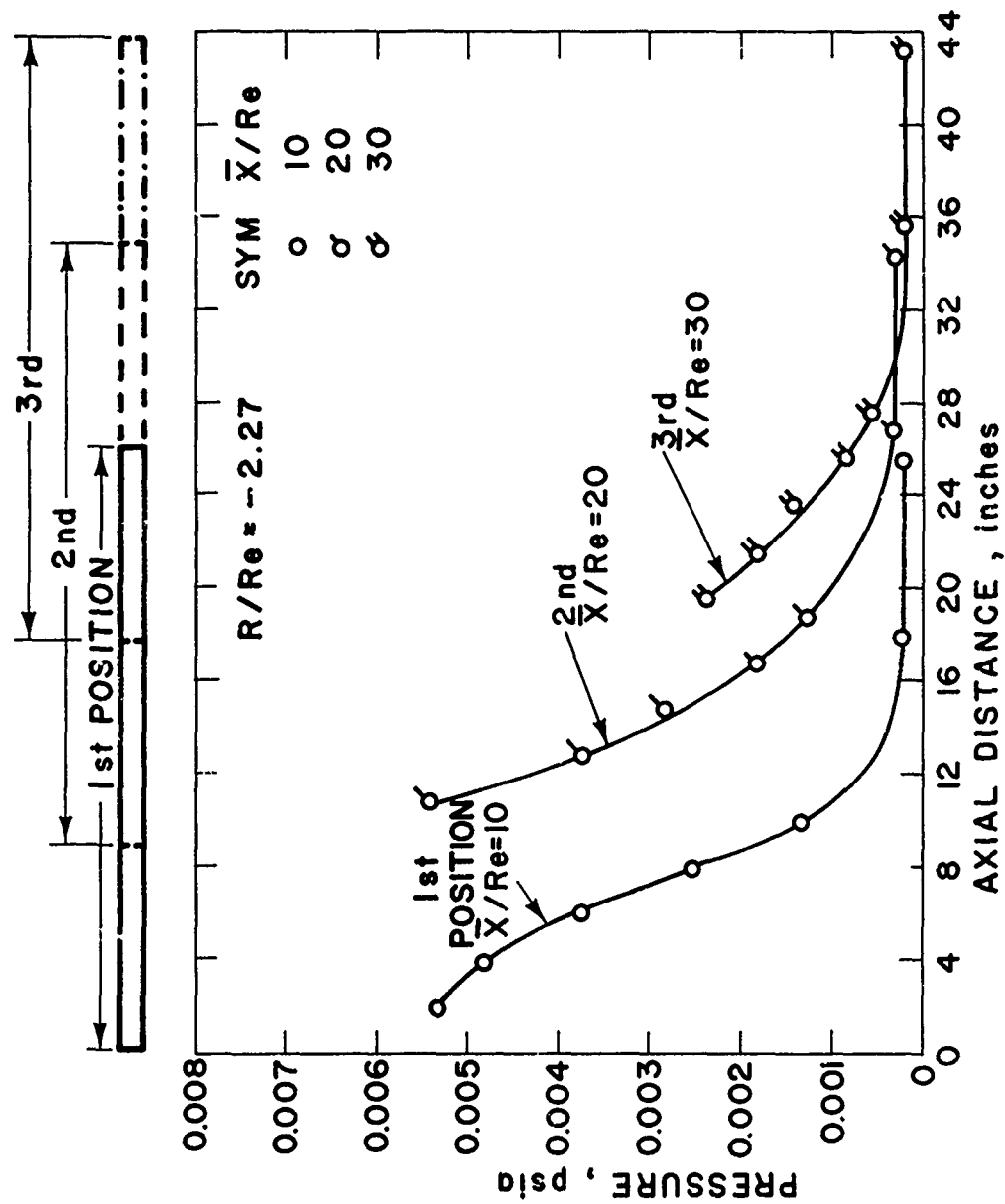


Figure 16. Measured Pressures Arrangement for Assessing Applicability of Infinite Cylinder Theory.

UNCLASSIFIED

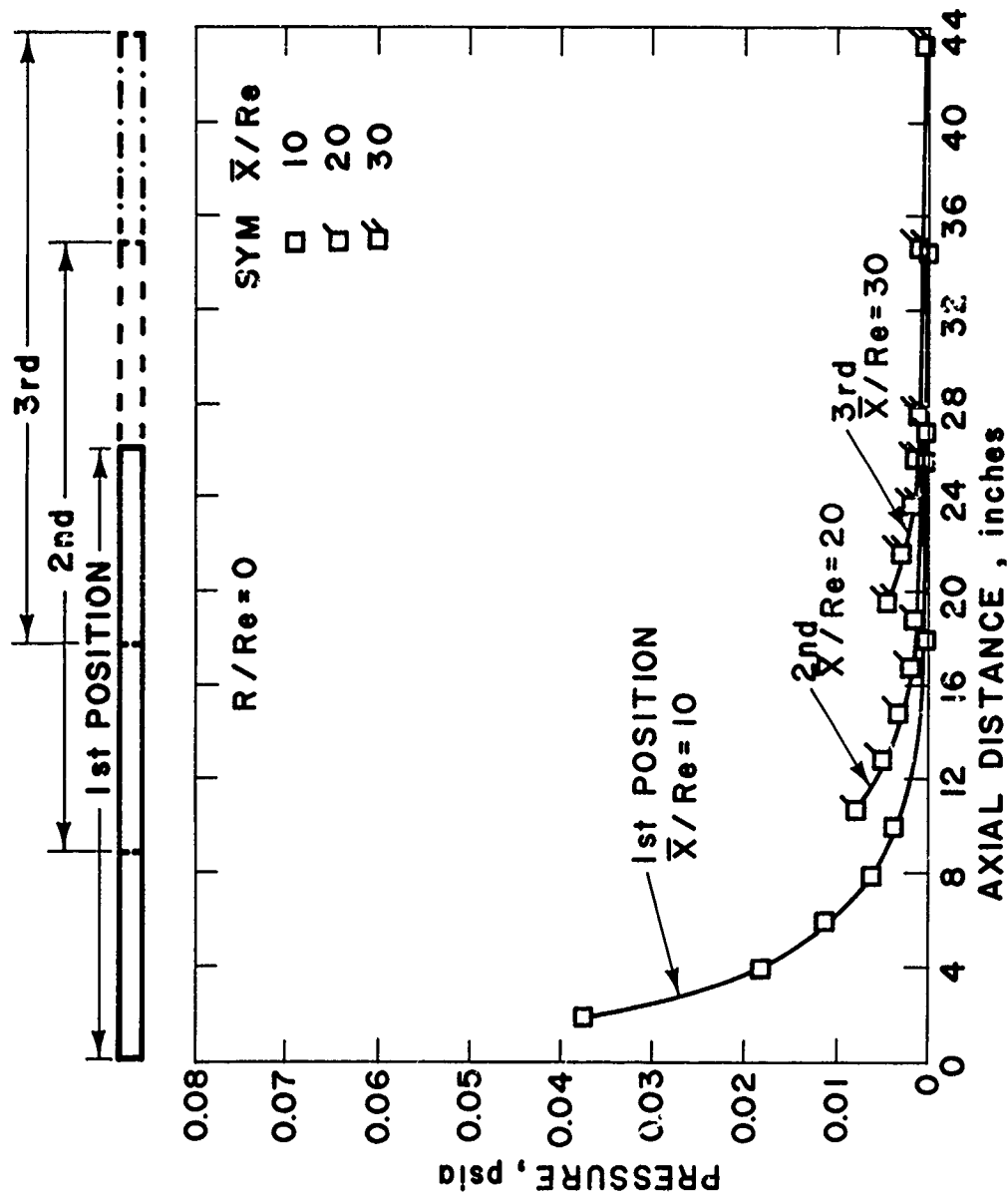


Figure 17. Measured Pressures Arrangement for Assessing Applicability of Infinite Cylinder Theory.

UNCLASSIFIED

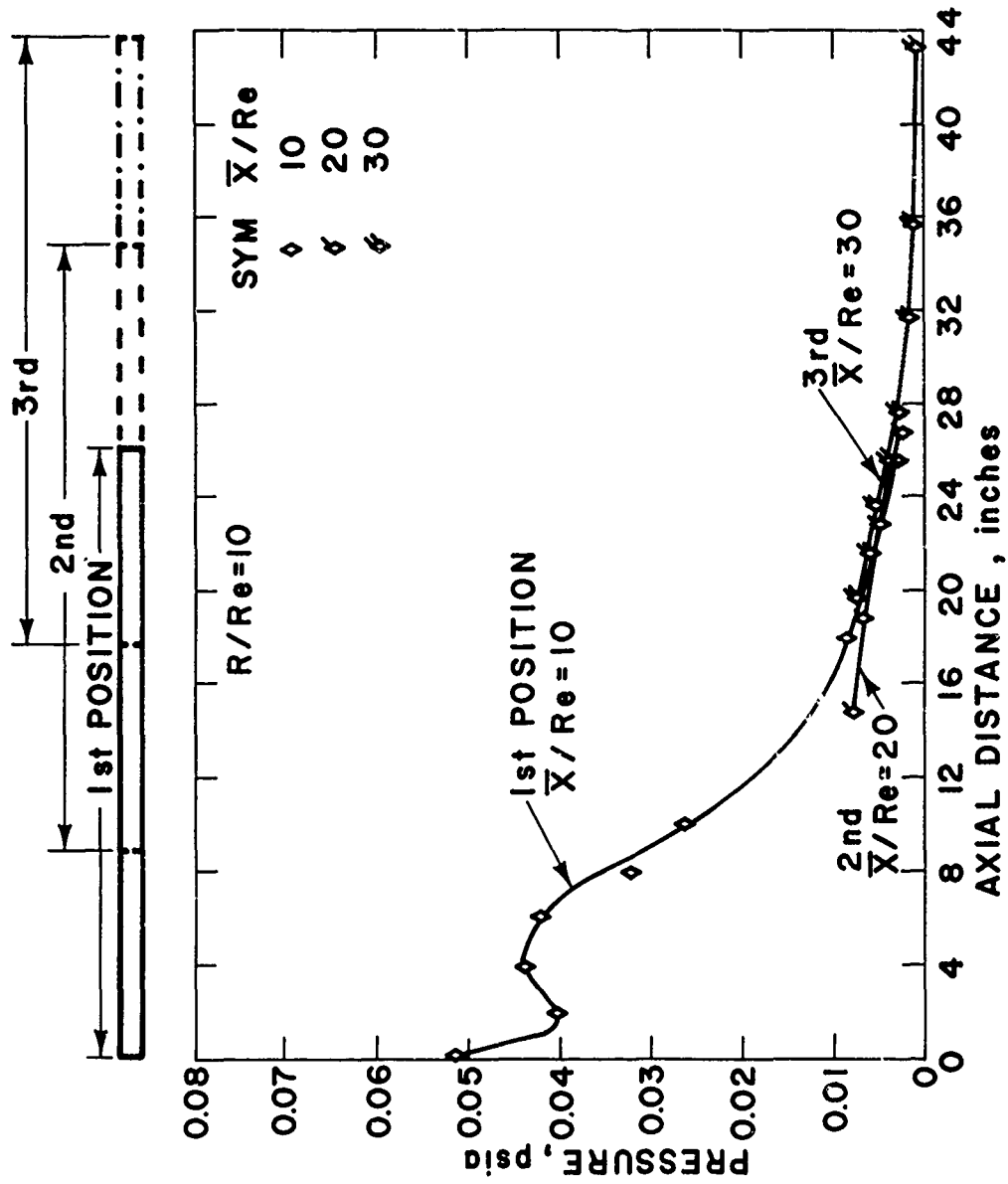


Figure 18. Measured Pressures Arrangement for Assessing Applicability of Infinite Cylinder Theory.

UNCLASSIFIED

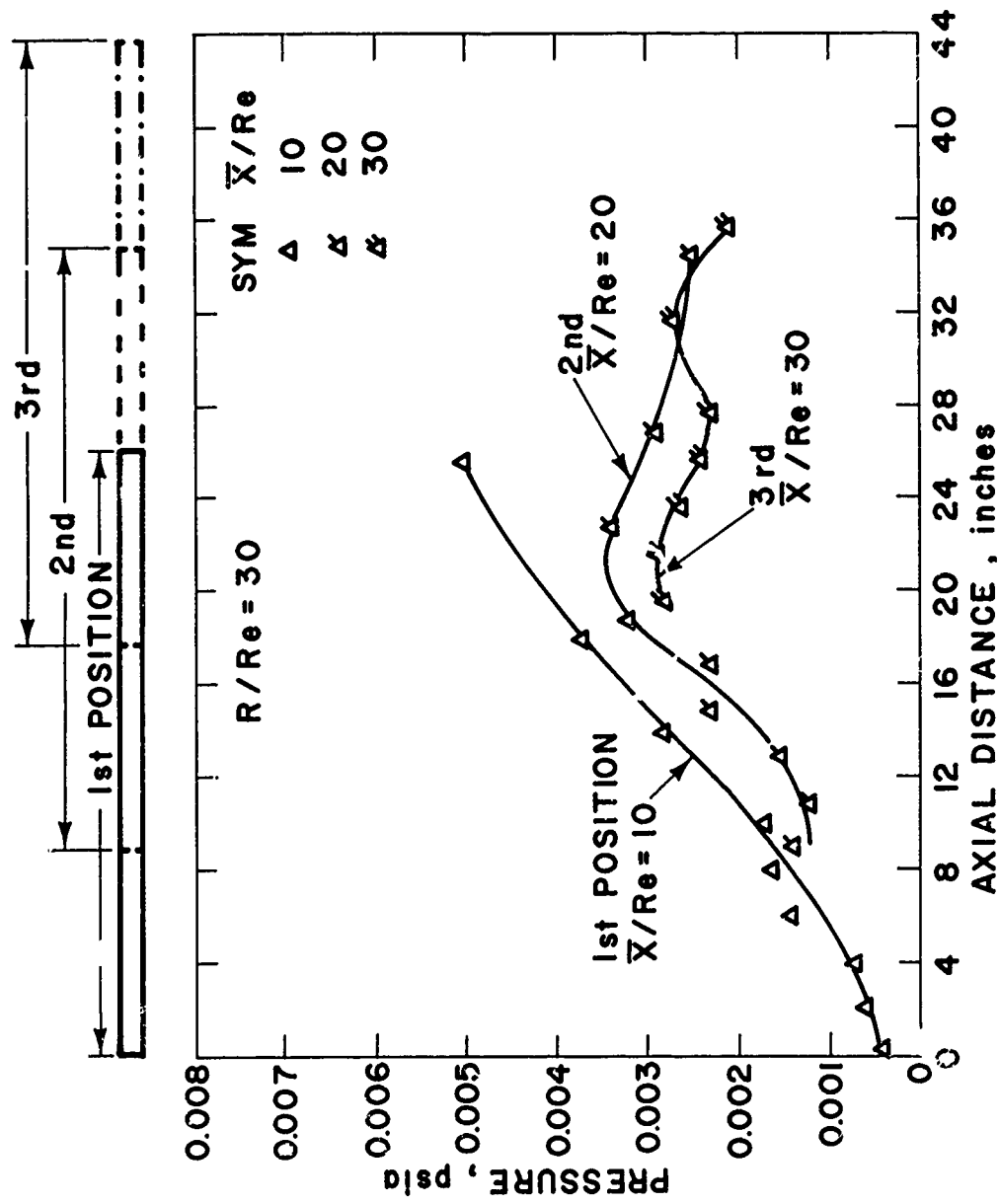


Figure 19. Measured Pressures Arrangement for Assessing Applicability of Infinite Cylinder Theory.

UNCLASSIFIED

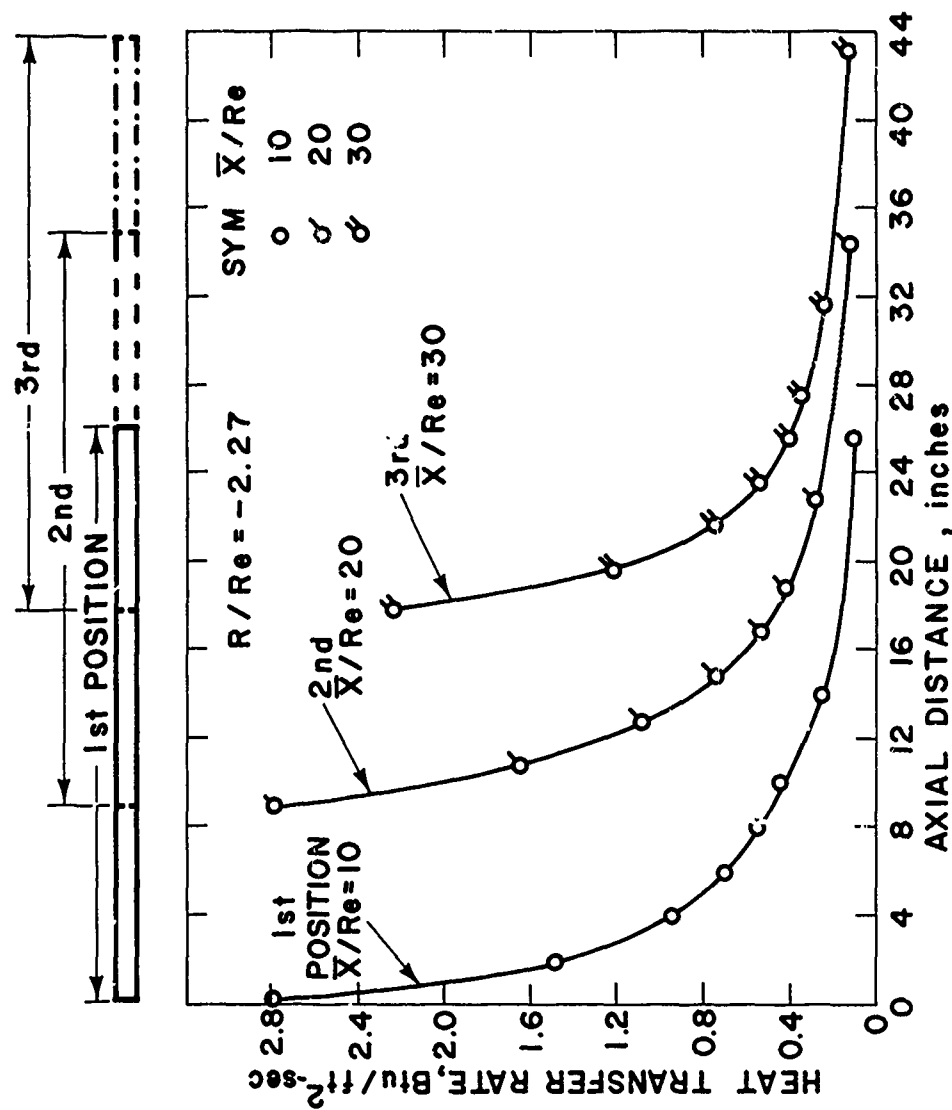


Figure 20. Measured Heat Transfer Rates Arrangement for Assessing Applicability of Infinite Cylinder Theory.

UNCLASSIFIED

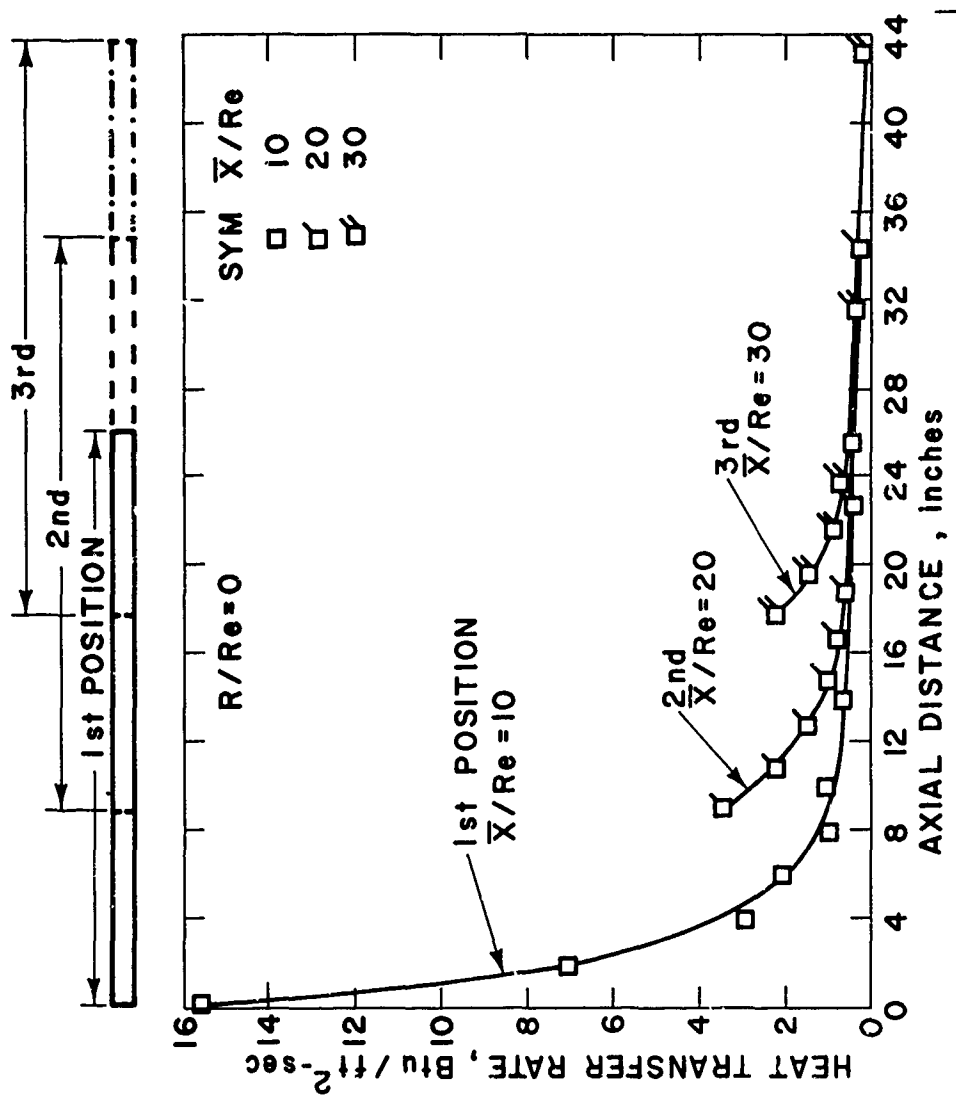


Figure 21. Measured Heat Transfer Rates Arrangement for Assessing Applicability of Infinite Cylinder Theory.



UNCLASSIFIED

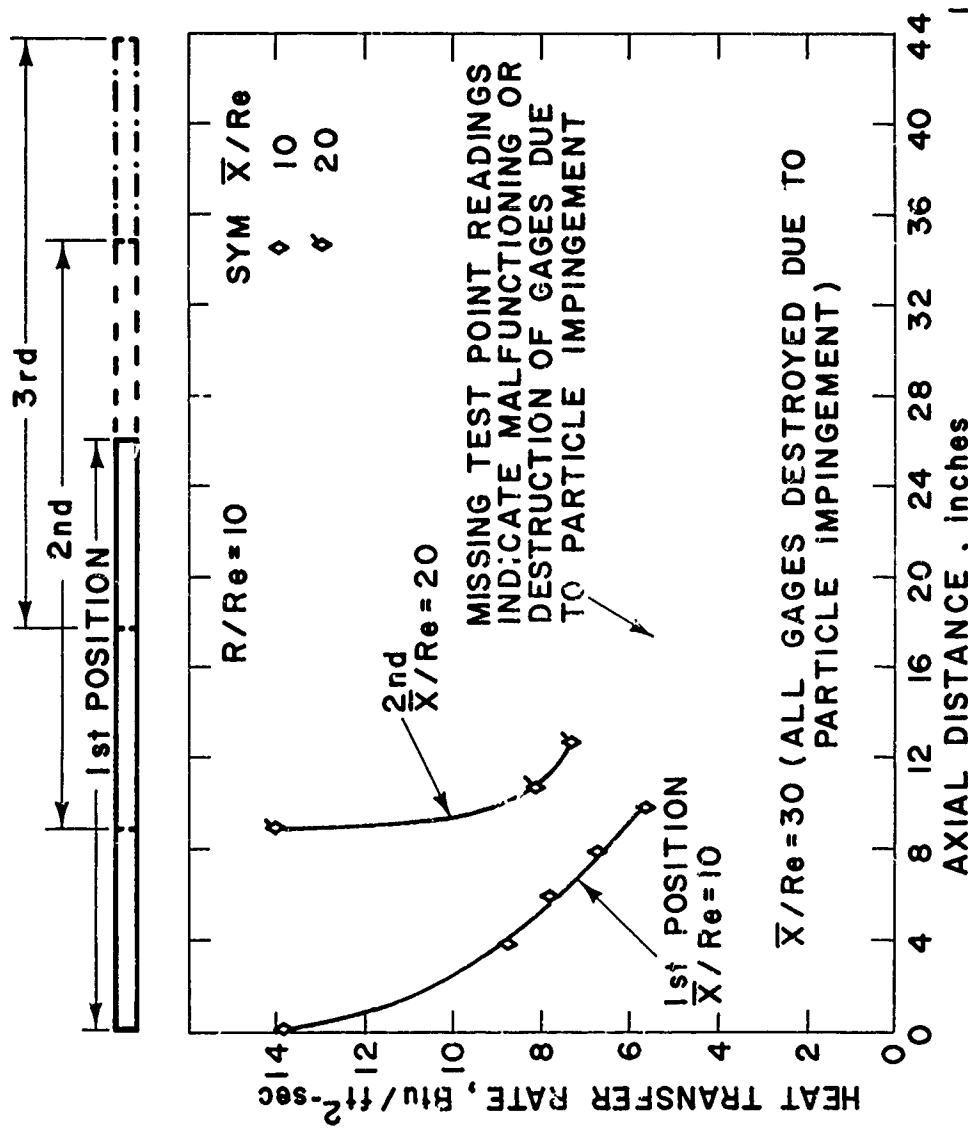


Figure 22. Measured Heat Transfer Rates Arrangement for Assessing Applicability of Infinite Cylinder Theory.

UNCLASSIFIED

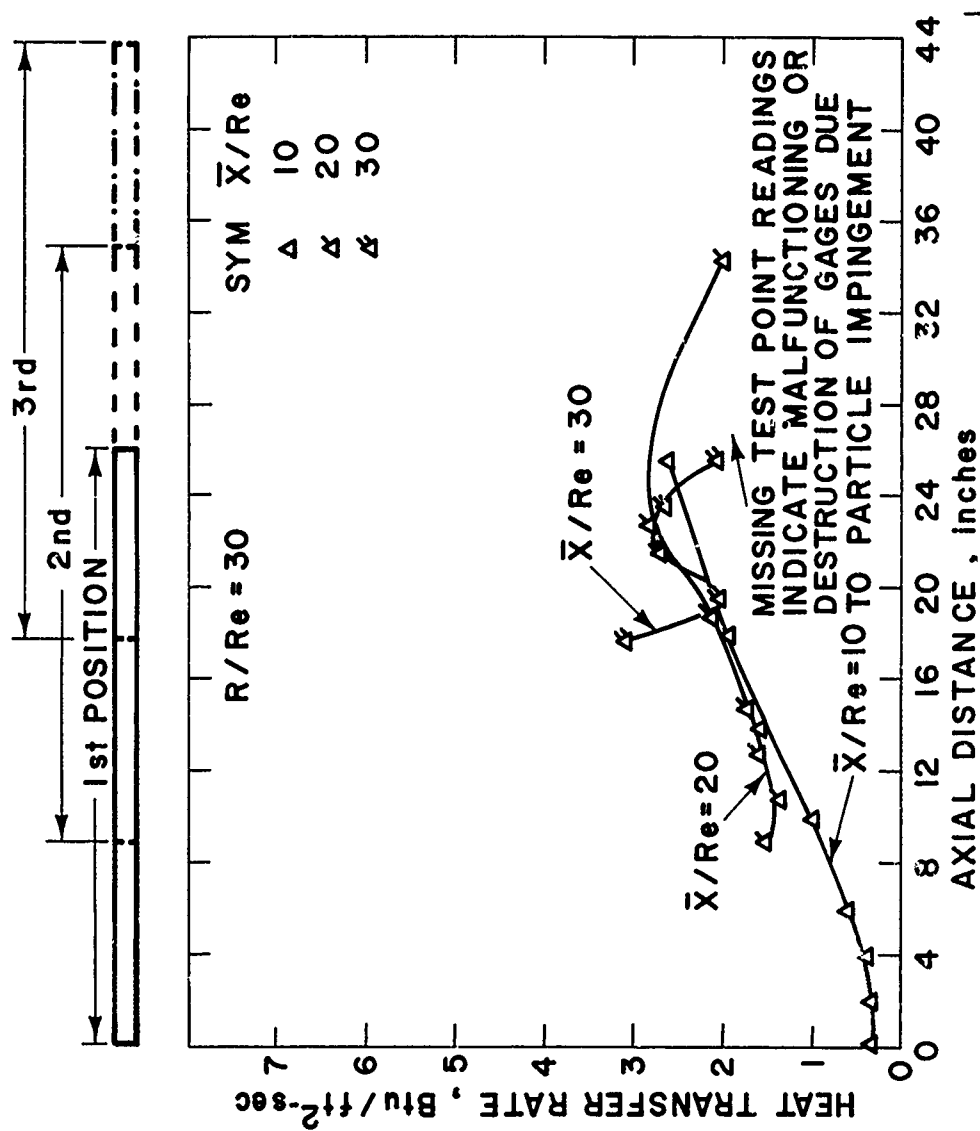


Figure 23. Measured Heat Transfer Rates Arrangement for Assessing Applicability of Infinite Cylinder Theory.

UNCLASSIFIED

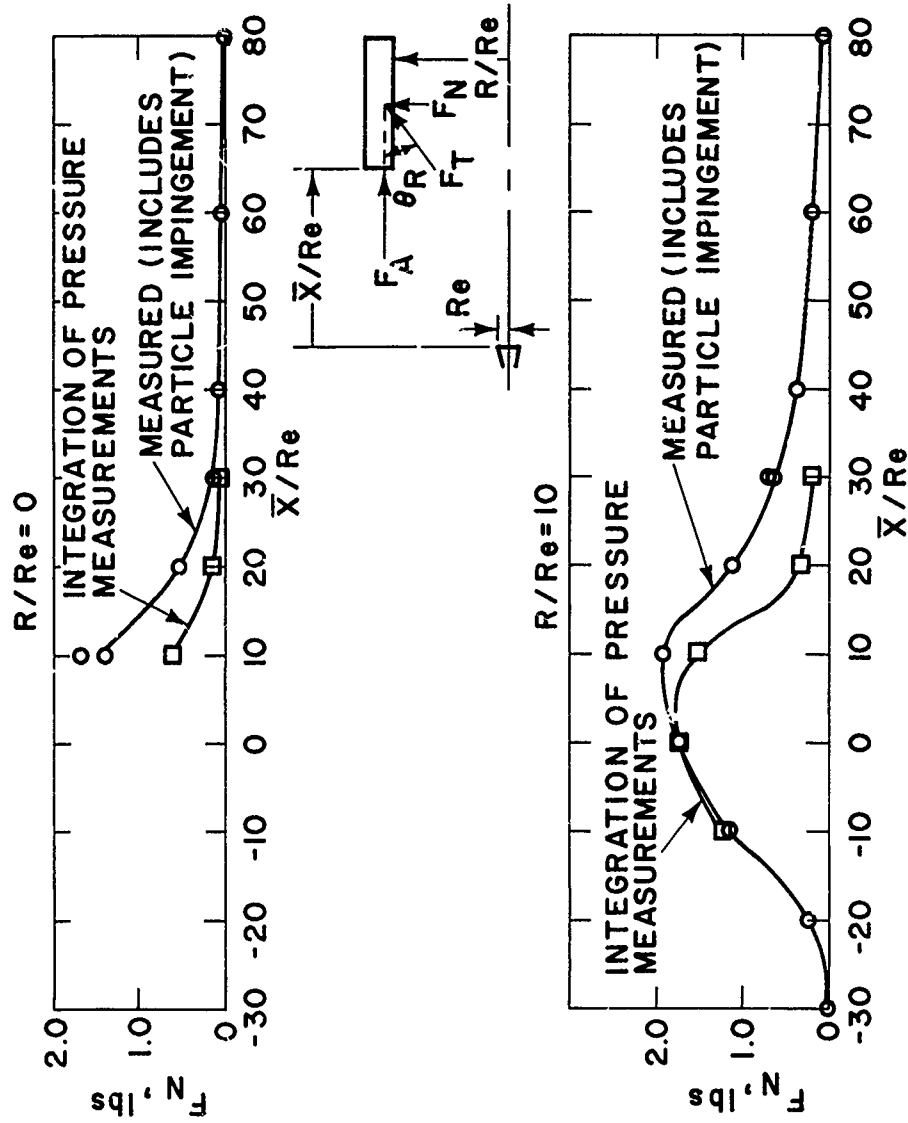


Figure 24. Comparison of Measured Total Normal Forces with Integrated Pressure Forces.

UNCLASSIFIED

UNCLASSIFIED

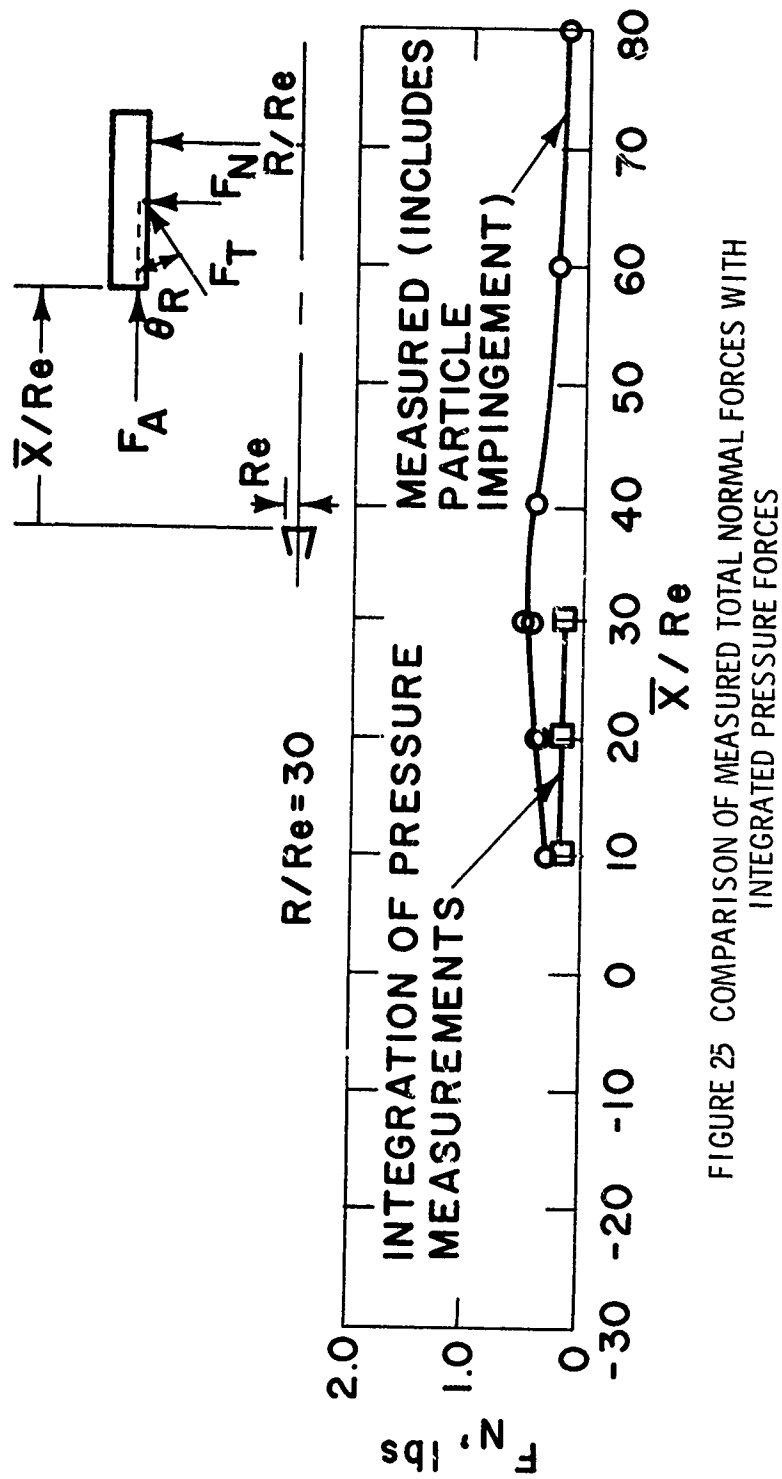


FIGURE 25 COMPARISON OF MEASURED TOTAL NORMAL FORCES WITH INTEGRATED PRESSURE FORCES

Figure 25. Comparison of Measured Total Normal Forces with Integrated Pressure Forces.

UNCLASSIFIED

## UNCLASSIFIED

### QUESTIONS, ANSWERS & COMMENTS:

Q./A. J. Laderman (Aeronutronic): Could you comment as to what extent erosion or ablation occurs and how you feel this might influence your force measurements?

A./L. Rute (AVCO Corp.): Well, we have not looked into these problems of erosion or the second point you mentioned. As a matter of fact, in the short duration techniques that were employed, I do not believe that we can look into these particular effects. We had particle buildup on the cylinder.

Q./F. C. Price (Aeronutronic): What was the Mach number of the nozzle you were using and what was the chamber pressure?

A./L. Rute (AVCO Corp.): The chamber pressure was 680 psi and the Mach number was on the order of three.

UNCLASSIFIED

645/646

**UNCLASSIFIED**

**SHOCK TUBE STUDIES OF HYPERVELOCITY  
IMPACT PHENOMENA**

by

W. J. Hooker, A. L. Morsell, and R. Watson  
Heliodyne Corporation  
Van Nuys, California

**UNCLASSIFIED**

**UNCLASSIFIED**

**SHOCK TUBE STUDIES OF HYPERVELOCITY  
IMPACT PHENOMENA**

by

W. J. Hooker, A. L. Morsell, and R. Watson  
HELIODYNE CORPORATION  
Van Nuys, California

**ABSTRACT**

Shock tube measurements are presented of the hypervelocity erosion from the surfaces of models due to impacts of solid particles that are injected and suspended in the test gas prior to firing. The data show that the ratio of particle size to surface roughness of the model is an important scaling parameter, and that the so-called "cosine-squared" law does not apply for small particles impacting on rough surfaces. The amount of mass removed from a particle impact on a conical surface varies from 0.25 to 1.0 times the mass removed from a blunt surface, depending on the surface roughness of the cones. By comparison, the cosine-squared law predicts a ratio of 0.03 for the  $10^\circ$  half angle cones used in the experiments. A discussion of some of the problems associated with achieving a suspended uniform distribution of powder in the shock tube test section is given with emphasis on the problem of small particle acceleration and survival in the high temperature test gas.

**UNCLASSIFIED**

647

**UNCLASSIFIED**

## 1. INTRODUCTION

Heliodyne has developed a shock tube facility<sup>(1-7)</sup> equipped with apparatus for suspending finely-divided powders of selected materials in the shock tube test gas. The facility was designed originally for studying the optical and electromagnetic properties of chemical species in the gas phase that could be obtained only by vaporizing a solid in a carrier gas. Shock wave heating of the powdered solid material and gas produces rapid ablation of the powder and results in a uniform mixture of the products of decomposition. The virtue of this device is that complex solid matter/gas chemistry is produced in a controlled one-dimensional flow field.

Since the techniques for producing, injecting and uniformly distributing finely divided powders in the driven section of the shock tube have been fully developed by us, it was decided that a similar technique with powders large enough so that they would not appreciably burn up during the shock tube test time, could be used for hypervelocity impact studies. A description of the operational features of the powder injection shock tube facility is given in Section 2, and details of the hypervelocity impact tests are given in Section 3.

**UNCLASSIFIED**



UNCLASSIFIED

## 2. POWDER INJECTION SHOCK TUBE FACILITY

The powder injection system presently used is represented in Fig. 1. To prevent agglomeration, the powder is processed under moisture-free conditions, and the demountable powder chamber, shown on top of the injection tank, is loaded with a measured amount of powder in a dry box. The powder chamber is separated from the injection tank by a small electrically-controlled valve. Larger electrically-controlled valves separate the injection tank from the shock tube and the dummy volume from the shock tube. The shock tube dump tank is isolated from the shock tube by an aluminum foil diaphragm. In order to avoid interference with the powder injection process, the diaphragm is contoured to match the inside of the tube. The powder chamber is just large enough to contain a few grams of powder, the injection tank has a volume about equal to that of the shock tube, and the dummy volume is approximately 6 times the volume of the shock tube. Just before injection the shock tube and dummy volume are evacuated, the injection tank is pressurized to several cm Hg, and the powder chamber is pressurized to 1,000 psig. The valve between the dummy volume and the shock tube is open; the other valves are closed. Upon initiation of an electronically-timed automatic firing sequence, the powder chamber valve is opened and the powder is blown violently into the injection tank. About one second later, long enough to achieve reasonable mixing of the powder with the gas in the tank, the valve connecting the injection tank with the shock tube is opened and the contents of the injection tank rush into the driven section of the shock tube and into the dummy volume tank. The

UNCLASSIFIED

UNCLASSIFIED

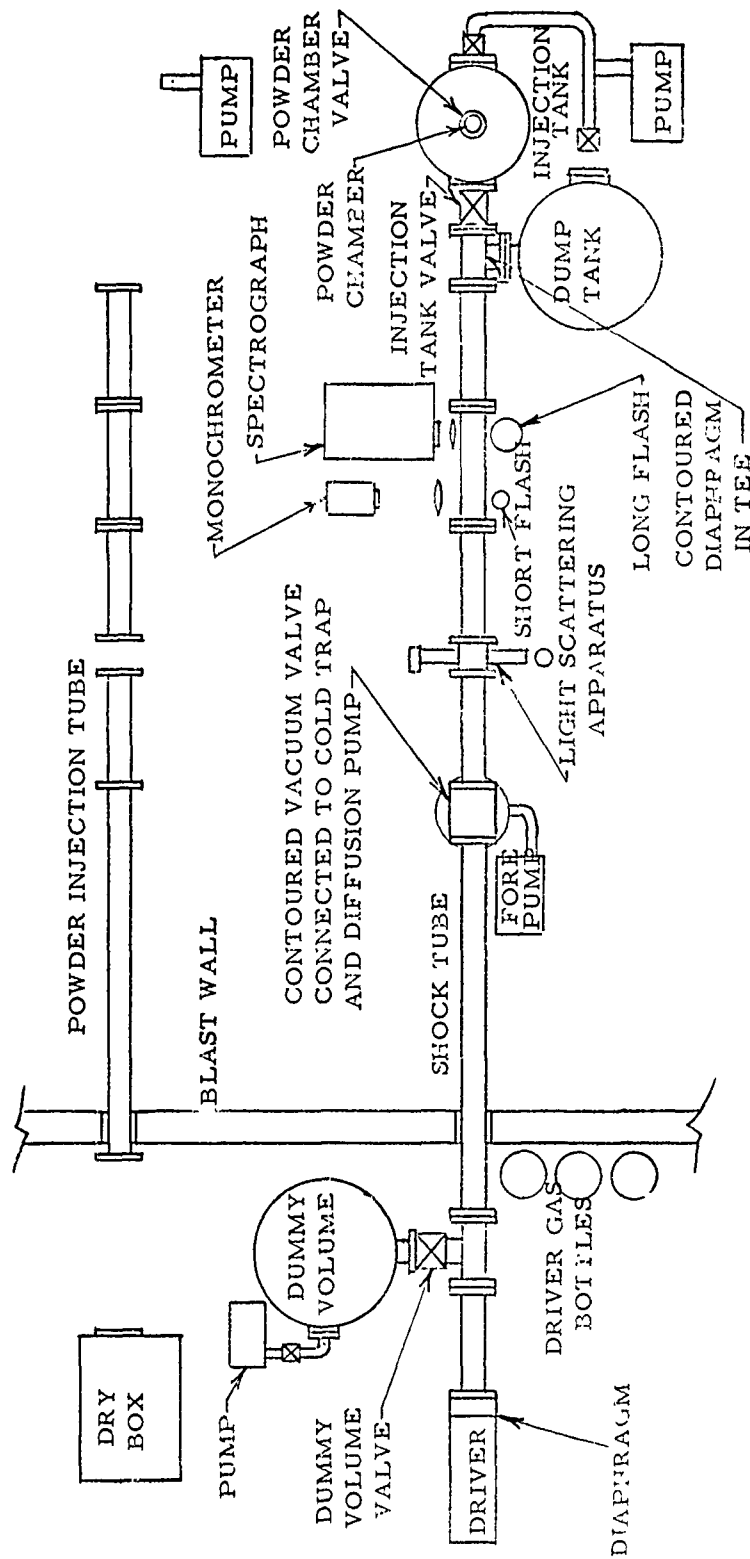


Figure 1. Schematic Diagram of Powder Injection System.

UNCLASSIFIED

UNCLASSIFIED

injection tank valve and the dummy volume valve are closed immediately after injection; and as soon as they are closed, the shock tube is fired.

The amount of powder suspended in the shock tube and the uniformity of the distribution of the powder have been measured by several means, the most direct of which are weight measurements of the quantity of powder which settles on small squares of stainless steel foil arranged at one-meter intervals along the inside of the shock tube. Because the weight differences are very small, and because absorption of water from the atmosphere can cause large weighing errors, one of the shock tubes has been coupled to a dry box and the measurements are made without ever exposing the powder samples to the laboratory room atmosphere. Fig. 2 shows the results of two such tests.

The lines on the figure at 1 1/2 and 6 1/2 meters from the injector bound a region for which a nearly uniform powder distribution is desirable. In this region the standard deviation of the weighings from the mean of  $3.24 \mu\text{g}/\text{cm}^3$  is  $0.29 \mu\text{g}/\text{cm}^3$ . Powder to the left of this region is never seen at an observation point and powder on the right gets turbulently mixed with driven gas at the contact front.

Another technique for measuring the powder distribution makes use of the fact that all the powder/gas mixture upstream of an observation station in a shock tube is swept by the station in a shock-heated condition when the shock tube is fired. If the powder decomposes rapidly to form a stable gas-phase compound, a measurement of spectral absorption from this compound as a

UNCLASSIFIED

UNCLASSIFIED

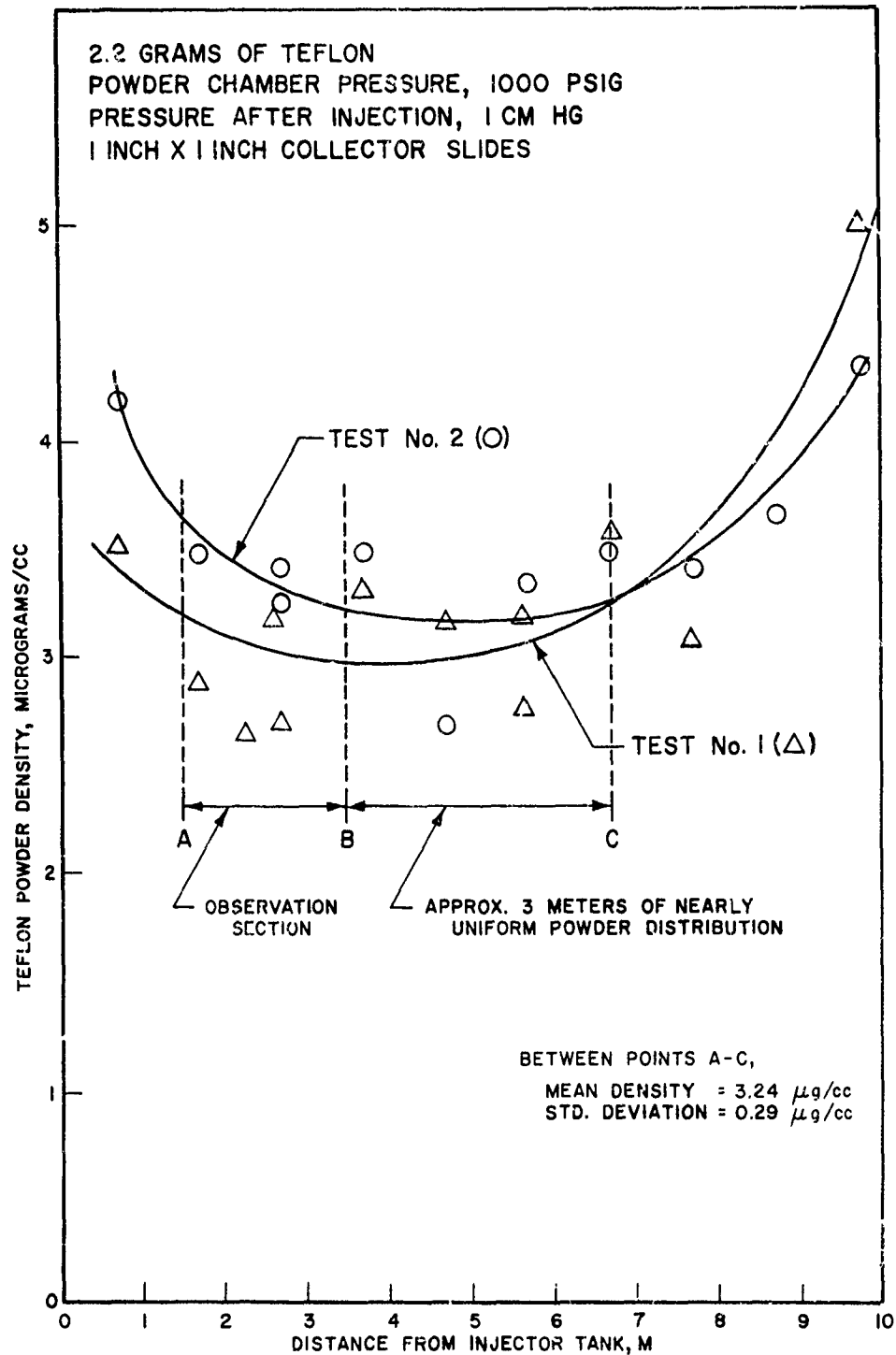


Figure 2. Teflon Powder Density Distribution Along the Driver Section, Obtained by Direct Weight Measurements.

UNCLASSIFIED

## UNCLASSIFIED

function of time will give a measure of the original powder distribution along the length of the tube. This measurement has been made on the teflon powder<sup>(8)</sup>, which decomposes to the relatively stable compound  $\text{CF}_2$  when heated in an inert argon diluent. Fig. 3 shows oscilloscope traces of  $\text{CF}_2$  absorption at  $2536 \text{ \AA}$  for four shock tube tests in which all parameters were maintained constant in order to deduce reproducibility of injection; both slow and fast sweep traces are shown to indicate the overall duration and uniformity of absorption. The 10 microsecond rise time on the fast sweep traces is the time required for the shock wave to traverse the observation port. The initial driven argon pressure for these tests was maintained at 1 cm Hg, and the injected teflon powder was maintained at approximately 4 mole percent. In each case, zero and one-hundred percent transmission lines were put onto the film shortly before the teflon powder/argon mixture was injected. The transmission through the teflon/argon mixture prior to shock arrival does not coincide with the one-hundred percent transmission line because of the loss of light by scattering from the teflon powder initially suspended in the test section. It is seen from Fig. 3 that the powder concentration is quite uniform in the useful test gas length upstream of the observation port.

A third technique for measuring injected powder uniformity is the light scattering method. Monitoring scattered light at a given station along the shock tube driven section provides a measure of injection reproducibility, as well as the settling rate of powder at that station. In Ref. 9, Deirmendjian shows by numerical computation that the intensity of radiation scattered approximately  $40^\circ$  from the forward direction is a direct measure of the total number

UNCLASSIFIED

UNCLASSIFIED

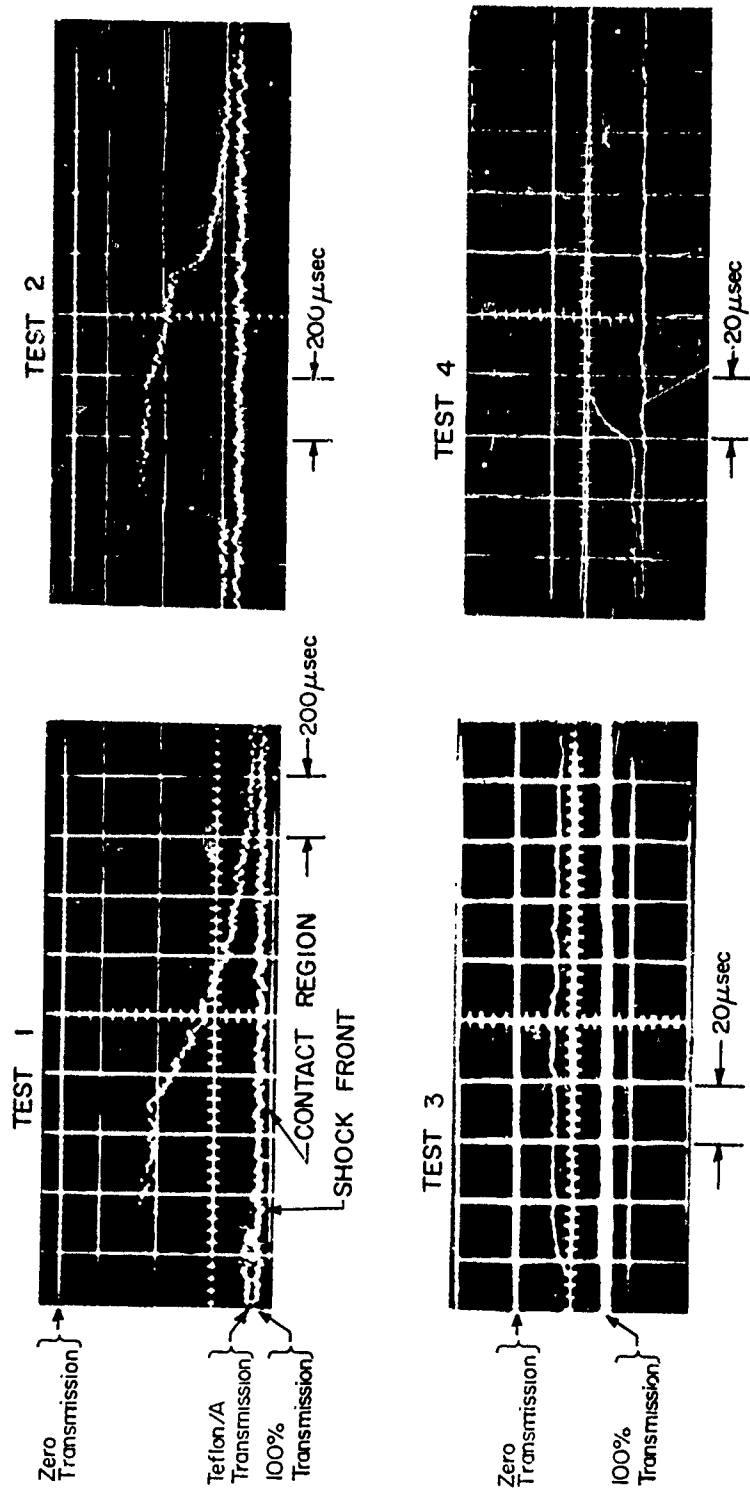


Figure 3. Teflon Powder Distribution Along the Driver Section of the Shock Tube as Determined by CF<sub>2</sub> Absorption at 2536A in Argon in Four Shock Tube Tests. The Gain Settings are the Same for all Four Records; Tests 1 and 2 are at Slow Sweep Speeds while Tests 3 and 4 are Fast.

UNCLASSIFIED

## UNCLASSIFIED

of particles in the scattering volume, independent of their size distribution. We have made use of this phenomenon in the powder injection shock tube experiments, and an oscilloscope record of such a measurement is shown in Fig. 4.

In Fig. 4 time increases from left to right. The top trace corresponds to the intensity of light transmitted across a diameter of the shock tube, while the bottom trace corresponds to the intensity of light scattered at  $43^\circ$  from the forward direction.  $I_0$  is the intensity of the transmitted light in vacuo, and  $I$  is the net intensity transmitted after the powder has been injected;  $I_{43^\circ}$  is the intensity scattered at  $43^\circ$ . After an initial transient of approximately one second, associated with the opening and closing of the injector valves, the  $I$  and  $I_{43^\circ}$  intensities are seen to be quite steady for several seconds, indicating that a quiescent powder/gas dispersion of uniform distribution has been achieved. The sharp change in signals at the time indicated by "shock arrival" is due to water vapor behind the contact front from the combustion driver. On the 1 sec/cm time scale shown, the actual experimental testing time is immeasurably small (being on the order of 100  $\mu$ sec).

Because the velocity of the shock-accelerated gas in a shock tube can be made very high, the techniques for suspending finely-divided powder in the driven section of the shock tube may be applied to the problem of producing high-velocity particles for hypervelocity impact studies, \* provided that the powder particles are large enough not to burn up while being accelerated.

\* Mirtch and Mark<sup>(10)</sup> used a particle-shock tube for studying the erosion of optical surfaces. The particles in their experiment were supported by a thin flat plate mounted near the shock tube axis, and were removed and accelerated by the shocked gas flow.

UNCLASSIFIED

Start of Injection  
Process Shock Arrival

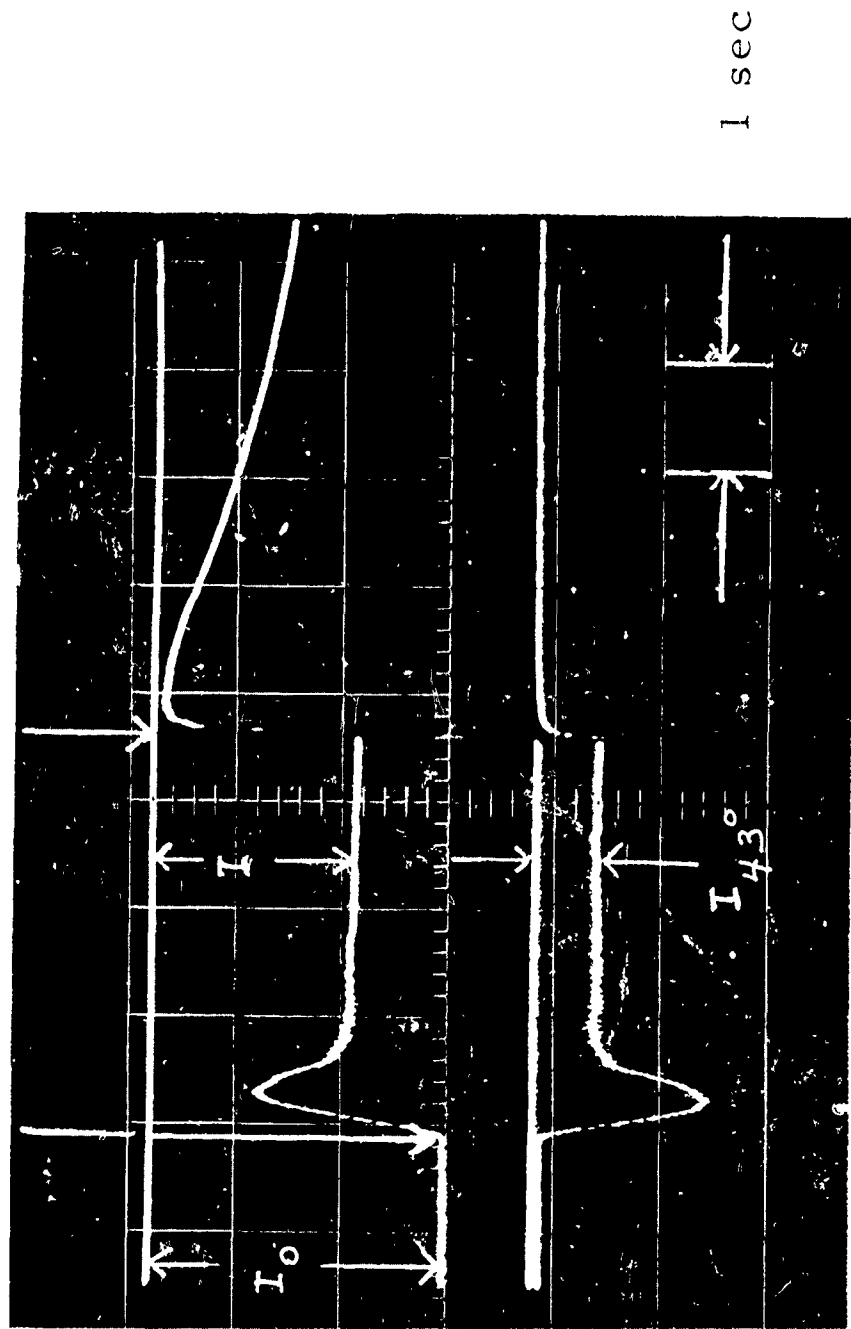


Figure 4. Transmitted and Scattered Light Signals from a Suspension of Carbon Particles in Air.



## UNCLASSIFIED

We have made calculations<sup>(1)</sup> of the burn-up times and trajectories of particles in a shock tube flow, and some of the results are shown in Figs. 5 through 7. The burn-up times for selected materials are shown in Fig. 5. Testing times for two different shock tube configurations are shown for comparison. Since the particle burn-up times shown in Fig. 5 were computed for flow in the free molecular regime, the burn-up time scales linearly with the particle dimension. Therefore particles of, say, two microns diameter would require an order of magnitude longer to burn up than the  $.2\mu$  particles for which the calculations were made. It should be noted, however, that a 2 micron particle is in a continuum flow regime behind the shock wave and, therefore, the burn-up times scaled linearly from Fig. 5 are actually too small. A map for computing "large" particle acceleration times is given in Fig. 6; the accelerating force is assumed to be continuum pressure drag. A typical particle trajectory in the free-molecular flow regime is shown in Fig. 7.

From a detailed consideration of the results shown in Figs. 5 through 7, it was decided that particles of approximately 5 microns diameter could be accelerated successfully up to shocked gas velocity in a shock tube.

UNCLASSIFIED

UNCLASSIFIED

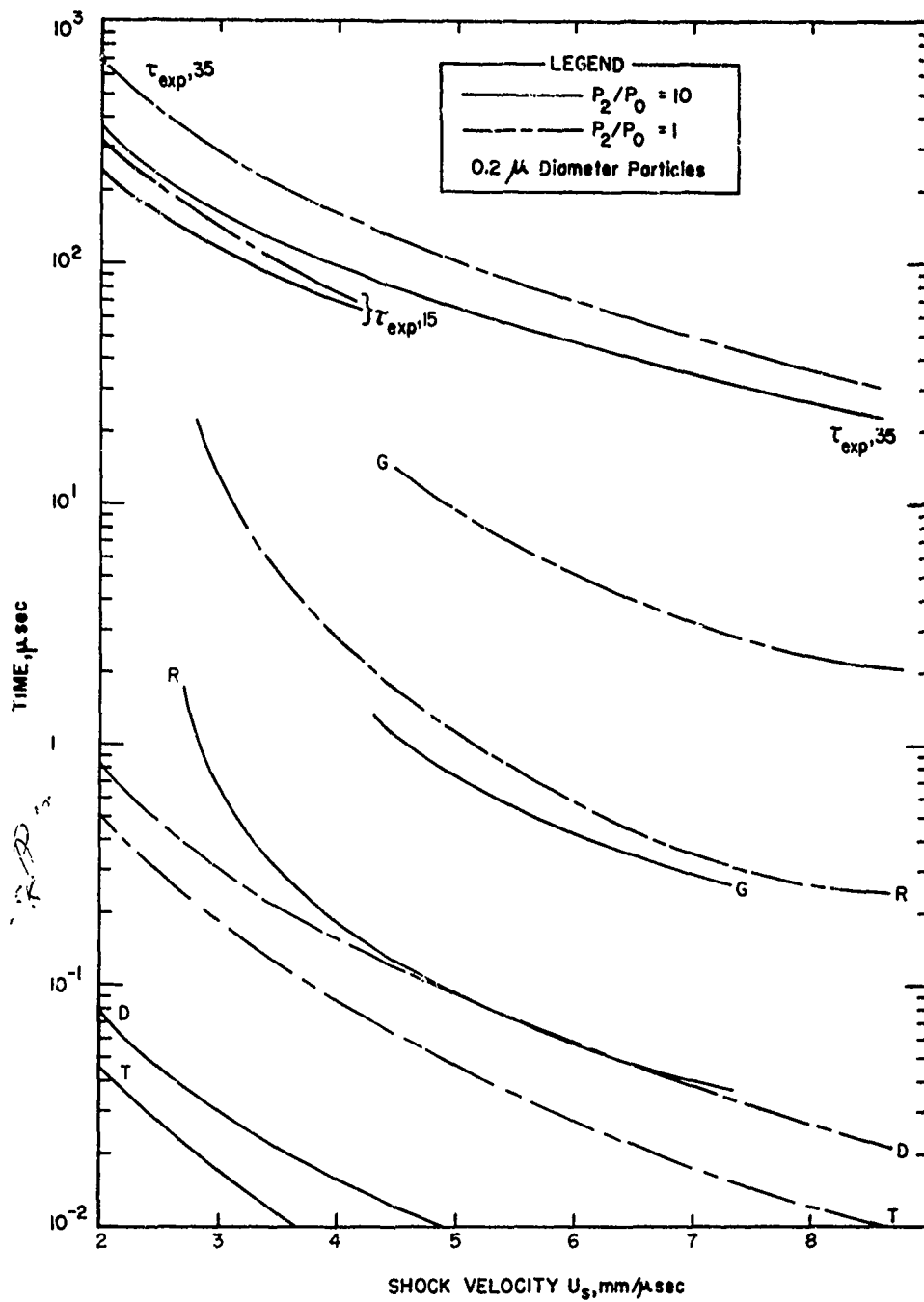


Figure 5. Shock Tube Testing Time and Particle Burn-Up Times for Various Materials vs Shock Velocity. T-Teflon; D-Delrin; R-Phenolic Refrasil; G-Graphite;  $\tau_{\text{exp},15}$ ,  $\tau_{\text{exp},35}$  - Experimental Testing Time at Distances of 15' and 35' Respectively, from the Diaphragm.

UNCLASSIFIED

UNCLASSIFIED

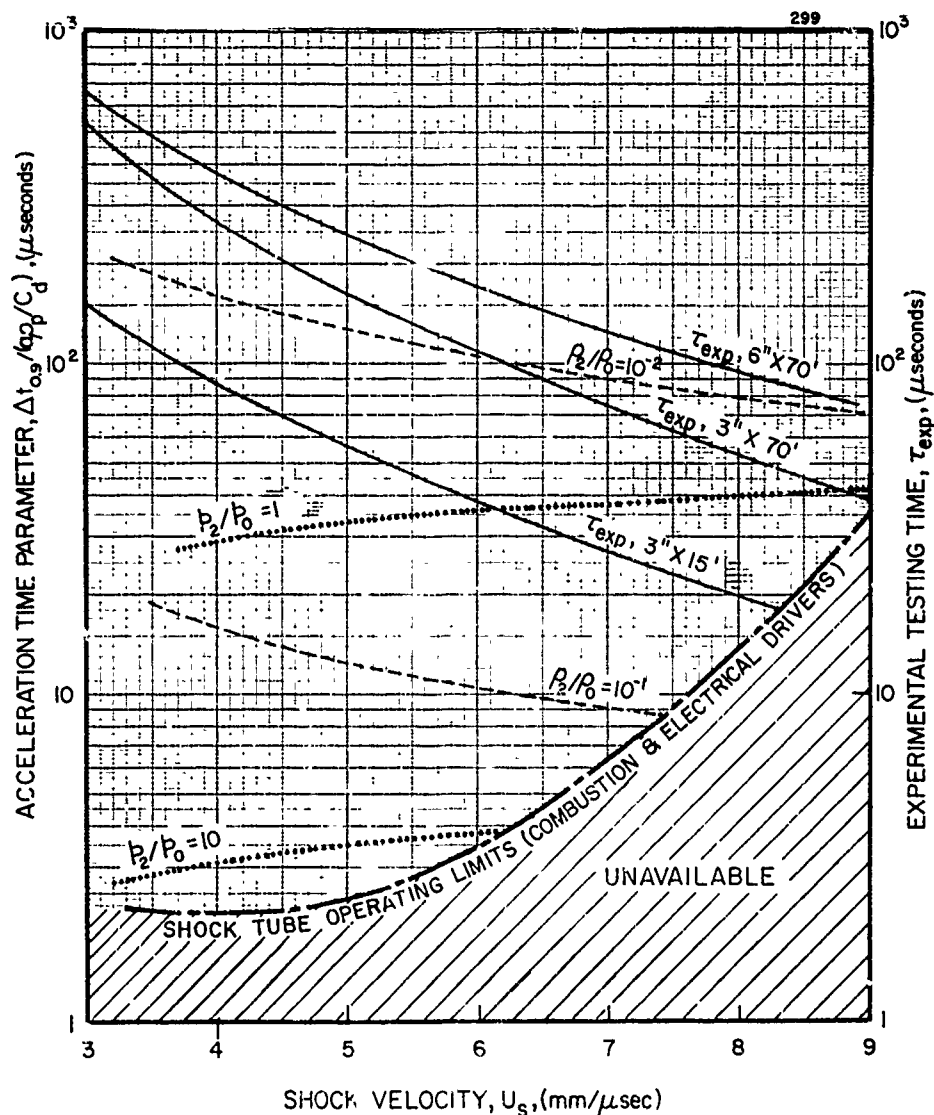


Figure 6. Particle Acceleration and Shock Tube Testing Times vs Shock Velocity.

$\Delta t_{0.9}$  = time for the particle to reach 90% of the shocked gas velocity, μ sec

$a$  = particle radius, microns

$\rho_p$  = particle density, g/cm<sup>3</sup>

$C_d$  = particle drag coefficient

$p_2$  = pressure behind the shock wave

$p_c$  = standard pressure (1 atm)

$\rho_2$  = density behind the shock wave

$\rho_o$  = standard density ( $1.29 \times 10^{-3}$  g/cm<sup>3</sup>)

$\tau_{exp}$  = experimental testing time, μ sec, for the shock tube geometries listed.

UNCLASSIFIED

UNCLASSIFIED

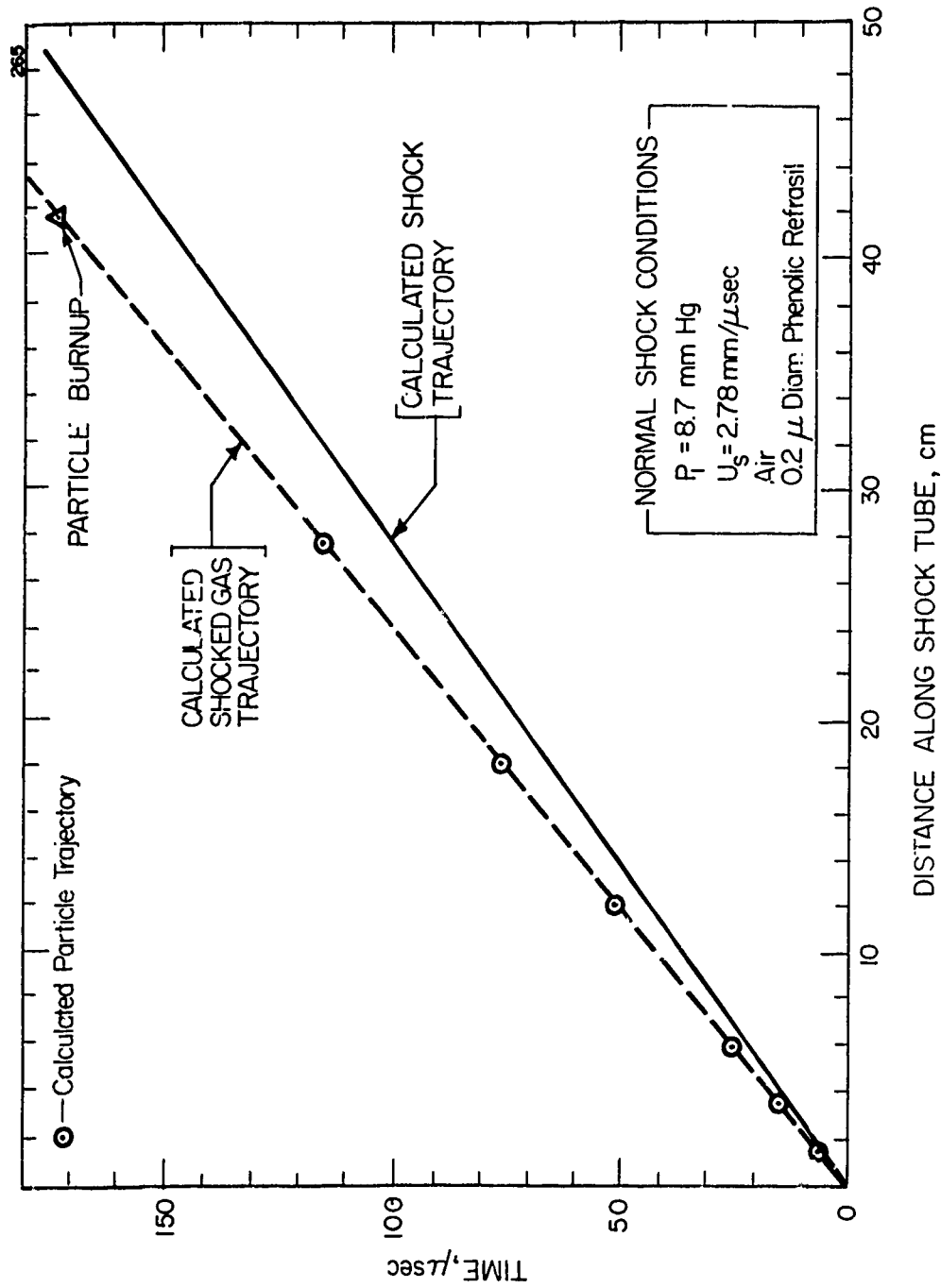


Figure 7. Wave and Particle Trajectories for 0.2  $\mu$  Diameter Phenolic Refrasil Powder.

UNCLASSIFIED

UNCLASSIFIED

### 3. EXPERIMENTAL MEASUREMENTS

In the very extensive literature<sup>(11-19)</sup> on hypervelocity impact phenomena, it is demonstrated that good correlation is obtained between the target crater mass removed and the normal component of kinetic energy of the impacting projectile (the cosine-squared, or Newtonian, approximation). The proportionality constant is dependent on the target and projectile materials, but has been found to be independent of projectile size for projectile diameters ranging from several inches down to 1/64 inch (400 microns). Performing hypervelocity impact tests with projectiles in the micron-size range would thus provide an important extension of the available literature data.

Further consideration of the mechanics of interaction of micron-size projectiles with material surfaces revealed that the scale of the surface roughness of the target, when compared to the projectile dimension, could be important. This is illustrated schematically in Fig. 8. All of the hypervelocity impact data reported in the open literature were obtained under test conditions similar to those shown in Fig. 8(a). Under these circumstances, the mean target surface inclination is clearly defined, and a meaningful impact angle  $\theta$ , is obtained. However, when the dimensions of the impacting projectile are reduced to the micron-size range, test conditions similar to those shown in Fig. 8(b) can be expected. In this latter situation the impact angle is not uniquely determined, and the Newtonian scaling relationship can be expected to become invalid. Thus, the

UNCLASSIFIED

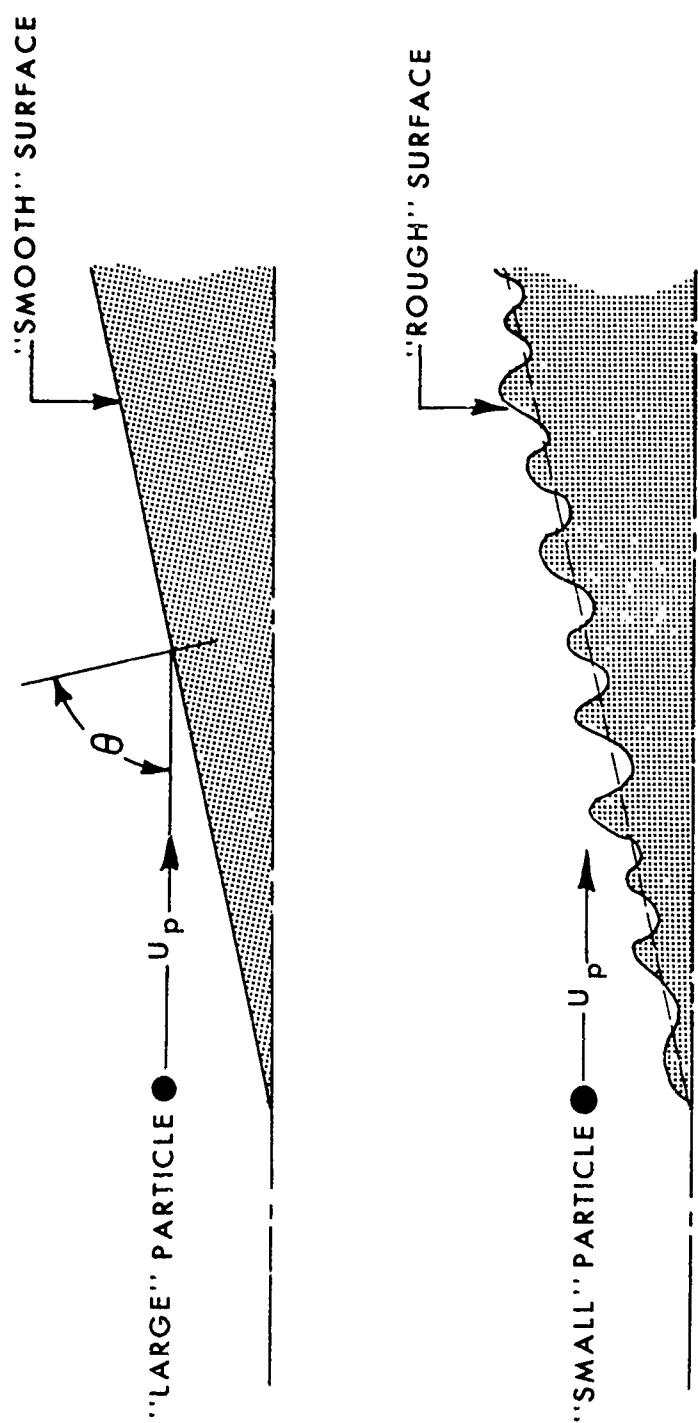


Figure 8. Impact of a Particle Onto a "Smooth" and "Rough" Surface.

## UNCLASSIFIED

ratio of surface roughness to projectile dimension can be expected to be an important scaling parameter.

Shown in Fig. 9 is a schematic of a powder injection shock tube facility for performing hypervelocity impact tests (the shock tube used for the tests to be described later in this paper did not have the sliding gate valves shown in Fig. 9. Instead, the entire driven section of the shock tube was filled with the injected particles).

A schematic of the target rake used for these studies is shown in Fig. 10. The three blunt targets and the conical target were arranged so that the bow shock waves generated by the supersonic flow behind the primary shock wave did not interfere with one another. The tip of the conical target was of a material different than the remainder of the target so as to eliminate any effects of near normal impact near the nose of the target. The technique used for determining hypervelocity impact damage in these experiments was to measure the total weight loss from the impacts. A view of the actual targets used in these experiments is shown in Fig. 11.

A preliminary series of shock tube measurements has been made by us to determine the angular dependence of mass removal by hypervelocity impact, and the influence of surface roughness on this mass removal. The particles used were 5 micron diameter Alundum. The shock tube conditions chosen for these experiments were 1 cm Hg initial pressure and shock velocity of approximately 4 mm/ $\mu$ sec. Prior to each experiment, the four lead targets were carefully weighed and then mounted in the holder. After the experiment, the lead models were re-weighed, and the mass difference noted. Since it was not possible, in this initial series of measurements,

UNCLASSIFIED

UNCLASSIFIED

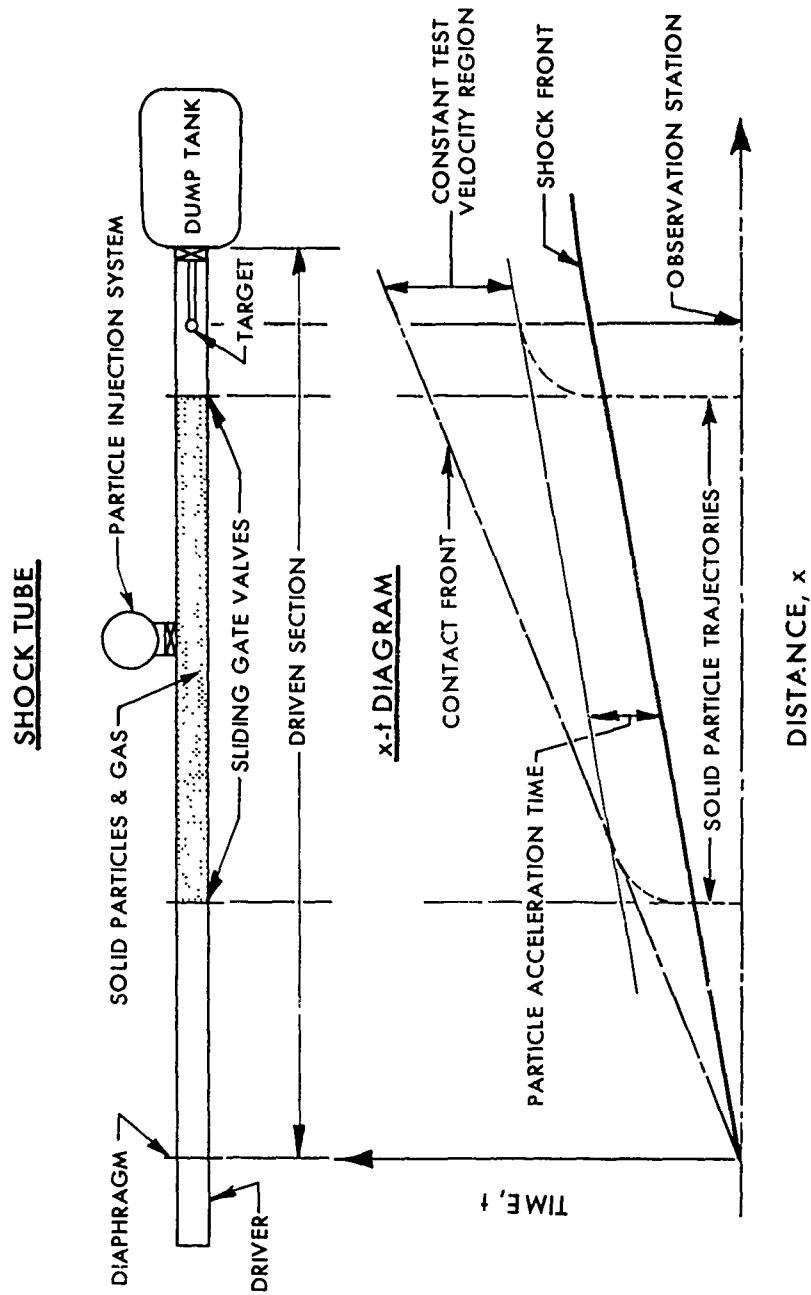


Figure 9. Schematic of Particle Injection Shock Tube, and Associated Time-Distance Diagram.

UNCLASSIFIED



UNCLASSIFIED

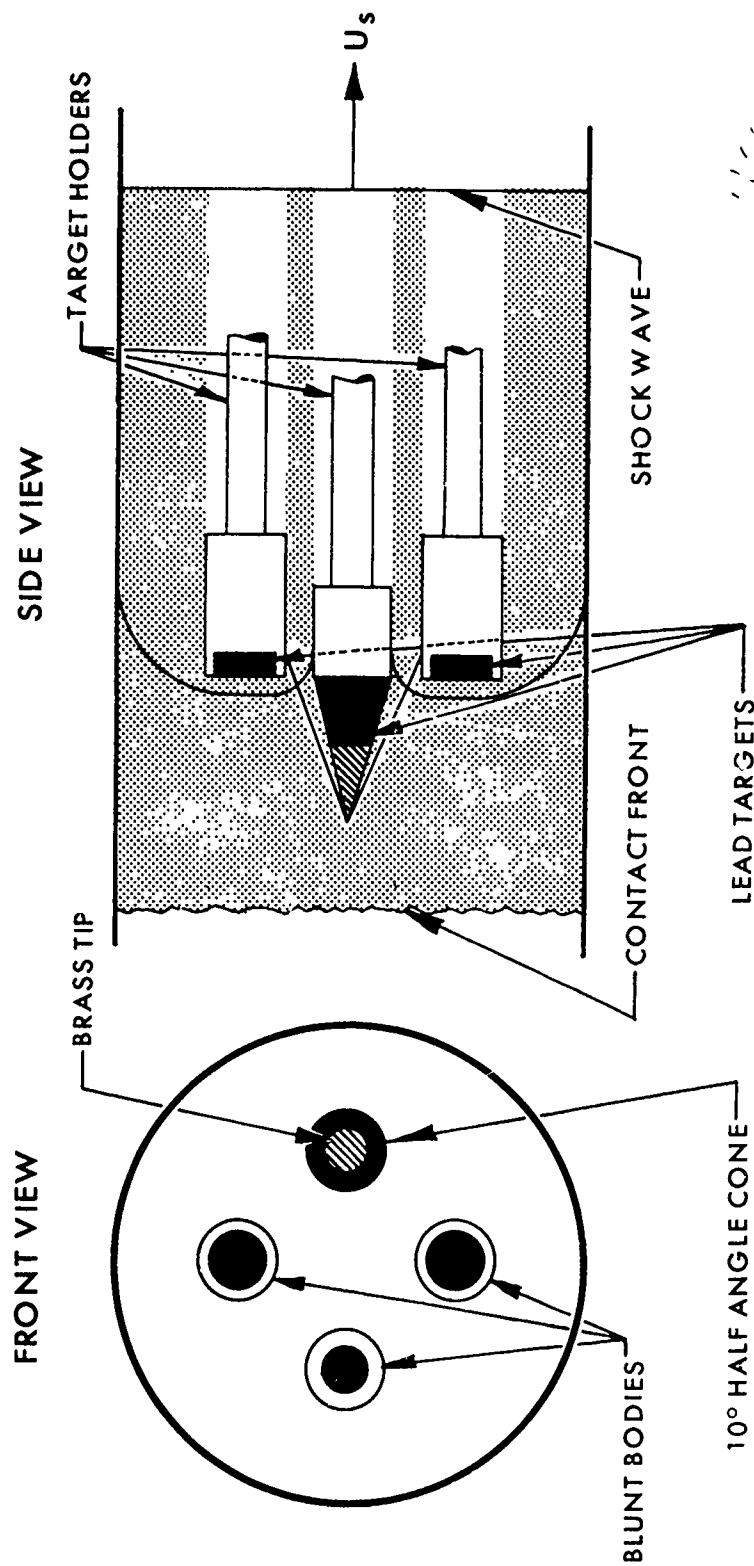


Figure 10. Schematic of the Targets Used in the Shock Tube Particle Impact Tests.

UNCLASSIFIED

UNCLASSIFIED

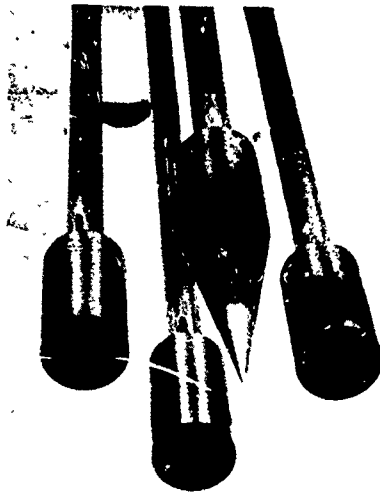


Figure 11. Target Used in the Shock Tube Impact Tests.

UNCLASSIFIED

## UNCLASSIFIED

to determine the actual number density of material particles in the shocked flow, it was decided to compute the mass loss from an impact on the conical model by normalizing it to the mass loss on the blunt models, as is shown below.

If, as is shown in Fig. 10 we let

$L$  = the length of the column of particles between the shock front and the contact front,

$n_p$  = the particle number density, and

$A_p$  = the projected, or swept, area of the target,

then the total number of particles,  $N_T$ , striking the target during the testing time is given by

$$N_T = A_p L n_p. \quad (1)$$

Therefore, the mass removed,  $M_R$ , per impact is given by

$$M_R = \frac{M_T}{N_T} = \frac{M_T}{A_p L n_p}, \quad (2)$$

where  $M_T$  is the total mass removed from the target.

During any one shock tube experiment,  $L$  and  $n_p$  are fixed, and the mass removed per impact on the conical surface divided by the similar quantity for the blunt surface is given by the ratio

$$\frac{(M_R)_{\text{cone}}}{(M_R)_{\text{blunt}}} = \frac{(M_T)_{\text{cone}}}{(M_T)_{\text{blunt}}} \times \frac{(A_p)_{\text{blunt}}}{(A_p)_{\text{cone}}}. \quad (3)$$

Using the data reduction method of Eq. (3), three independent data points were obtained for each experiment. One series of

## UNCLASSIFIED

experiments was made with models whose surfaces were relatively smooth when compared to the dimensions of the particles used (the conical models were cast in a polished mold, while the blunt models were trimmed with a razor blade). Photomicrographs of two areas of the models used in this series are shown at the top of Fig. 12. Another series of experiments were run, using models that had previously been exposed to the high velocity particle flow in the shock tube. The surfaces of these models were relatively rough, or "sand-blasted", in comparison to the particle dimensions, as is shown by the two figures in the lower left of Fig. 12. At the lower right of Fig. 12, we show the two left figures repeated, but we have drawn on them the edges of the craters formed by the impacts; we did this in order to improve the visualization of the result as shown by the fuzzy photographs. The reason the photographs are fuzzy is that the region photographed is slightly out of focus due to the curvature of the surface being viewed.

In Fig. 13 we show the results of these two series of experiments. Plotted is the mass removed per conical impact normalized by the mass removed by a blunt impact, versus the individual sample number. It is seen that the data groups about two points. Those corresponding to the previously mentioned smooth surface fall at a ratio of approximately 0.25, while those corresponding to the rough surface center about unity. For comparison purposes the fraction predicted based on the cosine-squared Newtonian law, namely 0.03, is shown.

What is immediately evident from Fig. 13 is that under no conditions is the mass loss from a conical impact within an order

UNCLASSIFIED

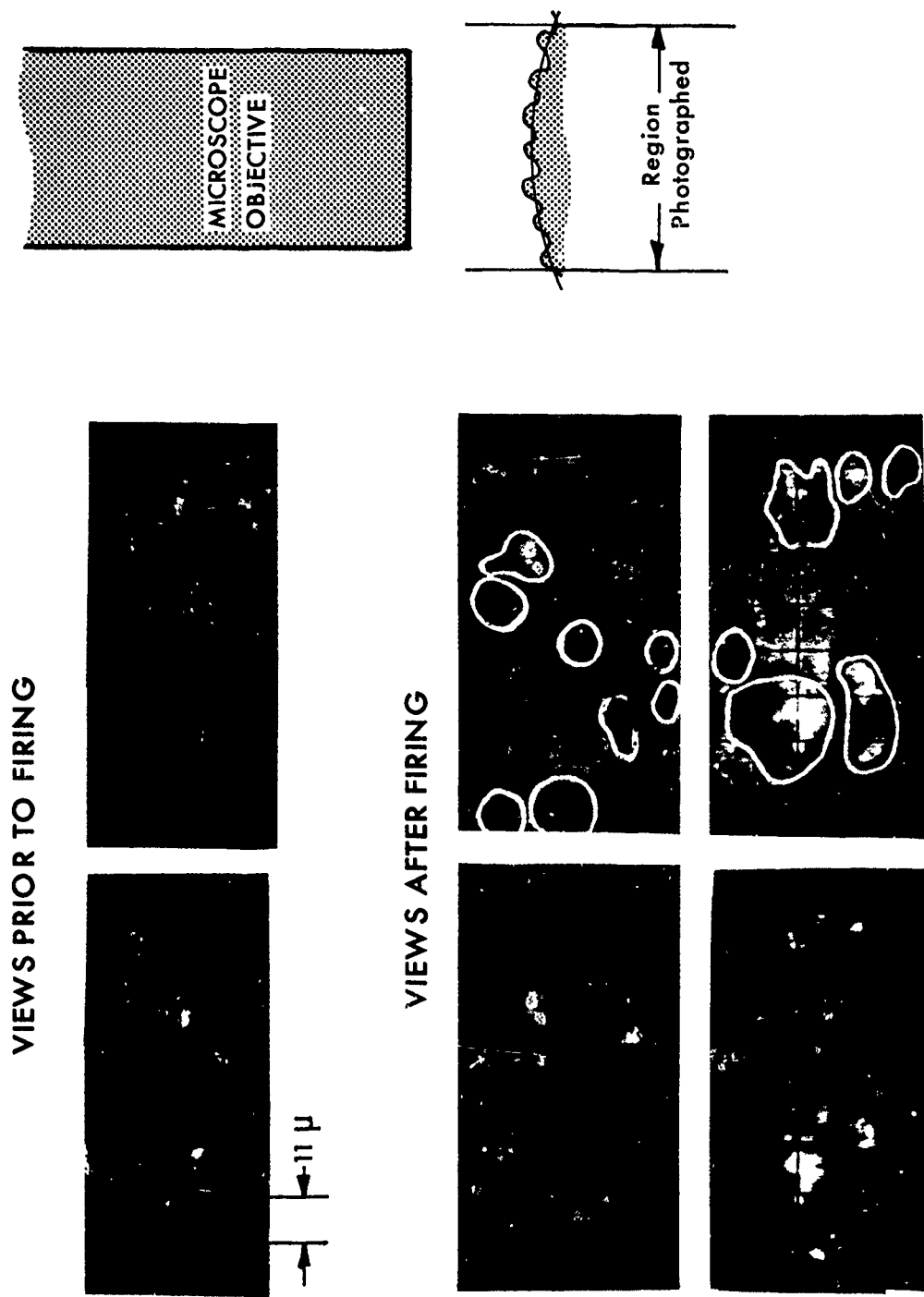


Figure 12. Photomicrographs of the Conical Lead Models Used in the Particle Impact Shock Tube Tests.

UNCLASSIFIED

UNCLASSIFIED

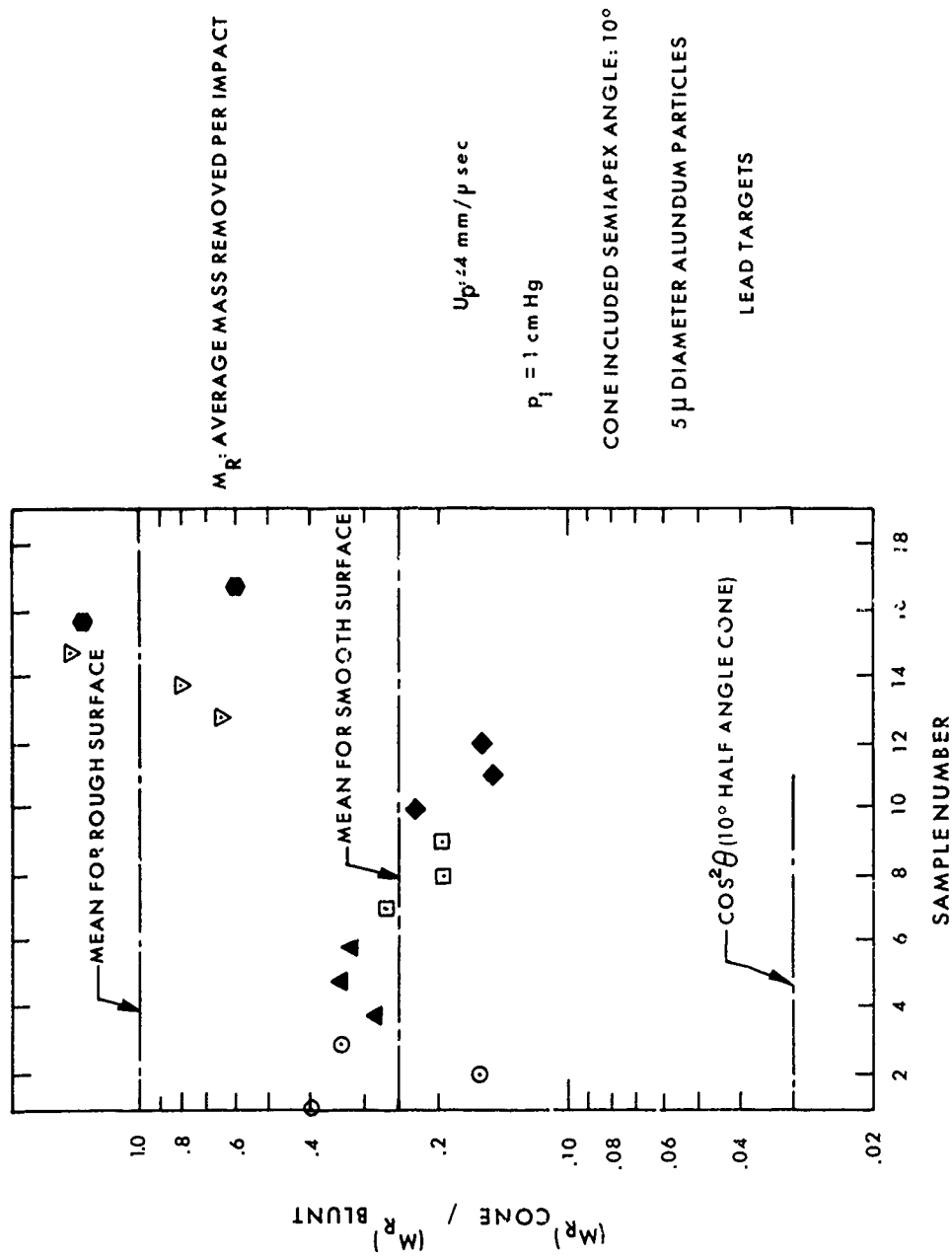


Figure 13. Ratio of the Mass Remove Per Conical Impact,  $(M_R)_{\text{Cone}}$  to the Mass Removed Per Blunt Impact,  $(M_R)_{\text{Blunt}}$ , versus Sample Number.

UNCLASSIFIED

**UNCLASSIFIED**

of magnitude as small as that predicted based on the cosine-squared law and, indeed, for the roughened surface the mass loss from a conical impact is the same, virtually, as that from a normal impact. This is a direct result of the fact that when the surface roughness dimensions are comparable to, or greater than, that of the dimensions of the impacting particles, every impact is nearly a normal incidence impact. In fact, an argument can be made that, if small protuberances are merely sheared by an impacting particle, rather than vaporized, the fraction shown on the ordinate of Fig. 13 can exceed unity.

**UNCLASSIFIED**

# UNCLASSIFIED

## REFERENCES

1. Hooker, W. J., A Summary of Calculations of Chemical and Fluid Dynamic Parameters in the SAPAG Facility, Heliodyne Corporation RN 17 (June 1965)
2. Tannenbaum, I. R., Techniques for Producing Submicron-size Plastic Particles, Heliodyne Corporation RN 19 (June 1965)
3. Nayfeh, A. H., Shock Wave Structure in a Dusty Ablating Gas, Heliodyne Corporation RN 23 (June 1965)
4. Holden, R. R. and Hooker, W. J., The Preparation and Injection of Teflon/Gas Dispersions for Shock Tube Investigations, Heliodyne Corporation RN 24 (June 1965)
5. Hooker, W. J., and Sellers, R. P. Jr., The Absorption Spectra of Shock-Heated Teflon/Argon and Teflon/Nitrogen Mixtures, Heliodyne Corporation RN 21 (June 1965)
6. Morsell, A. H., Electrical Conductivity of Shock-Heated Air and Air Plus Teflon Mixtures, Heliodyne Corporation RN 20 (June 1965)
7. Watson, R., Morsell, A. L., and Hooker, W. J., "Shock Tube Experiments with Dispersed Mixtures of Ultrafine Particles and Gases," Heliodyne Corporation (submitted for publication to Physics of Fluids), December 1966.
8. Hooker, W. J. and Morsell, A. L., Burn-up Rates of Powders Behind a Normal Shock Wave, Heliodyne Corporation RN 25 (June 1965)
9. Deirmendjian, D., Appl. Optics 3, 187 (1964)
10. Mirtich, Michael J., and Mark, Herman, Feasibility of Accelerating Micron-Size Particles in Shock-Tube Flows for Hypervelocity Degradation of Reflective Surfaces, NASA, Lewis Research Center, NASA TN D-3187, January 1966



## UNCLASSIFIED

11. Study of the Phenomena of Hypervelocity Impact. Summary Report. GMDRL: TR63-216, June 1963.
12. Posever, F. C., et al. Investigation of Structural Implications of Meteoroid Impact. Tech. Doc. Report, April 1962 - June 1964 (NAA) July 1964
13. Hermann, W. and Jones, A. H., Survey of Hypervelocity Impact Information, ASRL Report No. 99-1, MIT (1961)
14. Charters, A. C. and Locke, G. S., Jr., A Preliminary Investigation of High-Speed Impact: The Penetration of Small Spheres into Thick Copper Targets, NACA RM A-58 B-26 (1958)
15. Summers, J. L., Investigation of High Speed Impact: Regions of Impact and Impact at Oblique Angles, NASA TN D-94 (1959)
16. Whipple, F. L., Meteoritic Phenomena and Meteorites, Physics and Medicine of the Upper Atmosphere. Edited by: White, C. S., and Benson, O. O., University of New Mexico Press (1952)
17. Bjork, R. L., Effects of a Meteoroid Impact on Steel and Aluminum in Space. P-1662, Rand Corp. (16 Dec. 1958)
18. Bjork, F. L., "Meteoroid vs Space Vehicles", ARS Journal, (1961)
19. Lieblein, S., and Clough, N. (Lewis Res. Ctr.) and McMillan, A. R. (GMDRL), Hypervelocity Impact Damage Characteristics in Armored Space Radiator Tubes, Sept., 1964.

UNCLASSIFIED

## CONFIDENTIAL

### QUESTIONS, ANSWERS & COMMENTS:

(C) Q./W. C. Kuby (Univ. of Calif., Santa Barbara): I have one question to ask. It would appear that in both of the reasonings you gave for not extrapolating, it would indicate that one would expect more damage with the small particles than with the large particles. Yet the work of Persechini, again over a very small range in particle diameter, indicates that the damage does go down when the particle size decreases. The work, which we will hear more about later, from which I put up one slide, shows a great change in the damage. Now, of course we are marginal in hypervelocity; however, in some of the rocket tests we are coming up to it with velocities of 8,000 or 9,000 fps for the particles. The data of Sorensen includes data for particles of lower velocity than that. Do you have any comments on this?

(C) A./W. Hooker (Heliodyne): The only data that we have seen where I think a relatively clear argument can be made that you might expect completely different results is where you introduce, by putting models into a rocket plume, a liquid layer on the surface itself. I am not aware of any extensive hypervelocity impact data on the combination of liquid layer - solid backup layer but it can, I think, be argued that the way in which you say that material is removed, namely just by depositing a normal amount of kinetic energy into a solid, this material is not able to recede, i.e., the acoustic waves going through the material are exceeding the local shear strengths and this results in a completely different phenomenon in a liquid than it would in a solid. However, if the thickness of the liquid layer is comparable in dimension to that of the particle, you have a reflection problem. We

CONFIDENTIAL

# CONFIDENTIAL

## QUESTIONS, ANSWERS & COMMENTS:

started to work on this about one year ago and the work was terminated. It is the only argument that I know that is open in this area if you have a liquid layer that is thin compared to the particle. If you take legitimate data from a gun range and find that the particle size effect is going the inverse of what we are saying here, then I would like to see it and we would like to work on it ourselves.

# CONFIDENTIAL

675/676  
THIS DOCUMENT CONTAINS INFORMATION AFFECTING THE NATIONAL DEFENSE OF THE UNITED STATES WITHIN THE MEANING OF THE ESPIONAGE LAWS, TITLE 18, U.S.C., SECTION 793 AND 794, THE TRANSMISSION OF WHICH IN ANY MANNER TO AN UNAUTHORIZED PERSON IS PROHIBITED BY LAW.

**UNCLASSIFIED**

OPEN FORUM

Chairman: Prof. Richard F. Hoglund  
Purdue University

**UNCLASSIFIED**

**UNCLASSIFIED**

Effects of Impingement of Rocket  
Exhaust Gases and Solid Particles  
On A Spacecraft.

By: Clarke H. Lewis  
Applied Research Laboratories  
Aeronutronic Division, Philco-Ford  
Newport Beach, California

This work was sponsored by the  
Jet Propulsion Laboratory under Contract No. 951246

**UNCLASSIFIED**

# UNCLASSIFIED

## SECTION I INTRODUCTION

This presentation describes the major results of work performed under JPL Contract 951246 during the period 18 March 1966 - 25 October 1966. This contract has the general objective of determining the design restraints imposed upon a spacecraft by the impingement of gases and solid particles emanating from a solid propellant rocket.

The program was divided into two phases, one analytic and the other experimental. The analytic phase included a literature review of the important aspects of the problem and the development of analytic techniques to quantitatively describe the effects. Included in this effort were a review of gaseous impingement effects, the development of computational methods for predicting the high altitude rocket plume flow field for a gas particle flow, and a review of hypervelocity impact work.

The experimental phase was devoted to study of the impingement damage effects of micron sized particles such as are found in solid propellant rocket exhausts. A helium gas flow facility and a hydrogen-oxygen rocket motor were used to accelerate micron sized  $\text{Al}_2\text{O}_3$  particles to velocities ranging from 4000 ft/sec to over 10,000 ft/sec. These high speed particles impinged on instrumented target samples. Effects such as material removal, particle heating, and variation of surface reflectance were studied.

UNCLASSIFIED

# UNCLASSIFIED

## SECTION 2 IMPACTION DAMAGE STUDIES

### 2.1 GENERAL DESCRIPTION

The objective of these studies were to gain more information about the problem of surface damage due to particle cloud impaction, in particular, for the case of micron-sized  $\text{Al}_2\text{O}_3$  particles such as emanate from a solid propellant rocket motor. Considerable work has been done to date on hypervelocity impact of metal particles upon metal surfaces. This work has been concerned exclusively with single particle impaction and has involved particle sizes of 1/32 inch to 1/8 inch in diameter. These current experiments are concerned with delineating the differences between these single particle impacts and cloud effects.

Much of the conventional hypervelocity impact data can be represented by the correlation of Sorensen<sup>1</sup>, in which the volume of material removed per impact is given by

$$\frac{V}{V_0} = 0.12 \left( \frac{\rho_p}{\rho_t} \right)^{\frac{1}{2}} \left( \frac{\rho_p v^2}{S_t} \right)^{0.845} \quad (1)$$

If the particle impaction process could be considered as the sum of a series of independent single impactions, then the above equation could be applied directly to each impaction and the resultant material removal summed over the number of impacting particles to give the total damage. The experiments in this study provide a test of this possibility and also provide data from which one can ascertain the functional dependence of material removal on particle size, particle impaction velocity, particle impaction mass flux, and target surface strength. The ultimate objective of this work is to develop a model which can be

# UNCLASSIFIED

used to calculate damage to a surface due to the impingement of a solid propellant rocket exhaust containing  $\text{Al}_2\text{O}_3$  particles.

## 2.2 EXPERIMENTAL MEASUREMENTS

The experimental program consisted of two sets of experiments. In one set, helium gas was used in a Mach 5 supersonic nozzle to accelerate the  $\text{Al}_2\text{O}_3$  particles to mass average velocities between 4400 ft/sec and 5800 ft/sec. In the second set, the combustion products of a  $\text{H}_2\text{-O}_2$  rocket motor were used to accelerate the particles to about 9000 ft/sec. The  $\text{Al}_2\text{O}_3$  used in all of the experiments were from a single lot and had a number of peak of about 1.2 microns diameter and a mass mean of 5 microns diameter (Figure 1). A long slender nozzle with a length to exit diameter cylindrical specimens were made of either 1100-0 or 6016-T6 aluminum alloy and were aligned with axis parallel to the flow, exposing the flat face. The total surface regression of these specimens was measured and the temperature history of the specimen surface was recorded during each test. Surface reflectance was also measured before and after each test.

### 2.2.1 HELIUM TESTS

The Helium Flow Facility<sup>2</sup> was used to produce reproducible high velocity gas-particle flows into which were placed aluminum impaction samples. Prior to being mixed with the particles, the helium gas passes through a pebble bed heater, the temperature of which controls the velocity that the gas ultimately reaches at the nozzle exit. Velocities about 35% higher than that for room temperature helium are possible. During a test, the particle feed rate is measured directly, the gas stagnation pressure is measured in order to determine gas flow rate, and light transmission measurements are made at the nozzle entrance and exit to determine the particle mean velocity and spatial distribution. The samples are placed approximately 2 inches from the exit of the nozzle, which is within the Mach cone of the nozzle. The



## UNCLASSIFIED

transmission measurement is made about half way between the sample and the nozzle exit.

Initial tests using 6061-T6 and 1100-0 aluminum produced very small material losses<sup>3</sup>. At these experimental conditions, Sorensen's<sup>1</sup> correlation equation indicated large target mass loss should have been expected. These results indicated the possibility of a significant particle size scaling law. Consequently tests were conducted to more adequately document the two-phase flow velocity to better evaluate the validity of a scaling law. This was done by using transmission measurements at the nozzle entrance and exit to verify the particle mass mean velocity. In terms of the incident beam,  $I_0$ , the transmitted beam,  $I$ , can be expressed as<sup>4</sup>

$$I/I_0 = \exp \left[ - \frac{3\phi p_g u_g L}{p_p u_p D_{32}} \right] \quad (2)$$

At the nozzle entrance, the assumption is made that the particle velocity is that of the gas and a value of  $D_{32}$ , the volume to area mean particle diameter, is computed from the measured transmission. Using this computed value of  $D_{32}$  and the computed values of the gas density and velocity, particle velocity can be obtained from the measured transmission at the nozzle exit. Figure 2 contains plots of the particle velocity at the exit plane of the test nozzle for the different experimental conditions obtained in this study. These velocities were calculated using the Aeronutronic particle lag computer program. The experimentally derived values for the mass mean velocity ( $D_p \approx 5$  micron) agree well with the theoretical calculations.

Preliminary calculations had shown that the particle velocity loss through the shock layer in front of the specimen would be small.

## UNCLASSIFIED

A short series of experiments was conducted to verify this in light of the greatly reduced target mass loss. Since the shock layer thickness is proportional to the specimen diameter, the specimen diameter was varied over a factor of four, holding all other conditions constant. The variation in target mass loss as shown in Figure 4, was relatively small and indicates that the particle velocity drop in the shock layer is, in fact, small. Some of the variation obtained can be explained by the increased heat transfer with reduced specimen diameter causing a reduction in surface strength.

The remaining helium gas-particle tests had the objectives of determining the functional relationship of target mass loss with particle velocity and with surface strength as well as investigating the particle scaling effect. These results are shown in Figure 4. The target surface temperature was measured by a thermocouple located .100 inches back of the surface. A transient heat transfer analysis indicated that the surface temperature was within 5% of the measured thermocouple temperature. The shear strength used in the calculations was based on this temperature (Figure 5) for shear strength data.<sup>5</sup>

### 2.2.2 HYDROGEN-OXYGEN ROCKET TESTS

In order to obtain particle velocities higher than those available with the helium facility, the combustion products of  $H_2-O_2$  rocket engine were used to accelerate the  $Al_2O_3$  particles through a nozzle that was geometrically similar to the one used in the helium tests. The  $Al_2O_3$  particles are introduced into the combustion chamber by means of a water slurry. The chamber temperature is low enough so that the particles do not vaporize or melt, thus the particle size distribution in the nozzle flow is known. The target location was also the same as in the helium tests. Experimental verification of the particle velocities could not be made in these tests because a light transmission apparatus has not been provided in the hot firing test section. However, due to

UNCLASSIFIED

## UNCLASSIFIED

the geometric similarity of the two nozzles and the proven accuracy of the particle lag calculations for the helium nozzle, it can be assumed with confidence that the computed values of particle velocity are correct. (Figure 2)

6061-T6 and 1100-0 Aluminum alloys were used as target materials for these experiments. The two principal variables, other than material, were the total amount of impacting particles as controlled by run time, and the surface temperature of the sample as controlled by water cooling. The surface temperature was deduced from the temperature measured by a thermocouple placed below the surface. Below the thermocouple was a transverse passage for the flow of cooling water. The heat absorbed by the water was determined by measuring the water temperature rise and the flow rate. During the initial part of each test, the nozzle flow was free from any particles. Following Fay and Riddell<sup>6</sup> and Boison and Curtiss<sup>7</sup>, a gas phase convective heat flux was calculated which was used in conjunction with the specimen thermocouple to determine the surface temperature prior to the impaction of any particles. Both transient calculations and examination of the specimen temperature - time history indicate that temperature distribution in the specimen reached a steady value during the gas heating period (about 2 seconds). This equilibrium surface temperature has been used to determine the surface strength used in plotting the data in Figure 4. During the period of particle flow, it was evident that additional heating occurred due to particle impaction. As yet, it has not been possible to determine the surface temperature rise during particle impaction because the temperature distribution has been of a transient nature throughout the duration of the particle impact portion of the runs. The data from these tests shown in Figure 4 show the effect of this increased heat transfer. Proportionally more damage occurs as the amount of impacting particles increases, indicating that the surface strength is decreasing as the surface temperature is rising.

# UNCLASSIFIED

## 2.3 DISCUSSION OF RESULTS

While the analysis of the impingement damage data collected to date is still of a preliminary nature, several positive statements can be made. For the helium data and the  $H_2-O_2$  rocket data where the total amount of particles are small, the variation of damage with particle velocity does follow the functional form of Sorensen's correlation as shown in Figure 4. Also for these same data there appears to be little correlation between damage and the material type. From the helium data, verification of the particle lag calculations and the resultant nozzle design was obtained by the use of light transmission measurements of the flowing particle cloud. Based on the computed particle velocities and the surface strength based on temperature measurements, the experimentally obtained damage results were compared with Sorensen's correlation equation which is applicable to conventional hypervelocity impact tests. Figure 4 shows that the particle damage obtained from micron-sized  $Al_2O_3$  particles is from 100 to 1000 times less than that due to an equivalent volume of large particle ( $d_p \approx .125$  inch). These results show that particle heating can be significant and that part of the subsequent experiments should be designed so that the effect of the particle heating can be determined.

The apparent lack of correlation between damage and the different strength aluminum alloys at low temperatures has not been explained. The data does indicate that there is a significant particle size scaling factor. It is possible that the mechanical properties of projectile material may be more significant for the micron-sized particles used in this study than for large particles studied previously.<sup>1</sup> This could be associated with the lack of sensitivity of material removed to surface strength for the cold target tests. Whether this effect persists at higher temperatures cannot be determined as yet because of the heat transfer variations due to the particles.

UNCLASSIFIED

## UNCLASSIFIED

Surface reflectance was measured before and after tests for several specimens. In every case the normal reflectance after particle impaction was at least 50 times less than before; independent of the amount of particles involved. The apparatus used wasn't capable of measuring a greater variation. For all of these cases, the particle volume flux was  $5 \times 10^{-2} \text{ cm}^3/\text{in}^2 \text{ sec}$  or greater in order to obtain detectable material removal. Additional tests should be performed for the sole purpose of measuring surface reflectance degradation at lower particle impaction rates.

Certainly, in subsequent work, the problem of particle heating will be studied; the effect and nature of the significant surface strength for different classes of materials needs to be better understood; and the effect of angle of impact will be investigated.

# UNCLASSIFIED

## REFERENCES

1. N. R. Sorensen, Proc. of Seventh Symposium on Hypervelocity Impact, Vol. VI, page 281 (1965)/
2. W. C. Kuby, "Proposal for Effects of Impingement of Rocket Exhaust Gases and Solid Particles on a Spacecraft, "Aeronutronic Proposal No. P-15244(U), submitted to J. P. L., Aug. 1965.
3. W. C. Kuby, Fifth Monthly Progress Letter, "Effects of Impingement of Rocket Exhaust Gases and Solid Particles on a Spacecraft, " Aeronutronic Div., Philco-Ford Corp., J. P. L. Contract No. 951246, Sept. 2, 1966.
4. R. A. Dobbins, et. al., "Measurement of Mean Particle Sizes of Sprays from Diffractively Scattered Light, " AIAA Journal, Vol. 1, No. 8, page 1882, Aug. 1963.
5. Alcoa Aluminum Handbook, 1964.
6. J. A. Fay and F. R. Riddell, "Theory of Stagnation Point Heat Transfer in Dissociated Air, " J. Aero. Sci., 25, 73-85, 1958.
7. J. C. Boison and H. A. Curtiss, "An Experimental Investigation of Blunt Body Stagnation Point Velocity Gradient, " ARS Journal, page 130, Feb. 1959.

UNCLASSIFIED

ALUMINA PARTICLE SIZE  
DISTRIBUTION  
Norton Type 38-900

$\phi(D)$  = fractional number of particles (per  
unit size increment) of size  $D$ ,  
between  $(D-\Delta D)$  and  $(D+\Delta D)$

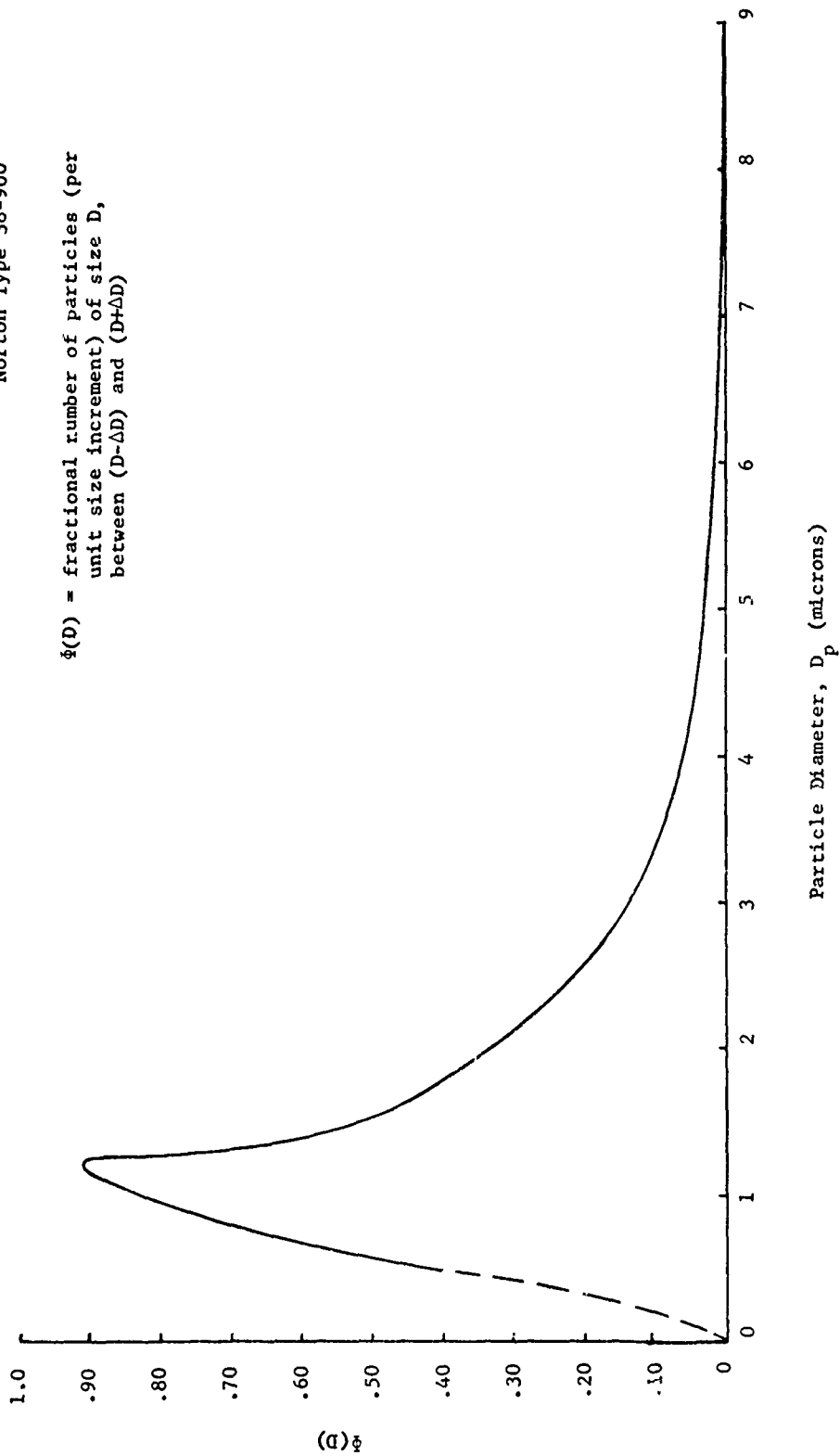


Figure 1. Particle Size Distribution

UNCLASSIFIED

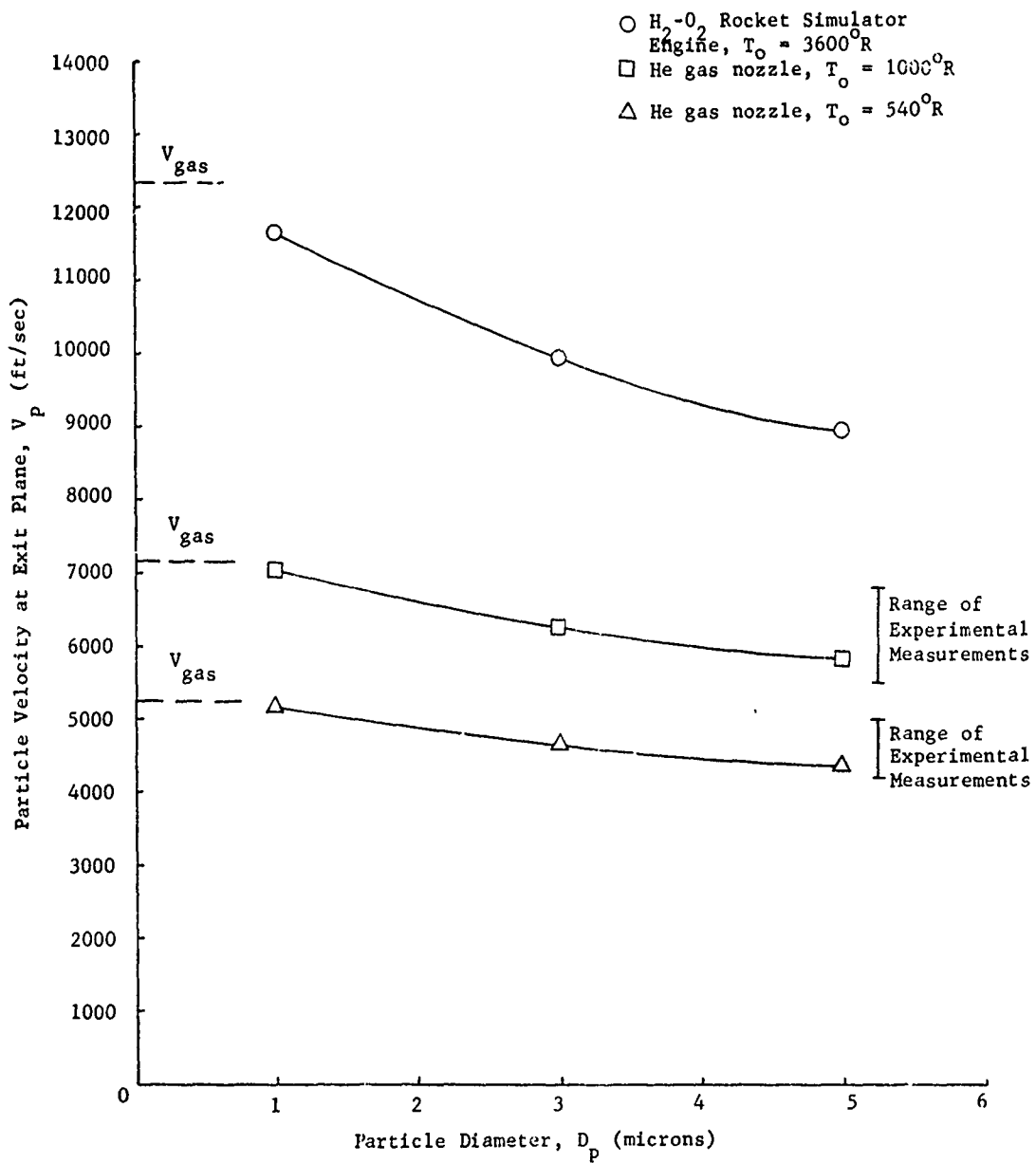


Figure 2.  $Al_2O_3$  Particle Velocity at Nozzle Exit Plane.

UNCLASSIFIED



UNCLASSIFIED

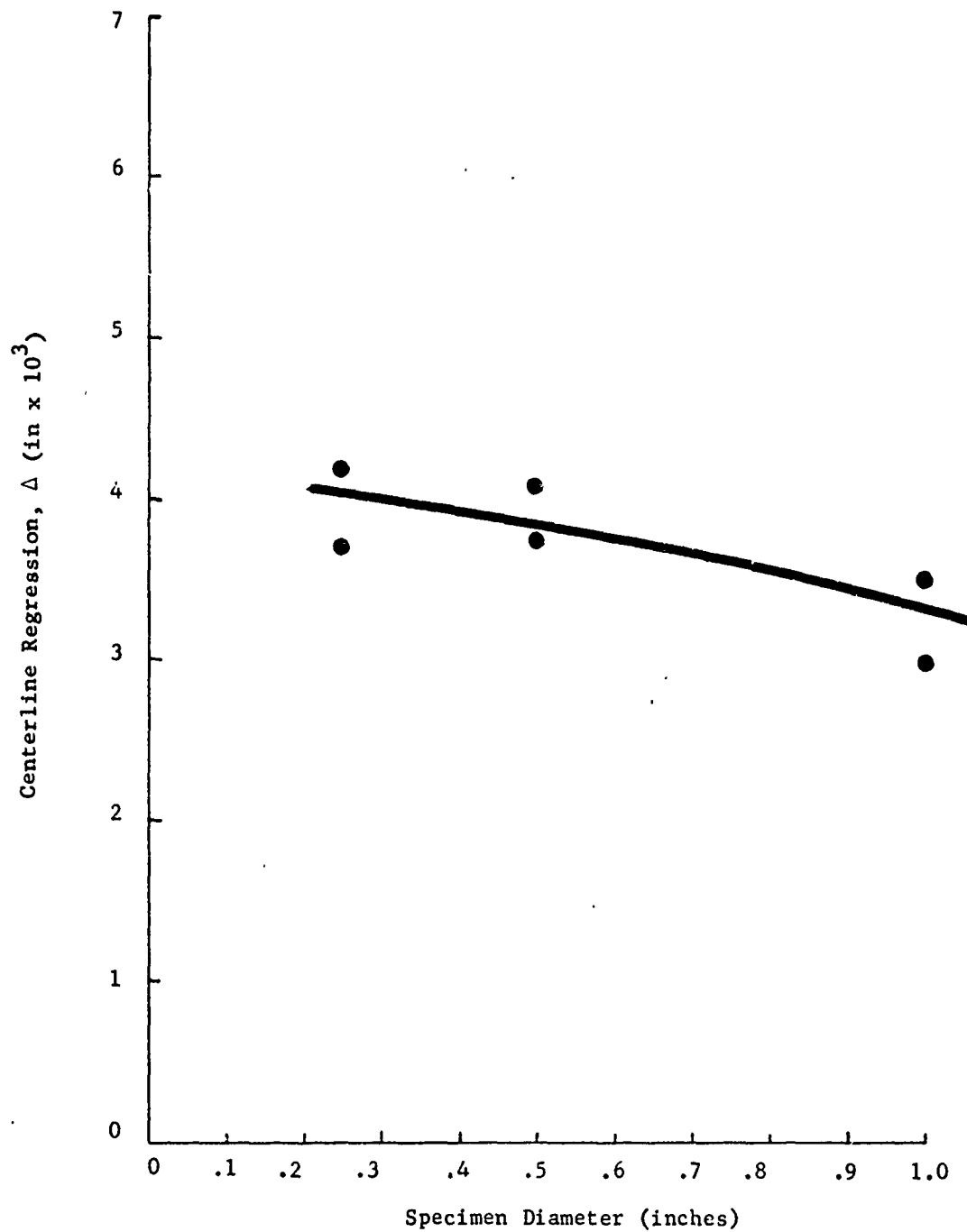


Figure 3. Impingement Damage as a Function of Specimen Diameter.

UNCLASSIFIED

UNCLASSIFIED

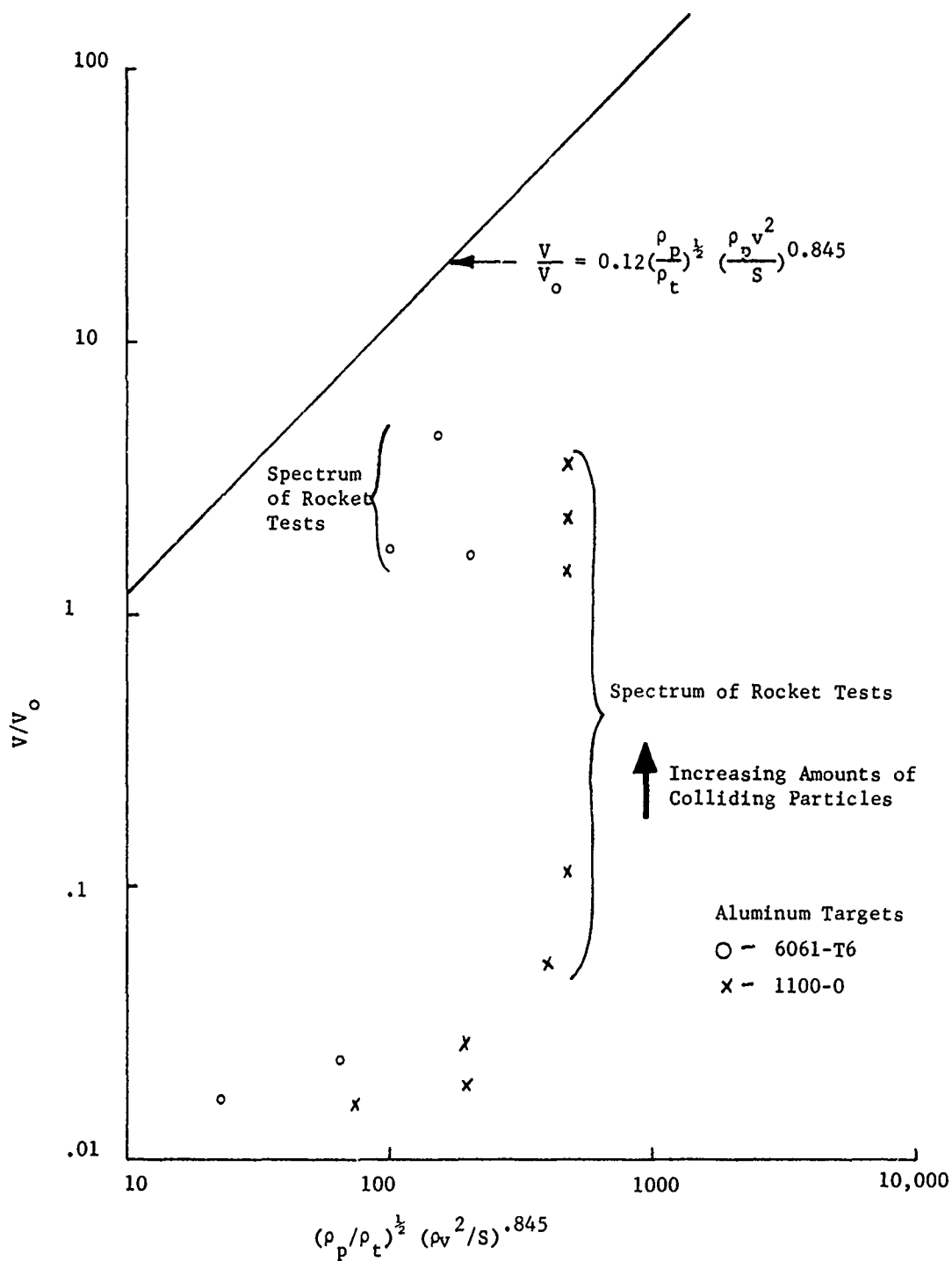


Figure 4. Normalized Volume Loss for  $Al_2O_3$  to Aluminum Impacts.

UNCLASSIFIED

UNCLASSIFIED

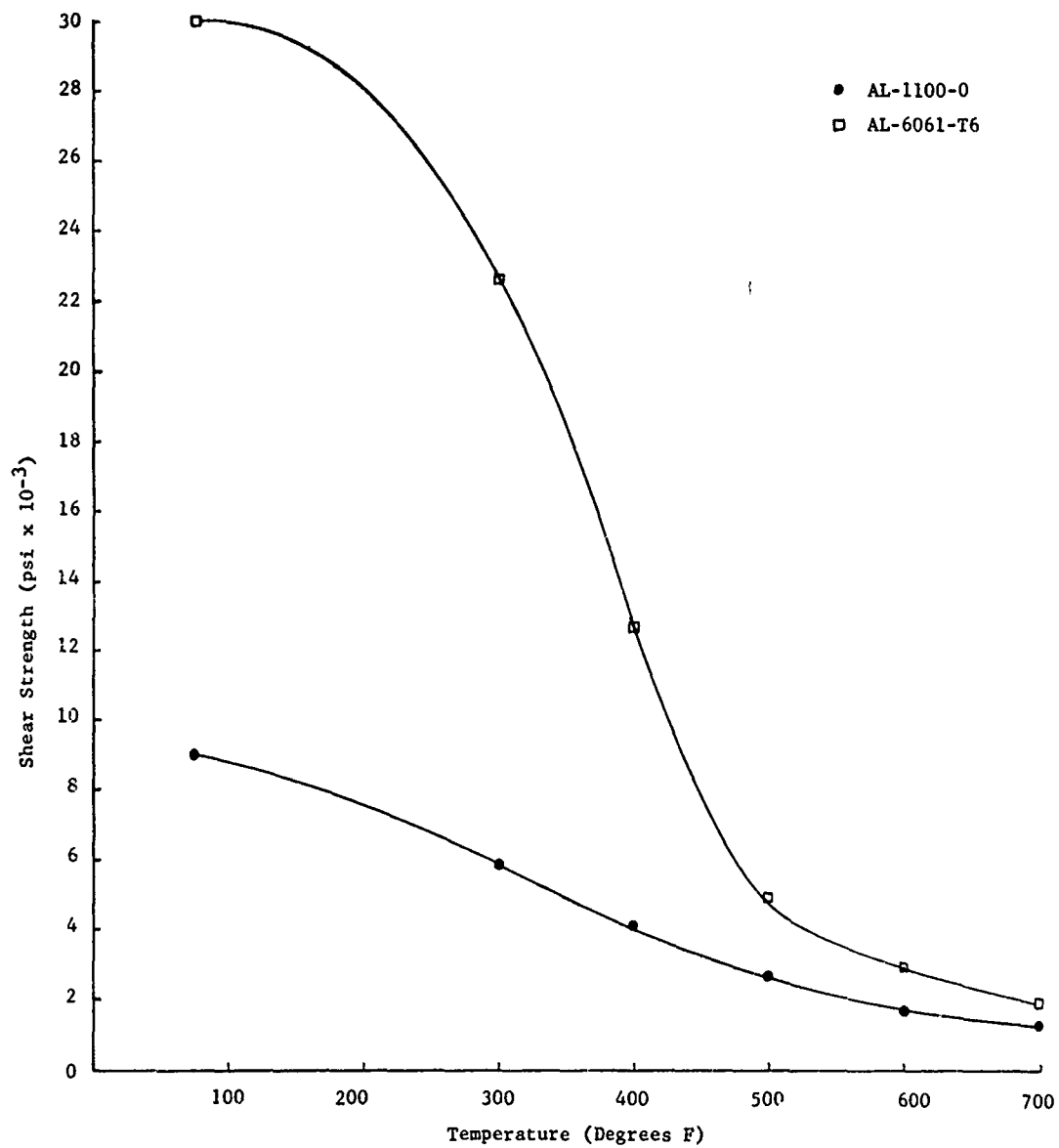


Figure 5. Shear Strength of 6061 and 1100 Aluminum Alloys.

UNCLASSIFIED

**UNCLASSIFIED**

**A LASER-DOPPLER TECHNIQUE FOR THE MEASUREMENT OF  
PARTICLE VELOCITY IN GAS-PARTICLE TWO-PHASE FLOW\***

**BY**

Robert N. James, Capt, USAF, and Ph. D. Candidate,  
Dept. of Aeronautics and Astronautics,  
Stanford University, Stanford, Calif.

Wayne R. Babcock, Senior Scientist, Physical Sciences  
Laboratory, United Technology Center,  
Sunnyvale, California

Howard S. Seifert, Professor of Aeronautics and Astronautics  
Stanford University, Stanford, Calif.

\* Work supported by the Rocket Propulsion Laboratory of the Air Force Systems Command, Edwards Air Force Base, under Contracts AF 04(611)-10926 and F04611-67-C-0056.

**UNCLASSIFIED**

## UNCLASSIFIED

A Laser-Doppler Technique for the Measurement of Particle Velocity in Gas-Particle Two-Phase Flow\*. ROBERT N. JAMES, Captain, USAF, and PhD Candidate, Dept. of Aeronautics and Astronautics, Stanford University, Stanford, California, WAYNE R. BABCOCK, Senior Scientist, Physical Sciences Laboratory, United Technology Center, Sunnyvale, California. and HOWARD S. SEIFERT, Professor of Aeronautics and Astronautics, Stanford University, Stanford, California, and Assistant for Research to the Vice-President, United Technology Center, Sunnyvale, California.

### ABSTRACT

In chemical propulsion, the use of metallic fuel constituents burning to particulate refractory oxides in rocket engines has forced attention to the understanding of two-phase nozzle expansion processes. In this study light from a helium-neon laser was reflected both from a fixed target and from moving particles. A lens concentrated the laser light and the light back-scattered from the particles was picked up by the same lens and directed into a Fabry-Perot scanning plate interferometer. The interferometer limited observation at any moment to those particles whose Doppler shifted frequency coincided with the interferometer transmission frequency. The light from the fixed target provided a frequency reference system, and calibrated movement of the interferometer mirror spacing provided continuous examination of velocity. Data in the form of lightscattering and number count vs velocity has been obtained for water droplets in subsonic flow, for aluminum spheres and alumina abrasive in cold supersonic flow and for aluminum and magnesium oxide in hot supersonic flow. Number count-velocity data was found to be a complicated function of

---

\* Work supported by the Rocket Propulsion Laboratory of the Air Force Systems Command, Edwards Air Force Base, under contract AF 04(611)-10926.

UNCLASSIFIED

## UNCLASSIFIED

particle size distribution and vector velocity distribution as well as instrument characteristics. Lightscattering velocity profiles followed theoretical predictions when collision effects were included for the spheres and agglomeration for the abrasive.

Precise determination of the velocity of micron sized particles is of material importance in both chemical propulsion and electrical colloidal propulsion. In electrical colloidal propulsion knowledge of the velocity of the particles leads directly to a determination of the charge/mass ratio of the particles; an essential parameter in both experimental and operational theoretical calculations. In chemical propulsion the use of metallic fuel constituents in modern rocket engines has brought attention to nonequilibrium aspects of two-phase nozzle expansion processes. Of primary importance is the velocity lag: the condensed particles are accelerated in a nozzle almost entirely by drag forces associated with lag or slippage of the particles relative to the expanding gas. Since velocity lags have been a cause of rocket performance losses, a number of studies have been directed toward delineation of the mechanism and magnitude of these lag effects.

Except for some results of Fulmer and Wirtz<sup>1</sup>, the experimental determination of the velocity lag has been essentially only semiquantitative. The specific intent of this investigation was to obtain particle velocities using a Doppler radar technique at optical wavelengths by taking advantage of the output of a helium-neon gas laser, light-scattering from particles, and the operating characteristics of the scanning plate Fabry-Perot interferometer.

Before discussing the present system in greater detail, it is of interest to comment briefly on the heterodyne or time-resolved method of measuring the doppler signal as compared with the space-resolved system being used.

## UNCLASSIFIED

One can see, from Figure 1, that if the Fabry-Perot unit were to be removed and the oscilloscopes, etc. replaced with a radio-frequency spectrum analyzer, the beat frequency generated by the interfering light waves could be detected. This system, in fact, was used by L. Mollenauer and W. Babcock<sup>2</sup> in the early stages of the work where it proved to be a very sensitive and useful tool in measuring the vibration and velocity characteristics of a target surface. However, limitations in available signal-to-noise ratios made the heterodyne system unattractive when compared with present techniques.

The dominant noise source is the particle signal. This is due to the fact that particles yielding a particular Doppler frequency at any instant are widely spread in position with respect to the focal spot diameter. As a result the particle signals appear as random pulses on the order of nanoseconds duration. Obviously, the spectrum generated is so broad that identification of the frequencies of interest becomes ambiguous. In the present optical spectrometer system, all beat frequencies are rejected and only those light frequencies to which the interferometer is resonant are passed, hence this source of noise is eliminated.

Our system is illustrated in Figure 1. Collimated light from a 200mw continuous single axial mode helium-neon gas laser with a wavelength of  $6328 \text{ \AA}$  is passed through a specialized beam splitter and is reflected both from a fixed target and from individual moving particles. A lens concentrates the laser light in a small region centered around the particle whose velocity is being measured. The light backscattered from the particle is then picked up by the same lens and directed into a Fabry-Perot scanning plate interferometer. The interferometer acts like a variable frequency narrow-band filter, limiting observation at any moment to those particles whose Doppler shifted frequency coincides with the interferometer transmission frequency. The light from the

UNCLASSIFIED

## UNCLASSIFIED

fixed target provides a frequency (ie:velocity) reference system, and calibrated movement of the interferometer mirror spacing between two adjacent orders of the source frequency provides continuous examination of velocity.

The signals are amplified by the photomultiplier system and fed to a Tektronix 564 storage oscilloscope. With this scope only the maximum signal remains on the screen at any velocity setting because smaller signals are covered by the larger ones. After a sufficient time all that can be seen is an envelope of maximum signals vs velocity. A one-to-one correspondence between frequency (velocity) and scope horizontal movement is obtained by linking the interferometer mirror movement to the scope horizontal movement.

Simultaneously, the signal is fed to a Tektronix 547 oscilloscope which allows precise visual setting of the "B" time base triggering level by virtue of the fact that the "B" gate output is used to drive a Z-axis amplifier for trace brightening of the particle signal. This adjustment is made by viewing the signals displayed on the 547 using the "A" time base and positioning the bright spot, generated by the trace brightener, at the desired signal amplitude. Any signal reaching this amplitude causes a one microsecond pulse to appear at the "B" gate output which is used, in addition to trace brightening, to drive a signals/unit-time counter as shown in Figure 2. Initially, a Hewlett-Packard 523C counter was used but was later replaced by a rate counter, the output of which drives the "B" input to the 564 storage scope. With the 564 in the chopped input mode, signal amplitude vs velocity is displayed on one half of the screen while a signal number vs velocity curve is generated on the remaining half. Figure 8, a photo of aluminum particles, illustrates typical results.



## UNCLASSIFIED

The Doppler shift for the moving scattering particle is obtained from the general expression<sup>4</sup>

$$f_r = f_o \times \left[ \frac{1 - \frac{\vec{V} \cdot \vec{k}}{c}}{1 - \frac{\vec{V} \cdot \vec{k}_1}{c}} \right] \quad (4)$$

where

$f_r$  = received frequency

$V$  = velocity of the particle

$k$  = unit vector in the direction of the incoming wave

$f_o$  = transmitted frequency

$k_1$  = unit vector in the direction of the scattered wave

For practical application, the geometry illustrated in Figure 3 leads to the expression

$$f_d = \frac{V}{\lambda_o} \left[ \cos \theta - \cos (\theta + \phi) \right]$$

The frequency transmission characteristics of the Fabry-Perot interferometer may be approximated for the central spot of the typical output ring structures by

$$\frac{I}{I_{\max}} = \left[ 1 + \frac{4R}{(1-R)^2} \sin^2 \left( \frac{2\pi d}{\lambda} \right) \right]^{-1}$$

Clearly, when  $2d/\lambda = n$  is an integer the interferometer is in resonance for the wavelength involved. To avoid ambiguity in the velocity display we must have the original mirror spacing such that the mirror movement for interorder resonance of the reference wavelength is just equal

UNCLASSIFIED

## UNCLASSIFIED

to the mirror movement required for resonance of the maximum Doppler shifted wavelength to occur. At mirror spacing  $d_0$  the reference wavelength,  $\lambda_0$  is resonant at order  $n$  (see Figure 4). Movement of the mirrors to spacing  $d_1$  gives resonance for  $\lambda_0$  at the next order,  $n+1$ . This same movement,  $d_0$  to  $d_1$ , allows wavelength  $\lambda_1$  to be resonant at order  $n$ . Therefore, the Doppler shift represented by  $\lambda_1 - \lambda_0$  is the maximum shift which can be used without ambiguity. With these limitations in mind it is easily shown<sup>2,3</sup> that the basic mirror spacing is given by

$$d_0 = \frac{c}{2 f_{d_{\max}}}$$

Which may be put in terms of the maximum velocity to be measured giving

$$d_0 = \frac{c \lambda_0}{2 v_{\max} [\cos \theta - \cos (\theta + \phi)]}$$

Since zero velocity is associated with mirror spacing  $d_0$  and  $v_{\max}$  is associated with  $d_1$ , any intermediate mirror spacing will be proportional to a velocity between zero and  $v_{\max}$ . The oscilloscope presentation of the reference markers and an intermediate wavelength (velocity) are shown in Figure 5. The presentation of the particle signal is of such a short duration (on the order of 100 nanoseconds in these tests) that it appears as a spike. As shown, the value of any intermediate velocity is obtained by the linear interpolation.

$$v = \frac{a}{b} v_{\max}$$

where  $a$  and  $b$  are the geometric measurements shown in Figure 5.

## UNCLASSIFIED

By sweeping through the velocity regime present in the flow we obtain an oscilloscope presentation which is the locus of maximum signals vs velocity. It was further concluded that this locus represented the largest particle with that velocity. For the optical and flow parameters of this study it was shown<sup>2,3</sup> that the likelihood of simultaneous multiple exposure of particles with the same velocity was remote.

Figure 6 illustrates the lightscattering vs velocity profiles obtained from the three particle materials used thus far in the cold-flow studies: water mist, aluminum oxide abrasive, and aluminum spheres. For particles of a unique velocity both in magnitude and direction, interferometer theory predicts the upper curve of the two water mist curves. The experimental results obtained from a very finely divided water mist at 11 psig chamber pressure exhausting through a 1/16" throat diameter converging nozzle are shown in the lower curve. The two curves compare very favorably.

The aluminum oxide abrasive used had a very narrow size distribution centered at .3 micron diameter. Constant lag two-phase flow theory for spherical particles of this same material predicts a velocity of approximately 450 meters/sec with a nitrogen chamber pressure of 100 psia exhausting through a 1/16" throat diameter supersonic nozzle. (Throat radius of curvature to throat-radius ratio was 150). The resultant experimental velocity profile is shown in the lower figure. The low velocity portion of the profile is very nearly that of the shape predicted by interferometer theory, but the high velocity portion is spread out. Noting the general low velocity compared to the two-phase theory prediction, and the irregular shape of the particles it was concluded that this profile was the result of the flow of irregular agglomerates of varying sizes.

UNCLASSIFIED

## UNCLASSIFIED

The last material investigated was aluminum in the form of .1 to 20 micron diameter spheres. The velocity profile predicted by the combination of interferometer, lightscattering and two-phase flow theories is shown in the upper figure in Figure 6. The experimental profile showed considerable broadening in the low velocity regime. This broadening was shown to be reliably predicted by collisions among the particles. The existence of significant collision broadening requires that the assumptions that all particles have no significant radial velocity component and that each particle has a unique velocity predictable by two-phase flow theory alone must be discarded. As a result the experimental velocity profile must be adjusted; this requires an iterative analysis combining the experimental results and the theories including the effects of collisions on the velocity vector.

The number count vs velocity data obtained from the three materials are shown in Figure 7. The prime value of the number-count data thus far has been its usefulness as an extremely sensitive indicator of particle existence in a velocity regime under investigation. Except for the water mist, detailed analysis of the counting technique showed it to be a complex function of interferometer characteristics, lightscattering characteristics, collisions, particle size distribution, velocity distribution of unique particle sizes, and velocity vector angle.<sup>2,3</sup> Theoretically the system appears partially to bias the count in favor of the larger sizes present at any velocity. Application of the number counting technique to more precise analysis will be the subject for future investigations.

The extension of the application of the velocity-measurement technique to hot flow has just recently begun. Figure 9 illustrates a typical result of the measurement of particle lightscattering and number count in the exhaust of a laboratory demonstrator hybrid rocket engine. This engine utilized gaseous oxygen at 60 psig as the

## UNCLASSIFIED

oxidizer and plexiglass impregnated with 20 percent aluminum by weight for the fuel. As shown, velocities up to 1300 meter/sec were measured with good signal-to-noise ratio even though the measuring system has not yet been optimized for hot flow tests. Similar results have been obtained using the same hybrid engine with 20 percent magnesium instead of aluminum.

It is anticipated that investigations will continue into the usefulness of the number counting technique, cold two-phase flow phenomena, and hot two-phase flow in general. Furthermore, any phenomena involving motion of particles would be amenable to analysis with this technique.

UNCLASSIFIED

# UNCLASSIFIED

## REFERENCES

1. Fulmer, R. D. and D. P. Wirtz: Measurement of Individual Particle Velocities in a Simulated Rocket Exhaust. AIAA Paper No. 65-11 (AIAA New York Meeting, January 25-27, 1965)
2. James, R. N., W. R. Babcock and H. S. Seifert: Application of a Laser-Doppler Technique to the Measurement of Particle Velocity in Gas-Particle Two-Phase Flow. Final Report, AF 04(611)10926. (also Stanford University Department of Aeronautics and Astronautics Report (SUDAAR) No. 265, June 1966).
3. James, R. N.: Application of a Laser-Doppler Technique to the Measurement of Particle Velocity in Gas-Particle Two-Phase Flow. PhD Thesis, Stanford University, June 1966.
4. Censor, D.: Detection of the Transverse Doppler Effect with Laser Light. IEEE Proceedings, Vol 52, August 1964, p. 987.

UNCLASSIFIED

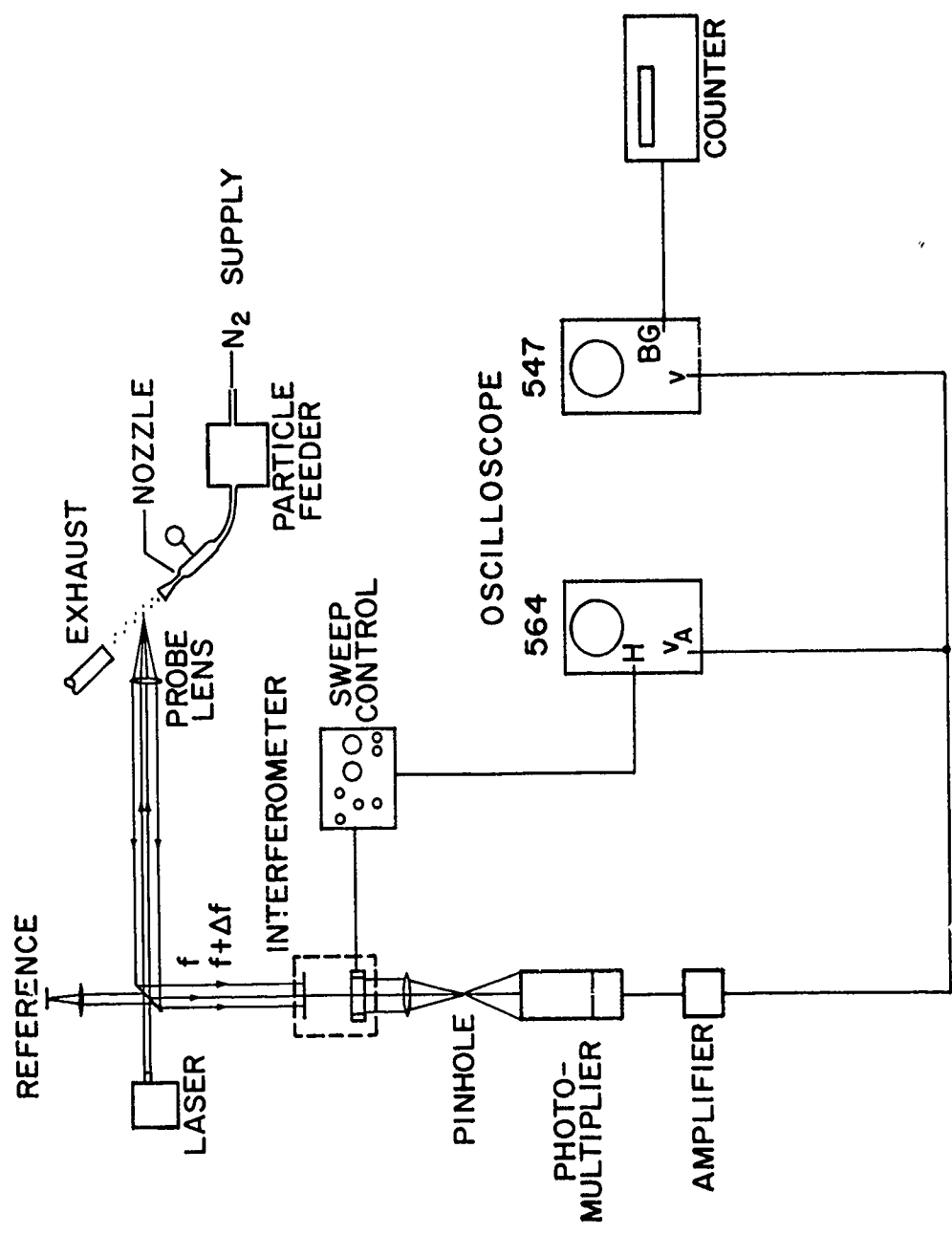
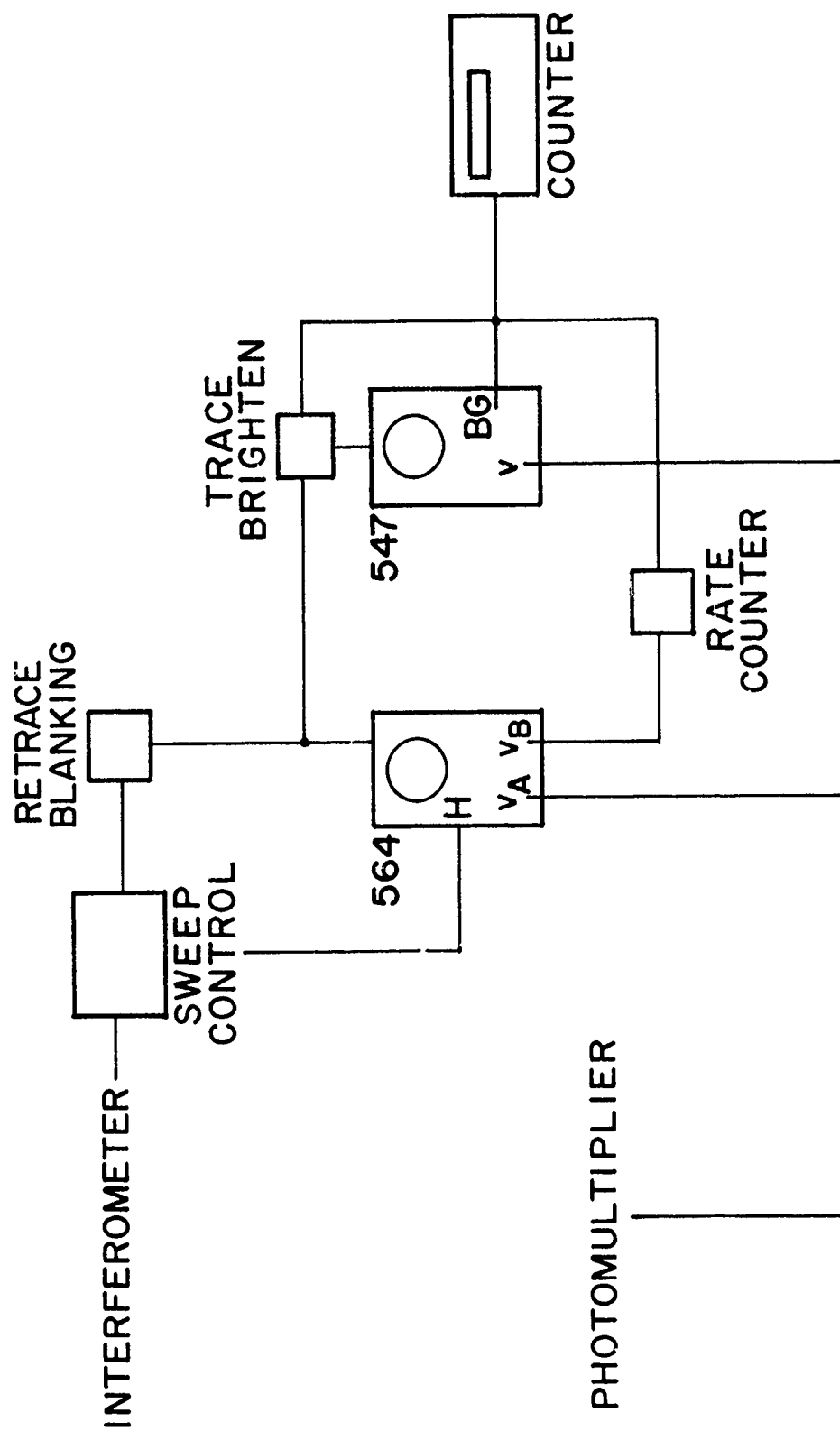


Figure 1. Experimental Layout.

UNCLASSIFIED

UNCLASSIFIED



UNCLASSIFIED

Figure 2. Block Diagram of Instrumentation.

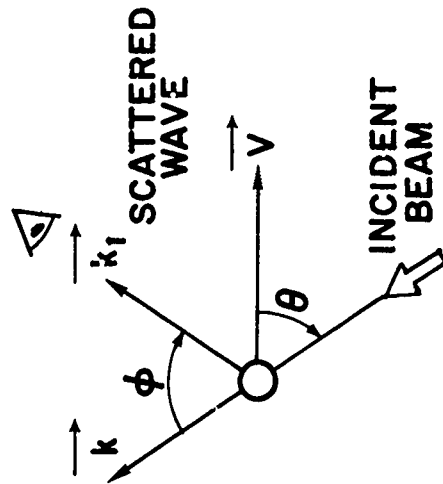


UNCLASSIFIED

$$f_d = \frac{V}{\lambda_0} [\cos \theta - \cos(\theta + \phi)]$$

$$\left[ \frac{1 - \frac{\vec{V} \cdot \vec{k}}{C}}{1 - \frac{\vec{V} \cdot \vec{k}_1}{C}} \right]$$

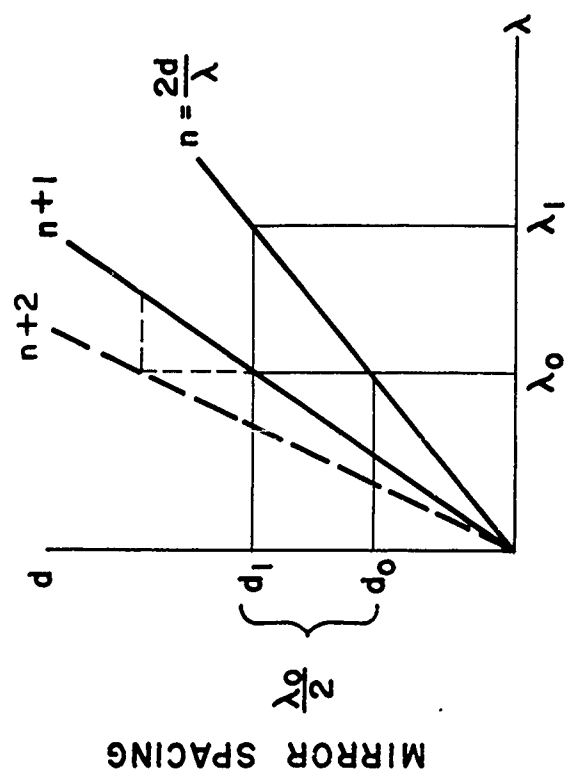
$$f_r = f_0$$



UNCLASSIFIED

Figure 3. Doppler Shift.

UNCLASSIFIED



$$\frac{I}{I_{\max}} = \left[ 1 + \frac{4R}{(1-R)^2} \sin^2 \frac{2\pi d}{\lambda} \right]^{-1}$$

$R = \text{mirror reflectance}$

$$d_0 = \frac{C}{2 |f d m c x|} = \frac{C \lambda_0}{2 V_{\max} [\cos \theta - \cos(\theta + \phi)]}$$

Figure 4. Velocity Measurement.

UNCLASSIFIED

UNCLASSIFIED

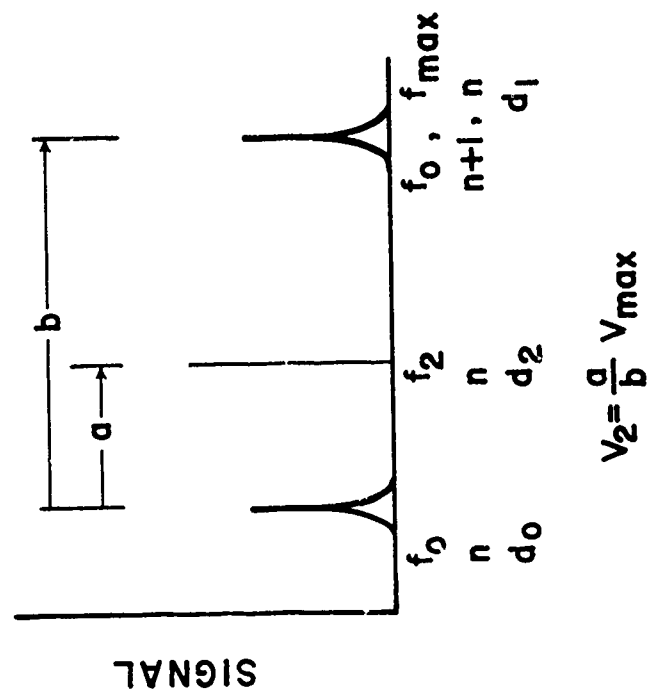


Figure 5. Oscilloscope Presentation.

UNCLASSIFIED

UNCLASSIFIED

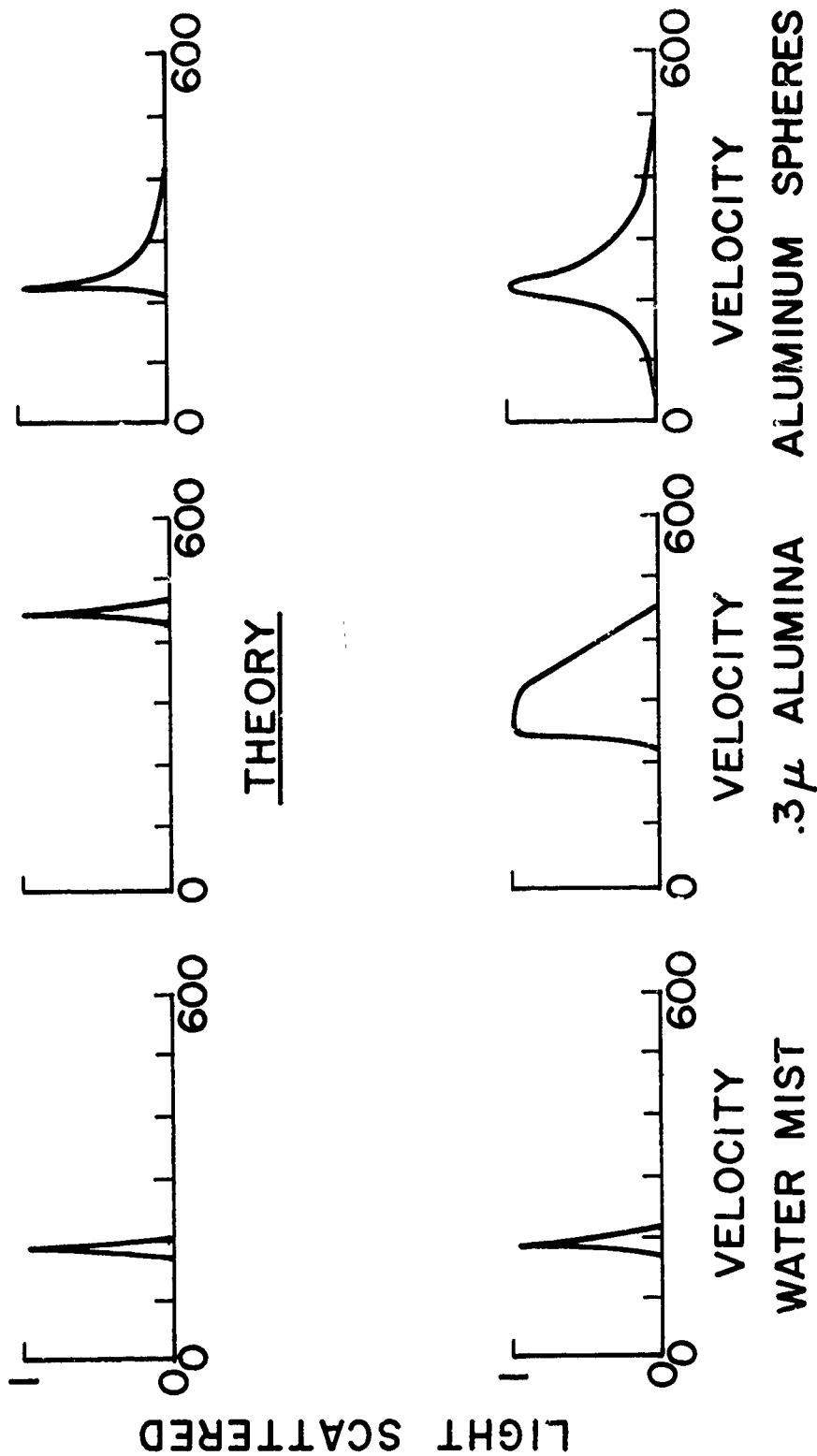


Figure 6. Light Scattering versus Velocity Profiles.

UNCLASSIFIED

UNCLASSIFIED

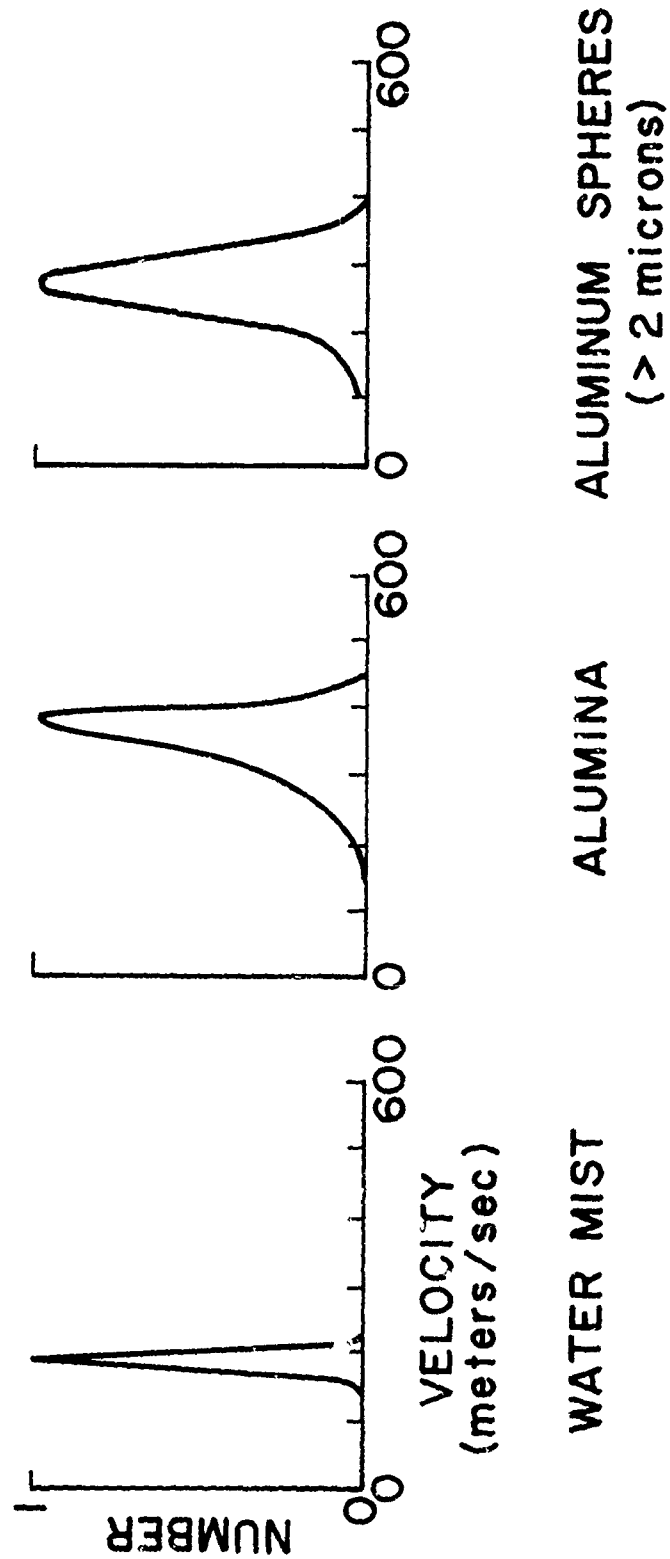


Figure 7. Number Count versus Velocity Data.

UNCLASSIFIED

UNCLASSIFIED

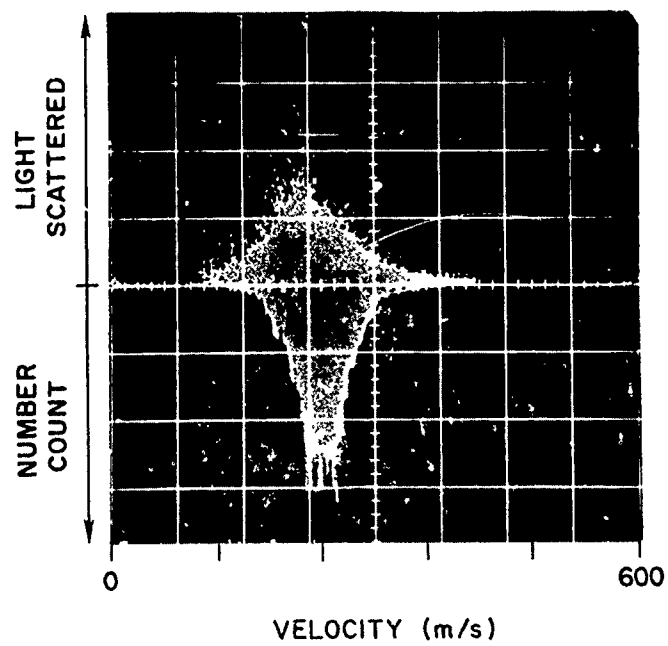


Figure 8. Cold Flow.

UNCLASSIFIED

UNCLASSIFIED

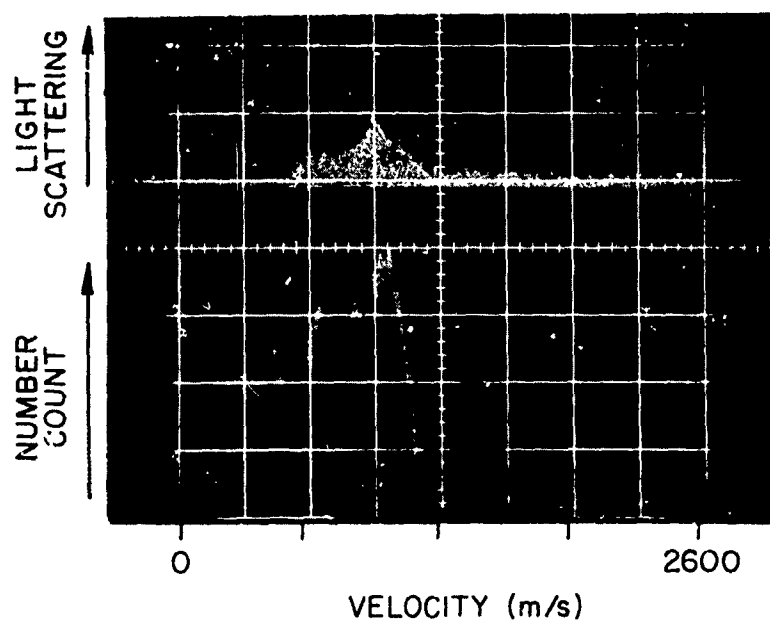


Figure 9. Hot Flow.

UNCLASSIFIED

## UNCLASSIFIED

### QUESTIONS, ANSWERS & COMMENTS:

Q. /R. F. Hoglund (Purdue University): I think the potential both for measuring particle velocities and for using particles as a tracer in otherwise unknown flow fields is obvious. Let me ask if you have tried cross beams to get three-dimensional information:

A. /H. S. Seifert (Stanford University): No, we have not. We only own one laser. There is an aspect that people may not appreciate and that is when you are ready to receive a specific wave length, there has to be a particle in the focal volume with the appropriate velocity. This is a statistical matter, so that if you look across beams, the gate might not be open for the two coincidental appropriate velocity functions.

Q. /R. F. Hoglund (Purdue University): Is it a pulsed laser?

A. /H. S. Seifert (Stanford University): No, it is a CW Laser, mono-mode. The wave length that is let through by the Fabry-Perot is an absolute wave length to 1/1000ths of an angstrom or something like that, so a laser that puts out several different wave lengths separated by 1/100th of an angstrom, would not be suitable.



**UNCLASSIFIED**

**THE MEASUREMENT OF GAS AND PARTICLE TEMPERATURE IN  
ROCKET MOTOR CHAMBERS AND EXHAUST PLUMES**

by

**J. M. ADAMS**

**Aerojet-General Corporation  
Sacramento, California**

**UNCLASSIFIED**

# UNCLASSIFIED

## THE MEASUREMENT OF GAS AND PARTICLE TEMPERATURE IN ROCKET MOTOR CHAMBERS AND EXHAUST PLUMES\*

by

J. M. Adams

Aerojet-General Corp.  
Sacramento, California

### I. INTRODUCTION

The spectrometric method of determining flame temperatures has been used successfully for many years<sup>1, 2, 3</sup>. Successful application of this method to the determination of gas and particle temperatures in rocket motor exhaust plumes and chambers is accomplished only when particular attention is directed to the factors in such a system which can confuse the spectrometric results. These factors include the "searchlight" effect, the light scattering properties of particles, the temperature gradient across the plume, the non-uniformity of particle concentration and the diffusion of air into the plume, causing after-burning.

Over the past year (1965-1966), we have conducted a program with the specific objective of developing the techniques for measurement of gas and particle temperatures, in the chamber and exhaust plumes, of metalized solid-propellant rocket motors. The ultimate objective of this program was to permit a more complete understanding of the combustion and expansion processes in beryllium and beryllium hydride solid propellant systems, a knowledge which would subsequently lead to the improvement of delivered specific impulse efficiency for future propellant systems.

---

\*The work reported herein was sponsored by Edwards AFRPL under Contract AF 04(611)-10545.

UNCLASSIFIED

## UNCLASSIFIED

During this program, measurements of gas and particle temperatures were obtained in the chamber and in the exhaust plume of motors containing metalized solid propellants. Exhaust plume measurements indicated that a large amount of thermal energy was lost from the system in the form of molten oxide particles, particularly during the last portion of the motor firing. It was observed that the "freezing front" (i. e. that region where the particles reach their freezing temperature) passed downstream of the exit plane at some time approximately halfway through the firing. Hence the heat of fusion of the particles made essentially no contribution to the motor specific impulse. Chamber measurements further indicated that considerable combustion occurred downstream of the grain surface, somewhere between the plenum (where the measurements were made) and the exit plane. This is corroborated by the particle temperature measurements. Although the measurements should be considered as preliminary until verified by further tests, they definitely help clarify the combustion-expansion phenomena. Further, they clearly demonstrate the valuable utility of this measurement technique in investigating propellant combustion.

From the knowledge gained during the present effort, earlier measurement techniques which were applicable only to optically-thin regions have been improved to allow treatment of the optically-thick case which is normally encountered in the chambers and plumes of large motors. It is now evident that the incorporation of this more general technique into the present system will permit meaningful and precise measurements which will lead to a more complete understanding of the combustion and expansion phenomena of metalized propellant systems.

## II. DESCRIPTION OF APPARATUS

The apparatus used for the present program is shown in

## UNCLASSIFIED

Figure 1; it has been described in detail elsewhere<sup>4</sup>. It includes a 0.5m Ebert spectrometer, a carbon arc lamp for the reference light source and associated optics. This apparatus, collectively called the Spectral Comparison Pyrometer, was used successfully to make the gas and particle temperature measurements described in this paper.

### III. DESCRIPTION OF METHOD AND ANALYSIS

To determine temperatures of both the gas and the condensed phase in a spectrally absorbing-emitting two-phase medium, it is necessary to determine the emittance and radiance associated with the continuum emission of the condensed-phase cloud and the spectrum line emission of the gas. The emittance is determined by measurement of the extinction of a beam of light from a reference light source (e. g. a tungsten ribbon lamp of known brightness temperature). This extinction occurs due to both absorption and scattering but each contribution can be isolated through the use of the Mie scattering theory\* with a knowledge of the complex refractive index and particle size distribution for the particles present. From this treatment, the absorptance of the particle cloud can readily be determined in the optically thin case. For a system in thermal equilibrium,<sup>†</sup> the emittance of the cloud is equated to the absorptance from Kirchhoff's Law.

Figure 2 presents the normal and hemispherical emittance as a function of optical depth,  $\delta$ , with  $\gamma_a/\gamma_t$  as a parameter. This curve, reproduced by permission of C. D. Bartky is the result of work by Bartky<sup>6</sup> and by Romanova<sup>7</sup> on special solutions of the radiative transfer equation<sup>8</sup>. An "optically thin" cloud of scatterers and absorbers corresponds to that region to the left of Figure 2 where the lines are

---

\*The details of the Mie scattering theory are given by Van de Hulst<sup>5</sup>.

†Although the reference light source and the cloud are, in general, not in thermal equilibrium with each other, no appreciable heating of the cloud occurs by absorption of the reference light source beam, and Kirchhoff's Law is applicable.

## UNCLASSIFIED

straight, values of  $\delta$  corresponding to the "knee" of the curves are associated with "optically thick" clouds. Finally when the emittance reaches its maximum value, a condition of "infinite optical depth" is said to exist.

### A. OPTICALLY THIN CLOUDS

Measurements of plume radiance and transmittance are made within a region defined by the acceptor optics as shown in Figure 3.\* This region takes the form of two colinear thin cones having a common apex at the centerline of the plume. It is the scattering and absorption of the reference light source beam and the emission of the gas and particles within this region which are considered. The depth and particle concentration along the cone centerline defines the optical depth. For the case of exhaust plumes of LKS motors, the optical depth is approaching the "optically thick" case, but the "optically thin" analysis can be used with an error in temperatures of less than 1%.

Light collected by the acceptor optics is passed to the spectrometer where it is spectrally dispersed across the exit slit, causing an emf to be generated by the detector. In the following equations,  $E_{ij}$  represents a resulting galvanometer deflection at  $\lambda_i$  and  $R_j$ , and  $K_{ij}$  is a system multiplication constant which includes the response characteristics of the optical system, spectrometer, phototube, and galvanometer. The galvanometer deflection is related to the radiance incident upon the phototube through the equation:

$$E_{ij}K_{ij} = R(\lambda_i, T_j), \text{ the radiance}$$

Prior to making measurements on a flame, with only the reference source on, measurements of galvanometer deflection are

---

\*The apparatus shown in this figure represents one particular configuration of that shown in Figure 1.

# UNCLASSIFIED

made at various source temperatures. The deflection is related to the continuum emission from the source at  $\lambda_1$  by equation 1, which also accounts for the transmissivity,  $\tau_w$ , of both lenses or windows on either side of the flame:

$$E_{10} K_{10} = \frac{\epsilon_s(\lambda_1, T_s) \tau_{w1}^2}{\lambda_1^5 \left( \exp\left(-\frac{C_2}{T_s}\right) - 1 \right)} \quad (1)$$

In the presence of the flame the measured galvanometer deflection at  $\lambda_1$  of the continuum is related to the radiance emitted by the particles with equation 2:

$$E_{12} K_{12} = \tau_{w1} \epsilon_p(\lambda_1, T_p) R_1^0(\lambda_1, T_p) \quad (2)$$

where the particle cloud emittance,  $\epsilon_p(\lambda_1, T_p)$  is given by:

$$\epsilon_p(\lambda_1, T_p) = 1 - \exp(-\tilde{N} \gamma_a t) \quad (3)$$

To better explain the relationship shown in Figure 2, equation 3 can be rewritten as:

$$\begin{aligned} \epsilon_p(\lambda_1, T_p) &= \tilde{N} \gamma_a t \quad \text{where } \tilde{N} \gamma_a t < 0.1 \\ &= \tilde{N} (\gamma_a + \gamma_s) t (\gamma_a / \gamma_t) \end{aligned}$$

which would give a straight line relationship between  $\ln \epsilon_p$  and  $\ln \tilde{N}(\gamma_a + \gamma_s)t$ , as is shown at the left of Figure 2. For a hypothetical cloud which has dimensions almost the same as those of the receptor "cones", radiation emitted from the far side of the region would be scattered and absorbed as it passed through the region toward the

UNCLASSIFIED

## UNCLASSIFIED

receptor. Thus the detector would see a lesser contribution from the more distant regions due to a net scattering loss. This condition, which probably could not arise in motor exhaust plumes, is termed the thin-transverse case and was analyzed by Adams<sup>9</sup>. The other extreme case, called the thick-transverse case, where the transverse and longitudinal dimensions are roughly equal, results in no net loss due to scattering of light emitted from far regions because scattering into the volume in a direction toward the receptor is equal to that light lost by scattering in this direction. Thus, the radiation collected by the receptor does not depend on the scattering cross section of the particles, and equations 2 and 3 result.

This is not characteristic of the reference light source beam as it traverses the plume, however. Because the source beam is anisotropic and because there is not thermal equilibrium between the plume and the source, light scattered out of the receptor cones is not scattered back entirely, but some absorption occurs outside of this volume. It will, for the present, be assumed that all the radiation from the reference source beam which is scattered out of a control volume is permanently lost. Actually, of course, some of this radiation is recovered.

Equations 1 through 7, relating the gas and particle temperature to the measurements of radiance cover the case just discussed and have been incorporated into an existing computer program which is used to reduce the exhaust plume measurements.

With the reference source on, the measured signal is the sum of the transmitted source intensity and that coming from the particle emission, and is given by equation 4:

# UNCLASSIFIED

$$E_{11}K_{11} = \tau_{w1} [1 - \exp(-\tilde{N} \gamma_{a1} t)] R_1^0(\lambda_1, T_p) + \tau_{w1}^2 [\exp(-\tilde{N}(\gamma_{a1} + \gamma_{s1})t)] R_1^0(\lambda_1, T_s) \epsilon_s(\lambda_1, T_s) \quad (4)$$

At  $\lambda_2$ , a spectrum line is generated by the trace element and emission from both the particles and the gas occurs. This radiance is determined from equation 5:

$$E_{22}K_{22} = \frac{\tau_{w2} \gamma_g}{\tilde{N} \gamma_{a2} + \gamma_g} [1 - \exp(-\tilde{N} \gamma_{a2} + \gamma_g)t] R_i^0(\lambda_2, T_g) + \frac{\tau_{w2} \tilde{N} \gamma_{a2}}{\tilde{N} \gamma_{a2} + \gamma_g} [1 - \exp(-\tilde{N} \gamma_{a2} + \gamma_g)t] R_i^0(\lambda_2, T_p) \quad (5)$$

With the reference source on, the resulting radiance is the sum of that from the continuum emission by the particles, the spectrum line emission by the gas (trace element) and that transmitted through the flame from the reference source beam. This sum is related to the resulting galvanometer deflection by equation 6:

$$E_{21}K_{21} = E_{22}K_{22} + \tau_{w2}^2 [\exp(-\tilde{N}(\gamma_{a2} + \gamma_{s2}) + \gamma_g)t] R_i^0(\lambda_2, T_s) \epsilon_s(\lambda_2, T_s) \quad (6)$$

where:

$$R_i^0(\lambda_i, T_j) = \frac{1}{\lambda_i^5 (\exp(\frac{C_2}{\lambda_i T_j}) - 1)} \quad (7)$$

## B. OPTICALLY THICK CLOUDS

### 1. Optical Depth

The number density of particles or droplets in a

UNCLASSIFIED



# UNCLASSIFIED

combustion chamber or plume can be calculated from the relation

$$\tilde{N} = \frac{\rho_g X}{(1-x) \rho_L \bar{V} L_u} \quad (8)$$

where  $L_u$ , the velocity lag =  $u_p/u_g$

$$\bar{V} = \text{mean particle volume} = \int_0^{\infty} f(D) \frac{\pi D^3}{6} dD \quad (9)$$

$$\text{The relation } \int_0^{\infty} f(D) dD = 1 \quad (10)$$

defines the normalized frequency function,  $f(D)$ .

$X$  is the mass fraction of particles

$\rho_L$ ,  $\rho_g$  are the condensed phase and gas densities, respectively.

The optical depth,  $\delta$ , is then given by:

$$\delta = \frac{\rho_g X}{(1-X) \rho_L L_u} \cdot \left( \frac{\gamma_a + \gamma_s}{\bar{V}} \right) \cdot t \quad (11)$$

Properties of  
propellant and  
system

Properties of  
particle size  
and refractive  
index

Actual  
thickness  
of plume

which we will write as:

$$\delta = \xi \cdot (\gamma_t / \bar{V}) \cdot t. \quad (11)'$$

# UNCLASSIFIED

## 2. Extinction Parameter

$$\text{Since } \gamma_t / \bar{V} = f_1(\bar{D}, \sigma) \quad (12)$$

where  $\bar{D}$  is the mean diameter and  
 $\sigma$  is the size distribution function,

$$\text{and since } \gamma_a / \gamma_t = f_2(\bar{D}, \sigma) \quad (13)$$

we can write

$$\gamma_a / \gamma_t = f_3(\gamma_t / \bar{V}), \quad (14)$$

which dependence is presented in Figures 4 and 5 for a cloud at beryllia particles.\* The refractive index for beryllia was determined from measurements of Kendall<sup>10</sup> and Bauer<sup>11</sup>. The dependence of the absorption index of beryllia on temperature was determined by a rather tenuous extrapolation of the data at room temperature, assuming a temperature dependence similar to that of alumina.

## 3. Particle Cloud Emittance

Having the relationship expressed by Figure 4 and 5, the emittance of a cloud can be determined from Figure 2, since

$$\epsilon_p = (\gamma_a / \gamma_t, \delta)$$

\*These figures were generated by varying  $D_{\max}$  of Figure 6 and obtaining  $\gamma_a$ ,  $\gamma_s$ ,  $\bar{V}$  for each distribution by integration of the form

$$\frac{\gamma_i}{\gamma_t} = \int_0^\infty \gamma_i(D) f(D) dD.$$

The resultant functions were cross-plotted to give Figures 4 and 5.

## UNCLASSIFIED

and hence

$$\epsilon_p = \epsilon(\tau_a/\tau_t, \tau_t/\bar{V}, \xi, t) \quad (15)$$

where  $\xi$  is determined from the propellant and system properties. The resulting relationship for a typical propellant is shown in Figure 7.

#### 4. Gas Emittance

For optically thick clouds, the gas emittance presents a slightly different but no less difficult problem than that which has just been discussed. The gas emittance in the optically thick region\* is determined from measurements conducted on the same gas in an optically thin region\* downstream. The gas spectral emission coefficient, given by

$$\tau_g = -\frac{1}{t} \ln(1 - \epsilon_g) \quad (16)$$

(for optically thin regions) is determined for the optically thick zone through the method shown by Buchele<sup>12</sup>. Having  $\tau_g$ , the gas emissivity can be determined from the parameters

$$\frac{\tau_g}{\tilde{N}(\tau_a + \tau_s) + \tau_g} \text{ and } [\tilde{N}(\tau_a + \tau_s) + \tau_g]_t$$

by computational technique which is similar to that used in the determination of particle cloud emissivity.

#### IV. RESULTS

The following paragraphs present some of the results of the

---

\*Condition on optical depth refers to particle cloud.

## UNCLASSIFIED

measurements of gas and particle temperature in small flames and rocket motors, and the optical properties of molten alumina. For a more complete description, the reader is referred to Colucci and Adams<sup>4</sup>.

### A. PRECISION, SMALL FLAMES

The precision of the temperature measurements is determined from the source variance, i. e., that variance from a large set of recorded measurements of radiancy from the reference light source. With the hydrogen/oxygen flame operating, a measured variance in flame temperature larger than the aforementioned source variance must be due to fluctuations in the flame temperature during the run. This variance is termed the temperature variance. When particles are added to the stream, still more uncertainty will result; due to the character of the particulate emission and the effect of scattering, the resulting variance calculated from the latter measurements is termed the gross temperature variance. This second variance is not necessarily indicative of precision but only indicates the temperature fluctuation during the measurement.

An estimate of the temperature variance can be obtained by examining data from measurements on  $H_2/O_2$  flames containing  $Al_2O_3$  particles. Table I presents some typical results of this investigation.\*

---

\* See Adams and Colucci<sup>13</sup> for details of the measurements and data reduction.

# UNCLASSIFIED

TABLE I  
PRECISION OF FLAME TEMPERATURE MEASUREMENTS

Std. Dev. $\sigma$ , °K	Degrees of Freedom	Remarks
16.5	25	Gas temperature, clean gas
40.8	50	Gas temperature with particles
140.0	50	Particle cloud

It is felt that the first value in the table represents a value very close to the minimum value which can be obtained in a measurement of this type. The second figure is larger because it reflects the uncertainty in the change of emittance from the particle cloud from  $\lambda_1$  to  $\lambda_2$ . the last number, representing the standard deviation in particle temperature, reflects the uncertainty in  $n'$ , the absorption index for molten alumina. Measurements of the absorption index are described in the following paragraphs.

## B. ABSORPTION INDEX OF MOLTEN ALUMINA

To relate particle temperature to the continuum emission of the particle cloud and to determine the effect on these measurements of scattering by the particles, a knowledge of the refractive index of the condensed phase is required. The refractive index is a complex number, i. e. ,

$$m = n - n'i \quad (17)$$

where  $n$  is a measure of the change in the speed of light in the medium (in this case,  $\text{Al}_2\text{O}_3(l)$ ) relative to the value in the surrounding medium, and  $n'$  is related to the absorption or attenuation of the light beam in the medium. Absorption in the medium can be described through the relation:

## UNCLASSIFIED

$$I = I_0 e^{-\gamma t} \quad (18)$$

where  $\gamma$  is the usual absorption coefficient and  $t$  is the thickness. It can be readily shown that  $n'$  is related to the absorption coefficient in the medium by the following:

$$\gamma = 2n'k = \frac{4\pi n'}{\lambda} \quad (19)$$

For a system of scatterers it can be shown (although not so readily) that the absorption cross section,  $\gamma_a$ , used to determine the emittance of the particle cloud by

$$\epsilon_p = 1 - \exp(-\tilde{N} \gamma_a t) \quad (20)$$

is approximately directly proportional to  $n'$ , i.e.

$$\gamma_a \propto n' \quad (21)$$

From the above it is obvious that in order to obtain accuracy in the determination of particle cloud emittance (and hence temperature),  $n'$  must be known to within close limits.

Data obtained by Gryvnak and Burch<sup>14</sup> indicate that a value of  $\gamma = 1 \text{ mm}^{-1}$  is likely at the melting temperature, where they observed a sharp increase in the alumina emittance. Unfortunately they could not measure the thickness of the molten sample and hence could not determine  $\gamma$  to a reasonable precision. However, using the value of  $\gamma = 1 \text{ mm}^{-1}$

UNCLASSIFIED

# UNCLASSIFIED

$$n' = \frac{\lambda \gamma}{4} = 0.00008 \text{ at } 1\mu.$$

Table II indicates the dependence of  $T_p$  on  $n'$ , using the data from a motor firing. This table was generated by calculating an absorption cross section,  $\gamma_a$ , for each given value of  $n'$ . The corresponding cloud emittance was then obtained from Equation 20. The calculation of particle temperature followed.

TABLE II  
PARTICLE TEMPERATURE, DETERMINED FROM SPECTROSCOPIC MEASUREMENTS - DEPENDENCE ON  $n'$ .

$m = 1.799 - n'i (15)$		
$T_p (.1 \text{ sec})^*$ °K	$T_p (.7 \text{ sec})^*$ °K	$n'$
3662	3805	.0005
3332	3453	.001
2804	2899	.005

\*Time refers to elapsed time from start of firing. Measurements made at the exit plane of rocket motor nozzle.

If the values presented in Table II were the only measurements of temperature available to us, we would suspect that  $n' > .001$ , since for values of  $n'$  less than .001, the temperatures determined from the spectral measurements are unreasonably high.

Fortunately there are other measurements on  $Al_2O_3$  particle cloud emission which can be used<sup>17</sup>. These were obtained on a  $H_2/O_2$  flame into which  $Al_2O_3$  particles were injected at temperatures from 2600°K to 3000°K. Particle absorption cross sections were determined from emittance measurements and are presented in Table III together with cross sections calculated from the Mie theory for various values of  $n'$ . The same treatment was given to the data of

# UNCLASSIFIED

Carlson and Du Puis<sup>16</sup> and these values are shown in Table IV.

The results of Carlson and Du Puis<sup>16</sup> agree with those of Adams<sup>17</sup> to within the uncertainty in all the measurements of both studies. From the data of both Tables III and IV the best value of  $n'$  appears to be  $\approx 0.005$  for the range of variables used in this study. The recommended complex refractive index of alumina, is given by

$$m = 1.799 - .005i \text{ (T} \approx \text{melting point of Al}_2\text{O}_3, \lambda \approx .6\mu\text{)}.$$

TABLE III  
DETERMINATION OF  $n'$  FOR MOLTEN ALUMINA, OBTAINED FROM  
EXPERIMENTS ON FLAMES CONTAINING PARTICLES<sup>17</sup>

Calculated $\gamma_a$ , Mie Scattering Theory:			
$n'$	$\gamma_a(\lambda = .588\mu)$		
0.0001	$1.1508 \times 10^{-13} \text{ cm}^2$		
0.0005	$5.7435 \times 10^{-13} \text{ cm}^2$		
0.001	$1.146 \times 10^{-12}$		
0.005	$5.623 \times 10^{-12}$		
0.01	$1.099 \times 10^{-11}$		
Measured $\gamma_a$ , Experiments on $\text{H}_2/\text{O}_2$ flames:			
Run	$\gamma_a(\lambda = .588 \mu)$	$T_g(^{\circ}\text{K})$	$n'$ (by interpolation)
1	$7.2 \times 10^{-12} \text{ cm}^2$	2685	0.0079
2	$3.9 \times 10^{-12}$	2466	0.0043
3	$6.5 \times 10^{-12}$	2750	0.0072
4	$8.5 \times 10^{-12}$	2885	0.0094
5	$7.6 \times 10^{-12}$	2700	0.0084

$$\text{avg. } n' = 0.0074 \pm 0.0019 \text{ (2500-2900)*}$$

\* Std deviation on measured  $\gamma_a = 0.5 \times 10^{-12}$  for 25-30 degrees of freedom.



# UNCLASSIFIED

TABLE IV  
DETERMINATION OF  $n'$  FOR MOLTEN ALUMINA, OBTAINED  
FROM MEASUREMENTS OF CARLSON<sup>16</sup>

Calculated $\gamma_a$ , Mie Scattering Theory*:		
$n'$	$\lambda = 1.3\mu$	$\lambda = 1.7\mu$
0.00005	$7.4 \times 10^{-11}$	$4.7 \times 10^{-11}$
0.0001	$1.475 \times 10^{-10}$	$8.336 \times 10^{-11}$
0.0005	$7.19 \times 10^{-10}$	$4.15 \times 10^{-10}$
0.001	$1.43 \times 10^{-9}$	$8.32 \times 10^{-10}$
0.005	$6.95 \times 10^{-9}$	$4.01 \times 10^{-9}$
Measured $\gamma_a$ , determined from emittance measurements <sup>†</sup> :		
$\gamma_a$ (all $\lambda$ )	T (°K)	$n'$ (by interpolation)
$1.94 \times 10^{-10}$	2320	0.000181
$2.74 \times 10^{-10}$	2460	0.000258
$6.3 \times 10^{-10}$	2600	0.000595
$1.65 \times 10^{-9}$	2800	0.00155
$3.33 \times 10^{-9}$	3000	0.00326

\*Conditions on particle size distribution from Figure 3<sup>16</sup>.

†Calculations shown in <sup>4</sup>. Emittance values obtained by averaging points above 2320°K in Figure 12<sup>16</sup>.

## C. GAS AND PARTICLE TEMPERATURE MEASUREMENTS

With the apparatus set up around the exit of the rocket motor as shown in Figure 3, measurements of particle cloud and gas spectral emittance and spectral radiance were taken at wavelengths around  $\lambda = 0.589\mu$ , at a position about 0.5 inch downstream of the exit plane of the nozzle. The motors used for these tests were of the configuration shown in Figure 8 which contains about one pound of propellant and, at a chamber pressure of 600-1000 psia, generates a thrust of 250-350 lb<sub>f</sub>.

\*See Table IX for summary of test conditions. This table relates motor test numbers to propellant type.

## UNCLASSIFIED

After the first two motor tests, \* the carbon arc reference source was placed close to the exhaust plume and measurements were taken at a point approximately 0.5 in. downstream from the exit plane. The fiber bundles and rotating sampling scanners had been eliminated in order to increase the radiance of the reference source approximately 15 times. Satisfactory determinations of temperature were then obtained from the light extinction and emission measurements; the results of Motor Test 3 are presented in Table VI.

TABLE VI  
MEASURED TEMPERATURES ON IKS-250 MOTOR NO. 3

Time, <u>sec</u>	Temp, <u>°K</u>
0.1	2804
0.2	2822
0.3	2845
0.4	2856
0.7	2899

The measurements, which show that the particles are still in the molten state, are an indication of conditions at the center of the plume. This is true because of the narrow "depth of field" of the receptor optical system; i. e., more light from the center of the plume strikes the detector than that from any other region.

---

\*No temperatures could be determined from the data of Tests 1 and 2 within reasonable limits because a lack of detectable penetration of the reference source beam through the plume or chamber precluded a determination of plume emissivity. As was shown earlier, for optically thick regions reasonable limits on emissivity can be established even in the absence of a good light extinction measurement. However, in motor tests 1 and 2, the plume was not optically thick, and hence, the minimum limit for emissivity is extremely low ( $\sim 0.2$ ). The measurements taken in the chamber (which is optically thick) were obscured because of melting of the viewport probe tips. The firings did serve the useful function of delineating unforeseen difficulties in measurement techniques on motors.

UNCLASSIFIED

## UNCLASSIFIED

Successful measurements of both gas and particle temperatures were made on the fourth motor test, with the apparatus positioned as in the third test. These results, which are presented in Figure 9, indicate that the thermal lag between particles and gas reached a value greater than  $700^{\circ}\text{K}$ . These measurements can be compared to theoretical temperatures presented in Table VII, which were calculated for the cases of frozen (at both chamber and throat) and shifting equilibrium, where the particles are either solidified or supercooled.

The particle temperatures determined from measurements on Test 3 are higher than those for Test 4, a difference which cannot be due to random fluctuations. The measurements made on Test 3 were of much less precision, as previously mentioned, because there was insufficient gain on the recording channel to obtain a reasonable galvanometer deflection. This condition was corrected on Test 4.

It can be seen from Figure 9 that the measured gas temperature, although initially at a relatively low value ( $1902^{\circ}\text{K}$ ) rises during the firing to a level above that predicted for the shifting equilibrium case No. 6 (Table VII). The particle temperatures are also seen to rise, always remaining far above the melting temperature. The excessive particle temperature suggests that combustion is occurring at this point in the exhaust plume, resulting in an "effective" particle temperature. If either active combustion is occurring at this station or if appreciable molten alumina exists here, the measured particle temperature will be higher than expected. In the former case, i. e., where active combustion is occurring near the droplet surface, the measurement will indicate a temperature somewhere between the freshly condensed liquid alumina temperature (near the reaction zone) and the surface temperature of the parent drop. If molten aluminum metal exists here, the emissivity based on the refractive index of the oxide is incorrect and a higher temperature results.

## UNCLASSIFIED

Gas and particle temperatures were also measured successfully in the exhaust plumes of two 1KS-250 motors having beryllium and beryllium hydride propellant. These measurements are presented in Figures 10 and 11, where the chamber pressure trace is also indicated for comparison.

Figure 10 indicates that little thermal lag occurred in the beryllium propellant test. The gas and particle temperatures appear to follow each other rather closely, but since they are both above the theoretical temperature at this station, some combustion must have occurred during the expansion process. This conclusion is strengthened by the chamber temperature measurements which were made in this propellant system; they are shown below.

Greater thermal lag is apparent from Figure 11 for the beryllium hydride propellant test. It can be seen from the figure that the beryllium oxide "freezing front" passed the measurement station at  $t = 0.3$  sec. As in the case of aluminum, the measurements indicate continuing combustion for the reasons previously given.

Some additional insight into beryllium propellant combustion was gained from measurements of gas and particle temperature in a plenum located just aft of a burning grain of beryllium propellant. These measurements are shown in Table VIII. The results are extremely interesting because they seem to indicate incomplete combustion in the chamber region. More measurements are definitely required, particularly with the well-characterized aluminum propellant which would serve as a good standard of comparison.

UNCLASSIFIED

# UNCLASSIFIED

TABLE VII  
THEORETICAL TEMPERATURE FOR 1KS-250 MOTORS AT  
MEASUREMENT STATION, ALUMINIZED PROPELLANT

One-dimensional case,  $P_c$ : 400 to 1000 psia      Expansion ratio: 9.74

Conditions in one-dimensional computation	Temperature, °K (Assuming no thermal lag)
1-Frozen equilibrium at chamber with supercooling of particles	1810
2-Frozen equilibrium at throat with supercooling of particles	1880
3-Frozen equilibrium at chamber with solidification of particles	2020
4-Frozen equilibrium at throat with solidification of particles	2100
5-Shifting equilibrium with supercooling of particles	2160
6-Shifting equilibrium with solidification of particles	2277

Axisymmetric case, <sup>1</sup> determination of radial temperature profile at  $A/A^*$  of 9.74.

$P_c$ , psia	Temperature, °K		
	Center	Min. Temp.	Edge
700	2000	1970	2319
400	2130	2090	2460

<sup>1</sup> Estimate for shifting equilibrium with supercooling. These numbers serve only to indicate the radial temperature profile across the plume.

# UNCLASSIFIED

TABLE VIII  
MEASURED TEMPERATURES, BERYLLIUM PROPELLANT  
CHAMBER PLENUM REGION, 1KS-250 MOTOR

	$T_g, ^\circ K$	$T_p, ^\circ K$
Upper* Limit	3430	3035
Lower Limit	3340	2880

Theoretical Temperature:  $3570^\circ K$

\*This uncertainty is due to the combined uncertainties in particle cloud emissivity and window transmissivity. The limits of emissivity are discussed under "Analysis for Optically Thick Clouds," presented earlier.

A calculation of particle temperature assuming convection to be the important heat transfer mechanism to beryllium drops of one-micron diameter indicates that the droplet temperature in the chamber could lag the gas temperature by only  $10^\circ K$ , a conservative result which is not borne out by the measurements. Instead, the measurements indicate that the phase change from  $Be_{(l)}$  to  $Be_{(g)}$  is occurring at temperatures lower than the saturation temperature (corresponding to the chamber pressure) and that this vaporization/ $Be_{(g)}$  diffusion process is the rate-controlling process which prevents sufficient combustion of beryllium in the chamber. The model for the combustion of beryllium is similar to that used in the studies of aluminum combustion, i. e., an evaporating droplet within a spherical laminar diffusion flame. An analytical study using this model should be very enlightening, resulting in a good prediction of particle temperatures and fraction of metal burned at various axial stations.

More tests are required with similar motors to increase the statistical confidence in the measurements and eliminate the

UNCLASSIFIED

## UNCLASSIFIED

possibility of some heretofore unknown systematic bias which could cause cause erroneous measurements. However, there is no reason to doubt the validity of the measurements, and there are several possibilities which can account for the difference between the calculated and theoretical temperatures (in addition to the considerations already mentioned):

1. Air is diffusing into and reacting with the gases in the exhaust plume. This phenomenon was observed to occur during radar attenuation studies<sup>18</sup> on exhaust plumes, where it accounted for appreciable increase in plume temperature. The effect can be minimized through the use of a nitrogen "blanket" in subsequent exhaust plume studies. Because of the close proximity of the measurement station to the nozzle exit, this effect cannot be very important.

2. The uncertainty in the thermodynamic data which must be used to establish the composition of the gas and the relationship between the internal energy of the gas and its temperature, could alone account for more than half the observed difference between the theoretical and measured temperatures.

3. Disequilibrium between the sodium and the surrounding gas could account for a higher observed temperature; however, a conservative estimate of the extent of this effect could account for an increase of less than  $10^{\circ}\text{K}$ .

### D. LIGHT SCATTERING AND EXTINCTION MEASUREMENTS\*

The particle size and number density used in the determination of cloud emittance could not be obtained from the light scattering measurements with much confidence. They were determined from the extinction parameter  $\gamma_t/\bar{V}$  at  $\lambda = 0.588\mu$ , obtained by measurements of extinction of the reference light source beam together with data on plume thickness, alumina mass fraction and gas density. A

\*The relationship between extinction parameter and the optical depth is given in equation 11. Figure 6 shows the particle size distribution (typical unimodal) used to generate the broken curve in Figure 12.

## UNCLASSIFIED

curve of extinction parameter versus particle diameter was generated from the Mie theory, and is presented in Figure 12, where the measured coefficients are also shown.<sup>†</sup> Also shown on this figure (footnote 3) is the value of extinction parameter for the particle size distribution of Figure 13. This latter curve was obtained from a photomicroscopic examination of a sample of particles taken during Test No. 4 with a high-voltage particle precipitator stationed about 4 ft downstream of the motor exit plane. There are two values of (number) mean particle diameter corresponding to the measured values of extinction parameter. The larger of the two possible diameters is the most probable, judging from the particle sample taken during the firing. Also, since the extinction parameter decreased (as the pressure increased) during the firing, it seems more likely that this is attributed to an increasing particle size (associated with the larger values of diameter on the curve (Figure 12)) since agglomeration of the particles should be proportional to pressure. The determination of mean particle diameter during the test is only incidental to the analysis and is not necessary to the computation of particle temperature. Instead, once  $\gamma_t/\bar{V}$  is determined from the extinction measurements, the parameter  $\gamma_a/\gamma_t$  can be found from which emissivity and then temperatures are computed. As shown earlier, the functional relationship or  $\gamma_a/\gamma_t$  to  $\gamma_t/\bar{V}$  depends on refractive index and the particle size distribution function; fortunately, the latter variable is relatively unimportant to this relationship (v, Figure 5).

<sup>†</sup>See Table IX for summary of test conditions.

UNCLASSIFIED



# UNCLASSIFIED

TABLE IX  
TEST CONDITIONS SUMMARY, 1KS 250 MOTORS

Motor Test No.	Propellant	Measurements Presented in:
1	Aluminum	---
2	Aluminum	---
3	Aluminum	Table VI
4	Aluminum	Figures 9, 12, 13, 14
5	Beryllium Hydride	---
6	Beryllium	Figures 10, 16
7	Beryllium Hydride	Figures 11, 15
8	Beryllium	Figure 15, Table VIII

The extinction coefficient at  $\lambda = 0.436\mu$  was also determined using a mercury arc lamp and is presented in Figure 14, together with a theoretical curve calculated for a typical unimodal distribution (see Figure 6). The data presented in Figure 14 serves to strengthen the conclusion that the effective particle diameter is in the range 0.5 to 0.7 $\mu$  for the aluminum propellant.

Extinction parameters were also measured at 0.589 $\mu$  on Motor Tests 7 and 8,\* again using the measured transmission of the reference light source in the exhaust plume. These measurements are shown in Figure 15, where the extinction parameter is related to mean particle size for a unimodal distribution. As in the cases of Motor Tests 3 and 4, the smaller of the two possible particle sizes was eliminated. The measurements of Sehgal<sup>19</sup> indicated a number mean for a beryllium propellant of less than 0.1 $\mu$ , which would seem to indicate that the smaller of the two sizes was the correct choice. However, examination of the photomicrographs of Sehgal show large spherical particles ( $\sim 1\mu$ ) surrounded by small single crystals of mean diameter

---

\*Table IX relates motor test number and propellant type.

## UNCLASSIFIED

less than  $0.1\mu$ . These small crystals which greatly contribute to the reported size distribution are believed to have come from fracture of the large particles after the beryllium oxide had frozen. This fracture can occur from at least two causes: (1) from the thermal stresses at freezing which occur either during freezing because the solid phase has a higher density than the liquid or after complete freezing due to inter-crystalline shear, and (2) from impingement upon the walls of the tank in which Sehgal collected his sample.

From the above arguments together with the measurements at  $\lambda = 0.589\mu$ , it is concluded that the mean particle diameter for the beryllium propellant is in the range  $0.7$  to  $0.8\mu$ . This conclusion is further strengthened by the measurements taken farther down the exhaust plume at  $\lambda = 0.436\mu$  (again using mercury arc lamp) during Motor Test 6, which are shown in Figure 16. For the motor tests with the beryllium hydride propellant, the particle size (from Figure 15) appears to be  $0.9$  to  $1.0\mu$ .

In an attempt to obtain particle sizes in the chamber region during Motor Tests 7 and 8, the mercury arc light source and scattering detectors were installed at the optical viewports installed at the chamber plenum region. The results of these tests indicated that no radiance from the mercury arc lamp could be detected at the three angles at which detectors were placed ( $0^\circ$ ,  $63^\circ$ , and  $117^\circ$ ). Calculations of the extinction parameter for the chamber region indicate that the transmitted beam intensity would be less than  $10^{-70}$  of the incident intensity if all the expected metal or metal oxide were present in the chamber region.

### V. CONCLUSIONS

This paper has described work on the spectroscopic measurement of gas and particle temperature in small flames and rocket

UNCLASSIFIED

## UNCLASSIFIED

motor exhaust plumes. The following conclusions are drawn:

1. The spectral comparison method is readily applicable to optically thin regions where the emission characteristics of the condensed phase present are well known. For optically thick regions, a slight revision to the technique is necessary. Successful measurements of gas and particle temperatures were obtained in both the optically thin case (rocket motor exhaust plume) and the optically thick region associated with a small motor chamber with a high condensed phase mass fraction. These measurements are reported herein.

2. The precision of the measurement is extremely good for the optically thin case with a standard deviation for a clean gas of less than  $20^{\circ}\text{K}$ . In the presence of particles, the standard deviation for the gas temperature is about  $40^{\circ}\text{K}$ , with the refractive index of alumina accounting for a larger uncertainty in particle temperature.

3. Sodium appears to be desirable for use as a trace element, since it has been shown to be in equilibrium with the gas for pressures at 1 atm and above. Calculations indicate that no appreciable disequilibrium between sodium atoms and their neighbors could occur in the expansion of an exhaust plume. Lithium, on the other hand, is undesirable because of its observed tendency for self-absorption.

4. Light scattering and extinction measurements appear to offer promise as a method for defining effective particle size in a cloud of particles, such that the cloud reflectance can be determined. However, light scattering measurements of good precision in an optically thick plume do not appear to be possible with a conventional light source. The applicability of a Q-switched laser for this purpose is described by Adams<sup>20</sup>.

## UNCLASSIFIED

5. Measurements of gas and particle temperature in the exhaust plume of a small motor are presented together with a discussion of differences between the measured and theoretical temperatures. It is concluded from these measurements that a more intense continuum reference source will be required for greater optical depths (larger motors).

UNCLASSIFIED

## UNCLASSIFIED

### VI. REFERENCES

1. Bundy, R. P. and H. M. Strong "Measurement of Flame Temperature, Pressure, and Velocity", Physical Measurements in Gas Dynamics and Combustion, Vol. IX Princeton Series, Princeton, 1954.
2. Gaydon, A. G. , Spectroscopy of Flames, Wiley, 1957.
3. Hett, J. H. and J. B. Gilstein, "Pyrometer for Measuring of Instantaneous Temperatures in Flames", J. Opt. Soc. of America 30, 11 (1949) 909.
4. Collucci, S. E. and J. M. Adams, "Flame Temperature Measurement of Metallized Propellants", Final Report to Edwards AFB, AFRPL-TR-66-203, Sept. 1966.
5. Van de Hulst, H. C. , Light Scattering by Small Particles, Wiley, 1957.
6. Bartky, C. D. and E. Bauer, "Predicting the Emittance of a Homogeneous Plume Containing Alumina Particles", Aeronutronic Publ. No. U-3232 Contract NONr 3907(00), Aug. 1965.
7. Romanova, L. M. , Opt. and Spectey, 14, 135 (1963).
8. Chandrasekhar, S. , Radiative Transfer, Dover, 1960.
9. Adams, J. M. and L. Cann. "The Spectrophotoelectric Measurement of Gas and Particle Temperature", Aerojet-General Corp. TP-139, June 1964.
10. Kendall, E. G. and J. D. McClelland, "Materials and Structures", Aerospace Rept. No. TDR-930(2240-66) TR-1, March 1962.
11. Carlson, D. J. , "Radiation from Rocket Exhaust Plumes", Aeronutronic Report. Presented at Joint Specialists Conference, Colorado Springs, Colorado, June 1966.
12. Buchele, D. , "A Self-Balancing Line Reversal Pyrometer", NACA TN 3656, August 1956.
13. Adams, J. M. and S. E. Colucci, "The Spectroscopic Measurement of Gas and Particle Temperature in Metalized Propellant Combustion", CPIA Bulletin No. 111, Vol III, (1966).

## UNCLASSIFIED

14. Gryvnak, D. A. and D. E. Burch, "Optical and Infrared Properties of Alumina at Elevated Temperatures", Philco Publ. U-2623 (AD 606 793), 1964.
15. Malitson, I. H. et al., "Refractive Index of Synthetic Sapphire", J. Opt. Soc. America 48, 1, Jan. 1958.
16. Carlson, D. J. and R. A. DuPuis, "Alumina Absorption and Emittance", Philco Publ. No. 2627 (1964).
17. Adams, J. M. "A Determination of the Emissive Properties of a Cloud of Molten Alumina Particles", J. Quant. Spectrosc and Radiative Transfer 7, No. 1, Jan. 1967, p. 273.
18. Coughlin, J. P. and S. W. Hollingsworth, "A Correlation between Measured and Computer Values of Microwave Attenuation for Solid Propellant Exhausts Part II: Theoretical Calculations and Correlations," Special Session, 20th Interagency Solid Propellant Meeting, Philadelphia, Pa., July 1964 (Vol. IV, Bulletin).
19. Sehgal, R., JPL Space Programs Summary 37-22(B) no date.
20. Adams, J. M., "Some Remarks on the Determination of Spectral Emissivity in an Optically Thick Particle Cloud", submitted for publication in AIAA Journal, Jan 1967.

UNCLASSIFIED

# UNCLASSIFIED

## NOMENCLATURE

$A_o$	= Cross-sectional area of incident beam at scattering volume
$A_s$	= Area of incident beam at light stop of scattering detector
$C_2$	= constant in Planck's equation, $1.4388 \times 10^4$ micron $^{\circ}\text{K}$
$D$	= diameter
$E_{ij}$	= Emf generated from radiance detected by phototube i - refers to wave length j - refers to reference source alone j - 1 - refers to radiance from both flame + reference source j - 2 - refers to radiance from flame alone
$f(D)$	= frequency function of D, defined such that $\int_0^{\infty} f(D) dD = 1$
$I$	= intensity of light
$I_o$	= plane-polarized component of light intensity perpendicular to plane of observation
$i_i$	= intensity function i - 1 plane polarized in direction perpendicular to observation plane i - 2 plane polarized in observation plane
$k$	= $2\pi/\lambda$
$K_{ij}$	= phototube c.o.s.a. at $E_{ij}$
$L_u$	= velocity lag, $u_p/u_g$
$n$	= index of refraction $n = n' + i$
$\tilde{N}$	= particle number density, $\text{cm}^{-3}$
$n$	= real part of refractive index
$n'$	= imaginary part of refractive index
$r$	= distance from light stop of scattering detector to scattering volume
$T_b$	= brightness temperature
$T$	= temperature, $^{\circ}\text{K}$
$t$	= thickness

# UNCLASSIFIED

$u$	= velocity
$\bar{V}$	= mean particle volume
$V$	= volume
$\dot{w}$	= mass flow rate, lbm/sec

## Greek Symbols

$\alpha$	= $\pi D/\lambda$ , particle size function, dimensionless
$\gamma_a$	= absorption cross section
$\gamma_s$	= scattering cross section
$\delta$	= optical depth = $\tilde{N}(\gamma_a + \gamma_s)t$
$\epsilon$	= emissivity
$\mu$	= Micron, $10^{-6}$ meter
$\lambda$	= Wavelength, micron
$\theta$	= Angle between center line of detector and center line of incident light beam.
$\rho$	= Reflectivity of particles, mirrors, etc., or density
$\sigma_i$	= Standard deviation
$\tau$	= Transmissivity
$X$	= Mass fraction of particles

## Subscripts

$a_i$	= absorption, at $\lambda_i$
$b$	= brightness
$L$	= liquid
$g$	= gas
$o$	= comparison source
$p$	= particles
$s_i$	= scattering, at $\lambda_i$
$w_i$	= window, at $\lambda_i$

UNCLASSIFIED



UNCLASSIFIED

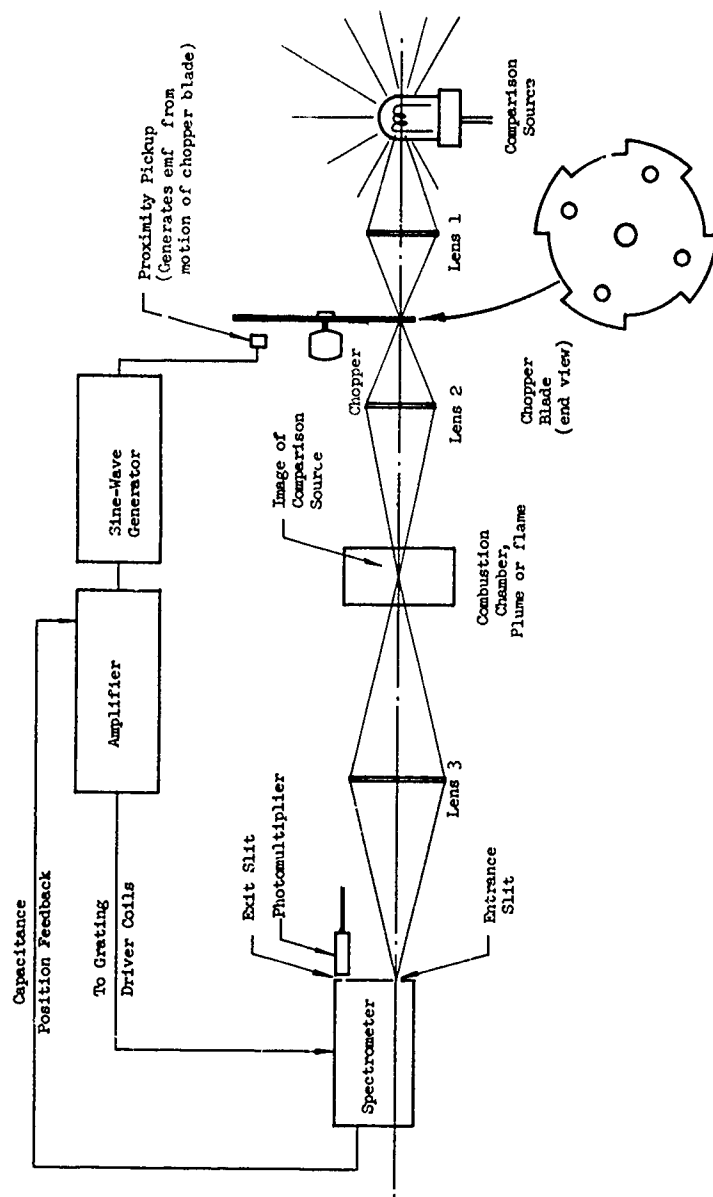
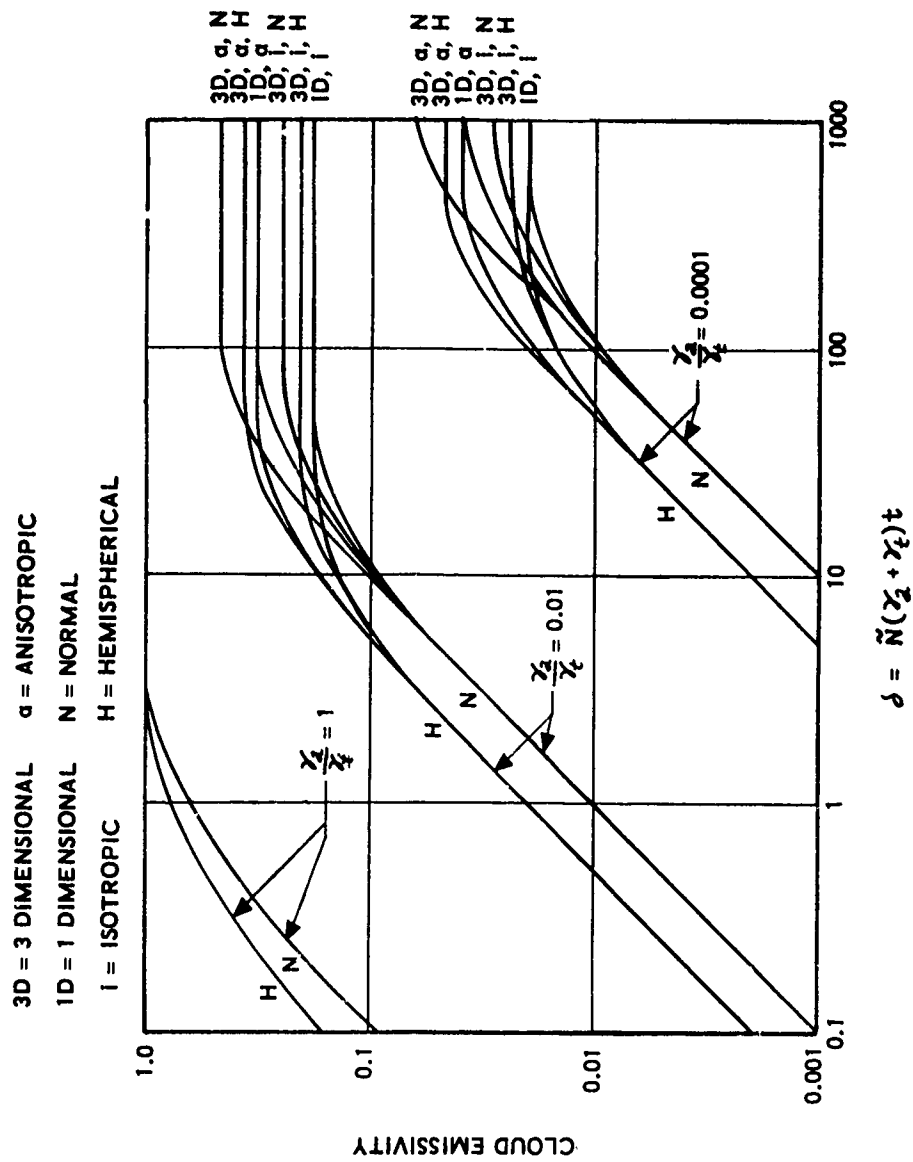


Figure 1. Optics and Electromechanical Schematic of Spectral Comparison Pyrometer

UNCLASSIFIED

**UNCLASSIFIED**



(Reproduced by permission of C.D. Bartky of Aeronutronic, Corp.)

Figure 2. Normal and Hemispherical Emittance as a Function of Optical Depth.

UNCLASSIFIED

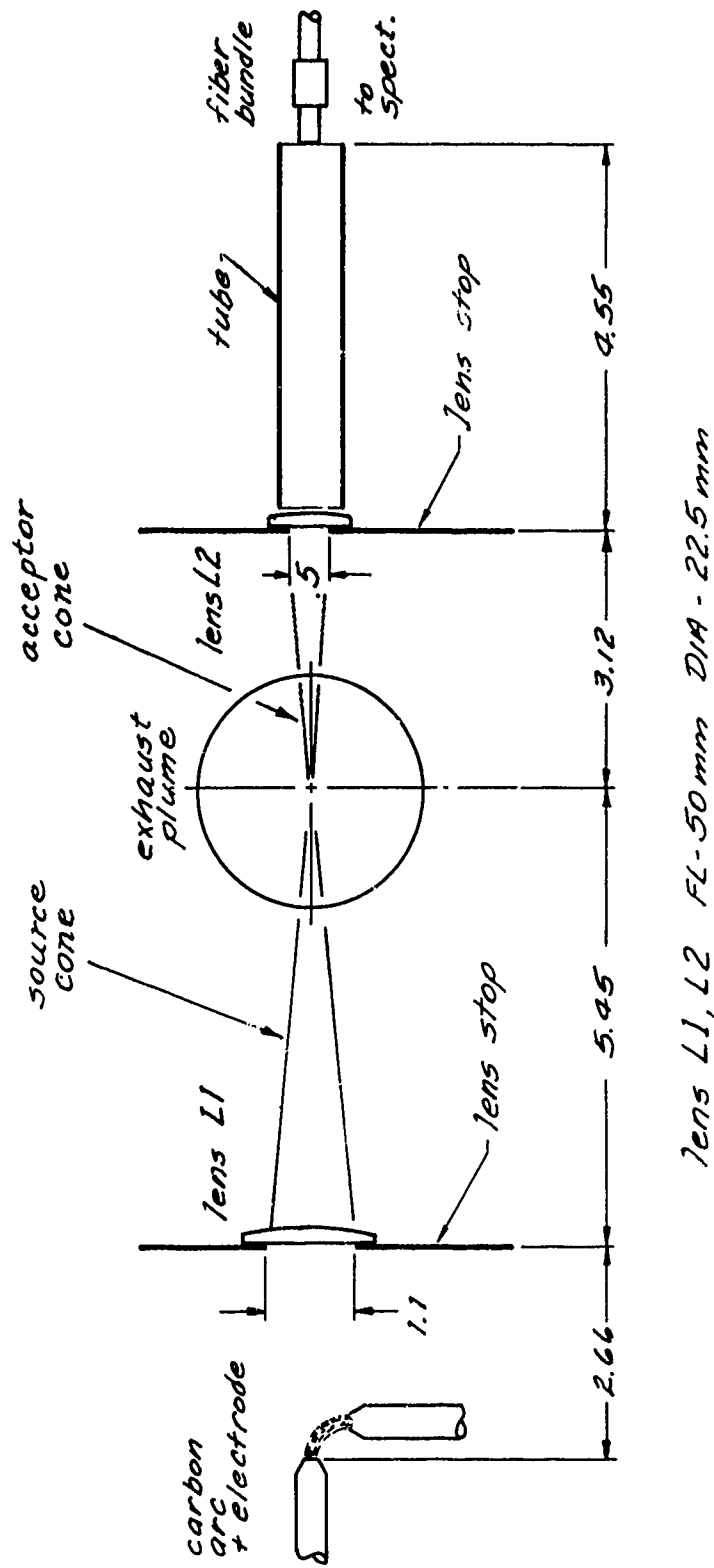


Figure 3. Experimental Layout for Gas and Particle Temperature Measurements.

UNCLASSIFIED

UNCLASSIFIED

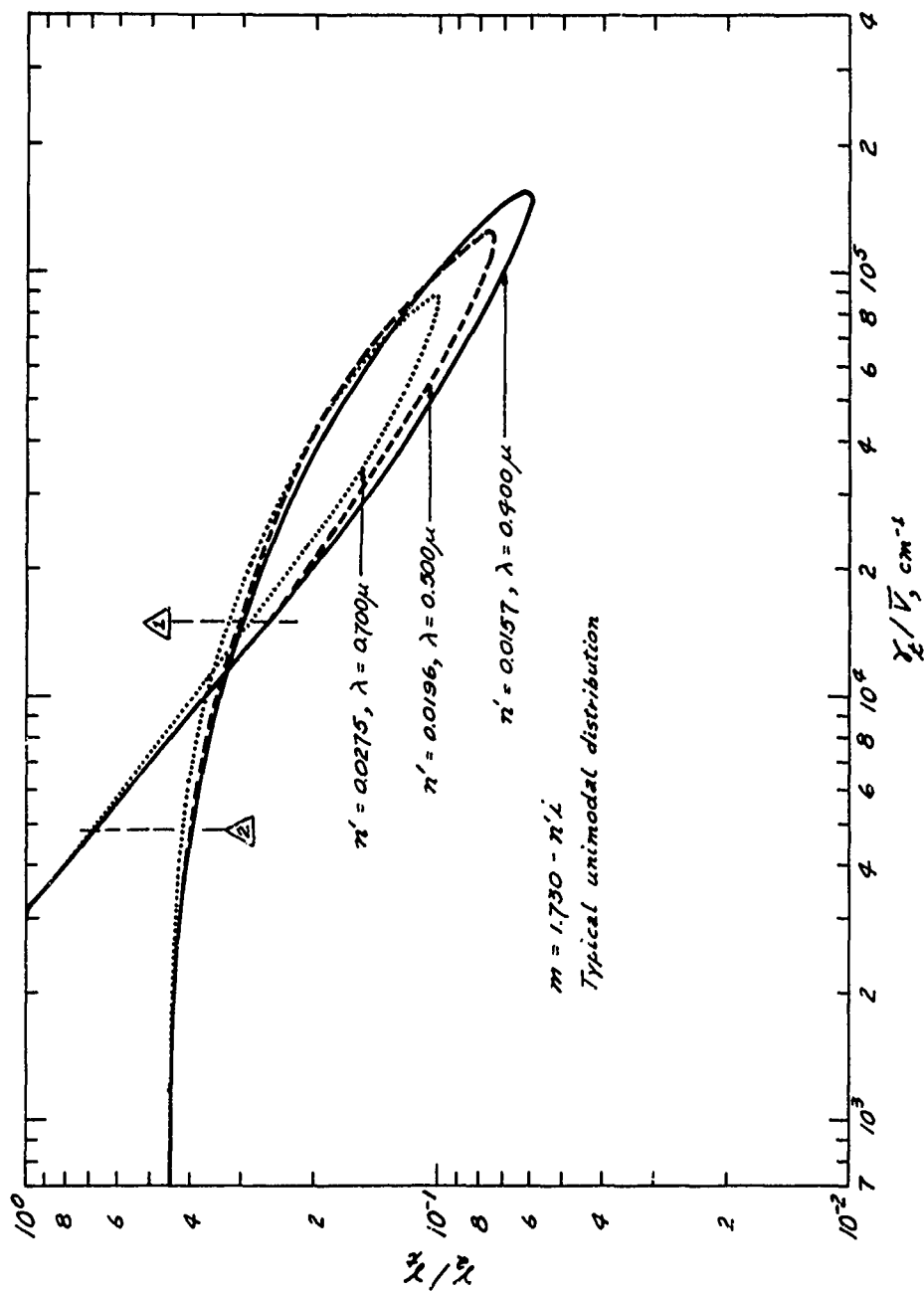


Figure 4. Absorption/Total Cross Section vs. Extinction Parameter for Beryllium Oxide Spherical Particles: Dependence on  $n'$  (Particle Size Distribution from Figure 6)

UNCLASSIFIED

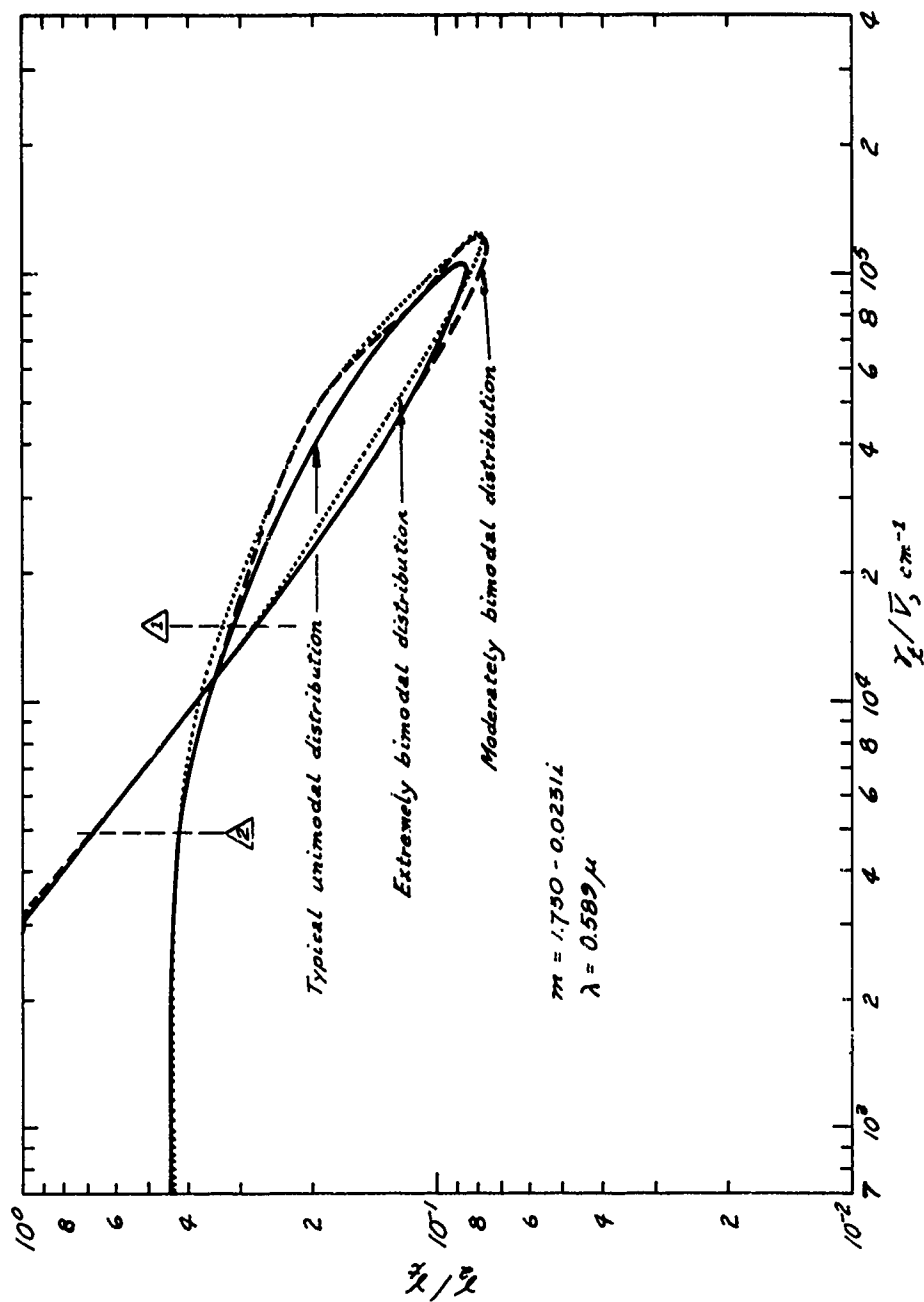


Figure 5. Absorption/Total Cross Section vs. Extinction Parameter for Beryllium Oxide Spherical Particles: Dependence on size distribution,  $f(D)$  (Particle Size Distribution from Figure 6)

UNCLASSIFIED

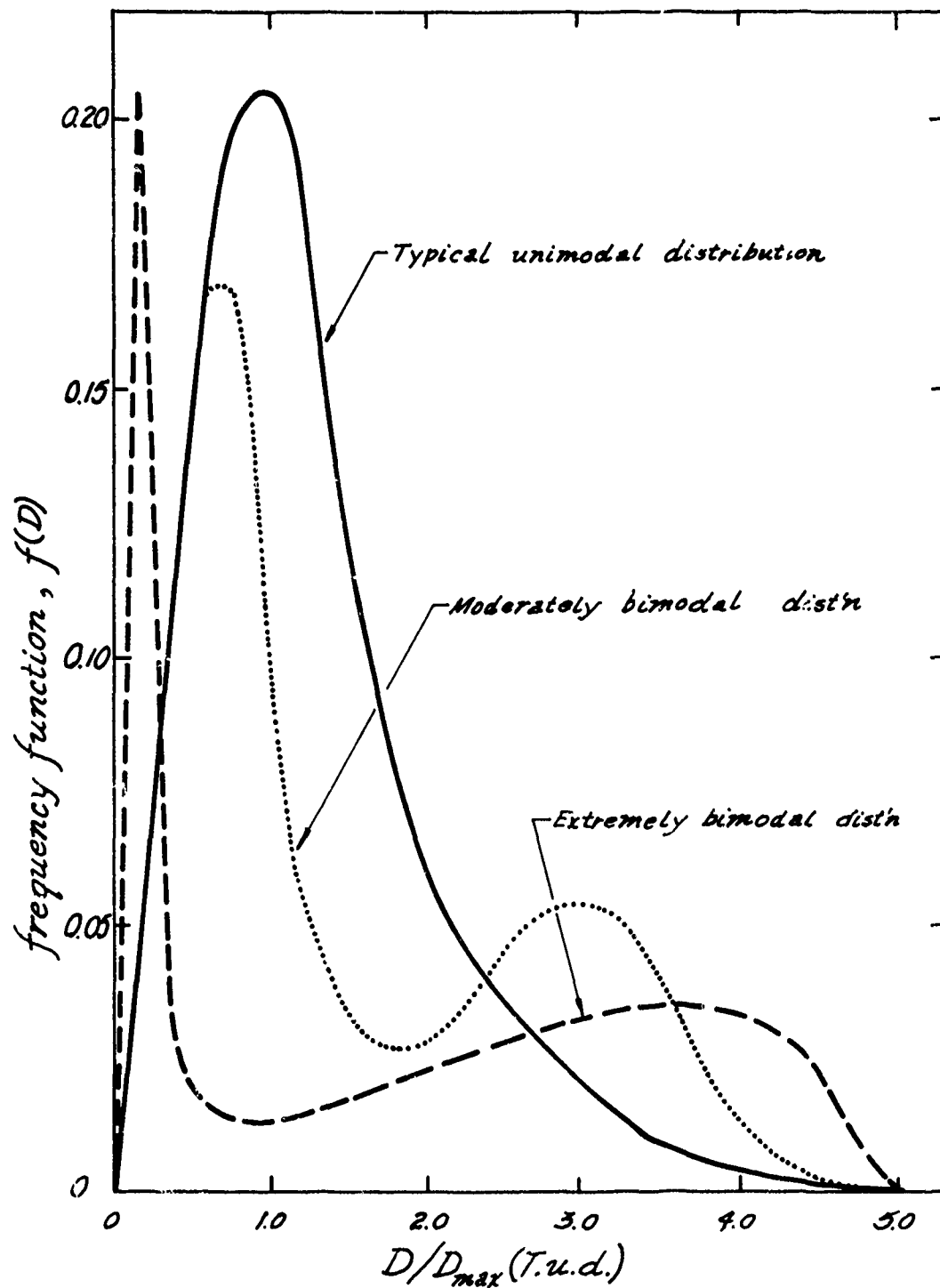


Figure 6. Particle Size Distributions Used in Generating Curves of Extinction Parameter Versus Mean Particle Diameter

UNCLASSIFIED

UNCLASSIFIED

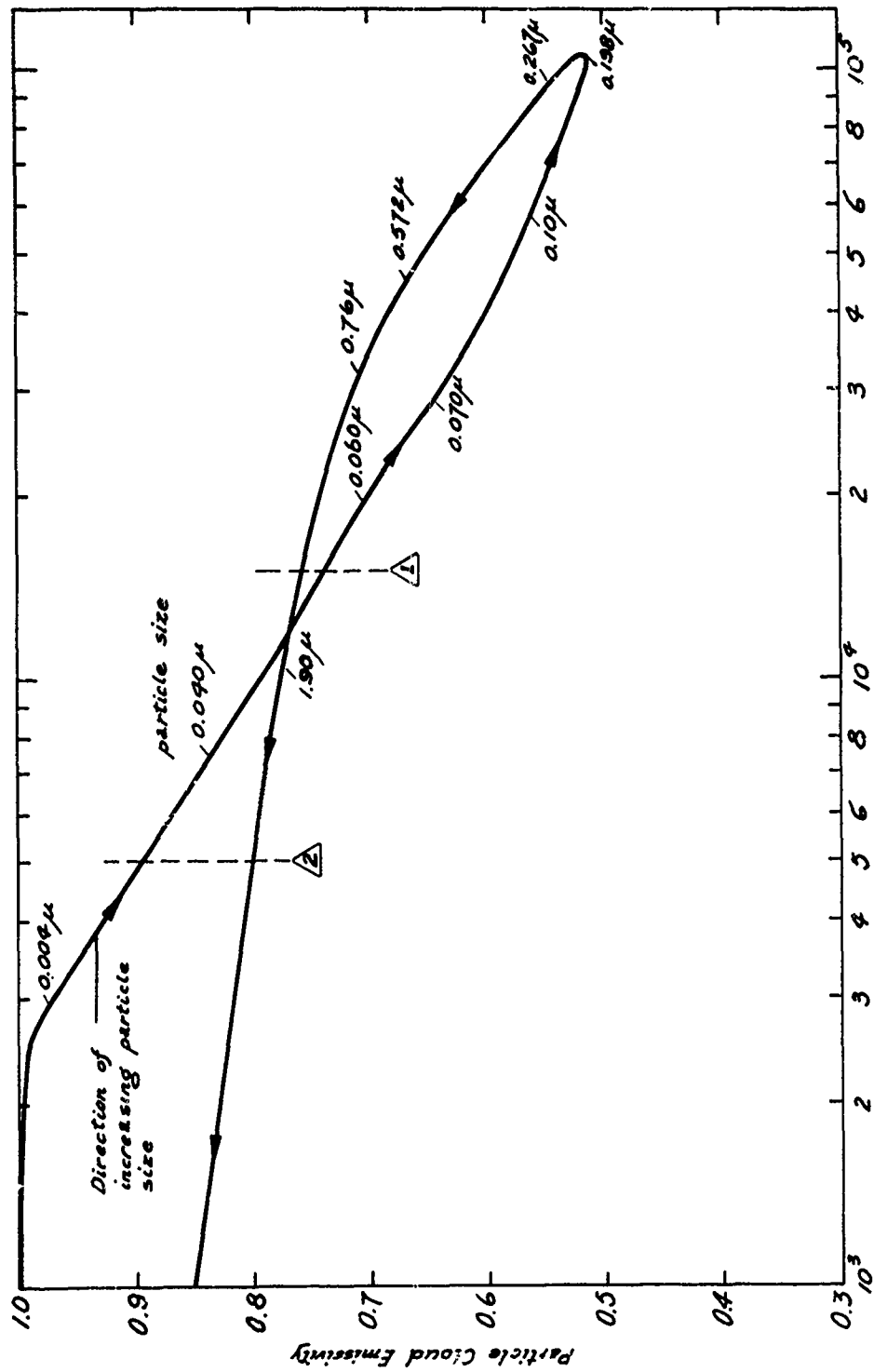


Figure 7. Particle Cloud Emittance vs. Extinction Parameter for Beryllium Oxide Spherical Particle Determined from Chamber Conditions in Small Motor (see Figure 8)

UNCLASSIFIED

UNCLASSIFIED

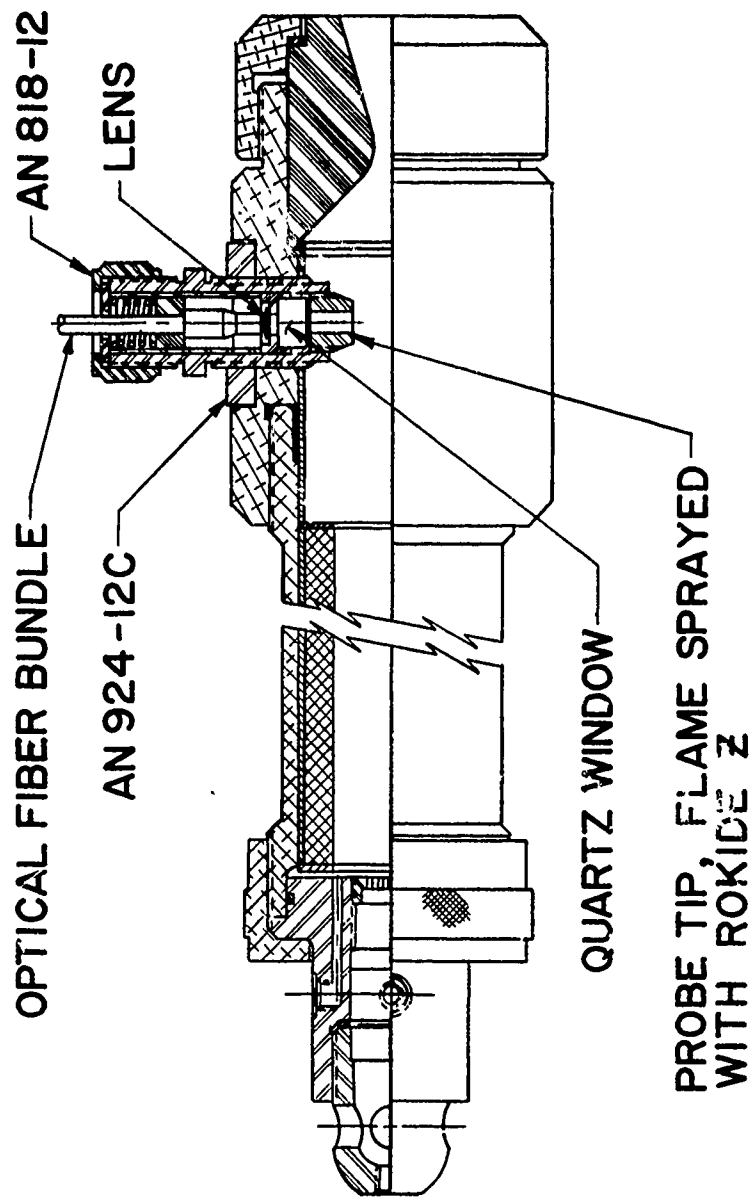


Figure 8. Test Motor Assembly

UNCLASSIFIED



UNCLASSIFIED

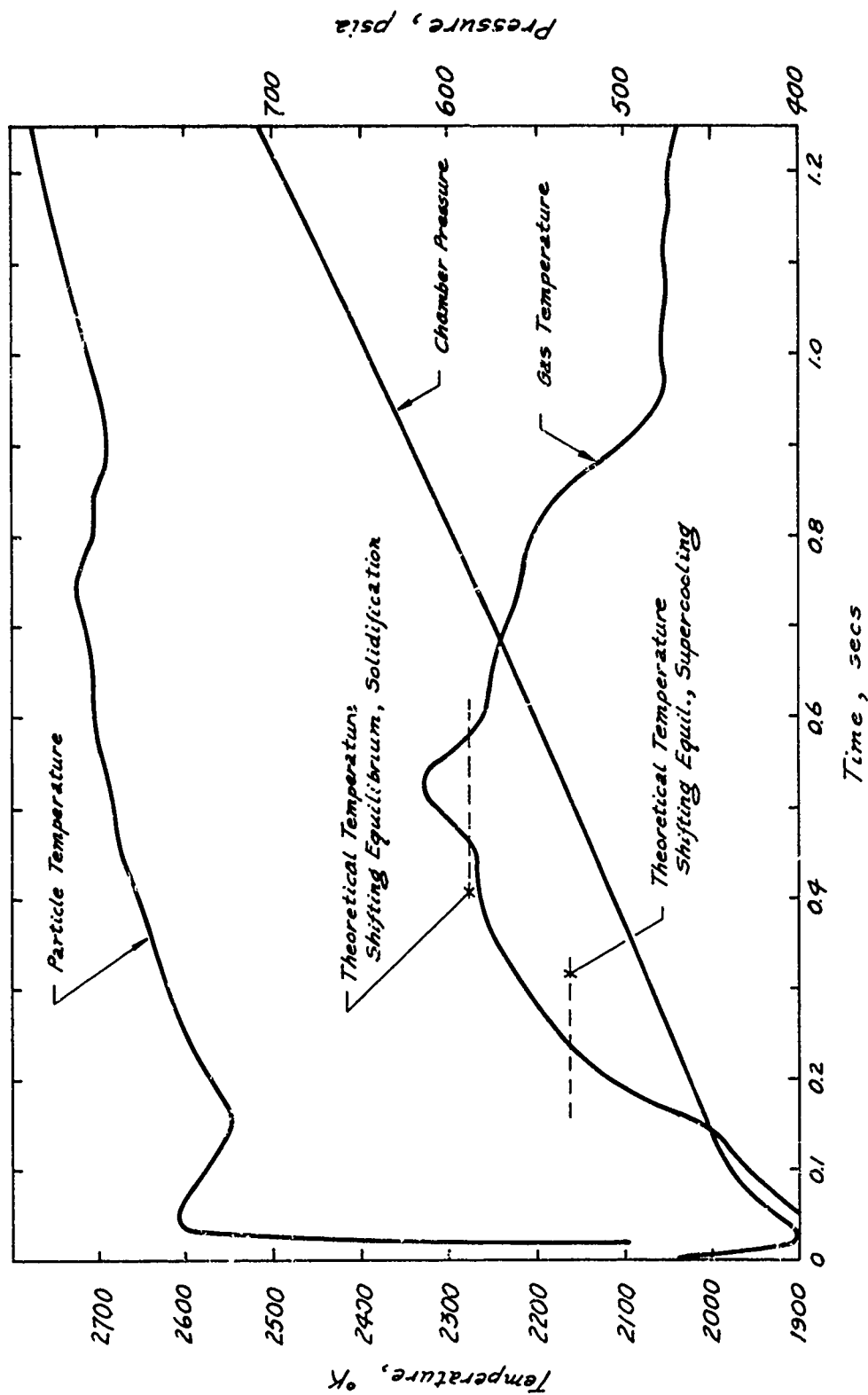


Figure 9. Measured Gas and Particle Temperatures, Exhaust Plume of 1KS-250 Motor, Aluminized Propellant

UNCLASSIFIED

UNCLASSIFIED

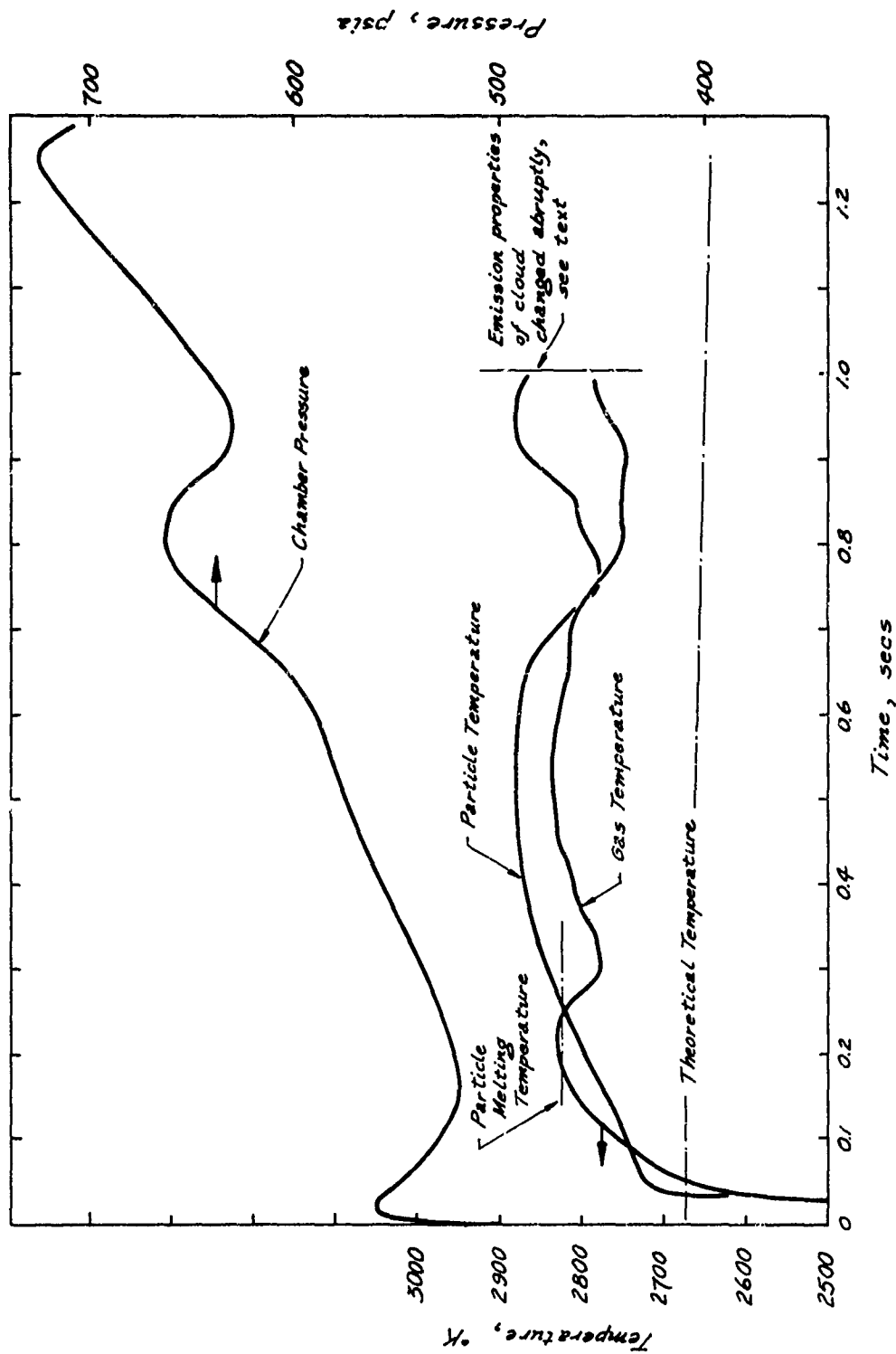


Figure 10. Measured Gas and Particle Temperatures, Exhaust Plume of 1 KS-250 Motor.

UNCLASSIFIED

UNCLASSIFIED

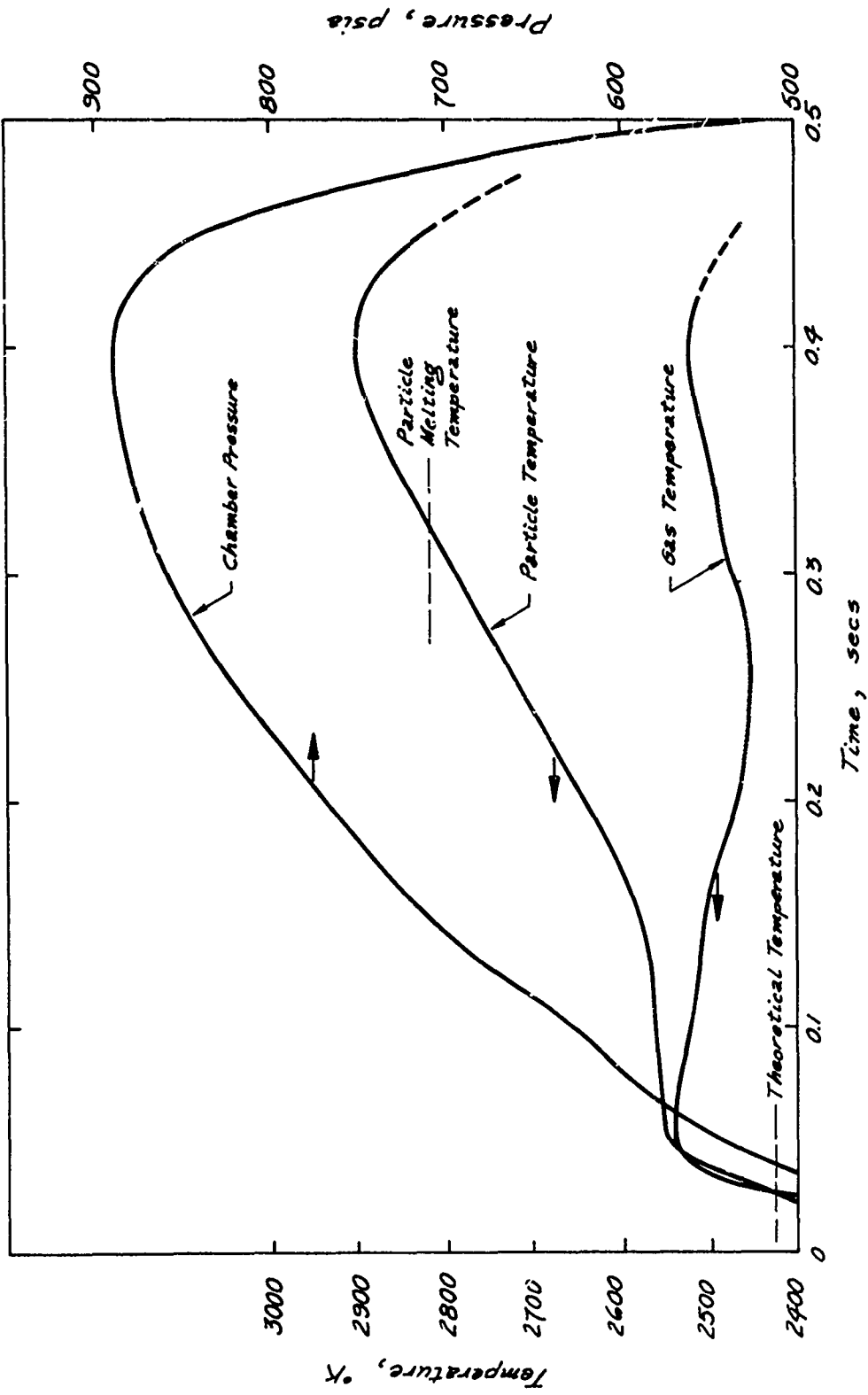


Figure 11. Measured Gas and Particle Temperatures, Exhaust Plume of IKS-250 Motor

UNCLASSIFIED

UNCLASSIFIED

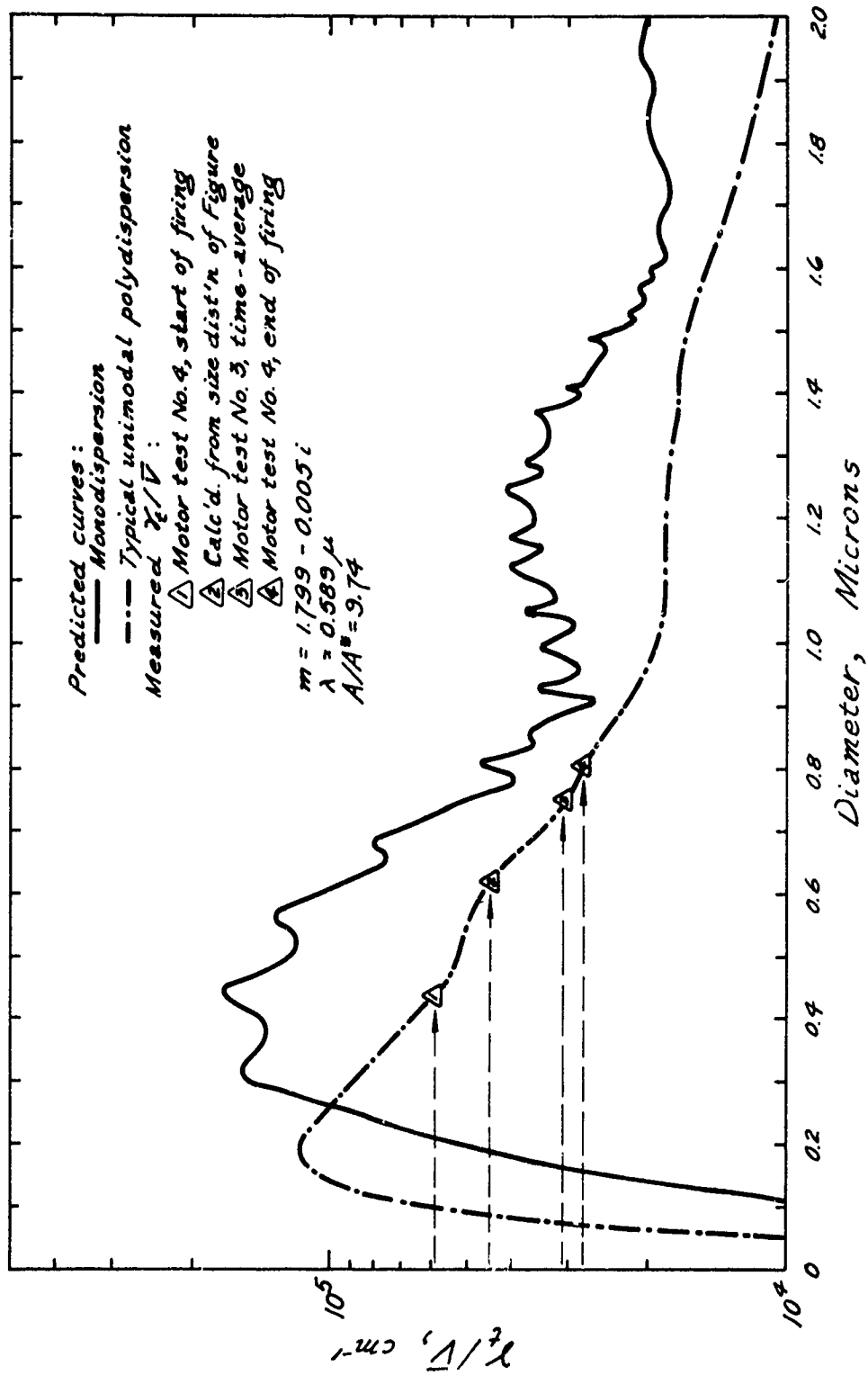


Figure 12. Extinction Parameter, Determined from Light Extinction Measurements in Exhaust Plume of 1KS-250 Motor (Tests No. 3 and 4) at  $\lambda = 0.589\mu$

UNCLASSIFIED

UNCLASSIFIED

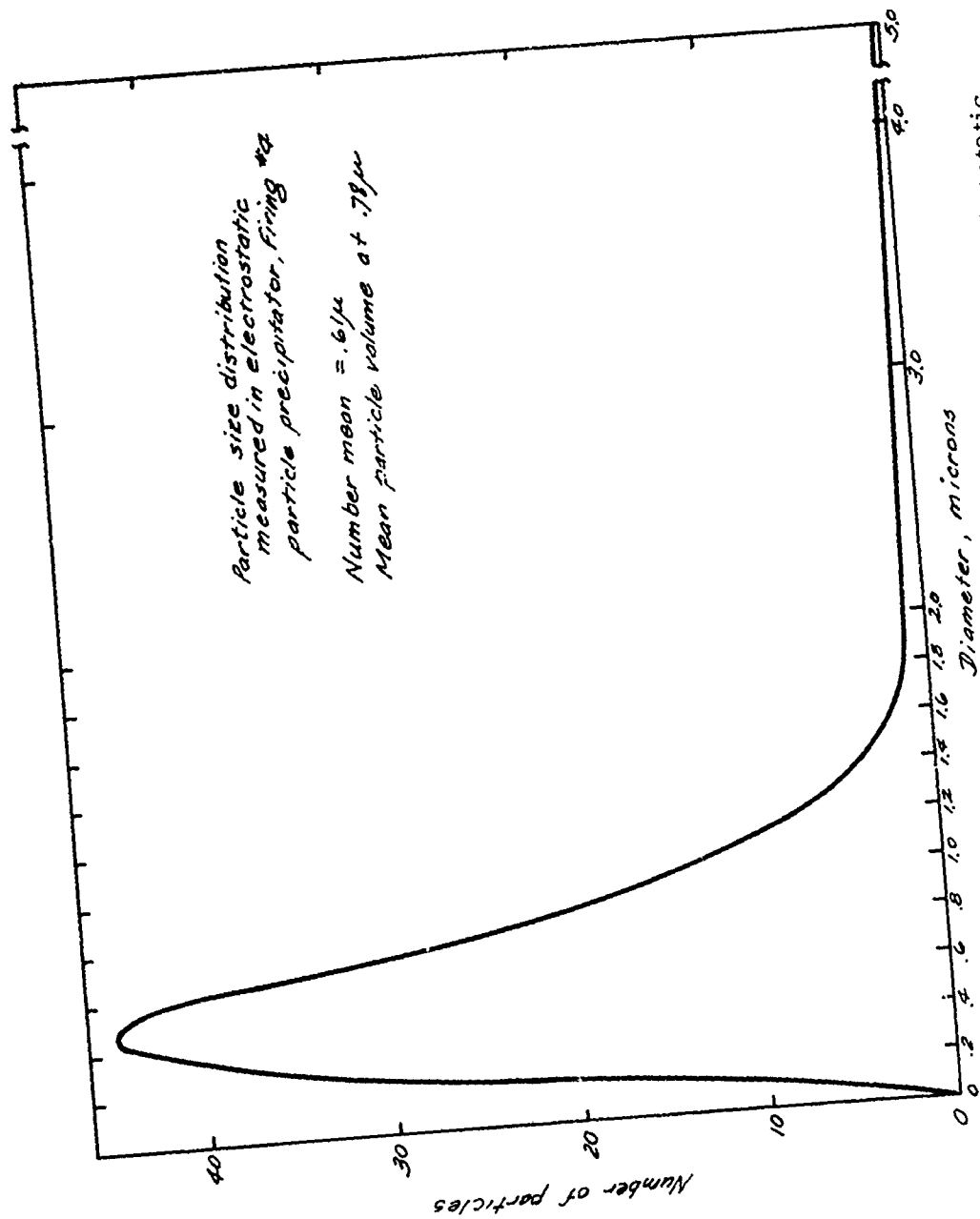


Figure 13. Particle Size Distribution Measured In Electrostatic Particle Precipitation, Motor Test No. 4

UNCLASSIFIED

UNCLASSIFIED

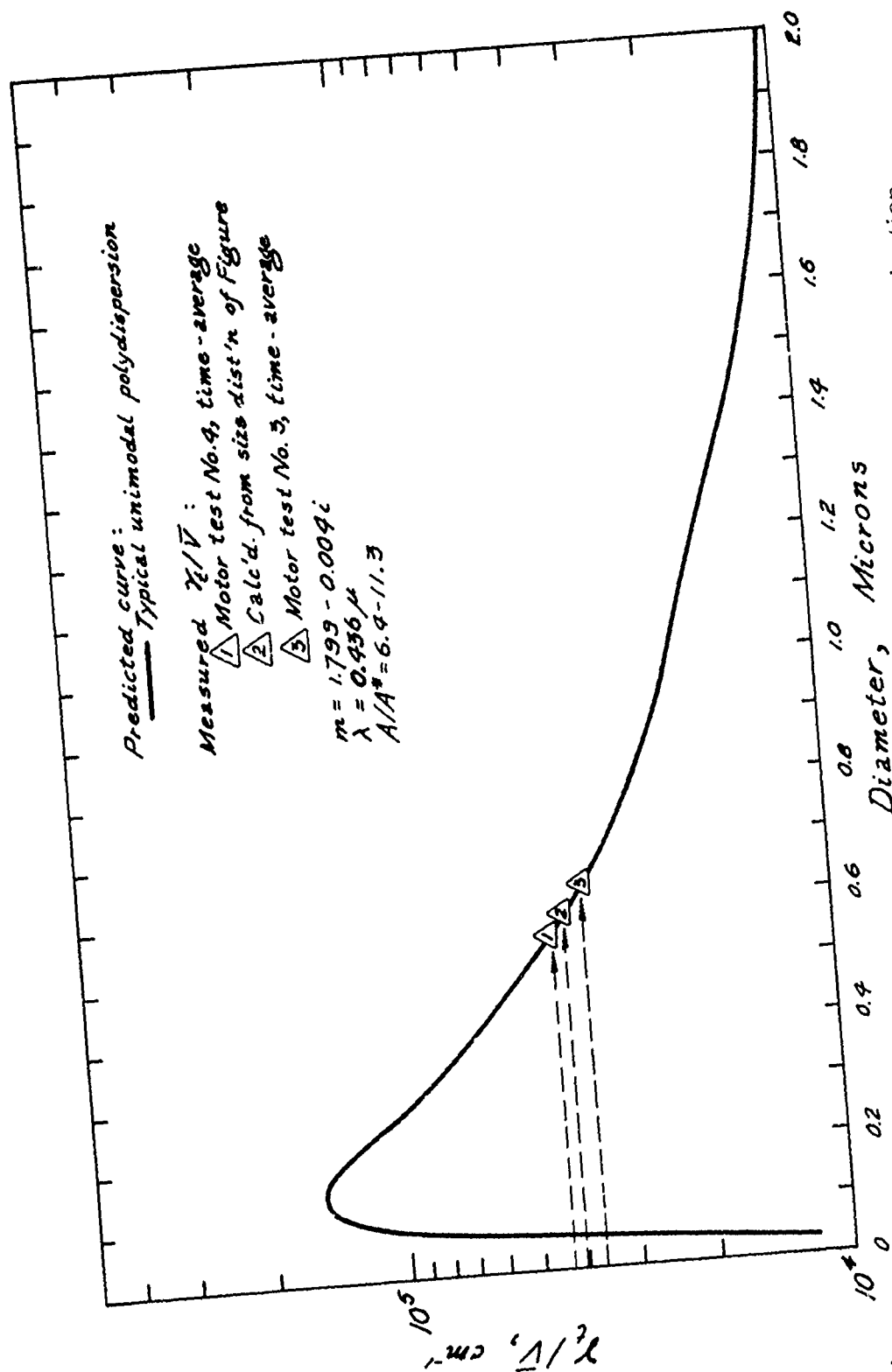


Figure 14. Extinction Parameter, Determined from Light Extinction Measurements in Exhaust Plume of 1KS-250 Motor (Tests No. 3 and 4) at  $\lambda = 0.436\mu$

UNCLASSIFIED

UNCLASSIFIED

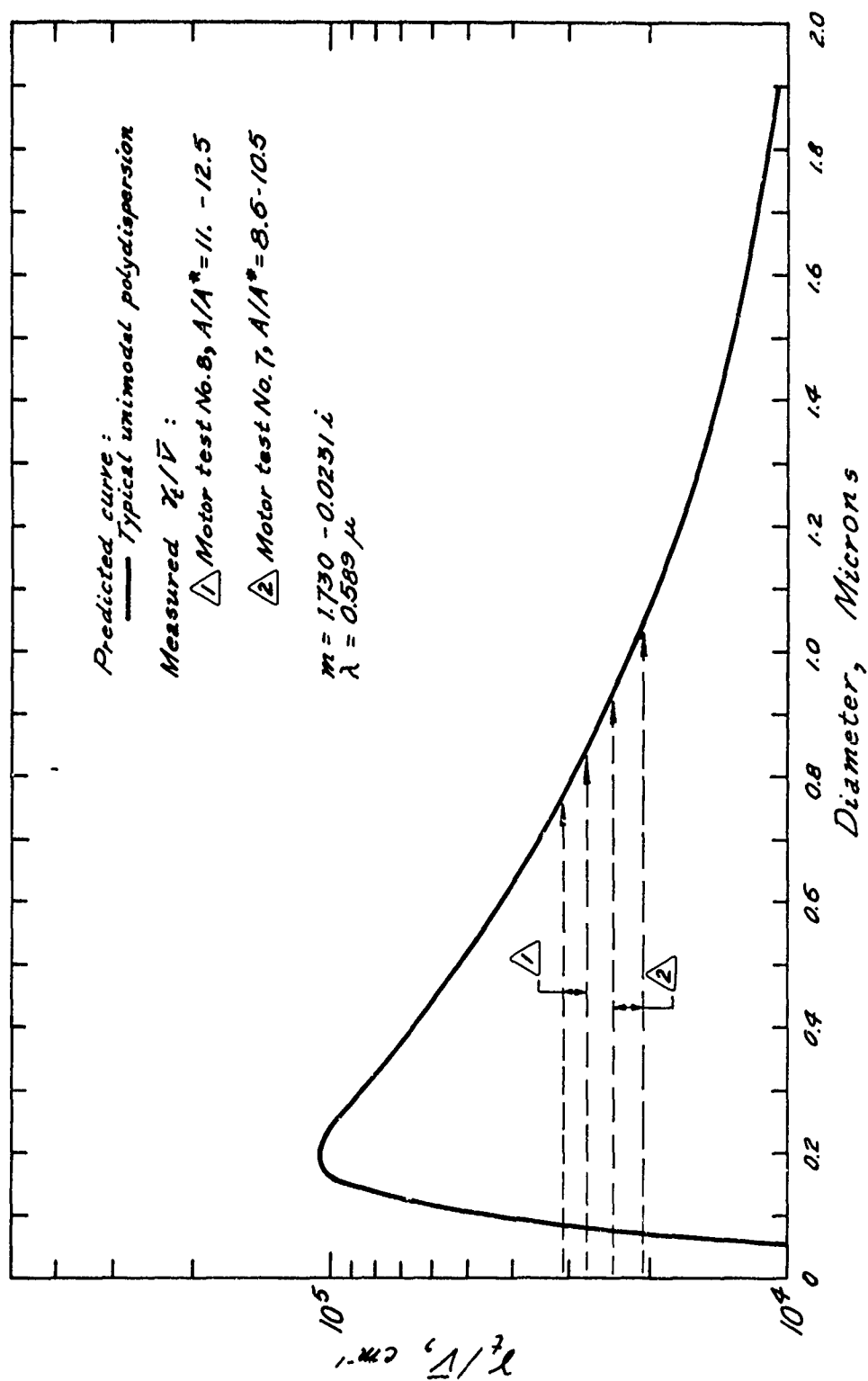


Figure 15. Extinction Parameter, Determined from Light Extinction Measurements in Exhaust Plume of 1KS-250 Motor (Tests No. 7 and 8) at  $\lambda = 0.589\mu$

UNCLASSIFIED

UNCLASSIFIED

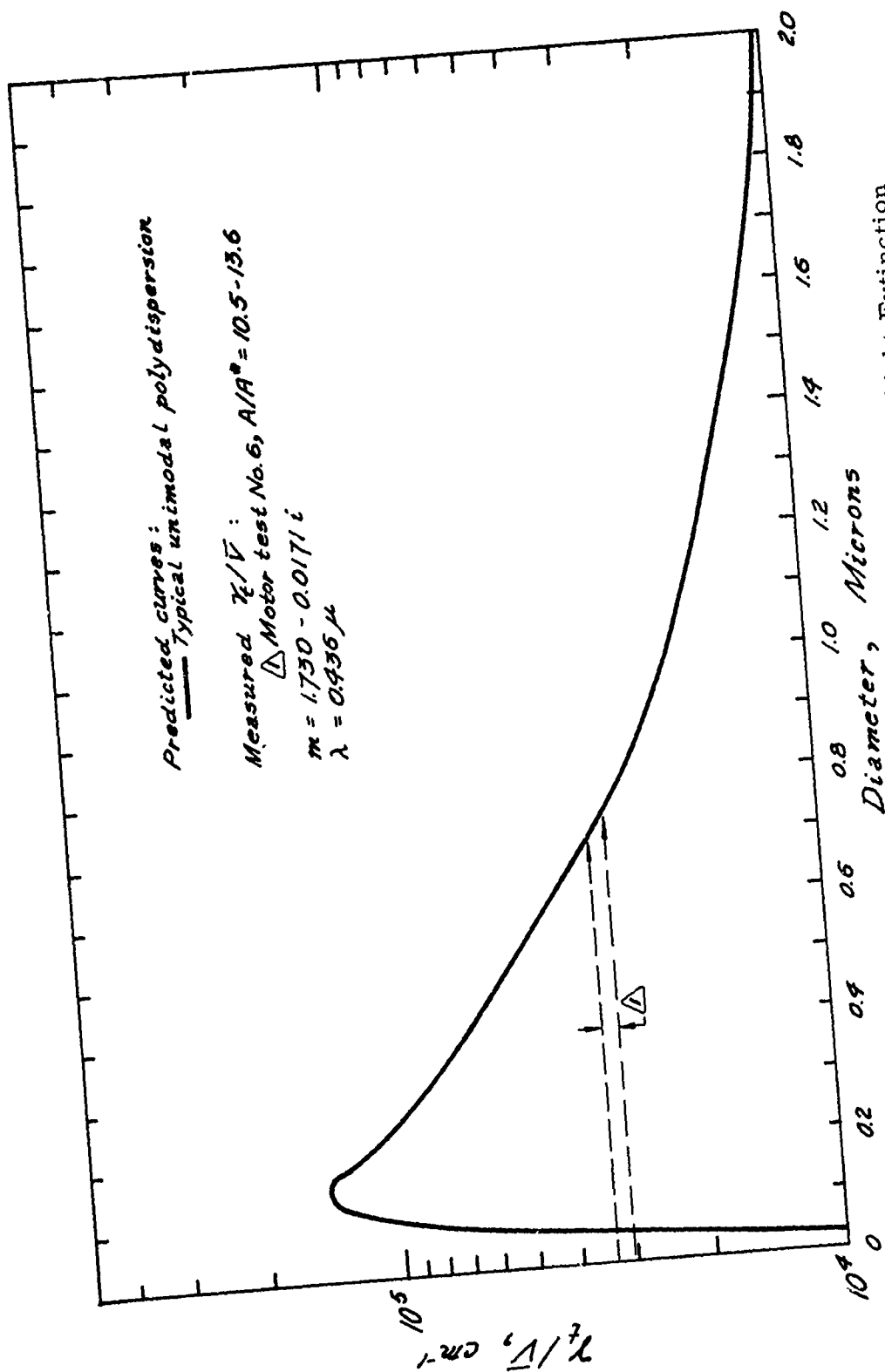


Figure 16. Extinction Parameter, Determined from Light Extinction Measurements in Exhaust Plume of 1KS-250 Motor (Test No. 6) at  $\lambda = 0.436 \mu$

UNCLASSIFIED

759/760



**UNCLASSIFIED**

**UNDEREXPANDED GAS-PARTICLE JETS**

by

Philip O. Jarvinen and James S. Draper

Mithras, Inc.  
Cambridge, Massachusetts 02138

**UNCLASSIFIED**

# UNCLASSIFIED

## UNDEREXPANDED GAS-PARTICLE JETS

Philip O. Jarvinen<sup>+</sup> and James Stark Draper<sup>++</sup>

Mithras, Inc., Cambridge, Massachusetts 02138

It was noted experimentally<sup>1</sup> that the addition of solid particles to supersonic jets issuing from underexpanded nozzles had a pronounced effect on the geometric characteristics of the exhaust plume. As the particle to gas loading was increased, the exhaust plume shrunk in size and the Mach disc moved toward the nozzle exit plane. This note describes a simple model for the gas-particle exhaust flow whose predictions are in agreement with the experimental data.

The assumption is made that the geometrical characteristics of gas-particle plumes are controlled by the specific heat ratio and exit Mach number of the gas phase of the two-phase flow. The particles are assumed to take part in determining the mass flow but not the expansion of the plume upon exit from the nozzle. The nozzle exit plane flow properties of the gas-particle flow are described by treating the mixture as an equivalent perfect gas<sup>2-4</sup> with zero lags and an effective value of  $\bar{\gamma}$  given by

$$\bar{\gamma} = \frac{1 + \phi \frac{C_{PS}}{C_P}}{1 + \gamma \phi \frac{C_{PS}}{C_P}}$$

The specific heat ratio for the gas phase is determined from the gas composition and specific heats and molecular weights of the individual components.

---

This work was supported by the US Air Force Cambridge Research Laboratories under Contract AF 19(628)-5912.

+ Principal Staff Engineer, Aerothermodynamics Division. Member AIAA.

++ Staff Engineer, Aerothermodynamics Division.

UNCLASSIFIED

# UNCLASSIFIED

The exit plane, gas-only Mach number, based on the exit velocity and temperatures of the gas-particle flow, is

$$M_g = \frac{V_e}{\sqrt{\gamma R T_e}}$$

The gas phase specific heat ratio and exit Mach number define a pseudo nozzle for the gas phase whose geometrical properties and chamber conditions are such as to produce the gas phase exit conditions. Properties of the pseudo nozzle such as  $(A_e/A^*)_P$ ,  $(P_e/P_c)_P$  and  $(T_e/T_c)_P$  are obtained from gas tables<sup>5</sup>. The chamber pressure, temperature and throat area of the pseudo nozzle are determined from these properties and the assumptions of identical exit conditions for the pseudo and actual nozzles. Then the exhaust plume flow properties are calculated by treating the gas phase separately from the solids and by assuming the gas phase exhausts from the pseudo nozzle.

The pseudo nozzle concept for gas-particle exhaust plume flows is tested by comparing its theoretical predictions with the experimental data of Lewis and Carlson<sup>1</sup> for the location of the Mach disc in gas-only and gas-particle jet flow. The analytical approximation of Hill and Draper<sup>6</sup> for the flow from a nozzle into a vacuum is used to specify the variation of density along the centerline of the jet.

$$\frac{x_{C,L}}{(y^*)_P} = \left[ \left( \frac{2}{\gamma + 1} \right) \frac{1}{\gamma + 1} \frac{\lambda}{\sqrt{\pi}} \frac{C^*}{C_{C,L}} \frac{P_c}{P_{C,L}} \right]_P^{1/2}$$

where

$$\lambda = \left[ \sqrt{\pi} \left\{ 1 - C_F/C_{C,L} C_{F_{max}} \right\} \right]_P^{-1}$$

## UNCLASSIFIED

The local Mach number is determined from isentropic flow relationships:

$$M_{C.L} = \left( \frac{2}{\gamma - 1} \right)^{1/2} \left[ \left( \frac{\rho_c}{\rho_{C.L}} \right)^{\gamma - 1} - 1 \right]^{1/2}$$

The Mach disc is located such that the pressure behind the shock wave is ambient pressure.

The variation of gas-only exit Mach number with particle to gas loading as predicted by the pseudo nozzle model is shown in Figure 1 for the two nozzles used by Lewis and Carlson. The exit Mach number decreases from the gas-only value with increasing particle to gas loading. A comparison of the pseudo nozzle results for the percentage change in the distance to the Mach disc as a function of particle mass fraction and the experimental data<sup>1</sup> shows good agreement (Figure 2). Theoretical calculations made for nozzle exit to ambient pressure ratios from  $P_e/P_\infty = 10$  to  $P_e/P_\infty = 10000$  indicated that the percentage change in position of the Mach disc is independent of pressure ratio as was observed experimentally. The pseudo engine results for the distance to the Mach disc, when compared with experimental results on an absolute basis, agree within the differences exhibited by experimental data<sup>8</sup>.

The model described above, with the theories of references 6 and 9, provide a simple method which may be used to locate gas density contours in and to describe the size and shape of high altitude exhaust plumes from solid propellant vehicles.

UNCLASSIFIED

# UNCLASSIFIED

## REFERENCES

1. Lewis, C.H. and Carlson, D.J., "Normal Shock Location In Underexpanded Gas and Gas-Particle Jets". AIAA Journal Vol. 2, No. 4, 4 April 1964.
2. Hoglund, R. F., "Recent Advances in Gas-Particle Nozzle Flows". ARS Journal Vol. 32, No. 5, May 1962.
3. Bailey, W. S. et. al. "Gas Particle Flow in an Axisymmetric Nozzle". ARS Journal Vol. 31, No. 6, June 1961.
4. Marble, F. E., "Nozzle Contour for Minimum Particle Lag Loss". AIAA Journal Vol. 1, No. 12, December 1963.
5. Wang, C. J., Peterson, J. B., and Anderson, R., "Gas Flow Tables" Space Technology Laboratories Report GM-TR-154, March 1957.
6. Hill, J. A. F. and Draper, J. S., "Analytical Approximation for the Flow from a Nozzle into a Vacuum". Journal of Spacecraft and Rockets, October - November 1966.
7. Adamson, T. C. Jr., and Nicholls, J. A., "On the Structure of Jets from Highly Underexpanded Nozzles into Still Air". Journal of the Aerospace Sciences, Vol. 26, No. 1, 1959.
8. Carlson, D. J. et. al. "Solid Propellant Exhaust Radiation Studies, Interim Technical Report No. 3 "Aeronutronic Publication No. U-3044, March 1965. Aeronutronics Division of Philco Corporation, Newport Beach, California.
9. Hill, J. A. F. and Habert, R. H., "Gasdynamics of High-Altitude Missile Trails", MITHRAS Report MC 61-18-R1 January 1963, MITHRAS, Inc., Cambridge, Massachusetts.

# UNCLASSIFIED

## NOMENCLATURE

$A^*$	=	nozzle throat area
$A_e$	=	nozzle exit plane area
$C$	=	Crocco number, $V/V_M$
$C^*$	=	Crocco number at the nozzle throat
$C_F$	=	vacuum thrust coefficient
$C_{F_{\max}}$	=	maximum vacuum thrust coefficient
$C_{F^*}$	=	specific heat of gas phase
$C_{P_S}$	=	specific heat of solid phase
$\phi$	=	ratio of the mass flow of solids to the mass flow of gas
$R$	=	gas phase gas constant
$T_e$	=	exit temperature from equivalent gas formulation
$V_e$	=	exit velocity from equivalent gas formulation
$X_g$	=	distance to Mach disc for gas-only flow
$X_s$	=	distance to Mach disc for gas-particle flow
$y^*$	=	nozzle throat radius
$\gamma$	=	gas phase specific heat ratio
$\overline{\gamma}$	=	gas-particle flow equivalent specific heat ratio
$\rho_c$	=	chamber density

UNCLASSIFIED

# UNCLASSIFIED

## Subscripts

c	=	chamber conditions
C.L.	=	properties on jet centerline
P	=	pseudo nozzle properties

UNCLASSIFIED

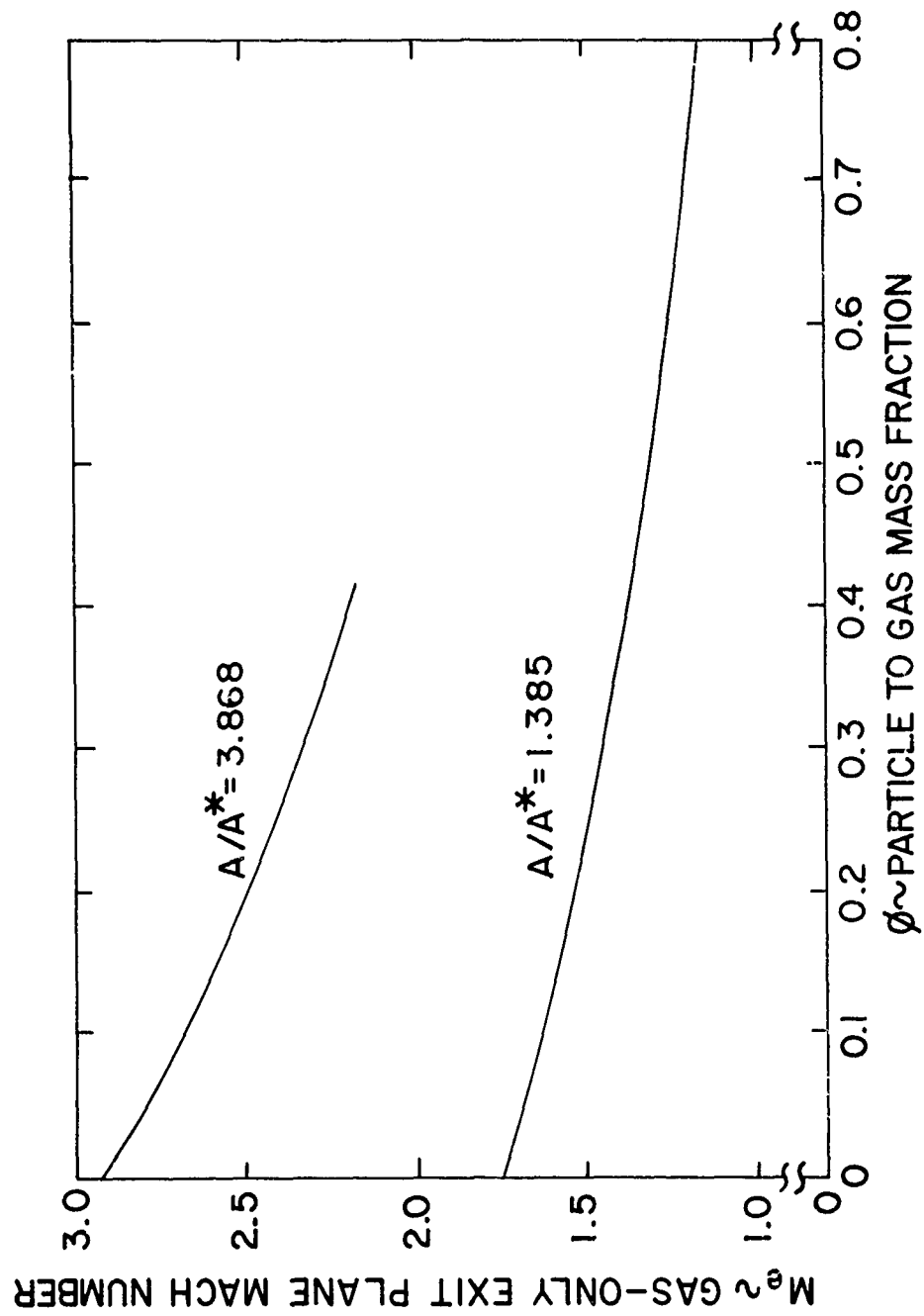


Figure 1. Variation of gas-only exit plane Mach numbers with particle to gas loading.

UNCLASSIFIED



UNCLASSIFIED

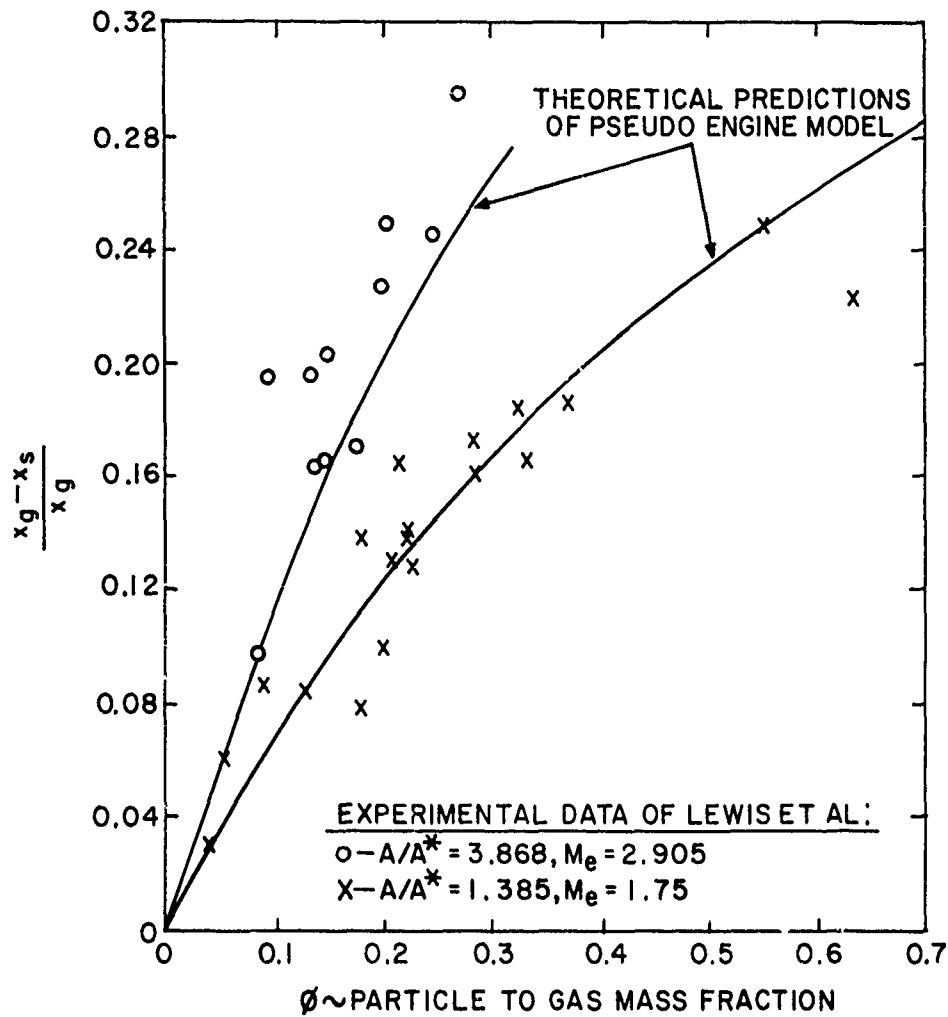


Figure 2. Comparison of pseudo engine model predictions with experimental data.

UNCLASSIFIED

**UNCLASSIFIED**

**PARTICLE DRAG COEFFICIENT  
IN GAS-PARTICLE FLOWS**

by

George Rudinger

Cornell Aeronautical Laboratory, Inc.  
Buffalo, New York

**UNCLASSIFIED**

# UNCLASSIFIED

## PARTICLE DRAG COEFFICIENT IN GAS-PARTICLE FLOWS

George Rudinger  
Cornell Aeronautical Laboratory, Inc.  
Buffalo, New York

All calculations of gas-particle flow involve the particle drag coefficient which describes the viscous interaction between the gas and the particles. Stokes drag is usually assumed for qualitative studies because it leads to convenient equations although everyone realizes that it is a poor approximation for Reynolds numbers greater than about one. For numerical work, it is usually assumed that the drag coefficient has the same values as for a single sphere in steady flow. Although this assumption appears plausible, particularly for particle concentrations normally encountered in rocket nozzles, it has not yet been satisfactorily verified. As part of our ONR - sponsored Project SQUID, we have been trying to determine effective drag coefficients experimentally, and I want to report briefly on the present status of this work.

I cannot go into experimental details, but the principle of the experiment is quite simple. If a shock wave passes through a gas-particle mixture, the flow in the relaxation zone behind the shock front is completely determined by the continuity equations for the gas and for the particles, the momentum equation of the mixture, and two sets of experimental data, such as the gas pressure and the particle velocity or concentration<sup>1</sup>.

The first experiments<sup>1</sup> were performed with a vertical aluminum shock tube having a cross section of 7.5 cm by 7.5 cm. Gas pressure

UNCLASSIFIED

## UNCLASSIFIED

was measured by means of a suitable pressure transducer, and the particle motion was recorded by means of streak records. A mixture of air and spherical plan beads of  $29\mu$  average diameter and of known composition was allowed to flow continually through the driven section of the shock tube, and a weak shock wave was then sent through this flow. A typical streak record is shown in Figure 1. The incident shock wave and its reflection from the closed bottom of the shock tube are also visible because of total reflection of the light beam from the shock front. The particle trajectories were traced and evaluated with the result shown in Figure 2 where the drag coefficient is plotted as a function of the particle Reynolds number. A straight line, as shown, fitted the experimental data very well. For comparison, the graph shows also the relationships for Stokes drag, the standard drag coefficient for single spheres, and an intermediate correlation proposed some time ago by Ingebo<sup>2</sup>.

Although the experimental results are well reproducible, the difference between them and customarily used relationships is so large that it becomes imperative to understand what causes the observed behavior of the drag coefficient and to rule out erroneous interpretations of the experimental data. The particles used for the experiments are too small to be seen in the streak record, and Figure 1 shows the motion of irregularities in the particle distribution in the shock tube. Since it could not be established whether or not the irregularities of the distribution move with the same velocity as the particles themselves, we attempted to produce more uniform gas-particle mixtures. These efforts were successful, but the streaks then were too faint for evaluation. With such mixtures it became possible to measure changes of the particle concentration in the relaxation zone behind the shock front by means of light scattering. Since according to the continuity equation, the product of particle concentration and particle velocity relative to the shock front is constant, the particle velocity is readily

## UNCLASSIFIED

determined from light scattering records.

The small particles used in these experiments were deposited on the shock tube walls in significant numbers. This deposit was removed by the high flow velocity of the gas produced by the shock wave and falsified the light-scattering measurements. A sufficiently high initial flow velocity in the shock tube was therefore required to prevent the deposit. Since no air supply was available to provide the required initial flow velocity of about 10 m/sec, a smaller shock tube was set up. At first, a few experiments were performed with a glass shock tube of about 1 cm diameter. The results agreed well with those shown in Figure 2, but to reduce possible effects caused by the boundary layer in such a narrow tube, a bigger tube of about 2.5 cm diameter and made of copper was finally used.

A typical pressure and light scattering record is shown in Figure 3. The initial flow velocity and the shock velocity are indicated in the figure as well as the average particle diameter and the loading ratio  $u$  (ratio of the particle flow rate to the gas flow rate). A number of experiments are shown in Figure 4 where the loading ratios and the particle size are also indicated. The straight line shown is not an empirical fit of the data but the line obtained with the first experiments shown in Figure 2. The good agreement with the newer data is evident. The larger particles seem to cause a shift upward and to the right, but this shift is not much larger than the scatter of the data. It is also interesting to note that the results seem to be independent of the particle loading, at least over the range of these experiments.

We have thus obtained substantially the same results with two different techniques and with three shock tubes of different sizes and materials. At this point, it seems that we cannot doubt the experimental results, but we still need an explanation. Several hypotheses

## UNCLASSIFIED

that one might consider are briefly indicated in the following:

Acceleration The flow around the particles is not steady so that the drop could be affected by the continuous readjustment of the flow. However, the change of the particle velocity relative to the gas burning the time in which the particle travels a significant distance - say one particle diameter - is only 0.1% of the relative velocity so that it should be permissible to consider the flow as quasi steady.

Delay of Wake Mixing The experiments are evaluated on the basis of one-dimensional flow; it is therefore implied that the effect of the particles is instantaneously distributed over the entire cross-section of the duct. In reality, this distribution takes place gradually through mixing of the particle wakes with the rest of the gas. As a result, the computed gas velocity might be in error<sup>3</sup>. It is possible to show, however, that any hypothesis which would affect the gas velocity without affecting also the measured particle velocity could not significantly modify the steep slope of the correlation shown in Figures 2 and 4.

Electrostatic Effects There is no doubt that the particles carry electric charges which could affect the calculated drag in some manner. Mathematically, this hypothesis means that the equation of motion for the particles should include a term for the electrostatic force in addition to the one expressing viscous drag. Although this effect cannot be completely ruled out at this time, it is hard to see why it should be independent of the particle concentration.

Surface Roughness The surface of the particles is not completely smooth, and md irregularities should be more significant for the smaller particles<sup>4</sup>. Since this aspect will be discussed by the next speaker, Dr. Selberg, no further comments are made here.

## UNCLASSIFIED

Oscillation or Rotation of Particles Photomicrographs of the glass particles immersed in oil reveal that many of them have small gas bubble inclusions. The center of gravity of the particles may therefore be slightly shifted from the center of the sphere. Shock impact and viscous drag may then lead to excentric oscillations or rotation of the particles. Nothing can be said at this time about the drag of such bodies.

Collisions Between Particles Since the particles have a size distribution, they will develop different velocities that may lead to collisions between particles. Such collisions have the same effect as an increased drag because they tend to destroy the oriented particle motion relative to the gas. Marble<sup>5</sup> has shown that such collisions may have effects of the same order of magnitude as those caused by viscous drag, but his theory applies only to much larger Reynolds numbers.

Turbulence It was pointed out by Torobin and Gauvin<sup>6</sup> that the turbulence level for an observer on a particle is much higher than the turbulence level for an observer on the wall of the duct because the particle velocity relative to the gas is much smaller than the gas velocity in the duct. It is not known what effect of such high turbulence levels on the drag could be.

Deposit on Walls There is some evidence that particles are deposited on the wall ahead of the shock wave in spite of the rather high flow velocity. It is therefore possible that the light scattering measurements behind the shock wave are somewhat affected by particles swept off the walls. However, this phenomenon would not have affected the early results obtained by means of streak records.

Some of these hypotheses have not yet been definitely ruled and,

UNCLASSIFIED

## UNCLASSIFIED

possibly, more than one, or additional ones, may have to be considered; but this is the present status of the program. We are continuing the work, and I hope to come up some day with a more definite answer to this problem.

UNCLASSIFIED



# UNCLASSIFIED

## REFERENCES

1. Rudinger, G. "Experiments on Shock Relaxation in Particle Suspensions in a Gas and Preliminary Determination of Particle Drag Coefficients". In Multi-Phase Flow Symposium (N.J. Lipstein, Editor), ASME, New York, 1963, pp. 55-61.
2. Ingebo, R. D. "Drag Coefficients for Droplets and Solid Spheres in Clouds Accelerating in Air Streams", NACA, TN3762, 1956.
3. Rudinger, G. "Reply to Comments by S. L. Soo". Physics of Fluids, Vol. 7, pp. 1884-1885, 1964.
4. Selberg, B. P. "Shock Tube Determination of the Drag Coefficient of Small Spherical Particles". NASA CR-418, 1966.
5. Marble, F. E. "Mechanism of Particle Collision in the One-Dimensional Dynamics of Gas-Particle Mixtures". Physics of Fluids, Vol. 7, pp. 1270-1282, 1964.
6. Torobin and W. H. Gauvin "Fundamental Aspects of Solids Gas Flow. Part V. The Effects of Fluid Turbulence on the Particle Drag Coefficient". Canadian Journal of Chemical Engineering, Vol. 38, pp. 189-200, 1960.

UNCLASSIFIED

UNCLASSIFIED

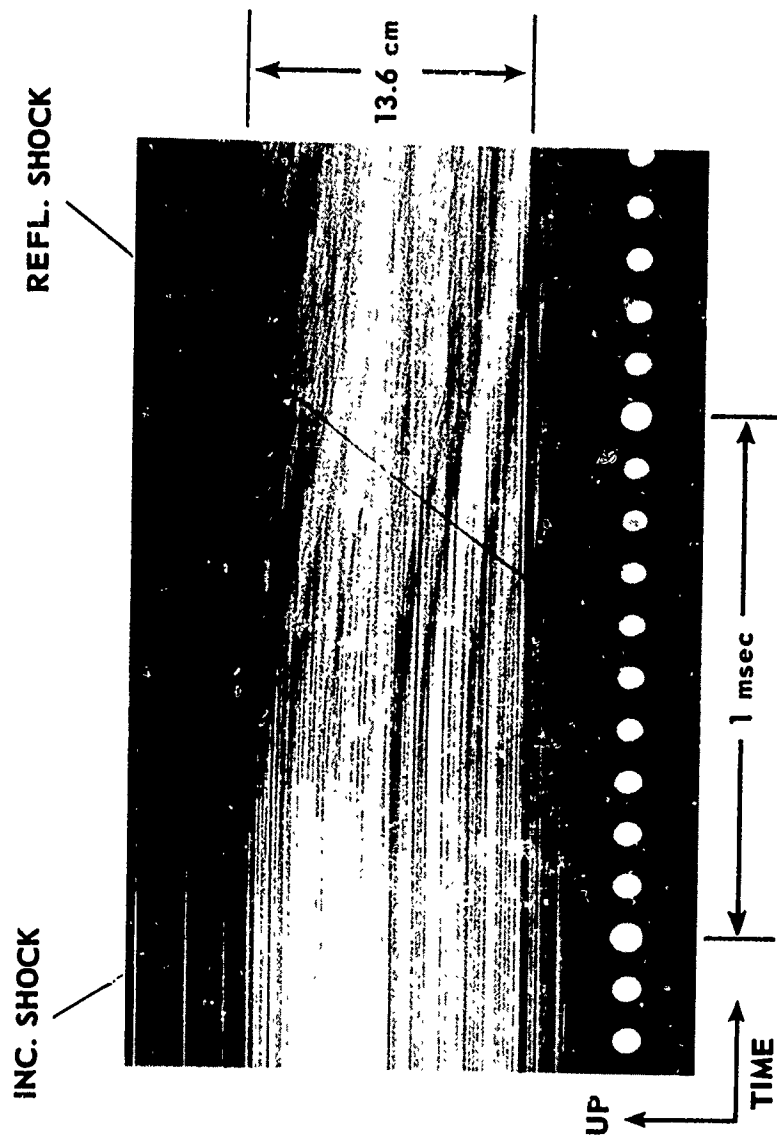


Figure 1. Typical Shock Tube Streak Record

UNCLASSIFIED

UNCLASSIFIED

DRAG COEFFICIENT (7.5-cm x 7.5-cm SHOCK TUBE)

$\eta \sim 0.2$ ,  $D = 29 \mu$

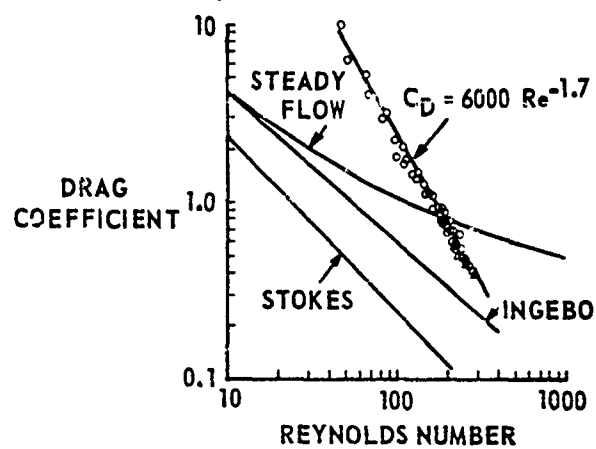


Figure 2

UNCLASSIFIED

UNCLASSIFIED

VERTICAL SHOCKTUBE  
(2.5 cm DIAMETER)

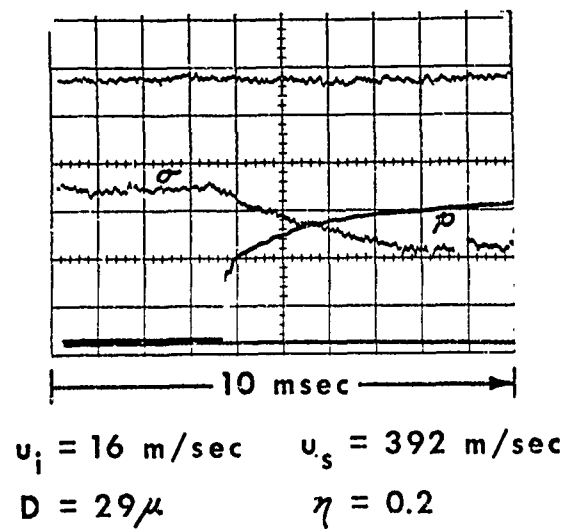


Figure 3. Typical Pressure and Light Scattering Record

UNCLASSIFIED

UNCLASSIFIED

DRAG COEFFICIENT (2.5-cm SHOCK TUBE)  
(SHOCK POINTS AND RELAXATION ZONE)

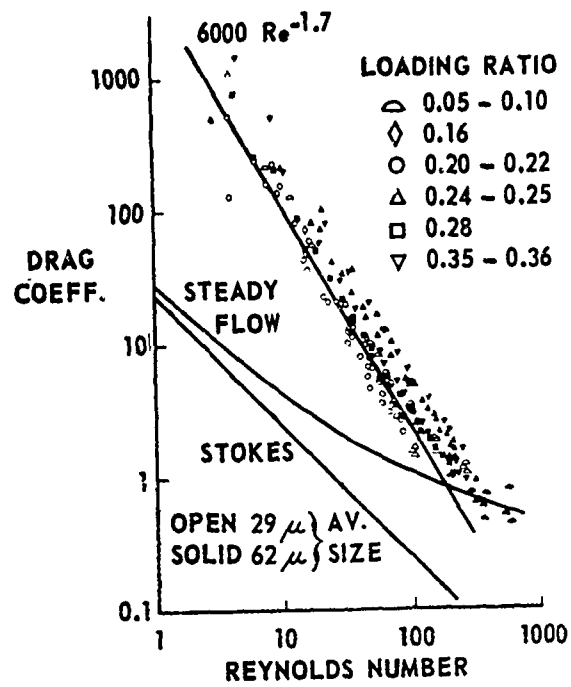


Figure 4

UNCLASSIFIED

779/780

**UNCLASSIFIED**

SHOCK TUBE DETERMINATION  
OF THE DRAG COEFFICIENT OF  
SMALL SPHERICAL PARTICLES

by

B. P. Selberg

The Aerospace Corporation  
San Bernardino Operations

**UNCLASSIFIED**

# UNCLASSIFIED

## SHOCK TUBE DETERMINATION OF THE DRAG COEFFICIENT OF SMALL SPHERICAL PARTICLES

With the addition of large mass fractions of metal particles in solid propellant rocket motors, and hence the existence of these particles and condensed liquid or solidified particles from the combustion products in the rocket nozzles, there has been a renewed interest in the  $C_D$  of small particles among those interested in solid propellant rockets. The liquid propellant researchers have also been interested in  $C_D$  of small evaporating or burning liquid drops. The first slide contains the results of most of the recent work on the  $C_D$  of small particles versus  $Re$ . The solid line indicates the classical steady state  $C_D$  for a sphere and is based on work done by many investigators. I would like to make two points about this graph, the first being the large discrepancies that exist between the different investigation results. Secondly, I would like to call your attention to the experimental results, which is indicated by the dashed line. This work, done by Crowe at the University of Michigan, was a theoretical and experimental study with burning and non-burning particles. His experimental results which are indicated here have been shifted above the steady state curve; he was unable to explain the reason for this shift. It should be noted, however, that for the  $Re$  number range which he covered, he obtained the same general trend as the classical steady state curve. The work that is going to be presented today is the follow-on to Crowe's work and was sponsored by NASA. Crowe was able to theoretically obtain expressions for compressibility and slip flow effects on the  $C_D$  of spherical particles. It was the original intent of this work to first determine why the shift existed in Crowe's data from the steady state curve and then experimentally study

UNCLASSIFIED

## UNCLASSIFIED

compressibility and slip flow effects. Because of the high scatter which existed in Crowe's data, approximately 30 per cent, it was necessary to construct a new and better-instrumented shock tube.

The next slide is a photograph of the new facility. The driver section is at the extreme left, out of the field of view. Once the shock wave is initiated, it travels down the shock tube to the right, interacts with the particles which are dropped by the particle injector. The particles are then accelerated by the convective flow behind the shock front and are then photographed to obtain the  $x$  versus  $t$  history. The particles were photographed by using a rotating drum camera in conjunction with a xenon flash lamp. The energy to the flash lamp was supplied by five high voltage switching circuits which were triggered by an audio-oscillator. With this optical system it was possible to obtain exposures 480 nanoseconds in duration. The shock speed was measured by two pressure transducers on each side of the test section in conjunction with a microsecond timer. The shock tube and the driver section could both be independently pressurized or evacuated such that the proper  $M_R/(Re)^{1/2}$ , which is the parameter that describes the flow regime under consideration, is obtained. The next slide indicates the equation of motion for a non-burning particle.

For our study the axial accelerations that the particles encountered were 100 g's and thus the normal acceleration due to gravity can be neglected and the equation can be written in a scalar form. If spherical particles are considered the equation takes a form indicated on the second line of the slide.

Where:

$\rho_p$	is the particle density
$a$	is the particle acceleration
$d$	is the particle diameter
$\rho_2$	is the convective flow density



## UNCLASSIFIED

$U_2$	is the convective flow velocity behind the shock front
$V_p$	is the velocity of the particles with respect to inertial space
$U_R$	is the relative velocity between the particles and the convective flow

From each experimental run the following quantities are needed to determine  $C_D$ , Re number and  $M_R$ :

- particle diameter
- convective flow velocity
- convective flow density
- viscosity of the convective flow
- particle velocity
- particle acceleration

The particle diameter was obtained from the image on the photograph film. The convective flow velocity and density were obtained from the normal shock relations in conjunction with the measured shock front velocity. The viscosity was obtained from the National Bureau of Standards tables using convective flow temperatures obtained from the shock relations. The particle velocity and the particle acceleration were both obtained from the position data recorded on the film. Whenever position data is used to obtain velocities and accelerations, there is always concern over the accuracy used to obtain the velocities and accelerations. For this reason two data reduction techniques were used to reduce the position data. These methods are indicated on the next slide.

The first method consisted of a third-order polynomial fit to the position of data. Since five position points existed, the highest order polynomial that could be passed through these points would be a fourth-order polynomial. In order to account for inaccuracy in measuring the position data and therefore not wanting the polynomial to pass

UNCLASSIFIED

## UNCLASSIFIED

through every position point, a third-order polynomial was chosen. A least squares technique was used to fit the best third-order polynomial to the position data. The particle's velocity and acceleration is then obtained by differentiating the polynomial one and two times, respectively. The second data reduction technique determined a  $\bar{C}_D$ . The equation for  $C_D$  can be rewritten as indicated in the slide, making the indicated change of variable and assuming that  $B$  is constant over the time interval of interest. By doing this the equation can be integrated and by substituting the proper boundary conditions, one obtains the last equation indicated on the slide. Here again a least squares technique was used to fit this equation to the data points. Once this is done and  $B$  is determined then  $\bar{C}_D$  is obtained. The assumption that  $B$  is constant over the time interval of interest is a good assumption in that  $C_D$  changes only about 2 per cent. We then attempted to determine the cause of the shift in  $C_D$  that Crowe observed. To this end experimental runs were made with glass particles, 150 - 250 microns in diameter, in the incompressible continuum regime. The next slide indicates the results of these runs using the  $\bar{C}_D$  method.

Here again we have the classical steady state curve with our experimental points falling considerably above this curve and with the best fit curve to the experimental points. We have verified the same general trend that Crowe's experiment determined. We have also obtained the same upward shift of  $C_D$ , however to a lesser extent. We have also reduced the experimental scatter. The next slide indicates the same experimental results but with the polynomial data reduction technique method. Again we have essentially the same results, i.e., the same shift and same scatter. Individual values of  $C_D$  and  $Re$  for both data reduction techniques were nearly the same. This established the validity of the data reduction techniques and indicates that the  $C_D$  obtained by both methods are correct. Probable error calculations for these runs indicated a 5 per cent probable error in  $Re$  number. As

## UNCLASSIFIED

you can see in the slide, the errors in Re number and  $C_D$  are considerably more than 4 and 5 per cent, respectively. We also could not explain the reason for the upward shift from the classical experimental curve. In order to try to explain this discrepancy, the natural first thing to do would be to recheck all of the experimental calibrations. This was done and resulted in the verification of the initial calibrations.

We then looked into possible causes such as boundary layer formation time, wake formation time, sphere rotation, acceleration effects, turbulence and particle effects. Boundary layer formation time and wake formation time can both be ruled out on the basis that these formation times are at least an order of magnitude less than the time between when the particle interacts with the shock front to the time when the first picture is taken. Sphere rotation was ruled out on the basis of work done by other investigators which indicated if rotation did exist, a decrease of  $C_D$  would be obtained. In any event the particle injector did not tend to rotate the particles. Acceleration effects were discarded on the basis of past investigations which all indicated that for acceleration effects to be important, the acceleration modulus had to be on the order of one or greater. For the present study, the acceleration modulus was  $\approx 10^{-3}$ . Schlieren photographs were taken of the shock front which indicated the shock front was normal and plane, thus no turbulence would be generated by the shock front. The only other mechanism which could generate turbulence would be the boundary layer. Since the convective flow velocities were so low for the present study, it was felt that any turbulence which was generated in the boundary layer would not have any mechanism by which to be transmitted to the center of the test section. Having ruled out everything but particle effects, we took a closer look at the particles. Upon a close examination the particles did have some significant roughness. Thus it was decided to conduct some new experiments

UNCLASSIFIED

## UNCLASSIFIED

with different particles. Some HF 295 gun powder balls, 280 - 350 microns in diameter, were chosen mainly due to the fact that they had more surface roughness than the glass balls. The same experiments were rerun with the same techniques with  $M_R < 0.15$ .  $C_D$  increases as much as 85 per cent were obtained over the best fit through the previous glass particles data. If this was indeed a surface roughness effect it was felt that by repeating more experiments with the glass beads at higher  $M_R$  numbers this effect should be seen. Thus more experiments were run with glass particles with  $0.15 < M_R < 0.3$ . Here again considerable increase in  $C_D$  was noticed with a similar increase in scatter. In order to tie down the apparent surface roughness effect even further, additional experiments were run with sapphire balls, 396.8 microns in diameter. These sapphire balls were individually lapped such that they had a surface finish of 1.5 microinches. Due to experimental constraints, it was necessary to conduct these experiments with  $0.14 < M_R < 0.32$ . The sapphire ball experiments indicated a decrease in  $C_D$  from the best set of the glass particle data and a decrease in scatter. The next slide indicates the results of these tests. Note that all the sapphire data lies below the glass particle data and that it is almost back to the classical steady state curve. It is felt that if we had been able to reduce the  $M_R$  number to values less than 0.15 we may have reached the steady state curve. The next series of slides are photomicrographs of glass particles, ball powder, and sapphire balls.

The first of the series is a photomicrograph of glass particles indicating magnification of 200. These magnifications are only relative for comparison of the different particles and are not representative of true magnifications. This first photomicrograph essentially indicates the particles are round with some large surface blemishes. The next photomicrograph is also of a glass particle. The magnification has been increased by approximately a factor of 10. The surface

## UNCLASSIFIED

here appears to be quite rough with little pits on the entire surface. The next photomicrograph is also of a glass particle the same magnification as the previous slide. However, here we are looking at some of the larger surface blemishes. The next photomicrograph is of ball powder. This slide indicates that the ball powder is rough with a few blemishes seen on the surface here and there. The next slide is a photomicrograph of ball powder again with an intermediate magnification. These surface blemishes now are becoming very apparent. The next photomicrograph is again ball powder at a high magnification comparable with that of the high magnification of the glass particles; the surface now is very rough, much rougher than that of the glass particles. The next slide is a photomicrograph of the sapphire balls at low magnification. This essentially indicates the sapphire balls are rough with no apparent surface roughness. The next slide is another photomicrograph of a sapphire ball with the high magnification comparable to the high magnification for the glass and ball powder. Although surface roughness does exist, it exists here to a lesser extent than of either the glass particles or the ball powder. The next photomicrograph is also of a sapphire ball at high magnification but one which has been washed. Note here that almost all of the roughness which was apparent in the last slide is now gone. This indicates that most of the roughness on the sapphire ball appears to be dust and other surface dirt which can be washed off.

The last slide indicates my conclusions:

1. Surface roughness can cause considerable shift in  $C_D$  for small spherical particles where viscous effects are important in both the slip flow and continuum regime, i. e., for Re numbers greater than 1.
2. Thus  $C_D$  for particles in rocket exhaust may be several hundred percent higher, for the regimes discussed in 1. above, than the

UNCLASSIFIED

## UNCLASSIFIED

usually accepted value which is obtained by modifying the steady state results for compressibility and slip flow effects. The particles from the propellant in the rocket exhaust will be rougher than those used in the present study. The condensed liquid particles in the nozzle, although smooth, will be deformed, while the solidified condensed liquid particles will most likely be comparable with the glass particles in the present study.

Much more work needs to be done to study the influence of the various contributing parameters: namely, compressibility, burning, slip flow, transition flow, free molecular flow, neighboring particles, electric charges, turbulence and controlled roughness.

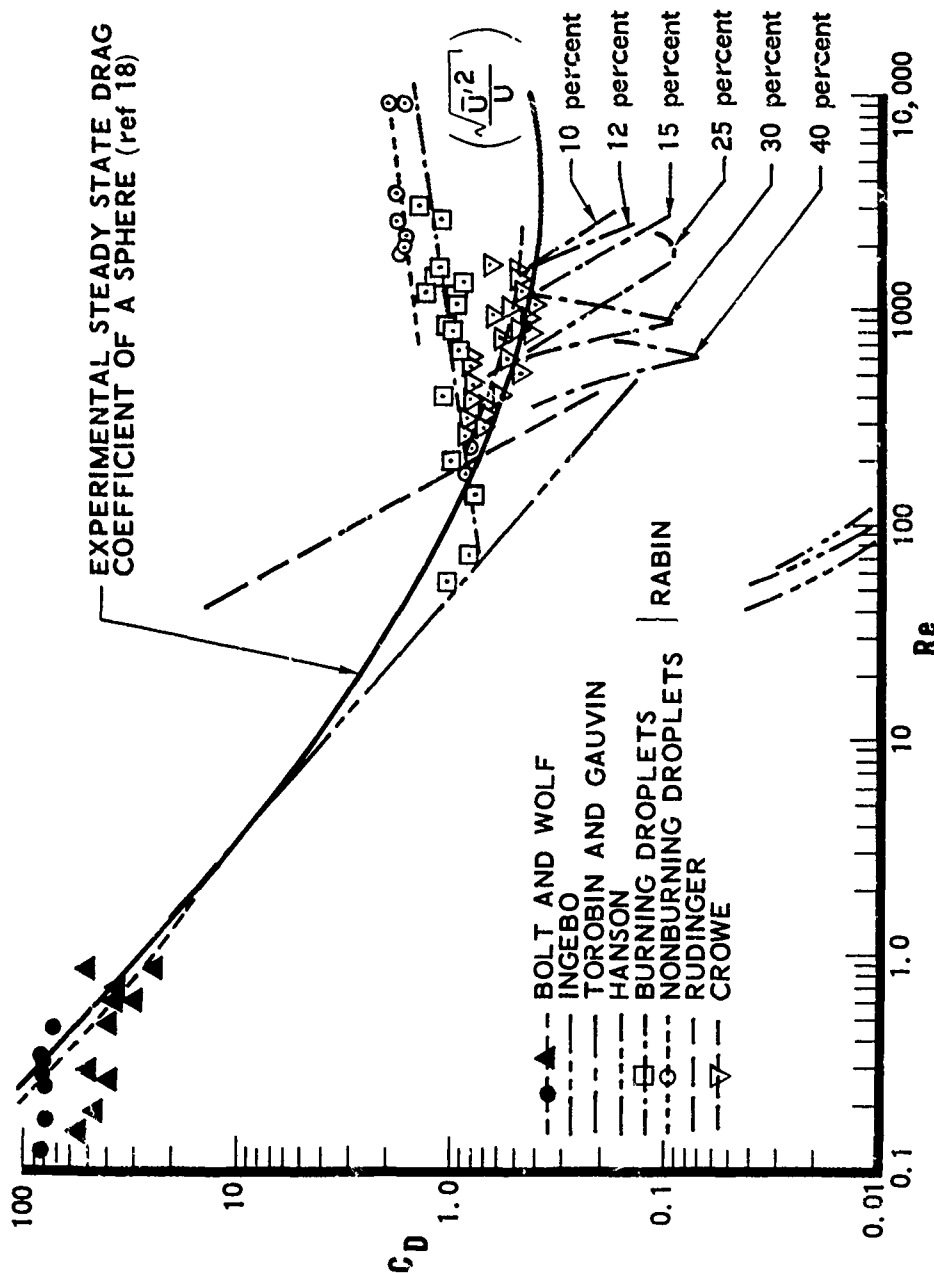


Figure 1 (Slide 1). Data on the Drag Coefficient of Spheres.

UNCLASSIFIED

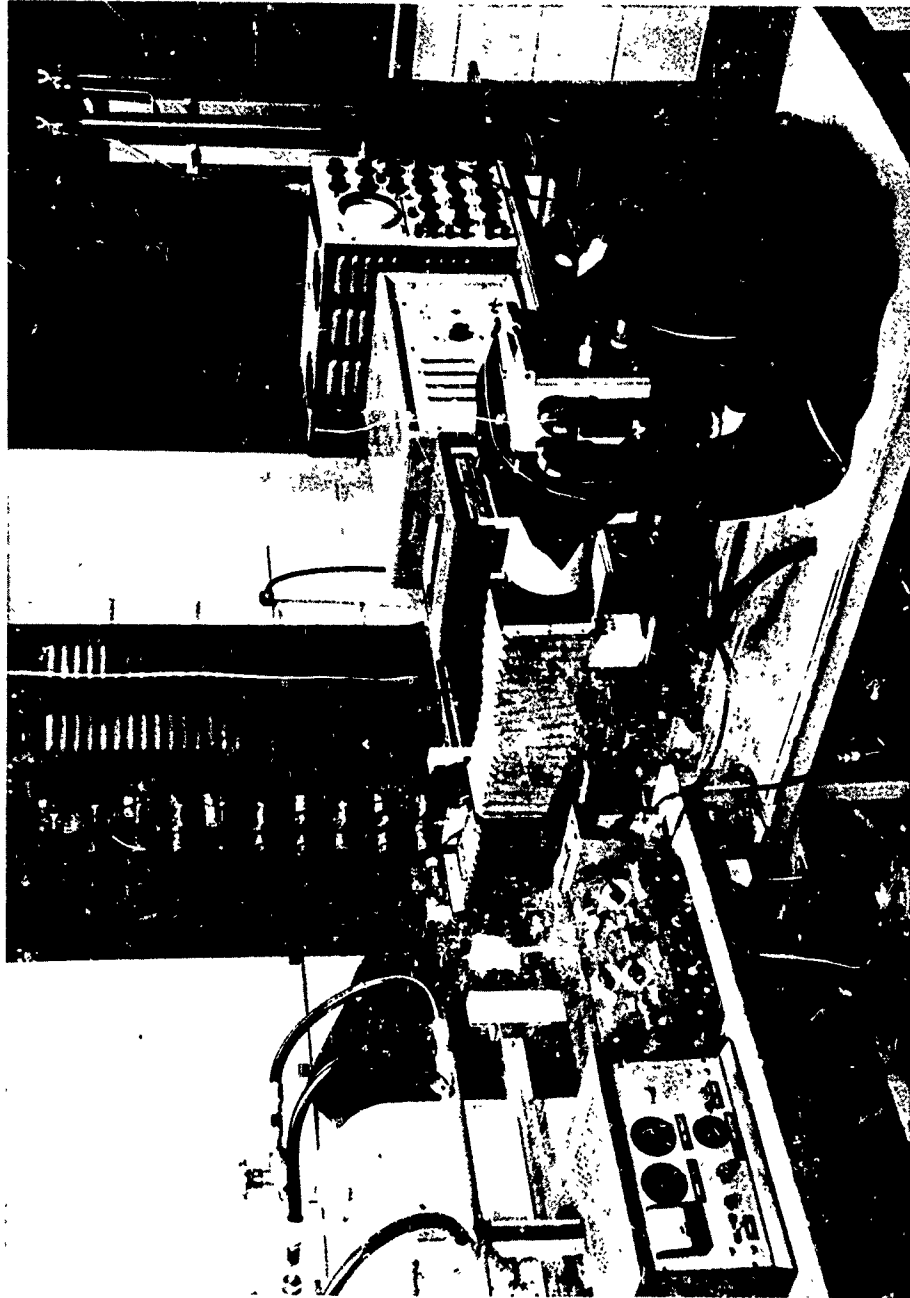


Figure 2 (Slide 2). General Shock Tube Facility.

UNCLASSIFIED



UNCLASSIFIED

- THE PARTICLE EQUATION OF MOTION IS

$$\frac{C_D \rho_2}{2} \left| \vec{U}_R \right| \vec{U}_R = m \vec{a}$$

- FOR SPHERICAL PARTICLES OF UNIFORM DENSITY

$$C_D = \frac{4\rho_p \alpha d}{3\rho_2 U_R^2} = \frac{4\rho_p \alpha d}{3\rho_2 (U - V_p)^2}$$

- FROM EACH EXPERIMENTAL RUN, THE FOLLOWING QUANTITIES ARE NEEDED TO DETERMINE  $C_D$ ,  $Re$ , AND  $M_R$

- PARTICLE DIAMETER
- CONVECTIVE FLOW VELOCITY
- CONVECTIVE FLOW DENSITY
- VISCOSITY OF THE CONVECTIVE FLOW
- PARTICLE VELOCITY
- PARTICLE ACCELERATION

UNCLASSIFIED

Figure 3 (Slide 3). Equation of Motion for a Non-Burning Particle.

UNCLASSIFIED

UNCLASSIFIED

- THIRD ORDER POLYNOMIAL FIT TO POSITION DATA
- THE EQUATION FOR  $C_D$  CAN BE WRITTEN AS

$$B (U_2 - \dot{x})^2 = \ddot{x} \quad \text{WHERE } B = \frac{3\rho_2 C_D}{4\rho_p d}$$

$$\text{LET } \dot{x} = p \quad \text{THEN } \ddot{x} = dp/dt$$

$$\frac{dp}{(U_2 - p)^2} = B dt$$

- ASSUMING  $B$  IS A CONSTANT OVER THE TIME INTERVAL OF INTEREST THE ABOVE EQUATION CAN BE INTEGRATED AND PUT INTO THE FOLLOWING FORM WITH THE PROPER BOUNDARY CONDITIONS

$$x = x_0 + U_2 t - \frac{1}{B} \ln [B(U_2 - V_{p_0}) t + 1]$$

Figure 4 (Slide 4). Data Reduction Techniques.

UNCLASSIFIED

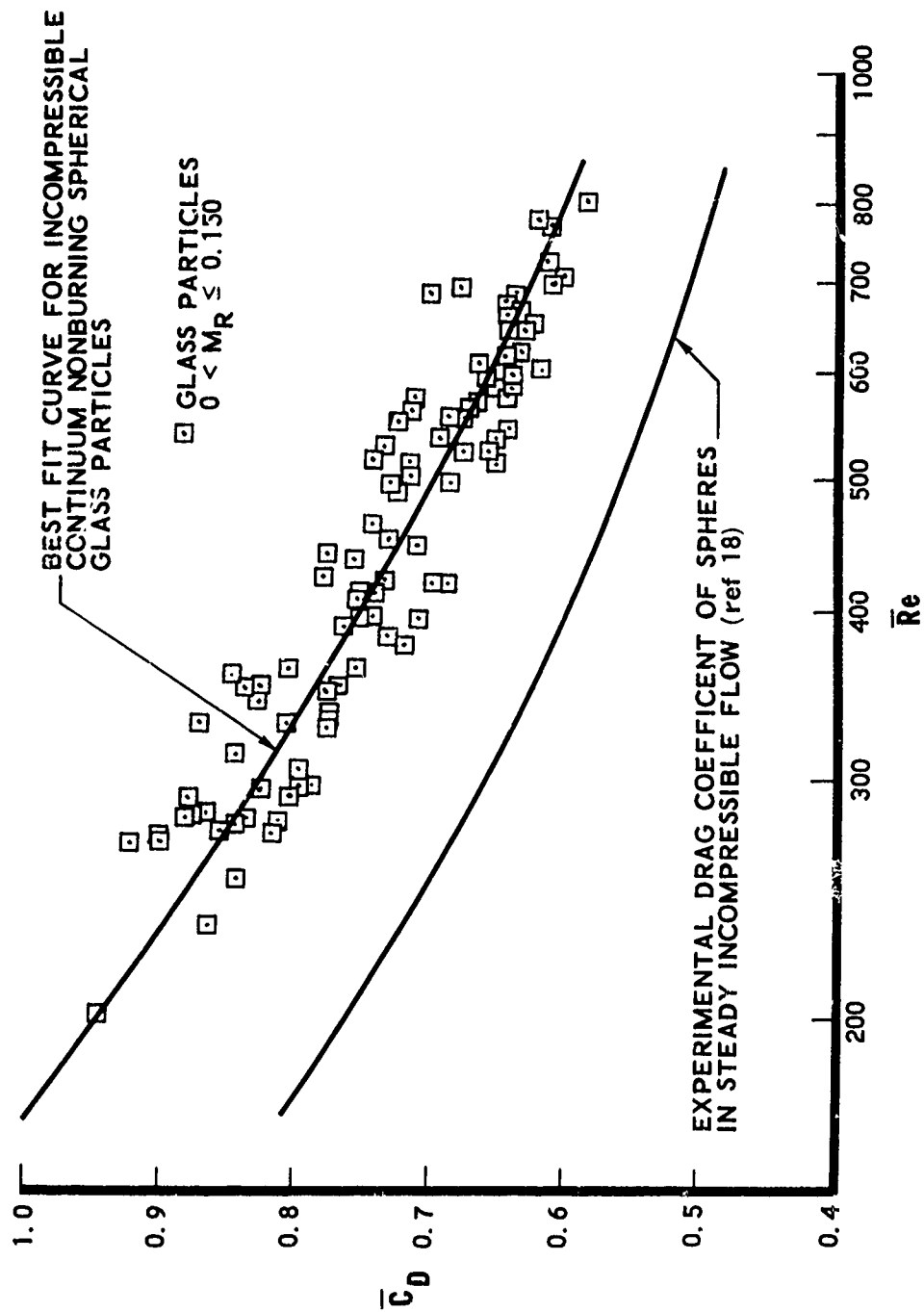


Figure 5 (Slide 5). Drag Coefficient versus Reynolds Number for Mean Drag Coefficient Method.

UNCLASSIFIED

UNCLASSIFIED

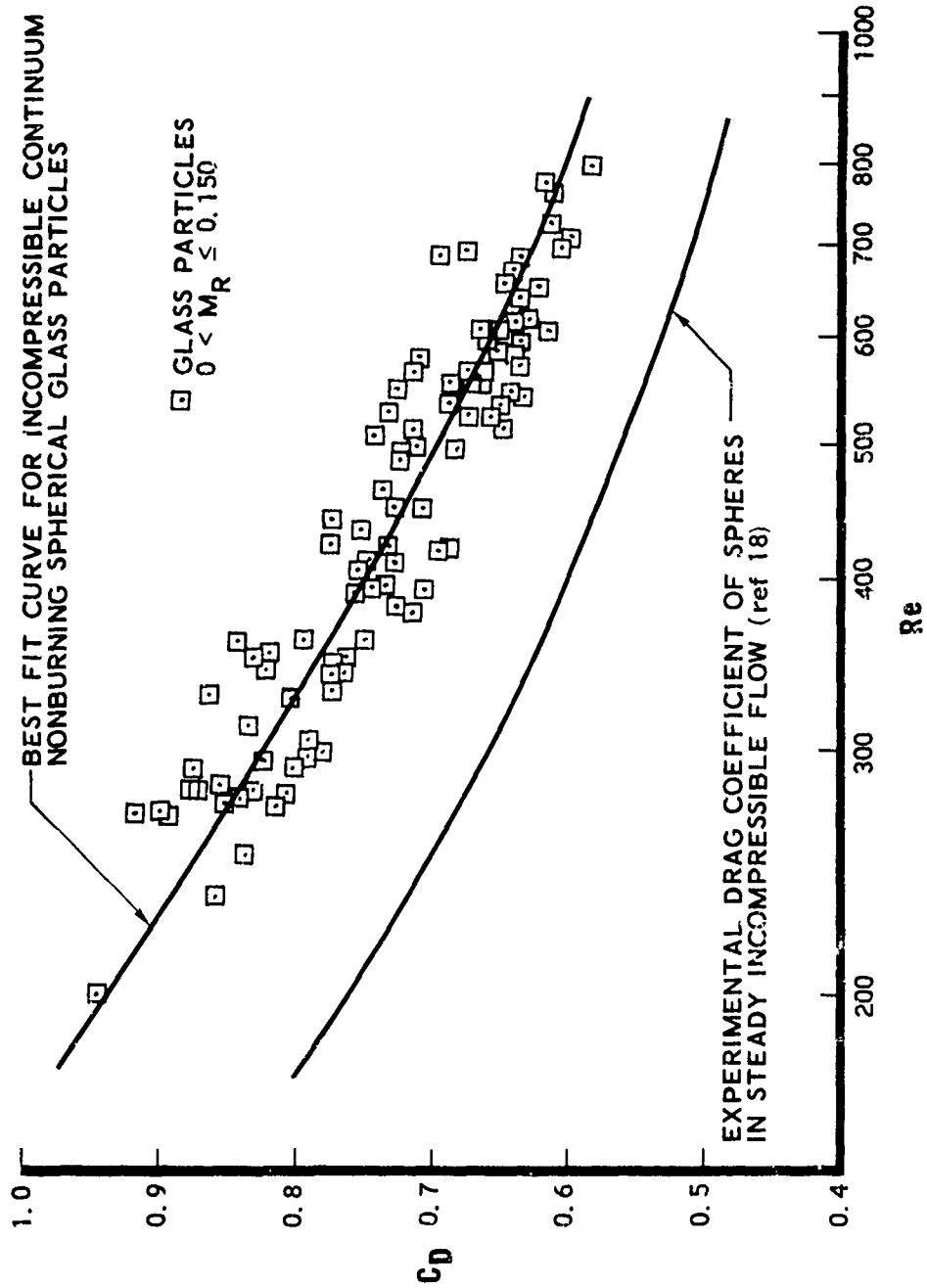


Figure 6 (Slide 6). Drag Coefficients versus Reynolds Number for  
Third Order Polynomial Data Reduction Technique.

UNCLASSIFIED

UNCLASSIFIED

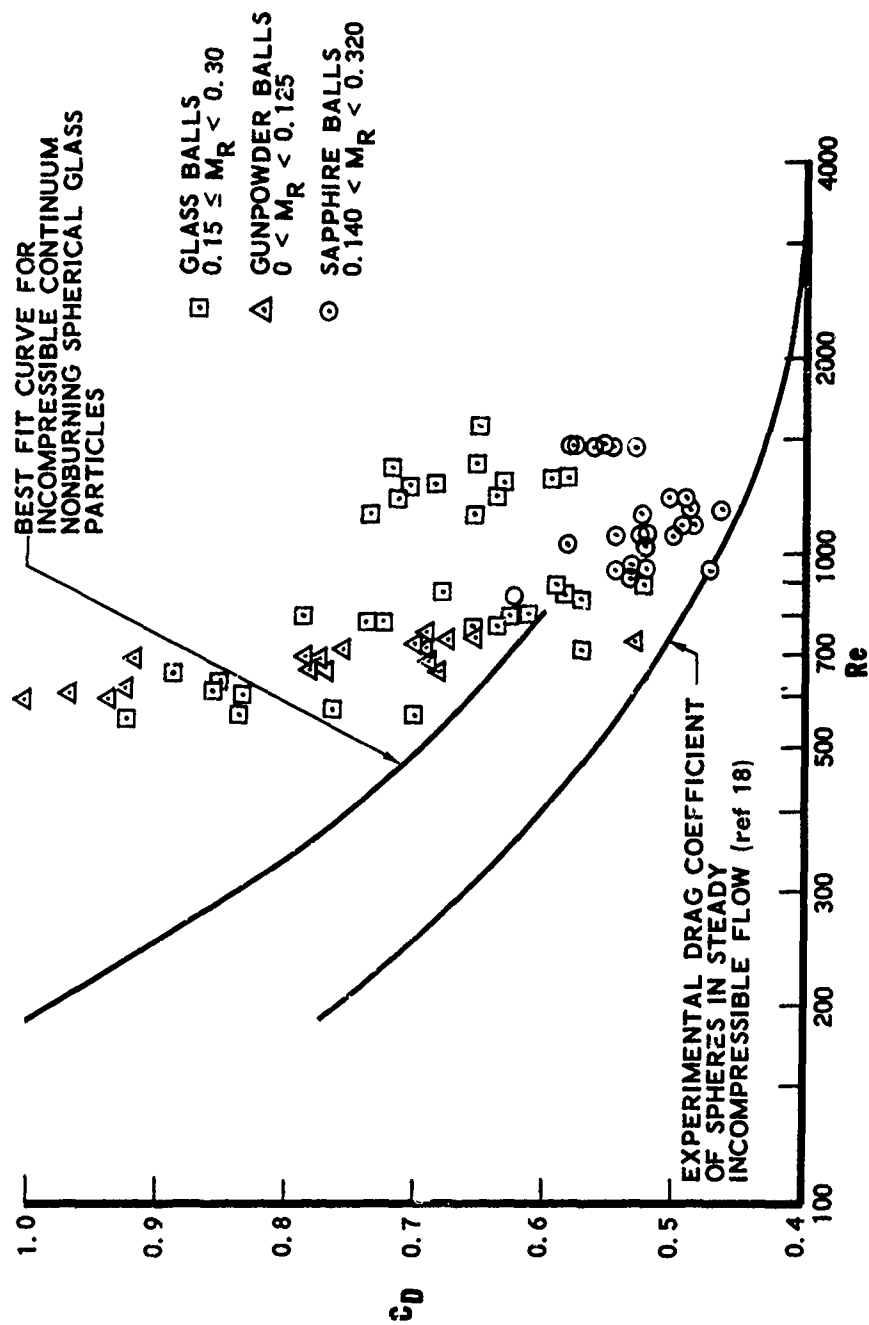


Figure 7 (Slide 7). Drag Coefficient versus Reynolds Number:  
Glass Particles, Ball, Powder, and Sapphire Balls.

UNCLASSIFIED

UNCLASSIFIED



Figure 8 (Slide 8). Photomicrograph of Glass Particles, Magnification = 200.

UNCLASSIFIED

UNCLASSIFIED

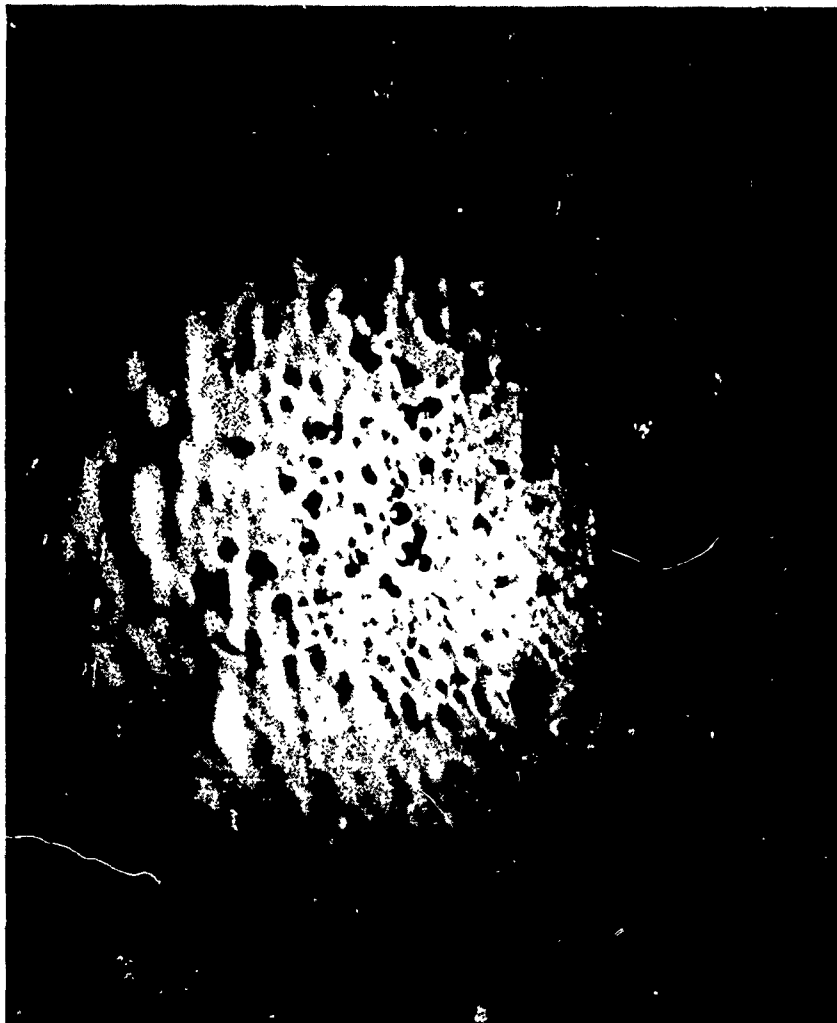


Figure 9 (Slide 9). Photomicrograph of Glass Particle, Magnification = 1840.

UNCLASSIFIED

UNCLASSIFIED

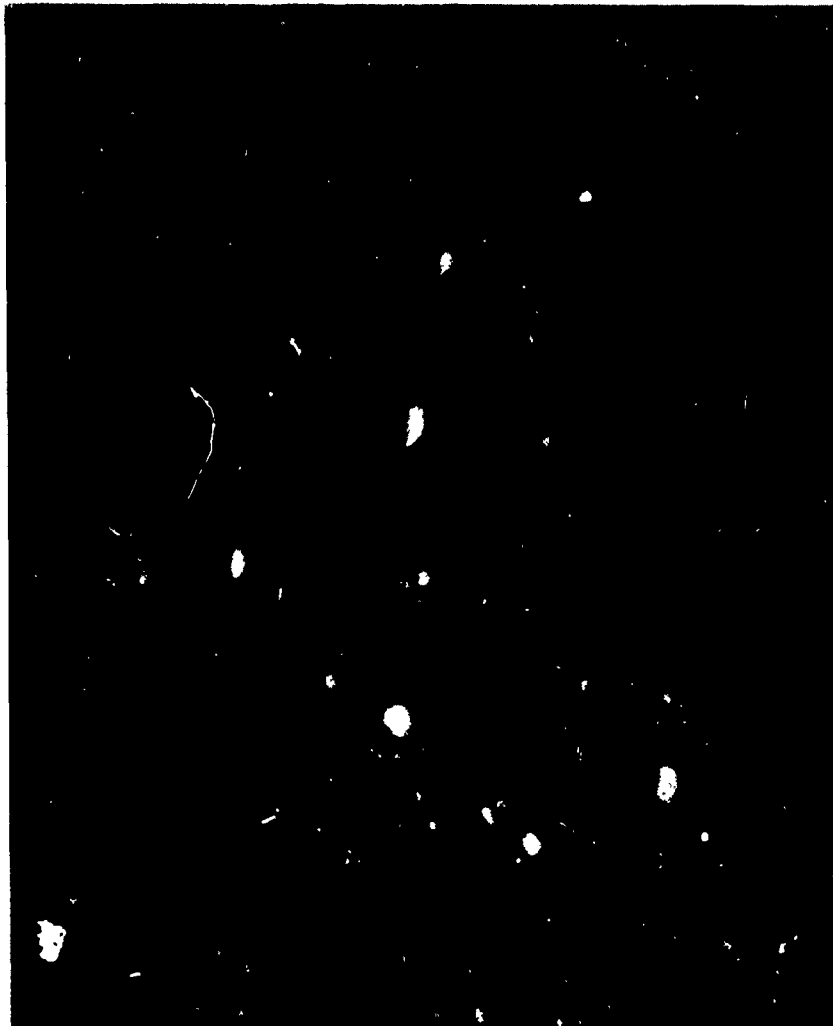


Figure 10 (Slide 10). Photomicrograph of Glass Particle, Magnification = 1840.

UNCLASSIFIED



UNCLASSIFIED

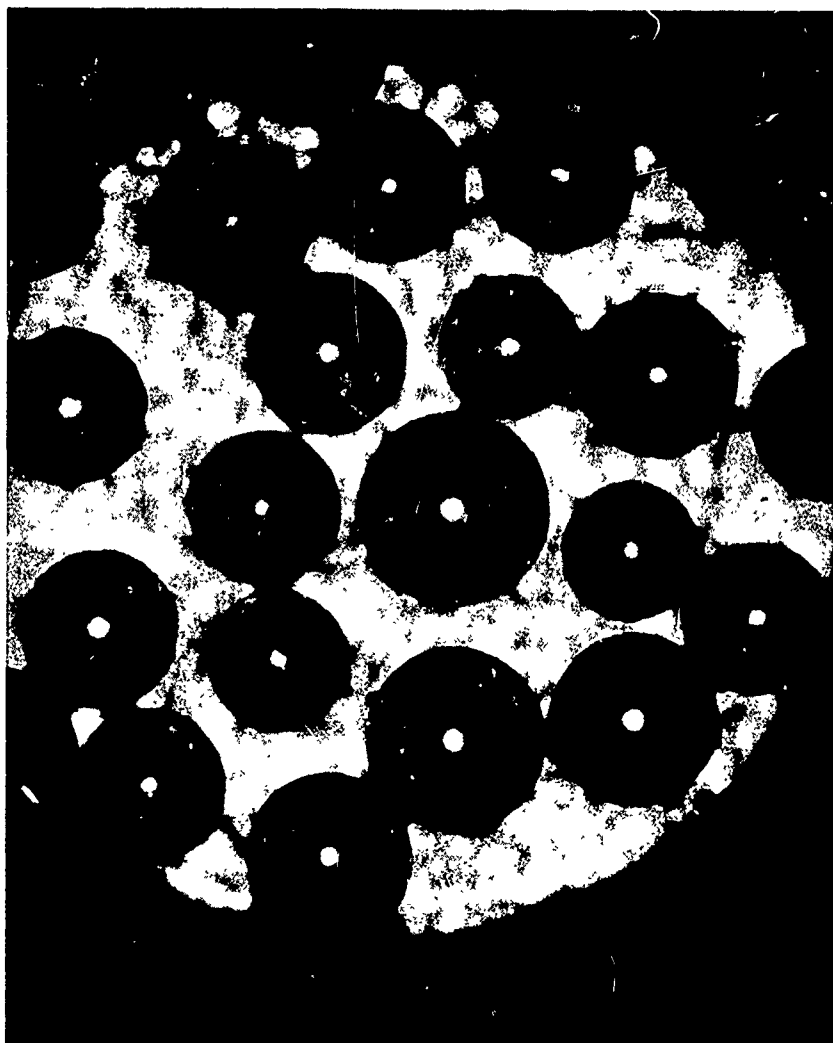


Figure 11 (Slide 11). Photomicrograph of HP 295 Ball Powder,  
Magnification = 110.

UNCLASSIFIED

UNCLASSIFIED

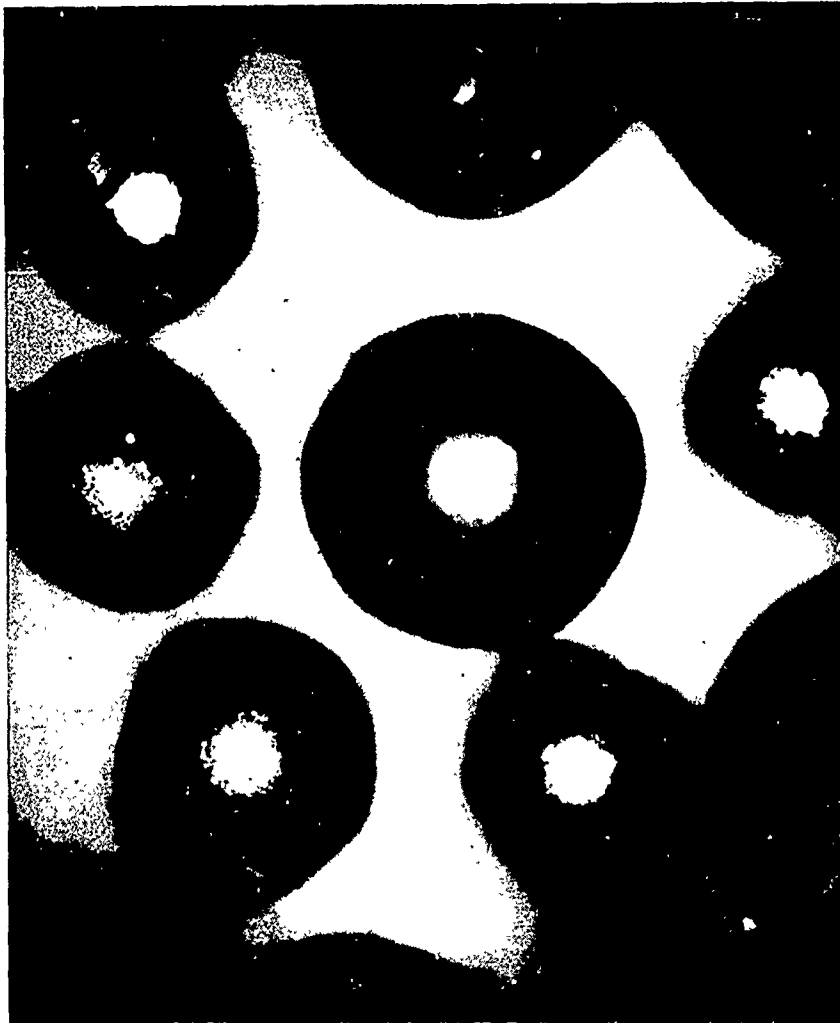


Figure 12 (Slide 12). Photomicrograph of HP 295 Ball Powder,  
Magnification = 190.

UNCLASSIFIED

UNCLASSIFIED



Figure 13 (Slide 13). Photomicrograph of HP 295 Ball Powder,  
Magnification = 1840.

UNCLASSIFIED

UNCLASSIFIED

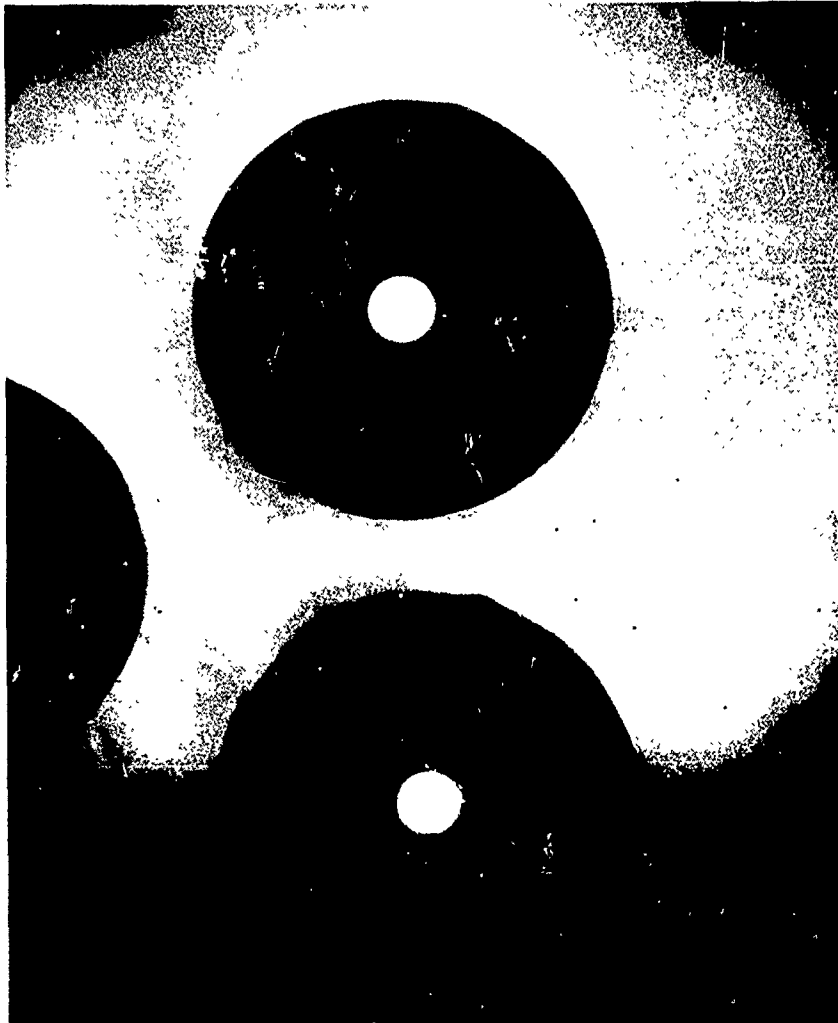


Figure 14 (Slide 14). Photomicrograph of Sapphire Balls,  
Magnification = 202.

UNCLASSIFIED

UNCLASSIFIED

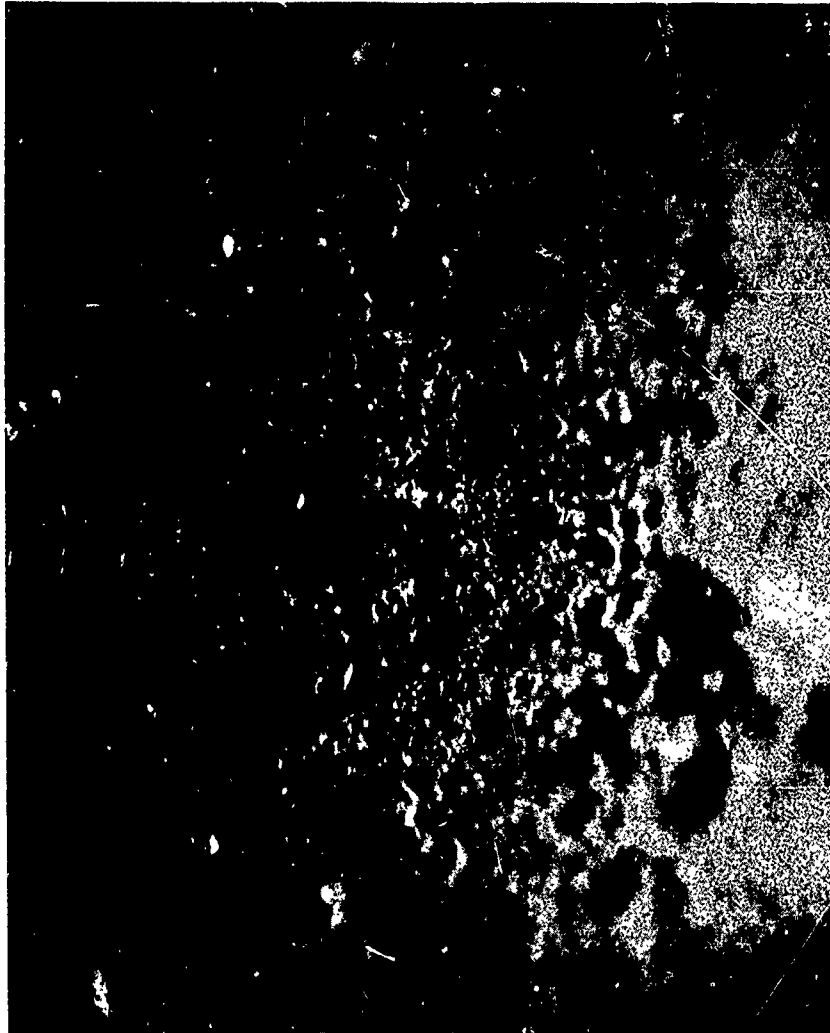


Figure 15 (Slide 15). Photomicrograph of Sapphire Ball,  
Magnification - 1850.

UNCLASSIFIED

UNCLASSIFIED



Figure 16 (Slide 16). Phot micrograph of a Washed Sapphire Ball,  
Magnification = 1760.

UNCLASSIFIED

UNCLASSIFIED

- SURFACE ROUGHNESS CAN CAUSE A CONSIDERABLE SHIFT IN  $C_D$  FOR SMALL SPHERICAL PARTICLES
- $C_D$  FOR PARTICLES IN ROCKET EXHAUSTS MAY BE SEVERAL HUNDRED percent HIGHER THAN THE USUALLY ACCEPTED VALUE
- MUCH MORE WORK NEEDS TO BE DONE ON THE INFLUENCE OF COMPRESSIBILITY, BURNING, ELECTRIC CHARGES, SLIPFLOW, TRANSITION FLOW, FREE MOLECULAR FLOW, NEIGHBORING PARTICLES, AND TURBULENCE AS WELL AS THE INFLUENCE OF CONTROLLED SURFACE ROUGHNESS

Figure 17 (Slide 17). Conclusions.

UNCLASSIFIED

# UNCLASSIFIED

## QUESTIONS, ANSWERS & COMMENTS

Q. /G. Rudinger (Cornell Aeronautical Lab.): There is certainly some evidence that roughness could cause some effect like those in your report. Did you remark that you did not evaluate any experimental data where there were two particles in close proximity?

A/B. P. Selberg (Aerospace): Yes.

Q. /G. Rudinger (Cornell Aeronautical Lab.): You mean you did not evaluate them or did not report them? Did you find any effect of neighboring particles?

A/B. P. Selberg (Aerospace): We had a technique where if a particle was within, I think it was 6 diameters of another particle, we would just automatically discard both of these. If one particle was within the wake of another one, within 12 diameters, we wouldn't even think of it and we selected these on the basis of some previous work where people claim these were the numbers; that within these distances they would see some difference in particle motion.

C/G. Rudinger (Cornell Aeronautical Lab.): It would be interesting to evaluate these records just to see if there is an effect. There is another thing; in your data, you find that the larger Reynolds number or the particles with the bigger drag coefficient are larger which means that the surface roughness effect becomes more important for bigger particles. This seems a little bit unreasonable.

From your table on glass particles, taking your data for two particles with the same Reynolds number, but one at low Mach number



## UNCLASSIFIED

and one at high Mach number, the one with the higher Mach number is the bigger particle. I also get larger drag coefficients for the larger particles; and when one extrapolates, one comes to your particles which are still larger. It seems somewhat surprising that the surface roughness would become more important for the larger particles.

C. /B. P. Selberg (Aerospace): For the HP 295 ball powder, the largest  $C_D$ 's were obtained with the smallest diameter powder having the largest relative Mach number. This is the trend I would expect if it were a surface roughness effect. For the glass particle data ( $.15 < M_R < .30$ ) again, the largest  $C_D$ 's were obtained with the smallest particles; however, no discernible  $M_R$  effect could be detected. If all of the glass particle data in which  $.15 < M_R < .3$  are examined, no correlation between  $C_D$ , surface roughness and  $M_R$  could be determined. It is felt that this lack of correlation is due to the fact that the surface roughness was not controlled from particle to particle.

C. /G. Rudinger (Cornell Aeronautical Lab.): Since I didn't find any effect of the particle concentration, it would indicate that each particle carries with itself a mechanism for the peculiar behavior; but as I say, a lot more work has to be done.

C. /L. J. Delaney (Aerospace): More work needs to be done especially in terms of Isp efficiency. In the region that we are usually concerned with, where we may have strong deviations of these drag coefficients, the particles in the rocket motors in general are liquid. Presumably, you would have, hopefully, a very smooth surface. Therefore, at least in terms of Isp efficiency, it may be stretching it a little bit to indicate that these drag coefficients are much higher than what we would normally use. Also, when we are in the solidification regime in the rocket nozzle, usually we are in the transition region and not in the slip flow region.

UNCLASSIFIED

## UNCLASSIFIED

C. /B. P. Selberg (Aerospace): It was the intent of this work originally to go into the slip flow and you would still have your viscous forces acting.

C. /L. J. Delaney (Aerospace): Yes, they are still there. As a matter of fact, this particular phenomena in terms of the rocket motor problem really doesn't answer much because when you try to calculate this particular effect, we know as soon as we have an imbalance or an accelerating force on the particle, it begins to distort so this whole model is really only somewhat of an approximation - which has many drawbacks.

C. /B. P. Selberg (Aerospace): Right - the only thing is that many people do take this steady state curve and modify it for Mach numbers.

C. /L. J. Delaney (Aerospace): That is true.

**UNCLASSIFIED**

COMMENTS ON TWO PHASE FLOW  
IN THE ROCKET CHAMBER

by

Captain H. W. Gale  
AF Institute of Technology  
Wright-Patterson AFB, Ohio

**UNCLASSIFIED**

# UNCLASSIFIED

## COMMENTS ON TWO PHASE FLOW IN THE ROCKET CHAMBER

Captain H. W. Gale

As a generalist in rocket design with a particular interest in unconventional motors I view the present activity in two phase flow as a resource for solving several key problems within the chamber in addition to those being explored downstream of the throat. Of these, deposition and flow of oxides on the inlet surfaces, particle size and particle distribution within the chamber, and the behavior of particles near the propellant surface appear most amenable to major advances due to the resources of data from existing and past studies. Previous difficulties in each area are cited and directions of improvement are suggested.

Deposition of oxide has been a chronic problem of motors due to resulting performance loss and mechanical difficulties. Among the conditions leading to deposition are uninsulated walls, inefficient combustion, short action times, and unusual inlet designs. The sole mechanism of deposition is usually considered to be particle impingement although this mechanism cannot be conveniently analyzed to yield quantitative results and does not yield qualitative results in agreement with experiments. Analysis of firings on the BATES motors at the Air Force Rocket Propulsion Laboratory and firings at Aeronutronics Division of Philco-Ford Corporation suggests that three regions of deposition can be defined, Figure 1. The first region is one of nearly stagnant flow or recirculatory flow such as occurs at the motor head end or at the aft end of cut off grains. The deposition form is a gray powder or spheroids. The powder is a thin loose film such as would result from brownian motion impact of already frozen particles against the wall. Spheroids will form if nuclei of sufficient size are available,

UNCLASSIFIED

## UNCLASSIFIED

about 56 microns for aluminum oxide. The origin of the nuclei can be inefficient combustion due to bad formulation, low pressures, etc., or can be from some other source such as fiberglass insulation. Paper-phenolic insulation was chosen for the BATES motor to avoid deposition which occurred with fiberglass insulation erosion at grain slots, reported in reference 8, apparently generated nucleation sites on asbestos phenolic insulation in some cases. The spheroids and powder can occur together if the spheroids are not so densely spaced as to cover the surface. Hermesen and Woolfolk developed an equation which describes the growth rate of aluminum oxide spheroids, Figure 2, reference 3. Spheroids above one eighth inch tend to coalesce into larger droplets which may detach or flow under the influence of gas shear or gravity.

The second region is one of flow swept surfaces where a sheet of oxide or a powder may be deposited. The sheet form is not dependent on area ratio as would be expected from a particle impingement source, nor does it require nuclei of the spheroid type. Rather sheet formation depends more on the wettability of the surface such that it will form on steel, graphite, or stable char layers but will not form on an active ablator such as nylon nor on a material at the melting temperature of the oxide. The Hermesen and Woolfold equations were redeveloped for surface plating deposition and yielded good agreement with data from the BATES motor for retained oxide weight (.2 pound predicted compared to .1 to .2 pound observed) and oxide thickness about .015 inches at high area ratios and zero near the throat. The equations indicate that an original deposit is required to initiate plating since the stable thickness is zero whenever the film surface temperature equals the wall surface temperature ( $T_s = T_w$ ). The stable film thickness of Figure 3 is that of frozen oxide, not including any liquid rivulets. Any liquid layer on the surface of the plating will be swept to the throat by the gas stream. Such a film could result from

## UNCLASSIFIED

smearing of spheroids growing on the surface and particle impingement. The spheroid smearing mechanism would predict about .4 pound deposited and .2 pound swept away for the BATES motor. According to data from water droplet heat transfer experiments by Captain Gagliardi at the Air Force Institute of Technology the particles will bounce from the film surface if their momentum is below a critical level, after a residence time of 1 to 10 milliseconds. The postulated residence time is in the same magnitude as the film freezing time, suggesting that the particles may lose thermal energy to the wall without adhering.

In the third region of very high flow velocity and high convective heat flux (area ratios less than 10) the deposition can occur as rough surface irregular buildups or with upstream plating, the throat region surface can experience corrosion instead of deposition. The deposition texture and dependence on area ratio fit a particle impingement model, based on work by Lundberg, reference 5. Inefficient combustion was the most probable source of particles large enough to impinge and adhere; for example, aluminum combustion at chamber pressure below 250 psia or beryllium combustion with flame temperatures below the melting point of the oxide were observed to cause severe deposition. Quantitative analysis of trajectories, impact frequency, and particle capture should be possible by extension of existing two phase flow computer programs. Due consideration should be given the varied wettability of materials in estimating deposition weight and performance loss. The oxide flow after deposition is very important.

A recent report, "Beryllium Erosion-Corrosion Investigation for Solid Rockets"<sup>8</sup>, has documented the importance of controlling oxide deposition and flow for successful nozzle design. Some motors in the past benefited by generation of a protective ceramic coating on the nozzle throats by flow of oxides downstream from the inlet. Examination of data from early BATES motor firings at AFRPL supports the

UNCLASSIFIED

## UNCLASSIFIED

idea. As demonstrated on the first wafer motor research contract<sup>1</sup> slag deposition on the throat can have disastrous consequences for restartable rockets. Subsequent development encountered no significant slag problem due to use of another propellant and insulation and careful inlet design. The plug nozzle controllable motors may have problems also.

Inlet surface stream-wise vortices can channel the film under some conditions into "rivers" approximating the throat width for plug nozzles. Such streams can have a significant effect on throat area and flow symmetry. Apparently no consideration has been given to stream-wise vortices in the past studies although the basic theories are already developed<sup>7, 9</sup>.

Distribution of the particles in the chamber trajectories should be considered in estimates of propellant performance and erosion-corrosion forecasts. Several recent reports, such as the report by Aeronutronics, have improved understanding but good quantitative techniques are not yet available, although available simplified analysis can be adapted<sup>2, 5</sup>.

The two phase flow particles enter the flow as metal-oxide globules on the surface of the propellant. At present we have no convenient model of the force balance which causes such particles to leave the surface only after achieving sufficient size. A good model should yield results in accordance with experiments on particle size distribution, "g" effects on burn rate, and instability-extinguishment. A model based on U. T. C. report "Investigation of Particle Growth and Ballistic Effects on Solid Propellant Rockets"<sup>4</sup> is proposed for discussion. As metal particles emerge from the burning surface they shield the adjacent surface from severe heating thus flow velocities along the face of the particle are low and essentially tangential to the

## UNCLASSIFIED

surface. Such flow results in an unbalanced pressure force toward the surface so long as any surface shadowing exists.

As the particle emerges from the surface forces accumulate due to increasing exposed cross sectional area and decreased shadowing. There are critical gas velocity limits such that medium particles are ejected immediately but small particles must grow until the balance of forces results in "ejection". According to this model at low pressures or with inefficient combustion the particles will agglomerate into a blanket until the evolution of gases or unsymmetric drag lifts an edge, initiating a rapid ejection by inducing oxidizer rich gases under the blanket with subsequent enhanced lift forces. The mechanism would lag pressure pulses at high pressures but would lead (self-initiated) at low levels, apparently coupling with instability as a damper at high pressures and as a contributor at low pressures. Presumably the drag data from the two phase flow studies would apply in calculating the forces on the particle if the local velocities can be estimated. Qualitative application of the model to "g" effects on burn rate as calculated in reference 4 explain why the assumption that a particle on the surface is embedded in a smooth flow led to an overestimate of drag forces. Further, an AIAA Technical Note by R. Wall indicated a linear correlation of burn rate increase with percent of wall area perpendicular to the acceleration vector, as suggested by this model.

Two phase flow is a vital concern upstream as well as downstream of the throat. These comments are intended to suggest areas of particular concern for unconventional motors. Data on hand may be sufficient to yield significant advances with little effort.

UNCLASSIFIED



# UNCLASSIFIED

## REFERENCES

1. "An Applied Research Program to Demonstrate the Feasibility of a Solid-Propellant Pulse Rocket", AFRPL-TDR-64-66, Contract AF 04(611)-8531, ARC, December 1964.
2. Byrne, W. M., Jr., "Radiant Heat Transfer to an Enclosure from Two Phase Flows", AIAA Journal of Spacecraft, Vol. 3, June 1966.
3. Hermesen, R. W., and Woolfolk, R. W., "Vapor Phase Combustion of Beryllium and Aluminum", AD 617938, UTC-2040-FR, December 1964.
4. "Investigation of Particle Growth and Ballistic Effects on Solid Propellant Rockets", UTC-2128-FR, Contract NOW 65-022f, Final Report, January 1965-December 1965.
5. Lundberg, R. E., "Drag of Objects in Particle-Laden Air Flow, Phase IV; Blunt Bodies and Compressibility Effects", DASA-1326, Stanford Research Institute, Menlo Park, California, November 1962.
6. Murphy, J. M., and Wall, R. H., "Effects of Grain Configuration on the Burning Rate of a Spinning Rocket Motor", AIAA Journal, February 1966.
7. Schlichting, "Boundary Layer Theory", New York: McGraw-Hill, Third Edition, p. 442.
8. Smallwood, W. L., "Beryllium Erosion Corrosion Investigation for Solid Rocket Nozzles", AFRPL-TR-66-205, Aeronutronic Division of Philco-Ford Corporation, November 1966.
9. Weiss, R. F., "Stability of the Stagnation Region to Three-Dimensional Disturbances", Contract AF 30(602)-2083, -2393, -2968, January 1965, AVCO-EVERETT Research Laboratory, Everett, Massachusetts.

UNCLASSIFIED

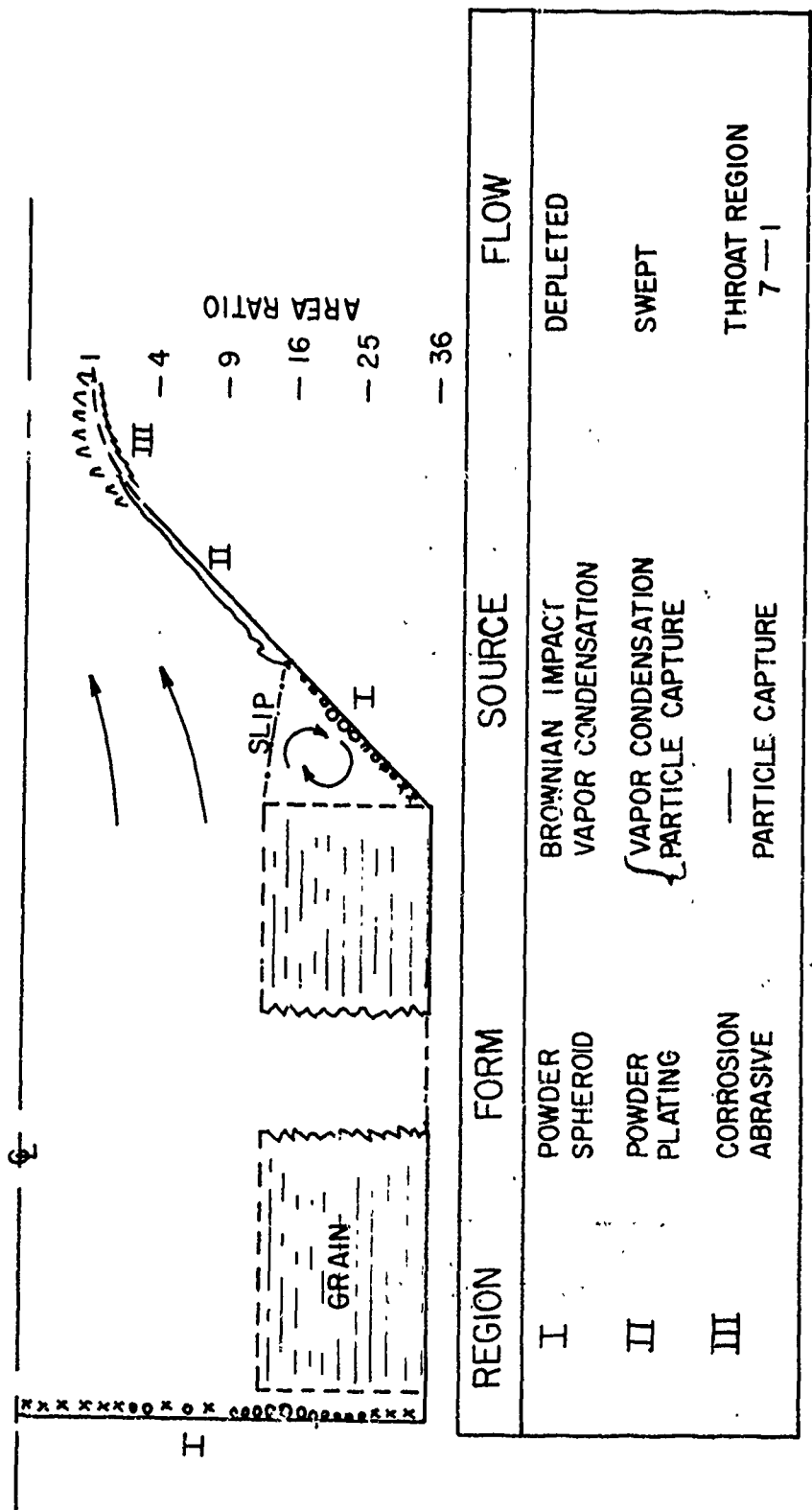


Figure 1. Oxide Deposition Regions.

UNCLASSIFIED

UNCLASSIFIED

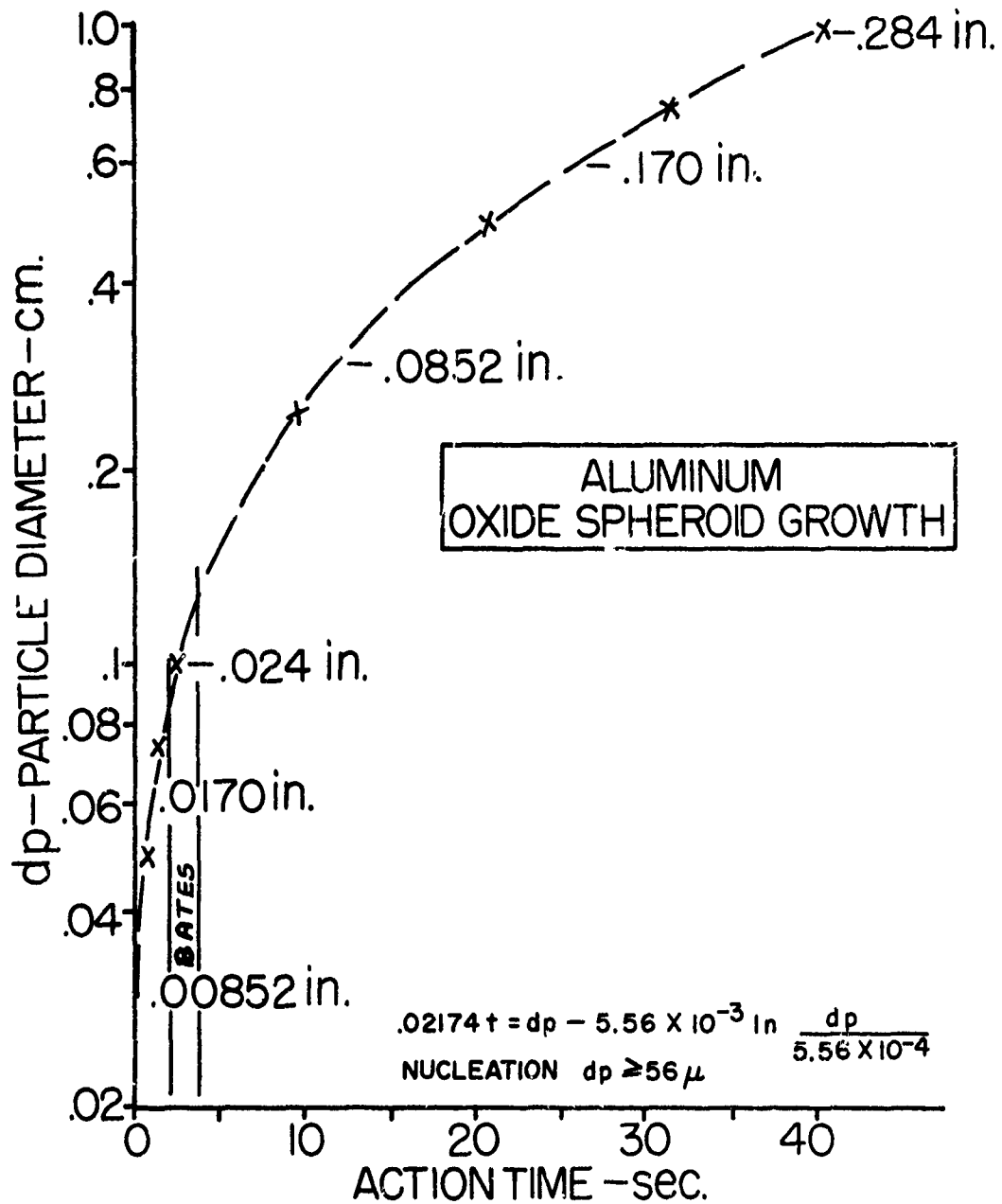


Figure 2. Aluminum Oxide Spheroid Growth (Reference 3).

UNCLASSIFIED

UNCLASSIFIED

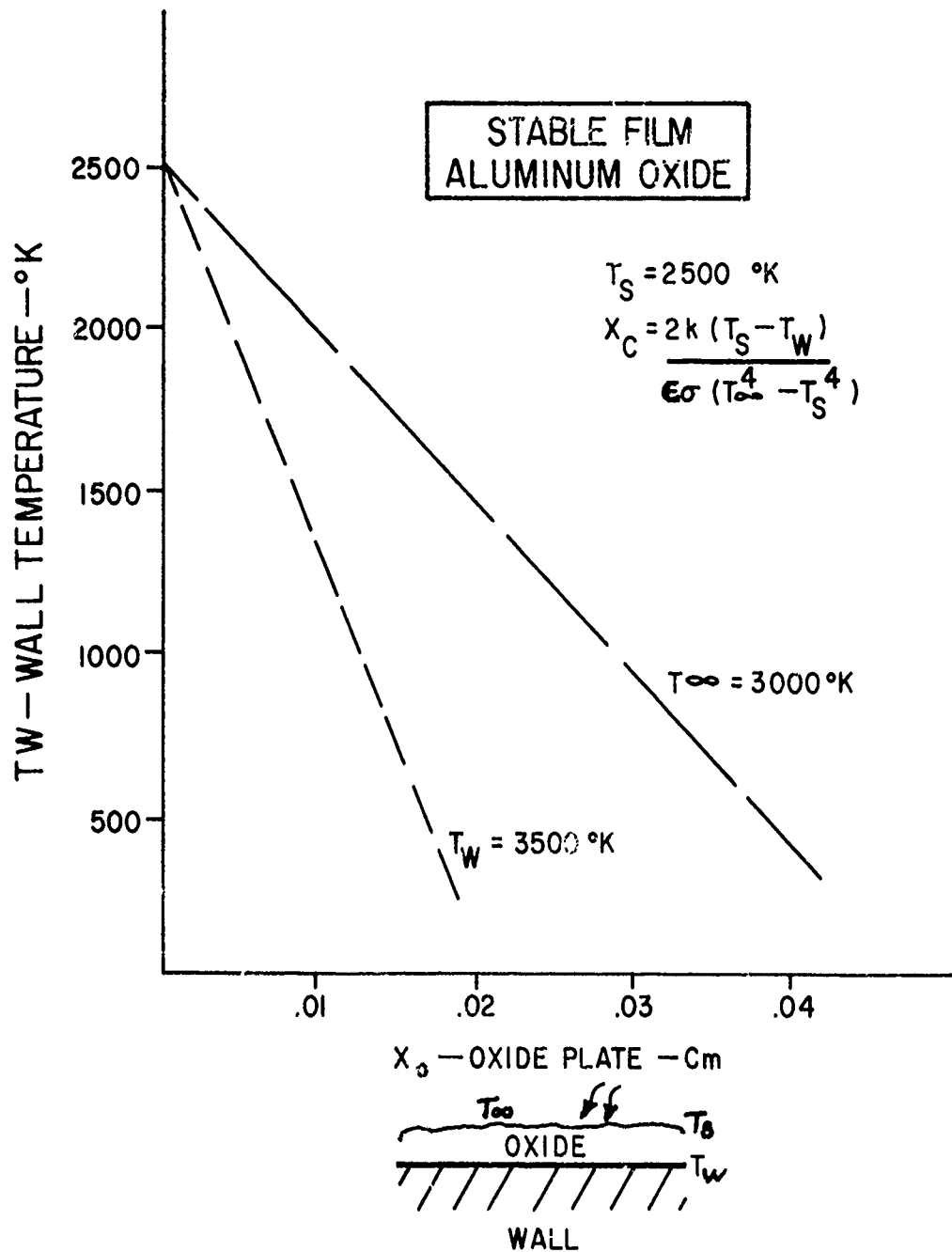
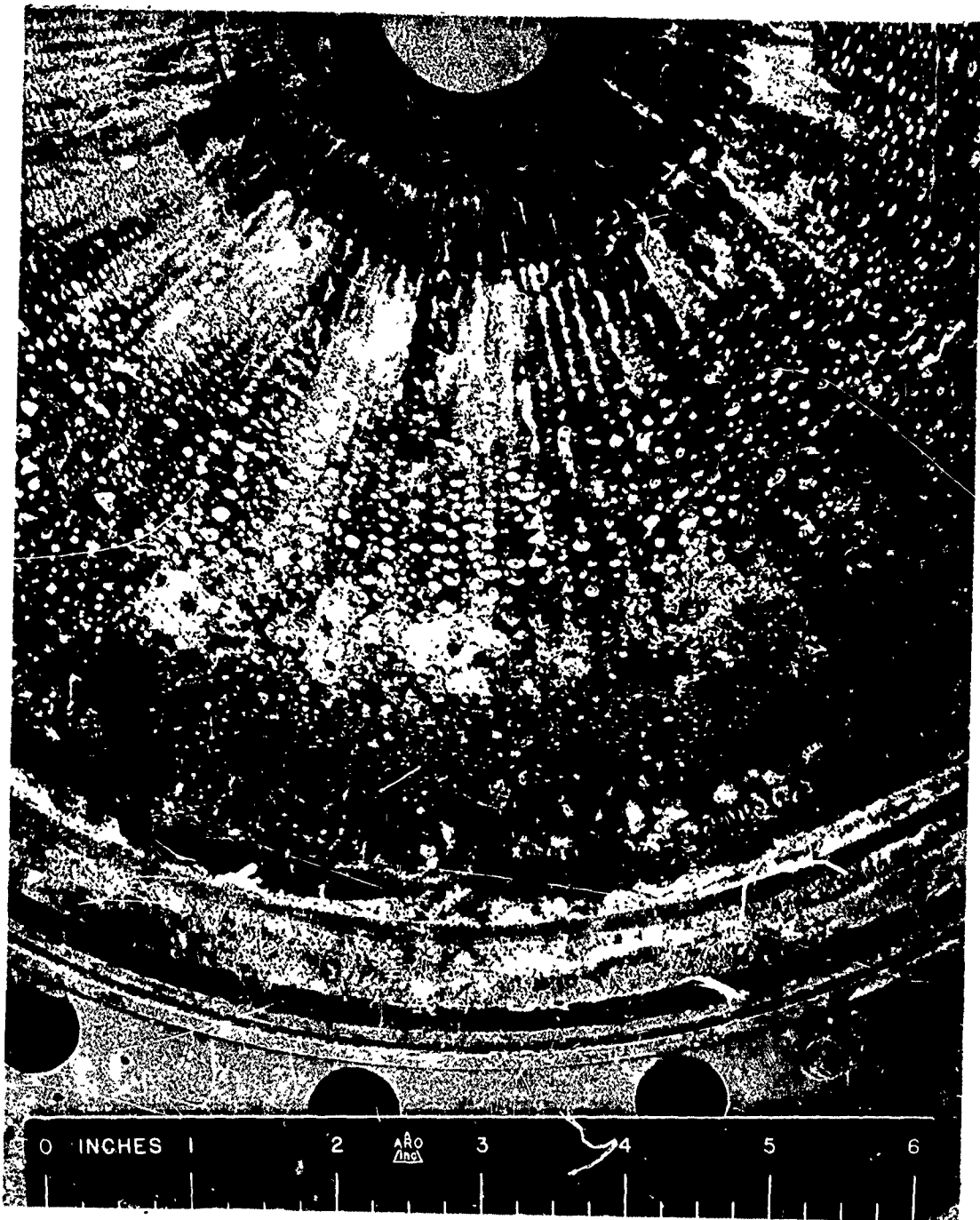


Figure 3. Stable Film Aluminum Oxide.

UNCLASSIFIED

UNCLASSIFIED



R — REYNOLD NO.

$\theta$  — MOMENTUM  
BOUNDARY THICKNESS

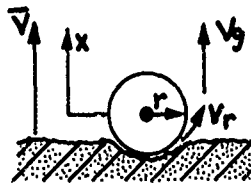
r — TURNING RADIUS

$$Re_{\theta} \sqrt{\frac{\theta}{r}} \geq 6-9$$

Figure 4. Streamwise Vortice Patterns.

UNCLASSIFIED

# UNCLASSIFIED



1. ACCELERATION = DRAG-COMBUSTION PRESSURE-CONTACT  
- "LIFT" - g LOAD

$$2. m\ddot{x} = \frac{1}{2} \rho v^2 C_D - P_{cb} A - P_o A_{cn} - \frac{1}{2} \rho \int V_r^2 dA - mg$$

## 3. ASSUME

(A) STOKES FLOW:  $C_D = 24/RE_d$

(B) DROPLET COMBUSTION:  
PRESSURE,  $P_{cb} = 0$

(C) WALL CONTACT AREA:  
 $A_{cn} = 0.001A$

(D)  $V_g$  VECTOR PERPENDICULAR TO  
WALL

(E) VIEW FACTOR:  $F_{1-2} = (\sin^2 \beta \cos \theta)$

(F) VERTICAL VELOCITY:  $V_g = \bar{V}$

(G) TANGENTIAL VELOCITY AVERAGE:

$$V_r = \frac{\bar{V}}{2} F_{1-2} = \frac{\bar{V}}{2} \left( 1 - \frac{r^2}{2r^2 + x^2} \right)$$

(H) MEAN GAS VELOCITY:  $\bar{V} = \frac{\dot{m}}{\rho A}$

$$4. m\ddot{x} = \bar{V} \mu 12 \pi r - \frac{\rho \pi r^2}{1000} - \rho_g \bar{V}^2 \frac{\pi r^2}{2} \left( \frac{r^2 + x^2}{2r^2 + x^2} \right)^2 - \rho_s \frac{4}{3} \pi r^3 g$$

5. ORDER OF MAGNITUDE SOLUTION  $\bar{V}$  CRITICAL AT "LIFTOFF":  
 $m\ddot{x} = 0, x = 0$

\* Eckert and Drake, Heat and Mass Transfer, McGraw-Hill, page 398.

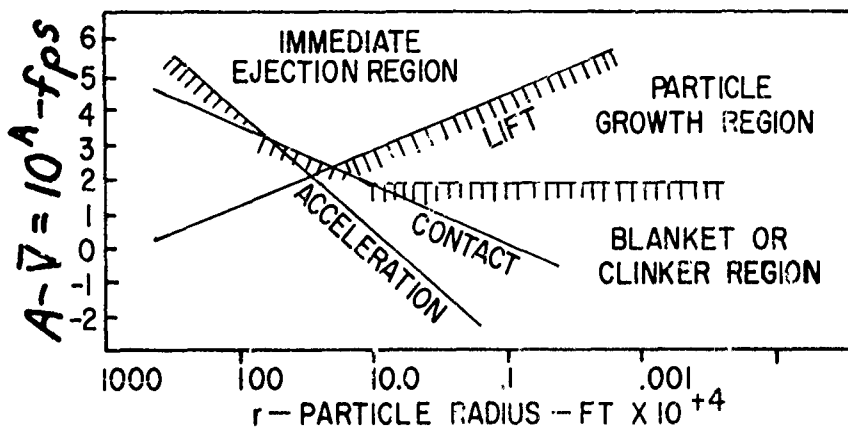


Figure 5. Particle Near an Ablating Wall.

# UNCLASSIFIED

819/820

**UNCLASSIFIED**

**METHODS FOR PREDICTING PARTICLE  
BEHAVIOR IN TWO-PHASE FLOW**

by

Richard J. Zeamer  
Hercules Incorporated  
Bacchus Works  
Magna, Utah

**UNCLASSIFIED**

# UNCLASSIFIED

## METHODS FOR PREDICTING PARTICLE BEHAVIOR IN TWO-PHASE FLOW

Richard J. Zeamer  
Hercules Incorporated  
Bacchus Works  
Magna, Utah

### Summary

Two distinct regimes of two-phase flow behavior are identified.

One regime involves the agglomerates of metal which form on the surface of the burning propellant and then ignite and burn up as they are carried by the gas stream.

These can cause erosion and slag inside rocket motors. These effects are confined to surfaces close to the propellant surface except in motors which have inefficient combustion.

The other regime involves the particles of metal-oxide which result from the burning of the metal in the propellant. These are generally so small that they do not cause erosion or slag except where turbulence or velocity gradients are extremely high, such as in split gaps and nozzle throats.

Efforts to predict impingement and erosion by use of combustion test techniques, flow analyses and particle motion calculations have shown some promising results. Analytic means of predicting particle behavior and its results on motor erosion performance are being developed.

UNCLASSIFIED



# UNCLASSIFIED

## METAL AGGLOMERATE BEHAVIOR

Metal agglomerates form on the burning surface of a solid propellant. These range tremendously in size, depending on the combustion efficiency of the propellant, from less than  $10\mu$  to more than  $800\mu$ .

The metal agglomerates leave the burning surface, are ignited, and travel with the gas stream. As they burn they diminish in size and, if left in the gas stream long enough, are completely burned up and annihilated. The metal ignition and burning rates, under such conditions, can be predicted by methods developed by Davis and Kuehl (see Appendix A).

Interval flows are mapped by electric conduction analog solution of the equations for incompressible irrotational flow (see Appendix B). The movement of the metal agglomerates from the propellant surface through the gas stream is calculated by the analog computer which so solves, for each particle, the equations of inertia and drag. The effect of change in size and mass of the agglomerated with time is allowed for. These equations are presented in Appendix B.

A typical result of mapping of flow and agglomerate paths is shown in Figure 1. In this case a severe impingement situation is predicted.

The flow and agglomerate path mapping result can be extended to a quantitative prediction of deposition, area by area, and as a function of time. This has been done for the split gap region by methods described in Appendix C. The results are shown in Figure 2. The impingement rate curve includes the results of flow and agglomerate plotting solutions for successively greater times after ignition. The

## UNCLASSIFIED

reduction in impingement rate with time is due mainly to the increasing distances between the propellant face and the wall.

The total accumulation of deposits, area by area, is determined by integration of the rate curve. This result for the split-gap area is shown by the upper curve on Figure 2.

The mapping technique, the results of which are illustrated in Figure 1, has been verified for two operational motors, the Polaris A3 stage and the X-258 Altair. The quantitative results, illustrated on Figure 2, have not yet been experimentally verified.

Severity of impingement appears to depend chiefly on initial agglomerate size. Small agglomerates have high drag force relative to inertia and tend to follow the gas flow. For large agglomerates the opposite is true; inertia is dominant and agglomerates tend to separate from the flow and impinge on obstacles in their paths.

The life time of agglomerates depends on the initial agglomerate size, chamber pressure, burning temperature of the gas and the metal being burned (aluminum burns about twice as fast as beryllium). This is illustrated in the following table of calculated results.

Metal	Chamber Pressure P. S. I. A.	Flame Temperature °R	Agglomerate size microns	Burn Time Millisec	Max. Travel at 50 ft. /sec. feet
Al	1000	6900	254	48	2.4
B1	470	6800	89	136	6.8
Be	737	6360	762	650	32.5

The analytic approach described above has already provided useful remedial information to designers of rocket motors in which two-phase flow problems could affect motor integrity and performance.

UNCLASSIFIED

## UNCLASSIFIED

With some additional development effort it could be made a precision analytic method.

### COMBUSTION STUDIES

The metal agglomerate impingement studies described above have been based on data on the size of the agglomerates which form on the propellant surface and which are swept into the gas stream.

This data has been obtained from window bomb tests made at Allegany Ballistics Laboratory for the Minuteman PSP and other programs. In these tests which strands of propellant have been burned under pressure and the burning surface, greatly magnified, has been photographed. The agglomerates are clearly visible and can be scaled as to size and counted. Movies are available which vividly illustrate agglomerate formation as well as the associated combustion of the propellant. The contrast between efficient and inefficient combustion is dramatic. A wide range of examples have been tested and the data is available for further analysis.

### METAL - OXIDE PARTICLE BEHAVIOR

Combustion of metal in a rocket motor produces metal oxide particles. These are usually very small compared to the metal agglomerates, and range in size from less than a micron to around 5 microns. However, various factors such as combustion efficiency, pressure, temperature, combustion environment, flow geometry factors can cause sizes to be much larger.

Calculations of particle paths in the chamber using techniques described for metal agglomerates, shows that these particles follow

## UNCLASSIFIED

the gas flow very closely and do not ordinarily separate or impinge to a degree that could cause problems.

Deposition of these particles does, however, occur at a relatively low rate from turbulent flow. The force carrying the particles to the wall are the lateral components of drag resulting from the random motions of the gas. This type of deposition has been calculated by methods derived from eddy diffusivity theory. Details are presented in Appendix D.

The particles so deposited do not adhere unless the wall surface temperature is less than the melting point of the metal oxide. Therefore, the surfaces where such deposits can be expected to occur are graphite throats, early in firing before they have heated and nozzle split line cavities where gas is allowed to flow.

The eddy diffusivity method has been applied to several nozzle split-line deposition problems. Typical buildup rates that have been calculated are 1.9 mils/sec at 60 ft/sec and 320 psia and 2.9 mils/sec at 45 ft/sec and 820 psia. To date there has been no experimental verification of these predictions.

The eddy diffusivity method should be useful in predicting the rate of buildup of oxide deposit in nozzle throats after ignition when the throat is still cool and before melt off of the oxide begins.

More work should be done in the mechanism of small particle deposition. There is need both for theoretical development and for experimental investigations.

A body of test firing ballistic data is available from the Minute-man PSP Program (in which 52 subscale motors and 2 full scale motors

UNCLASSIFIED

**UNCLASSIFIED**

were fired with various advanced beryllium propellants) is available for analysis of this type.

**UNCLASSIFIED**

UNCLASSIFIED

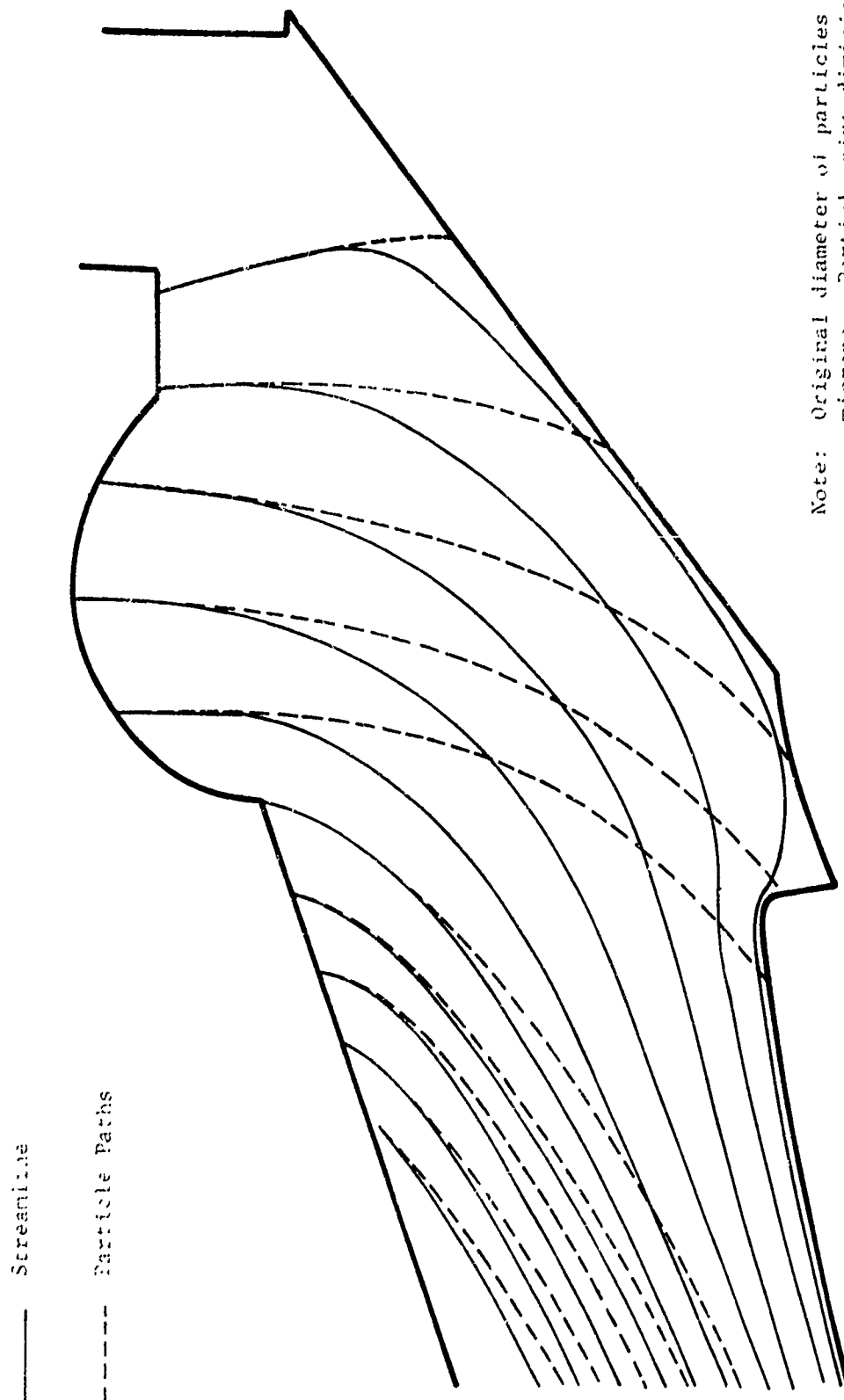


Figure 1. Two-Phase Flow Behavior Between Propellant Burning Surface and the Backside of a Submerged Nozzle at 2 Seconds after Ignition.

UNCLASSIFIED

UNCLASSIFIED

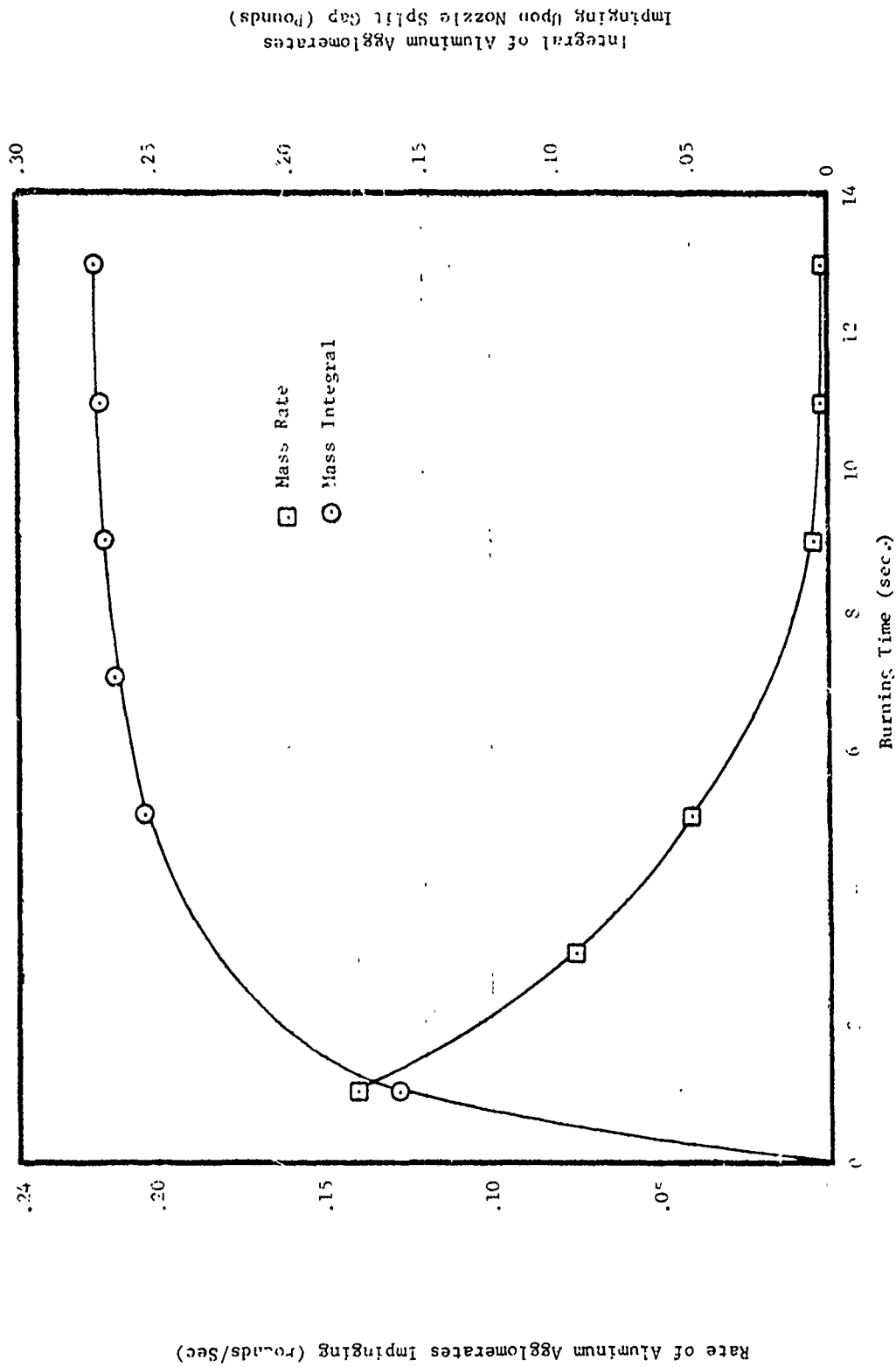


Figure 2. Nozzle Split Gap Rate of Agglomerate Impingement vs Time, and Total Accumulation vs Time.

UNCLASSIFIED

# UNCLASSIFIED

R. J. Zeamer  
Hercules Incorporated  
Bacchus Works  
Magna, Utah

14 March 1967

## APPENDIX A

### Ignition Delay

"Ignition and Combustion of Aluminum Particles in Hot Ambient Gases",  
R. Friedman & A. Macek, Kinetics and Combustion Division, Atlantic  
Research Corp., Combustion Flame Vol. 6, 9-19 (1962)

1. Gives experimental and theoretical results for ignition of Al.
2. Plot: apparent ignition time vs. diameter<sup>2</sup>.
3. Derives equation for ignition delay time.

$$t_i = \frac{P_p d^2}{12 \lambda g} \left[ C \ln \left( \frac{T_a - T_o}{T_a - T_i} \right) + \frac{L}{T_a - T_m} \right]$$

Conditions:

- (a) Single particle - No radiation from other particles
- (b) Heat transferred through stagnant ambient medium of temperature  $T_a$  at distance far from sphere.
- (c)  $T_i$ , ignition temperature is uncertain.
- (d) Provides estimate of  $t_i$  (apparent).

Must calculate then a true delay time by

$$t_{ap.} = t + \theta \quad \left( e^{\frac{-t}{\theta}} - 1 \right)$$
$$\theta = \frac{d^2 P}{18 \mu}$$

UNCLASSIFIED



## UNCLASSIFIED

### Further Work Needed:

- (1) Experimental work with multiple particles. (Window Bomb data may help).
  - (a) Window Bomb setup to track burning agglomerates.
  - (b) Develop empirical relations for metal propellants.
- (2) Develop equation utilizing convective and radiant heat transfer.

### Burning

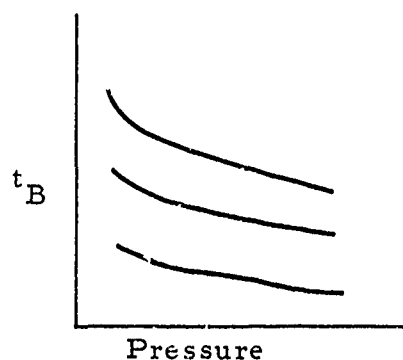
Combustion of Metals, George H. Marstein, Cornell Aeronautical Laboratory, AIAA Journal, Vol. 1, No. 3 550-562 (March 1963).

$$t_{\text{Residence}} = t_{\text{Ignition Delay}} + t_{\text{Burning}}$$

$$t_{lg} = \frac{Pd^2}{12\lambda} \left[ C \ln \left( \frac{T_a - T_o}{T_a - T_i} \right) + \frac{L}{T_a - T_m} \right] \text{ (Friedman \& Macek)}$$

Solid Propellants: The combustion of particles of metal ingredients, A. Davis, Armed Services Technical Information Agency, Arlington Hall Station, AD 299892

- (1)  $t = kd^{1.8}$
- (2) Plots the effect of pressure, gas composition and particle size on the burning time of aluminum particles.



### Further Work Needed:

- (a) Obtain K for pressures of interest
- (b) Need data for our propellants, higher conc. of aluminum.

# UNCLASSIFIED

"Ignition and Combustion of Aluminum and Beryllium", F. K. Kuehl, United Aircraft Corp., Research Lab., AIAA Journal, Vol. 3, No. 12, 2239-2247 (Dec. 1965)

1. Gives ignition delay time - more complete than Friedman and Macek.  
Includes convective heat transfer.

$$t_{lg} = \frac{P_s r_{ps}^2}{1.0 + 0.3 P_r^{1/3} Re^{\frac{1}{2}}} \left\{ C_{Ps} \ln \left( \frac{T_g - T_{Pi}}{T_g - T_{pmp}} \right) - \frac{L}{M(T_g - T_{pmp})} \right\} + \frac{P_s r_{Pl}^2}{3K_g} \left[ 1.0 + 0.3 Pr^{1/3} Re^{\frac{1}{2}} \right] \left\{ C_{Pl} \ln \left( \frac{T_g - T_{MP}}{T_g - T_{lg}} \right) \right\}$$

2. Metal combustion - develops Eqn. for vapor phase combustion

$$t_B = \frac{4 \pi P r_A^{(3-n)}}{M S (3-n)}$$

where:

P = density of particle

r = radius of particle droplet

n = burning rate exponent

M = Mol. weight of particle

S = burning rate coefficient

$$t_B \text{ (APPROX)} = \left[ \frac{2 \pi r}{M} \right] \frac{r_A^3}{W}$$

where:

$$W = S r^n$$

- (a) Provides basis for calculating K in  $t = K d^{1.8}$  eqn. if burning rate of metal is available.
- (b) Data in article includes W as function of oxidizer composition for 10 and 20 ATM.
- (c) Ignition delay equation still can be improved for multiple particle system by including radiation effects.

# UNCLASSIFIED

# UNCLASSIFIED

## APPENDIX B

Reference: Analog Simulation of Gas and Particle Flow in Solid Propellant Motors, by K. S. Cook.

1. Assume gas is frictionless and incompressible, then flow in a plane will satisfy Laplace equation, which also applies to electric current in potential flow.

$$\frac{\delta^2 \phi}{\delta x^2} + \frac{\delta^2 \phi}{\delta y^2} = 0 \quad \text{where} \quad \frac{\delta \phi}{\delta x} = -\mu, \quad \frac{\delta \phi}{\delta y} = -\nu$$

Since  $\phi$  and the stream function,  $\psi$ , are orthogonal, then

$$\frac{\delta \phi}{\delta x} = \frac{\delta \psi}{\delta y} \quad \text{and} \quad \frac{\delta \phi}{\delta y} = -\frac{\delta \psi}{\delta x}$$

and if one is considered the potential function for a certain flow case, the other is the stream function.

If simulating plane gas flow by an electric field in a flat conducting sheet, the gas streamlines may be made analogous to either the electric streamlines (paths of current flow) or to the electric potential lines (lines of constant voltage), provided proper boundary conditions can be applied.

$$\begin{aligned} \text{Hence: } U &= -k' \frac{\delta \psi \epsilon}{\delta y} = -k' \frac{\delta V}{\delta y} & (V = \text{voltage}) \\ V &= k' \frac{\delta \psi \epsilon}{\delta y} = k' \frac{\delta V}{\delta x} \end{aligned}$$

## UNCLASSIFIED

where  $k'$  is a proportionality constant to relate the gas and electric fields and subscript  $e$  denotes the electric field.

Two boundary conditions which must be satisfied in a rocket motor are:

1. There must be no gas flow normal to the case or other non-burning surfaces.
2. There is an equal rate of gas generation per unit area of burning surface and it leaves normal to the surface.

### Equations of Particle Motion

"Analog simulation of particle trajectories in Fluid Flow", Norum, Adelberg and Farrenhopf, Proceedings of 1962 Spring Joint Computer Conference.

#### Assumptions:

- (1) The only force acting on the particle is the drag force from the gas.
- (2) Particles are spherical.
- (3) No interaction between particles.
- (4) No effect of the particles on the gas flow.

#### Equations Used:

$$\dot{x} = \left( \frac{C_D R_e}{24 K} \right) W_x dt$$

$$\dot{y} = \left( \frac{C_D R_e}{24 K} \right) W_y dt$$

$$W_x = U - \dot{x}$$

#### Nomenclature:

$U$  = gas velocity in  $x$  direction

$V$  = gas velocity in  $y$  direction

$C_D$  = coefficient of drag

$R_e$  = Reynolds  $n$

$W$  = relative velocity between particle and gas

UNCLASSIFIED

## UNCLASSIFIED

$$W_y = V - \dot{y}$$

$$K = \frac{2l p A^2}{9\mu}$$

$$\frac{C_D R_e}{24} = f(Re)$$

$$R_e = \frac{2AlgW}{\mu}$$

$$W^2 = W_x^2 + W_y^2$$

Part of input is plot of curve  $C_L$  vs  $R_e$ .

$A$  = radius of particle

$\mu$  = viscosity

$\dot{x}$  = particle velocity in x direction

$\dot{y}$  = particle velocity in y direction

$x$  = coordinate axis parallel to motor centerline

$y$  = coordinate axis perpendicular to motor centerline

### Method of Using the Conductive Model

1. Select a cross section of the motor where the gas flow can reasonably be approximated by flow in a plane.
2. The cross section selected is drawn on conductive paper.
3. Boundary conditions are applied.
  - (1) Using the equations  $\mu = -k' \frac{\delta V}{\delta y}$  and  $V = k' \frac{\delta}{\delta x}$  indicates that the gas velocity in a given direction is proportional to the voltage gradient  $90^\circ$  from that direction. To force this condition, the non-burning boundaries are made constant potential lines by laying a conductive strip along them. In most cases this will produce two streamlines, separated at one end by the burning surface and the other by the nozzle or discharge area. One of the streamlines is grounded and the other is connected to some voltage,  $V_0$ .
  - (2) The second boundary condition, along the burning surface, is enforced by a special voltage gradient.

## UNCLASSIFIED

4. A special 5-point probe which senses the voltage at each point of contact is used to determine the voltage gradient and subsequently the velocity at a specific point on the model.

UNCLASSIFIED

# UNCLASSIFIED

## APPENDIX C

### Accumulation of Agglomerates Calculation

$$M_{\text{total}} = V\Delta t \rho_p f_a \sum_{i=1}^n f_i \left( \frac{D_i}{D_o} \right)^3$$

where

- $V\Delta t$  = propellant volume burned in region of influence during a small time
- $\rho_p$  = propellant density
- $f_i$  = fraction of each size particle in total metal distribution
- $f_a$  = fraction of total propellant mass which is aluminum
- $D_o$  = particle diameter upon leaving burning surface
- $D_i$  = particle diameter upon impact on surface of interest
- $n$  = number of various particle sizes under consideration

Example of calculation of mass impinging upon split gap region in the time interval 2 to 4 seconds.

For 89 particles, we observe that trajectories 12 thru 17 impinge upon surface of split gap.

$$\begin{aligned} M_{89} &= 2\pi RL \rho_p r_b f_a \sum f_i \left( \frac{D_i}{D_o} \right)^3 \\ &= 2\pi r_b \rho_p f_a \sum f_i RL \left( \frac{D_i}{D_o} \right)^3 \\ &= 0.0582 (.075) (17.85) (.4) \left( \frac{89}{89} \right)^3 + (.075) (17.75) (.4) \left( \frac{89}{89} \right)^3 \\ &= 0.0561 \text{ lb.in.} \end{aligned}$$

## UNCLASSIFIED

Similarly, we compare trajectories for 52 , 64 , 114 , and 140 , and obtain  $M_1 = 0, 0, 0.0126$  and  $0.0057$  respectively.

Then for time interval 2 to 4 seconds, we obtain

$$\begin{aligned} M_2 \text{ sec} &= 0.0561 + 0.0126 + 0.0057 \\ &= 0.0744 \text{ lb}_m \end{aligned}$$

And

$$\begin{aligned} M_{\text{total}} &= M_0 + M_2 \text{ sec} + M_4 \text{ sec} + M_6 \text{ sec} + \dots \\ &= 0.14 + 0.0744 + 0.04 + 0.0111 + 0.0034 + 0.0015 \\ &= 0.27 \text{ lb}_m \end{aligned}$$

UNCLASSIFIED

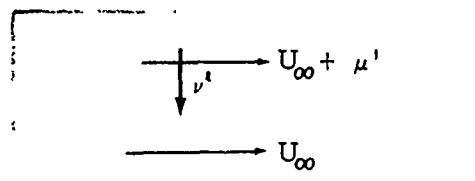


# UNCLASSIFIED

## APPENDIX D

### Particle Deposition by Eddy Diffusivity

We can assume that particle movement toward a wall parallel to the bulk motion of the fluid in turbulent flow will be by the deviating velocity in that direction. Since it can be either positive or negative, we employ the root mean square value  $\nu' = \sqrt{\bar{\nu'^2}}$ .



From Figure 1.

Rate of mass transfer/unit area

$$= \rho \nu'$$

Two layers of fluid in parallel planes

Figure 1

$$\text{Rate of momentum transfer/unit area} = \rho \mu' \nu' = \rho \overline{\mu' \nu'}$$

Because 2 is slower than 1, the shear stress on 1 will be equal to the momentum transfer

$$\tau_{gc} = -\rho \mu' \nu'$$

Since mechanism is similar for small particles, 2-3  $\mu$ , and molecular eddy diffusion, we will assume that (1) eddy diffusivity correlation can be used to approximate movement of particles and (2) all particles within a certain distance (mixing length) of the wall will be candidates for deposition on the wall.

Woertz developed an empirical expression for eddy diffusivities

## UNCLASSIFIED

from calcium chloride diffusion into air, carbon dioxide and helium gas stream

$$E = 0.008 U_{avg} A_o \sqrt{f}$$

where

$$\begin{aligned} U_m &= \text{average velocity of the gas stream, } \frac{\dot{Q}}{A} \\ A_o &= 1/2 \text{ the width of the duct} \\ f &= \text{fanning friction factor} \end{aligned}$$

Schubauer developed an expression for cases where the diffusion distance is small compared with the mixing length.

$$E = \frac{Ux}{2} \left( \frac{\nu'}{U} \right)^2$$
$$\begin{aligned} x &= \text{distance in direction of flow} \\ U &= \text{time average velocity at a point} \\ \nu' &= \text{root mean square deviating velocity} \end{aligned}$$

Assuming that the wall is like a fine screen which does not hamper the gas flow toward it, but catches and holds the particles, then the rate of deposition is

$$\dot{\delta} = \frac{W \nu'}{2 \rho_p}$$

where

$$\begin{aligned} W &= \text{lb of } Al_2O_3 / \text{unit volume of gas, lbm/ft}^3 \\ \nu' &= \text{deviating velocity normal to wall, ft/sec} \\ \rho_p &= \text{density of particles, lbm/ft}^3 \end{aligned}$$

The factor 2 is to account for the time when  $\nu'$  would be directed away from the wall. It is necessary to obtain a value for  $\nu'$ .

UNCLASSIFIED

# UNCLASSIFIED

Example:

Data	U avg, gas velocity (measured)	= 94 ft/sec
	$\rho_f$ , density of gas (mixture)	= 0.35 lbm/ft <sup>3</sup>
	$\rho_p$ , density of particles, Al <sub>2</sub> O <sub>3</sub> ( )	= 249 lbm/ft <sup>3</sup>
	$\mu_f$ , viscosity of gas (mixture)	= 0.2256 lbm/ft hr.
	2A <sub>o</sub> , height of split gap	= 0.0104
	x, length of flow path	= 0.177 ft.
	W, weight of particles/unit volume	= 0.124 lbm/ft <sup>3</sup>
	r <sub>k</sub> , hydraulic radius	= $\frac{(2A_o)L}{L + 2A_o}$
		since L > A <sub>o</sub>
		≈ A <sub>o</sub>

$$Re = \frac{U \text{ avg } \rho_f 4r_k}{\mu_f} = \frac{(94)(0.35)(4)(0.0052)(3600)}{(0.2256)}$$

$$= 1.14 \times 10^4$$

From Perry's Chemical Engineering Handbook, page 382.

$$f = 0.0088$$

$$\sqrt{f} = 0.096$$

$$E = 0.08 U \text{ avg } A_o \sqrt{f}$$

$$= (0.08)(94)(0.0052)(0.096)$$

$$= 0.00375 \text{ ft}^2/\text{sec}$$

$$\nu' = \sqrt{\frac{UE}{0.5x}}$$

$$= \left[ \frac{(94)(0.00375)}{(0.5)(0.177)} \right]^{\frac{1}{2}}$$

$$= 2.0 \text{ ft/sec}$$

$$\dot{\delta} = \frac{W \nu'}{2 \rho_p}$$

$$= \frac{(0.124)(2.0)}{2(249)}$$

$$= 0.499 \times 10^{-3} \text{ ft/sec}$$

$$= 6.0 \text{ mils/sec}$$

**UNCLASSIFIED**

Reference

T. K. Sherwood and R. L. Pigford, Absorption and Extraction, McGraw-Hill Book Co. Inc. , page 38-47.

**UNCLASSIFIED**

841/842

**UNCLASSIFIED**

AN EXPERIMENTAL STUDY OF THE DRAG COEFFICIENT  
OF BURNING ALUMINUM DROPLETS

by

R. L. Marshall,

G. L. Pellett

and

A. R. Saunders

NASA Langley Research Center  
Langley Station, Hampton, Va.

**UNCLASSIFIED**

# UNCLASSIFIED

## AN EXPERIMENTAL STUDY OF THE DRAG COEFFICIENT OF BURNING ALUMINUM DROPLETS

By Roy L. Marshall, Gerald L. Pellett, and Andrew R. Saunders

Langley Research Center  
National Aeronautics and Space Administration  
Hampton, Virginia

### INTRODUCTION

A knowledge of the dynamics of motion of burning particles and droplets is important in heterogeneous combustion in multi-phase flow systems. In this paper the dynamics of 200-500 micron aluminum droplets which burn as they fall through stagnant ambient air are examined.

C. T. Crowe, J. A. Nicholls and R. B. Morrison<sup>1</sup> summarized the earlier experimental results on the drag coefficients of burning particles. Since these data largely pertain to burning hydrocarbon droplet systems, which differ in many respects from the burning aluminum system, the extrapolation of results to the present study is highly questionable. In their experiments Crowe, et al examined burning gun powder particles accelerating in a gas stream, and found an increase in the drag coefficient as compared to the standard drag curve for spheres. Leont'ye<sup>2</sup> measured the drag coefficients of burning carbon spheres and found an increase in the drag. The drag of burning metal droplets appears to have been largely neglected although the experimental data on burning particles indicate a larger effective drag force in the presence of combustion.

### EXPERIMENTAL TECHNIQUE

Experiments to measure the influence of combustion on the

UNCLASSIFIED

## UNCLASSIFIED

drag of burning aluminum droplets have a unique set of requirements. First, a clean and rapid high temperature ignition must be achieved. Secondly, an accurate history of the droplet's relative velocity and acceleration must be determined. Thirdly, the burning rate must be measured, and most important the nature of burning must be characterized. Nelson<sup>4</sup> used a flash-heating technique to ignite high specific area foils to study the combustion of zirconium droplets in a gaseous media. Prentice<sup>5</sup> adapted the technique to study certain aspects of aluminum combustion. A similar technique of ignition was employed in the present study. Here small aluminum foils of predetermined mass were dropped along the axis of a helical xenon flashtube. When the foil reached the center of the helix, 24,000 joules stored in a 1140 microfarad capacitor bank were discharged through the flashtube. The resulting thermal radiation caused rapid melting and ignition of the foil. With the exclusion of the small period of time (0.1 sec) that the burning droplet was in the helix of the flashtube its displacement history was observed by high speed cameras over the entire trajectory. By intercepting the particle at some point in the trajectory, the change in mass may then be obtained by reweighing and comparing to the original foil mass. Since the flashtube is separated from the gaseous oxidizer, the chemical composition, temperature, pressure, and relative velocity (zero in this case) of the test gas can be controlled to permit an idealized examination of the drag coefficient.

The results reported in this paper are for falling droplets in the 200-500 micron range burning in air at atmospheric pressure. The relative humidity was approximately 50 percent and the temperature approximately 77° F.

### BEHAVIOR OF THE ALUMINUM DROPLET

The primary objective of the experiment was to obtain numerical values of the drag coefficient as a function of Reynolds number for different burning aluminum droplet sizes. It has been pointed out by

## UNCLASSIFIED

Prentice<sup>5</sup> that when aluminum burns in air it has a tendency to form oxide caps, to spin, and to fragment. Some of these phenomena as observed in the NASA-LRC studies are illustrated in the still plate streak photograph of the Figure 1. The most obvious event is that of fragmentation. Approximately three quarters along the trajectory of the burning droplet a primary puffing event was observed. These events introduce uncertainties, and if the values of the drag coefficient and corresponding Reynolds number are to be meaningful, the behavior of the particle, its flame zone and the sequence of events that these quantities undergo must be well characterized.

In many of the experiments in which still plate streak photographs were taken, events could be observed but not characterized. Some insight into this problem was obtained when a chopping disk was incorporated as a rapid shutter and a timing device. Figure 2 is typical of these pictures taken at a relatively high photographic exposure. In general, as the particle leaves the flashtube it burns with no noticeable irregularities. It continues to fall until it reaches the point of the primary puff where there is a sudden increase in brightness. The brightness rapidly decreases and then the particle will often start to spiral. The spiraling ceases and as the particle continues to fall it will suddenly fragment, usually producing one major particle.

Additional details of droplet appearance and flame structure of freefalling burning droplets were obtained by high speed Fastax motion pictures. Figure 3 is a sequence of frames of a burning aluminum droplet impinging upon a glass slide. These pictures were taken early in the combustion history and show the particle preceded by a highly luminous crescent shaped flame with no evidence of particle spin. The details of these Fastax photographs show the ratio of the crescent shaped flame diameter to droplet diameter to be approximately 2.7:1. The combustion of the droplet began to terminate when the flame first struck the slide; part of the surrounding oxide smoke particles were

UNCLASSIFIED



## UNCLASSIFIED

deposited on the slide and a portion upon the particle.

A photomicrograph of the quenched droplet of Figure 3 is shown in Figures 4 and 5. Figure 4 shows the oxide pattern deposited on the slide. It is important to note that the ratio of the diameter of the outer oxide smoke to the particle diameter is approximately 5:1 which is very much greater than 2.7:1 observed on the same particle prior to particle quench. This suggests that flame to particle diameter ratios inferred from slide interception must be carefully interpreted.

Figure 5 is a photomicrograph of the same particle in which the slide has been rotated  $90^\circ$  to show a side view. The purpose of this was to show how the larger particles were squashed on impact.

One of the difficulties in calculating the drag coefficient and Reynolds number is estimating the change in the droplet diameter that occurs when a particle is heated to its boiling point. Assuming that the particle is still a sphere on the glass slide, the ratio of the diameter immediately after the vapor diffusion flame was extinguished to the diameter when the particle was cool was calculated to be 1.16. This is in agreement with values obtained by a formula Prentice<sup>5</sup> used to calculate density changes. This correction was applied to values of Reynolds number and drag coefficients calculated later.

High speed, high magnification Fastax movies of the type shown in Figure 3 are certainly informative but they are limited by representing only a small portion of the complete particle history in each experiment. What was really needed for the drag coefficient study was a complete trajectory history of the burning droplet and its flame zone. Figure 6 is a single still plate film on which multiple exposures of a single burning aluminum droplet were photographed while it was falling. Certain portions of this picture have been enlarged to show detail of the droplet and flame structure.

## UNCLASSIFIED

In the initial portion of the trajectory the droplet was burning in a manner similar to that shown on the slide of the Fastax movie in Figure 3. As the particle continued to burn the intensity of the flame and the particle decreased somewhat with time. Suddenly the particle brightened, then the crescent flame rapidly expanded, contracted and disappeared. The luminosity of the particle then began to decrease before fragmentation.

### DRAG COEFFICIENT AND REYNOLDS NUMBER

Examination of the equation for the drag force which included the inertia, body force and a mass transfer term indicated that accurate measurements of the particle velocity, acceleration, instantaneous mass and rate of mass change were necessary to calculate drag coefficients. In these experiments displacement as a function of time of the burning droplet was recorded by a high speed camera. These data were then curve fitted and differentiated to yield the velocity and acceleration. In these experiments the particle injection apparatus imparted an initial velocity to the droplet. After leaving the flashtube small droplets which had not accelerated to their terminal velocity would do so very quickly, whence they would then start to decelerate. Accurate values of the mass of large droplets was not easily obtained by slide interception and at this writing the data is still in the process of reduction.

Figure 7 is a plot of the drag coefficient as a function of Reynolds number on which the standard drag curve for spheres in steady flow and values for burning gun powder<sup>1</sup> have been shown for reference. The burning aluminum droplet data are preliminary values for the 250 micron diameter droplets burning in air. The results indicate that the terminal velocity was less than that of a non-burning sphere of the same size and density and that there was a corresponding several-fold increase in the drag coefficient as shown.

UNCLASSIFIED

# UNCLASSIFIED

## SUMMARY

Examination of the results of these experiments indicate the following:

1. An aluminum droplet burning in ambient (50 percent relative humidity) air generally follows a set sequence of events: puff, often spiral and then fragment.
2. The motion of the droplet relative to the stagnant gas created a crescent-shaped flame zone that preceded the droplet.
3. A rapid expansion of the vapor-phase diffusion flame is associated with the primary puff after which the vapor-phase diffusion flame disappeared.
4. Measurements to calculate the drag coefficient and Reynolds number should be made above, i. e., before the primary puffing event.
5. Calculated values of the drag coefficient as a function of Reynolds number indicate a several-fold increase in the drag coefficient of a burning aluminum droplet resulting from combustion in air.

# UNCLASSIFIED

## REFERENCES

1. Crowe, C. T.; Nicholls, J. A.; and Morrison, R. B.: Drag Coefficient of Inert and Burning Particles Accelerating in Gas Streams. Ninth Symposium (International) on Combustion, Academic Press Inc., 1963, pp. 395-406.
2. Leont'yeva, Z. S.: Combustion of a Carbon Particle Moving in a Gas Flow. Bull, Acad, Sci. USSR, No. 12, Dec. 1951, pp. 1801-1811.
3. McLean, W. G.; and Nelson, E. W.: Engineering Mechanics, second ed., Schaum Pub. Co., c. 1962, p. 288.
4. Nelson, L. S.: The Combustion and Explosion of Zirconium Droplets Ignited by Flash Heating. SC-RR-65-569, Sandia Corp., Jan. 1966.
5. Metal Combustion Study Group: Aluminum Particle Combustion Progress Report - April 1, 1964 - June 30, 1965. Techn. Progr. Rept. 415 (NOTS TP 3916), U. S. Naval Ord. Test Station, Apr. 1966.

UNCLASSIFIED

UNCLASSIFIED

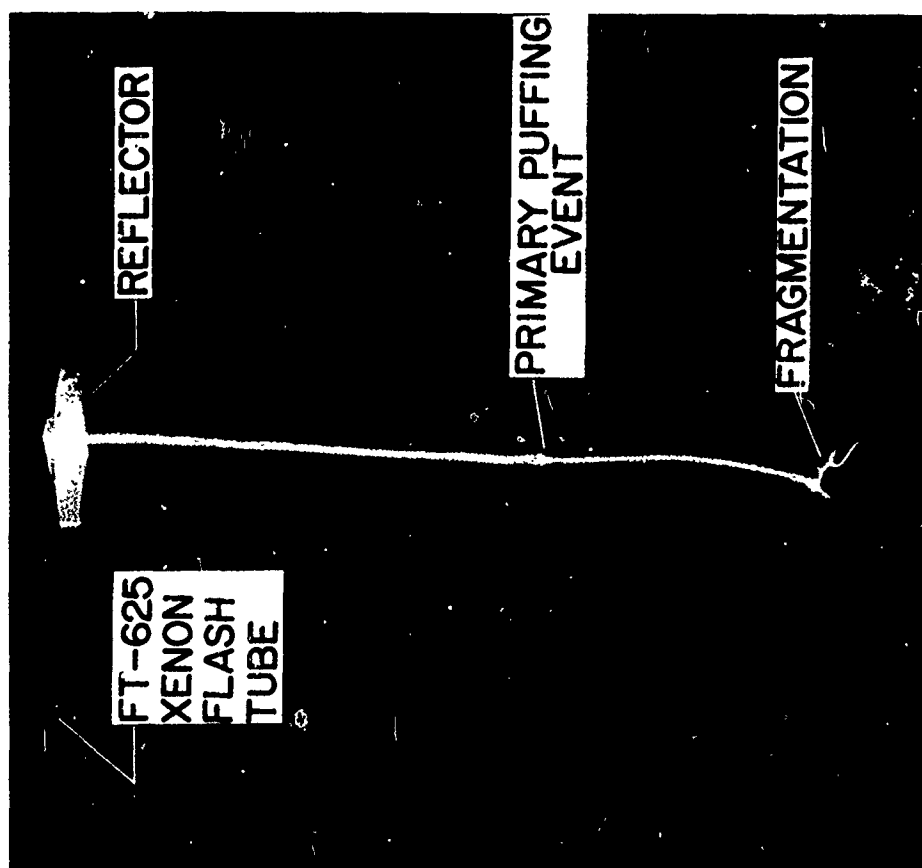


Figure 1. Still-plate photograph of a burning aluminum droplet.

UNCLASSIFIED

UNCLASSIFIED

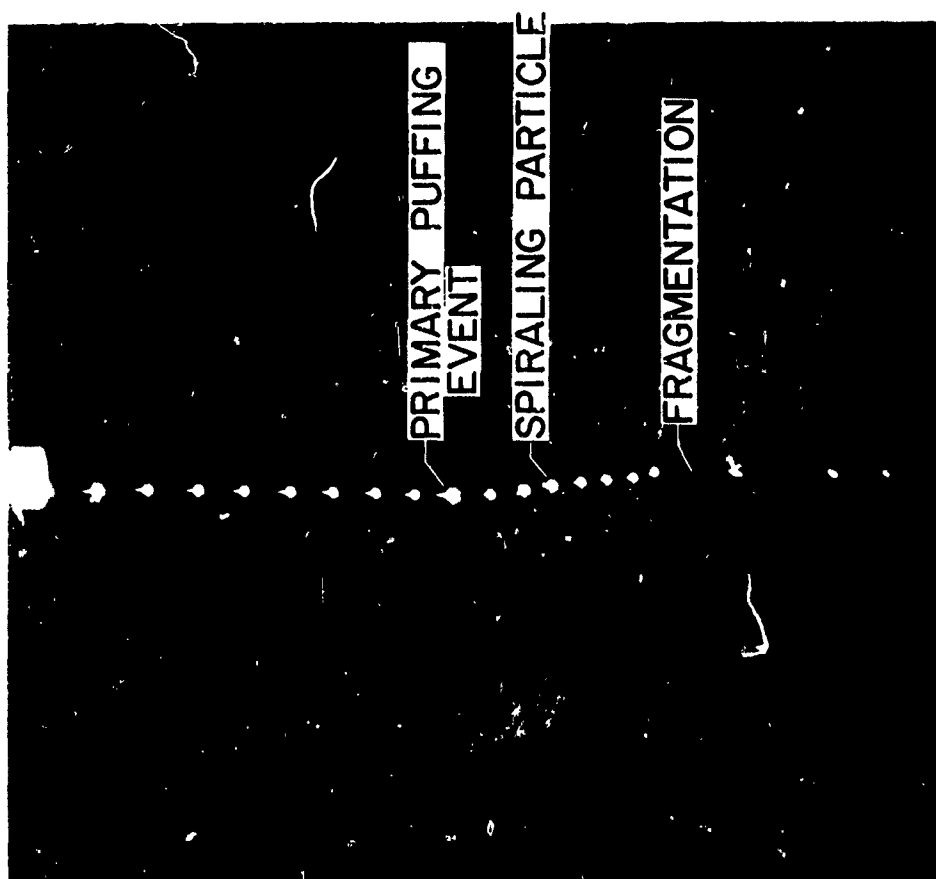


Figure 2. Chopped still-plate photograph of a 350 $\mu$  burning aluminum droplet.

UNCLASSIFIED

UNCLASSIFIED

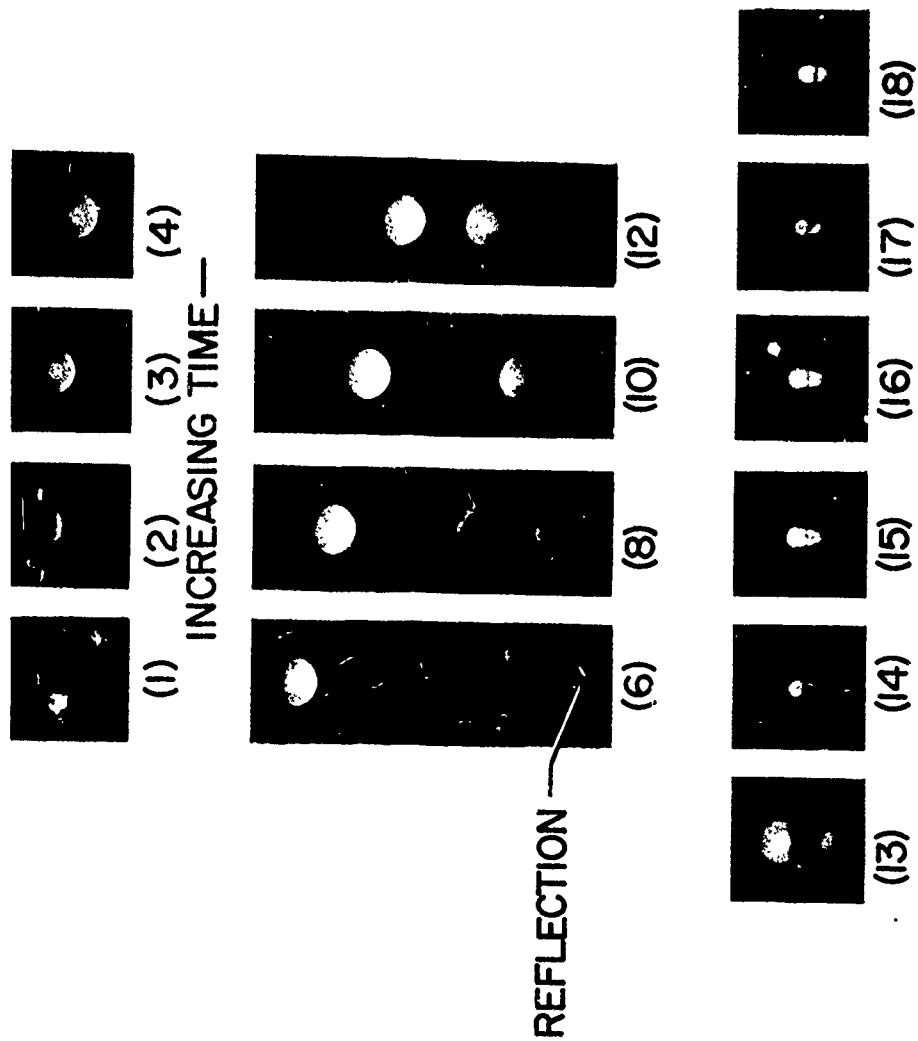


Figure 3. Burning aluminum droplet impinging on glass slide fastax framing rate 3600 fps, ( ) indicates frame number.

UNCLASSIFIED

UNCLASSIFIED

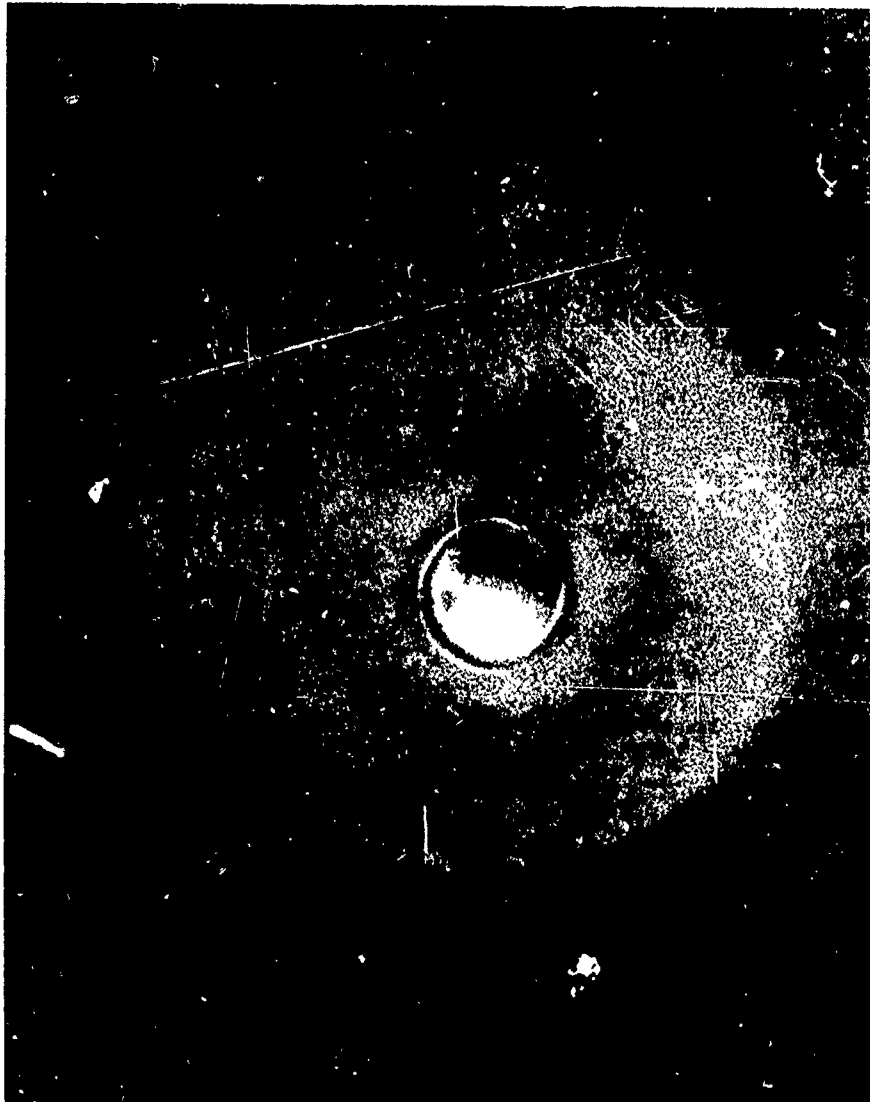


Figure 4. Quenched aluminum particle (top view).

UNCLASSIFIED



UNCLASSIFIED



Figure 5. Quenched aluminum particle (side view).

UNCLASSIFIED

UNCLASSIFIED

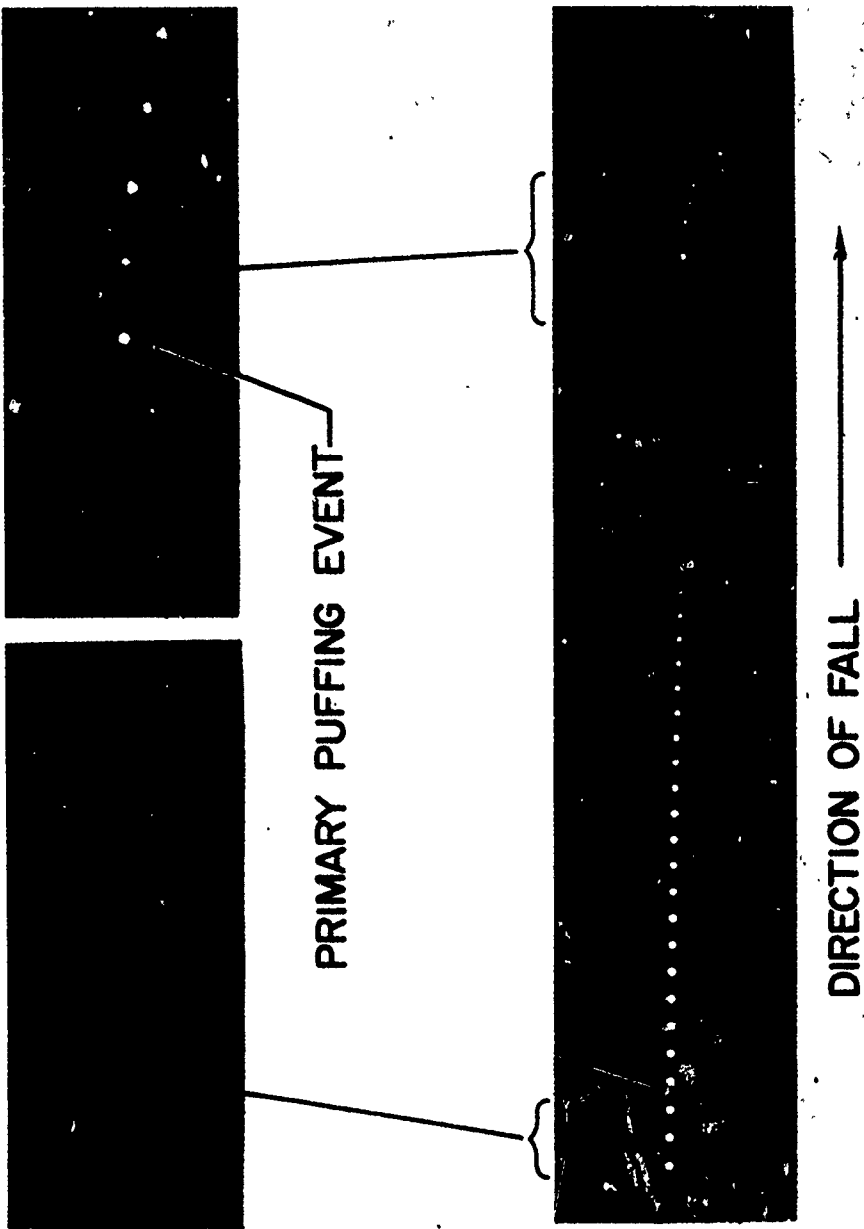


Figure 6. Time resolved history of a burning aluminum droplet and associated flame zone.

UNCLASSIFIED

UNCLASSIFIED

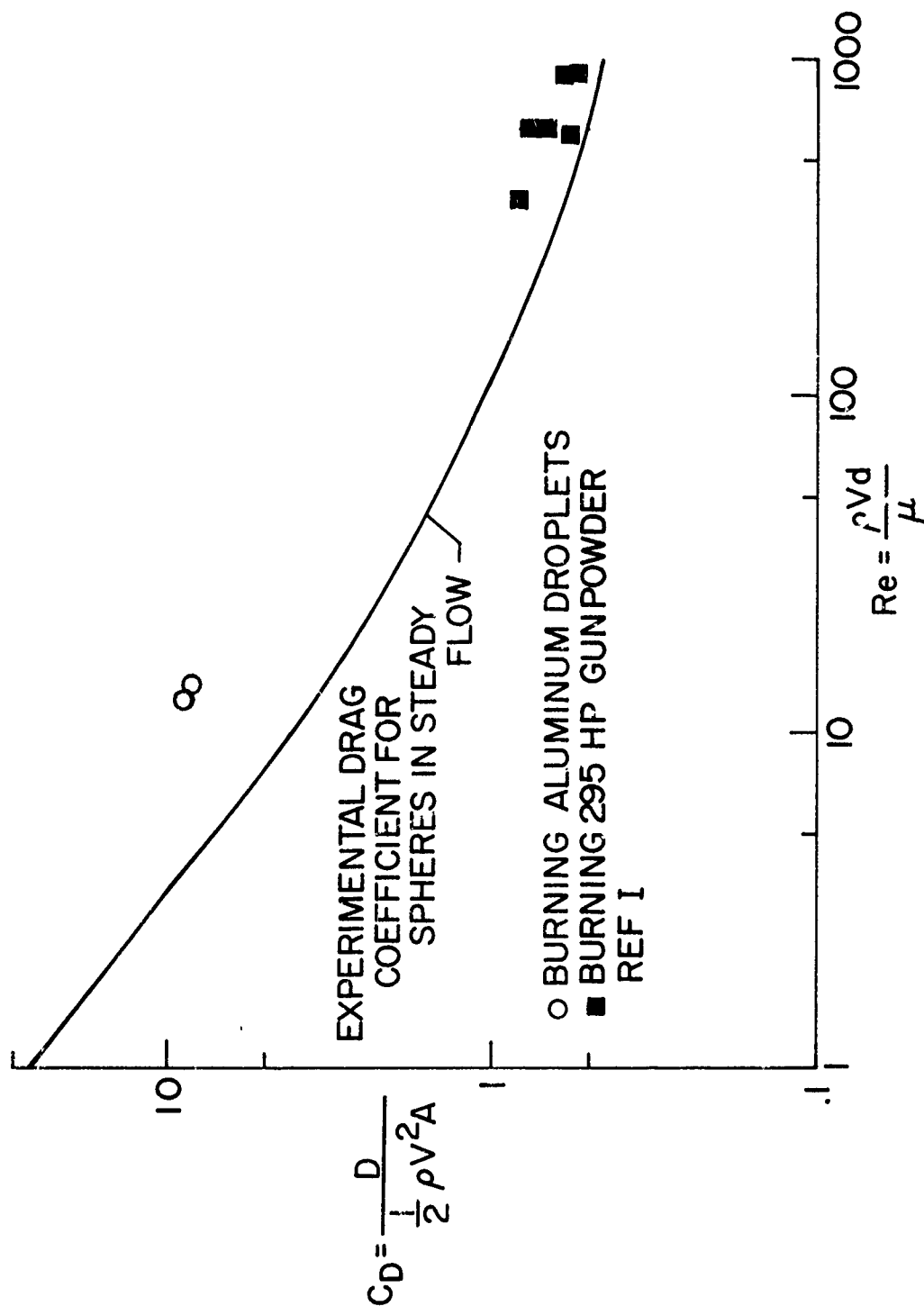


Figure 7. Drag coefficient versus Reynolds number for burning particles.

UNCLASSIFIED

Unclassified

Security Classification

DOCUMENT CONTROL DATA - R&D		
<small>(Security classification of title, body of abstract and indexing annotation must be entered when the overall report is classified)</small>		
1. ORIGINATING ACTIVITY (Corporate author) Air Force Rocket Propulsion Laboratory Edwards, California 93523		2a. REPORT SECURITY CLASSIFICATION CONFIDENTIAL
		2b. GROUP 4
3. REPORT TITLE (U) Proceedings of the Air Force Rocket Propulsion Laboratory Two-Phase Flow Conference		
4. DESCRIPTIVE NOTES (Type of report and inclusive dates) Final Report		
5. AUTHOR(S) (Last name, first name, initial)		
6. REPORT DATE August 1967	7a. TOTAL NO. OF PAGES 450	7b. NO. OF REFS
8a. CONTRACT OR GRANT NO.	9a. ORIGINATOR'S REPORT NUMBER(S) AFRPL-TR-67-223, Vol. II	
b. PROJECT NO. 305901		
c.	9b. OTHER REPORT NO(S) (Any other numbers that may be assigned this report)	
d.		
10. AVAILABILITY/LIMITATION NOTICES In addition to security requirements which must be met, this document is subject to special export controls and each transmittal to foreign governments or foreign nationals may be made only with prior approval of AFRPL (RPPR-STINFO), Edwards, California 93523		
11. SUPPLEMENTARY NOTES	12. SPONSORING MILITARY ACTIVITY AFRPL Edwards, California 93523	
13. ABSTRACT (U) Two-phase flow and related phenomena have received only limited treatment in other conferences. Furthermore, no concentrated effort has been put forth to clarify existing areas of contradiction, compare state-of-the-art data, or identify research efforts toward those areas where additional information is needed. Therefore, the purpose of this conference was to provide an opportunity for those directly concerned with two-phase flow and related phenomena to review current technology, and highlight points of controversy. The papers in this report include topics of: (1) Particle formation and growth mechanisms; (2) Performance losses in two-phase nozzle flows; (3) Particle size determination techniques; and (4) Two-phase plume phenomena (radiation, attenuation, impingement). The report also contains the questions, answers, and comments that were made during the conference.		

DD FORM 1473  
1 JAN 64

Unclassified

Security Classification

Unclassified

Security Classification

14 KEY WORDS	LINK A		LINK B		LINK C	
	ROLE	WT	ROLE	WT	ROLE	WT
Particle Formation Particle Growth Mechanisms Performance Losses Two-Phase Flow Phenomena Particle Size Determination Two-Phase Plume Phenomena						

#### INSTRUCTIONS

1. **ORIGINATING ACTIVITY:** Enter the name and address of the contractor, subcontractor, grantee, Department of Defense activity or other organization (*corporate author*) issuing the report.

2a. **REPORT SECURITY CLASSIFICATION:** Enter the overall security classification of the report. Indicate whether "Restricted Data" is included. Marking is to be in accordance with appropriate security regulations.

2b. **GROUP:** Automatic downgrading is specified in DoD Directive 5200.10 and Armed Forces Industrial Manual. Enter the group number. Also, when applicable, show that optional markings have been used for Group 3 and Group 4 as authorized.

3. **REPORT TITLE:** Enter the complete report title in all capital letters. Titles in all cases should be unclassified. If a meaningful title cannot be selected without classification, show title classification in all capitals in parenthesis immediately following the title.

4. **DESCRIPTIVE NOTES:** If appropriate, enter the type of report, e.g., interim, progress, summary, annual, or final. Give the inclusive dates when a specific reporting period is covered.

5. **AUTHOR(S):** Enter the name(s) of author(s) as shown on or in the report. Enter last name, first name, middle initial. If military, show rank and branch of service. The name of the principal author is an absolute minimum requirement.

6. **REPORT DATE:** Enter the date of the report as day, month, year, or month, year. If more than one date appears on the report, use date of publication.

7a. **TOTAL NUMBER OF PAGES:** The total page count should follow normal pagination procedures, i.e., enter the number of pages containing information.

7b. **NUMBER OF REFERENCES:** Enter the total number of references cited in the report.

8a. **CONTRACT OR GRANT NUMBER:** If appropriate, enter the applicable number of the contract or grant under which the report was written.

8b, 8c, & 8d. **PROJECT NUMBER:** Enter the appropriate military department identification, such as project number, subproject number, system numbers, task number, etc.

9a. **ORIGINATOR'S REPORT NUMBER(S):** Enter the official report number by which the document will be identified and controlled by the originating activity. This number must be unique to this report.

9b. **OTHER REPORT NUMBER(S):** If the report has been assigned any other report numbers (*either by the originator or by the sponsor*), also enter this number(s).

10. **AVAILABILITY/LIMITATION NOTICES:** Enter any limitations on further dissemination of the report, other than those

imposed by security classification, using standard statements such as:

- (1) "Qualified requesters may obtain copies of this report from DDC."
- (2) "Foreign announcement and dissemination of this report by DDC is not authorized."
- (3) "U. S. Government agencies may obtain copies of this report directly from DDC. Other qualified DDC users shall request through \_\_\_\_\_."
- (4) "U. S. military agencies may obtain copies of this report directly from DDC. Other qualified users shall request through \_\_\_\_\_."
- (5) "All distribution of this report is controlled. Qualified DDC users shall request through \_\_\_\_\_."

If the report has been furnished to the Office of Technical Services, Department of Commerce, for sale to the public, indicate this fact and enter the price, if known.

11. **SUPPLEMENTARY NOTES:** Use for additional explanatory notes.

12. **SPONSORING MILITARY ACTIVITY:** Enter the name of the departmental project office or laboratory sponsoring (paying for) the research and development. Include address.

13. **ABSTRACT:** Enter an abstract giving a brief and factual summary of the document indicative of the report, even though it may also appear elsewhere in the body of the technical report. If additional space is required, a continuation sheet shall be attached.

It is highly desirable that the abstract of classified reports be unclassified. Each paragraph of the abstract shall end with an indication of the military security classification of the information in the paragraph, represented as (TS), (S), (C), or (U).

There is no limitation on the length of the abstract. However, the suggested length is from 150 to 225 words.

14. **KEY WORDS:** Key words are technically meaningful terms or short phrases that characterize a report and may be used as index entries for cataloging the report. Key words must be selected so that no security classification is required. Identifiers, such as equipment model designation, trade name, military project code name, geographic location, may be used as key words but will be followed by an indication of technical context. The assignment of links, rules, and weights is optional.

Unclassified

Security Classification

END

DATE

FILMED

4-68